Phenanthroline-based Copper Complexes for Water Splitting Applications

–

Photo-physical and spectroscopic investigations

PADERBORN UNIVERSITY

FACULTY OF SCIENCE – DEPARTMENT OF CHEMISTRY

Dissertation

for awarding the academic title

Dr. rer. nat.

by

Kai Stührenberg, M.Sc.

from Amelinghausen, Germany

Paderborn, 2017.

Board of Examiners

Prof. Dr. Thomas Kühne (Chairman)

Prof. Dr. Matthias Bauer

PD Dr. Hans Egold

Prof. Dr. Hans Joachim Warnecke

Acknowledgments

First of all I like to thank Prof. Dr. Matthias Bauer for assigning me to a project of global relevance and always giving me honest and friendly advice. I am grateful and proud of the opportunity you gave me and the work we have done. In addition, I would like to thank you for your trust in me granting three student research assistants.

A special thanks goes to A. Hillebrand and P. Dierks. Working with you has been a privilege and you contributed a lot to this work and my personal development. Your support, critical questions and most importantly humor brought me back down to earth, when I needed it. N. Dickmann and R. Rodriguez, thank you for support in the last half year of my thesis. You took some of the preparative workload of my shoulders, when I had to concentrate on writing. M. Huber thank you for intense und personal conversations. Thank you T. Hirschhausen for sorting some of my crystals. ;) I wish you all the best for the future. You will go your way, I have no doubt of that. We will stay in touch.

“Unterarbeitskreis” Stühnenberg in 2017.

(From left to right: Nicole Dickmann, Renè Rodriguez, Philipp Dierks and Kai Stühnenberg)

Thank you working group Bauer for the kind and friendly climate, which is quite important, since we have spent more time together during our Ph.D. time than I spend with Anne or at home or someone/somewhere else. L. Burkhardt, R. Schoch, P. Müller and P. Zimmer, I would like to thank you for all the fruitful serious and not serious discussions, where you passed on your knowledge to me.

Working group Bauer in 2017.

Of course, the central analytic department under the leadership of Dr. Flörke had a large impact on this work. Mr. Dr. Flörke, even when I came with a bucket full of different crystals, you were always motivated to give the first crystal as much attention as the last crystal. Thank you for your commitment. The flexibility and spontaneity in sample acquisition was in particular for sensitive NMR samples important. Thank you Mrs. Stolte and Mr. Dr. Egold for enabling that and useful discussions. Mrs. Busse and Mrs. Gloger are thanked for conduction the elemental analysis. I would like to thank Mr. Dr. Weber, Mrs. Knaup and Mrs. Zukowski for the mass spectra.

Mrs. Dr. D. Hackenberger and Prof. Dr. L.J. Goossen are thanked for trying to perform decarboxylative cross coupling reactions with my ligand system.

Mr. Dr. C. Wilhelm and Prof. Dr.-Ing. S. Ernst are thanked for DRUVS spectra acquired under difficult conditions.

Mrs. Dr. S. Masing, thank you for a life-long friendship starting in primary school and independent of long physical distances between us. Every up and down has strengthen our relationship.

Mr. D. Bade, our calls are usually a mixture of insanity, inspiration and motivation. Thank you for being my personal halligan tool.

Thank you for being my friends in in difficult hours: B. Niezborala, J. Cubic, J. Wolff, B. Klüppel, R. Schoch, A. Hillebrand. I will never forget that.

The “Amelingäuser” Crew, thank you for always making me feel as if I have never been away: S. Brakelmann, M. Busemann, R. Buchholz, M. Köhler, L. Kröger, D. Kröger and F. Meyer.

A very special thanks goes to my second family, Karin, Ingo, Renè and Andrè, who were, are and will be there supporting me, although you sometimes do not realize your impact.

Anne you bring me down to earth, when no one else can and give me all of your love. You have been my love since these old days in the Minzeweg and I will love you to the end of my time.

Finally, I like to thank my parents for supporting me all the way. You would say, that I owe you nothing, but I owe you everything.

I thank everyone who made an impact on shaping me on this long journey in any kind, because you made me who I am today.

“Friendship to is not the daily contact, it is the assurance that you can rely on someone regardless of what and when.”

This dissertation was written with a maximum coffee turn over frequency of 6 d^{-1} and a maximum program crash number of 7 per day at an average of 1.2 d^{-1}.

Publications

1. Busser, G. Wilma; Mei, Bastian; Weide, Philipp; Vesborg, Peter C. K.; Stührenberg, Kai; Bauer, Matthias; Huang, Xing; Willinger, Marc-Georg; Chorkendorff, Ib; Schlögl, Robert; Muhler, Martin: "Cocatalyst Designing: A Regenerable Molybdenum-Containing Ternary Cocatalyst System for Efficient Photocatalytic Water Splitting", ACS Catal. **2015**, 5, 5530.

2. Liebhäuser, Patricia; Keisers, Kristina; Hoffmann, Alexander; Schnappinger, Thomas; Sommer, Isabella; Thoma, Anne; Wilfer, Claudia; Schoch, Roland; Stührenberg, Kai; Bauer, Matthias; Dürr, Maximilian; Ivanović-Burmazović, Ivana; Herres-Pawlis, Sonja: "Record Broken: A Copper Peroxide Complex with Enhanced Stability and Faster Hydroxylation Catalysis", Chemistry **2017**, 23, 12171.

3. Stührenberg, Kai; Müller, Patrick; Burkhardt, Lukas; Dierks, Philipp; Flörke, Ulrich; Bauer, Matthias: "Bis(2,9-dimethyl-1,10-phenanthroline) copper(I) complexes revised: A HERFD and V2C study of the model compound and the impact of halogen substituents.", manuscript in preparation.

4. Stührenberg, Kai; Burkhardt, Lukas; Neuba, Adam; Bauer, Matthias: "UV/VIS and X-ray absorption spectroelectrochemical behavior of 2,9-bis(halomethyl)-1,10-phenanthroline) copper(I) complexes", manuscript in preparation.

5. Stührenberg, Kai; Wilhelm, Christian; Neufeld, Sergej; Schmidt, Wolf Gero; Bauer, Matthias: "Spectroscopic analysis of different colors of the same complex – impact of higher structures", manuscript in preparation.

Attended Beamtimes

Institution	Beamline	Date
Angstrømquelle Karlsruhe ANKA Karlsruhe, Germany	XAS	03.06.2014 – 06.06.2014
European Synchrotron Radiation Facility ESRF Grenoble, France	BM25a ID26 BM25a	04.07.2014 – 08.07.2014 16.11.2016 – 22.11.2016 20.07.2017 – 24.07.2017
Deutsches Elektronen Synchrotron DESY Hamburg, Germany	Petra III P65 Petra III P65 Petra III P65	25.07.2016 – 29.07.2016 15.09.2016 – 20.09.2016 04.06.2017 – 07.06.2017

Financial grants and cooperations involved in this work

Institution	Project	Principle Investigator
University Paderborn, Commission for Research and Junior Academics	Kupfer-basierte Photosensibilatoren zur photokatalytischen Wasserspaltung	Kai Stühренberg, University Paderborn
University Paderborn, Commission for Research and Junior Academics	Kupfer-basierte Wasseroxidationskatalysatoren als Beitrag zur katalytischen Wasserspaltung	Kai Stühренberg, University Paderborn
German Research Foundation	Research Unit 1405 Dynamics of Electron Transfer Processes within Transition Metal Site in Biological and Bioinorganic systems	Prof. Dr. Gerald Henkel, University Paderborn
Swedish Research Council	Time-resolved *in situ* methods for design of catalytic sites within sustainable chemistry (2013-27768-99267-37)	Prof. Dr. Per-Anders Carlsson, Chalmers University of Technology

Abbreviations

(neg)	negative ion mode (ESI mass spectroscopy)
(pos)	positive ion mode (ESI mass spectroscopy)
abs.	absolute
Amp.	amplitude
AO	atom orbital
ATR	attenuated total reflection
bpy	bipyridine
br	broad peak (IR spectroscopy)
Bz	benzyl group
calc.	calculated data
CAN	diammonium cerium(IV) nitrate
$CHCl_3$	chloroform
cm	centimeter
COSY	correlation spectroscopy (NMR spectroscopy)
cps	counts per second
d	doublet (NMR spectroscopy)
DAPy	diazapyridinophane
DCM	dichloromethane
dd	doublet of doublets (NMR spectroscopy)
DFT	density functional theory
DMP	2,9-dimethyl-1,10-phenanthroline
DMSO	dimethyl sulfoxide
DRUVS	diffuse reflectance UV/VIS spectroscopy
ED	electron donor
EI	electron impact ionization
eq.	equivalents
ESI	electrospay ionization
EtAc	ethyl acetate
EtOH	ethanol
eV	electronvolt
EXAFS	extended x-ray absorption fine structure
exciplex	excited state complex

exp.	experimental data
g	gram
GC	gas chromatography
GS	ground state
h	hours
HMBC	heteronuclear multiple bond correlation (NMR spectroscopy)
HMQC	heteronuclear multiple quantum coherence (NMR spectroscopy)
HOMO	highest occupied molecular orbital
Hz	Hertz [s^{-1}]
I2M	interaction of two M-O units
ISC	intersystem crossing
K	Kelvin
KOH	potassium hydroxide
KO-*t*-Bu	potassium tert-butoxide
L	ligand (mass spectrometry)
LDA	lithium diisopropylamide
LiHDMS	lithium bis(trimethylsilyl)amide
LMCT	ligand to metal charge transfer
LUMO	lowest unoccupied molecular orbital
M	mol/l or molecule isotope peak (mass spectrometry)
M	target molecule (mass spectrometry)
m	middle intensity (IR spectroscopy)
MeCN	acetonitrile
MeOH	methanol
mg	milligram
min	minutes
MLCT	metal to ligand charge transfer
MS	mass spectrometry
MV	methyl viologen dichloride
mV	millivolt
N	equivalent concentration, normality
$NaCO_3$	sodium carbonate
n-BuLi	*n*-Buthyllithium
neg	negative ion mode (mass spectrometry)

nm	nanometer
nm	nanometer
PCl_3	phosphorus trichloride
PHEMDs	photo-hydrogen-evolving molecular devices
phen	1,10-phenanthroline
pos	positive ion mode (mass spectrometry)
ppm	chemical shift (NMR spectroscopy)
PS	photosensitizer
quin	quintet (NMR spectroscopy)
r.t.	room temperature
rpm	rounds per minute
s	singlet (NMR spectroscopy)
s	strong intensity (IR spectroscopy)
SCE	saturated calomel electrode
SHE	standard hydrogen electrode
t	triplet (NMR spectroscopy)
$TBA[PF]_6$	tetrabutylammonium hexafluorophosphate
TCSPC	time correlated single photon counting
TEA	triethylamine
Tf	triflat group
TfOH	trifluoromethanesulfonic acid
TGA	thermogravimetric analysis
THF	tetrahydrofuran
TLC	thin layer chromatography
TLC	thin-layer chromatography
TOF	turnover frequency [h^{-1}]
TON	turnover number [-]
TRANES	time-resolved area normalized emission spectroscopy
TRES	time-resolved emission spectroscopy
TR-XRF	total reflection X-ray fluorescence spectroscopy
Ts	tosyl group
UV	ultra violet
V	Volt
VIS	visible

vs	very strong intensity (IR spectroscopy)
w	weak intensity (IR spectroscopy)
W	Watt
WNA	water nucleophilic attack
WRC	water reduction catalyst
XANES	x-ray absorption near edge structure
δ	chemical shift (NMR spectroscopy) or deformation vibration (IR spectroscopy)
v	valence vibration (IR spectroscopy)

Table of Contents

1 **Abstract**

Abstract

The future environmental issues are inseparably connected with today's energy source mix, which is mainly based on fossil fuels, and are already today commonly known as climate change and greenhouse effect. In order to retain the planet earth from severe climate changes, it is important to change the basis of our energy system towards renewable and sustainable sources. The utilization of nearly unlimited sources, like solar energy, is in this context a reasonable choice as point of origin.

Since today's society is more mobile than ever, a likewise mobile energy carrier is needed, which must be able to work independent from weather conditions. Here, solar energy can be applied to split water into the storable gases hydrogen and oxygen. Photocatalytic processes can be applied to facilitate this water splitting reaction, which can be divided into two half reactions: the generation of hydrogen by reductive photocatalytic water splitting and evolution of oxygen by water oxidation. The established available catalysts are mainly based on noble metals because of their assumed superior efficiency. This questions the long-term economic and ecologic competitiveness of these systems, since noble metals are expensive, potentially not environmental-friendly and exhausted under dubious conditions.

This dissertation pursues the goal to further establish copper as central metal for water splitting applications by thorough spectroscopic analysis in order to conclude structure-property relationships. On the one hand copper(I) complexes are implemented to function as photosensitizers in water reduction catalysis, while copper(II) species provide the opportunity of establishing earth abundant water oxidation catalysts.

Photoactive copper(I) complexes of 2,9-bis(halomethyl)-1,10-phenanthroline were synthesized and characterized by a variety of spectroscopic methods. Chemical standard analytic, like single crystal X-ray diffraction, NMR spectroscopy and mass spectrometry, provided structural confirmation and insights into coordination geometry and electronic properties. More elaborate X-ray absorption spectroscopy was used to verify and deepen this knowledge. During the cycle as photosensitizer, copper(I) is photo-oxidized to copper(II). The related structural and electronic changes during this photooxidation were investigated in detail using an combination of electrochemistry with UV/VIS absorption spectroscopy. The analysis of the spectroscopic data was also

supported by computational chemistry to identify and assign transitions in the experimental data.

In the case of water oxidation catalysis, precursors of copper(II) water oxidation catalysts were synthesized by conversion of a copper(II) salt with commercially available and tailored non-redox innocent ligands. Afterwards, this complexes were identified by a combination of single crystal X-ray diffraction and IR spectroscopy. Although the synthesis was assumed to be straightforward, a variety of interesting species – varying in molecular structure as well as higher structures – were obtained in dependency on reaction parameters.

Kurzfassung

Die zukünftigen Umweltprobleme sind untrennbar mit der heutigen Zusammensetzung der Energiequellen verbunden, welche hauptsächlich auf fossilen Brennstoffen beruhen, und sind bereits heute gemeinhin bekannt als Klimawandel und Treibhauseffekt. Um schwere klimatische Veränderungen des Planeten Erde zu verhindern ist es wichtig die Basis unseres Energiesystems hin zu erneuerbaren und nachhaltigen Quellen zu ändern. Der Einsatz einer fast unerschöpflichen Quelle, wie Sonnenenergie, ist in diesem Zusammenhang als Ausgangspunkt eine sinnvolle Wahl.

Da unsere heutige Gesellschaft mobiler ist als je zuvor, wird auch ein in gleicherweise mobiler Energieträger benötigt, der in der Lage ist unabhängig von Wetterbedingungen zu arbeiten. Hier kann Sonnenenergie genutzt werden, um Wasser in die speicherbaren Gase Wasserstoff und Sauerstoff zu spalten. Photokatalytische Prozesse können eingesetzt werden, um die Wasserspaltungsreaktion zu ermöglichen, welche in die Erzeugung von Wasserstoff durch reduktive Wasserspaltung und die Erzeugung von Sauerstoff durch oxidative Wasserspaltung eingeteilt werden kann. Die etablierten verfügbaren Katalysatoren basieren hauptsächlich auf Edelmetallen, weil diese eine vermeintlich höhere Effizienz besitzen. Dies stellt die langfristige ökonomische und ökologische Konkurrenzfähigkeit dieser Systeme in Frage, da Edelmetalle unter bedenklichen Bedingungen abgebaut werden, teuer und potenziell nicht umweltfreundlich sind.

Diese Dissertation verfolgt das Ziel durch gründliche spektroskopische Analyse Struktur-Eigenschaftsbeziehungen ableiten zu können, um Kupfer als Zentralmetall für Wasserspaltungsanwendungen weiter zu etablieren. Kupfer(I)-Komplexe sind auf der einen Seite implementiert, um als Photosensibilisator zu fungieren, während Kupfer(II)-Spezies die Möglichkeit eröffnen unedle Metalle als Wasseroxidationskatalysatoren zu etablieren.

Photoaktive Kupfer(I)-Komplexe von 2,9-bis(halogenmethyl)-1,10-Phenanthrolin wurde synthetisiert und durch eine Vielfalt von spektroskopischen Methoden charakterisiert. Chemische Standardanalytik, wie Einkristall-Röntgendiffraktometrie, NMR-Spektroskopie und Massenspektrometrie lieferten die strukturelle Bestätigung und Erkenntnisse über Koordinationsgeometrie und elektronische Eigenschaften. Die aufwendigere Röntgenabsorptionsspektroskopie wurde benutzt, um dieses Wissen zu

bestätigen und zu vertiefen. Während des Zyklus als Photosensibilisator wird Kupfer(I) zu Kupfer(II) photo-oxidiert. Die damit zusammenhängenden strukturellen und elektronischen Veränderungen während dieser Photooxidation wurden durch eine Kombination aus Elektrochemie und UV/VIS-Absorptionsspektroskopie im Detail untersucht. Die Auswertung der spektroskopischen Daten wurden zusätzlich durch quantenmechanische Rechnungen gestützt, um Übergänge in den experimentellen Daten zu identifizieren und zu zuordnen.

Im Fall der Wasseroxidationskatalyse wurden die Präkursoren der Kupfer(II)-Wasseroxidationskatalysatoren durch Umsetzung von Kupfer(II)-Salzen mit kommerziell erhältlichen und maßgeschneiderten, redox-aktiven Liganden synthetisiert. Diese Komplexe wurden nachfolgend durch eine Kombination aus Einkristall-Röntgendiffraktometrie und IR-Spektroskopie identifiziert. Obwohl die Synthese vermeintlich unkompliziert zu sein schien, wurde eine Vielzahl interessanten Spezies – sich in Molekülstruktur aber auch in höheren Strukturen unterscheidend – in Abhängigkeit der Reaktionsparameter erhalten.

2 **Introduction**

2.1 Worldwide Energy and Climate Situation

Mankind is heading towards an energy crisis in the face of increasing population and economic growth, while fossil resources are simultaneously declining. In fact, fossil fuels are being consumed by mankind 500000 times faster than they are reproduced by nature.[1]

Although the full usage of all fossil-based fuels – like oil, natural gas and coal – available on earth would at least satisfy the energy consumption for several centuries[2] unsolved issues rise. In the following decade, the topic of energy availability will addressed increasingly, since security issues of environmental and economical nature[3] will rise and may potentially destabilize whole communities because of restricted access and uneven distribution of energy resources. In addition, the emission of CO_2 is endangering today and will further alter the global climate in the future on a very shorter timescale. These anthropogenic emissions are equilibrated between atmospheric and near-surface layers within 10 to 30 years.[4] This is why approximately 50 % of emitted CO_2 stay available at the atmosphere, while the remainder is absorbed by biosphere and by the ocean altering the pH value of the latter. Since there are no destruction mechanisms for CO_2 it must be removed by convection. This is happening by convection of near-surface and deep ocean water on a timescale between 400 and several thousand years.[4,5] Since the CO_2 concentrations were determined between 210 ppm and 300 ppm for the last 650000 years, the recent increase in excess of 380 ppm are alarming.[6]

Hence, the energy supply has to be sustainable to conquer this challenge. Future energy supply and climate development are inseparably connected with development of cost-efficient, sustainable and renewable energy.[7] Global energy demand, which is covered to an amount of 80 % by fossil fuels, considering industrial progress and a population growth of about 2 %.[2,3] Moreover, the expected world total primary energy supply in 2040 has to be increased to 1.25×10^{11} J based on recent policies under consideration according to the *International Energy Agency*.[8]

One way out of this dilemma is the application of solar energy within a reasonable sustainable energy mix. According to the advocates of the hydrogen evolving community, hydrogen produced from water will replace fossil fuels rising to the main energy provider in the second half of the 21st century.[9] Today, the majority of

hydrogen is produced from fossil fuels by industrial steam reforming making it essential to implement sustainable processes.[10] Based on today's technical potential, the annual worldwide energy consumption could be saturated three to a hundred times by direct solar energy.[11] The incoming sunlight on earth in 60 to 90 minutes with an energy of approximately 10^{22} J could cover the demand of whole mankind for one year.[12,13] The save long-term storage of this chemical fuel is another issue, which has to be solved. Since mobility is the engine of social wealth, the solar energy has to be transferred into mobile energy carrier. The fuel cell has a high potential here, due to the fact that only hydrogen has to be carried along for operation, which can react with atmospheric oxygen to water. In this case the main concern is the low cost hydrogen production through utilization of sunlight to supply fuel cells. But the long-term storage of hydrogen is at least up to today associated diffusion processes and hydrogen embrittlement.[14] That is the reason why conversion mechanisms towards smaller, easier storable molecules or basic chemicals are investigated.[15]

2.2 Water Splitting

The splitting of water came to attention to the scientific public in the early 1980-ies, where the Texas A&M University´s public information office over interpreted a statement of chemistry professor J. O´M. Bockris about an water splitting device. The office stated, that a breakthrough discovery in the field of photolysis of water to hydrogen and oxygen by sun light with 12 % efficiency was achieved. Furthermore, it was implied that the cell could be easily developed for commercial uses. Other Scientists in the field were upset, because the statements were given before a publication in a peer-reviewed journal and doubt that this cell would function at all. In addition, concerns were expressed that the claim would raise false hope and expectations in the general public. Bockris cleared this issue in a later interview agreeing with other leading scientists that the commercialization of this kind of fuel generation is only in its pioneering phase.[16]

Today, the water splitting issue is mainly still on a level of fundamental research, although several significant milestones were reached within this time. Unfortunately, a general commercial implementation of water splitting apparatus to gain hydrogen as fuel took not place. The main reasons are the high demands for those systems. The thermolysis of water is only possible over 2200 °C[12] and for the spontaneous dissociation in its elements 237 kJ/mol[17] energy is required. Based on these facts, efficient catalysis system are needed to reduce the amount of energy to split water. This is sometimes archived by harsh reaction conditions, which then potentially destabilized and decompose the catalytic systems resulting in short lifetimes. These extreme conditions – vide infra – lead also to less attractive water splitting apparatus, since the chemicals introduce an enormous hazard potential. Due to this obstacles, the complex overall water splitting process is typically divided into it half reactions water reduction – hydrogen evolution – and water oxidation – oxygen evolution –, respectively.

Despite all issues, research is still searching for efficient and stable systems and the effort is steadily increased as can be seen in figure 2-1 based on the nearly exponential increasing publications in the area. This takes account to the increasing importance a general perception for renewable energy sources. The number of publications in the field of water reduction is dominating followed by contributions for water oxidation. This

already indicates that most of the researches divide the complex water splitting issue into two smaller parts in order to gain deeper insight into the systems. General terms like water splitting and artificial photosynthesis lead to significantly less total publications, although a similar exponential-like development is observable. The data was retrieved by searching the term denoted in figure 2-1 in *Web of Science*.[18]

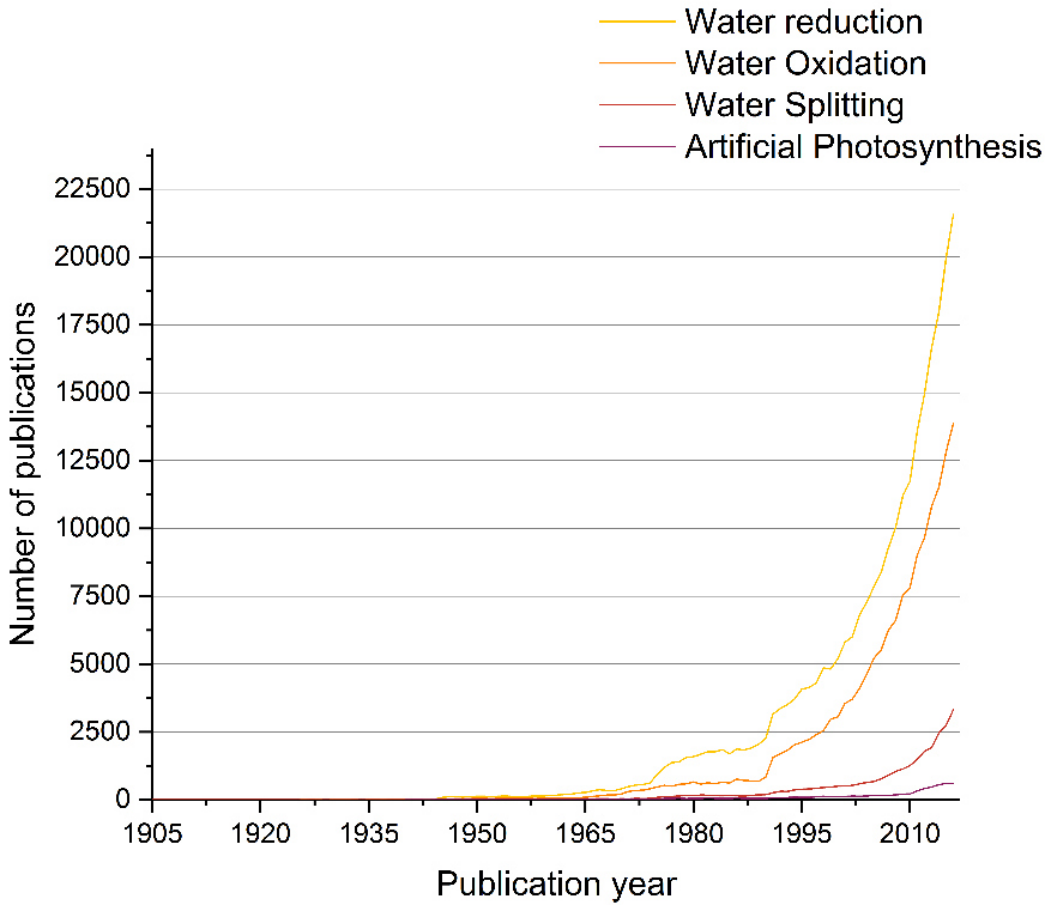

Figure 2-1: Development of publications in the area of water splitting.[18]

In the following passages an overview of water splitting systems will be given focusing on the relevant topics of this work. In addition, the historic context will be described to classify this work into the existing and continuing research in this area.

2.2.1 Overall water splitting

The central aim is the development of an overall water splitting system, which generates hydrogen and oxygen simultaneously as a light generated solar fuel. The formal overall water redox reaction is shown in equation (2-1). In this reaction, where the oxygen atom is oxidized on the one hand and the hydrogen atoms are reduced on the other, only light is needed to drive the process. Thus there is no need to apply sacrificial substances as later discussed.

$$H_2O \xrightarrow{h\cdot\nu} H_2 + \frac{1}{2}O_2 \qquad \textbf{(2-1)}$$

Unfortunately, the overall water splitting systems have still obstacles to overcome. The full water splitting process is a multielectron reaction. In addition to that, the fact of a different amount of redox equivalents is impeding the splitting.[19,20] This leads to a discrepancy in the electron balance. Therefore, the system has to accumulate four electrons to facilitate the oxidative part of the reaction resulting in Coulomb repulsion effects and high charge densities. In addition, both half-cell reactions – reduction and oxidation – exhibit large overpotentials on typical metal-based electrodes making the use of tailored and finely tuned catalytic systems necessary.

In fact, the majority of these systems, which are able to split water fully according to the aforementioned scheme, are heterogeneous. Within this field large number of non-noble electrochemical-based applications can be found.[21] Most of recent publications focus on photo-induced catalysis[22], which can be further divided into noble metal-based[23][24] and catalysts consisting of earth abundant metals[25][26], the latter is already dominating today´s research. In addition, biomimetic approaches[27], suspension-based systems[28] and even metal free catalysts[29] are under intense investigation.

Although the final research step must be a connected full water splitting system, in research most of the homogenous systems are considered by dividing the overall water splitting into a reductive and oxidative part using sacrificial species to facilitate the chemical reaction. Additionally, the presence of both a two-electron and a four-electron process complicates the comprehension and optimization by means of suitable analytics. The division into a reductive and an oxidative part is described by in equations (2-2) and (2-3), respectively. In the case of the water reduction, hydrogen is

gained through a two-electron reduction of two water molecules. While in the oxidation of water, water undergoes a four-electron oxidation. To conclude, two electrons are needed to evolve one hydrogen molecule, whereas four electrons are generated when one oxygen molecule is formed.

$$2\,H_2O + 2\,e^- \xrightarrow{h\cdot\nu} H_2 + 2\,OH^- \qquad \textbf{(2-2)}$$

$$2\,H_2O \xrightarrow{h\cdot\nu} O_2 + 4\,H^+ + 4\,e^- \qquad \textbf{(2-3)}$$

After optimizing and understanding the isolated reductive and oxidative processes both have to be recombined in a functioning system, which might be a suspension or mixture or an electrochemical cell set-up. In a distant future, this final construction may provide us with hydrogen just by – exaggerated speaking – filling in water and letting the solar energy work. As well as in today's recent research, in the following two chapters both essential half reactions will be discussed.

2.2.2 Reductive water splitting

As early as 1912, the Italian photochemist Giacomo Ciamician predicted that solar energy could be used to solve future energy crisis. Intriguingly, he formulated in a *Science* publication, that smoke-free industrial colonies will be build, glass buildings will be designed for photochemical processes and the "guarded secret of the plants […] will have been mastered by human industry".[30]

This vision appears even today still very futuristic. One step to the vision of Ciamician was realized in the 1970s, where the first photocatalytic water splitting systems were established. These consisted of heterogeneous, semiconducting metal species[31] – like TiO_2 – as shown in the case of a photoelectrochemical set-up by *Honda* and *Fujishima*.[32,33] A short period of time later, in 1979, homogenous splitting systems were firstly developed.[34,35] The first homogeneous system for reductive water splitting was published by *Sutin* and *Creutz*[35] under application of $[Ru(II)(bpy)_3]^{+2}$ as photosensitizer (PS), which is nowadays a standard model for noble metal based PSs, and a macrocyclic Co(II) water reduction catalyst (WRC). A remarkably detailed study was performed including optical spectroscopy, quenching and back reaction analysis as well as different reaction conditions.

This was the starting point for a tremendous research activity, as can be seen in figure 2-1, and the establishment of a new field of research, which was divided in different areas, since this is an interdisciplinary issue. Although many years of research were spent in this area, the first reproducible system for full water splitting under visible light was reported in 2001 by *Arakawa* et al..[36] A mixture of Pt-WO_3 and Pt-$SrTiO_3$ (Cr-Ta-doped) photocatalysts and a IO_3^-/I^- redox shuttle were used to split water stoichiometrically by means of visible light only (>420 nm and even >500 nm). The band gaps of the photocatalysts were tuned to give an efficient system with the iodide-based shuttle. Even though the estimated quantum efficiency was as low as 0.1 % (at 420.7 nm), the long-term stability enabled a high amount of gas evolution.

In general, photocatalytic water reduction systems consist of a PS, a WRC and an sacrificial electron donor (ED), which is called a three component system when all components are not joined, as depicted in figure 2-2. Optionally, an electron relay (ER) can be used to mediate the electron transfer to the catalyst. These systems are able to evolve hydrogen under irradiation of light by the mechanism in figure 2-2. An

exemplary system for reductive photocatalytic water splitting consists of ethylenediaminetetraacetic acid or trimethylamine as ED, methyl viologen dichloride as electron relay, $[Ru(bpy)_3]^{+2}$ as PS and a WRC based on Pd, Pt or Fe, for instance.[37,38] The idealized reductive photocatalytic water splitting is described by equation (2-2), which shows that hydrogen is gained by reduction water. In addition, two hydroxide species are formed indicating that this reaction requires two reduction equivalents per hydrogen molecule. Consequently, the general trend is to apply an excess of PS to account for this stoichiometry.

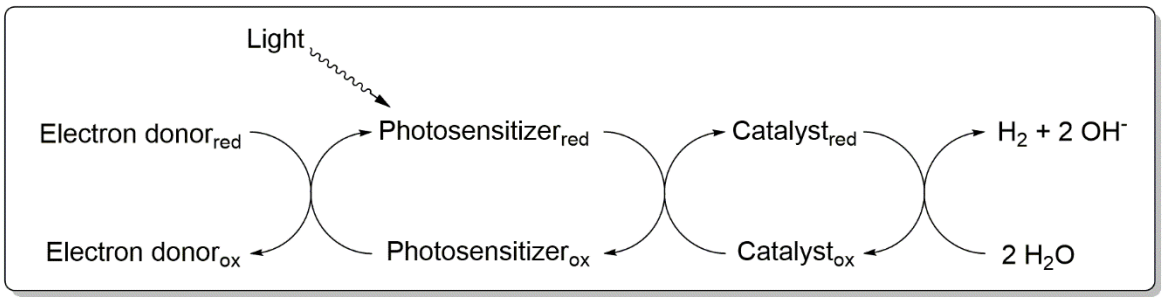

Figure 2-2: Scheme of the photocatalytic water reduction.

For the WRC, the reduction of protons solely has a high overpotential and a large activation barrier leading to the necessity of an efficient catalyst material. The catalyst must be able to abstract two electrons per equivalent hydrogen from excited PSs and react with water, as described in equation (2-2). Water reduction catalysts based on platinum has proven to do so with a remarkable efficiency.[39,40] Beside colloidal platinum[41–44], molecular platinum(II) complexes were applied in the field of reductive water splitting.[38,39]

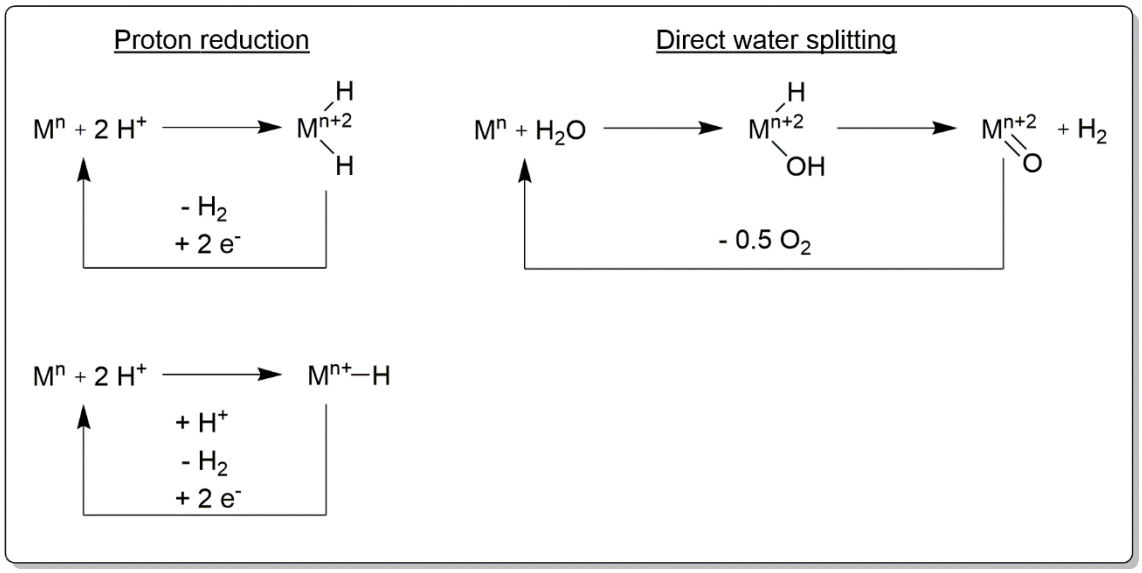

Figure 2-3: Proposed general mechanism for reductive water splitting.

The mechanism of oxidative addition by bond cleavage is a well-established concept and a key reaction in the field of organometallic chemistry.[45] The cleavage of water is nearly as well implemented[46] today, and several general mechanistic aspects can be pointed out.[47–49] As presented in figure 2-3[47–49], the potential mechanisms are divided into proton reduction and direct processing of water itself. The first mentioned reaction type – especially applicable in acidic solutions – begins with an addition of one or two protons to the catalytic metal center. More specifically, this can be differentiated in homolytic and heterolytic pathways, which only differ in the intermediate species. In the homolytic – usually performed by two-center catalysts – case, either the metal is first reduced to a [M] species or the proton addition to $[M\text{-}H]^+$ takes place first followed by a proton addition or one electron reduction giving the metal hydride intermediate. The heterolytic pathway shows a decomposition of the metal hydride species by proton attack, instead of an disproportionation of the metal hydrides, as described for the homolytic process before. It seems likely, that a dihydrogen complex is formed in this case, before emitting elemental hydrogen.[47–49]

As discussed in chapter 2.2.4, the short-term replacement of such noble metals is needed to establish a more sustainable process. In nature, hydrogenase enzymes based on iron and/or nickel are able to produce hydrogen.[50] Intriguingly, these systems are able to facilitate hydrogen evolution near the potential of the reversible hydrogen electrode and high TOFs as high as 100 – 10000 mol hydrogen per mol catalyst per second.[51] In order to mimic natures metallosulfur catalysts, several design approaches were proposed. An example is the left species in figure 2-4, in which two iron centers are bridged by the characteristic bis(μ-S) motive.[52] A second promising molecular design are cobaloximes, as depicted in

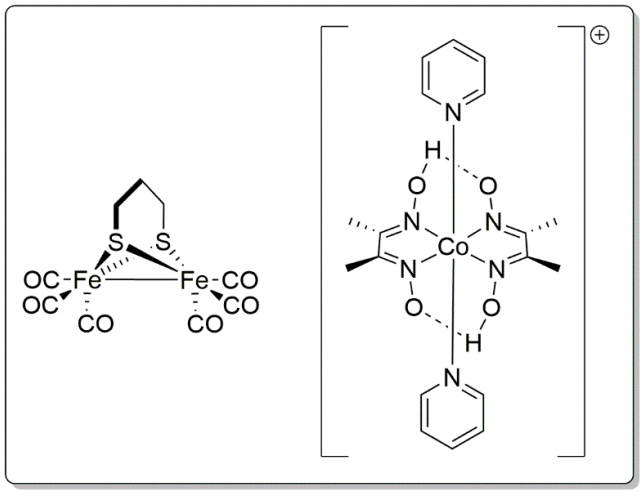

Figure 2-4: Common structural examples of an artificial [FeFe]-hydrogenase (left) and a cobalt diglyoxyme complex (right).[47-49]

figure 2-4. Due to simple synthesis the application of these complexes is widely used, especially in dyads.[53][54]

Dyads – in published articles also called organized systems or photo-hydrogen-evolving molecular devices (PHEMDs) – pursue the approach of connecting PS and WRC by means of a linker unit in a single molecule (figure 2-5[39]).[55,56] The linker functions as an electron transfer way between both centers and can be realized by annulated aromatic ring systems or aliphatic chains with heteroatoms, like peptide groups.[38,57] The aim of all connectors is to enable efficient and energy loss-free electron transfer. Which topologic method – three component systems or dyads – should deliver better results in general is controversially discussed.[38,58] While some authors stress that dyads should be more efficient, since a potentially more direct electron transfer is ensured without contribution of a statistic electron transfer by collision in solution,[38] other researchers state, that all synthesized dyads have been more inefficient than three component systems.[58] Despite of that, the robustness of dyads seems generally higher, most likely by preventing undesired side reactions, making it a reasonable alternative.[59]

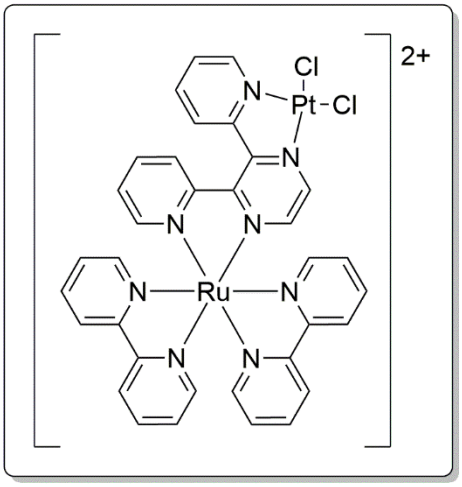

Figure 2-5: Example of a dyad for photocatalytic water reduction.[39]

2.2.3 Oxidative water splitting

The production of solar energy driven fuels as renewable and sustainable energy process by means of full water splitting makes it necessary to investigate also the oxidative part. This fundamental sub-process in the conversion of electricity or sun light into storable chemical fuels – water oxidation – is considered to be the bottleneck in the development of solar fuels.[19,60,61] This is due to the nature of this four electron process highly oxidizable, stable and reversible compounds were needed. Heterogeneous approaches for water oxidation were conducted as early as in the beginning of the 20th century, where the research focused mainly on electrode dependent overpotentials.[62] In the following years transition metal oxides, especially ruthenium oxides, were found to be efficient water oxidation catalysts[63] introducing once again the issue of sustainability and earth abundancy.

In nature, the oxidation of water is realized by a Ca-Mn_4 cluster within the terminal reaction of photosystem II.[64] The thermodynamic potential needed for water oxidation is as high as 1.23 V vs SHE at pH = 0 and exhibits a high complexity due to the participation of four electrons and four protons to finally form the O-O bond. Research indicates a nucleophilic attack of an O=Mn^V species on a Ca^{2+} ligated water molecule, which are additionally coordinated by amino acids and/or parts of a Mn_4 cluster.[65] Based on the natural model, biomimetic complexes were prepared to mimic the synergistic effects of this cluster.

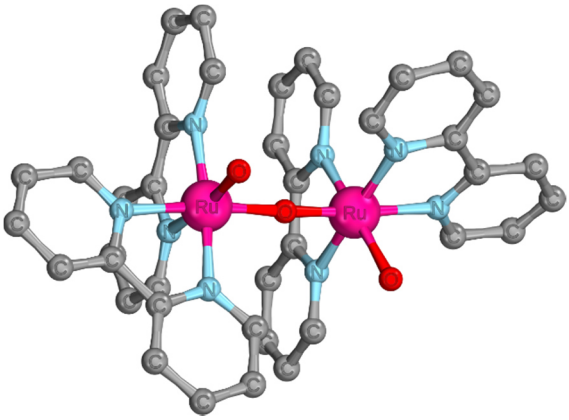

Figure 2-6: Representation of the blue dimer from crystal structure. (Hydrogens and anions are omitted for clarity.)

Inspired by nature, the path of dinuclear molecular water oxidation catalysts was laid by Meyer and co-worker in 1982, where the famous so-called “blue dimer” was published. This dinuclear complex is consisting of two Ru(III)-OH_2 function bridged by one oxo group resulting in an overall structure of cis,cis-$[(bpy)_2(H_2O)Ru(\mu\text{-}O)Ru(H_2O)(bpy)_2]^{4+}$ [66], as depicted in figure 2-6.[67] In lower oxidation states, like III and II, the complex is prone to reductive cleavage of the dinuclear species, which is a common behavior.[68] Beside electrochemical oxidation of water, the blue dimer is capable of evolving oxygen by adding an excess of Ce(IV) with an TON of at least 13.[69] It is considered that the coordination of the anion reduces the activity significantly by blocking coordination sites.[61]

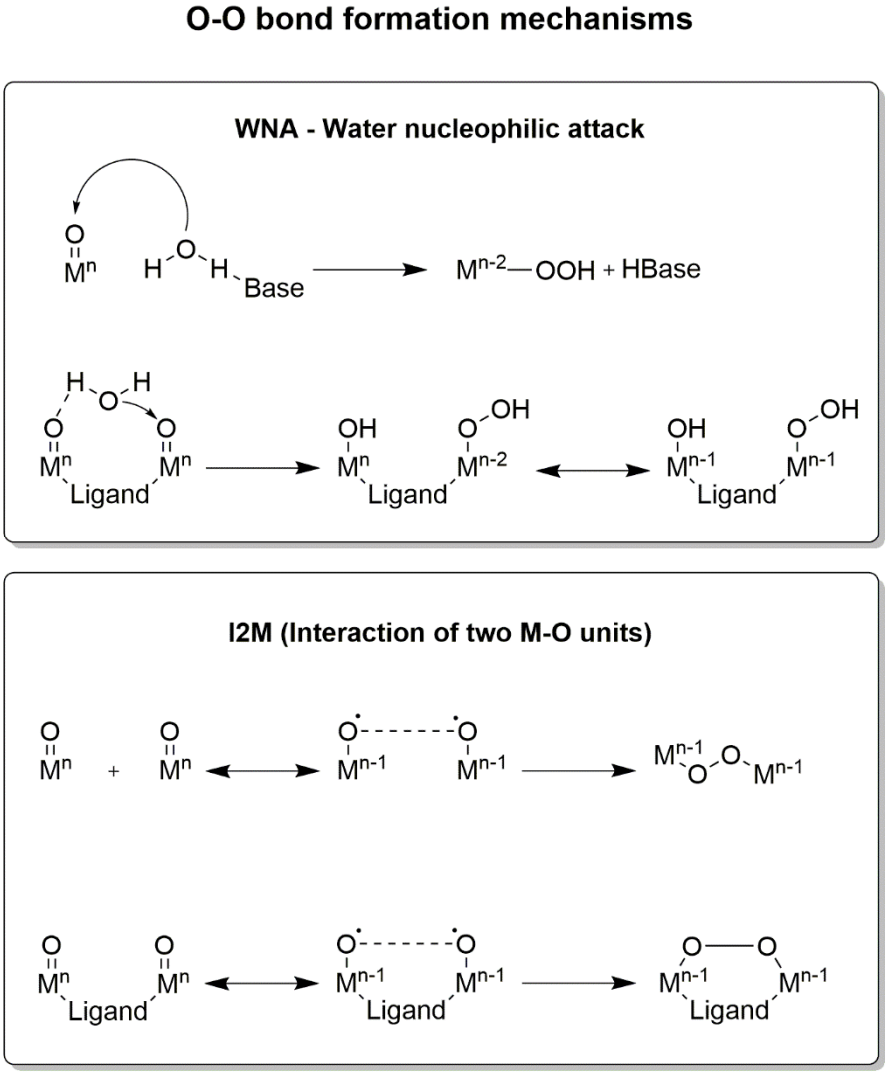

Figure 2-7: Established O-O bond formation mechanisms by WNA and I2O depicted for mono- und dinuclear complexes.

Within the research sector of water oxidation, the main work focused on expensive and rare noble metals like ruthenium, which in fact have a sufficient activity but are beside the high cost mined under partly questionable conditions.[70–74] Therefore the aim to implement earth-abundant and cheaper metals as base for efficient water oxidation catalysts. Copper as central ion represents a compromise between cost and efficiency. Unfortunately, the research sector of water oxidation with copper catalysts is merely rudimentary investigated indicating the necessity of fundamental research in this area. In the following, the existing published work will be presented to give an overview on this topic.

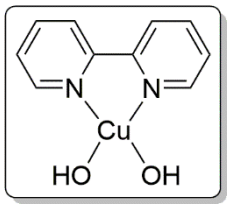

Figure 2-8: [Cu(bpy)(OH)$_2$].

In an article by *Meyer* et al. published in *Nature Chemistry* in 2012 it is shown that a copper(II) complex (figure 2-8), which is coordinated by a **bpy** and two hydroxo functions under basic conditions, exhibits a low overpotential under electrochemical water oxidation conditions resulting in an efficient catalysis.[75] The ease of the synthesis of this substance based on commercially available compound increases the interest additionally. Under electrochemical conditions, [Cu(bpy)(OH)$_2$] exhibits a TOF of estimated 100 s^{-1} in basic media with an overpotential as large as ca. 750 mV.[75]

Even simple copper(II) salts – like $CuSO_4$ or $Cu(NO_3)_2$ – in basic buffer solutions were found to have a significant electrochemical water oxidation activity.[76] Interestingly, there is evidence for mono-, di- and even larger copper species depending on reaction conditions. In high concentrated carbonate-containing solutions, the reaction is second order in [Cu^{II}] indicating a μ-peroxide or bis(μ-oxo) bridge as potential rate determining step. Whereas in CO_2-saturated $NaHCO_3$ solutions at pH = ca 6.7 a mononuclear active species is considered, but when increasing to pH = ca. 8.2 there is evidence for a mixture of mono- and dinuclear species catalyzing the oxidation.[76] This example shows the sensitive equilibrium between mono- and polynuclear species involved, which can be tuned by simple parameters as the pH value. Based on the studies, it is considered, that only hydroxo coordinated copper(II) complexes exhibit a significant catalytic water oxidation activity.

In 2013, *Meyer* et al. published electrochemical water oxidation with an anionic polypeptide-ligated copper(II) hydroxo complex in a well-defined and characterized catalytic cycle with overpotential of ca. 520 mV and a TOF of 33 s^{-1}.[77] The triglycylglycine (TGG) ligand is four-times negatively charged in basic media. A reaction mechanism for water oxidation catalysis was proposed based on previous mechanistic studies on Ru[78] and Ir[79] and electrochemical evidence, as depicted in figure 2-9.[77]

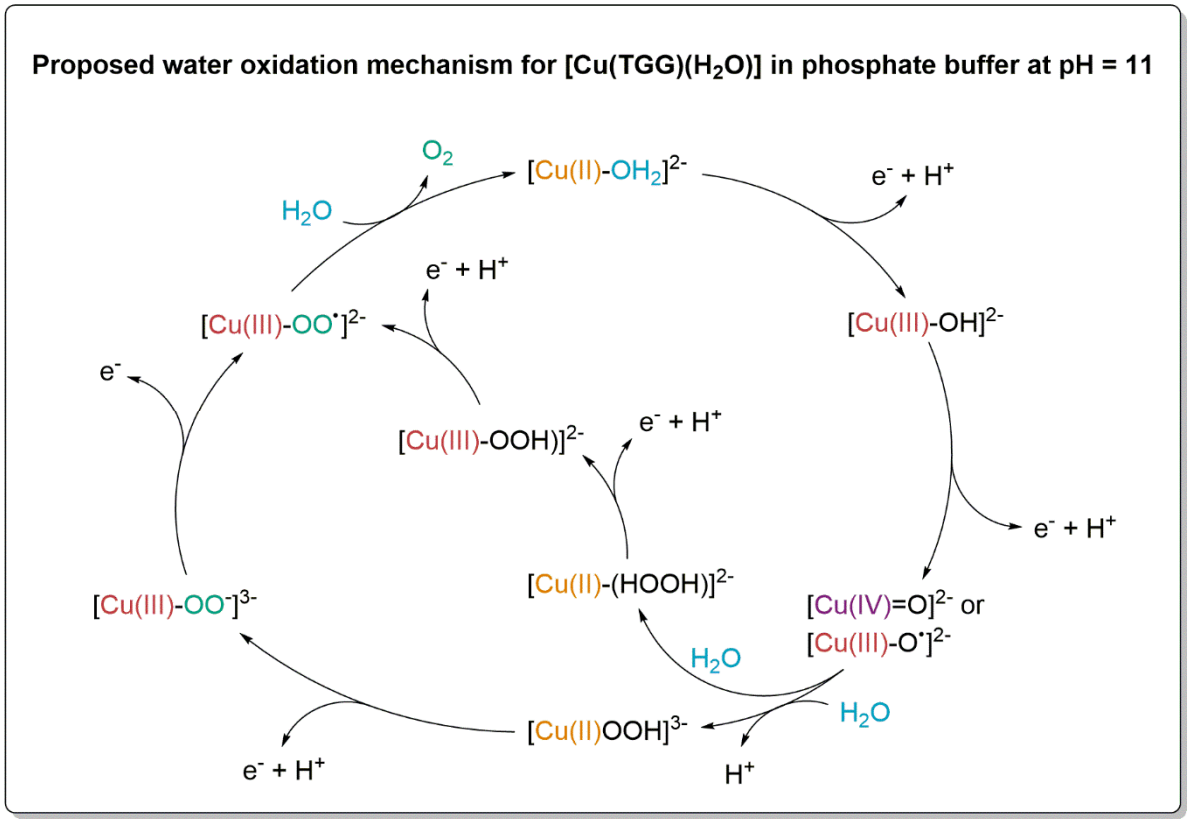

Figure 2-9: Proposed water oxidation mechanism for [Cu(TGG)(H_2O)] in phosphate buffer at pH = 11.[77]

The homogenous oxidative half reaction of water splitting based on earth abundant materials has only recently drawn increasing attention and is a key reaction for the implementation of an overall water splitting system. Especially in the field of copper-based systems nearly no research has been conducted. Since reactive oxygen species are involved in the splitting mechanism, these system are prone to decompose, for instance by oxidation of the ligand scaffold.

2.2.4 Earth abundancy

To create worldwide applicable systems, it is mandatory to implement simple synthesizable compounds based on affordable substances from the general chemical feedstock ideally even from unprocessed raw materials, which are available all over the world. Materials produced in a large amount decreases the cost additionally. In the case of metal complexes this refers to ligands as well as metal precursors. The cost for the metal applied plays a key role within such systems. Since noble metal exhibit superior properties – for hydrogen catalysis represented by the classical volcano plot[80] –, expensive metals like Ruthenium, Platinum and Rhodium are used for reactions and processes in the first place and up to now.[81] Despite the cost factor, noble metals are exhausted under partial unsocial and exploitative conditions.[70–73]

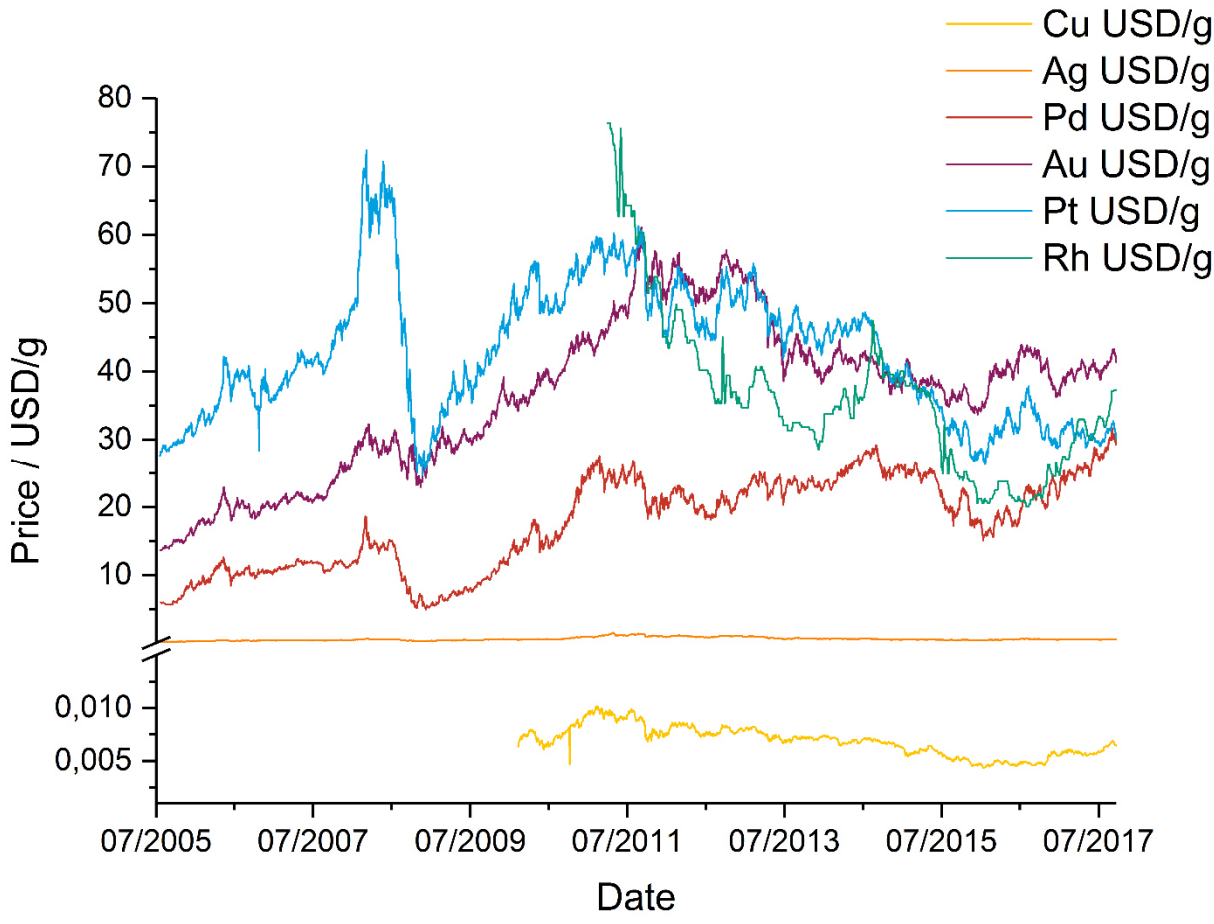

Figure 2-10: Price development of different metal as traded at the stock exchange Frankfurt (Germany).[82]

This questions the long-term competitiveness of these catalytic systems. Earth abundant, non-noble metals are offering an ecological and economical more sustainable perspective. This is the reason why this work pursues the aim to contribute

to the implementation of earth abundant metal into sustainable catalytic system for energy production. Especially copper exhibits a compromise between a sufficient availability, relatively low cost and delivering a good catalytic activity at the same time, which makes it attractive and competitive in comparison to noble metals.

The enormous financial differences between noble metals and copper is shown in figure 2-10 based on data from stock exchange Frankfurt.[82] In comparison to other commonly used noble metals, copper is more than two orders magnitude cheaper. This means that even if copper complexes are one or nearly two orders of magnitude lower in activity the application of copper would still be attractive from a financial point of view.

2.2.5 Photocatalytic Water Splitting

Light to energy conversion processes are called artificial photosynthesis[20,32,55,83] and can be considered analogue to photosynthesis in green plants. In the context of Ciamician´s vision, the term “artificial leaf” was also established.[84] Photocatalytic water splitting represents an important sub-issue within this broad topic, since solar energy is free of charge, available in a large amount and a functional system does not depend on auxiliary energy.[85] Research in the area of photocatalytic processes for water splitting applications is an interdisciplinary task in the intersection of physical, analytical, organic and inorganic chemistry. The long-term objective is the development of industrial applicable, long-lasting and environment friendly systems which are able to split water in hydrogen and oxygen simultaneously that no additional electron donors or acceptors need to be implemented. Because the energy generation using hydrogen gas emits only water, an emission free cycle of water splitting and fuel cell usage is possible.[44] On this way a sustainable mobile energy supply for anyone can be realized. Hydrogen generation and the conversion into energy will be a key technology in the future green energy mix to provide the everyday energy demand.[86]

In order to deliver the activation energy for that process, a special PS, which meets the high physico-chemical requirements. Beside intense MLCT absorption bands in the spectral range of incident sun light and a high chemical stability against irreversible oxidation and reduction reactions under reaction conditions, the energy states of the excited electrons and the longevity of the photo-induced exited stated are crucial for a well-working PS. In most of the photocatalytic water splitting systems the photosensitizer is limiting catalysis efficiency, thus the research on these species is playing a major role. In comparison to noble metal photosensitizers, copper-based systems exhibit economic and ecological advantages while outperforming the performances first mentioned complexes.[87]

2.2.5.1 Photosensitizer

When the aspect of sustainability is focused, it is striking that the photocatalytic water splitting is up to now almost exclusively based on noble metals to initiate the reduction process. Electron transfer model systems are commonly ruthenium based and are well descripted in literature. The most prominent and most investigated PS - this substance is topic of more than 8000 publications[88,89] – is $[Ru(bpy)_3]^{+2}$ was first synthesized by *F. H. Burstall*[90] in 1936. Later, in the 1970s, *Crosby* et al. characterized the spectroscopic properties in detail assigning the red luminescence to its ^{3}MLCT excited state.[91] $[Ru(bpy)_3]^{+2}$ was considered to be a non-photoactive compound, until *Gafney* and *Adamson* reported electron transfer quenching by $[Co(NH_3)_5Cl]^{2+}$ in 1972.[92] After several years of further research, it was shown that this complex exhibits a good stability, striking photo-redox properties accompanied with long-living excited state characteristics. Subsequently, $[Ru(bpy)_3]^{+2}$ was used in water splitting reactions[93], which was another key step to today's popularity in photochemistry.

$[Ru(bpy)_3]^{+2}$ exhibits suitable MLCT transitions with broad, intensive absorption maxima and a relatively long lifetime of the excited state.[17,47,89,94] These complexes are significantly more potent oxidation and simultaneously reduction agents than in the ground state, for which reason these states are easily quenched by electron donors or acceptors, respectively, resulting in shortened lifetimes and decreased electron transfer rates to catalysts.[57] In fact, the self-exchange energy transfer rates for this complex are determined in acetonitrile at r.t. with an ionic strength is 0.02 M to $8.3 \times 10^6\ M^{-1}\ s^{-1}$.[95] In comparison, the quenching rates for the common electron relays, for instance methyl viologen, are generally two or three orders of magnitude faster than the exchange energy rate of the mentioned complex[96] indicating that the excitation of the PS is crucial to the whole process.

In order to offer a general overview of the photo-redox properties, figure 2-11 was adapted from *Balzani* et al.[97]:

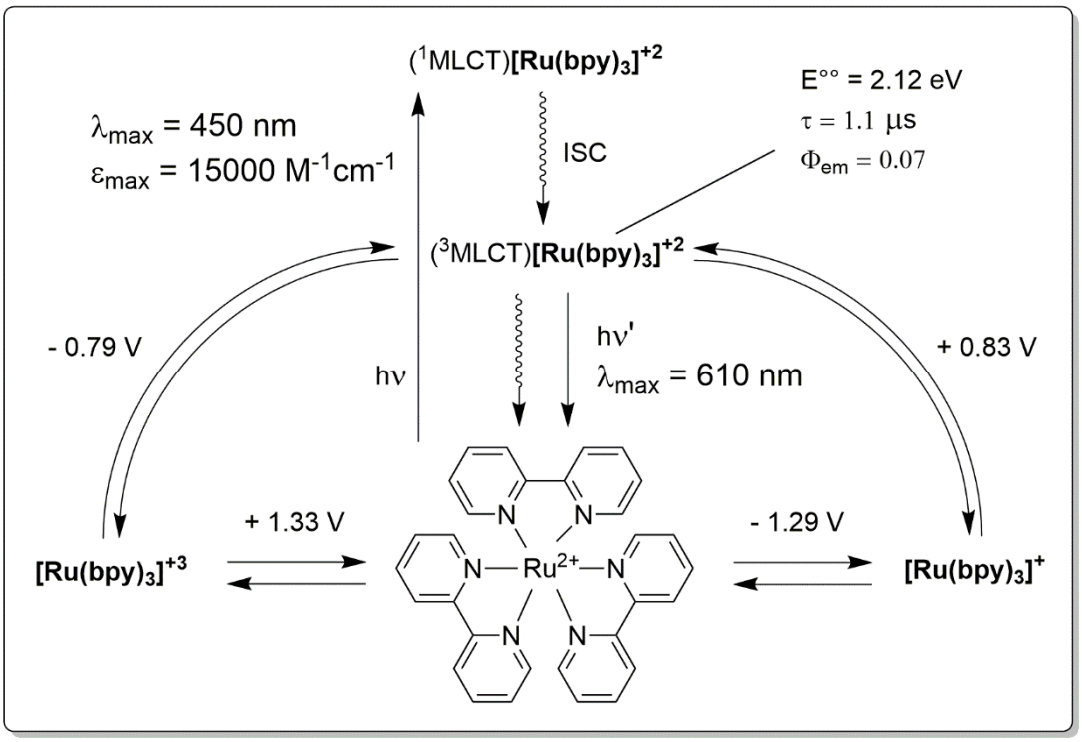

Figure 2-11: Photoredox properties of $[Ru(bpy)_3]^{+2}$ adapted from *Balzani* et al.. (Measured in deaereted acetonitrile at 298 K, potential values are referred to SCE)

The singlet ground state (^{1}GS) of the PS is excited by a photon to the ^{1}MLCT state, as depicted in figure 2-11. This is a matter of transitions of metal centered dπ orbitals to ligand π* orbitals, which are accumulating electrons resulting in a photon-induced charge separation and a formal oxidation of the metal. The mentioned transitions are usually the lowest electronic energy changes within this kind of complexes. After several femtoseconds, a transition of the excited short living ^{1}MLCT state to a longer living triplet ^{3}MLCT state, which can relax to its ground state either by light emission or by non-radiative routes. Electrons in the ^{3}MLCT are also able to provide the WRC with a sufficient reduction potential for water splitting.[57] By application of an ED, the electron balance of the PS is regenerated in order to regain the initial species. Because of the high reactivity, the excited states can easily be quenched by electron donor or acceptor compounds under reduction of lifetimes and lower electron transfer efficiency, provided that no arrangements were established to prevent this reaction.[57]

Since Ruthenium is an expensive noble metal, the long-term competitiveness of such photocatalytic water reduction systems is questionable. Therefore, the development of water splitting systems with easily accessible non-noble metals were established in the area of PSs before arranging them as catalysts.[98] Non-noble metals offer an ecological and economical sustainable perspective. That is the reason why copper is increasingly established as central metal of photoactive complexes by applying the biomimetic principles of the *entatic* strain analogue to copper based electron transfer enzymes. To approach both, the Cu(I) and Cu(II) oxidation state, which are involved in the photoexcitation, on the potential energy surface, tetradentate ligands are preferably used. Ligands supporting coordination geometries, which lie in between the ideal environments quadratic-planar for Cu(II) and tetrahedral for Cu(I), are necessary to facilitate this *entatic* effect. In this context, it is additionally investigated in what way a mixed N,P-donor coordination and diverse substituents are impacting lifetime, stability and the so-called exciplex quenching in order to synthesize a PS with high quantum yields and suitable MLCT transitions excitable with UV/VIS light. The first efficient noble-metal-free system for photo-induced water reduction was published by *Beller* et al.[87] recently in 2013. Beside a copper based PS, TEA as sacrificial ED and $[Fe_3(CO)_{12}]$ as WRC was applied to reach TONs above 800 (eq. hydrogen/eq. copper) within six hours reaction time. This results are outperforming both the established $[Ru(bpy)_3]^{+2}$ systems and $[Ir(bpy)(ppy)_2]$ systems significantly. In this special case the copper(I) ion is heteroleptic coordinated by a 2,9-dimethyl-4,7-diphenyl-1,10-phenanthroline and a phenoxathiin, which is substituted by two phenoxaphosphinines.

In fact, research was initially focused on noble metal based PS, but the interest in cheaper alternatives like complex ions out of the first period of transition metals is increasing. Copper(I) systems are in some characteristics even more attractive than ruthenium complexes. When comparing the redox potential, it is striking that the Cu^{2+}/Cu^{+} couple at 0.16 V has a lower reduction potential than Ru^{3+}/Ru^{2+} with 0.25 V under standard conditions verifying an easier reducing of the formal oxidized Cu(II) species.[99] In addition, copper complexes with nitrogen donor ligands exhibit relatively high extinction coefficients and long lifetimes, which are absolutely comparable to the related ruthenium compounds.[100,101]

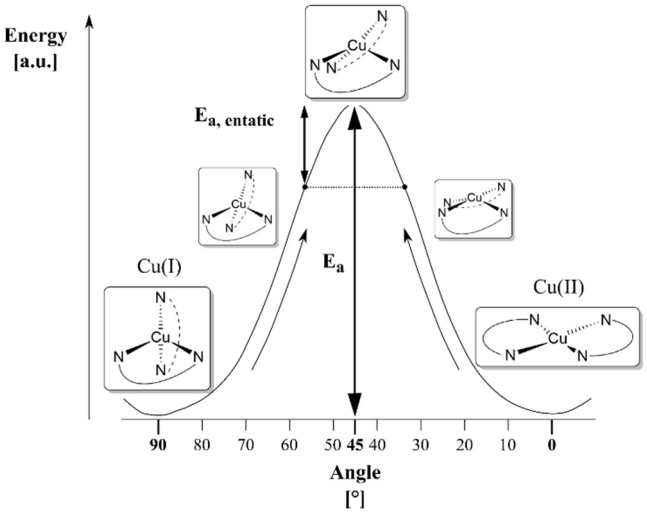

Figure 2-12: Energy in dependence of the torsion angle of a copper-based photosensitizer according to the entatic state principle.

Vallee and *Williams*[102] were first to postulate the influence of the aforementioned *entatic state* in copper containing metalloenzymes in which the coordination sphere of the copper ion is already come closer to the geometry of the excited state in order to minimize the reorganization energy and thus promote the electron transfer as depicted schematically in figure 2-12.[103,104,105] This principle was subsequently also applied in the area of coordination chemistry.[106,107,108] By regulating the geometry, two characteristics, namely activation and pre-organization, can be influenced, which are crucial for the redox properties.[106,107] Copper(I) complexes favors a tetrahedral coordination, while copper(II) prefers a quadratic-planar or a quadratic-pyramidal geometry for a pentadentate species, respectively.[89,109–111] The quadratic-planar character was additionally verified by theoretical studies.[105,112] During the photo-induced excitation a reorganization of the inner coordination sphere in terms of a D_2 flattening distortion takes place, which is driven by an increasing overlap of ligand σ-donor orbitals with formal half occupied d_{yx}-metal orbitals.[113] The configuration of coordinating ligand atoms regarding to their σ- and/or π-donor properties and the second coordination sphere plays also a role in the following processes. [104,114]

The photoexcitation of copper(I) bis(phenanthroline) complexes takes initially place according to the *Franck-Condon principle* meaning the ligand sphere is firstly not able to react to the sudden affinity change towards the quadratic-planar

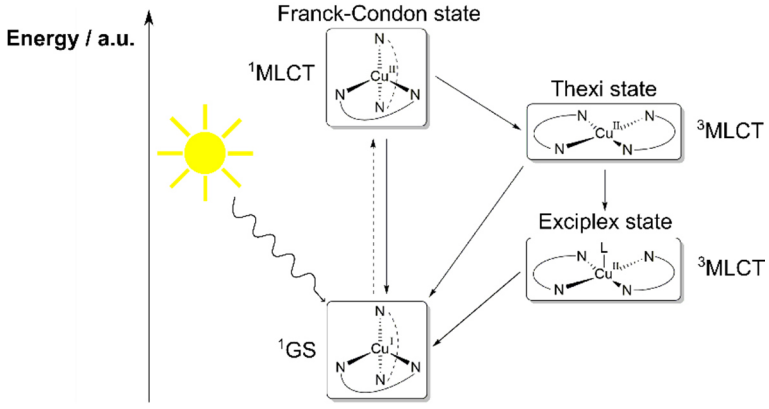

Figure 2-13: Photophysics of copper(I) PS - Excitation and induced structural changes.

coordination geometry in the generated copper(II) center, as depicted in figure 2-13.[89] Emanating from this species, the so-called *Franck-Condon state*, either a recombination under emission of electromagnetic radiation or a vibrational relaxation, for instance a Jahn-Teller distortion, is possible. The higher the reorganization energy, also called *Franck-Condon barrier*, the less stable the *Franck-Condon state* and the lower the tendency of quenching.[115] Steric demanding phenanthroline ligands, especially in 2,9-position, are able to increase the *Franck-Condon barrier*, thus improve the electron transfer.[115–117] The relaxed state, namely *thexi state*, can re-form the ground state either by radiative or non-radiative transitions. In doing so the energetic distance to the ground state decreases in descending order from *Franck-Condon* over *thexi* towards the *exciplex state*.[89] To conclude, efficient ligands move in the area of conflict between the need of rigidity to provide an as planar geometry as possible according to the *entatic state* and a sufficient flexibility to coordinate Cu(I) ions, which prefer a tetrahedral ligand sphere. Based on the shown excitation processes, distorted copper(I) complexes are promising photoactive model materials.

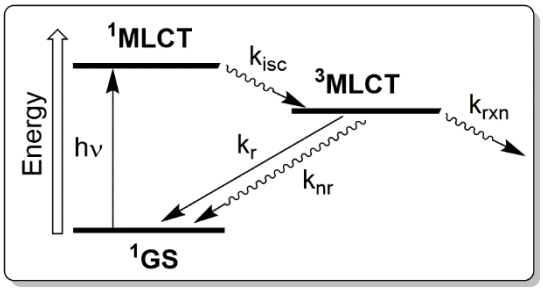

Figure 2-14: Time constants involved in the decay of an excited copper(I) PS.[57]

The aforementioned processes are associated with time constants as shown in figure 2-14.[57] The initial excitation leads to an ^{1}MLCT state, which undergoes an intersystem crossing to the long living ^{3}MLCT state. This state is able to transfer the photo-excited electron to another compound, represented by k_{rxn}. Furthermore, this state can relax by radiative/emissive or non-radiative pathways back to the ground state. The electron transfer from the PS to the WRC is realized by whether an oxidative or a reductive quenching mechanism (figure 2-15).[37,118,119] In the oxidative case, the ground state of the PS becomes photo-excited resulting in an excited state, which is quenched by the WRC. Afterwards the oxidized PS is reduced by an ED to regenerate the ground state species. Reductive quenching mechanism starts also with a photoexcitation, but then the excited state is additional reduced by an ED leading to a negatively charged ion.

The ionic species undergoes quenching and is reoxidized to the initial ground state PS.

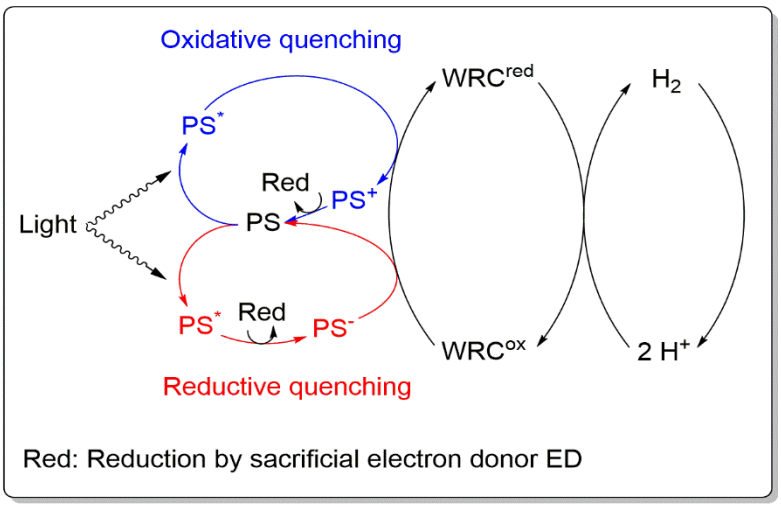

Figure 2-15: Oxidative and reductive photosensitizer quenching mechanisms.

In general, it is to state that copper(I) complexes with heteroatom tend to low lying and accessible MLCT states.[120] The possibility of systematic ligand modification of copper complexes in order to fine-tune those states and thus optimize lifetime, absorption and emission characteristics show the competitiveness to the conventional ruthenium species, particularly because the latter cannot be configured *ad libitum* because of a low lying metal based excited triplet state.[17,120,121] Additionally, the subsequent occupied anti-bonding e_g*-type molecular orbital is weakening the metal-ligand interaction leading to a higher probability of ligand dissociation.[17]

Tetradentate coordinated d^{10} copper(I) complexes, however, possess only a low affinity for increasing the coordination number and exhibit ideally a D_{2d} symmetry, while the d^9 configured copper(II) with D_2 symmetry is coordinationally unsaturated and hence are able to stabilize itself though another ligand leading in sum to a pentadentate coordinated complex.[100,117,121,122] In presence of *Lewis* bases and anions the coordination number is expanded under formation of an excited state complex, shortly named as exciplex, which cause a so-called exciplex quenching resulting in shorter lifetimes due to acceleration of non-radiative transitions.[118,120,121,123] In comparison, d^{10} copper(I) systems are anticipated to exhibit a greater lability than, for instance, low spin d^6 ruthenium(II) complexes.[124]

One of the intense investigated and well available ligand class associated with photo-induced electron excitation, which exhibits low lying π*-orbitals resulting in a facile oxidizability of copper and accessible low lying MLCT states, are polypyridines.[89,120,121,125] Especially 1,10-phenathroline (phen) derivates have proven its worth by tuning the properties of copper(I) complexes based the principle of the *entatic state* and *Franck-Condon barrier* through variation of substituents in 2,9-position. A first electrochemical proof of principles was given by *James* and *Williams*[126], who discovered that copper(I) complexes of 2,9-dimethyl-1,10-phenantroline (DMP) deliver a 400 mV more positive oxidation potential compared to the corresponding unsubstituted derivative early in 1961. The substitution pattern is verifiable responsible for a change in the complex geometry, the possibility of extension of the coordination sphere and therefore direct modification of MLCT states.[117,122] This approach allows the stabilization of copper(I) bis(phenanthroline) species and prevent ligand exchange reactions.[89,127]

Beside the electronic influence of π* orbitals, this ligand type provides the possibility of tuning the electronic behavior by means of the substitution pattern. The more pronounced the steric demand, the more is the photoluminescence maxima shifted to higher energies because no planar coordination environment can be established for the formal oxidized copper(II) state.[117] Heteroleptic copper(I) complexes with one phenanthroline and one diphosphane ligand are distinguished by extraordinary long excited state lifetimes and simultaneously decreased exciplex quenching rates, which makes such systems interesting for photocatalytic water splitting purposes.[125,128,129] In addition, the spatial volume occupied is at least held or can even be increased by application of bidentate phosphine ligands, while lowering the MLCT states.[116]

In order to summarize the field and give a brief review on phenanthroline based N,N- and N,P-donor ligands, the properties of important compounds, as can be seen in figure 2-16 were described in table 2-1. In general, the nitrogen donor systems exhibit nanosecond scale lifetimes, which are about three orders of magnitude shorter than for the NP complexes. Furthermore, the first are easier to oxidize and show their absorption maxima at lower energy, although the molar attenuation coefficient is presumably higher for that wavelength. Bulkier ligands shield the copper ion from quenchers, thus resulting in longer lifetimes. In addition, substituents attached to the

backbone have a significant impact in photo-physics and catalytic water splitting performance.

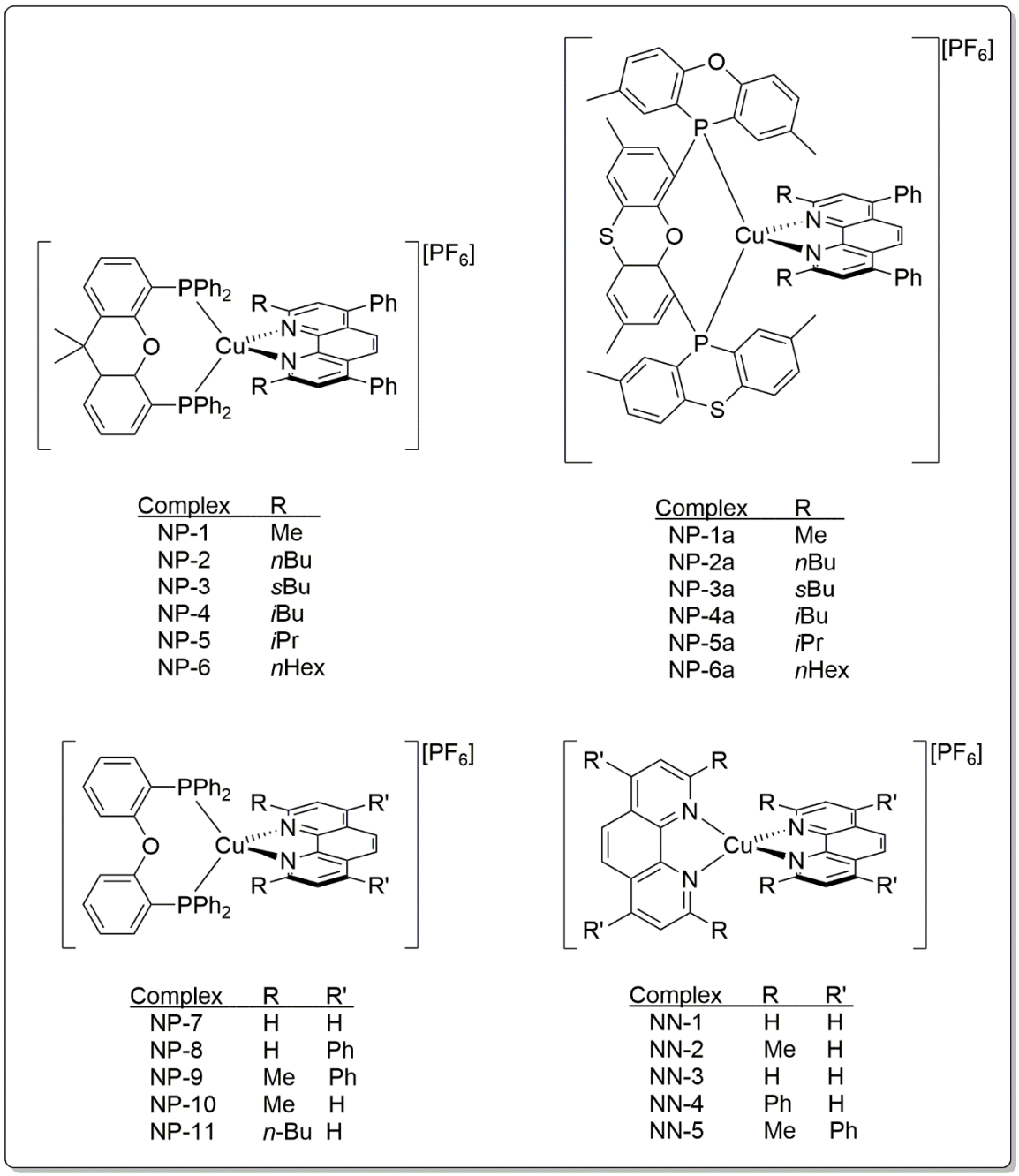

Complex	R
NP-1	Me
NP-2	*n*Bu
NP-3	*s*Bu
NP-4	*i*Bu
NP-5	*i*Pr
NP-6	*n*Hex

Complex	R
NP-1a	Me
NP-2a	*n*Bu
NP-3a	*s*Bu
NP-4a	*i*Bu
NP-5a	*i*Pr
NP-6a	*n*Hex

Complex	R	R'
NP-7	H	H
NP-8	H	Ph
NP-9	Me	Ph
NP-10	Me	H
NP-11	*n*-Bu	H

Complex	R	R'
NN-1	H	H
NN-2	Me	H
NN-3	H	H
NN-4	Ph	H
NN-5	Me	Ph

Figure 2-16: Exemplary phenanthroline-based copper photosensitizer.

Table 2-1: Overview of published copper(I) phenanthroline photosensitizer.

PS	Absorption		Emission				CV data		Performance in reductive water splitting			Ref
	λ_{max} [nm]	ε [$M^{-1}cm^{-1}$]	λ_{max} [nm]	Φ_{abs}	τ_0 [µs]	τ_{cat} [ns]	E_{ox} [V]	E_{red} [V]	Time [h]	Volume H_2 [ml]	TON_H	
NN-1	458	6880	-	-	<0.020	-	+0.19	-	-	-	-	[130]a)
NN-2	454	7950	740	-	0.085	-	+0.64	-	-	-	-	[130]a)
NN-3	460	-	-	-	-	-	-	-	24	2.6	60	[131]b)
NN-4	448	3440	715	-	0.250	-	+0.58	-	-	-	-	[130]a)
NN-5	478	13200	765	-	0.070	-	+0.58	-	-	-	-	[130]a)
NP-1	389	5701.9	569	0.08	(6.4±0.1)	180	+0.93	-2.05	24	37	862	[132]c)
NP-1a	386	5432.7	545	0.05	(16.3±0.1)	130	+0.90	-2.03	65	37	873	[132]c)
NP-2	389	5838.5	565	0.27	(15.6±0.1)	130	-	-	40	41	954	[132]c)
NP-2a	389	4810.2	535	0.34	(40.3±0.4)	90	-	-	8	46	1085	[132]c)
NP-3	387	4848.9	546	0.75	(54.1±0.6)	440	+1.02	-2.12	60	57	1330	[132]c)
NP-3a	386	4215.6	518	0.52	(51.2±0.5)	82	-	-	6	54	1251	[132]c)
NP-4	-	-	-	-	-	-	-	-	45	9.6	224	[132]c)
NP-4a	-	-	-	-	-	-	-	-	10	44	1029	[132]c)
NP-5	-	-	-	-	-	-	-	-	24	54	1270	[132]c)

NP-5a	-	-	-	-	-	-	-	-	6	49	1147	[132]c)
NP-6	-	-	-	-	-	-	-	-	65	17	400	[132]c)
NP-6a	-	-	-	-	-	-	-	-	6	43	1005	[132]c)
NP-7	391	-	700	0.0018	0.19	-	-	-	5	<1	-	[128]d),[87]e)
NP-8	-	-	-	-	-	-	-	-	24	<1	-	[87]e)
NP-9	-	-	-	-	-	-	-	-	24	20	477	[87]e)
NP-10	383	-	570	0.15	14.3				21	1.8	42	[128]d),[87]e)
NP-11	378	-	560	0.16	16.1	-	-	-	-	-	-	[128]d)

a) Photophysical data were measured in neat dichloromethane. The emission wavelength was corrected, ± 4 nm. Excited state lifetimes were measured in argon-saturated dichloromethane, ± 5 %. The oxidation potential was measured in 0.1 M TBAH/CH_2Cl_2, (0.01 V vs Ag/$AgNO_3$, which was found to be + 0.35 vs SCE using ferrocene as an internal standard.

b) Reaction conditions: Cu PS (ca. 3.5 mmol), [$Fe_3(CO)_{12}$] (ca. 5 mmol), THF/TEA/water (4:3:1, 10 mL), pH 11.5, 25 °C, Xe light irradiation (output 1.5 W), without light filter, 24h. TON(Cu)=n(H)/n(CuPS).

c) Optical measurements were performed in degassed THF at room temperature. Quantum yield measured at an optical density of ca. 0.1 (error: about 10%). The lifetimes τ_0 were measured in dilute solution with an optical density of about 0.1, 0.02 mM (388 nm). The lifetimes τ_{cat} were measured under comparable catalytic conditions: 0.35 mM copper PS and 0.5 mM [$Fe_3(CO)_{12}$] in a mixture of THF/triethylamine/water (4:1:1). The electrochemical measurements were carried out in dry MeCN under an argon atmosphere with 0.1M [Bu_4N][PF_6] as a supporting electrolyte. Peak potentials are versus Fc/Fc^+. Reaction conditions: copper PS (3.5 mmol), [$Fe_3(CO)_{12}$] (5mmol),10 mL THF/TEA/water (4:3:1), 25 °C, Xe-light irradiation (output:1.5 W). Gas evolution was quantitatively measured by an automatic gas burettes, while gas analysis was performed by GC. (Error: 1% -17 %). TON_h=n(H)/n(CuPS).

d) Photophysical data were measured in DCM at room temperature with ± 10 % error for the quantum yield and ± 5 % error for the lifetime results.

e) Reaction conditions: Cu PS (ca. 3.5 mmol), [$Fe_3(CO)_{12}$] (ca. 5 mmol), THF/TEA/water (4:1:1, 10 mL), pH 11.5, 25 °C, Xe light irradiation (output 1.5 W), without light filter, gas evolution measured quantitatively by automatic gas burettes, gas analysis by GC. The results differ between 1 to 20%, except for volumes <10 mL (up to 40%). TON(Cu)=n(H)/n(CuPS).

3 **Outline**

This work pursues to accelerate the establishment of copper in water splitting applications by thorough spectroscopic evaluation of the synthesized complexes. Based on these insights, the potential of the copper complexes will be discussed in context of the existing literature. Two main areas will be dealt with sequentially:

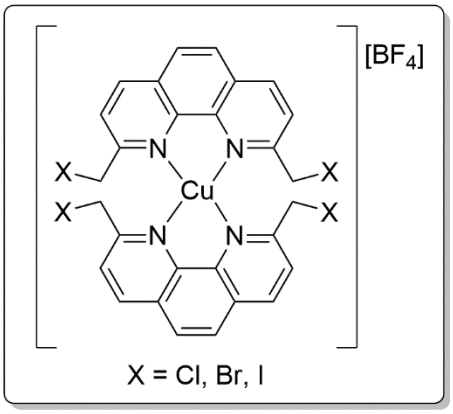

Figure 3-1: Series of studied DMP-X-based copper(I) complexes.

First, a series of copper(I) complexes will be introduced. The ligand system of these homoleptic complexes is based on DMP, which is substituted with chlorine, bromine and iodine atoms in 2,9-position figure 3-1. Significant differences in a variety of spectroscopic methods are induced by this substitution pattern opening the possibility of predicting properties in such a series. In detail, information were obtained regarding optical and electronic properties as well as the flattening ability according to the entatic state principle. In particular, spectroelectrochemical methods have proven to provide valuable information for the photoexcitation process. Based on the entatic state aspect a cyclic pyridinophane-based copper(I) complexes were synthesized, which unfortunately did not meet the optical requirements for good PS and were therefore not further pursued. Finally, an assay of reductive photocatalytic water splitting reactions were performed to assess of the efficiency as PS. Additionally, analogue copper(II) complexes to mimic the photo-excited state and as reference for the spectroscopic data were synthesized.

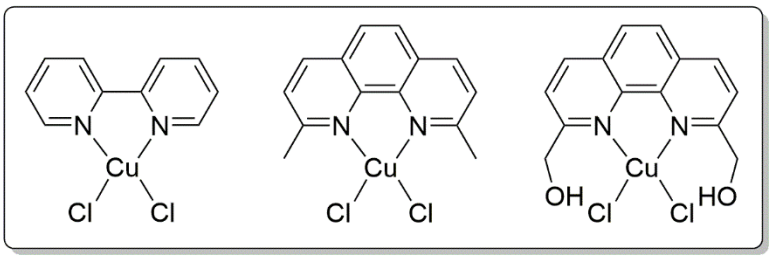

Figure 3-2: Excerpt of synthesized WOC precursors.

In the second part, the emphasis lies on an investigation of copper(II) complexes as WOC. The preparative way to the species depicted in figure 3-2 were presented. The copper(II) compounds are identified by single crystal X-ray diffraction and IR spectroscopy. In addition, chemical and electrochemical water splitting reactions were performed and discussed.

4 **Results**

4.1 Ligand synthesis of phenanthroline-based systems

4.1.1 Azapyridinophane ligands

Azapyrinonophanes were investigated as potential ligands for photoactive copper(I) species. The route of synthesis and spectroscopic results of the ligand type are presented in this section and was content of the master thesis of *Anke Hillebrand*.[133]

The synthetic strategy follows an adapted route first published by *Mamo* and *Pappalardo* et a. in 1985.[134,135] Symmetric diazapyridinophanes **DAPy** were built up by sodium *p*-toluenesulfonamide **NaTs-NH$_2$** and 2,6-bis(bromomethyl)pyridine followed by the removal of the tosyl groups with sulfuric acid. The resulting diazapyridinophane facilitates further substitution reactions to vary the steric and electronic properties of the ligand.

NaTs-NH$_2$ was synthesized by a condensation reaction with hot sodium ethoxide solution in a slight excess (figure 4-1). After 2 h of refluxing, the sodium salt precipitated as colorless needles, which were filtered off.[135] The ^{1}H- and ^{13}C-NMR signals shifted considerably about 0.2 ppm related to the sulfonamide, the purity was confirmed by elemental analysis.

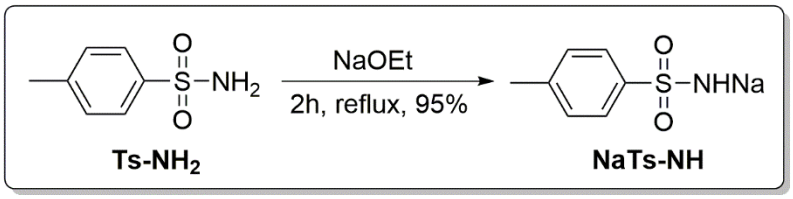

Figure 4-1: Synthesis of NaTs-NH$_2$.

The second key substance was synthesized by a four step route, starting with the commercial available 2,6-pyridinedicarboxylic acid **DMPy-OOH**. Firstly, the carboxylic acid was activated by thionyl chloride followed by esterification with methanol.[136,137] Alternatively, the ester **DMPy-OOMe** could be prepared in methanol in the presents of catalytic amounts of sulfuric acid[138] or hydrogen chloride and 2,2-dimethoxypropane.[139] Although different literature of all routes reports nearly quantitative yields, the esterification with the methanol/sulfuric acid system led to yield of only 55 %. On this account, thionyl chloride was used to prepare the acyl chloride by heating the carboxylic acid in tenfold excess thionyl chloride. The surplus reagent was distilled off under reduced pressure (850-900 mbar) after 45 minutes reaction time. In contrast, *Park* et al.[140] postulated the activation and esterification as a one-pot synthesis with

100% yield but were not able to recover the excess thionyl chloride. Methanol was added dropwise under cooling after the distillation was completed. Furthermore, the resulting mixture was heated again for 45 minutes. After that the excess methanol was distilled off and crude product was dissolved in saturated aqueous sodium hydrogen carbonate solution. The aqueous layer was extracted with DCM to obtain **DMPy-OOMe** in 95 % yield. Because **DMPy-OOH** shows a characteristic pattern in ^{1}H NMR studies induced by hydrogen bridge interactions, non-converted reagent could simply be identified. In addition, the formed methyl group was detectable at 3.98 ppm. All signals in ESI mass spectrum could be assigned presenting the sodium adduct as the most intense peak (calc. 218.04 m/z; exp. 218.05 m/z). Due to these facts, the diester was used in the next synthetic step without further purification.

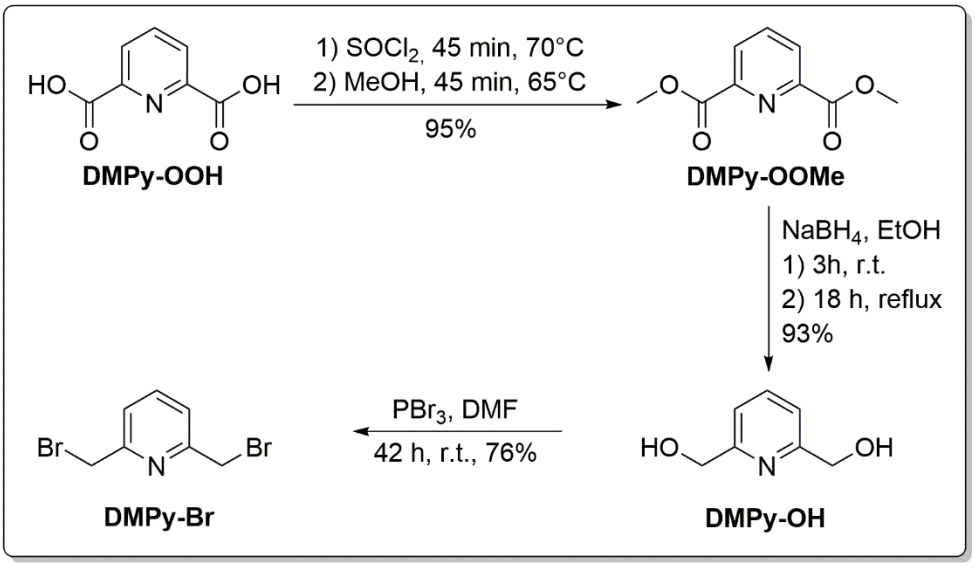

Figure 4-2: Synthesis of DMPy-Br.

DMPy-OOMe was then reduced by sodium borohydride in EtOH to give pyridine-2,6-diyldimethanol **DMPy-OH**. As suggested by literature[141], a ratio of reduction agent to diester of 27:1 was applied under cooling and in small portions. After stirring for 3 h at r.t. the reaction mixture was refluxed for 18 h. Then the solvent was evaporated, the residue diluted in sodium hydrogen carbonate solution and it was heated to reflux for 5 minutes. Water was added and the flask was cooled overnight inducing a colorless precipitation, which was filtered off. A second fraction was obtained by evaporation of half the solvent and storing the mixture overnight in the fridge again. The combined solid were long-term extracted with 300 ml acetone per extraction step, which took 4-12 h each. The colorless solid **DMPy-OH** was obtained by solvent evaporation in 93 %

yield. The ^{1}H NMR spectrum showed a characteristic broad signal for the hydroxyl group at 3.29 ppm. Furthermore, the purity was proven by elemental analysis, thus it was used without additional purification procedures.

The last step in the synthesis of the key compound **DMPy-Br** was performed by addition of phosphorous tribromide to a cooled solution of **DMPy-OH** inducing an orange coloration and a black precipitate as described in literature.[142,143] After stirring at r.t. for 2 days, water was added to quench the reaction and dissolve the precipitate. It was extracted with diethyl ether, which gave pale yellow needles in high purity and 76 % yield upon evaporation. Mass spectra showed the expected typical bromine pattern and elemental analysis permitted further conversions without further purifications steps.

In order to generate the macrocycle, the **DMPy-Br** was stepwise converted with an excess sodium *p*-toluenesulfonamide salt **NaTs-NH$_2$** (1:2) in DMF. The first equivalent of **NaTs-NH$_2$** was dissolved in hot DMF, before a DMF solution of **DMPy-Br** was added dropwise over 20 minutes. After stirring the mixture for 40 minutes at 80 °C, the second equivalent sodium salt was added. The solution turned orange instantaneously and was heated for another 4 h. Evaporating the solvent resulted in a brown, viscous residue, which was washed with water, MeOH, EtOH, and acetone to leave a bright brown powder.[142,143]

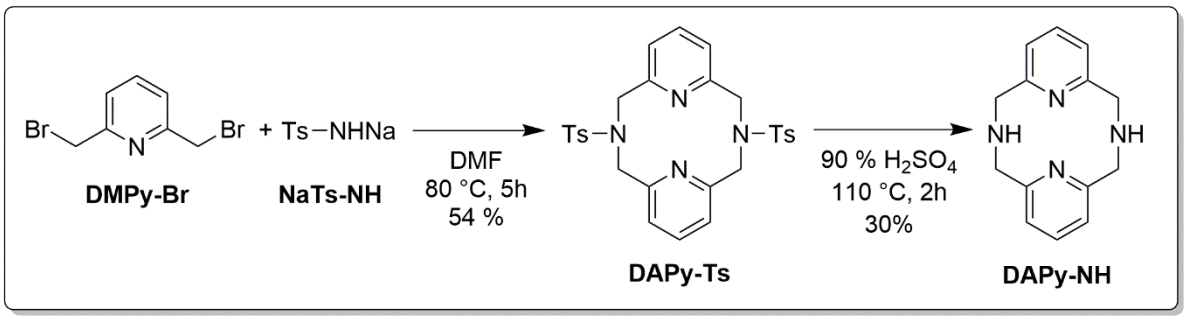

Figure 4-3: Synthesis of DAPy-Ts and DAPy-NH.

Interestingly, the ^{1}H, ^{13}C and ^{15}N NMR spectra led to the assumption, that the product contains two similar species, revealed by a doubled set of signals. In contrast, the mass spectrum showed only signals of the product, presuming that the second species exists either only in solution or is too instable for detection in mass spectrometry. A general statement regarding those macrocyclic compounds is the characteristic tendency to bind ions in its cavity.[144] To conclude, a proton may be bound within the center of the cycle by the coordinating nitrogen atoms. To verify this assumption, nBuLi

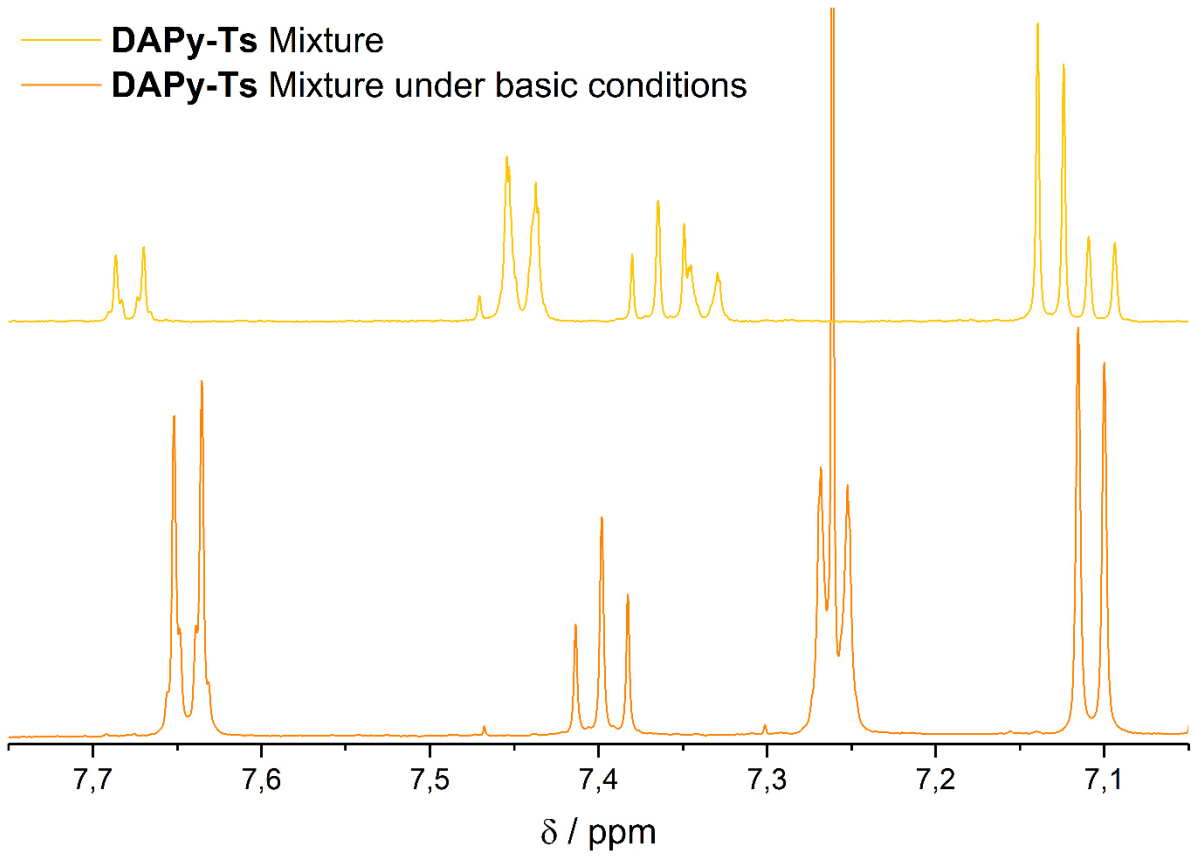

Figure 4-4: **^{1}H NMR spectra comparison between DAPy-Ts and it's the same sample under basic conditions.**

was used at – 78 °C to generate a Brønsted basic milieu in order to intercept a possible ring proton (figure 4-4). A slight peak shift is indebted by the change of the solvent from DCM-d_2 to $CDCl_3$. All in all, there is still an uncertainty in what extent the lithium ion may compete or fully replace the potentially bound proton, especially because previous studies, which try to protonate the supposed not protonates species by acetic acid or deuterated hydrochloric acid, remained unsuccessful. Furthermore, not only the dimer compound **DAPy-Ts**, but the analogue trimer species ($[M+Na]^+$ at 822.23 m/z) was detectable in the mass spectra with very low intensity, giving an additional coordinative possibility to explain the NMR behavior.

As can be seen in figure 4-3, the tosyl groups were removed with concentrated sulfuric acid at 110 °C for 2 h.[135] During the reaction the pale yellow solution turned brown and was added dropwise to an excess of sodium hydroxide solution under cooling. A light brown precipitated was filtered off, washed with chloroform and the solvent was evaporated from the resulting filtrate. A bright yellow solid **DAPy-NH** remained in 30 % yield. In order to increase the yield, the reaction was even performed in 96% sulfuric

acid and the reaction time was extended up to four hour but no improvement was observed.

Comparable to **DAPy-Ts**, two similar species were visible in the NMR spectra and the mass spectrum reveals no foreign signals indicating that the same postulated cation affinity effect as before was found. Additionally, the tosylated and untosylated trimer species are still verifiable with low intensity.

To vary the substituents of the diazapyridinophanes, *Bottino* et al.[135] published the methylation of such derivates under *Eschweiler-Clarke* conditions with excess formic acid and acetaldehyde. Comparable to that, a *Leuckart-Wallach* reaction was used to alkylate primary and secondary amines leading to yields of 61 – 85 %.[135] For that reason, the analogue reaction with benzaldehyde was performed with unsubstituted diazapyridinophane **DAPy-NH**.

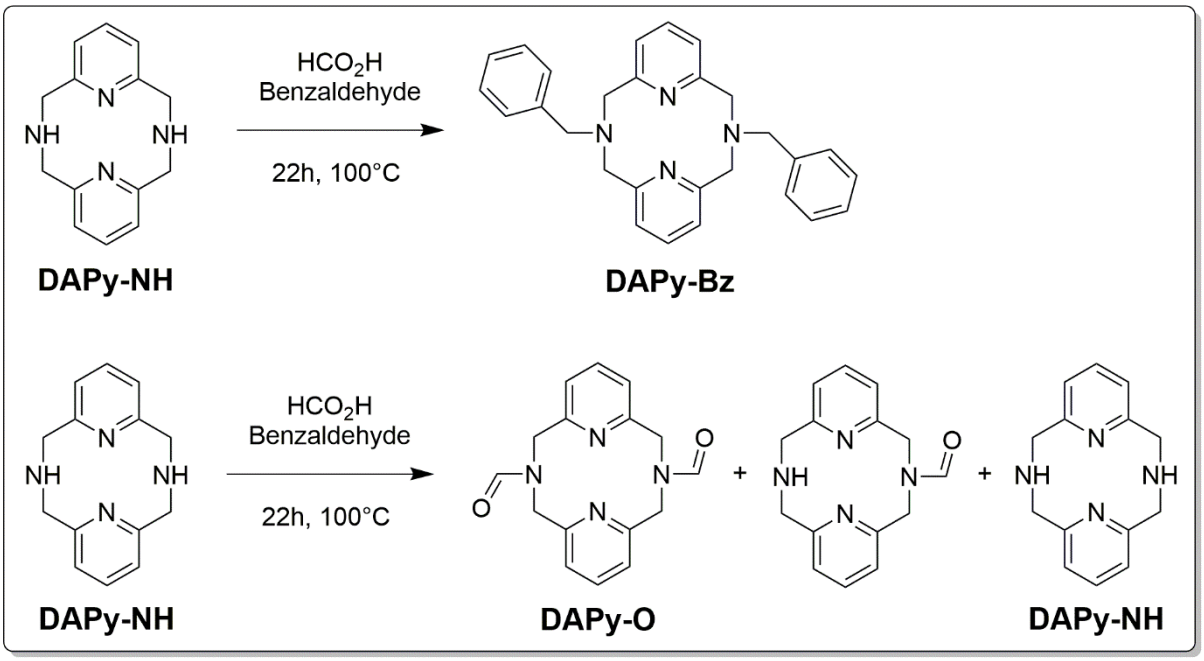

Figure 4-5: Proposed Leuckart-Wallach reaction (top) and experimental result of the reaction (bottom).

DAPy-NH was converted with formic acid and benzaldehyde over 22 h at elevated temperatures and then quenched with conc. hydrochloric acid. The volatile components were removed, the residue was dissolved in water and added dropwise to a sodium hydroxide solution. After extraction and subsequent evaporation of the organic solvent, the crude product was obtained. NMR spectra revealed a mixture of different species, which were identified as the reagent **DAPy-NH** itself, the dialdehyde **DAPy-O** and the singly substituted aldehyde by GC-MS, as depicted in figure 4-5.

Although the target molecule was not successfully synthesized so far, no reaction has been published for the synthesis of diazapyridinophanedicarbaldehyd **DAPy-O** itself or related species with or without any catalyst yet.[145,146]

A second approach included a deprotonation step followed by addition of a halogen compound to realize the functionalization of the ring amines through generation of a simple salt. Therefore, **DAPy-NH** was dissolved in THF, cooled down to – 78 °C and 2 eq. *n*-BuLi was added dropwise turning the solution red. After transferring 1-bromo-propane into the reaction mixture and further processing, the obtained NMR spectra showed only reagent signals.

The final successful route included the amination of benzaldehyde by **DAPy-NH** with an excess of sodium borohydride, like suggested by *Hasserodt* and *Gros*[147] for an comparable 1,4,7-triazacyclononane system. Benzaldehyde and the unsubstituted di-azapyridinophane **DAPy-NH** were dissolved in EtOH and heated at 50 °C for 2 h. Then sodium borohydride was added in portions to the cooled solution followed by heating for 2 h again. The volatile compounds were removed and the residue was dissolved in sodium hydroxide solution. Afterwards the aqueous phase was extracted with DCM and successive solvent evaporation.

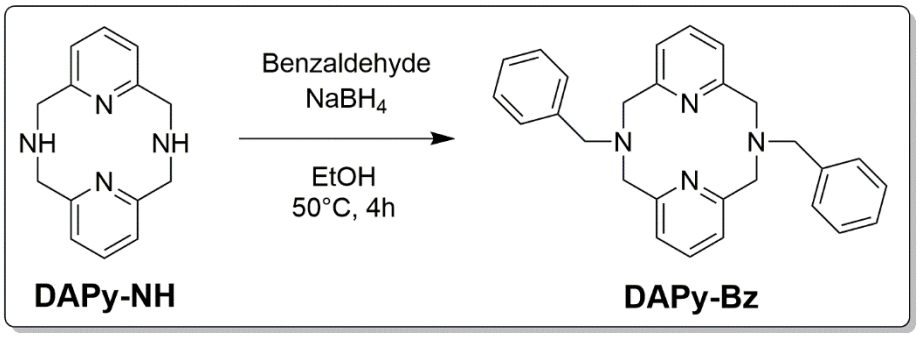

Figure 4-6: Synthesis of DAPy-Bz.

NMR analysis of the crude product revealed a suitable signal at 4.6 ppm for the benzylic CH_2 group, but the final evidence was delivered by mass spectrometry exhibiting the appropriate molecule isotope peak (m/z = 421.24 $[M+H]^+$). Due to the fact that sublimation and recrystallization from different solvent were not successful, another purification method, for instance flash chromatography, has to be examined.

Established cyclic diazapyridinophanes **DAPy-Ts**, **DAPy-NH** and **DAPy-Bz** and the novel **DAPy-O** were synthesized as macrocyclic ligands. Intriguingly, signs for coordination of simple and small cations were given by NMR spectroscopy. This

evidence lead to the assumption that the species exhibit good coordination properties, which should lead to easily accessible copper complexes.

4.1.2 DMP-X-based ligands

In order to develop a rational design for phenanthroline-based PS, the influence of different halogenated Cu(I) complexes of 2,9-Bis(halomethyl)-1,10-phenanthroline on optical, electrochemical and catalytic properties was investigated. The synthesis of ligands **DMP-Cl** and **DMP-I** as well as the optical characterization of the resulting homoleptic copper(I) compounds is content of the Bachelor Thesis of *Philipp Dierks*.[148]

An overview of the synthesized 2,9-dimethyl-1,10-phenanthroline derivatives is provided in figure 4-7.

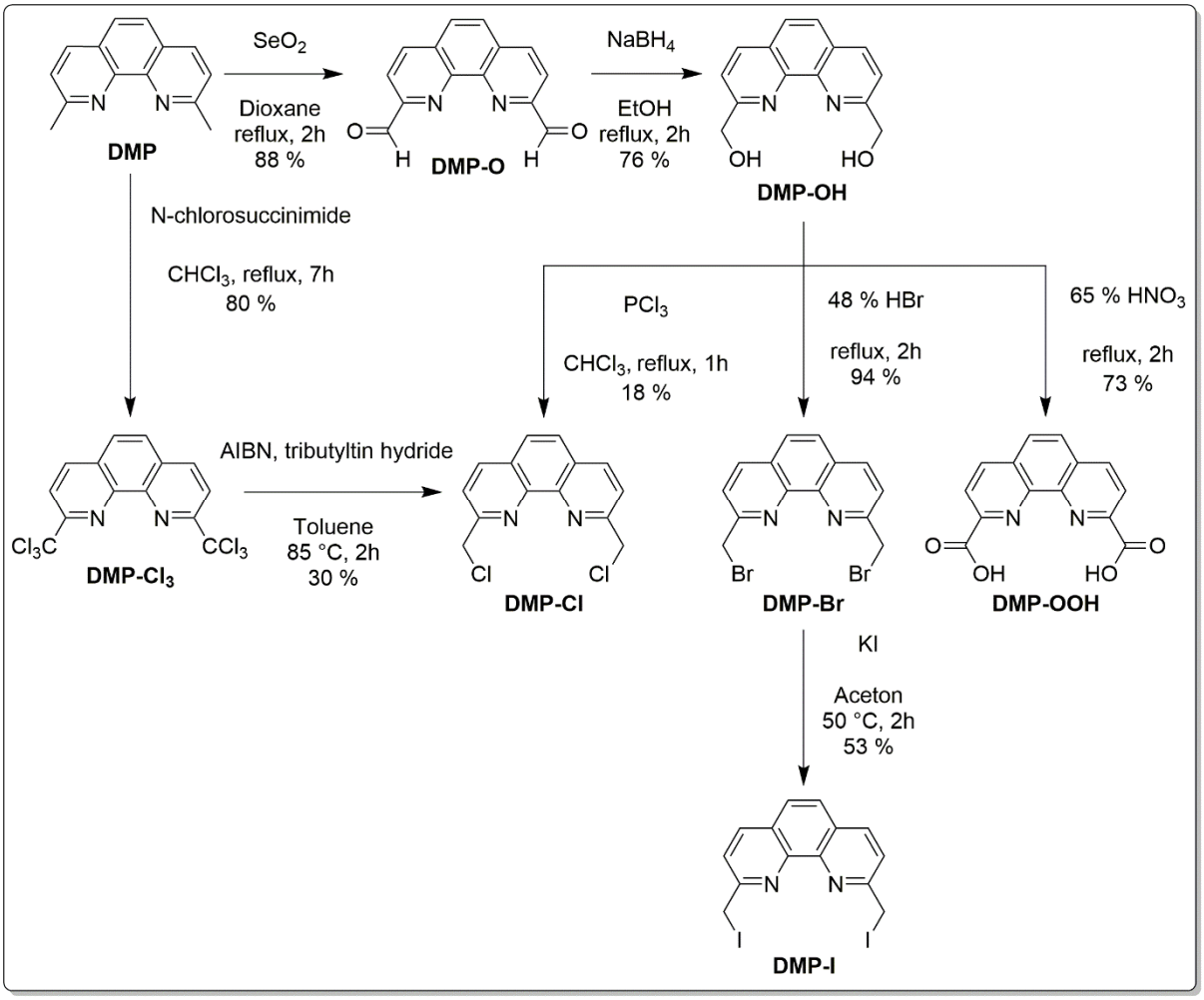

Figure 4-7: Overview over synthesized 2,9-Dimethyl-1,10-phenanthroline derivatives.

Starting from **DMP**, the dialdehyde species **DMP-O**[149,150] was obtained in 88 % yield by oxidation with selenium(IV) dioxide under elimination of water. In the next step it was reduced by sodium borohydride leading to **DMP-OH**.[149] The reaction mechanism proceeds most likely over a Lewis adduct by coordination of sodium with the carbonyl

group increasing the nucleophilicity of the carbonyl carbon atom, which is then able to react with the borohydride as can been seen in figure 4-8.

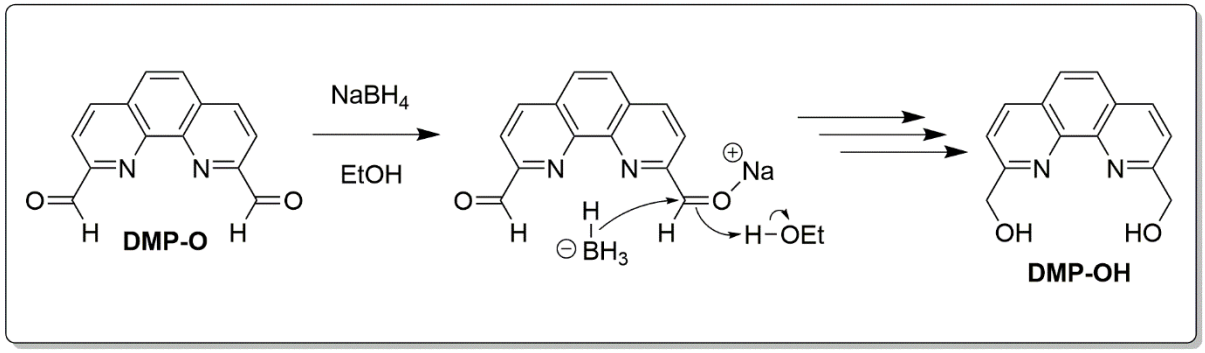

Figure 4-8: Proposed mechanism for reduction of 1,10-Phenanthroline-2,9-dicarbaldehyde DMP-O.

DMP-OH can then be either halogenated by hydrogen bromide or phosphorous trichloride to **DMP-Br**[149,151] and **DMP-Cl**[149,152], respectively or oxidized by nitric acid to give **DMP-OOH**[149,151].

The bromination is realized by a S_N2 reaction in refluxing conc. HBr. After treating with an aqueous sodium carbonate solution, compound **DMP-Br** is obtained as a precipitated solid, which was chromatographically purified. The typically expected reaction mechanism of the benzylic substitution is depicted in figure 4-9.[153] The hydroxyl function is first protonated to become a better leaving group, followed by a nucleophilic attack of the bromide ion.

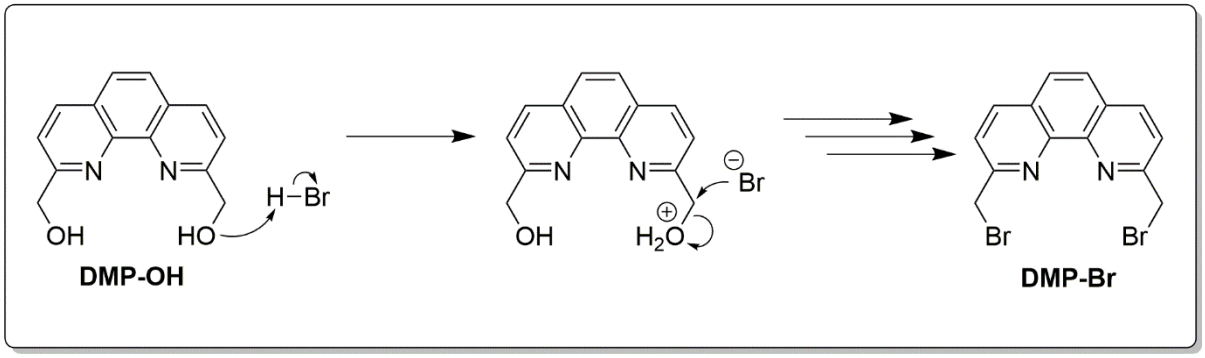

Figure 4-9: Proposed mechanism for the bromination of (1,10-phenanthroline-2,9diyl)dimethanol DMP-OH.

Conversion of the diol **DMP-OH** with an excess phosphorous trichloride in chloroform resulted in an immediately precipitation of a colorless, flocculent solid, which was obviously not the orange reagent. This suspension was heated to reflex for one hour. After distilling the solvents off, the solid, orange residue was treated with aqueous sodium carbonate solution and the insoluble yellow solid was separated. Finally, the colorless product was obtained in 18 % yield by chromatographic purification. The reaction mechanism is proceeding most likely by an nucleophilic attack of oxygen on the oxophilic phosphorous, as depicted in figure 4-10.[154]

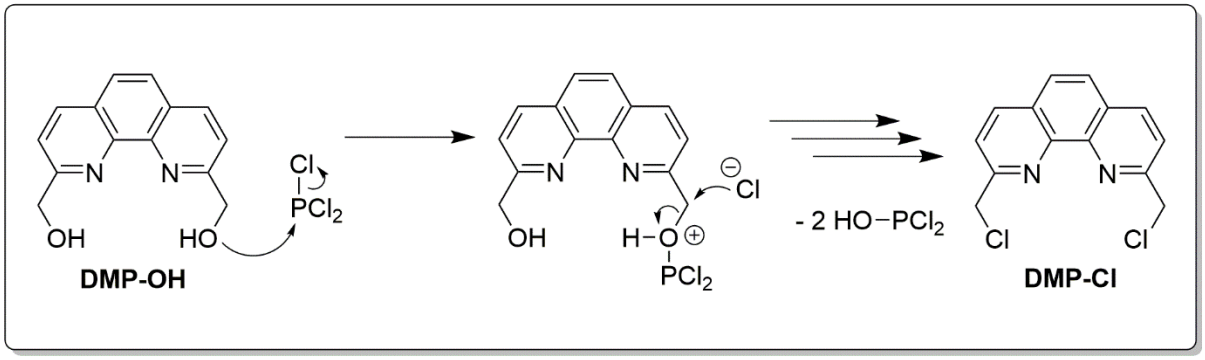

Figure 4-10: Proposed mechanism for chlorination of (1,10-phenanthroline-2,9-diyl)dimethanol DMP-OH.

Due to the low yield, a second, two-step synthetic procedure, based on **DMP** was conducted. Adapted from literature[149,152], **DMP** was converted with an excess *N*-chlorosuccinimide to obtain **DMP-Cl$_3$** in yields between 80 % and 99 %. A radical dechlorination is performed by utilizing azobisisobutyronitrile and 4 eq. tributyltin hydride to radical defunctionalize **DMP-Cl$_3$** to the mono chloromethyl derivate **DMP-Cl**.

Analogue to the bromination with HBr, a reaction with conc. HCl was performed, but no reaction was detected and the reagent was regained. To favor the substitution, copper(I) chloride was added as a catalyst. A catalyst coordination by the oxygen atom should weaken the carbonyl bond in order to increase electrophilicity. In this case, the reagent was obtained likewise. Chlorination of **DMP-OH** with thionyl chloride and triethylamine under reflux conditions and subsequent treatment with aqueous sodium carbonate solution resulted in a precipitate, in which the desired product could not be detected.

In an approach to synthesize **DMP-I**, the **DMP-OH** was converted with hydroiodic acid in expectance of an analogue mechanism as in figure 4-9. The resulting red solution was heated to reflux for 2 h and treated with $NaCO_3$ solution until a pH value of 9 was

reached. The precipitate was collected and analyzed by NMR spectroscopy identifying the reactant only.

Finally, a *Finkelstein* reaction[155] was performed to obtain **DMP-I**. **DMP-Br** is converted to **DMP-I**, as schematically depicted in figure 4-10. This reaction is realized by adding **DMP-Br** to an excess potassium iodide in acetone. After a few minutes, a yellow coloration was observable in addition to a precipitation of a colorless solid potassium bromide, which causes the equilibrium to shift towards the desired **DMP-I**. Due to the benzylic position, a substitution is generally more favored. In addition, the reaction mixture was heated at 50 °C for 2 h. After solvent evaporation, the remaining orange-black solid was washed with water in order to separate the sodium salts. The crude product was purified by means of chromatography, confirmed by NMR and mass spectrometry and obtained in 56 % yield.

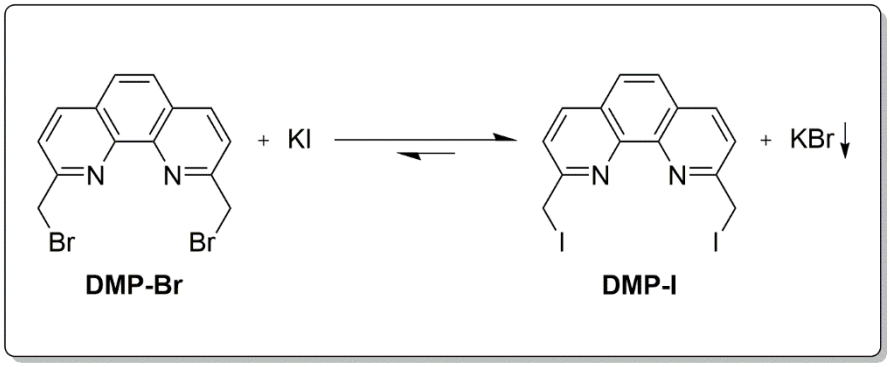

Figure 4-11: Finkelstein reaction for iodination of 2,9-bis(bromomethyl)-1,10-phenanthroline DMP-Br.

Interestingly, the carbon atom in α position to the iodine exhibits a significant high field to 7.0 ppm in comparison to its bromine analogue, which has a shift of 35.0 ppm. This is a common range for such type of carbon atoms – like benzyl iodide[156] – and can be attributed to the heavy-atom effect, which originates from spin-orbit coupling inducing another angular momentum.[157,158] An overview of chosen NMR data is given in table 4-1, showing the dramatic change for the C_α signals, while all other signals do not change significantly.

Table 4-1: Chosen NMR data of DMP, DMP-Cl, DMP-Br and DMP-I.

Signal	DMP	DMP-Cl	DMP-Br	DMP-I
H_{Me} [ppm]	2.95[a]	5.11[a]	4.97[a]	4.85[b]
C_{Me} [ppm]	26.0[a]	47.7[a]	35.0[a]	7.0[b]
N [ppm]	298.8[a]	298.8[a]	299.5[a]	302.4[b]
Signals marked with a and b were acquired in $CDCl_3$ and MeCN-d_3, respectively.				

After NMR acquisition of **DMP-I** the coloration turned from yellow to rose in within two hours indicating a decomposition. This assumption was proven by a classical iodine proof using the starch indicator. The resulting iodine-starch-complex had a typical blue coloration indicating iodide anions in solution very sensitively, even a iodine concentration in the range of 10^{-5} M still results in a dark blue coloration.[159]

To investigate the stability of **DMP-I** towards different solvents and light, the ligand was exposed to an excess of solvents both with regular laboratory light and without illumination of light by wrapping the sample into aluminum foil. For water splitting relevant solvents MeCN and water, as well as THF, DCM, $CHCl_3$ and Acetone, since this is synthesis solvent, were chosen for this series. It was found, that the decomposition is faster when exposed to light than their non-illuminated reference samples. In case of water, the ligand exhibits neither a visible solubility nor was a decomposition observable. The yellow color of the solution remained in acetone and MeCN even when illuminated verifying the stability in these solvents. Because of the importance for water splitting measurement, the MeCN sample was additionally analyzed by NMR spectroscopy confirming the assumption on a middle timescale. Finally, after two months the MeCN solution was tested positive in the starch reaction, too. Interestingly, the DCM solution decolored within several hours. Discoloration took approximately one day in THF and $CHCl_3$ solutions.

Samples held under exclusion of light exhibit the same decomposition behavior but delayed for approximately one week. This indicates an increasing rate of decomposition by light but not an induction of the reaction.

To obtain **DMP-F**, a *Finkelstein* reaction of **DMP-Br** with NaF in acetone was unsuccessfully performed verified by ^{19}F-NMR spectroscopy and EI mass spectrometry. The synthesis was not further pursued due to increasing health risks of other fluorinating agents.

During his advanced practical course in inorganic chemistry, *P. Dierks*[160] tried to synthesize phosphine substituted DMP-PR_3 ligands, which will be discussed in the following. His efforts were primarily based on a substitution of **DMP-Br** with lithium diphenylphosphide **LiPPh$_2$** as described before by *R. Ziessel*.[161] First, a suitable solvent had to be found, whose properties should allow dissolving **DMP-Br** and resist reacting with *n*-BuLi for this the substitution reaction at the same time. Therefore DMF (solubility: ca. 3.3 g/l), MeCN (solubility: ca. 2.0 g/l) and THF (solubility: ca. 2.0 g/l) was applied for diphenylphosphane **HPPh$_2$** deprotonation test reactions with *n*-BuLi. The reaction parameters were chosen as stated in literature.[161] After deprotonation at – 80 °C, the reaction solutions turned intense orange indicating a successful deprotonation. The reaction was quenched by 1 eq. D_2O resulting in the deuterated species **DPPh$_2$**. To verify the presence of this compound, in situ NMR samples were prepared under air exclusion with a $CDCl_3$ capillary for referencing. ^{31}P-NMR broadband proton decoupled spectra show the characteristic triplet generated by an $^1J_{PD}$ coupling at around – 40 ppm and is in accordance with literature.[162] Based on ^{31}P NMR spectra, MeCN was dismissed as a potential reaction solvent due to a higher amount of side reactions and a potentially lower conversion estimated by these spectra.

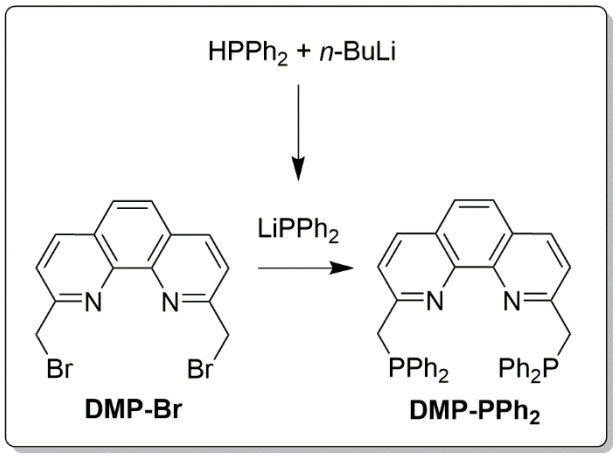

Figure 4-12: Synthesis of DMP-PPh2 by substitution of DMP-Br.

Consequently, the first step – formation of **LiPPh$_2$** –was conducted first THF at – 80 °C by adding *n*-BuLi to $HPPh_2$. The nucleophile **LiPPh$_2$** was then transferred dropwise to a pale yellow solution of **DMP-Br** in THF. During intensification of the yellow color, a fine solid precipitated. After one hour reaction time, a NMR sample was extracted indicating only two different phosphorus species, one of them being **HPPh$_2$**. The

second signal was detected at – 15.0 ppm, which is in the range of the target molecule.[161]

Since lithium bromide is formed in the anticipated reaction process of this S_N2 substitution, the precipitate was considered as the lithium salt, which is insoluble in THF. The solid was filtered off and dried. To verify the aforementioned hypothesis, the precipitate was investigated by a flame test exhibiting a for lithium characteristic crimson red flame color. In addition, a slightly brownish precipitate was obtained when treating an aqueous solution of the precipitated solid with $AgNO_3$ indicating the presence of halide ions in solution. These results were another indication that the substitution reaction took place.

The reaction was quenched by abs. EtOH and the solvents were removed *in vacuo*. An orange solid was obtained and DCM was determined as suitable mobile phase by TLC. The solid was then purified by manual column chromatography (silica gel) under air exclusion, as described in literature[161]. One fraction was collected and the remaining yellowish silica phase, which did not elute, was extracted by $CHCl_3$. Both exhibited the same chemical shift at 20.6 ppm in ^{31}P-NMR spectra. Additionally, ESI mass spectrometry did not confirm the target molecule or a decomposition product.

The same reaction was performed in DMF to ensure that the solvent does not interfere in any kind with deprotonation or substitution. After quenching the reaction with abs. EtOH and evaporation of the solvent, a ^{31}P-NMR spectrum of the remaining brown, high viscous liquid shows a large signal of $HPPh_2$ and significantly less intense signals at – 10.0 ppm and 65.3 ppm indicating an inefficient reaction with no conversion to the target molecule at ca. – 13 ppm.[161] For further reaction approaches, a better leaving group would most likely be beneficial.

The amine derivative, **DMP-Amine**, would open the possibility to introduce several substituents simply by means of S_N reactions varying the steric demand and electronic properties of this tetradentate ligand. To gain this compound, a two-step synthesis adapted from *Liu* et al. [163] was conducted.

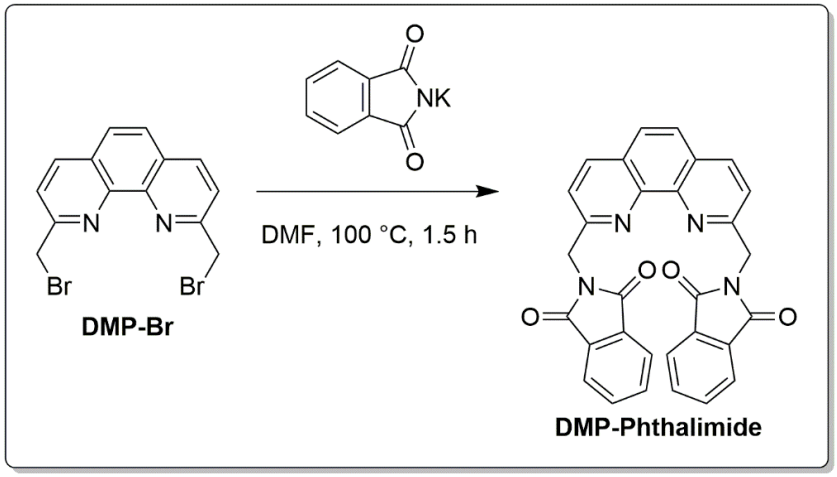

Figure 4-13: Synthesis of DMP-Phthalimide.

DMP-Br was converted with potassium phthalimide in DMF at 100 °C for 1.5 h resulting in a homogenous yellow solution. The solution was let cool to r.t., when a brown high-viscous liquid formed, then ice was added. This resulted in a yellow turbid solution. The solid was filtered off correlating to roughly 16 % yield. Due to impurities this yield will not be accounted to the total yield, The solvent was evaporated leading to a precipitation of brown solid and chromatographically purified leading to one main fraction with colorless needles being the product. The total yield of this reaction was determined as 76 %.

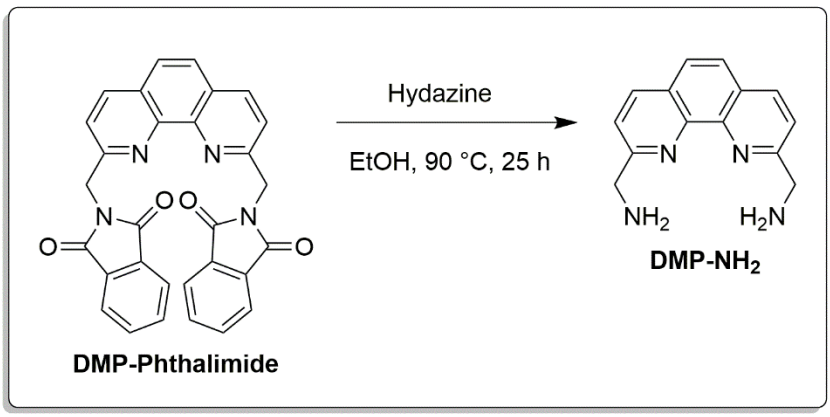

Figure 4-14: Synthetic route to DMP-NH_2.

In the next step, **DMP-Phthalimide** was reacted to become **DMP-NH_2** by means of hydrazine, as depicted in figure 4-14. After letting the reaction mixture cool down to r.t., 6 N HCl was used to acidize to a pH value of 1. The solution was then stirred at 100 °C for one hour and the solvent was evaporated, accordingly. A pale yellow solid was obtained and alkalized to a pH value of 14 by an aqueous 50 % KOH solution. The resulting orange-yellow solution was extracted with $CHCl_3$ and the

combined organic phases were dried over $MgSO_4$. The ^{1}H-NMR spectrum reveals a mixture of species, while an IR spectrum showed a broad potential δ NH bending vibration at ca. 1600 cm^{-1} and a broad signal at 3250 cm^{-1} that may be signed to v NH vibrations. Since C=C and OH vibrations are responsible for the same set of signals, mass spectrometry was applied to resolve this issue, which delivers no assignable signals. A test reaction to gain an azo dye with $NaNO_2$/HCl and 1-naphtol/KOH resulted in a brown precipitation. According to comparable compounds such an coloration is to be expected.[164] A reference reaction between 2-aminofluorene with 1-naphthol under the above described conditions showed a violet coloration. This may indicate the exclusion of systematic errors during synthesis. In addition, the conversion with iodomethane in the presence of ammonium hydroxide remained unsuccessful indicating an unsuccessful reaction. Except for the weak proof of a brownish precipitate during azo coupling, there were no signs indicating the positive synthesis of the target molecule.

Since the phthalimide is a good leaving group, an introduction of a phosphine substituent by means of a S_N2 type reaction was conducted. Therefore, diphenylphosphane was deprotonated by *n*-BuLi to give the characteristic orange colored lithium diphenylphosphide in THF at – 80 °C, which was added to a **DMP-Phthalimide** containing solution resulting in a black solution. A *in situ* NMR sample was prepared, showing most likely triphenylphosphane at – 7.3 ppm and tetraphenyldiphosphane at – 26.7 ppm.[165,166] The latter may be a coupling byproduct as proposed by literature.[167] The main signal is observed at – 15.0 ppm, while additional signals were detected at – 15.9 ppm, – 21.8 ppm and – 22.4 ppm, which all lay in the range of comparable target molecules.[161,165,166] The sample was exposed to air resulting in two typical signals for phosphorous oxides at 28.7 ppm and 30.7 ppm.[165] In addition, a pale brown precipitation was observed, which shows that only the signals – 15.9 ppm, – 21.8 ppm and – 22.4 ppm remained unaltered indicating an air sensitivity of the main product. Then $[Cu(MeCN)_4][BF_4]$ was added and the solution turned more brownish und brightened. A ^{31}P-NMR spectrum of this solution shows a single signal at – 14.9 ppm. This may be a sign for a potential equilibrium of different phosphorous species in solution, which is then broken by coordination to copper. Crystallization approaches and additional analytic delivered no additional insights.

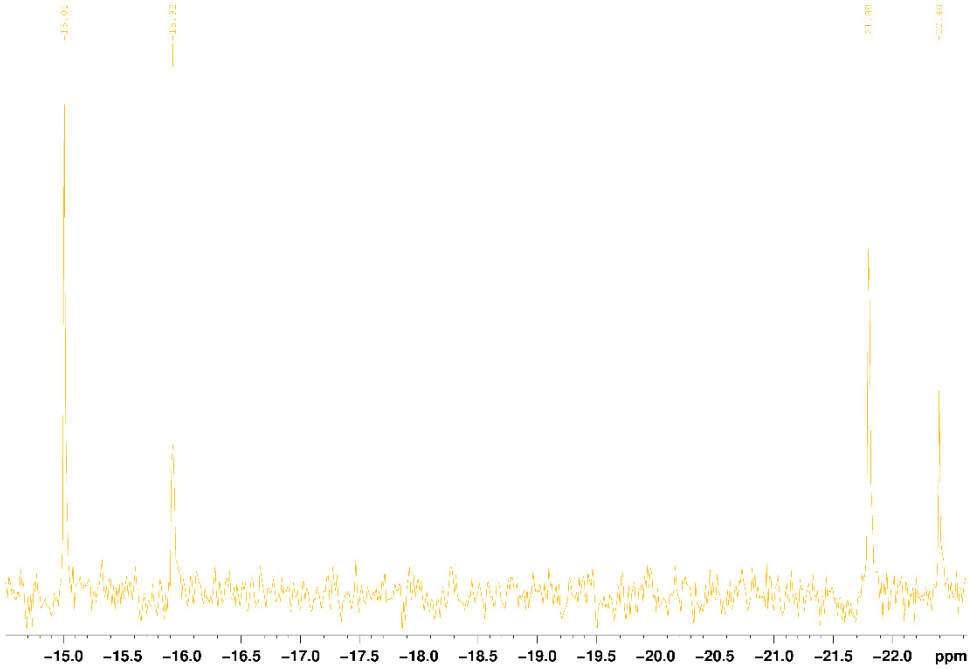

Figure 4-15: ***In situ*** **^{31}P-NMR spectrum of the reaction mixture to synthesize DMP-PPh$_2$.**

The ligands **DMP-Cl**, **DMP-Br**, **DMP-I**, **DMP-Cl$_3$**, **DMP-Phthalimide** and the potentially non-innocent ligands **DMP-OH** and **DMP-OOH** were synthesized. Unfortunately, the attractive phosphine-containing **DMP-PPh$_2$** could not be obtained despite literature instructions. The mono-halogenated set of ligand series is delivering photoactive copper(I) complexes in which altered properties throughout this row will be analyzed. In addition, the non-innocent ligands could be able to stabilize higher copper oxidations states, which is necessary for water oxidation catalysis.

4.1.2.1 UV/VIS absorption spectroscopy of DMP-X-based ligands

Elucidating the electronic structure of the synthesized ligands, UV/VIS spectra were recorded and compared to TD-DFT calculations. Since the halogen analogous ligands exhibit – as in the **DMP** case– two main signals, the electronic spectra of **DMP**, **DMP-Cl**, **DMP-Br** und **DMP-I** were found to be dominated by π-π* transitions, as depicted in figure 4-16. Additionally, this is consistent with literature[120] and verified by TD-DFT calculations. These signals and especially those to lower energy are not symmetrical indicating – consistent to calculations – a set of transitions. One contributing factor for this property is that halogen p-orbitals give rise to additional transitions and are mixing with π-π* transitions, as depicted in figure 4-17. **DMP** exhibits four times more intensity than the halogenated ligands, which is consistent with TD-DFT calculations. The halogen atoms decrease the transition dipole moment of the π-π* transitions resulting in lower intensities.

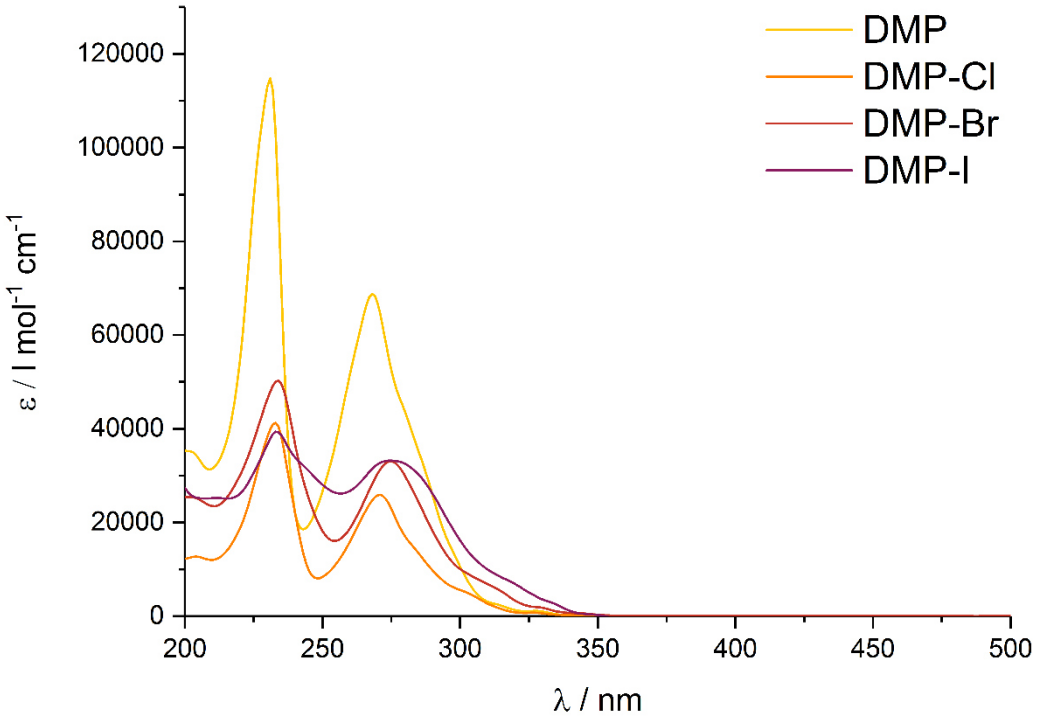

Figure 4-16: UV/VIS spectra of ligands DMP, DMP-Cl, DMP-Br and DMP-I.

The n-σ* of halogen atoms are most likely not visible as individual signal, since the signal intensity is too low (≈300 L · mol^{-1} · cm^{-1}).[166]

A general trend is the peak shifting to higher wavelengths with increasing period of the halogen atom, although the effect within the series of DMP-X ligands is weakly

pronounced, as depicted in table 4-2. Calculated signals exhibit the same behavior, which can be seen exemplarily when comparing the highest energy signals in figure 4-48. This indicates, that the halogen substitution has only a small impact of the conjugated π system.

Table 4-2: UV/VIS absorption data of DMP, DMP-Cl, DMP-Br and DMP-I.

Signal	DMP	DMP-Cl	DMP-Br	DMP-I
λ_{max},1 [nm]	231 (114798)	233 (41234)	234 (50269)	233 (50064)
λ_{max},2 [nm]	268 (68771)	271 (25909)	275 (33062)	275 (33213)
Molar attenuation coefficients [l·mol^{-1}·cm^{-1}] are shown in brackets.				

Experimental and calculated spectra of ligand **DMP** exhibit two main signals, which are shifted to higher energies in case of the calculated spectra, but both are showing a comparable peak distance deviating by ca. 5 % indicating just that shift. Calculations show π-π* transitions as the dominating absorption throughout the spectrum. The

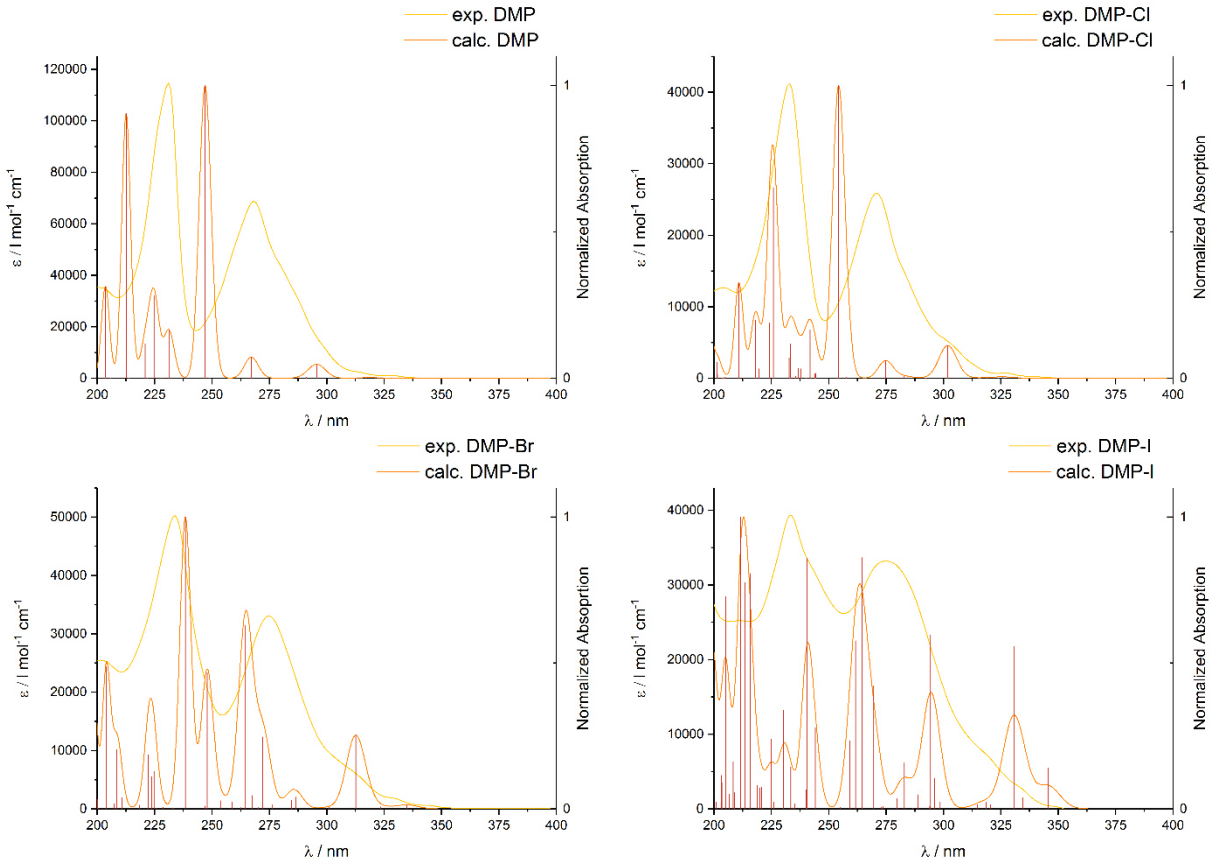

Figure 4-17: Experimental and calculated UV/VIS absorption spectra of DMP-X ligands.

low-intense signals to higher wavelength are most likely responsible for the broadening in the experimental spectrum. The same behavior is observable for **DMP-Cl**, but in addition the amount of contributing transition are increasing due to contributions of chlorine p-orbitals between 255 nm and 225 nm. In accordance with the experimental spectra, the calculated spectra of **DMP-Br** and **DMP-I** show an enlarging amount of transitions and intensity. In the range of 275 nm and 205 nm, the bromine p-orbitals are involved in a significant ratio up to 50 % whether in a donor or an acceptor orbital. Iodine p-orbitals are involved in nearly every transition of **DMP-I** throughout the spectrum, since the contribution over HOMO to HOMO-6 is >37 % for each molecular orbital. In addition, this is the only case were the halogen p-orbitals contribute in a distributed, smeared out manner over a large set of HOMO and LUMO states near the HOMO-LUMO gap.

Three main signals are dominating the UV/VIS spectra of the DMP-X-based ligands, which all originate as π-π^* transitions, as indicated by literature and TD-DFT calculations. The halogenation leads to a significant drop in absorption intensity leading to comparable molar attenuation coefficients within the series. The heavier the halogen atom, the more the halogen p-orbitals into come into play complicating the spectra. The spectroscopic data of the ligands will later be used as reference for the subsequent copper(I) complexes.

4.1.2.2 Steady state luminescence spectroscopy of DMP-X-based ligands

Emissive excited states can be probed by steady state luminescence spectroscopy in order to get deeper insights into the photoemission properties. The respective UV/VIS absorption spectra are always shown together with the acquired luminescence plots in order to provide a better overview.

In the case of the luminescence spectra of **DMP**, one broad band between 340 nm and 440 nm is observed, as can be seen in figure 4-18. Within this band, several features are visible. The most intense signal at 366 nm is followed by a less intense peak at 383 nm with a shoulder at 403 nm for all measured wavelengths, which is conform with literature.[168,169,170] The signal to highest energy involves most likely singlet n-π* transitions of the nitrogen lone pair to delocalized, phenanthroline π*-type orbitals, while lower energy signals are given rise by singlet π-π* transitions of the phenanthroline.[170,171] Excitation at higher wavelengths than depicted does not lead to a change of the band pattern but results in decreasing signal strength, since the irradiated energy is too low for these excitations.[169] Interestingly, the emissive states were populated comparably regardless of excitation at 231 nm or 280 nm, most likely because of the close proximity of these excited states.[170]

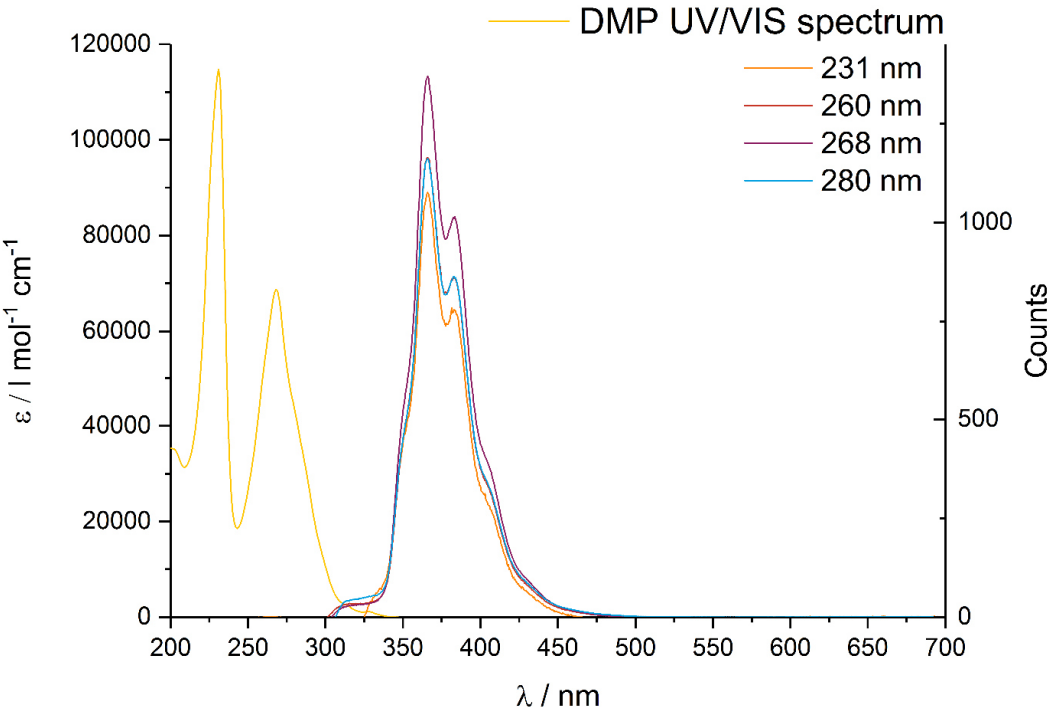

Figure 4-18: Steady state luminescence spectra of DMP.

Steady state spectra of the halogenated ligands show the pattern discussed before with no significant deviations, as can be seen in figure 4-19. In comparison to the unsubstituted **DMP**, an additional and intense feature was detected between 430 nm and 640 nm. This broad band shows two distinct peaks at about 491 nm and 531 nm throughout the series. Although no additional feature is detected in the UV/VIS absorption spectra, this band is assigned to n_x-π* transitions originating from halogen lone-pair electrons. Possibly, the corresponding absorption is at higher energy than the solvent cut-off as indicated by the mirror image rule. The excitation behavior in the case of **DMP-Cl** is in accordance with this hypothesis, since the intensity of the n-π* / π-π* block is increasing with decreasing excitation energy.

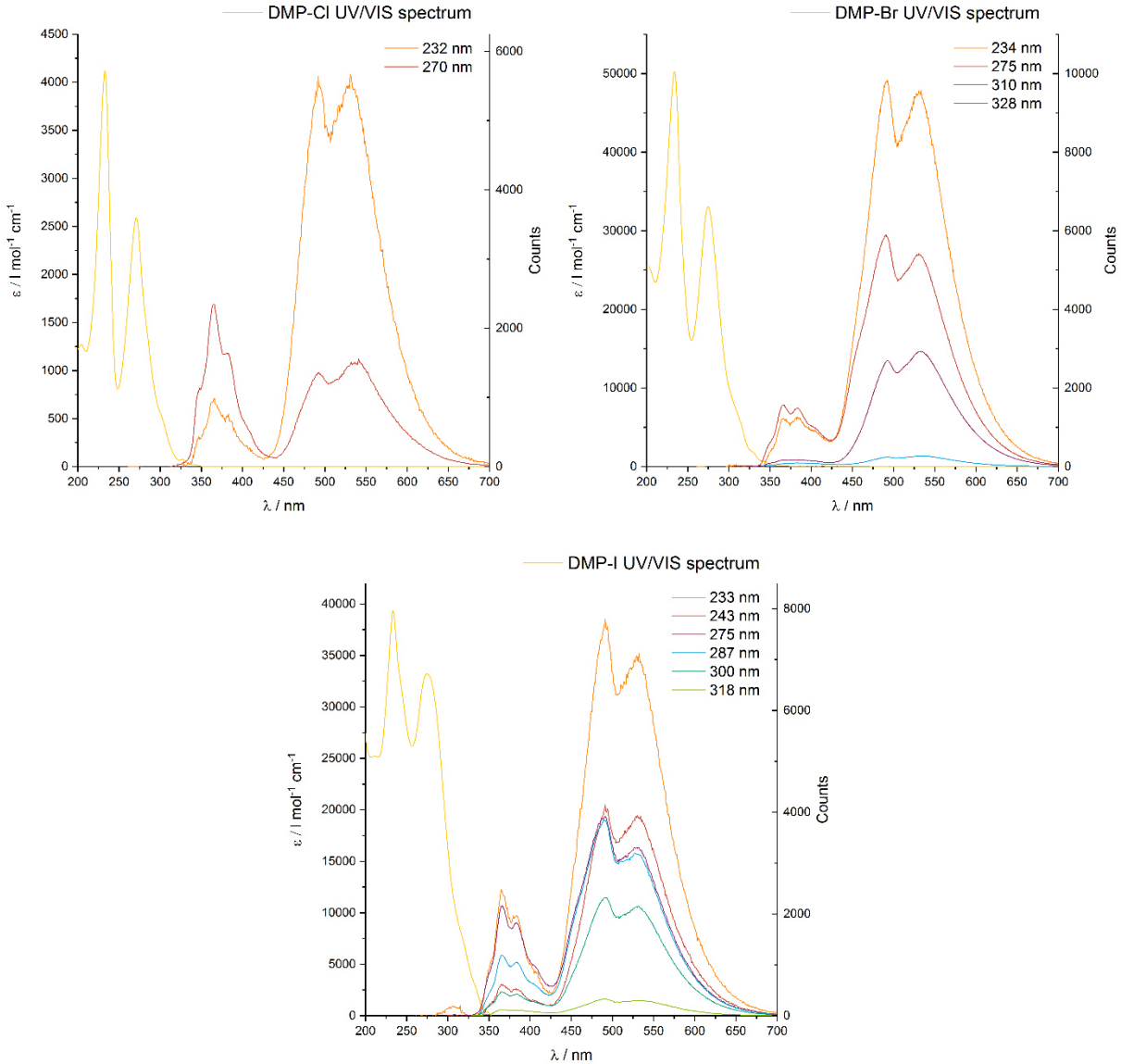

Figure 4-19: Steady state luminescence spectra of DMP-Cl (top left), DMP-Br (top right) and DMP-I (bottom).

This is also the case for the **DMP-Br** and **DMP-I**, where the intensity of the n-π* / π-π* emission is neglectable at excitation wavelengths higher than 300 nm, but luminescence of the new feature does also decrease in intensity. Despite the different halides, only slightly shifts for the postulated n_x-π* transitions are observable in the case of **DMP-Br** and **DMP-I** (table 4-3). Different intensities of the two n_x-π* transitions, signals shifts and the absence of this pattern in the **DMP** case exclude clearly the luminescence generation from an impurity. An exciplex formation is also not likely, since the sample concentrations were as low as 10^{-5} M.

Table 4-3: Proposed assignment of steady state luminescence signals of DMP-X-based ligands.

Signal	DMP	DMP-Cl	DMP-Br	DMP-I
π* ← n_N [nm] shoulder	351	348	346	349
π* ← n_N [nm]	366	365	366	365
π* ← π [nm]	383	383	384	384
π* ← π [nm]	403	404	402	403
π* ← n_X [nm]	-	493	491	491
π* ← n_X [nm]	-	538	531	531

Significant differences can be seen in the steady state luminescence spectra between **DMP** and the halogenated ligands. DMP only exhibits, what is assigned to be n_N-π* and π-π* transitions. When introducing halogen atoms another signal set is observed at higher emission energy, indicative of n_x-π* transitions, which differ slightly in shape and wavelength.

4.1.2.3 IR spectroscopy of DMP-X-based ligands

In this chapter, ligands are characterized and compared by IR spectroscopy with the aim to differentiate and identify these ligands most time-efficient. All spectra were additionally calculated to assign the correct vibrations at a TPSS/def2-TZVP level of theory for ligands and TPSSh/def2-TZVP level of theory for complexes. Since the carbon scaffold is constant, the IR spectra will be shown in a limited range to focus on the different substituents excluding the comparable v C-H_{Aryl} und v C-H_{Alkyl} signals, although the v C-H_{Alkyl} for instance exhibits shifts from 3035.6 cm^{-1} (3041.5 cm^{-1}) for **DMP** via 3039.5 cm^{-1} (3057.6 cm^{-1}) for **DMP-Cl** and 3031.8 cm^{-1} (3078.7 cm^{-1}) for **DMP-Br** to 3037.5 cm^{-1} (3087.6 cm^{-1}) for **DMP-I**. The calculated values are given in brackets.

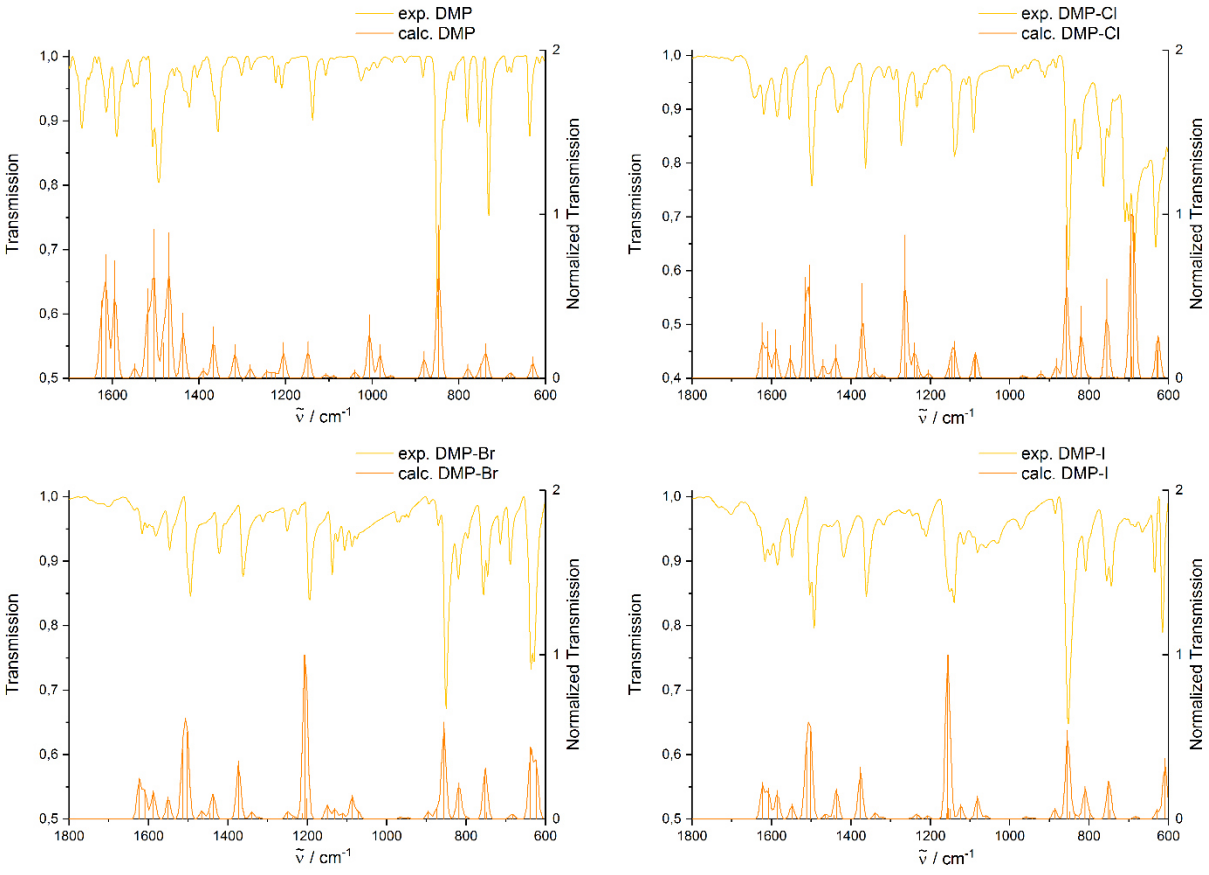

Figure 4-20: Experimental and calculated spectra of DMP-X based ligands.

For the halogenated ligands, it can be stated that the ligand spectra differentiate only the isolated C-X stretching vibration as expected verifying the possibility of distinguishing the ligands by IR spectroscopy. In addition, the shift decreases with increasing period of the halogens, as expected for heavier atoms.[166,172,173]

Table 4-4: Comparison of C-X vibrations in halogenated ligands.

Ligand	Vibration	$\tilde{\nu}_{exp}$ [cm^{-1}]	$\tilde{\nu}_{calc}$ [cm^{-1}]	$\tilde{\nu}_{lit.}$ [cm^{-1}][166,172,173]
DMP-Cl	ν_{as} C-Cl	687	688	830 - 560
DMP-Br	ν_{as} C-Br	636	638	680 - 515
DMP-I	ν_{as} C-I	615	609	610 - 485

A differentiation of DMP-X ligands can be realized based on IR spectroscopy, since the isolated ν_{as} C-X vibration can be assigned in each case. The concordance with computational frequency calculations is remarkable, easing the correlation between theory and experiment.

4.1.3 Macrocyclic phenanthroline-based ligands

In order to synthesize macrocyclic ligands, which are able to strain the coordination sphere according to the *entatic state* principle, the initial synthetic route was planned with a C-C coupling reaction as key step, as described in figure 4-21. Therefore, two mayor target molecules were selected, namely **Phen-Br** and **DMP-B(OH)$_2$**, which should undergo coupling in a *Suzuki* reaction. Especially the dibromo compound **Phen-Br** is a versatile species for further coupling approaches, since *Grignard* or *Stille* reagents could be preparable.

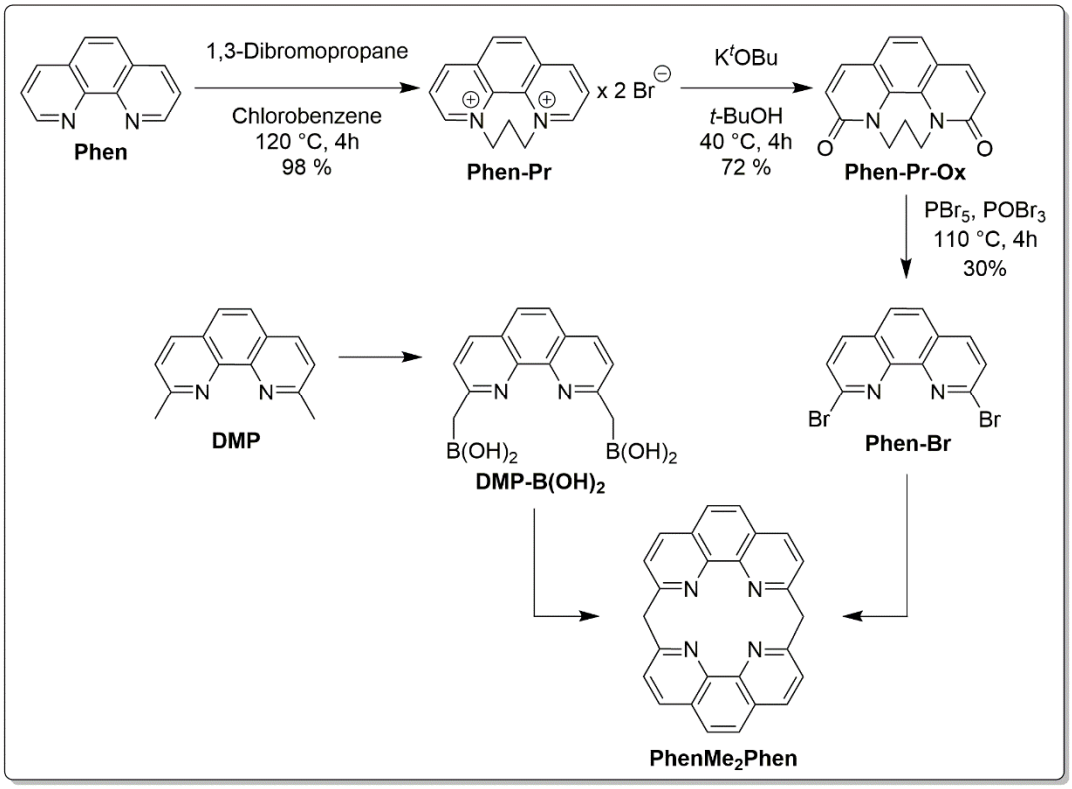

Figure 4-21: First synthetic route towards PhenMe$_2$Phen.

Synthesis of propane protected phenanthroline **Phen-Pr** was easily achieved in nearly quantitative yields according to *Jiang* et al. published in 2012.[174] Although the next step is known in literature[174], oxidation of the activated species **Phen-Pr** by potassium *t*-butoxide and subsequent aqueous treatment to the dione **Phen-Pr-Ox** was connected with a high amount of byproducts, which were hard to separate. By means of flash chromatography 12 % of the used crude product, which were obtained by extraction with chloroform could be gained as a clean fraction.

Synthesis of **Phen-Br** with phosphorus pentabromide in phosphorus oxibromide was successful.[174] A substitution of phosphorus oxibromide with dry chloroform as solvent led to no reaction. Surprisingly, only small scale neat reactions between the dione **Phen-Pr-Ox** and phosphorus pentabromide gave the product in 30 % yield and acceptable purity.

The other key compound **Phen-B(OH)$_2$** should be prepared by deprotonation of 2,9-dimethyl-1,10-phenanthroline **DMP** und subsequent conversion with trialkyl borate, but this reaction failed.

Due to this problems, the synthesis strategy was changed to a direct way of coupling, as specified in figure 4-21. **Phen** and **DMP** was reacted with itself – initially one sided – based on publications of *Abruña* et al.[175] and *Ziessel* et al.[176], respectively. In the first case a linkage of **phen** was achieved by LDA with diiodomethane as bridge building block, resulting in a not isolatable but by means of ESI MS detectable target species **7**. Oxidative coupling of **DMP** with LDA and bromine led to comparable results, in which only ESI MS proofed the existence of the molecule **DMP-DMP**.

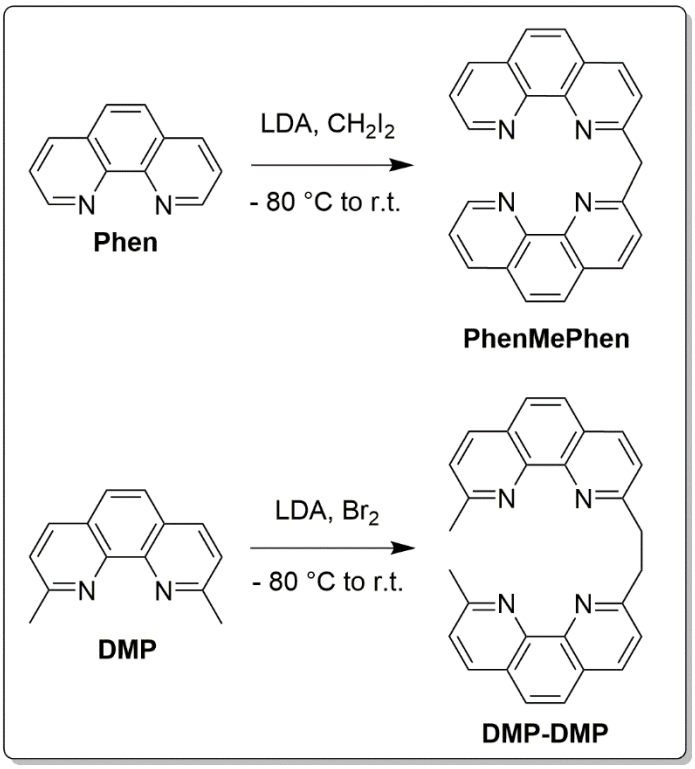

Figure 4-22: Direct coupling approaches of 1,10-phenanthroline and 2,9-dimethyl-1,10-phenanthroline.

Because the insufficient results could be attributed to the type of chemical reaction, the deprotonation behavior was investigated. Therefore, **phen** and **DMP** were applied in screening procedures with four different bases, namely LDA, *n*-BuLi, potassium *t*-butoxide and lithium bis(trimethylsilyl)amide. D_2O was used to quench the reaction in order to get insight into the initial deprotonation position. ^1H and ^{13}C NMR spectra revealed a large amount of by-product and reagent itself. It can be stated that the direct

deprotonation of **DMP** was not successful.

Another shortcut to macrocyclic phenanthrolines was published by *S. Ogawa*[177] in 1977. He postulates the formation of **PhenMe$_2$Phen** by thermal reaction of **DMP** with 2,9-dichloro-1,10-phenanthroline under TGA surveillance, which showed the appropriate hydrogen chloride evolution during the reaction. The analogous reaction of **DMP** with 2,9-dibromo-1,10-phenanthroline **Phen-Br** should then lead to the same ligand **PhenMe$_2$Phen** under formation of hydrogen bromide, as described in figure 4-23. An acidic gas was detected, although mass spectra did not detect the target molecule.

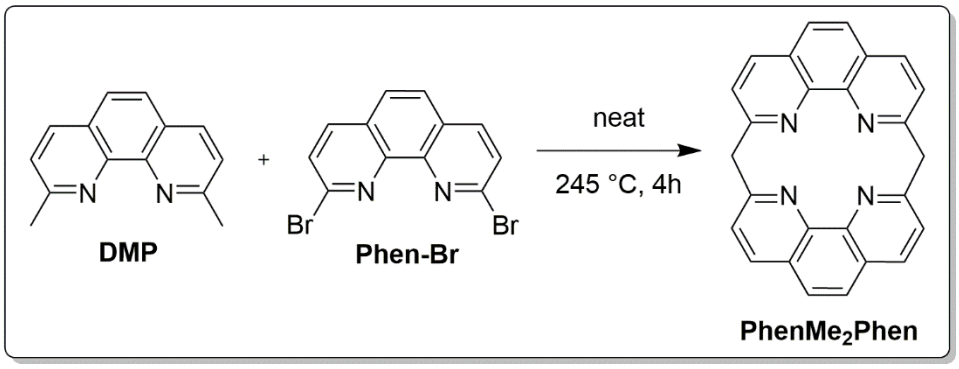

Figure 4-23: Direct coupling of DMP with Phen-Br.

Due to the inefficient direct synthesis of macrocyclic phenanthroline ligands, the synthesis strategy was turned around, as can be seen in figure 4-24, generating the cycle first and then forming the phenanthroline afterwards. A suitable precursor compound was tetraazacyclotetradecine **TACTD**, which then should be converted with Meldrum´s acid to a tertiary amine species. Subsequent heating to reflux in diphenyl ether should lead to the tetraone species resulting in the linked phenanthroline species by establishing aromaticity after substitution of both ketones by halogen atoms.

As depicted, the **TACTD** could be obtained either with or without a copper ion as structural template, while the last method was already described in literature.[178] The first approach led to a mixture of reagents and only a small amount of the target **TACTD**, which is contaminated high amount of with reagents and the one-side-opened target cycle, indicated by ^{1}H-NMR analysis, since a diaminobenzene signal set to 1,3-dibromopropane ratio of 3:2. EI mass spectrometry supports this results showing reagent signals, signals for the one-side-open **TACTD** at 256.16 m/z (calc. 256.17 m/z), the **TACTD** at 296.16 m/z (calc. 296.20 m/z)a That is the reason

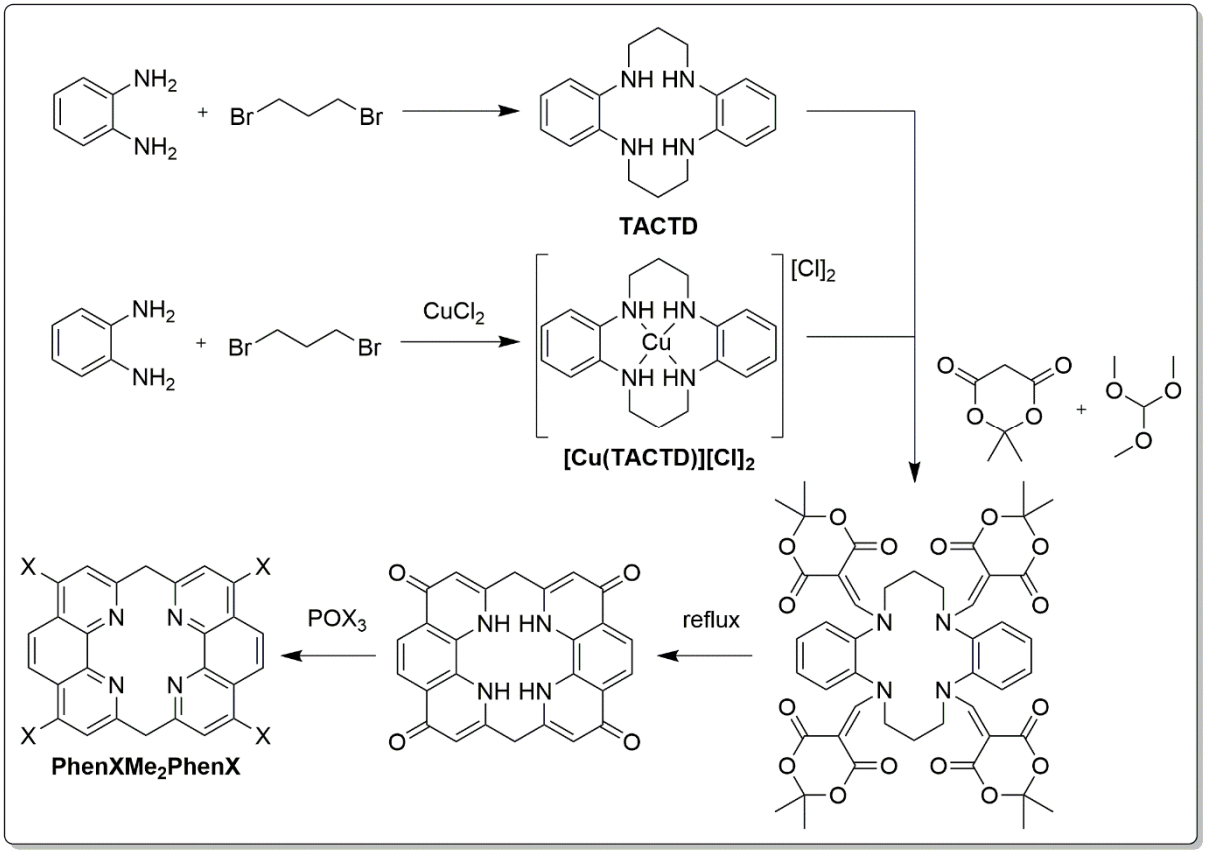

Figure 4-24: Synthetic route to coupled phenanthroline via a tetraazacyclotetradecine TACTD intermediate.

why a template procedure was chosen in order to increase the yield. Surprisingly, this reaction did not deliver any yield at all according to NMR and mass spectrometry.

A similar synthetic strategy like in figure 4-24 was applied in the following route, which starts with a dipyridine based system, as depicted in figure 4-25. This synthesis is related to a literature known procedure by *Schneider* at al..[179] The di(pyridin-2-yl)methane is accessible whether a *Wolff-Kishner* reaction of the corresponding ketone or by coupling 2-fluoropyridine with 2-methylpyridine by means of *n*-BuLi. The first led to detectable product ions in the mass spectra, although a diverse other species are visible. The latter reaction has to be performed again, but the first mass spectrometry results showed no molecule isotope peak. In both cases NMR spectra revealed a large amount of by-products. That is the reason why this route was not further pursued, but this synthetic approach will be further explained here. After a *Tschitschibabin* conversion to the dibromide species, the dialdehyde compound can be obtained by conversion with LDA and DMF subsequently. Tosylhydrazine is then reacted with the dialdehyde to give the tosylhydrazone, which undergoes a ruthenium-based catalytic

coupling reaction. Finally, another coupling reaction would be performed for C-C bond formation to phenanthroline systems.

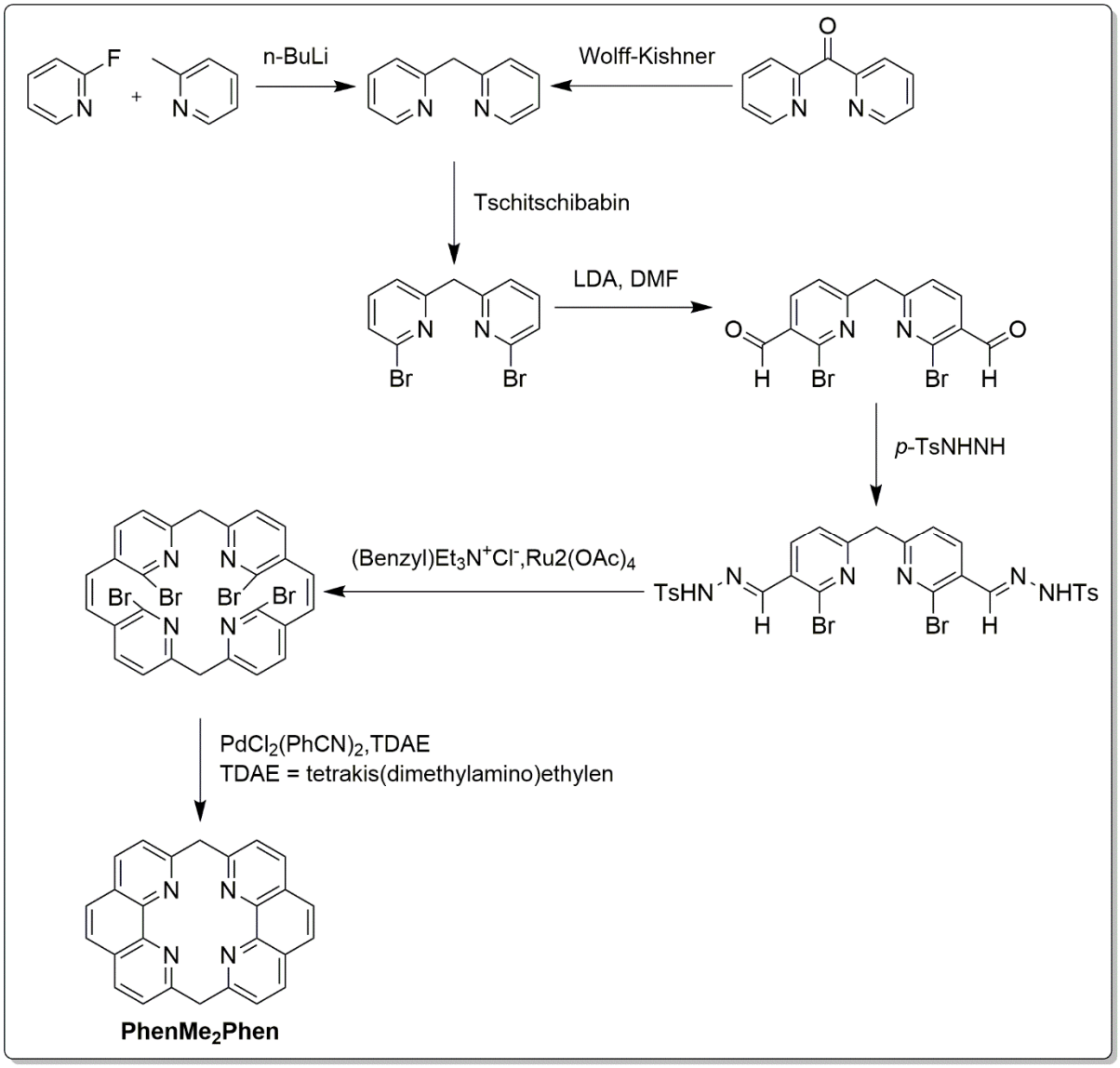

Figure 4-25: Syntheses of PhenMe$_2$Phen based on di(pyridin-2-yl)methane.

Macrocycle **PhenC(O)OCPhen** was synthesized in a one pot, two step synthesis. First **DMP-OOH** is converted in sulfonyl chloride as solvent to its acid chloride as can be seen in figure 4-27. One acid oxygen atom attacks the sulfur atom and chloride functions as a leaving group. After a rearrangement, a nucleophilic attack of chloride takes place and the resulting tetrahedral state decomposes under elimination of SO_2 and HCl.[180] The excess thionyl chloride is distilled off under precipitation of a yellow solid, which was dissolved in 40 ml dry THF (0.02 M).

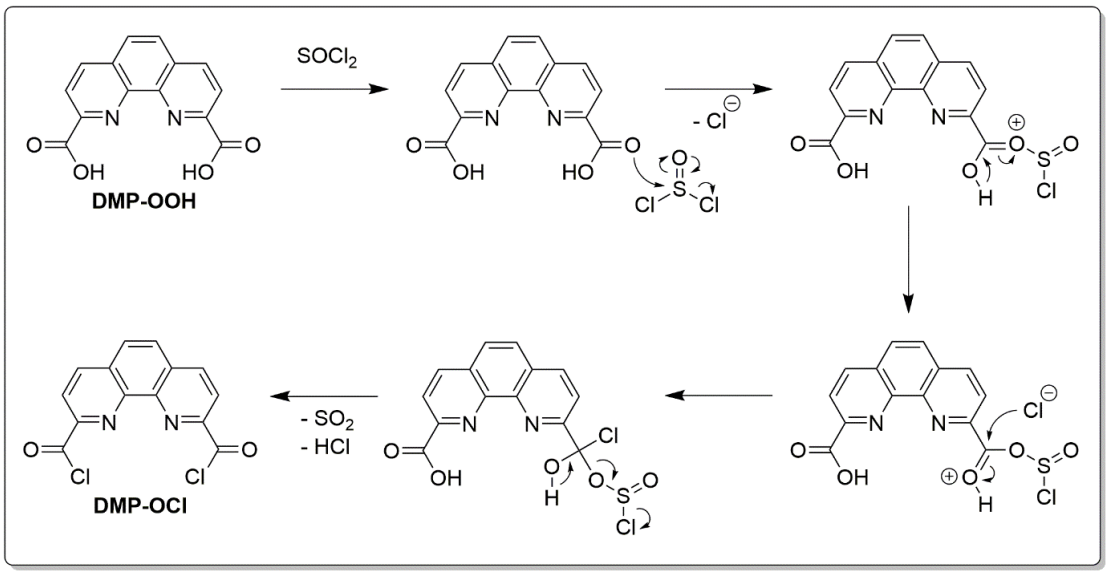

Figure 4-27: Proposed reaction mechanism of DMP-OOH with $SOCl_2$.

In the next step **DMP-OH** was suspended in dry THF/MeCN ($3 \cdot 10^{-3}$ M) and added by a syringe at ca. 10^{-5} mol/ml speed to ensure low concentration thus oppressing polymerization reactions. The proposed reaction mechanism is depicted in figure 4-26 and involves a nucleophilic attack of to alcohol oxygen. The resulting tetrahedral transition state decomposes under elimination of hydrogen chloride. This reaction takes place twice to give **PhenC(O)CO_2Phen**.

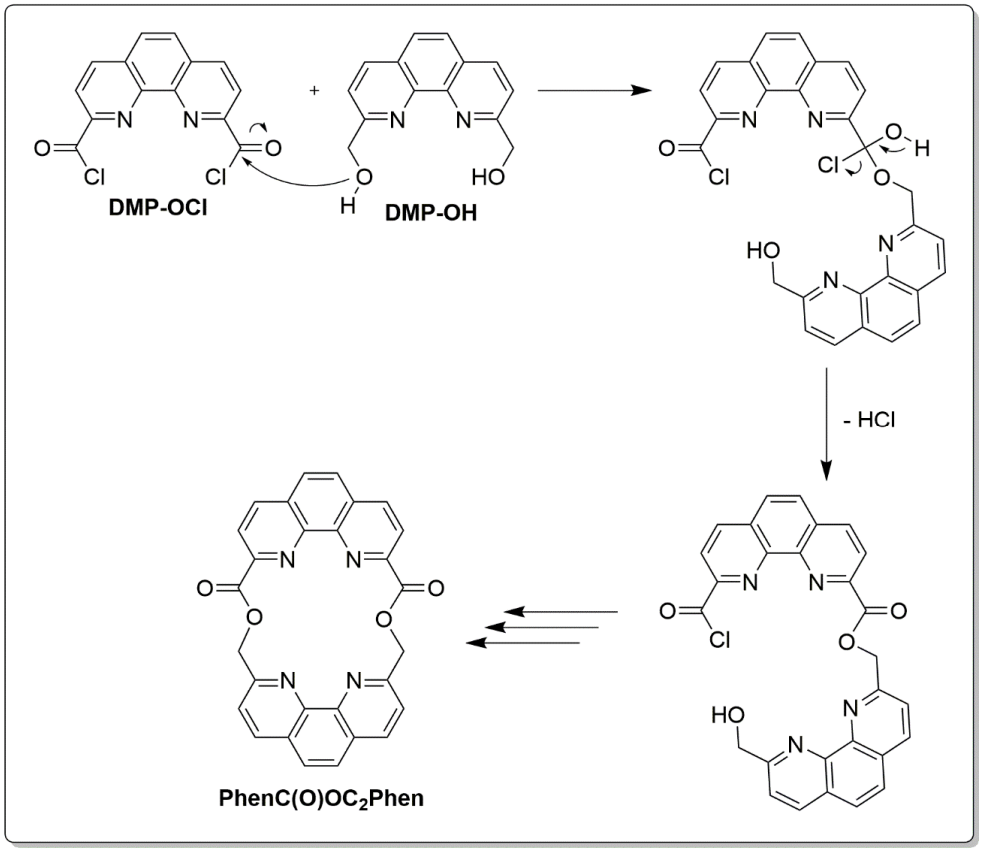

Figure 4-26: Proposed mechanism for esterification of DMP-OCl and DMP-OH.

The pale orange solution was stirred overnight, where the color intensified. After filtration a small amount of orange-red solid –in the following referred to as S1 – was obtained, which became paler when dried. The solvent of the filtrate was evaporated, washed with water, with MeOH, with ethyl acetate and diethyl ether. The yellow methanolic filtrate was evaporated because a significant amount of solid was extracted resulting in solid S2-MeOH. The solid residue S2, which was insoluble in all mentioned solvents, was collected, too. TLC analysis was inconclusive, since the substances smeared over a large range in all tested eluent mixtures on silica plates.

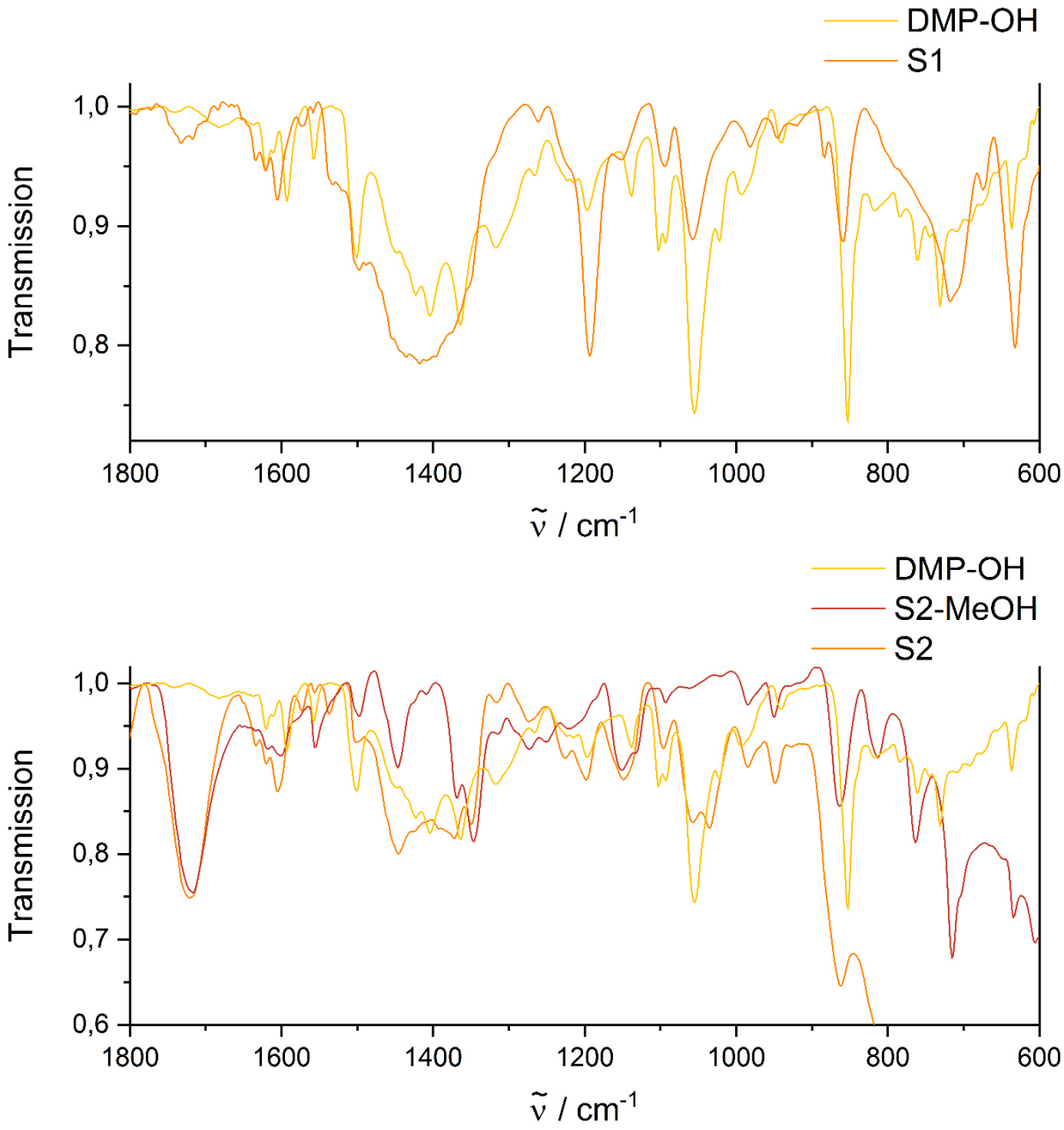

Figure 4-28: IR spectra of obtained solids after cyclisation of DMP-OOH and DMP-OH.

Since esters are identified with ease in IR spectra, ATR-IR spectroscopy was utilized to identify the target substance (figure 4-28). The resulting ester should have an intense v C=O vibration between 1750 cm^{-1} and 1715 cm^{-1}.[172,173] Additionally, a v_{as} (C-O-C) and v_{as} (O-CH_2-C) must be detected around 1250 cm^{-1} and 1050 cm^{-1} respectively to verify a ester structure element.[172] IR analysis of the pale orange-red solid S1 reveals an insignificant intensity for the spectral range of v C=O valance vibrations around 1700 cm^{-1} indicating that whether **DMP-OOH** nor DMP-OO-DMP are present. In fact, when overlaying the sample spectrum and the **DMP-OH** spectrum all signals are represented. This shows, that the sample was rather consisting of **DMP-OH** only.

The solid S2 from the yellow methanolic filtrate S2-MeOH was analyzed by IR spectroscopy showing an intense v C=O vibration was observable at 1716 cm^{-1}. This signal is asymmetric and broad in shape suggesting multiple different C=O fragments. In addition, signals at 1346 cm^{-1} and 1151 cm^{-1} indicated a successful synthesis of an ester species. Here, the thesis of more than one species is confirmed by detecting broad peaks or signals with small energetic differences.

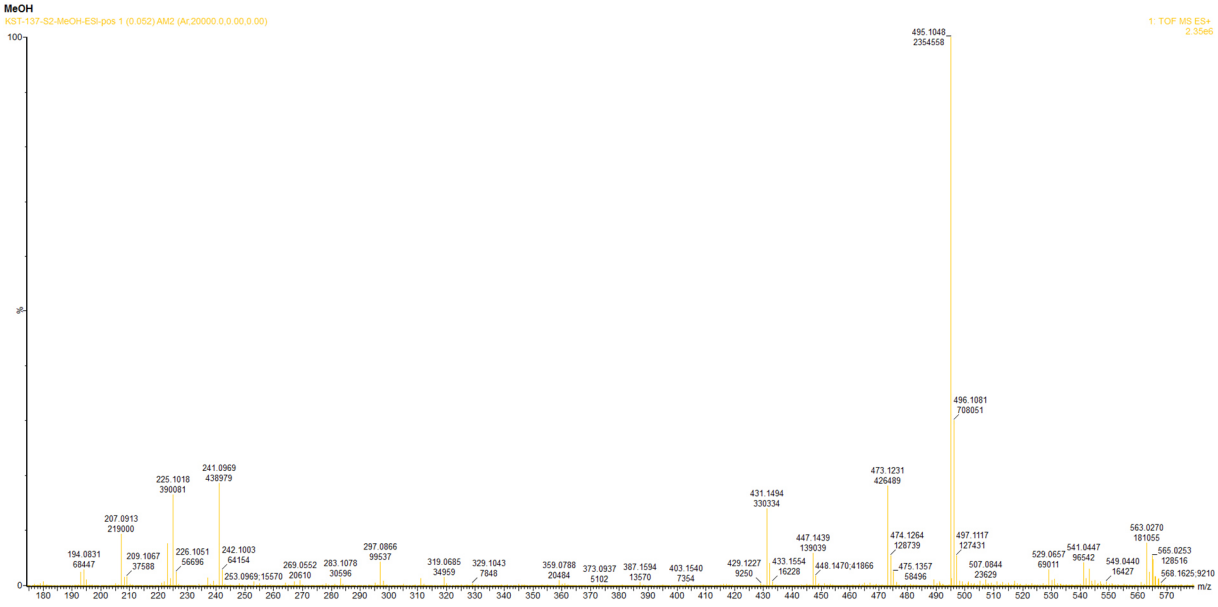

Figure 4-29: ESI MS spectrum S2 of PhenC(O)CO_2Phen in MeCN.

ESI MS was conducted (figure 4-29) and verified the successful coupling product at 495.10 m/z (calc. 495.11 m/z) as sodium adduct and at 473.12 m/z (calc. 473.12 m/z) as [M+H]. A direct decomposition product was identified 431.15 m/z (calc. 431.15 m/z) as [M-CO_2+3H], which disconnects one side of the macrocycle. The ion at 225.10 m/z (calc. 225.10 m/z) can be assigned to [**DMP-OH**–OH+2H], which can be a result of

further decomposition of the opened macrocycle. Compared to the ESI MS spectra of **DMP-OOH** and **DMP-OH**, no proof was found for presence of **DMP-OOH** in the sample, while [**DMP-OH**+H] was detected signal at 241.10 m/z (calc. 241.10 m/z) was observed.

The remaining solid after washing S2 exhibits the same v C=O vibration in absorption and shape. Most of the signals were also represented by the spectrum of S2-MeOH although broadening. Two differences are striking. Between 1346 cm^{-1} and 1446 cm^{-1} – in the spectral range of v_{as} (C-O-C) – only a broad peak with three main spikes is observable and at around 1045 cm^{-1} at least to signals nearly fully merged arises, which were not present in S2-MeOH but in **DMP-OH**. ESI MS analytic of S2 shows nearly no [M+H] ions, as depicted in figure 4-29. The macrocycle was detected additionally unassigned heavier ions, which are identical to the measurement of S2-MeOH.

Performing MPLC did not lead to a significant increase in purity, hence it was tried to separate the macrocycle by complexation und successive crystallization. Tetrakis(acetonitrile)copper(I) tetrafluoroborate and the macrocycle were dissolved in DCM, which resulted immediately in a dark purple / wine red solution. A purple precipitation was then observed, which was filtered off. During the filtration procedure the joint broke exposing the solid most likely to air. It was then tried to gain crystalline material out of the brownish orange filtrate by diethyl ether diffusion technique. After four days, the solution became less colorful, more brownish and a fine precipitate was observable. 14 days later, the solution was turquoise and the filtered off solid became grey and was not soluble in regular solvents except MeOH. An NMR spectrum shows only weak, not assignable aromatic signals.

Although many coupling approaches were presented, finally only one route let to a macrocyclic phenanthroline compound. The most promising **PhenC(O)CO_2Phen** was synthesized and identified. Pyridine-based diazapyridinophane could be built up by a straight forward literature-known procedure. New substitution patterns of the alkyl amine functions were obtained.

4.2 Phenanthroline-based Cu(I) complexes as photosensitizers

4.2.1 DMP-X-based Cu(I) complexes

4.2.1.1 Synthesis of DMP-X-based Cu(I) complexes

The synthesis of homoleptic copper(I) complexes was realized by transferring a dry solvent into a vessel of ligand and copper(I) precursor. Then, a significant solvent coloration is observable indicating the success of complexation. As precursor tetrakis-(acetonitrile)copper(I) tetrafluoroborate was used, which possesses a weak coordinating anion ensuring a lesser amount of quenching anion coordination to copper. Due to the weak coordinating MeCN ligand, this copper(I) compound is air sensitive and was manipulated under inert gas atmosphere.

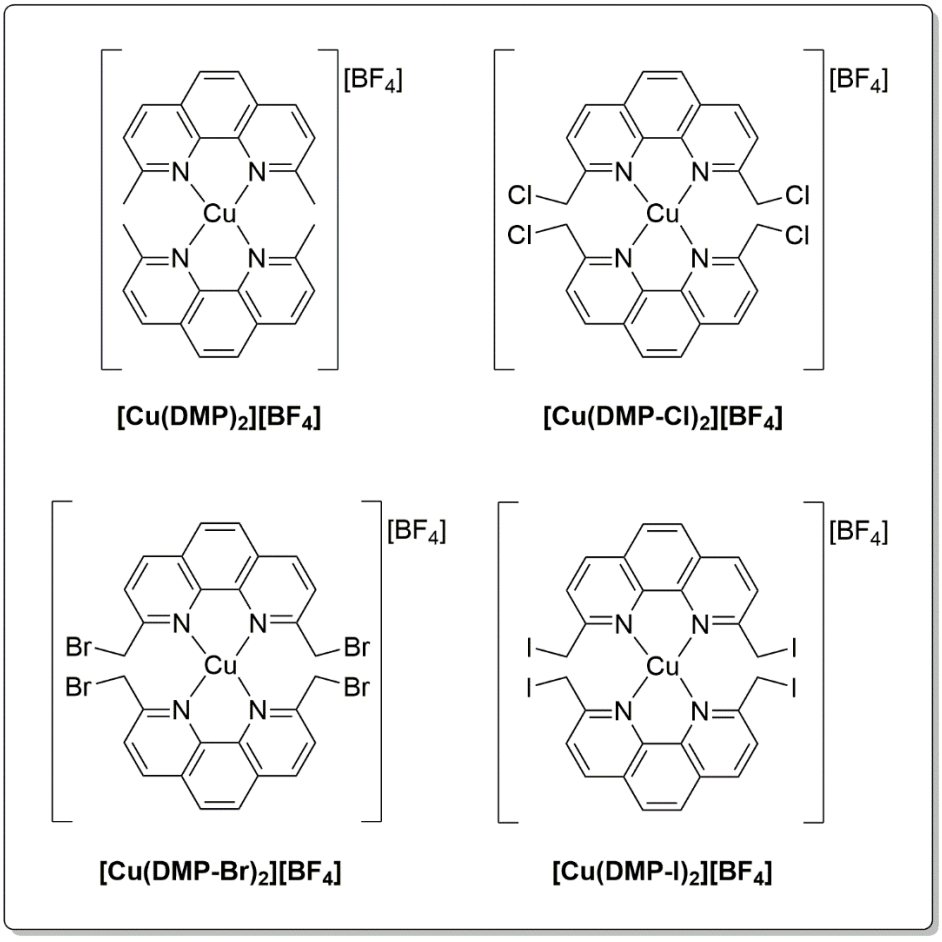

Figure 4-30: Schematic representations of $[Cu(DMP)_2][BF_4]$ and $[Cu(DMP\text{-}X)_2][BF_4]$ complexes.

A series of $[Cu(DMP\text{-}X)_2][BF_4]$ complexes were synthesized and are depicted in figure 4-30. Additional copper(I) complexes with other anions were crystalized by chance due

to impurities of the originally used copper(II) precursors and will be mentioned at the end of this chapter.

In a general synthesis procedure, ligand and tetrakis(acetonitrile)copper(I) tetrafluoroborate was transferred to a flask under inert gas conditions. Dry solvent was added until a homogenous solution was observed. This solution was filtrated by means of Schlenk technique and a crystallization was initiated with dry diethyl ether. The resulting crystals were filtered off without inert atmosphere, since the tetra-coordinated copper(I) compounds were stable at r.t. and in air as solid and in solution as verified by dissolution, purging with air and recrystallization.

Figure 4-31: Crystals of $[Cu(DMP)_2][BF_4]$.

In order to compare the impact of 2,9-dihalogen substitution on the photo-properties, **$[Cu(DMP)_2][BF_4]$** is used, which is the major model and reference compound investigate photo-physical behavior upon light excitation in copper chemistry.[181,182] The complexation reaction was performed in DCM, which turned orange-red immediately after contact with ligand and copper(I) precursor. This compound tends to form large crystalline chunks as can be seen in figure 4-31 in its red-orange mother liquor. This crystals were collected in 90 % to quantitative yields depending on the length of ether diffusion.

$[Cu(DMP\text{-}Cl)_2][BF_4]$ was obtained as orange needles in 75 % yield from a red DCM solution by *P. Dierks*.[148] Figure 4-32 shows orange needles in its depleted yellow mother liquor.

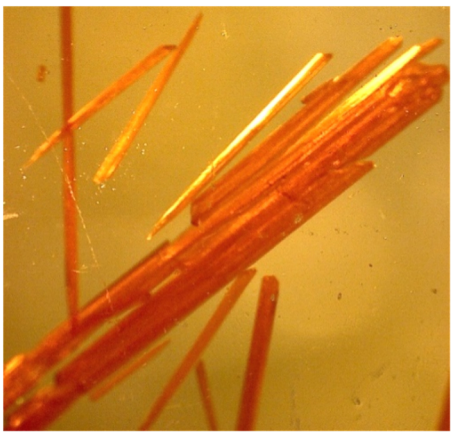

Figure 4-32: Crystals of $[Cu(DMP\text{-}Cl)_2][BF_4]$.

For the complexation of **[Cu(DMP-Br)$_2$][BF$_4$]** can either DCM or MeCN be used resulting in the same type of red-orange crystalline prisms as depicted in figure 4-33. Crystallization approaches of MeOH/Et$_2$O and DCM/Et$_2$O in a fridge resulted in feather-like, branched polycrystalline structures, while MeOH/THF and DCM/cyclopentane did not lead to ordered structures. Although this complex is stable in air and in solution, a long-term decomposition in aerated DMSO is observed by ^{1}H-NMR spectroscopy exhibiting a significant signal broadening for the aromatic and especially the bumpy methyl signals (figure 4-34). The last mentioned signal is low field shifted for 0.6 ppm while signals of the phenanthroline backbone peak were averagely shifted to lower frequencies by 0.28 ppm. In addition, a FID shortening is visible indicating all

Figure 4-33: Crystals of [Cu(DMP-Br)$_2$][BF$_4$].

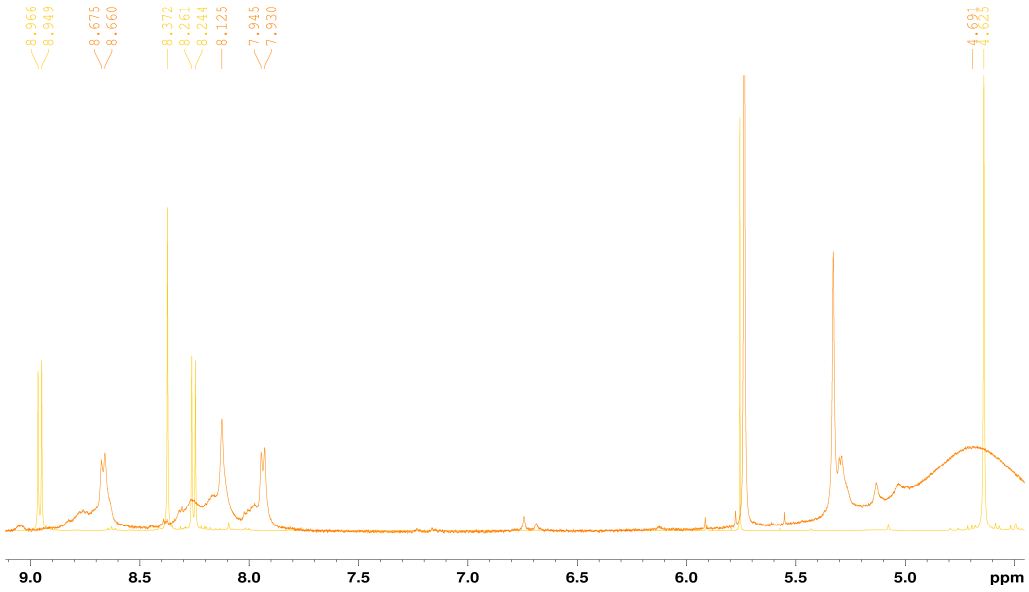

Figure 4-34: ^{1}H-NMR spectra of [Cu(DMP-Br)$_2$][BF$_4$] in DMSO-d$_6$. Yellow: Freshly prepared sample, orange: sample after three days.

in all at least a partial oxidation to a paramagnetic copper(II) species. In addition, it was found that, this complex is not long-term stable over a half a year in MeCN either.

When a significant amount of undissolved tetrakis(acetonitrile)copper(I) tetrafluoroborate was filtered off before performing the diethyl ether diffusion, it resulted in a parallel crystallization of the precursor itself and tri- and tetra- coordinated complexes in one single crystal. Recrystallization of the precursor is most likely induced by several factors. First, its concentration was $1.5 \cdot 10^{-6}$ M indicating large diffusion lengths and the ratio between ligand and precursor was significant lower than 2:1 due to the filtration procedure. In addition, the crystallization of the precursor may be favored owing to thermodynamic or kinetic reasons. In any case, the precursor must exchange acetonitrile ligands in the more nonpolar and significant less Lewis basic medium DCM, which is unfavorable due to its the weaker electron donation abilities.

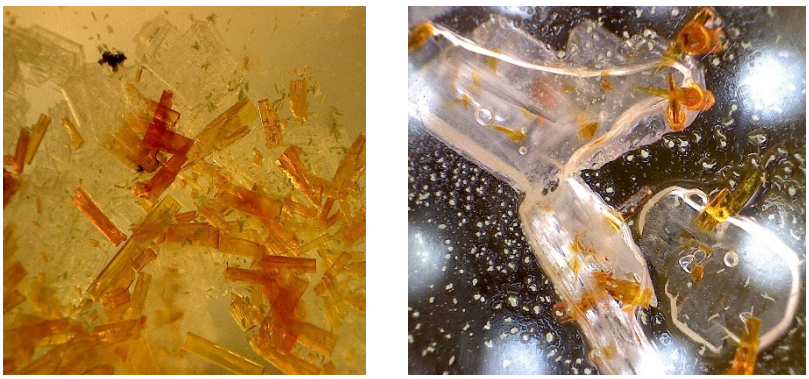

Figure 4-35: Crystals of [Cu(DMP-Br)(MeCN)][BF_4] / [Cu(DMP-Br)(MeCN)$_2$][BF_4] (orange-red) ratio 2:1 and [Cu(MeCN)$_4$][BF_4] (colorless).

Figure 4-36: Crystals of [Cu(DMP-I)$_2$][BF_4].

The synthesis of the heaviest homologue **[Cu(DMP-I)$_2$][BF_4]** was synthesized in MeCN and DCM by *P. Dierks*.[148] In both cases a dark red solution was obtained and after filtration and red-orange crystals were collected as shown in figure 4-36. Interestingly, the complex was significantly more stable regarding to halogen abstraction than its ligand. Even after two months in a closed vessel of MeCN and with normal light irradiation, the starch detection reaction[159] was negative.

Utilizing the general procedure from 4.2.1, **DMP-OH** was converted with **[Cu(MeCN)$_4$][BF$_4$]** in DCM/MeOH and MeCN/MeOH in an attempt to synthesize **[Cu(DMP-OH)$_2$][BF$_4$]**. When choosing DCM as the only solvent, solution turns orange immediately and an orange solid precipitated. It can be stated, that the color is not as intense as in the case for the [Cu(DMP-X)$_2$][BF$_4$] type of complexes. MeOH was added to increase solubility and led to a homogenous orange solution. During crystallization only a olive precipitate was obtained out of an orange solution. The solvent system was then changed to MeCN, which shows a comparable orange coloration and precipitation. Even upon addition of MeOH the solution remained turbid. After filtration and diethyl ether diffusion, very small green polycrystalline material could be grown, which were not suitable for X-Ray diffraction.

To verify the ligand coordination evaluate the direct electronic influence of the halogen series on the copper complex, NMR was utilized, since it is a measure of electron density.[183,184] In case of **[Cu(DMP)$_2$][BF$_4$]** no influence on the carbon atom is observed, but the proton signals are slightly shifted to lower field. More distinct changes are observed for the DMP-X copper(I) complexes. The proton signals of the methyl moieties are shifted to lower field after complexation, a trend which is also exhibited by the corresponding carbon atoms. When the ligands were coordinated to Cu(I), the nitrogen signals decline by ca. 50 ppm for all complexes verifying a complexation and a decrease in electron density. Interestingly, the chemical shift of the nitrogen atom remains relatively constant within the series indicating no significant difference in electronic properties.

Table 4-5: Chosen NMR data of [Cu(DMP)$_2$][BF$_4$], [Cu(DMP-Cl)$_2$][BF$_4$], [Cu(DMP-Br)$_2$][BF$_4$] and [Cu(DMP-I)$_2$][BF$_4$].

Signal	[Cu(DMP)$_2$][BF$_4$]	[Cu(DMP-Cl)$_2$][BF$_4$]	[Cu(DMP-Br)$_2$][BF$_4$]	[Cu(DMP-I)$_2$][BF$_4$]
H_{Me} [ppm]	4.42[a] (2.95)[a]	4.61[b] (5.11)[a]	4.54[b] (4.97)[a]	4.55[b] (4.85)[b]
C_{Me} [ppm]	26.0[a] (26.0)[a]	47.1[b] (47.7)[a]	34.0[b] (35.0)[a]	6.2[b] (7.0)[b]
N [ppm]	254.2[a] (298.8)[a]	254.6[b] (298.8)[a]	255.1[b] (299.5)[a]	251.6[b] (302.4)[b]

Signals marked with a and b were acquired in CDCl3 and MeCN-d_3, respectively. Values in brackets correspond to the uncomplexed ligands.

The synthesis of [Cu(DMP-X)][BF_4] type species was performed by straightforward conversion of [Cu(MeCN)$_4$][BF_4] under inert gas conditions resulting in red to orange crystals. In addition, chosen NMR data was presented showing the successful coordination by a shift of ^{15}N signals obtained by ^{15}N-^{1}H-HMBC to an averaged value of 254 ppm.

4.2.1.2 Single crystal X-ray diffraction of DMP-X-based copper(I) complexes

X-ray structures of the established **[Cu(DMP$_2$)][BF$_4$]** complex and its series of 2,9-dihalomethyl-1,10-phenanthroline copper(I) complexes **[Cu(DMP-Cl)$_2$][BF$_4$]**, **[Cu(DMP-Br)$_2$][BF$_4$]** and **[Cu(DMP-I)$_2$][BF$_4$]** were obtained. Ligands exhibit an increasing steric demand and forces the complex to stay in a distorted tetrahedral geometry thus preventing a significant flattening, which will be shown in the UV/VIS discussion in chapter 4.2.1.4. An overview of the most important structural parameters is given in table 4-7.

This section starts with the introduction of **[Cu(DMP$_2$)][BF$_4$]** as a reference compound for comparison of the DMP-X analogues. When analyzing the crystal structure it is striking, that both ligands coordinate the central atom in a different manner. Instead of spanning a plane with the copper ion, one ligands exhibits an out-of-plane coordination in which the copper ion is in a 0.5 Å distance away from the ligand plane. Thus, the ligand-Cu-ligand coordination angle is ca. 150°. In this arrangement, both ligands are not facing each other, as expected for an ideal tetrahedral coordination geometry. This property is also frequently found frequently in literature.[185] To get a measure for the flattening – a geometric key feature for the distortion – the angle between N-Cu-N planes in which both coordinating nitrogen atoms of a single ligand and the copper ion lay in one level is presented. Here, values of 80.8° and 88.1° were observed (figure 4-37), which is slightly smaller than in the ideal case of an undistorted tetrahedron and rises most likely from the discussed ligand distortion. This is to a greater extent observable in the right complex depicted in figure 4-37, since the distorted ligand is significantly more tilted out of the coordination plane. The geometry optimized structure gained from calculations shows the expected angle of 90° indicating that crystal package effects may be responsible for the distortion.

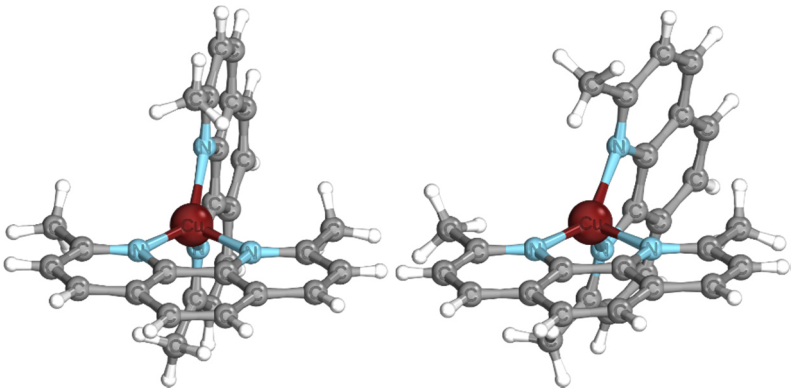

Figure 4-37: Representation of two crystal structures of [Cu(DMP)$_2$][BF$_4$] with 88° (left) and 80° (right) torsion angle.

Table 4-6: Structural parameters of $[Cu(DMP)_2][BF_4]$ and $[Cu(DMP)_2][BF_4]_2$ gained by X-ray diffraction, EXAFS and DFT calculations.

	$[Cu(DMP)_2][BF_4]$			$[Cu(DMP)_2][BF_4]_2$	
	X-ray diffraction	EXAFS	DFT	X-Ray diffraction	DFT
Cu-N distances [Å]	2.0041(16)	2.026±0.02	2.00	1.980(3)	2.00
	2.0484(15)		2.01	1.986(3)	2.00
	2.0515(16)		2.00	1.990(3)	2.01
	2.1275(16)		2.00	2.004(3)	2.01
N-Cu-N angles [°]	81.38(6)	-	83.38	82.38(11)	83.83
	81.44(6)		83.37	81.25(11)	83.80
Torsion angle N-Cu-N planes [°]	80.79	-	89.98	57.77	66.73

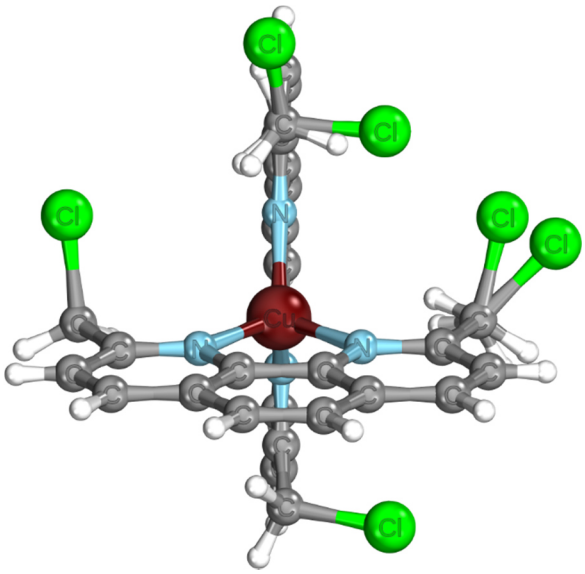

Figure 4-38: Representation of $[Cu(DMP\text{-}Cl)_2][BF_4]$ from crystal structure including the observed disorder.

The analysis of all three DMP-X complexes reveal comparable, distorted tetrahedral geometries. **DMP-Cl** is coordinating the Cu(I) ion in its ligand plane but is tilted ca. 20 ° resulting in a ligand non-facing alignment between both ligands. **$[Cu(DMP\text{-}Br)_2][BF_4]$** and **$[Cu(DMP\text{-}I)_2][BF_4]$** show a similar although not significantly less pronounced rotation behavior (10 ° and 13 °) with almost no deviation of the copper ion from the ligand planes. That may indicate a higher steric demand

straightening the ligand to a face-to-face arrangement.

Interestingly, **[Cu(DMP-Cl)$_2$][BF$_4$]** exhibits a disorder of one chlorine atom per ligand over four positions to a significant extend (ca. 60/40 for each chlorine), as depicted in figure 4-38. In contrast to the other crystal structures, both chlorine atoms per ligand are not aligned in a trans position, but are arranged in the same direction. This orientation leads to closest Cl-Cl distances of 3.49 Å and 4.98 Å for each pair of identical fractional occupation. The disorder induced by rotation of Cl-C_{Me}-C_{Phen} plane versus neighboring C_6 ring from ligand backbone is probably possible because of the lower steric demand in comparison with its heavier analogues. In all other complexes the torsion angle between the halogen atom and the plane spanned by the neighboring C_6 ring is mainly between 82° and 89° as can be seen in figure 4-39. Not surprisingly, the distances between halogen atoms through space increases with increasing period due to the increasing steric demand. DFT calculation and XAS data are in total agreement with results of the single crystal diffraction, verifying a nearly identical coordination geometry. Chosen copper bonding distances and angles are shown in table 4-7, where the subsequent EXAFS data from chapter 4.2.1.3 was added.

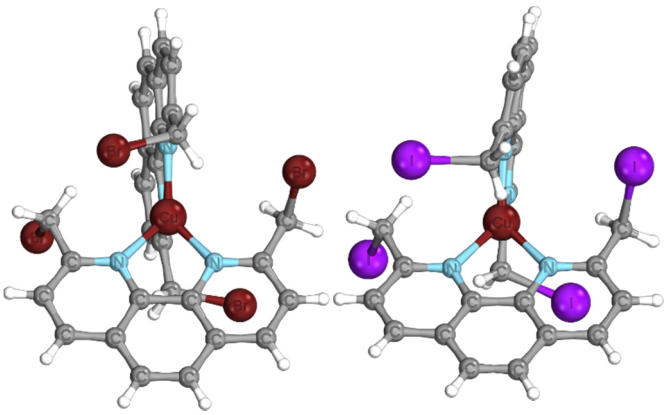

Figure 4-39: Representations of [Cu(DMP-Br)$_2$][BF$_4$] and [Cu(DMP-I)$_2$][BF$_4$] from crystal structures.

Table 4-7: Structural parameters of $[Cu(DMP\text{-}Cl)_2][BF_4]$, $[Cu(DMP\text{-}Br)_2][BF_4]$ and $[Cu(DMP\text{-}I)_2][BF_4]$ gained by X-ray diffraction, EXAFS and DFT calculations.

	$[Cu(DMP\text{-}Cl)_2][BF_4]$			**$[Cu(DMP\text{-}Br)_2][BF_4]$**			**$[Cu(DMP\text{-}I)_2][BF_4]$**		
	X-ray diffraction	EXAFS	DFT	X-Ray diffraction	EXAFS	DFT	X-Ray diffraction	EXAFS	DFT
Cu-N distances [Å]	2.039(2) 2.045(3) 2.048(2) 2.053(2)	2.039	1.99 1.99 2.02 2.02	1.995(7) 2.018(8) 2.024(8) 2.028(8)	2.027	2.02 2.02 2.02 2.02	2.014(10) 2.030(10) 2.038(11) 2.046(11)	2.029	2.00 2.00 2.00 2.00
N-Cu-N angles [°]	81.80(10) 81.91(9)	-	83.2 83.2	81.6(3) 83.0(3)	-	82.6 82.6	82.8(4) 82.7(4)	-	83.2 83.2
Torsion angle N-Cu-N planes [°]	89.8	-	88.0	86.5	-	90.0	87.5	-	89.9
X-X distance [Å]	3.50 4.98 4.62 5.53 5.52 5.57	-	4.04 5.35 5.34 7.02	5.41 5.81 5.85 6.04	-	5.72 5.73 5.73 5.74	5.75 6.00 6.06 6.34	-	6.00 6.00 6.00 6.00

Single crystal X-ray diffraction confirmed the successful synthesis of $[Cu(DMPX)_2][BF_4]$ complexes and delivered insights into the coordination geometries. Torsion angles approaching 90 ° indicating a typical distorted tetrahedral geometry. The detected disorder in the case of **$[Cu(DMP\text{-}Cl)_2][BF_4]$** shows residual rotational degrees of freedom. Intriguingly, the Cu-N distances for **$[Cu(DMP\text{-}Br)_2][BF_4]$** do not fit on the row, since a significant contraction is – even in comparison to **$[Cu(DMP\text{-}I)_2][BF_4]$** with higher

steric demands – observed. This knowledge will be of further importance, especially for the interpretation of the UV/VIS spectra.

4.2.1.3 X-ray absorption and emission spectroscopy

The XAS and XES analysis were performed by *R. Schoch* and *P. Müller*. First, results for the **[Cu(DMP)$_2$][BF$_4$]** / **[Cu(DMP)$_2$][BF$_4$]$_2$** pair will be presented, while the **DMP-X**-based complexes follow afterwards.

Starting with **[Cu(DMP)$_2$][BF$_4$]** and **[Cu(DMP)$_2$][BF$_4$]$_2$** experimental HERFD-XANES spectra were compared to TD-DFT simulations to get an deeper understanding of the impact of geometric and electronic differences.

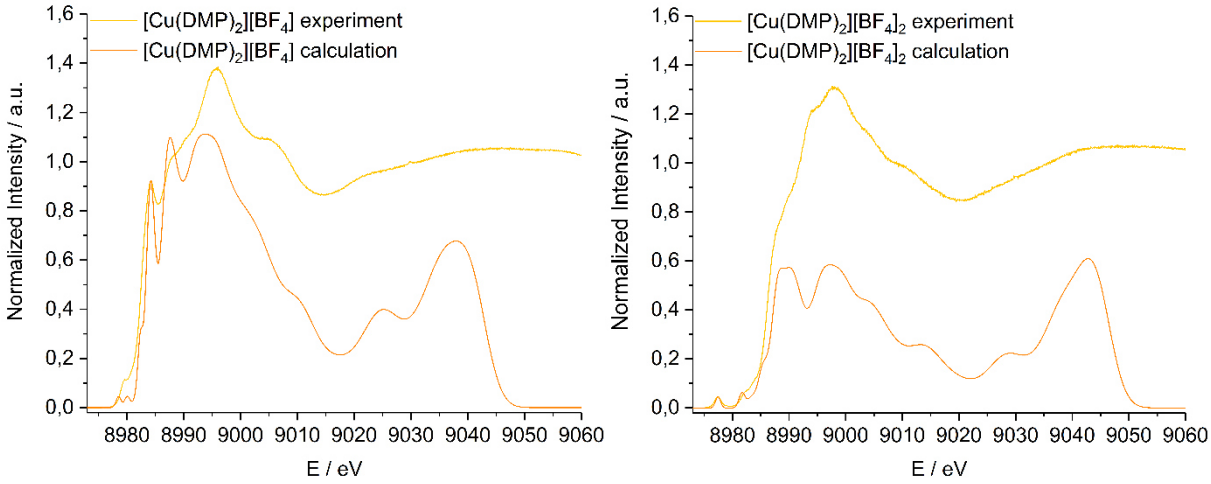

Figure 4-40: Experimental and calculated HERFD-XANES spectra of [Cu(DMP)$_2$][BF$_4$] and [Cu(DMP)$_2$][BF$_4$]$_2$.

In both cases the general shape of the spectra is very well reproduced by TD-DFT calculations, as can be seen in figure 4-40. **[Cu(DMP)$_2$][BF$_4$]$_2$** exhibits a pronounced prepeak located at 8977.46 eV indicative of an electronic d^9 configuration, which facilitates a 1s to LUMO transition. The LUMO is shown in figure 4-41 and consists

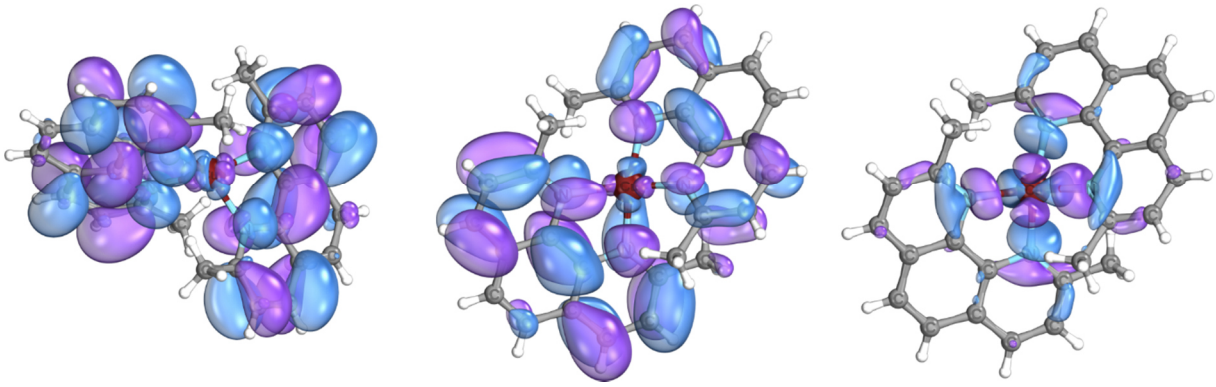

Figure 4-41: Relevant LUMO orbitals – degenerate LUMO/MULO-1 from [Cu(DMP)$_2$][BF$_4$] (left), LUMO +1 (middle) and LUMO (right) from [Cu(DMP)$_2$][BF$_4$]$_2$.

mostly of copper 3d orbitals (55%) with an admixture of Copper p and ligand p orbitals. These admixtures give rise to a dipole transition and thereby increase the intensity of the prepeak compared to a pure quadrupole. The second feature at 8982.3 eV is characterized by transitions in the ligand π* system.

[Cu(DMP)$_2$][BF$_4$] does not show a distinct prepeak, since the aforementioned transition is not possible in a d^{10} configuration. The LUMO in this case mainly consists of carbon and nitrogen p-orbitals originating from the ligand π* system. Accordingly the feature at 8980 eV can be assigned to a MLCT transition revealing the same as the one in the Cu(II) case. This signal is shifted to lower energies, because the ionization threshold is smaller in the Cu(I) case supporting the assignment before.

Additionally, the electronic structure was investigated by means of VtC emission spectra in comparison to DFT calculations.

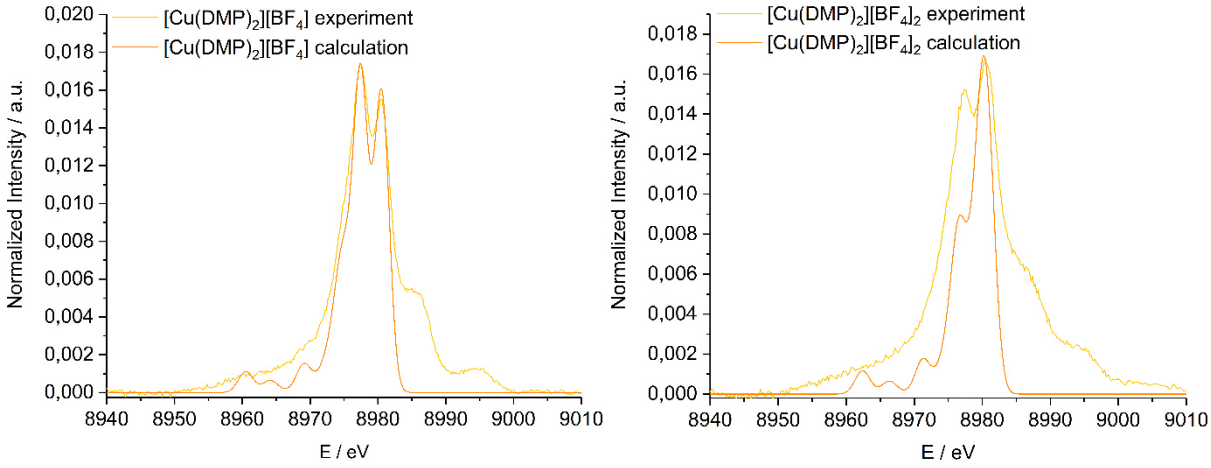

Figure 4-42: Experimental and calculated VtC spectra of [Cu(DMP)$_2$][BF$_4$] and [Cu(DMP)$_2$][BF$_4$]$_2$.

These spectra can be divided into three key parts, defined as the two main peaks and the three low intensity signals to lower energy. The latter signals both low in energy and intensity are characterized by transitions from the ligand π system into the 1s orbital. Due to the strong delocalization in the ligand backbone, a more precise correlation is not possible. The second key feature (8977.4 eV) is dominated by binding combinations of copper 3d-orbitals with ligand p-orbitals. The third and highest energy feature is of the same character for Cu(II), but in case of Cu(I) this feature is mainly described by copper 3d-orbitals with only little admixture. Spectra of Cu(I) in the geometry of the Cu(II) complex and vice versa were calculated because admixture and energy of other orbitals are symmetry dependent. The characteristic angles between the N-Cu-N planes in the investigated copper(I) and copper(II) species are 80° and

54°, respectively, resulting in a “broadening” of the main peak in both plotted VtC spectra.

On the one hand X-ray absorption spectroscopy was conducted on the $[Cu(DMP\text{-}X)_2][BF_4]$ series as solid samples to verify the X-ray diffraction data and more importantly on the other hand to have reference data for the XAS spectroelectro-chemical studies, which were already recorded. The Cu-N distances of the EXAFS fits are in accordance with the mean distances gained by X-ray diffraction.

In case of the discusses series, the edge location of the XANES spectra clearly indicate copper(I) species as shown in figure 4-43. **$[Cu(DMP\text{-}Br)_2][BF_4]$** is exhibits a slightly different behavior than the other three compound does not fit into the series. First, the

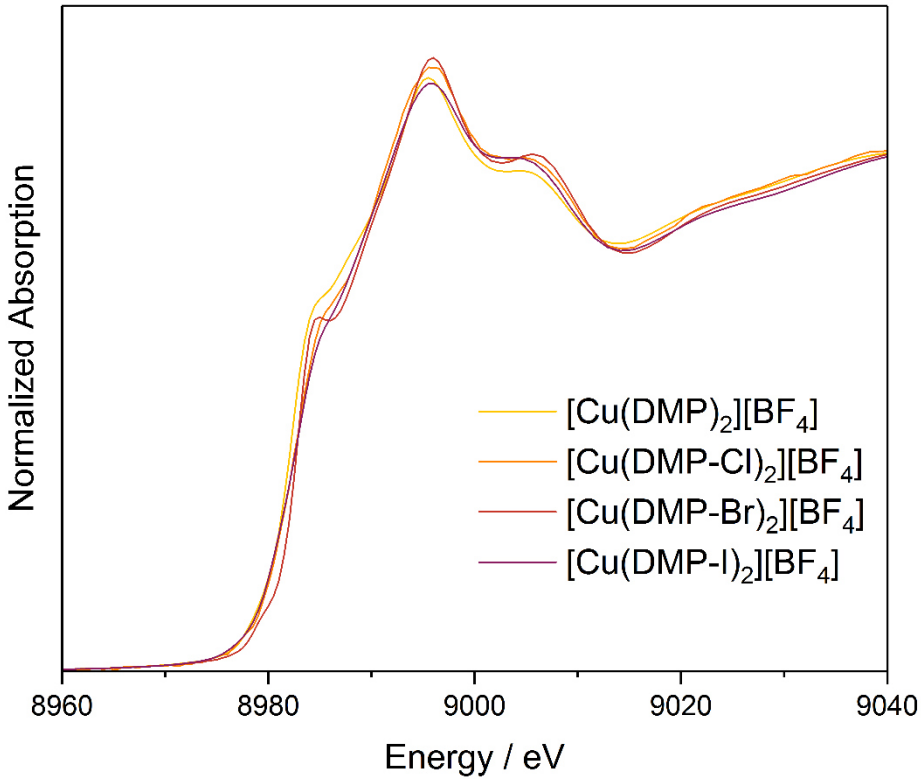

Figure 4-43: XANES spectra of $[Cu(DMP\text{-}X)][BF_4]$ solid samples.

edge is shifted to higher energy, but the slope is significantly higher. In addition, the edge feature at 8984.8 eV, which is only observable as shoulder in the other spectra is more pronounced.

Table 4-8: EXAFS analysis fitting parameter of $[Cu(DMP\text{-}X)_2][BF_4]$ samples.

Complex	Abs-Bs[a]	N(Bs)[b]	R(Abs-Bs)/Å[c]	σ/Å [d]	R/%[e] χ^2_{red} [f] E_f/eV[g] Afac[h]
$[Cu(DMP)_2][BF_4]$	Cu-N	4.3	2.032±0.020	0.095	2.126
	Cu-C	5.8	2.856±0.029	0.112	0.7672
	Cu-C	0.8	3.097±0.031	0.092	26.36
	Cu-C	3.4	3.299±0.033	0.039	$6.57\cdot10^{-6}$
	Cu-C	6.7	3.923±0.040	0.112	-
$[Cu(DMP\text{-}Cl)_2][BF_4]$	Cu-N	3.9	2.039±0.020	0.081	3.582
	Cu-C	2.9	2.813±0.028	0.081	0.7666
	Cu-C	0.5	2.931±0.029	0.032	30.78
	Cu-C	1.4	3.325±0.033	0.084	$1.19\cdot10^{-5}$
	Cu-C	8.6	3.940±0.039	0.063	-
	Cu-Cl	1.5	3.865±0.039	0.059	-
$[Cu(DMP\text{-}Br)_2][BF_4]$	Cu-N	3.9	2.027±0.020	0.087	0.3289
	Cu-C	7.7	2.859±0.029	0.112	0.9164
	Cu-C	7.4	3.334±0.033	0.11	20.24
	Cu-C	5.4	3.115±0.031	0.102	$5.48\cdot10^{-6}$
	Cu-C	5.9	3.970±0.040	0.112	-
	Cu-Br	0.4	4.457±0.045	0.067	-
$[Cu(DMP\text{-}I)_2][BF_4]$	Cu-N	4	2.029±0.020	0.081	0.1044
	Cu-C	3.4	2.801±0.028	0.063	0.8528
	Cu-C	7.4	2.991±0.030	0.112	24.71
	Cu-C	9.5	3.298±0.033	0.112	$9.05\cdot10^{-6}$
	Cu-C	3	3.997±0.040	0.067	-
	Cu-I	0.5	4.263±0.043	0.081	-

a) Abs=X-ray absorbing atom, BS=backscattering atom
b) number of backscattering atoms
c) distance between absorbing and backscattering atom
d) Debye-Waller-like factor
e) fit index
f) reduced χ^2 error (considers beside error to experiment the number of independent points and number of varied parameters)
g) Fermi energy, that account for the shift between theory and experiment
h) amplitude reducing factor
i) Atom distances obtained from single crystal structure

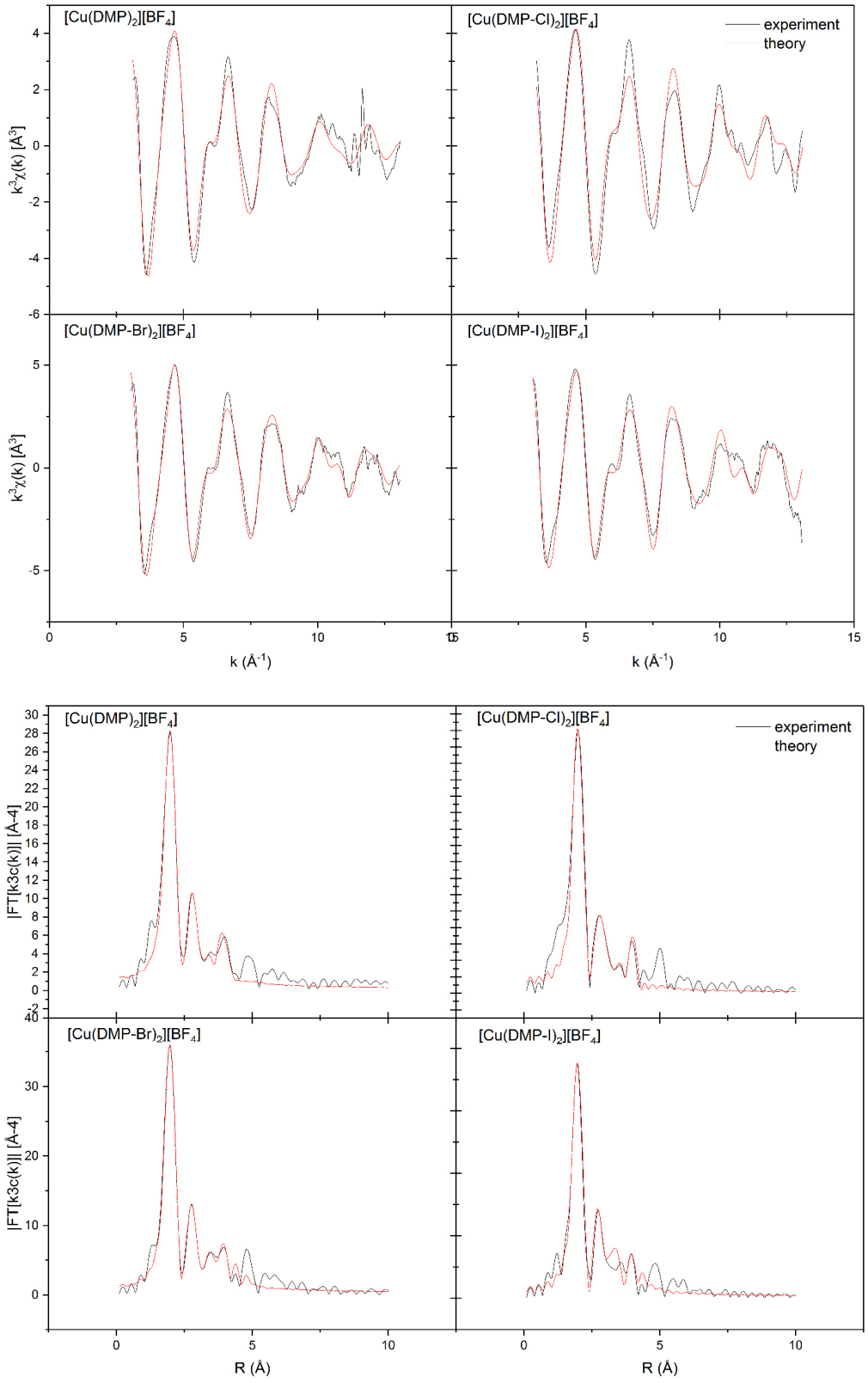

Figure 4-44: Comparison between experimental EXAFS data and their fits in k- and R-space.

Regular EXAFS as well as HERFD-XANES and VtC emission spectroscopy was applied on **[Cu(DMP)$_2$][BF$_4$]** and **[Cu(DMP)$_2$][BF$_4$]$_2$** giving insights into the electronic HOMO and LUMO states. The results show a good accordance of calculated and experimental spectra. Based on the different oxidations states, both complexes exhibit a significant different electronic structure. While the copper(I) species is determined to possess a ligand p-orbital based LUMO, the LUMO in the copper(II) case exhibits more than 50 % metal-d-orbital character. Regular XANES of the [Cu(DMP-X)$_2$][BF$_4$] shows an singular behavior for **[Cu(DMP-Br)$_2$][BF$_4$]** in comparison to the other copper(I) complexes.

In conclusion, differences in electronic structures can be used to investigate entailing geometric changes. Furthermore, these results can be used to validate other experimental properties because they readily show if the HOMO levels are calculated properly and how strongly they might be shifted. By means of this methods the proposed mechanism for an photoexcitation in terms of HOMO-LUMO transitions are verified.

4.2.1.4 UV/VIS spectroscopy of DMP-X-based copper(I) complexes

In the following, the experimental optical spectra will be discussed by means of literature and TD-DFT calculated spectra. For reasons of comparison, all calculations were performed with the same parameters as denoted in chapter 6.2.13. Especially, the descriptions of interesting π-π* are sensitive to the chosen exchange functional[186]. Charge transfer transitions are general poorly described.[187,188] In addition, the lack of orbital relation and missing consideration of two-electron terms introduce an error[188,189]. This is the reason why the same functional was used in order to introduce an error, which is at least consistent. In this given case, the calculations are showing that the general pattern is consisting of three broadened main signals at high energy and one peak with decreased intensity at higher wavelengths is reproduced.

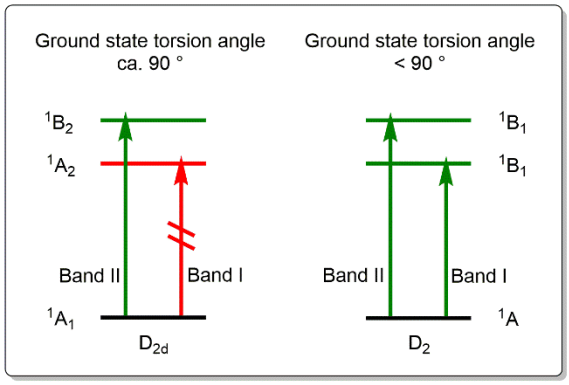

Figure 4-45: Correlation between ground state distortions and resulting MLCT transitions.

After complexation, two MLCT bands are usually observed in a copper(I) diimine complex. These are strongly dependent on the steric environment with respect to solvent attack blocking and inter-substituent interactions, especially in the 2,9 position, as mentioned before. The high energy band – also referred to as II band – at about 450 nm rises from $S_2 \leftarrow S_0$ transition and exhibits a red-shifted, broad $S_1 \leftarrow S_0$ shoulder, which is also called I band, resulting from a symmetry-forbidden dynamically flattened D_{2d} geometry (figure 4-45).[190,191]

While the MLCT peaks show no direct correlation between halogen and intensity, the signal undergoes a red shift ending with the **[Cu(DMP-Cl)$_2$][BF$_4$]**, where the reference compound is located. All π-π* transitions were red-shifted and decreasing in intensity accordingly, as listed in table 4-9. This indicates a declining energy difference between these states. Regarding to the MLCT states, the $S_2 \leftarrow S_0$ transition is dominant in all synthesized complexes excluding **[Cu(DMP-Cl)$_2$][BF$_4$]** to a significant degree due to the low absorption intensity and less structured signals, as can be seen in figure 4-46. When comparing all synthesized complexes, an intensity reduction of the $S_2 \leftarrow S_0$

MLCT transition in the order **[Cu(DMP-Br)$_2$][BF$_4$]** > **[Cu(DMP-I)$_2$][BF$_4$]** > **[Cu(DMP-Cl)$_2$][BF$_4$]** is observed. **[Cu(DMP-Br)$_2$][BF$_4$]** exhibits a three times weaker MLCT signal than the aforementioned reference species. Due to the broad peak and low intensity the absorption maximum for the **[Cu(DMP-Cl)$_2$][BF$_4$]** could only be assigned to the range between 400 nm and 425 nm.

Table 4-9: UV/VIS absorption data of [Cu(DMP)$_2$][BF$_4$], [Cu(DMP-Cl)$_2$][BF$_4$], [Cu(DMP-Br)$_2$][BF$_4$] and [Cu(DMP-I)$_2$][BF$_4$].

Signal	[Cu(DMP)$_2$][BF$_4$]	[Cu(DMP-Cl)$_2$][BF$_4$]	[Cu(DMP-Br)$_2$][BF$_4$]	[Cu(DMP-I)$_2$][BF$_4$]
λ_{max},1 [nm]	203 (80581)	207 (64586)	207 (44614)	205 (71594)
λ_{max},2 [nm]	226 (109340)	233 (103306)	236 (92375)	241 (74392)
λ_{max},3 [nm]	273 (87094)	273 (96592)	280 (67869)	281 (57337)
λ $S_2 \leftarrow S_0$ [nm]	456 (9522)	400–425 (790)	449 (3428)	456 (2246)
Molar attenuation coefficients ε [l·mol^{-1}·cm^{-1}] are shown in brackets.				

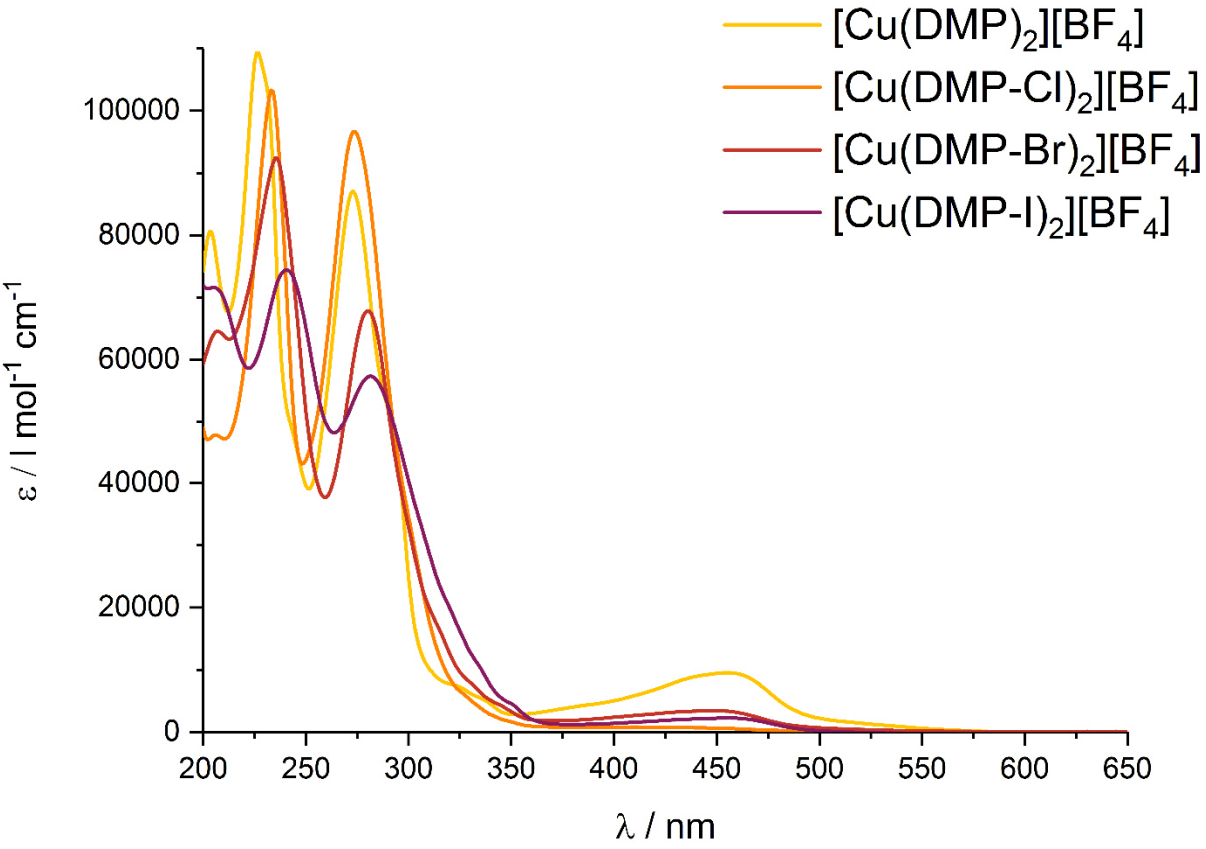

Figure 4-46: UV/VIS absorption spectra of [Cu(DMP)$_2$][BF$_4$], [Cu(DMP-Cl)$_2$][BF$_4$], [Cu(DMP-Br)$_2$][BF$_4$] and [Cu(DMP-I)$_2$][BF$_4$] at 10^{-5} M in MeCN.

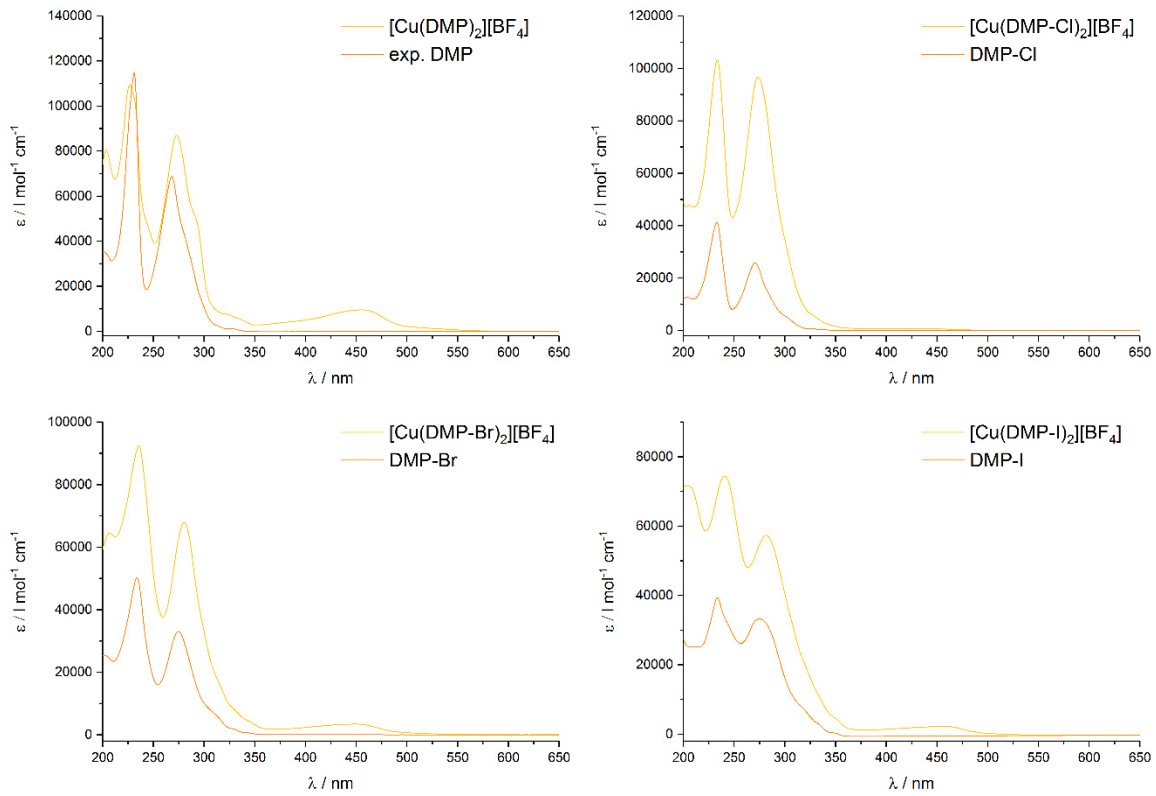

Figure 4-47: Comparison of UV/VIS spectra of DMP-X ligands and their homoleptic copper(I) complexes.

Low energy $S_1 \leftarrow S_0$ shoulders are clearly assignable at ca. 470 nm for **[Cu(DMP)$_2$][BF$_4$]**, **[Cu(DMP-Br)$_2$][BF$_4$]** and **[Cu(DMP-I)$_2$][BF$_4$]** with decreasing absorption intensity. **[Cu(DMP-Cl)$_2$][BF$_4$]** does not exhibit any significant intensity in this area compared to the other substances. This correlates with the average Cu-N bond length in the halogenated compounds. These bond lengths may be a measure of the bulkiness of the 2,9 substituents as shown for alkyl substituents and are directly affecting the ground state optical behavior.[192–194] It was observed, that increasing steric demand in 2,9-alkylsubstituated phenanthroline copper(I) complexes results in a MLCT band shift to higher energies because of destabilization of ground and MLCT states.[122,191–194] The shape and demand of the substitution shifts $S_2 \leftarrow S_0$ transition and changes the intensity of the $S_1 \leftarrow S_0$ band due to the geometry manipulation from D_{2d} to D_2.[195] The $S_1 \leftarrow S_0$ band can be applied as a measure for the degree of flattening, since the transition dipole moment of a D_{2d} complex is close to zero for this band.[196] **[Cu(DMP)$_2$][BF$_4$]** shows only a very small population of the $S_1 \leftarrow S_0$ band indicating no significant flattening, but exhibits the highest intensity within the discussed series resulting in a higher population of the relaxed MLCT state in this comparison.[197] The amount of dynamic flattening is decreasing from **[Cu(DMP)$_2$][BF$_4$]** > **[Cu(DMP-Br)$_2$]-**

[BF4] > **[Cu(DMP-I)2][BF4]** verifying the increasing steric demand thus leading to a reduction of flattening. In addition to the classical metal to ligand charge transfer transitions around 450 nm , a low-intense, broad signal is observable at 330 nm.[120,198] Results of TD-DFT calculations in these regions, as depicted in figure 4-48, verifies MLCT transitions, which are underlining this thesis.

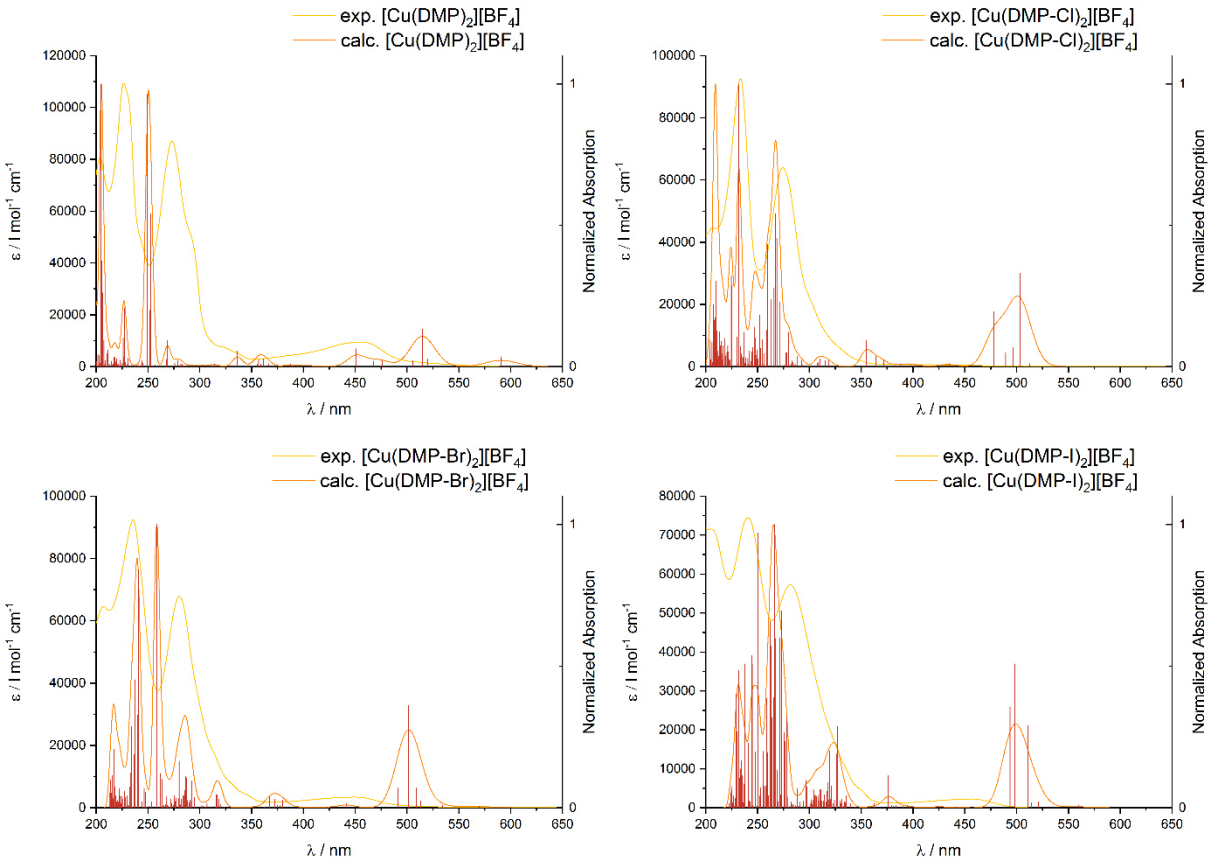

Figure 4-48: Experimental and calculated UV/VIS spectra of DMP-X-based copper(I) complexes.

For spectroelectrochemistry discussed later in this work, an UV/VIS analysis of **[Cu(DMP)2][BF4]2** is necessary and will be conducted in the following supported by TD-DFT calculations based on the crystals structure. The three already discussed ligand-based features were also observable in this case, as depicted in figure 4-49. As expected no MLCT transition around 450 nm is observed because the electronic system changed from d^{10} to d^{9} resulting in a significant higher excitation energy for the next copper valence electron, which is also indicated by TD-DFT calculations as shown in the following. The calculated UV/VIS spectra is determined by a large amount of

transitions resulting in a very complex spectrum compared to its copper(I) analogue. The overall conformity of experiment and calculation As observed in the experimental spectrum, two main features are also found in the calculation at 206 nm and 260 nm. Both consists of π-d transitions contaminated with π-π* transitions. All signals between

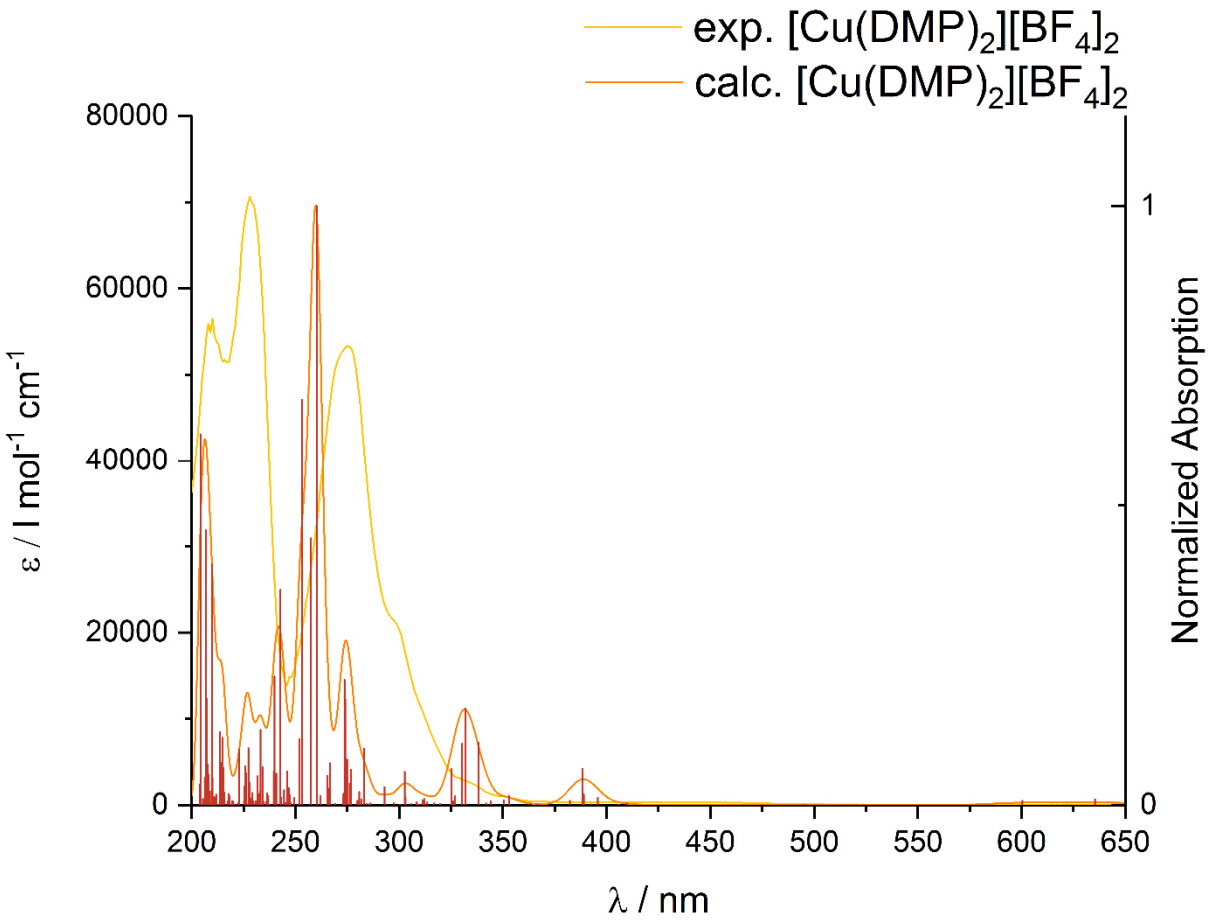

Figure 4-49: Experimental and calculated UV/VIS spectrum of copper(II) reference compound $[Cu(DMP)_2][BF_4]_2$.

theses peaks are mainly established by π-π* processes, except for the transition closely around 240 nm, which is given rise by π-d transitions. A large ratio of this transition type is also found for the peaks at 275 nm and 303 nm. One of these may correspond to the shoulder at 299 nm, which would be consistent with spectroelectrochemistry analysis in chapter 4.2.1.7. The signal at 388 nm gains also its intensity from LMCTs, while π-π* processes are mainly responsible for the signals 331 nm. The broadening in comparison to the copper(I) spectrum is due to the larger amount of transitions as indicated by calculations. Although the calculation deviates from the acquired spectrum, a general overview was given to classify the location of the transitions. A typical, broad d-d transition for tetragonal distorted copper(II) complexes

resulting from $^2E_g \leftarrow {}^2T_{2g}$ around 620 nm is not visible whether in the experiment nor in calculations.

UV/VIS spectroscopy revealed additional information on geometry dynamics. Typical for phenanthroline ligands, π-π* transitions ware observed in the UV region of the spectrum, which are red-shifted upon coordination. The copper(I) complexes exhibit a characteristic MLCT band around 460 nm, which can be divided into an $S_2 \leftarrow S_0$ and $S_1 \leftarrow S_0$, with the latter indicating the dynamic flattening. Based on this fact, is was found, that the amount of flattening decreases in the order **[Cu(DMP)$_2$][BF$_4$]** > **[Cu(DMP-Br)$_2$][BF$_4$]** > **[Cu(DMP-I)$_2$][BF$_4$]**. **[Cu(DMP-Cl)$_2$][BF$_4$]** exhibits the lowest MLCT absorption making MLCT assignments difficult. In addition, the absorption spectrum of **[Cu(DMP)$_2$][BF$_4$]$_2$** was analyzed and the missing MLCT transitions were observed as key difference. This is in accordance with the XAS/XES assessment in chapter 4.2.1.3, since a clear MLCT is observed in the copper(I) but not in the copper(II) case.

4.2.1.5 Steady state luminescence spectroscopy of DMP-X-based copper(I) complex

All copper(I) DMP-X complexes are investigated by means of steady state luminescence spectroscopy and compared to their ligand spectra to determine the effect of complexation since there are possible chelation-enhancing luminescence (CHEF) or chelate-enhancing quenching (CHEQ) effects.[199] Although known as Lewis basic exciplex quencher[89,113,123,200], MeCN was applied as solvent, since it is also used for water reduction catalysis.

For **[Cu(DMP)$_2$][BF$_4$]**, the luminescence signals and the pattern is comparable to the ligands spectra and exhibit no peak shifting, although the flank to lower energy decays slower (figure 4-50). Increasing the excitation wavelength over 290 nm results in a decreasing luminescence intensity as observed for the ligand spectrum. Under these parameters, no distinct emission with copper contribution could be detected. The heavy atom effect favoring non-emissive decays may have an influence on this behavior, too.

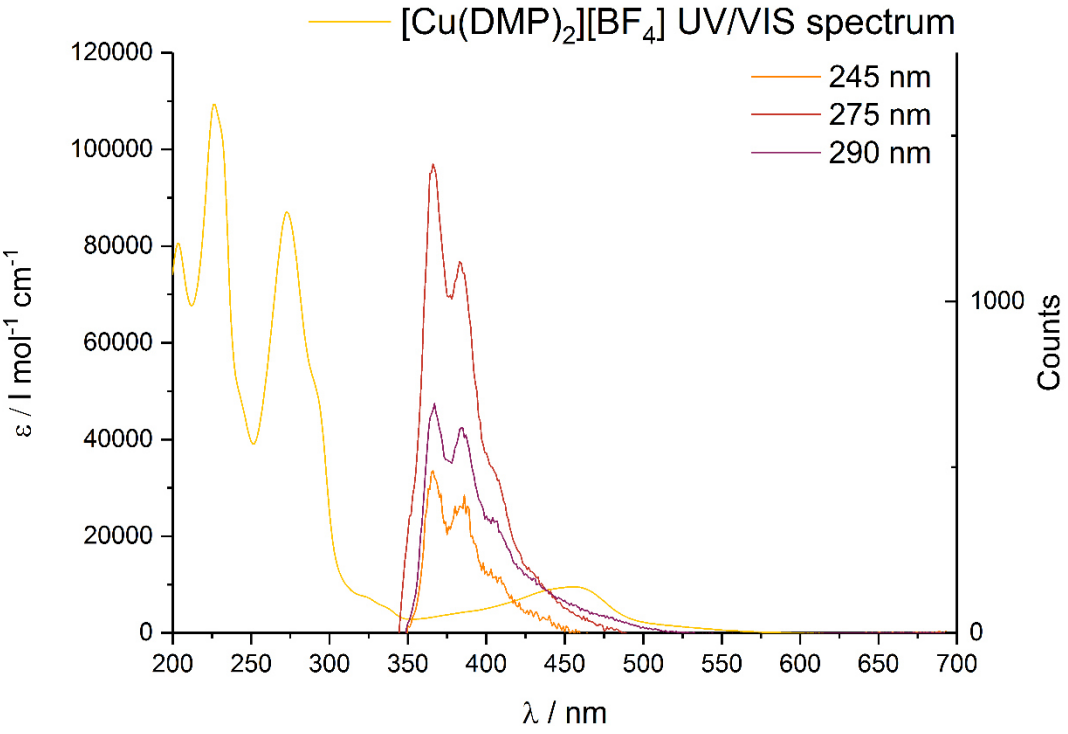

Figure 4-50: Steady state luminescence spectra of [Cu(DMP)$_2$][BF$_4$].

In steady state luminescence spectra for **[Cu(DMP-Cl)$_2$][BF$_4$]**, **[Cu(DMP-Br)$_2$][BF$_4$]** and **[Cu(DMP-I)$_2$][BF$_4$]** exhibit comparable structures for the low energy $\pi^* \leftarrow n_X$ band (figure 4-51). The poor spectra quality in the case of **[Cu(DMP-Cl)$_2$][BF$_4$]** is due to the

weak luminescence. As seen before, higher excitation wavelengths result in a decreasing luminescence intensity, while temporary increasing the population of emitting π-π* transitions around 360 nm. The broad signal in the range of 450 nm – 650 nm shows two identical features. This is not the case for **[Cu(DMP-Br)$_2$][BF$_4$]** and **[Cu(DMP-I)$_2$][BF$_4$]**.

[Cu(DMP-Br)$_2$][BF$_4$] loses its high energy emission properties and additionally the signal pattern changed significantly in comparison to the ligand luminescence spectrum. The first signals highest in energy are blue shifted for 7 nm and are broadened to higher energy indicating further emissive state here. The peak to lowest energy is not shifted at all.

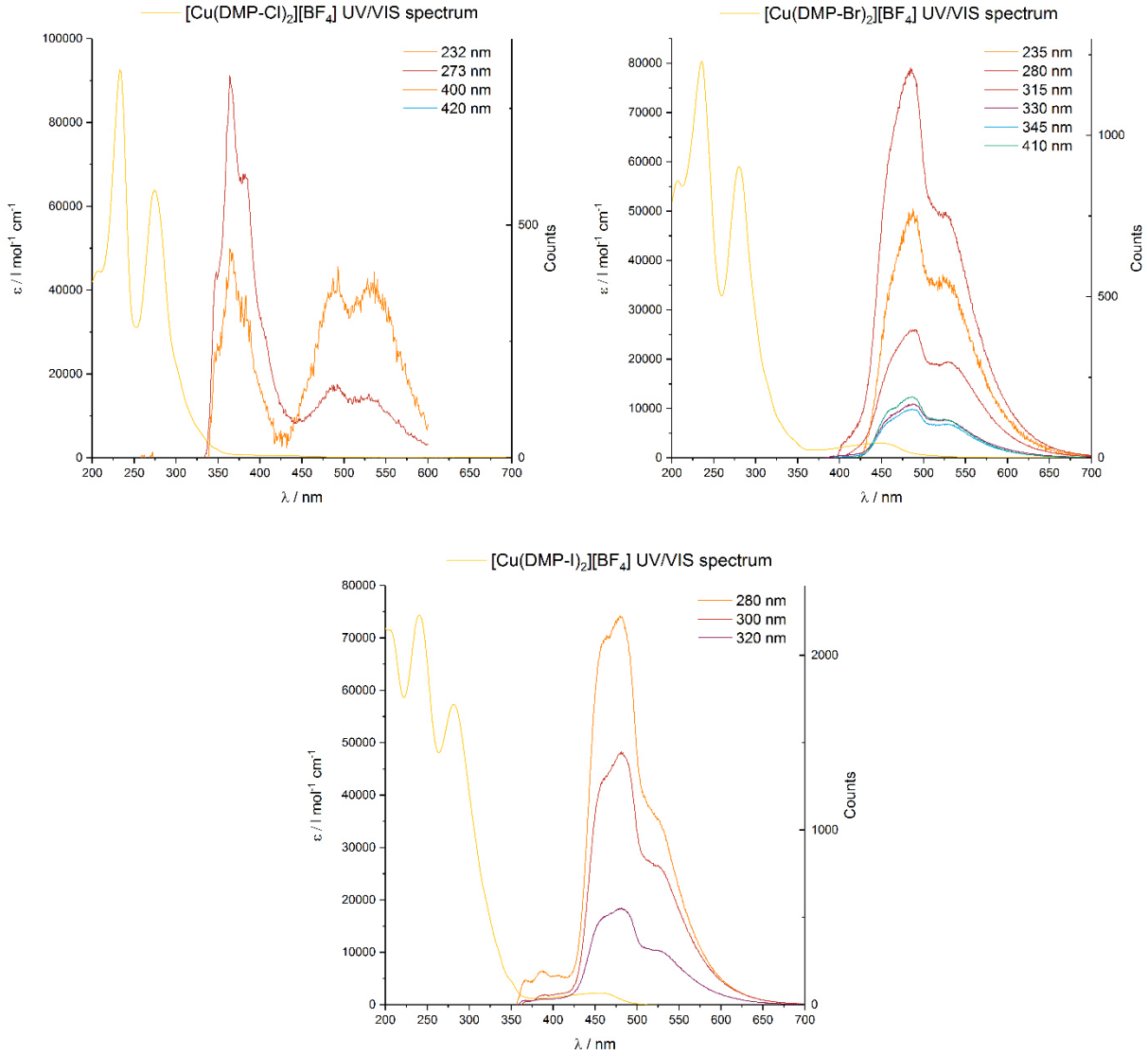

Figure 4-51: Steady state luminescence spectra of [Cu(DMP-Cl)$_2$][BF$_4$] (top left), [Cu(DMP-Br)$_2$][BF$_4$] (top right) and [Cu(DMP-I)$_2$][BF$_4$] (bottom).

The same luminescence behavior is observable for **[Cu(DMP-I)$_2$][BF$_4$]**, where the blue shifted shoulder at 462 nm is even more pronounced and a partially separation of this peak can be interpreted at 280 nm excitation energy. The most red shifted signal at 523 nm is in accordance with the ligand spectrum, although not as emissive in comparison with the main peak. The high energy signals of the ligand can be reproduced in the complex´s spectrum with a very weak intensity.

Table 4-10: Assignment of steady state luminescence signals of [Cu(DMP-X)$_2$][BF$_4$]-based ligands.

Signal	[Cu(DMP)$_2$][BF$_4$]	[Cu(DMP-Cl)$_2$][BF$_4$]	[Cu(DMP-Br)$_2$][BF$_4$]	[Cu(DMP-I)$_2$][BF$_4$]
$\pi^* \leftarrow n_N$ [nm] shoulder	351	-	not assignable	not assignable
$\pi^* \leftarrow n_N$ [nm]	366	365	-	367
$\pi^* \leftarrow \pi$ [nm]	383	383	-	386
$\pi^* \leftarrow \pi$ [nm]	401	401	-	405
$\pi^* \leftarrow n_X$ [nm]	-	492	484	462
$\pi^* \leftarrow n_X$ [nm]	-	-	not assignable	481
$\pi^* \leftarrow n_X$ [nm]	-	532	530	523

The missing signal set in the unsubstituted cases, the altered ratio between the two features of this band and slight shifts shows that no impurity or systematic error was give rise to the assigned $\pi^* \leftarrow n_X$ transitions. The comparison between the luminescence spectra of ligands and their copper(I) complexes are in itself consistent indicating clearly that the halogen atoms are the origin of the most red shifted luminescence signals. An exciplex formation is not likely, since the sample concentrations were as low as 10^{-5} M.

The steady state luminescence spectra can be classified into three main emission type, namely $\pi^* \leftarrow n_N$, $\pi^* \leftarrow \pi$ and $\pi^* \leftarrow n_X$. Luminescence of excited MLCT states are not observed because of the quenching solvent. A general – but minor – red-shift trend is observed upon coordination. Again, **[Cu(DMP-Br)$_2$][BF$_4$]** has a unique behavior in the discussed series because in the range between 325 nm and 400 nm a full luminescence signals set is missing, although it is observable for **DMP-Br**.

4.2.1.6 TC-SPC spectroscopy of DMP-X-based copper(I) complexes

The results of the time-resolved measurements are giving insights into dynamic photophysical behavior by investigating decay traces. This emission decays are fitted by methodology described in chapter 6.2.10 to extract the physical data. Due to the fact, that an increasing amount of free iterated parameters will result in a better fit, in this case the number of emitting states cannot be determined distinctly by the applied fit. Instead of giving the exact number of components, the least number of getting acceptable fit results is denoted, which is the most likely count of emissive states. Because of this determination issues, the overall lifetime and distinct major components of the fitted decay are used to discuss the spectra.

In the case of **[Cu(DMP)$_2$][BF$_4$]** decay curves were recorded at 372 nm, 342 nm and 425 nm, since steady state luminescence was detected in this regions. Additionally, decay curves at 500 nm, 535 nm, 720 nm and 775 nm were detected although no luminescence was observed, since this are the ranges of MLCT luminescence emission according to literature.[120,201] The luminescence decays at 775 nm, 535 nm and 500 nm are not meeting an acceptable level of luminescence indicated by a large amount (>75 %) of scattering light with lifetimes around 10 ps dominating the decay. This result was expected since no significant luminescence intensity was detected in the first place. Intriguingly, photon counting at 720 nm reveals a decay, which consists at least of two components. The dominating decay exhibits a lifetime of 1.23 ns (±1.7 ps) in a two component fit, where the overall lifetime is determined as 1.52 ns (±4 ps). According to literature[182], the lifetime of the detected MLCT luminescence is 2 ns and is ranged in the same magnitude.

When considering the decays at 342 nm, 372 nm and 425 nm it can be stated, that the decays of the main components are located at approximately 1.3 ns indicating a comparable emissive species, which are assigned to π*-π transitions.

Table 4-11: Results of TC-SPC decay curve fitting for $[Cu(DMP)_2][BF_4]$.

Luminescence [nm]	Number of Components	$[Cu(DMP)_2][BF_4]$
342	≥1	1.83 ns (±4 ps)
372	≥1	1.48 ns (±3 ps)
425	≥2	1.90 ns (±10 ps)
500	-	-
535	-	-
720	≥2	1.52 ns (±4 ps)
775	-	-

Consistent with the photo-physical results of $[Cu(DMP\text{-}X)_2][BF_4]$ complexes from before, the weaker intense luminescence leads to a poor signal-to-noise ration. This is reflected by a large ratio of lifetimes shorter than $3 \cdot 10^{-12}$ s making an adequate decay analysis impossible.

Since the direct lifetime emission properties could only insufficient be characterized, time-resolved area normalized emission spectra of all **$[Cu(DMP\text{-}X)_2][BF_4]$** were conducted to prove the origin of the detected luminescence data. Isoemissive points between two spectral features indicate that the luminescence is based on the same excitation from the investigated complex.

As can be seen in figure 4-52 for **$[Cu(DMP)_2][BF_4]$**, after excitation the luminescence intensity is shifting from 370 nm to 473 nm within the first 7 ns exhibiting an isoemissive point at 432 nm. This simple pattern is also observable for **$[Cu(DMP\text{-}Cl)_2][BF_4]$** and **$[Cu(DMP\text{-}I)_2][BF_4]$**, but the isoemissive points are constantly shifted to higher wavenumbers to 470 nm and 520 nm, respectively. This may indicate an initial population of singlet ligand-based π-π* transitions at short lifetimes.[100] Afterwards long-living metal-based components out of MLCT excitations give rise to an increasing intensity at lower energy.[100]

The TRANES spectrum for **[Cu(DMP-Br)$_2$][BF$_4$]** is significant more complex, although the general trend of increasing signal strength at higher wavelength is also observed. In addition, an isoemissive point at 346 nm and an intersection point at 440 nm were detected. In addition, the signal intensity at 320 nm is initially rising reaching its maximum at 2.71 ns and then decreases again. The feature at 404 nm however does only exhibit a monotonous declining behavior. A contamination of other compounds seems unlikely, since single crystals were used for preparing the sample.

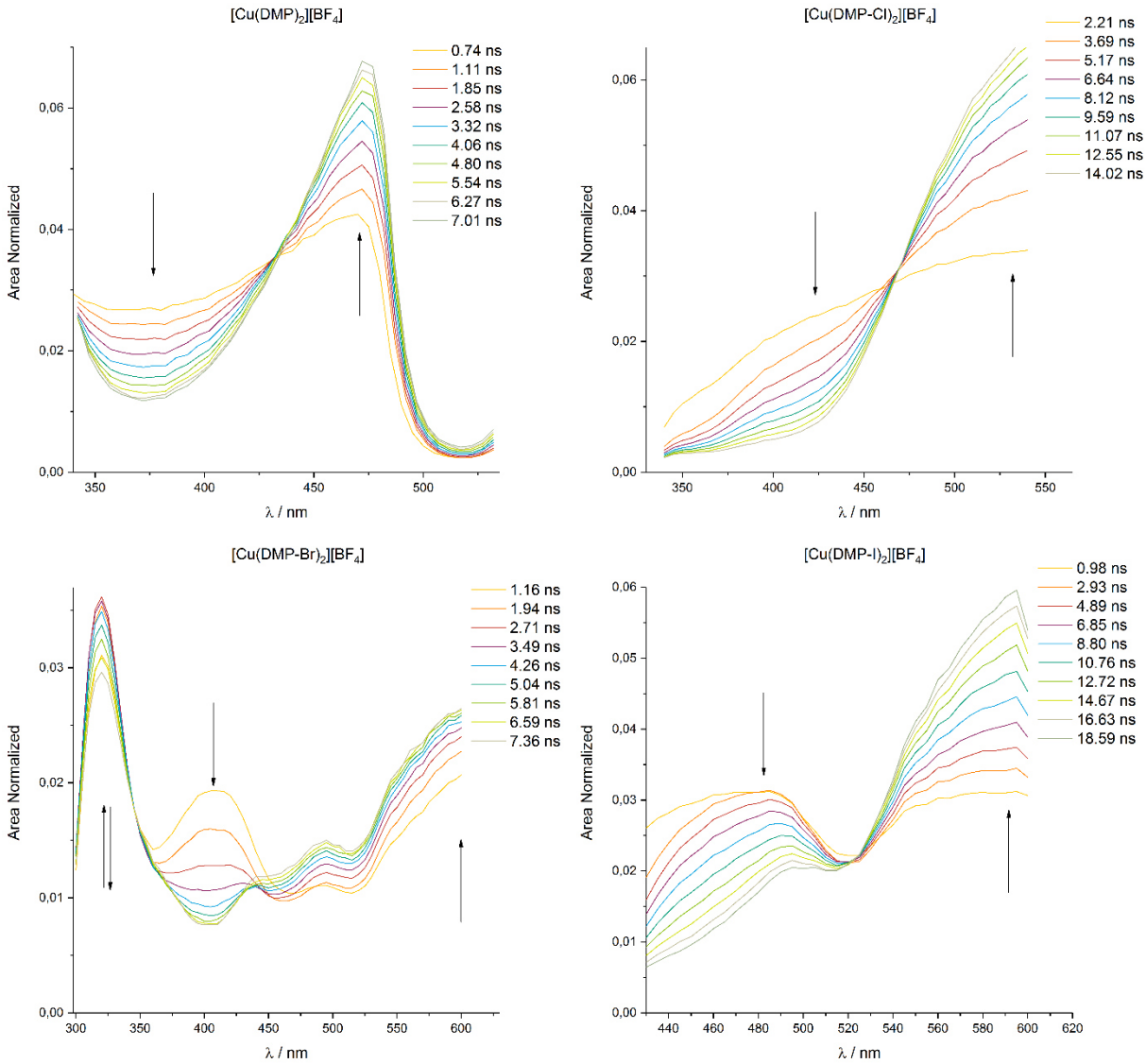

Figure 4-52: TRANES spectra for [Cu(DMP-X)$_2$][BF$_4$] complexes.

The decay time result for an MLCT of **[Cu(DMP)$_2$][BF$_4$]** were in the range of literature-known values, whereas the [Cu(DMP-X)$_2$][BF$_4$] complexes exhibits poor emission properties within the experimental set-up. Despite of that TRANES spectra delivered more detailed insights into the emission properties. One isosbestic point for all of these complexes is observed, which shifted to higher wavelengths with increasing size of the substituted halogen atom, except for **[Cu(DMP-Br)$_2$][BF$_4$]**. The spectroscopic results for **[Cu(DMP-Br)$_2$][BF$_4$]** show a unique and more complex behavior – as seen before and also seen for spectroelectrochemistry in chapter 4.2.1.7 – for this compound. The measured lifetimes were very short indicating singlet excited states most likely only.[100]

4.2.1.7 Electro- and spectroelectrochemistry of DMP-X-based copper(I) complexes

One key element of photosensitizer is a reversible transition between participating oxidation states. This behavior can be elucidated by electrochemical analysis of oxidation and reduction of the photosensitizers central metal. In case of copper photosensitizers the relevant transition is Cu^{II}/Cu^{I}, which is at the best a reversible one electron reaction indicating a fast, unhindered electron transfer. Cyclic voltammetry delivers a redox potential, which is a measure of the ease of this particular redox process. The results of cyclic voltammetry measurements and the square wave results for the copper(I) complex series are shown in figure 4-53. All measurements were performed as described in chapter 6.2.11 and in 10^{-3} M complex solution and 0.1 M TBA[PF_6] in MeCN. Unfortunately, an adequate baseline fit is not accessible due to additional redox-activity, which will be discussed in detail.

The reference compound **[Cu(DMP)$_2$][BF$_4$]** exhibits a pseudo-reversible behavior with the redox potential being located at 0.30 V vs. Fc/Fc^+ in MeCN (figure 4-53). The redox transition is verified by means of square wave. In the case of **[Cu(DMP-Cl)$_2$][BF$_4$]**, the Cu^{II}/Cu^{I} redox potential shifted significantly cathodic to 0.59 V vs. Fc/Fc^+. This is most likely due to the higher steric demand in 2,9 position as described in literature and chapters 2.2.5.1 and 4.2.1.4, respectively. Further enhancement of this demand by heavier homologues have only minor effect on increasing redox potentials over 0.60 V vs. Fc/Fc^+. for **[Cu(DMP-Br)$_2$][BF$_4$]** to 0.62 V vs. Fc/Fc^+ for **[Cu(DMP-I)$_2$][BF$_4$]**. This is in accordance with the decreasing flattening ability determined by UV/VIS spectroscopy. In addition, this results are in agreement with similar steric studies and typical redox potentials in literature[100], especially by *McMillin* et al.[117,125] and *McCusker* at al.[130][202].

Intriguingly, an less intense transition in the cyclic voltammogram of **[Cu(DMP-Cl)$_2$][BF$_4$]** in the range of 0.00 V vs. Fc/Fc^+ is observable, which is not the reference Fc/Fc^+ system. This may indicate a partly decomposition of the complex, since the signal increased with increasing number of cycles. Then most likely chloride ions are emitted into the solution, which are then reduced to chlorine.[203–205] That is also the reason why, the anodic signal is more pronounced, since changed aggregation state is an potential barrier and entails a significantly irreversible behavior.

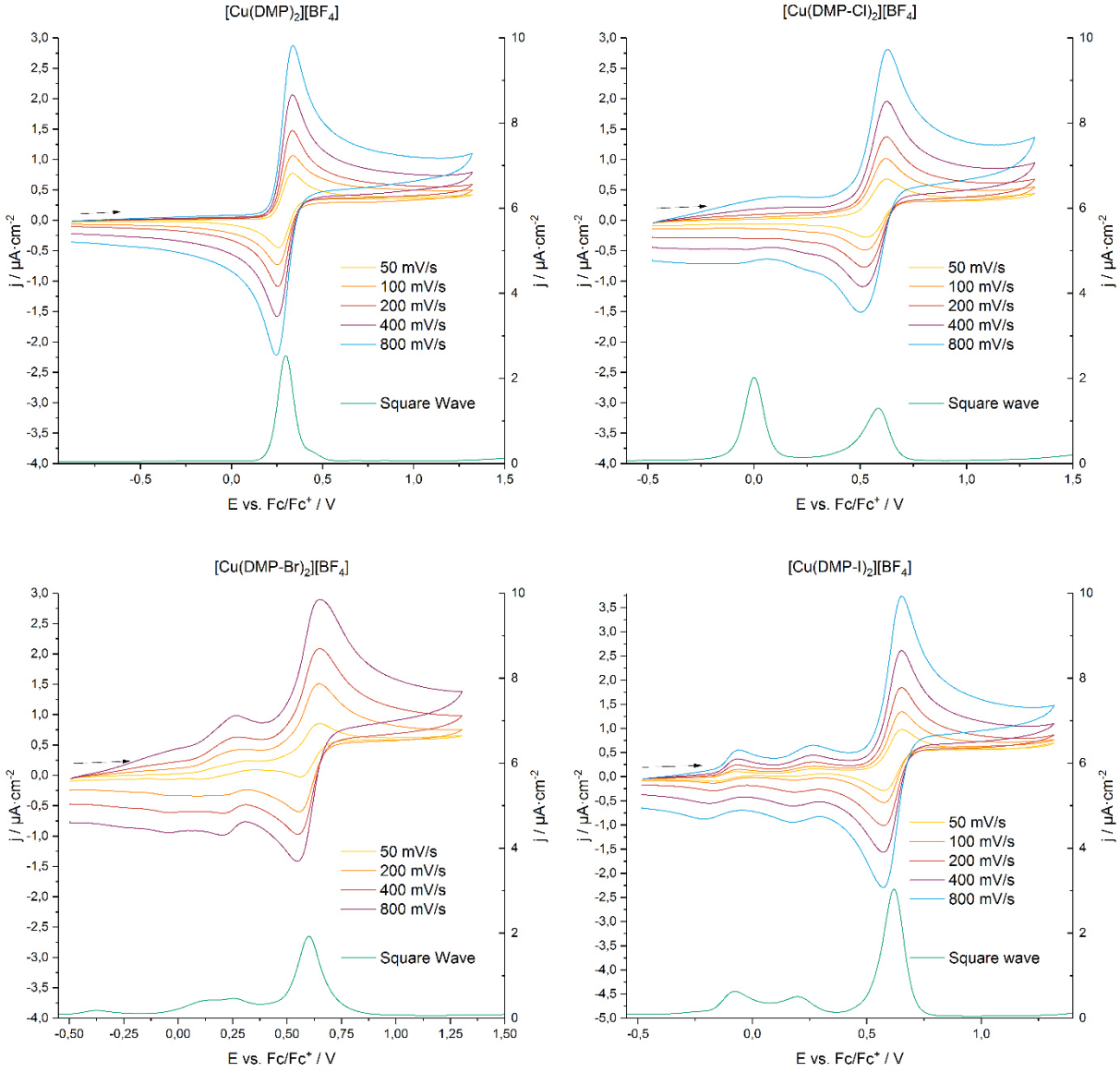

Figure 4-53: Cyclic voltammetry and square wave spectra of 10^{-3} M [Cu(DMP-X)$_2$][BF$_4$] complexes in MeCN.

This is even more distinct in **[Cu(DMP-Br)$_2$][BF$_4$]** and **[Cu(DMP-I)$_2$][BF$_4$]**, where two additional features can be observed. In the case of **[Cu(DMP-Br)$_2$][BF$_4$]**, a broad signal with two peaks is observable. The signal at 0.25 V vs. Fc/Fc$^+$ can be assigned to 2 Br_3^- → 3 Br_2^- + 2 e^-, as described in literature.[203–205] The reaction 3 Br^- → Br_3^- + 2 e^- was assigned to the second feature at 0.15 V vs. Fc/Fc$^+$.[203–205] A comparable behavior is observable for **[Cu(DMP-I)$_2$][BF$_4$]** at 0.20 V vs. Fc/Fc$^+$ and -0.08 V vs. Fc/Fc$^+$ with analogue reactions as described before.[203,205,206]

Table 4-12: Data from cyclic voltammetry of $[Cu(DMP\text{-}X)_2][BF_4]$ complexes.

Complexes	$E^0(Cu^{II}/Cu^{I})^a$ [V]	$2\ X_3^- \rightarrow 3\ X_2^- + 2\ e^-$ [V]^a	$3\ X^- \rightarrow X_3^- + 2\ e^-$ [V]^a
$[Cu(DMP)_2][BF_4]$	0.30	-	-
$[Cu(DMP\text{-}Cl)_2][BF_4]$	0.59	not assignable	not assignable
$[Cu(DMP\text{-}Br)_2][BF_4]$	0.60	0.25	0.15
$[Cu(DMP\text{-}I)_2][BF_4]$	0.62	0.20	-0.08
a) Measured as 10^{-3} M $[Cu(DMP\text{-}X)_2][BF_4]$ solution in MeCN versus Fc/Fc^+.			

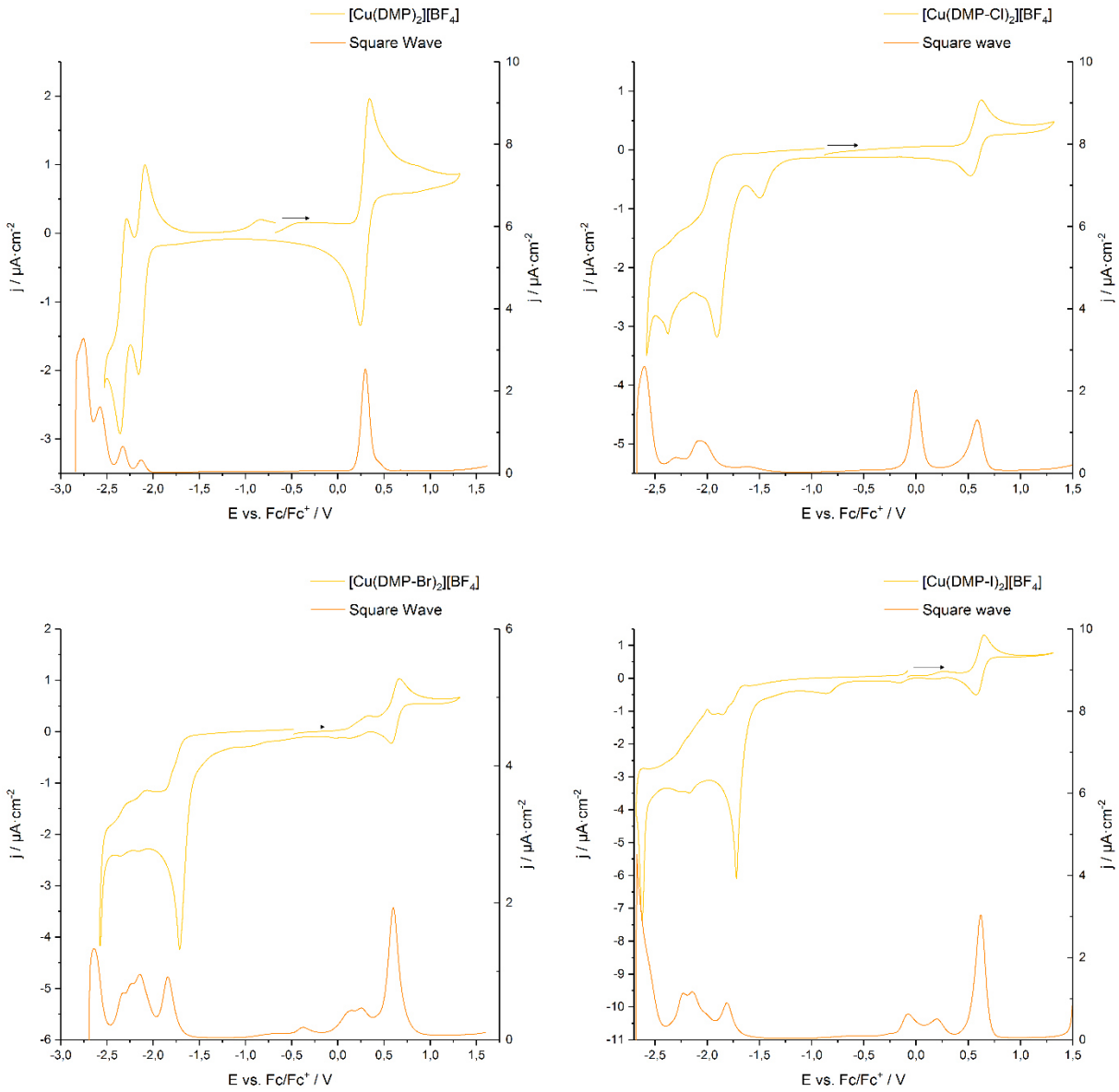

Figure 4-54: Cyclic voltammetry overview for the $[Cu(DMP\text{-}X)][BF_4]$ series.

Beside the interesting Cu^{II}/Cu^{I} redox transition additional reduction signals were observed when sweeping to cathodic potentials, as can be seen in figure 4-54. Two only partly or not reversible reduction signals were obtained in the case the discussed series, which could be caused by ligand reductions and/or by a Cu^{I}/Cu^{0} redox transition.[89,207] *McMillin* et al. found no Cu^{I}/Cu^{0} signal for $[Cu(DMP)_2][PF_6]$, but for several other $Cu(NN)_2^+$ complexes at ca. – 2.18 V vs. Fc/Fc^+ in MeCN solution. Based on the acquired data no distinct assignment could be conducted. Especially, the irregular and irreversible CV and broad square wave signals for the copper complexes with halogenated ligands impedes proper analysis. Despite of that it can be stated, that the oxidation potentials shift to higher potentials with increasing period of halogen atoms indicating an easier reduction, as denoted in table 4-13. In addition, all reductions for the halogenated species are irreversible.

Table 4-13: Reduction signals of $[Cu(DMP\text{-}X)_2][BF_4]$.

Complexes	Additional Signal [V][a]	E^0(Ox1) [V][a]	E^0(Ox2) [V][a]
$[Cu(DMP)_2][BF_4]$	-	-2.12	-2.33
$[Cu(DMP\text{-}Cl)_2][BF_4]$	-1.50[bc]	-2.07[bd]	-2.29[b]
$[Cu(DMP\text{-}Br)_2][BF_4]$	-	-1.84	-2.22[d]
$[Cu(DMP\text{-}I)_2][BF_4]$	-	-1.81[d]	-2.19[d]

a) Measured as 10^{-3} M $[Cu(DMP\text{-}X)_2][BF_4]$ solution in MeCN versus Fc/Fc^+.

b) Reduction peak visible only.

c) Assignment of reduction signal. No significant square wave signal.

d) Broad signal, most likely more signals. CV signals not clearly assignable.

The electrochemical oxidation can be monitored during electrolysis by a variety of spectroscopic methods showing a spectrum for the oxidized copper(II) species. This is particularly interesting, like in this case, when data for the analogous Cu(II) complexes are lacking. Despite common opinion, isosbestic points are not a direct proof for a smooth, quantitative formation of redox species or that an equilibrium between two species is present.[208,209] Instead isosbestic point indicates an unchanged reaction stoichiometry and that no side reaction take place during oxidation or reduction, respectively. The absorbance of the involved species at this point is constant as long

as the ratio between the substances are held constant.[208,209] Ideal two species can also be pretended by fast chemical reactions after electrochemical electron transfer. Performing the re-electrolysis to the initial species and comparing these data to the former, is a probe for the chemical stability and verifies the reversibility of the electrochemical process.[208,209]

Spectroelectrochemistry of the synthesized copper(I) complexes was obtained in a 10^{-3} M sample solution in MeCN with TBA[PF_6] as conduction salt in the *Metrohm-Autolab* set-up as described in chapter 6.2.11. First, each spectra set for each compound is discussed separately to lead then to a general property overview. The intensity changes in the spectra are indicated with arrows.

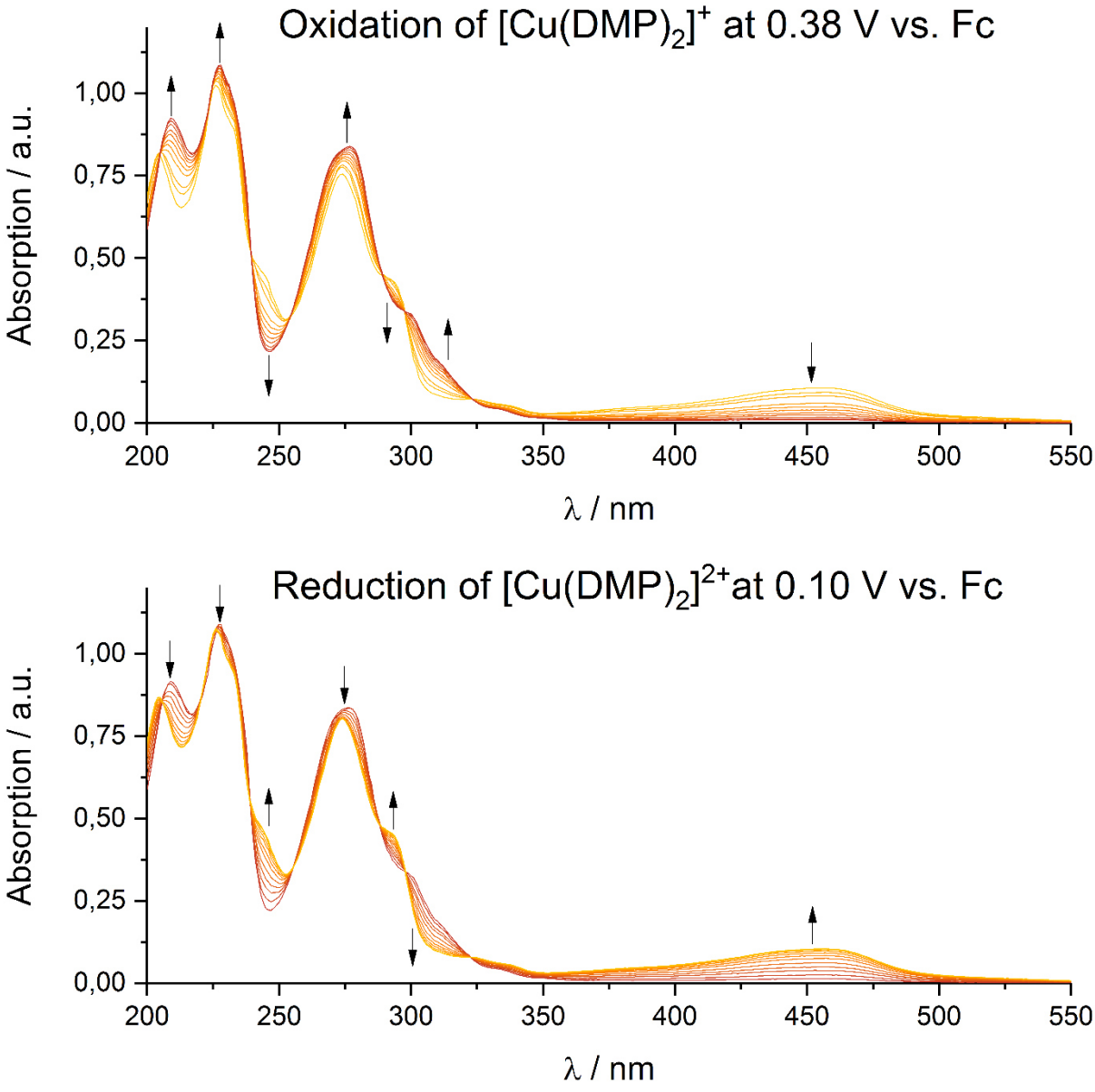

Figure 4-55: UV/VIS spectroelectrochemistry of [Cu(DMP)$_2$][BF_4].

The most striking feature for **[Cu(DMP)$_2$][BF$_4$]** is the loss of the copper(I) specific MLCT transitions at 456 nm with increasing electrolysis, as can be seen in figure 4-55. Since the higher energy $S_1 \leftarrow S_0$ shoulder is also a MLCT transition, the intensity decreases here consequently, as calculated. The flank around 300 nm exhibits three isosbestic points giving rise to a signal intensification between 300 nm an 325 nm. According to calculations, here may be a mixture of π-π*, d-π*, π-d and d-d transitions. The last mentioned would consequently give rise to increasing intensities upon oxidation. Comparison of UV/VIS spectra at the end of the oxidation process and from single crystals of **[Cu(DMP)$_2$][BF$_4$]$_2$** verifies the successful oxidation without side processed. After ending the reduction process, the steady state spectrum is consistent with the spectrum at before starting the experiment indicating full reversibility. A typical,

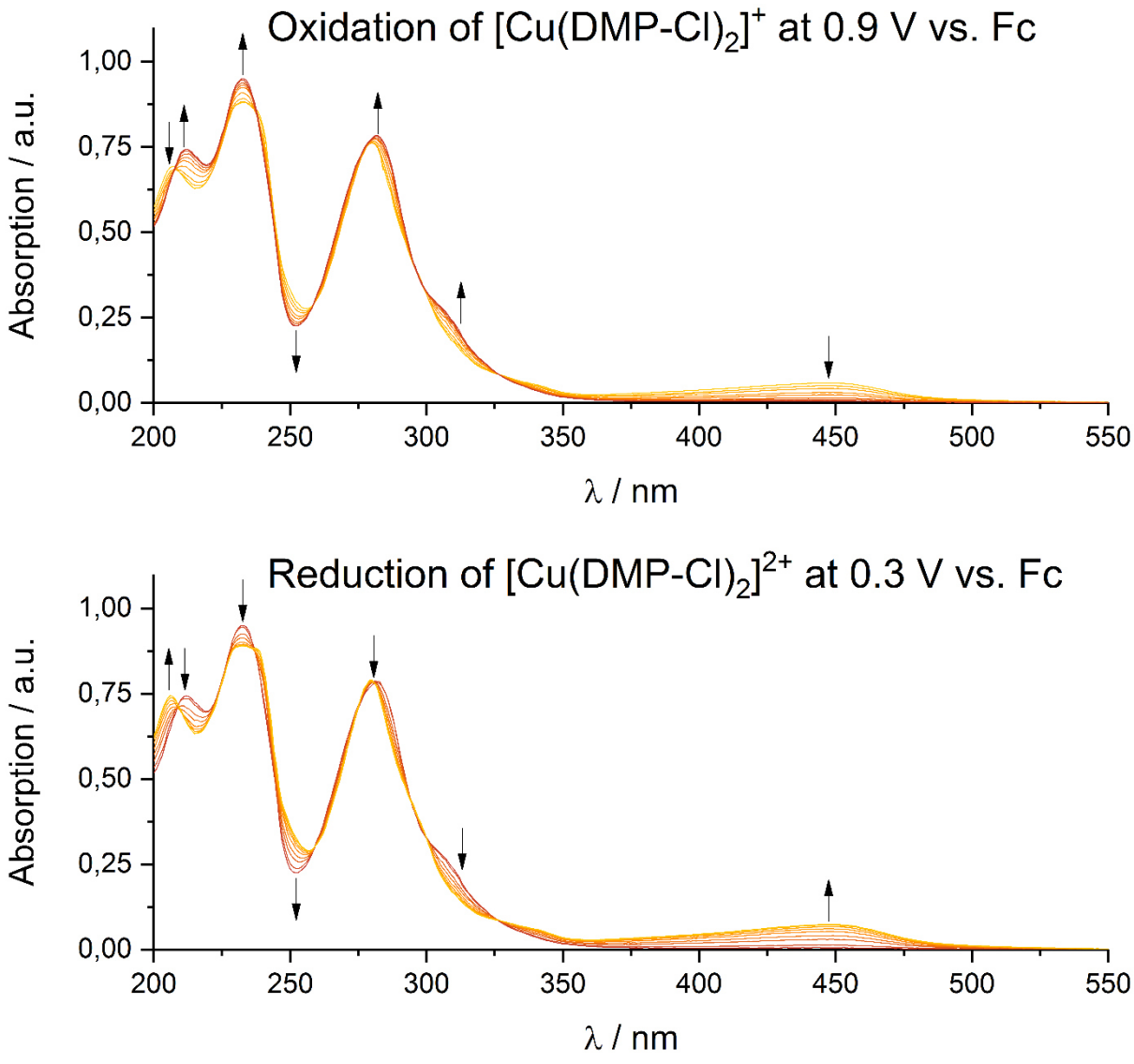

Figure 4-56: UV/VIS spectroelectrochemistry of [Cu(DMP-Cl)$_2$][BF$_4$].

broad d-d transition for tetragonal distorted copper(II) complexes resulting from $2E_g \leftarrow 2T_{2g}$ around 620 nm is not visible.

A consistent optical behavior can be observed for **[Cu(DMP-Cl)$_2$][BF$_4$]** (figure 4-56), although the structure in the shoulder at ca. 300 nm is altered. In the region between 295 nm and 298 nm all traces are parallel aligned, therefore no isosbestic points could be assigned. In comparison to the aforementioned reference compound here should be two isosbestic points. These points are indicated red in table 4-14 to differentiate them from assigned isosbestic points.

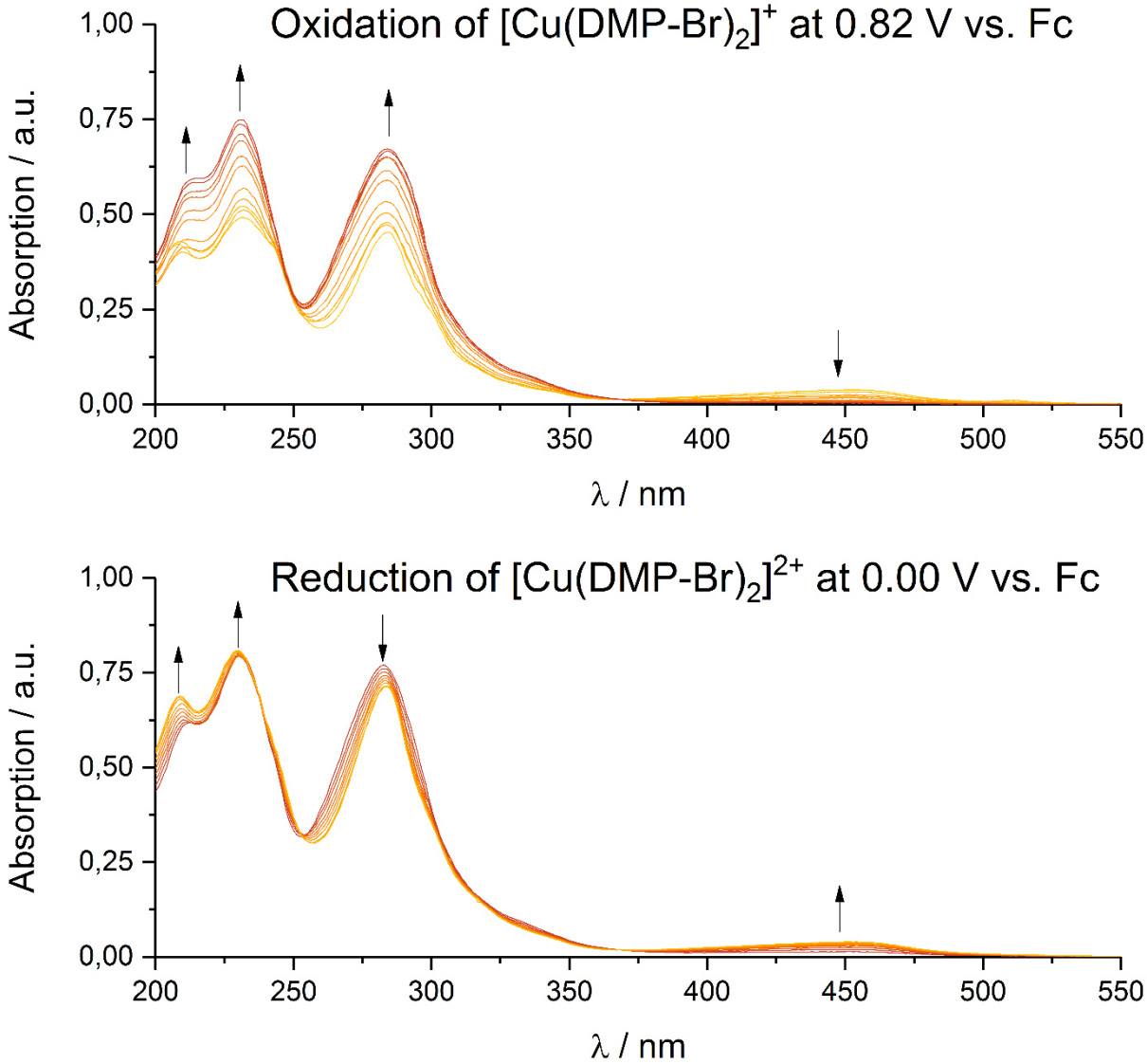

Figure 4-57: UV/VIS spectroelectrochemistry of [Cu(DMP-Br)$_2$][BF$_4$].

The results for **[Cu(DMP-Br)$_2$][BF$_4$]** (figure 4-57) are significantly different from the discussed spectra. In the range of π-π* transitions, no isosbestic point or even intersections are detected. Instead, just constant signals increase or decrease is

observable, although the absolute number of three features remains unchanged. Despite of that, the successful oxidation is verified by declining intensity of the MLCT band around 450 nm. Only one intersection point at 247.6 nm can be observed, when oxidizing the complex. Interestingly, two intersection points at 237.6 nm and 253.3 nm can be assigned during the reduction step indicating that a small amount of the complex may be decomposed during the electrochemical oxidation and reduction. The majority, however, resisted destructive processes, since the general signal pattern und the maximal remained the unchanged.

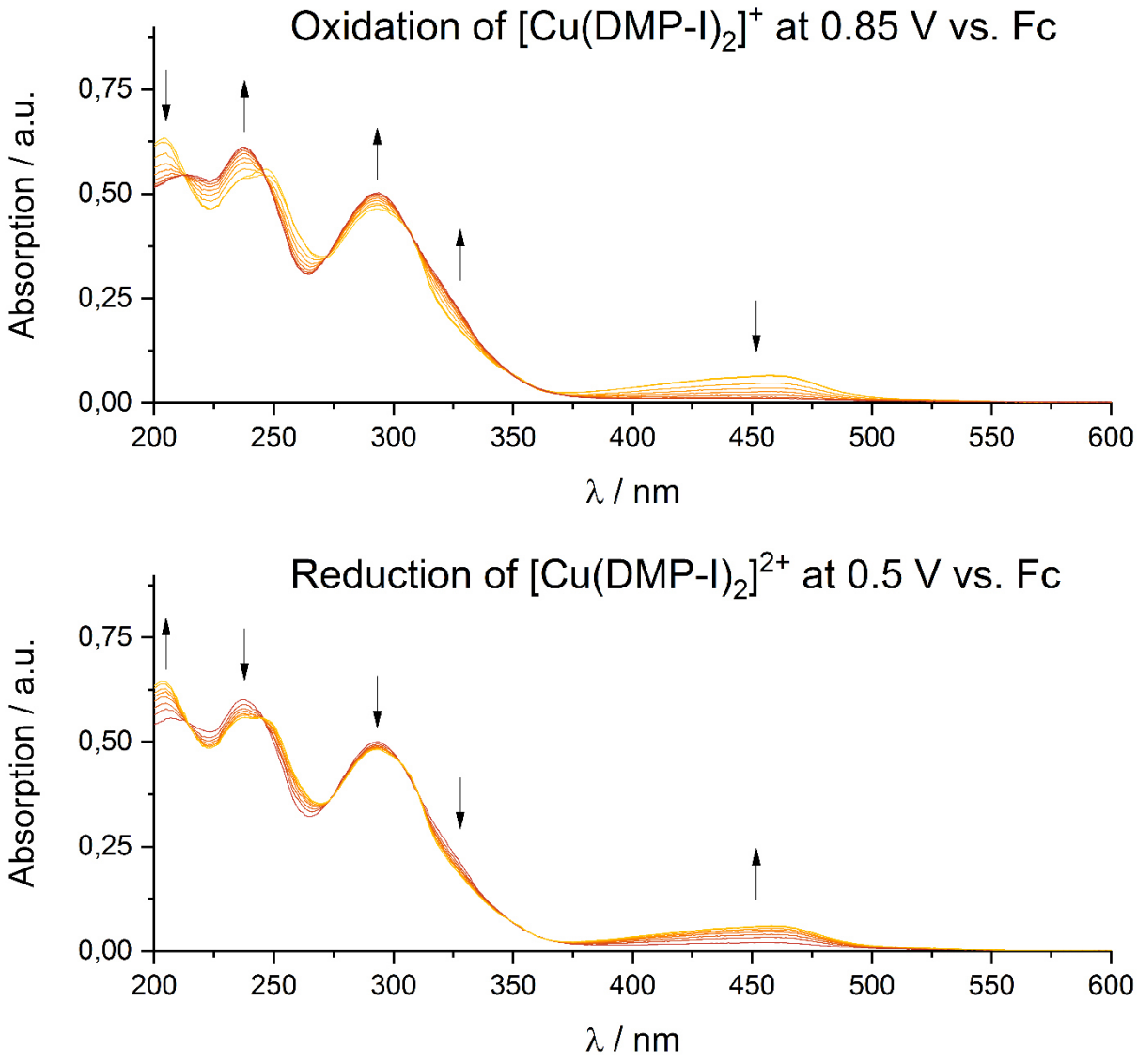

Figure 4-58: UV/VIS spectroelectrochemistry of [Cu(DMP-I)$_2$][BF$_4$].

In the case of **[Cu(DMP-I)$_2$][BF$_4$]** (figure 4-58), the spectroelectrochemical behavior is more comparable to **[Cu(DMP)$_2$][BF$_4$]** and **[Cu(DMP-Cl)$_2$][BF$_4$]** indicating a singular behavior of **[Cu(DMP-Br)$_2$][BF$_4$]**. For each of the three main features one isosbestic point is assignable during oxidation and reduction, although these are significantly

shifted as expected based on UV/VIS spectra of the Cu(I) complex series. The key differentiator to **[Cu(DMP)$_2$][BF$_4$]** and **[Cu(DMP-Cl)$_2$][BF$_4$]** is the missing at around 295 nm as in the **[Cu(DMP-Br)$_2$][BF$_4$]** case. In the oxidative case, the intersection points at 306.9 nm and 348.1 nm are most likely not fully resolved, since for each of these points two more isosbestic or crossing points are observable in the reduction part.

Table 4-14: Isosbestic points in UV/VIS spectroelectrochemistry spectra of DMP-X-based copper(I) complexes.

Isosbestic points	[Cu(DMP)$_2$][BF$_4$]	[Cu(DMP-Cl)$_2$][BF$_4$]	[Cu(DMP-Br)$_2$][BF$_4$]	[Cu(DMP-I)$_2$][BF$_4$]
1 [nm]	205.0 (205.6)	207.5 (204.9)	–	212.8 (214.0)
2 [nm]	239.5 (239.1)	237.1 (236.9)	– (237.6)	246.0 (245.8)
3 [nm]	254.6 (255.4)	258.4 (258.9)	247.6 (253.3)	272.3 (274.0)
4 [nm]	289.1 (288.2)	295.6 (294.2)	–	–
5 [nm]	297.6 (297.7)	298.9 (300.0)	–	306.9 (302.9, 310.3)
6 [nm]	323.4 (322.7)	326.5 (326.0)	368.5 (369.0)	348.1 (348.1, 361.0)

Values without brackets were assigned from the oxidative and values in brackets were assigned from the reductive part.

Red marked: Point not or not clearly assignable as isosbestic points, but are at least intersection points or ranges.

To sum up, all spectra sets show reversibility of the Cu^{II}/Cu^{I} transition within this given set-up. This was additionally verified by cyclic voltammetry before and after each step. Only **[Cu(DMP-Br)$_2$][BF$_4$]** exhibits signs of potential decomposition side products during the oxidation-reduction cycle, due to lack of several intersection points, which are observed in the other cases. This finding is surprising, since the **DMP-I** ligand was determined as the most instable ligand within the series.

The successful oxidation to Cu(II) is proven by total lack of the MLCT transition in the range of 450 nm, since the oxidation entails the change of electronic configuration from d^{10} to d^9, thus eliminating the mentioned transition and giving rise to possible d-d transitions. For **[Cu(DMP)$_2$][BF$_4$]** and **[Cu(DMP-Cl)$_2$][BF$_4$]**, a decrease in intensity for the flank at ca. 340 nm is observed, which is consistent with the loss of $S_1 \leftarrow S_0$ MLCT

transitions as assigned by literature[190,191] and calculations in this work. π-d transitions in the same region could be responsible for the decrease or plateaus in UV/VIS spectra of **[Cu(DMP-Br)$_2$][BF$_4$]** and **[Cu(DMP-I)$_2$][BF$_4$]**.

4.2.1.8 IR spectroscopy of DMP-X-based copper(I) complexes

ATR-IR spectroscopy was conducted to identify the complexes with easy and verify a complexation by comparison with the ligands spectra. The overall accordance of experimental and calculated spectra is sufficient to assign and compare signals, although the largest shift deviation is about 36 cm^{-1}. To improve readability, calculated values are denoted in brackets.

In contrast to the IR analysis results of the isolated ligands in chapter 4.1.2.3, a single characteristic C-X stretching vibration could not be assigned in the case of their copper(I) complexes. Instead of that this vibration is coupled to ring centered vibrations and smeared out over a significant wavenumber range according to calculations, which exhibit the same period dependency as discussed before. Assigned signals are listed in table 4-15. According to the calculation, the striking intense signal around 1040 cm^{-1}, which is detected in every spectrum, is mainly generated by the two ligand scaffold and methyl rocking vibrations. That is why there is no significant shift within the series.

Table 4-15: Assignment of C-X involving vibrations in DMP-X-based copper(I) complexes.

Ligand	$\tilde{\nu}$ ranges [cm^{-1}]	$\tilde{\nu}$ [cm^{-1}]
[Cu(DMP-Cl)$_2$][BF$_4$]	578 – 734 (586 – 744)	578.6 (587.8), 628.7 (641.4), 648.0 (658.2), 688.5 (696.0), 711.7 (725.4), 734.8 (742.2)
[Cu(DMP-Br)$_2$][BF$_4$]	521 – 638 (530 – 636)	522.7 (530.0), 541.9 (555.9), 638.4 (636.4),
[Cu(DMP-I)$_2$][BF$_4$]	496 – 615 (500 – 620)	496.6 (501.0), 520.9 (526.5), 614.1 (620.5)
Calculated values are denoted in brackets.		

In the case of **[Cu(DMP-Cl)$_2$][BF$_4$]**, the calculated spectra is nearly constantly shifted about 10 cm^1 to the experimental spectrum for the range of C-Cl involving vibrations. The intense signals at 689 cm^{-1} (calc. 696 cm^{-1}) and 712 cm^{-1} (calc. 725 cm^{-1}) is assigned to scaffold vibration including a small amount of ν_{as} C-Cl. These vibrations

are shifted to lower wavenumbers for **[Cu(DMP-Br)$_2$][BF$_4$]**. The highest absorption for a ν_{as} C-Br containing vibration is detected at 638 cm^{-1} (calc. 636 cm^{-1}) exhibiting additionally ring bending vibrations. A second vibration of comparable intensity, as for **[Cu(DMP-Cl)$_2$][BF$_4$]**, was whether calculated nor experimentally observed. Even more shifted are the ν_{as} C-Br involving vibrations for **[Cu(DMP-I)$_2$][BF$_4$]**, which are acquired at 496 cm^{-1} (calc. 501 cm^{-1}). Here, scaffold vibrations play also a part in this signals.

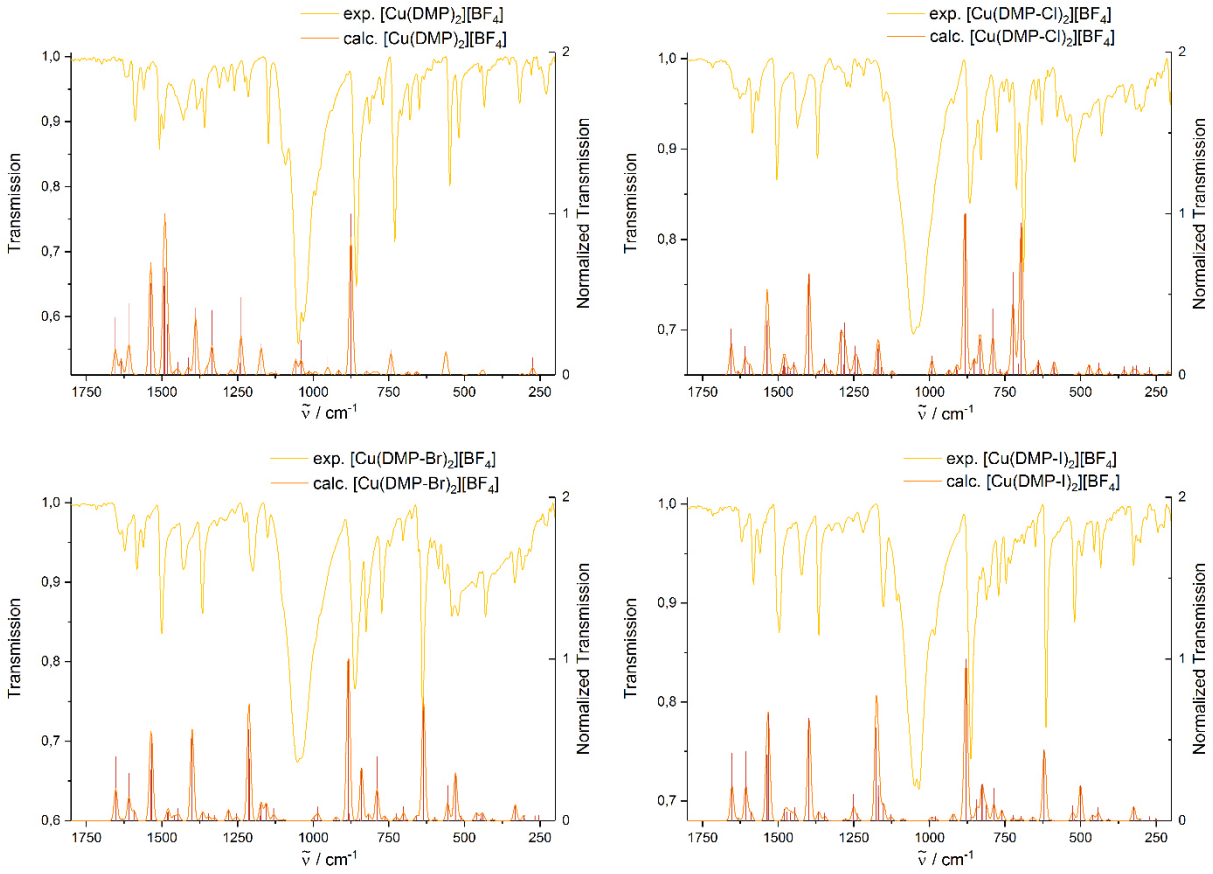

Figure 4-59: Experimental and calculated IR spectra of DMP-X-based copper(I) complexes.

An assignment of a single, isolated vibration for the identification of each species was not possible, although the fingerprint range in total identifies each compound. Combined vibrations are described and compared to literature and calculation. The latter made it possible to assign observed signals.

4.2.1.9 Water reduction catalysis of DMP-X-based copper(I) complexes

Photo-catalysis utilizing copper(I) complexes are common in literature due to their straight forward synthesis and the ease of tuning their photo-physical properties, as discussed extensive in chapters 2.2.5 and 2.2.5.1. Since **[Cu(DMP)$_2$][BF$_4$]** is a literature known complex and well investigated, it was reasonable to test the catalytic set-up with this substance, although no reference for the catalytic performance under comparable conditions was found.

The water reduction catalyst was chosen based on a solid activity and establishment in water splitting reactions. An easy preparation of the catalyst is also crucial to ensure reproducibility and therefore a good comparability between the photosensitizers. All this requirements are met by [K_2PtCl_4], which forms colloid platinum *in situ* under reductive, illuminated reaction conditions.[42–44,210,211] Although, colloidal particle of [K_2PtCl_4] are known to exhibit an induction period up to 40 min[35,39], no such behavior was observed in any case for other catalytic reactions within the working group.

In the following the explicit course of action for water reduction catalysis runs is specified, while the general procedure is described in chapter 6.2.12. **[Cu(DMP)$_2$][BF$_4$]** was previously dissolved in MeCN (13.3 ml) and [K_2PtCl_4] was dissolved in triethylamine (3.33 ml)/water (3.33 ml). Initially, a total concentration of 0.35 mM **[Cu(DMP)$_2$][BF$_4$]** (7 µmol, 3.79 mg) and of 0.5 mM [K_2PtCl_4] (10 µmol, 4.15 mg) was prepared regarding to the whole reaction volume of 20 ml, adapted from *Beller* et al.[212]. In several runs no significant gas evolution was detected after temperature and blind correction. The PS is most likely the catalysis determining substance due to the formation of reaction radical cations during photo-excitation resulting in decomposition reactions, although no significant color change was observable. Because of the fact that the PS is most likely the bottleneck[213], the amount of copper complex was increased to 15 µM (8.5 mg) without any effect. Because of the presence of small black particles, the reduction of [K_2PtCl_4] to form platinum(0) species was considered successful. According to previously published research[43][211], particle and cluster size are an important parameter showing that increasing size is correlated with decreasing catalytic activity.

Interestingly, a similar catalytic run from *Karnahl* et al. delivers a significant gas volume by using a less amount of $[Cu(DMP)_2][PF_6]$ and a assumed less efficient iron based water reduction catalyst.[131]

The model complex **$[Cu(DMP)_2][BF_4]$** delivered no satisfactory results. Since the other $[Cu(DMP\text{-}X)_2][BF_4]$ complexes exhibited inferior optical behavior in populating the MLCT states, as shown before, these were not tested.

4.2.2 DMP-based Cu(II) complexes as models for the excited state

Since Cu(II) is the formal photo-oxidized and flattened state, these kind of homoleptic tetra coordinated coordination compounds were synthesized as model species. Hence, these should give deeper insight into the photo-chemistry of copper indicating a possible geometric shape of the photo-excited state.[89]

In addition, samples of **$[Cu(DMP)_2]^+$** and **$[Cu(DMP)_2]^{2+}$** for HERFD-XANES and VtC emission spectra, several anions and reaction parameters were investigated. Since the **$[Cu(DMP)_2]^+$** exhibits no additional coordination molecules, a key problem was to ensure no coordination of solvents or anions beside two **DMP** ligands for $[Cu(DMP)_2]^{2+}$, although Cu(II) is prone to an attack of Lewis bases due to the flattened geometry and the low electron density of the copper ion. In the following, the synthesis and obtained structures will be discussed.

The general synthesis procedures typically included dissolving of the ligand and the copper(II) precursor in the solvent and then adding one solution dropwise to the other. In case of a precipitation, more solvent was added in order to solve the solid before continuing the addition. When the resulting precipitate was not soluble in the chosen solvent, it was filtered off and dissolvent in a more effective solvent. In most cases MeOH was sufficiently used as solvent and a diethyl ether diffusion was performed to obtain single crystals.

First, a simple complexation reaction between **DMP** and $CuCl_2$ was performed. Intriguingly, two different types of single crystals were obtained during the approach of synthesizing the $[Cu(DMP)_2]^{2+}$ structure motive. The choice of solvent decides, which species is favored establishing a switchable system. When using a polar solvent like MeOH for crystal growth by diethyl ether, only green **$[Cu(DMP)_2(Cl)][Cl]$** crystals are formed. The structural motive **$[Cu(NN)_2(Cl)][Cl]$** is very common, since copper(II) favors a penta coordinate structure indicating the problem of preventing such behavior.[89,110,111] In the special case of DMP ligands based complexes, this is the first example, beside an bridged ligand of *Noll* et al..[214] The diimine ligands are coordinating the copper ion in a distorted and flattened tetrahedral geometry opening another coordination site, which is here held by one of the two chloride anions.

Table 4-16: DMP complexes of copper(II) obtained by variation of copper(II) sources.

Complex	Crystals	Additional ligand	Torsion angle
$[Cu(DMP)_2(Cl)][Cl]$	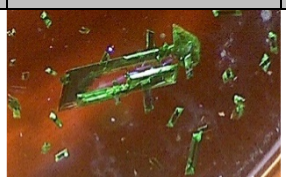	Cl Cu-Cl 2.32 Å	76.1 °
$[Cu(DMP)_2(Br)][Br]$	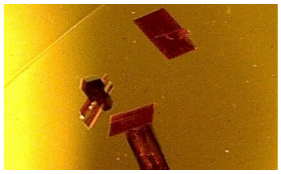	Cu-Cl 2.26 Å Cu-(μ-Cl) 2.34 Å	Ligands parallel
$[Cu_2\text{-bis}(\mu\text{-}Cl)(DMP)_2(Cl)_2]$	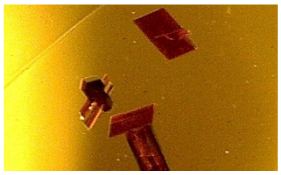	Cu-Cl 2.26 Å Cu-(μ-Cl) 2.34 Å	Ligands parallel
$[Cu(DMP)_2(MeOH)][ClO_4]_2$	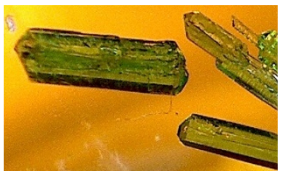	MeOH Cu-O 2.12 Å	65.0 °
$[Cu(DMP)_2(NO_3)][NO_3]$		NO_3 Cu-O 2.05 Å	76.2 °
$[Cu(DMP)_2(MeCN)][BF_4]_2$		MeCN Cu-N 2.01 Å	75.7 °
$[Cu(DMP)_2(BF_4)][BF_4]$	 Green crystals	BF_4 Cu-F 2.19 Å	66.4 °
$[Cu(DMP)_2][BF_4]_2$	 Brown crystals	None	54.4 ° 59.7 °

An additional distinct feature in these complexes is the fact, that the ligand planes and the N-Cu-N planes deviate lifting the copper ion out of the ligand planes. For **[Cu(DMP)$_2$(Cl)][Cl]** the deviation of both planes are 25.5 ° and 13.5 °, which results in a plane to copper distance of 0.66 Å and 0.37 Å, respectively. This is exceeding the highest literature known values of 0.61°Å[214] and 0.62 Å[215] significantly.

By changing the solvent to DCM – a lesser polar solvent -, **[Cu$_2$-bis(μ-Cl)(DMP)$_2$(Cl)$_2$]** is formed, which can be considered as a dimer of the aforementioned complex in which the before free anions are establishing a bis(μ-Cl) bridge between two copper ions. The central [Cu$_2$-bis(μ-Cl)(Cl)$_2$] unit can be described as kite with two non-bridging chloride pushed out of the kite´s plan. Both ligand planes in a parallel alignment with a distance of 2.03 Å, while the bridging chloride atoms are located 0.12 Å and 0.20 Å out of plane, which is also true for both copper atoms by 0.15 Å and 0.18 Å, respectively. All bond lengths are almost unaffected by the additional coordination compared to the monomeric species. Motives like this are also common in copper coordination chemistry.[145,146]

To suppress anion coordination, the anion was switched to perchlorate, since the negative charge is distributed over a larger volume. By crystallization from MeOH/Et$_2$O **[Cu(DMP)$_2$(MeOH)][ClO$_4$]$_2$** was obtained as green crystals. The bond length between copper and the methanol oxygen – 2.12 Å – is 0.11 Å shorter in comparison to all published [Cu(NNNN)(MeOH)] structures, where the copper ion is penta-coordinated.[146] The central copper ion is lifted out of both ligand planes by 0.34 Å and 0.42 Å. One **DMP** ligand is significantly bended with about 9.4 °, although the ligands environment in the crystal is a not bended ligand at 3.48 Å and an oxygen of the anion at 3.09 Å distance.

With nitrate as anion, crystals of **[Cu(DMP)$_2$(NO$_3$)][NO$_3$]** were obtained from complex-ation reaction in MeOH, which resulted in a precipitation of polycrystalline bright green material. Only one comparable complex has been mentioned in literature.[216] Redis-solving this solid in MeOH gave a red solution and green single crystals after slow diffusion of diethyl ether. The crystal reveals the direct coordination of an anion´s oxygen atom at 2.05 Å with another oxygen and the nitrogen atom being at a distance of 3.06 Å and 4.07 Å, respectively. Here, one of the ligands is also bend by 14.8 °. It has to be mentioned, that red crystals were obtained from a solution were the MeOH

was allowed to evaporate under room conditions. Due to the color and the experience in the reactions before, formation of a bridged dinuclear copper(II) complex is likely explanation. Unfortunately, the crystal quality was too poor to be analyzed by X-ray diffractometry.

Since halide, perchlorate and nitrate anions did not deliver a tetra coordinate Cu(II) complex, the weakly coordinating tetrafluoroborate was utilized to accomplish the aim. **DMP** and $Cu(BF_4)_2$ was dissolved in MeOH resulting in a green solution, which then darkened. Brown crystals were obtained by subsequent diethyl ether diffusion. The asymmetric unit exhibits two copper(II) complexes. One of them is coordinated by an additional ligand, which could not be resolved. The results of this experiment are not mentioned in table 4-16 because of poor crystal quality.

To investigate the behavior of another Lewis base solvent MeCN the same reaction was performed in MeCN. X-ray diffraction verifies **$[Cu(DMP)_2(MeCN)][BF_4]_2$** to be the green crystals gained (figure 4-60, left). The highest ligand bending (11.8 ° and 10.2 °) was in this work was observed for this compound. 11.8 ° is an exceptional value for the angle between the two terminal ring planes and is under the seven highest angles for published copper phenanthroline complexes in the *Cambridge Structural Database*[146], one of them[217] exhibiting the same chemical connectivity. During the transfer of these crystals from a vessel into the high viscous preparation oil, turned brown and starts to fissure when handling in air. A recrystallization of the mother liquor resulted in mainly dark brown crystals, which were finally confirmed as **$[Cu(DMP)_2][BF_4]_2$**. In air and at r.t., solvent is emitted by **$[Cu(DMP)_2(MeCN)][BF_4]_2$** to give the brown tetra coordinate copper(II) complex.

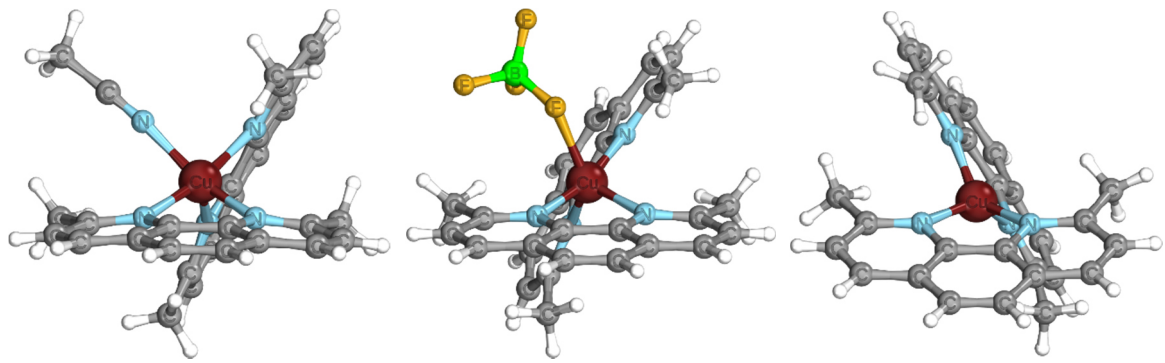

Figure 4-60: Comparison of $[Cu(DMP)_2(MeCN)]^{2+}$ (left), $[Cu(DMP)_2(BF_4)]^{+}$ (middle) and $[Cu(DMP)_2]^{2+}$ (right).

As a byproduct of this reaction another crystalline species was grown in small amounts, in which the copper center is directly coordinated by one fluorine of the anion turning the crystals color to green (figure 4-60, middle). The ligand bending angles in **[Cu(DMP)$_2$(BF$_4$)][BF$_4$]** (9.9 ° and 4.7 °) queues in the row before. This tension is also shown by a high deviation between N-N-Cu planes and ligand planes (22.4 ° and 15.9 °) lifting the copper up to 0.58 Å out of the ligands planes. Only two copper phenanthroline complexes are known to exhibit a larger difference.[214,217] This crystal structure was unknown to literature, although the general type of this compounds was known as discussed before.

Unfortunately, all reactions between DMP-X ligands and copper(II) precursors including $CuCl_2$, $Cu(BF_4)$ and anion exchanges of the afore mentioned solution with KPF_6 did not result in crystalline species. Most promising results was obtained when complexing **DMP-Br** with $Cu(BF_4)_2$ the methanolic solution turned orange and small red crystals and polycrystalline pale green crystals unsuitable for X-ray diffraction were obtained.

After variating anions and the reactions solvents it was possible to isolate crystals of **[Cu(DMP)$_2$][BF$_4$]$_2$** for analytic purposes. During the preparative way of getting to the target molecule additional copper(II) complexes with extraordinary geometric features were obtained. A significant ligand bending is a feature of pentacoordinate copper(II) complexes and **[Cu(DMP)$_2$(MeCN)][BF$_4$]$_2$** exhibits one of the highest known angles between both peripheral phenanthroline rings.[146] In **[Cu(DMP)$_2$(BF$_4$)][BF$_4$]** the copper ion is pushed out of the ligand planes by up to 0.58 Å, which is also quite unusual. Since there is no strong interaction between the bended ligands and another ligand or anion within about 3 Å, the distortion is probably an effect of the crowded copper center in order improve the orbital overlap. All three mentioned complexes were depicted in figure 4-60 for comparison.

The only obtained macrocycle **PhenC(O)CO$_2$Phen** was converted with $CuCl_2$ to a yellow solution, which was resistive to all applied crystallization approaches. The minimum geometric structure of quantum mechanical calculation (figure 4-61) show an extreme distorted coordination environment, which is also reflected in strongly bend phen moieties (15.6° and 8.9°). Both NN donor atoms are not able to coordinate the copper ion in their ligand planes (0.56 Å and 0.64 Å plane-copper distances) lifting the copper into a location, where it is coordinated in a 161° angle. This assessment indicates that the constrains introduced by the **PhenC(O)CO$_2$Phen** ligand lead to an unfavorable coordination geometry.

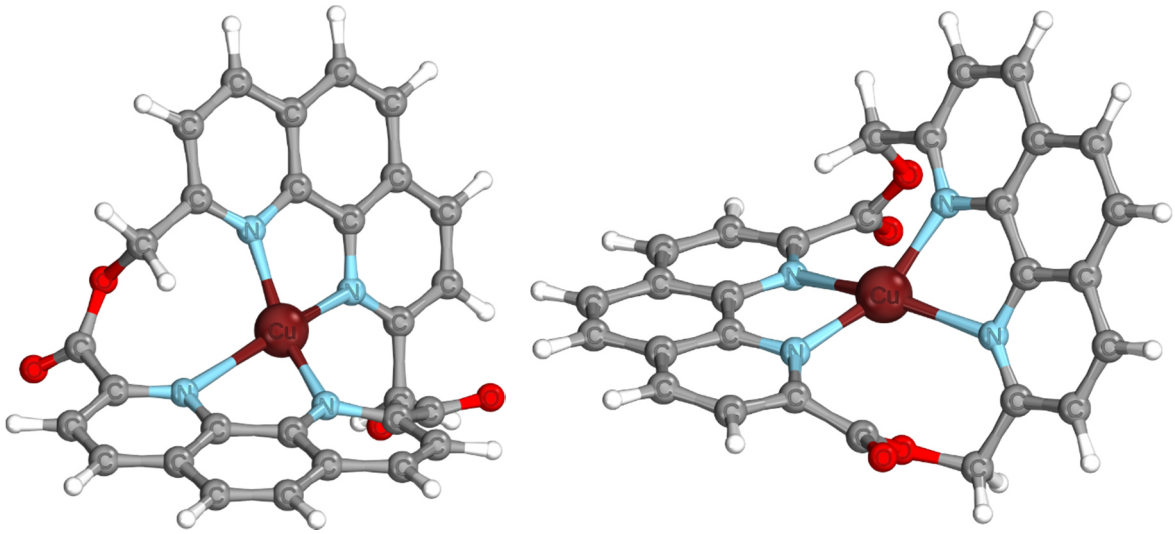

Figure 4-61: Energetic minimum structure of [Cu(PhenC(O)CO$_2$Phen)]$^{2+}$.

A variety of different Cu(II) complexes were synthesized. The issue of coordination by additional ligands was solved by varying the copper precursors and reaction parameters. All complexes reveal significant flattened geometries as discussed before and exhibit in part extreme bended ligands. Crystals of **[Cu(DMP)$_2$][BF$_4$]$_2$** were used of HERFD-XANES and VtC emission spectroscopy in chapter 4.2.1.3.

4.2.3 Copper(I) DMP complexes obtained by contaminated Cu(II) precursors

The synthesis of DMP based copper(II) complexes with $Cu(ClO_4)_2$, $CuCl_2$ and $CuBr_2$ was performed as model for the flattened photo-oxidized state but frequently it was found, that Cu(I) complexes were formed although high quality, trace metal based copper(II) precursors were used for synthesis. In figure 4-62 the results of EXAFS measurements for the exemplary compounds CuCl, $CuCl_2$, CuBr and $CuBr_2$ in R-space can be seen. It is obvious, that both copper(II) species are contaminated with additional compounds. The radial distribution function of $CuCl_2$ exhibits an observable shoulder at 2.22 Å, which matches exactly the Cu-Cl distance in CuCl. Since the copper(II) salts were a few years old, new $Cu(BF_4)_2 \cdot 4.04\ H_2O$, in the following only denoted as

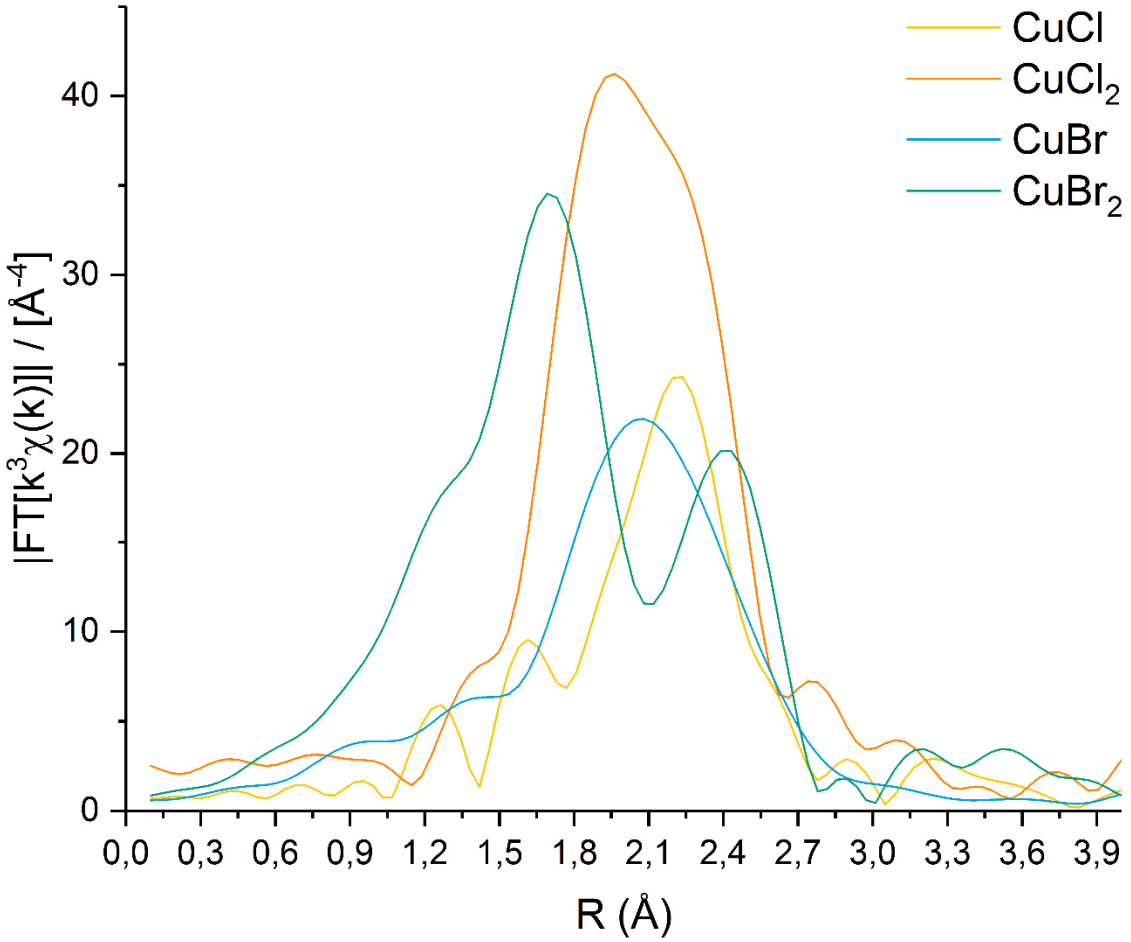

Figure 4-62: Fourier transformed and background removed EXAFS spectra of CuCl, CuBr and copper(I) contaminated $CuCl_2$ and $CuBr_2$ in R space.

$Cu(BF_4)_2$, was purchased reducing the behavior of forming Cu(I) complexes almost completely. A disproportionation to Cu(I) and Cu(III) seems the most probable

explanation.[218,219] Because of this unusual behavior and the open questions the here mentioned complexes are discussed separately and shown in table 4-17.

Table 4-17: Copper(I) DMP complexes and crystals obtained by contaminated Cu(II) precursors.

Complex	Copper precursor	Crystals	Additional ligand	Torsion angle
$[Cu(DMP)_2][BF_4]$	$Cu(BF_4)_2$	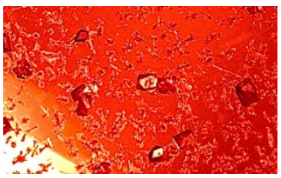	None	88.1 °
$[Cu(DMP)_2][Br]$	$CuBr_2$	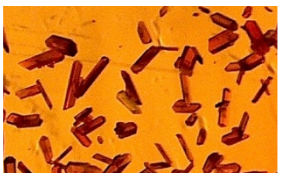	H_2O Cu-O 3.13 Å	77.4 °
$[Cu(DMP)_2][Br]$	$CuBr_2$	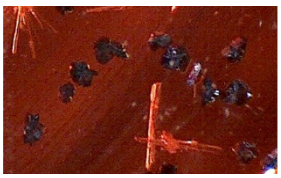 Dark brown crystals	Br Cu-Br 2.705(5) Å	73.1 °
$[Cu(DMP)_2][CF_3SO_3]$	$Cu(CF_3SO_3)_2$		None	85.6 °
[Cu(DMP)(Br)]	$CuBr_2$	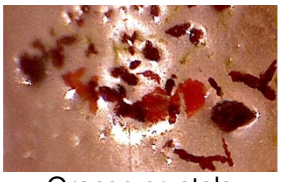 Orange crystals	Br Cu-Br 2.190(3) Å	-
$[Cu_2$-bis(μ-Br)$(DMP)_2]$	$CuBr_2$	 Red crystals	Br Cu-Br 2.3893(7) Å 2.5293(7) Å	-

[Cu(DMP-Br)$_2$][Br]	$CuBr_2$	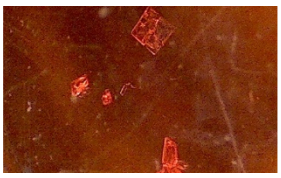	None	86.6 °
[Cu(DMP-Br)$_2$][ClO$_4$]	$Cu(ClO_4)_2$		None	88.1 °

Orange-red crystals of **[Cu(DMP)$_2$][BF$_4$]** were obtained by the above described procedure beside colorless crystals, which were most likely **DMP**. The geometric structure of **[Cu(DMP)$_2$][CF$_3$SO$_3$]** is similar to the aforementioned, since both complexes exhibit typical bond lengths and ligand-ligand torsion angles.

Red crystals of **[Cu(DMP)$_2$][Br]** were grown by pentane diffusion of the reaction solution in acetone. In addition, the solvent/antisolvent combinations acetone/chloroform and acetone/Et_2O were used to obtain crystals with comparable habitus. Due to coordination of water with a distance of 3.13 Å the ligand-ligand torsion angle is flattened to 77.4 °. In addition, all bonding lengths were slightly widened to averaged 2.024(6) Å in comparison to **[Cu(DMP)$_2$][BF$_4$]**. In another reaction brown crystals of **[Cu(DMP)$_2$][Br]** were obtained. In this case, the bromide anion is disordered over three positions, one of them is located in a 2.71 Å distance to the central copper ion leading to a flattened torsion angle of 73.1 °. Coordination of an additional ligand resulting in a pentacoordinate structure is flattening the ligand-ligand torsion angle significantly by steric repulsion.

[Cu(DMP)(Br)] and **[Cu$_2$-(μ-Br)$_2$(DMP)$_2$]** – depicted in figure 4-63 – are special cases in this series and can be assumed as monomer and its dimer. Both complexes were crystalized from the same reaction solution together with **[Cu(DMP)$_2$][Br]** simultaneously. Both ligand and copper(II) bromide were dissolved in MeOH and the latter was added dropwise to the ligand solution. The reaction mixture turned immediately bright green and a majority of the used mass precipitated as green polycrystalline material, which was filtered off. The green solid is considered to be **[Cu(DMP)$_2$][Br$_2$]**, since a significant amount precipitated and the later introduced crystals of **[Cu(DMP)$_2$]-**

[BF_4]$_2$ · MeOH were also green. Diethyl ether diffusion of MeOH and DCM solution of the reaction mixture led to the above mentioned complexes as single crystals.

The monomer is only known as a structure analogue with chloride and the bromide deviates only by 0.30 Å from the ligand plane, while **[Cu_2(μ-Br)$_2$(DMP)$_2$]** was already published in 1985.[220] The last mentioned complex exhibits a gap of 1.63 Å between both ligand planes and both copper ions were deviated 0.21 Å from the ligand planes towards each other. A Cu-Cu distance of 3.06 Å is slightly larger than published before. Copper and bromide atoms are forming a quadrilateral kite (Br-Cu-Br angle: 76.9 ° and Cu-Br-Cu angle: 103.1 °) with rectangular twisted ligand planes.

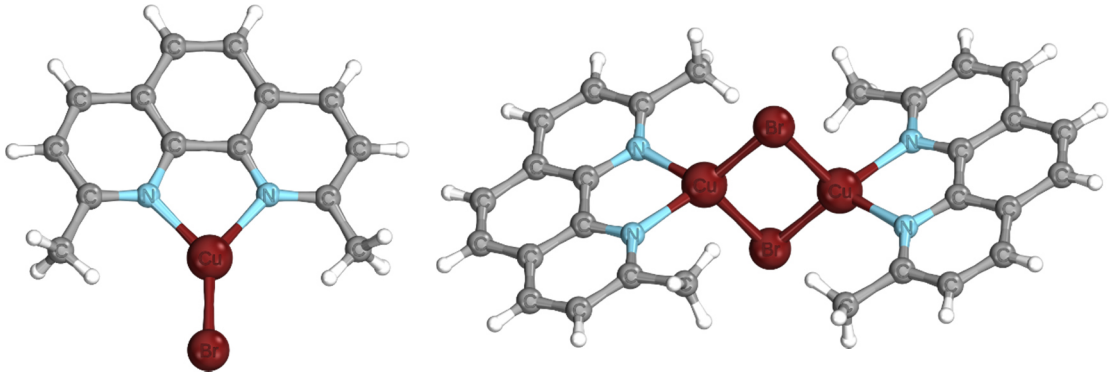

Figure 4-63: Representations of [Cu(DMP)(Br)] (left) and [Cu_2(μ-Br)$_2$(DMP)$_2$] (right) from crystal structures.

DMP-Br was converted with Cu(I) contaminated $Cu(ClO_4)_2$ in MeOH resulting in a green solution, which turned brown. After filtration a brown-orange solid was obtained beside an orange filtrate. During solvent evaporation orange crystals grew and were analyzed by X-ray diffractometry. As indicated by the color, the copper(I) complex **[Cu(DMP-Br)$_2$][ClO_4]** was identified. ^{1}H-NMR data verified the oxidation state as diamagnetic, since this method is very sensitive to paramagnetic residues due to the

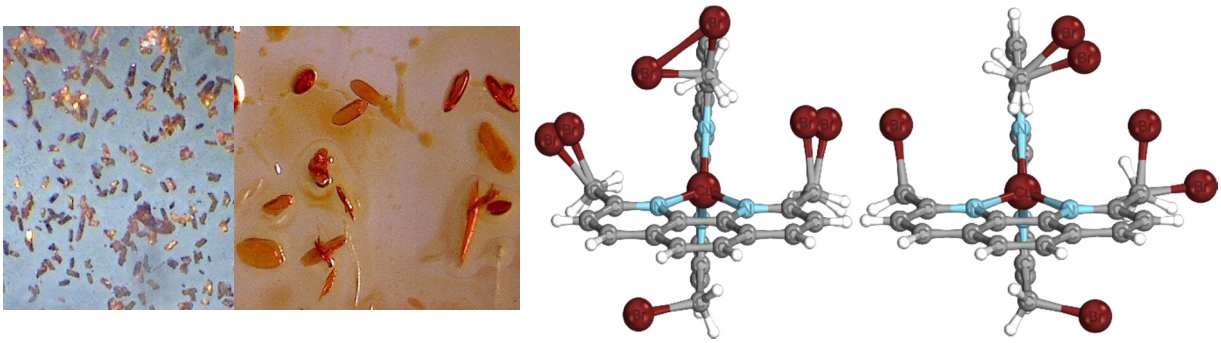

Figure 4-64: Crystals of [Cu(DMP-Br)$_2$][ClO_4] (left) and representations of disorder in [Cu(DMP-Br)$_2$][ClO_4] (right).

large magnetic dipole of the unpaired electron in Cu(II) inducing magnetic field fluctuations. This results in a fast relaxation of the nuclei, which can be observed as a short FID and broadened signals.[157,184] Interestingly, this crystal structures exhibits an comparable halogen atom disorder than **[Cu(DMP-Cl)$_2$][BF$_4$]**, but in the left representation in figure 4-64 three instead of two halogen atoms are disordered over two positions each, although one bromine is only disarranged by a 91:8 ratio, which is the left bromine. The other two bromine atoms are disordered by 67:33 and 73:27. In the right complex representation in figure 4-64, the disorder is nearly identical to **[Cu(DMP-Cl)$_2$][BF$_4$]**, since halogen atoms are arranged in a cis-like conformation.

DMP-Br was also complexed with Cu(I) contaminated $CuBr_2$ in MeOH to give a yellowish orange solution from which red-orange crystals of **[Cu(DMP-Br)$_2$][Br]** were obtained by diffusion of diethyl ether. One single bromide is here disordered over two positions in a 90:10 ratio.

Additional copper complexes were eventually synthesized with copper(I) contaminated precursors, as shown by XAS. These complexes exhibit the general geometric copper(I) parameters, with deviations in the case of [Cu(DMP)$_2$][Br], because of longer ranges coordination of bromide and water, respectively.

4.2.4 Phenanthroline-based homoleptic Cu(II) complexes

The aim was to generate homoleptic **phen** based complexes comparable to the $[Cu(DMP)_2]^{2+}$ type ones. This synthesis were performed time parallel to the aforementioned synthesis of the analogues.

Green crystals of **$[Cu(Phen)_2(Cl)][Cl]$** formed out of a turquoise solution, which exhibits two crystallographic different, but chemical identically cations in the symmetric unit. Compared to **$[Cu(DMP)_2(Cl)][Cl]$**, the **phen** ligands are unstrained. The first published examples for the iodide analogue and the chloride and bromide cations in 1977[221] and 1988[222] respectively. The torsion angle is flattened by 8 ° indicating also the presence of a less tensed system. This lead to a slightly shortened Cu-Cl distance (2.32 Å → 2.29 Å). The bromide complex **$[Cu(Phen)_2(Br)][Br]$** was analogously obtained. Beside a slightly longer Cu-Br bond length and a more pronounced flattening, the complex is structural comparable to **$[Cu(Phen)_2(Cl)][Cl]$**. When changing the anion to nitrate, **$[Cu(Phen)_2(NO_3)][NO_3]$** was obtained as blue crystals out of a turquoise solution. The nitrate coordination pattern and bond length are in accordance with literature[223], while the torsion angle is significantly more flattened.

For **$[Cu(Phen)_2(CF_3SO_3)][CF_3SO_3]$** so far mainly bpy derivates are published, the here discussed structure is not known in literature. On one side the tosyl anion attacks the copper ion by coordinating one oxygen atom at a 2.32 Å distance. All other atoms were not within a binding range. The second tosyl moiety coordinates copper from the opposite side with an distance of 3.17 Å just within both uncharged van-der-Waals radii.[224] That may be an elemental reason why the ligands are as flattened as 40 °.

In an complexation reaction with $Cu(ClO_4)_2$, blue crystals of **$[Cu(Phen)_3][ClO_4]_2$** were grown, although the ligand to metal ratio was 2:1. Cu-N bonds were paired in two groups, the axial positions – represented by nitrogen atoms of two different ligands – give expanded distances up to 2.39 Å, while the other four coordinative bonds ranged around 2.03 Å. The octahedron is slightly distorted, since the angle between the axis and the coordinating atoms in the equatorial position deviates between 78.0 ° and 104.0 °, which is consistent with literature.[225]

Table 4-18: Phen complexes of copper(II) obtained by variation of copper(II) sources.

Complex	Copper precursor	Crystals	Additional ligand	Torsion angle
$[Cu(Phen)_2(Cl)][Cl]$	$CuCl_2$	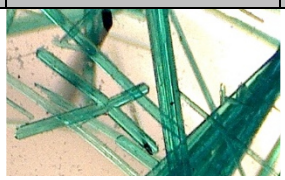	Cl Cu-Cl 2.2889(11) Å	68.4 °
$[Cu(Phen)_2(Br)][Br]$	$CuBr_2$		Br Cu-Br 2.4437(4) Å	64.8 °
$[Cu(Phen)_2(NO_3)][NO_3]$	$Cu(NO_3)_2$	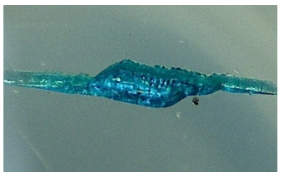	NO_3 Cu-O 2.1524(15) Å 2.749 Å	49.9 °
$[Cu(Phen)_2(CF_3SO_3)][CF_3SO_3]$	$Cu(CF_3SO_3)_2$		CF_3SO_3 Cu-O 2.316(3) 3.168	40.7 °
$[Cu(Phen)_3][ClO_4]_2$	$Cu(ClO_4)_2$	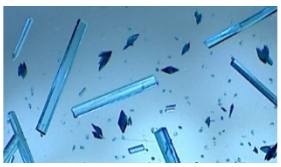	None	85.5 ° 86.2 ° 86.9 °
$[Cu_2\text{-}(\mu\text{-}OH)(Phen)_4][BF_4]_3$	$Cu(BF_4)_2$	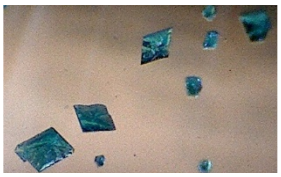	µ-OH Cu-O 1.955(6) Å 1.929(6) Å	71.1 ° 77.6 °

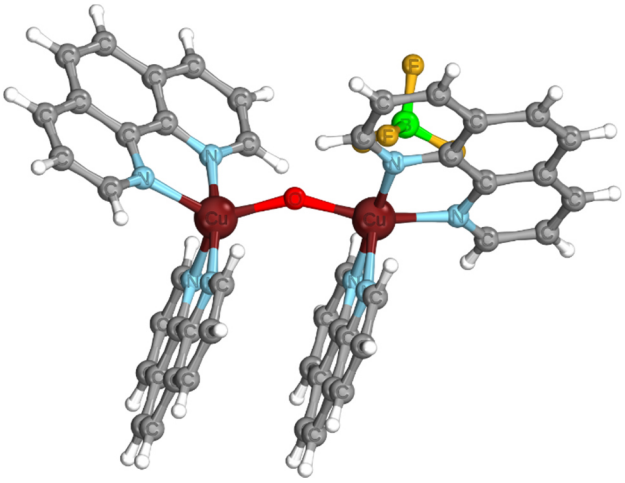

Figure 4-65: Representation of $[Cu_2\text{-}(\mu\text{-}OH)(Phen)_4(BF_4)]^{2+}$ from crystal structure. The hydrogen position of the bridging hydroxy unit could not be determined by X-ray diffraction.

First conversion approaches of **phen** with $Cu(BF_4)_2$ resulted in an immediate precipitation of a bright blue solid. The solvent ratio was then increased until a homogenous solution was reached after combining ligand and copper salt solution. An aliquot was then used for a diethyl ether diffusion. Finally blue crystals of **$[Cu_2\text{-}(\mu\text{-}OH)(Phen)_4][BF_4]_3$** were obtained. This is one of the rather rare examples[226] of an mono-hydroxo fragment bridging two copper complexes consisting of (poly-)pyridine based ligands only. Most likely tetrafluoroboric acid led to the bridging hydroxy function. The Cu-O-Cu angle of 148.6 ° and the Cu-O bond lengths of averaged 1.94 Å lead to a nearly parallel alignment of two ligands. The other two **phen** molecules are turned away from the central Cu-O-Cu unit and provide weak interactions with another set of the same **phen** ligands. Additionally, one copper is coordinated by a fluorine atom of the anion in a 2.90 Å, which is also shown in figure 4-65. Since the Cu-Cu distance is 3.74 Å, no significant copper-copper interaction is detected.

A series of copper(II) complex with **phen** ligands was synthesized. Due to the lesser steric demand of the **phen** in comparison to **DMP**, the copper center is even more prone to attacks of Lewis bases resulting in penta-coordinate complexes, with the exception of **$[Cu(Phen)_3][ClO_4]_2$**.

4.3 Pyridine based cyclic systems

4.3.1 Copper(I) and Copper(II) complexes of Diazapyridinophanes

This results are originated from *Anke Hillebrand's* master thesis.[133]

Copper(I) complexes of the tosylated **DAPy-Ts** and the unsubstituted diazapyridinophane **DAPy** were synthesized based on a general procedure[227], which uses abs. DCM and $[Cu(MeCN)_4][BF_4]$ as copper(I) precursor. Afterwards their properties were investigated by means of NMR, XAS, CV and UV/VIS spectroscopy.

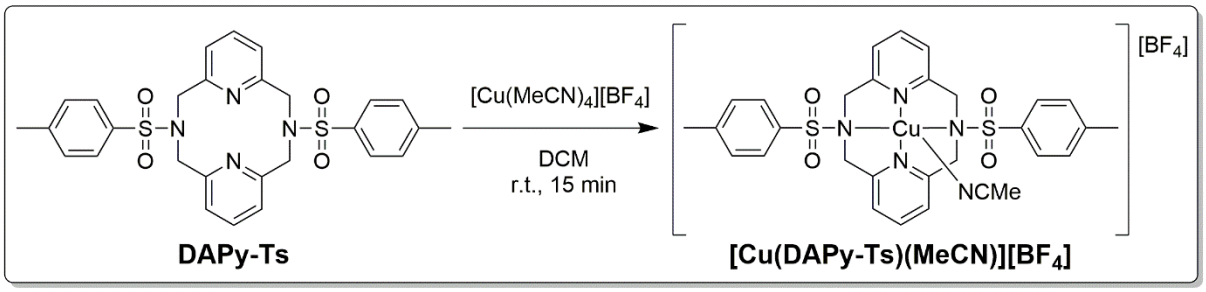

Figure 4-66: Synthesis of [Cu(DAPy-Ts)(MeCN)][BF_4].

To obtain **[Cu(DAPy-Ts)(MeCN)][BF_4]**, **DAPy-Ts** and the copper salt were dissolved in DCM. The resulting yellow solution was stirred for 15 min and filtered followed by a diethyl ether vapor diffusion to gain yellow crystals, which grew overnight. After decanting the crystals were dried *in vacuo*. In case of the X-ray analysis of **[Cu(DAPy-Ts)(MeCN)][BF_4]** (figure 4-67), the crystals were directly taken from the mother liquor.

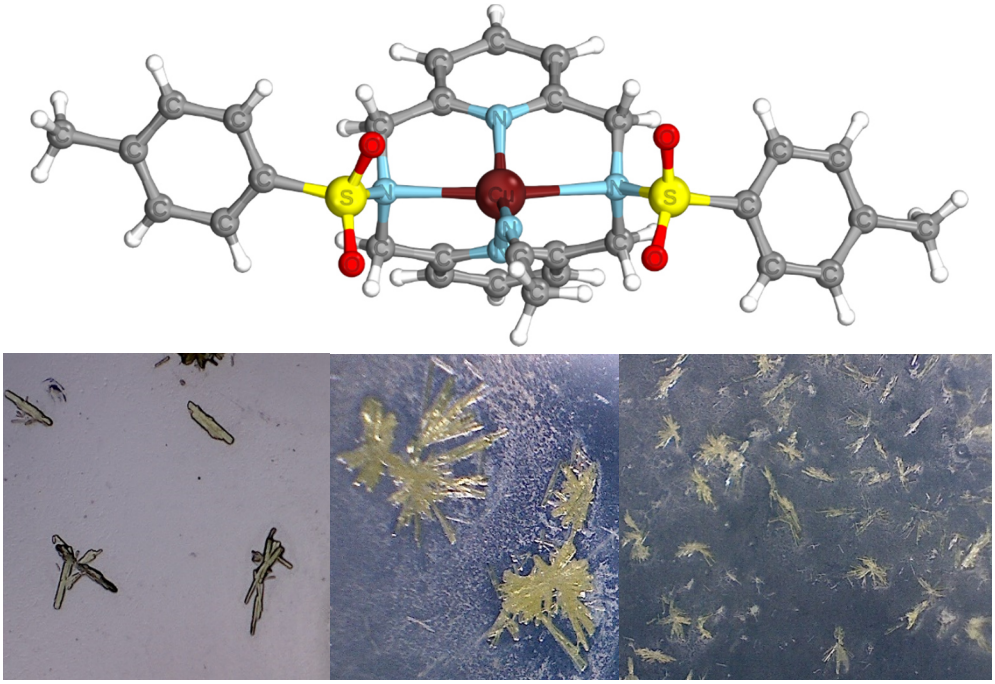

Figure 4-67: Pictures and Crystal structure of [Cu(DAPy-Ts)(MeCN)][BF_4].

The copper(I) is pentadentate coordinated by four nitrogen atoms of **DAPy-Ts** and one additional acetonitrile, which has its origin in the copper(I) precursor. The ligand exhibits a folded geometry like described in literature before[227] opening the complex to Lewis base attacks. The bond of bridging nitrogen atoms to the central ion is widened to 2.45 Å and 2.47 Å because of the C-N-C bond angle does not support a closer coordination.

The crystals **[Cu(DAPy-Ts)(MeCN)][BF_4]** were kept under argon before further analysis but it could be proved that the compound is stable even after two weeks of storing at atmosphere. In contrast the color of its solution changes into green within in 24 hours and later even into blue, when exposed to atmosphere. Then blue crystals were precipitating from the reaction mixture or measuring solutions, dependent on concentration and storage, after days or weeks. The formed blue crystals were

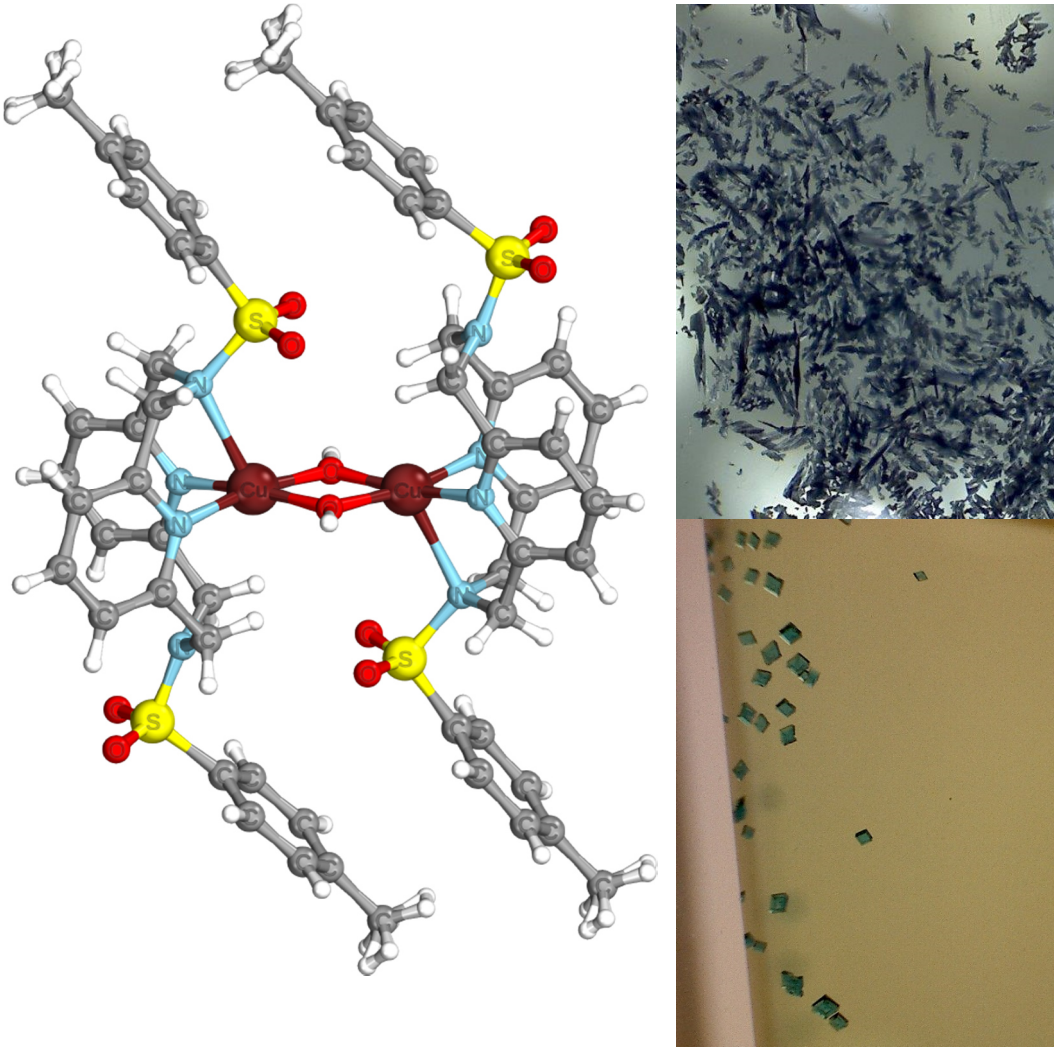

Figure 4-68: Representation of [Cu_2-bis(μ-OH)(DAPy-$Ts)_2$][$(BF_4)_2$] (left) from crystal structure and crystal habitus (right).

identified by X-ray analysis as **[Cu$_2$-bis(μ-OH)(DAPy-Ts)$_2$][(BF$_4$)$_2$]** an oxidation product of **[Cu(DAPy-Ts)(MeCN)][BF$_4$]**, as can be seen in figure 4-68. It seem likely, that the complex activated water and induced the reaction to HBF$_4$ under coordination of the hydroxo bridges. The Cu(II) ions are coordinated asymmetrically by three nitrogen atoms of **DAPy-Ts** at 1.99 Å, 1.99 Å and 2.39 Å. The remaining nitrogen exhibits a significantly longer Cu-N distance of 3.50 Å. The two hydroxo bridging functions at an distance of 1.91 Å are forming two arches with an 102.5 ° Cu-O-Cu angle. The interatomic copper bond distance was determined to 2.99 Å. This complex is not dissolvable in standard solvents for ESI MS, therefore no ESI mass spectrum was recorded. EI Mass delivered only ligand fragments.

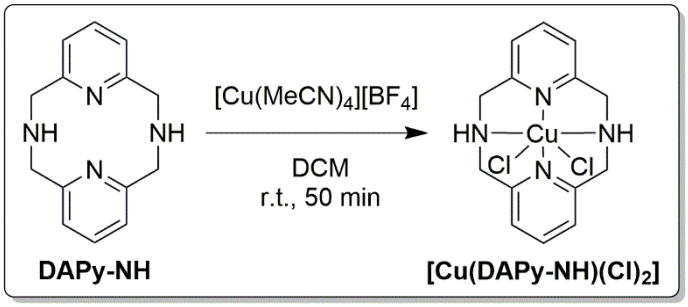

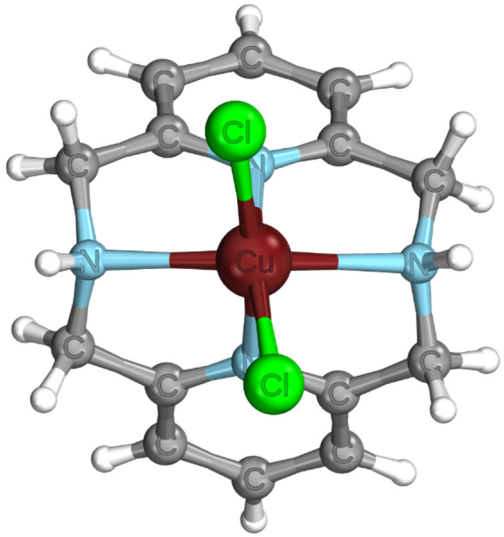

Figure 4-69: Synthesis and crystal structure of [Cu(DAPy-NH)(Cl)$_2$].

The detosylated ligand **DAPy-NH** was converted with [Cu(MeCN)$_4$][BF$_4$] under inert gas conditions by adding DCM to a mixture of both solids resulting in a red solution. After stirring for 50 min the reaction mixture was filtered giving a colorless solid. Subsequent ether vapor diffusion led to colorless crystals overnight, which were not separated by filtration. 48 h later the solution turned green and a brown solid and green needles precipitated. X-Ray structure analysis of the green crystals led to **[Cu(DAPy-NH)(Cl)$_2$]** as shown in figure 4-69. Both chlorine ligands were most likely introduced by a reaction or decomposition of the solvent DCM, analogue to known reactions from the available literature.[228] In order to synthesize the desired Cu(I) complex the solvent needs to be changed. The target complex might be significant more instable due to the missing steric shielding and the lower donor potential. In comparison to the aforementioned

complexes, the secondary nitrogen coordination is significantly tighter showing Cu-N distances of 2.31 Å. This may on the one hand be influenced by packaging effects, although the closest next contact is in a 4.12 Å distance. On the other hand, an increased Lewis acidity of the copper ion due to the higher oxidation state, pulling more electron density to the metal.

The secondary Cu-N distances and the lack in steric shielding in the structure of **[Cu(DAPy-Ts)(MeCN)][BF_4]** show a drawback of this ligand system indicating a higher instability then the non-cyclic species shown before. This sensitivity is also verified by easy oxidation to **[Cu_2-bis(μ-OH)(DAPy-Ts)$_2$][(BF_4)$_2$]**. A second oxidation took place in the case of a conversion of **DAPy-NH** in DCM to **[Cu(DAPy-NH)(Cl)$_2$]**. Although the exact mechanism was not investigated, this finding is an additional indicator for the aforementioned instability.

4.3.2 Spectroscopic characterization of [Cu(DAPy-Ts)(MeCN)][BF_4]

UV/VIS spectroscopy of **[Cu(DAPy-Ts)(MeCN)][BF_4]** in DCM with a concentration of $1.08 \cdot 10^{-5}$ mol/l was performed resulting in the spectrum below. A rather intensive transition band at 260-280 nm was revealed, which is assigned to π-π* transition of the pyridine moiety.[89] The results of *Mirica* et al.[227] based on UV/VIS spectra of the structural comparable complex [Cu(^{t}Bu$_2$N$_4$)MeCN][OTf] also measured in DCM shows a maxima at 264 nm for the free ligand and further transitions at 300 and 365 nm, which was not observed, here. As mentioned in chapter 4.2.1.4, classical MLCT are located to higher wavelength as detected in figure 4-70. A lack in population of such states is and indicator for a weak performance as PS.

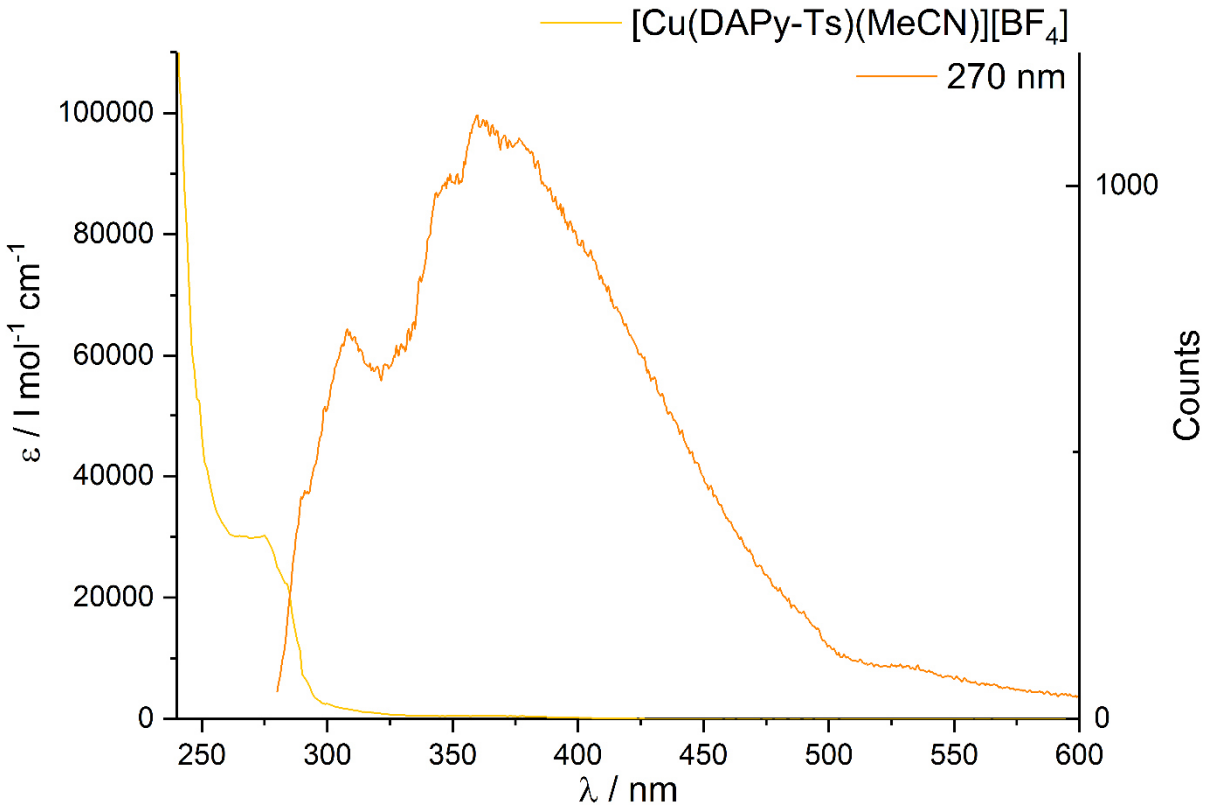

Figure 4-70: UV/VIS spectrum of [Cu(DAPy-Ts)(MeCN)][BF_4] in DCM.

Based on the observed maxima of **[Cu(DAPy-Ts)(MeCN)][BF_4]** the luminescence spectra was started to record at 280 nm using the same sample as for UV/VIS spectra and a wavelength of 270 nm for the excitation. The luminescence spectrum reveals emissive transitions until ca. 400 nm, which are probably induced by relaxation after π-π* excitation as indicated by literature.[89] MLCT states may be populated despite the aforementioned analysis based on the broad shoulder starting at 425 nm and the slow decaying feature at ca. 525 nm.

For examination of the coordination structure and oxidation states of metal centers X-ray absorption spectroscopy (XAS) is a predestinated method and was consequently applied for **[Cu(DAPy-Ts)(MeCN)][BF$_4$]**. Using XANES (X-ray absorption near edge structure) spectroscopy information about the oxidation state and the coordination geometry of a metal center can be obtained. For this complex, a Cu K-edge spectrum was recorded, which is shown in figure 4-71 together with spectra of Cu_2O and CuO as references for copper in oxidation state +I and +II, respectively.

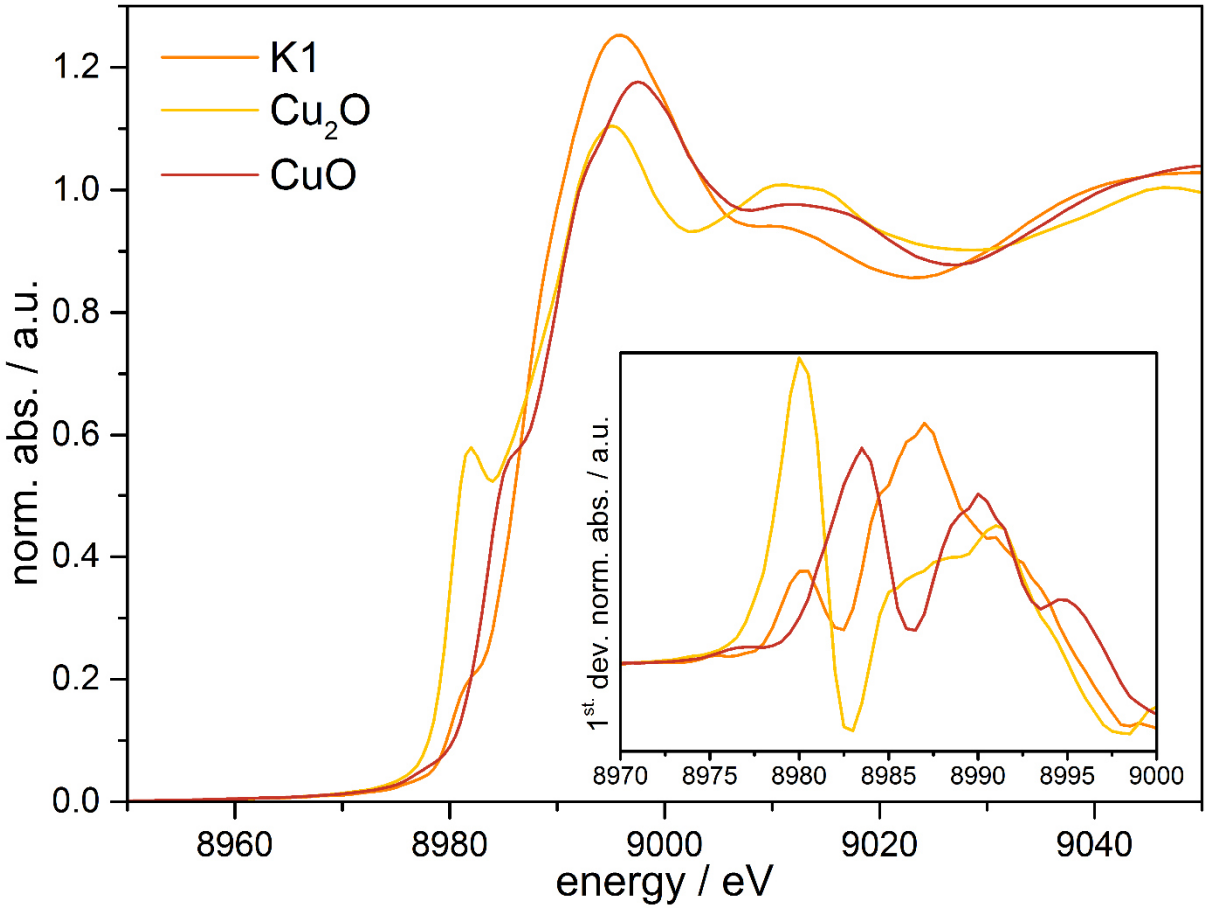

Figure 4-71: Normalized Cu-K-edge X-ray absorption spectra of [Cu(DAPy-Ts)(MeCN)][BF$_4$], Cu_2O and CuO and the corresponding first derivations as inset.

The identification of the copper oxidation state in **[Cu(DAPy-Ts)(MeCN)][BF$_4$]** is relative complex, since the determination of the edge position is hindered due to transitions close to the absorption edge. Comparison of the prepeak intensities of **[Cu(DAPy-Ts)(MeCN)][BF$_4$]**, Cu_2O and CuO reveals a relatively small intensity for **[Cu(DAPy-Ts)(MeCN)][BF$_4$]**. Such small intensities are characteristic for quadrupole transitions like in Cu(II) d^9 configuration.[229] Together with the shoulder-like shape of the prepeak the conclusion for the presence of a Cu(II) species is obvious. But with regard to the energetic positions of the first maxima in the first deviation of the

absorption spectra, indications for a Cu(I) complex are also present. The maxima of **[Cu(DAPy-Ts)(MeCN)][BF$_4$]** and of Cu_2O are both at 8980 eV, while the maximum of CuO appears at 8983.5 eV. This is also visible in the position of the whiteline maximum in the absorption spectra. Here the maximum of **[Cu(DAPy-Ts)(MeCN)][BF$_4$]** is at 8995.5 eV and Cu_2O at 8995.0 eV. The whiteline maximum of CuO lies at 8997.5 eV. Since the ligand in **[Cu(DAPy-Ts)(MeCN)][BF$_4$]** allows only a distorted tetrahedral coordination, deviations of the prepeak intensity compared to the Cu(I) reference can be explained. The energetic position of the prepeak is not influenced by this effect, which allows the conclusion of the presence of Cu(I) in **[Cu(DAPy-Ts)(MeCN)][BF$_4$]**.

Through evaluation of the extended X-ray absorption fine structure (EXAFS) range above the absorption edge element specific information can be obtained about the number of neighbor atoms, their type and their distances to the absorbing atom. In table 4-19 the fitting results and structural parameters of the analysis of **[Cu(DAPy-Ts)(MeCN)][BF$_4$]** are shown.

Table 4-19: EXAFS analysis fitting parameters of K1 and corresponding atom distances obtained through single crystals analysis.

Abs-Bs[a)]	N(Bs)[b)]	R(Abs-Bs)/Å[c)]	σ/Å [d)]	R/%[e)] χ^2_{red} [f)] E_f/eV[g)] Afac[h)]	R(Abs-Bs)/Å[i)]
Cu-N	1.0±0.05	1.891±0.018	0.050±0.005	28.72	1.8706
Cu-N	2.0±0.1	1.995±0.019	0.059±0.006	$8.2313 \cdot 10^6$	2.0631
Cu-N	2.1±0.2	2.498±0.025	0.112±0.011	7.897	2.4588
Cu-C	2.9±0.3	2.796±0.027	0.112±0.011	1.220	2.9550

a) Abs=X-ray absorbing atom, BS=backscattering atom, b) number of backscattering atoms, c) distance between absorbing and backscattering atom, d) Debye-Waller-like factor, e) fit index, f) reduced χ^2 error (considers beside error to experiment the number of independent points and number of varied parameters), g) Fermi energy, that account for the shift between theory and experiment, h) amplitude reducing factor, i) Atom distances obtained from single crystal structure

The distances of the coordinating nitrogen atoms could be divided into three, as can be seen in table 4-19. A nitrogen contribution of one atom at 1.891 Å can be assigned to a coordinating acetonitrile molecule. Two further nitrogen contributions of two atoms each at distances of 1.995 Å and 2.498 Å can be attributed to the ligand system. A

carbon shell at 2.796 Å is originated by the carbon backbone of the ligand. Due to spectrum quality, only the first carbon shell containing three atoms could be adjusted. For all contributions the distances are very similar to the distances obtained through single crystal analysis, as can be seen in table 4-19.

To investigate the redox processes cyclic voltammetry measurements were performed in degassed DCM and by means of a conducting salt $[NBu_4][PF_6]$ (c=0.2 mol/l). The sample was prepared under argon in a concentration of $2.3 \cdot 10^{-3}$ mol/l and transferred into the measuring cell by argon pressure. Measurements with the platinum working electrode indicated a fast production of depositions at the Pt surface, which made the spectra not reproducible. That is the reason why a glassy carbon electrode was used for the shown cyclic voltammogram. For scan speed of 100 mV/s, the complex shows an oxidation wave at 0.73 vs. Fc/Fc^+ and a reduction wave at – 0.20 vs. Fc/Fc^+. The measurement was repeated for 200 mV/s leading to a shift of the maxima to higher current density and absolute potentials as expected. Interestingly, the distance of

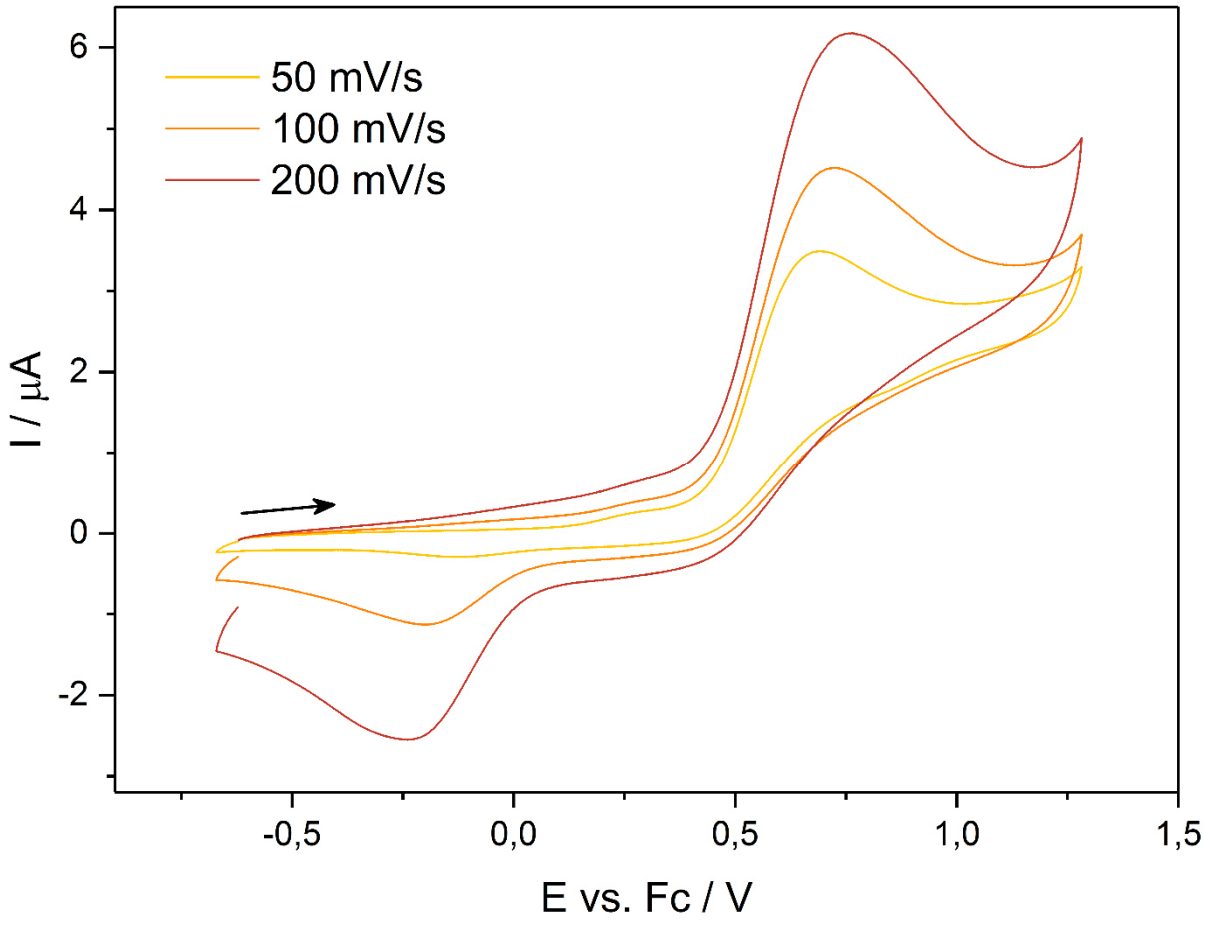

Figure 4-72: CV of $[Cu(DAPy\text{-}Ts)(MeCN)][BF_4]$ in DCM (c=2.3 mol/l) with $[NBu_4][PF_6]$ (c=0.2 mol/l) at 50, 100 and 200 mV/s.

0.93 V and the significantly different peak currents are indicative of an irreversible behavior, which is usually not the case due to the reversible Cu^{II}/Cu^{I} transition. The above-mentioned, comparable system of Cu(I) and Cu(II) complexes of ^{t}Bu-N_4 with OTf as anion were introduced by *Mirica* et al..[227] The CVs were recorded in MeCN with Bu_4NBF_4 as conducting salt (100 mV/s). The Cu(I) complex shows a mainly irreversible transition (0.01 V vs. Fc/Fc^+; – 0.50 V vs. Fc/Fc^+) close to the potentials recorded for the Cu(II) species. CVs in MeCN have also been measured for the **[Cu(DAPy-Ts)(MeCN)][BF_4]** system but did not lead to replicable results but large changes in every measuring cycle indicating undesired surface reactions. Beside the expected peak shift and decrease in current, no reduction peak is observable at 100 mV/s. It is most likely the complex is decomposing in the oxidative regime. For that reason, no reducible species are existent when reaching the cathodic potential. In the case of faster scan speed an increasing reduction wave is observable, because the oxidized species may be stable enough to survive the shorter cycle time. The cathodic wave is not as far shifted to negative values as the literature reference, which indicates that the oxidized state can be reduced easier.

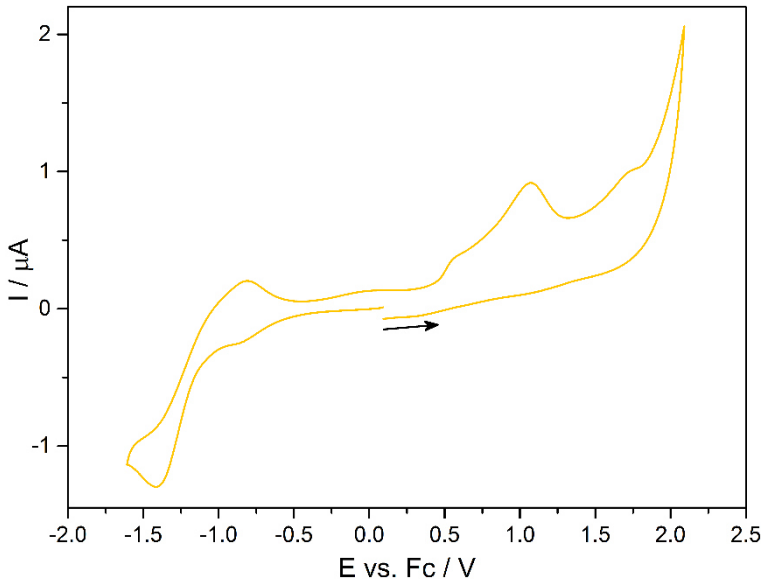

Figure 4-73: Cyclic voltammogram of DAPy-Ts in DCM (c=2.3 mol/L) with [NBu_4][PF_6] (c=0.2 mol/L).

To identify the possible influence of the ligand on the previous measured spectra, the cyclic voltammogram of the ligand is displayed in figure 4-73. When cycling to anodic potentials, a pronounced irreversible oxidation peak at 1.06 vs. Fc/Fc^+. On the cathodic side a reduction signal at – 1.40 vs. Fc/Fc^+ is detectable, which indicate a reduction of the pyridine moiety.[207,230]

Finally, experimental IR spectra of **DAPy-Ts** and **[Cu(DAPy-Ts)(MeCN)][BF$_4$]** are compared to calculated spectra obtained by DFT calculations. Starting with lowest wavenumbers, the signals 669 cm^{-1}, 779 cm^{-1}, 818 cm^{-1} and 918 cm^{-1} four marked signals are correlated to out-of-plane bending vibrations of pyridines and bending vibrations of the tosyl moieties. The following transition at 1090 cm^{-1} is mainly characterized by stretch vibrations in the tosyl substituents, while in the subsequent vibration at 1151 cm^{-1} the SO_2 moieties are involved. A reliable direct correlation of any additional peaks between 1180 cm^{-1} and 1620 cm^{-1} is not possible because of wavenumber shifts, different fine structures and different amount of peaks. The area

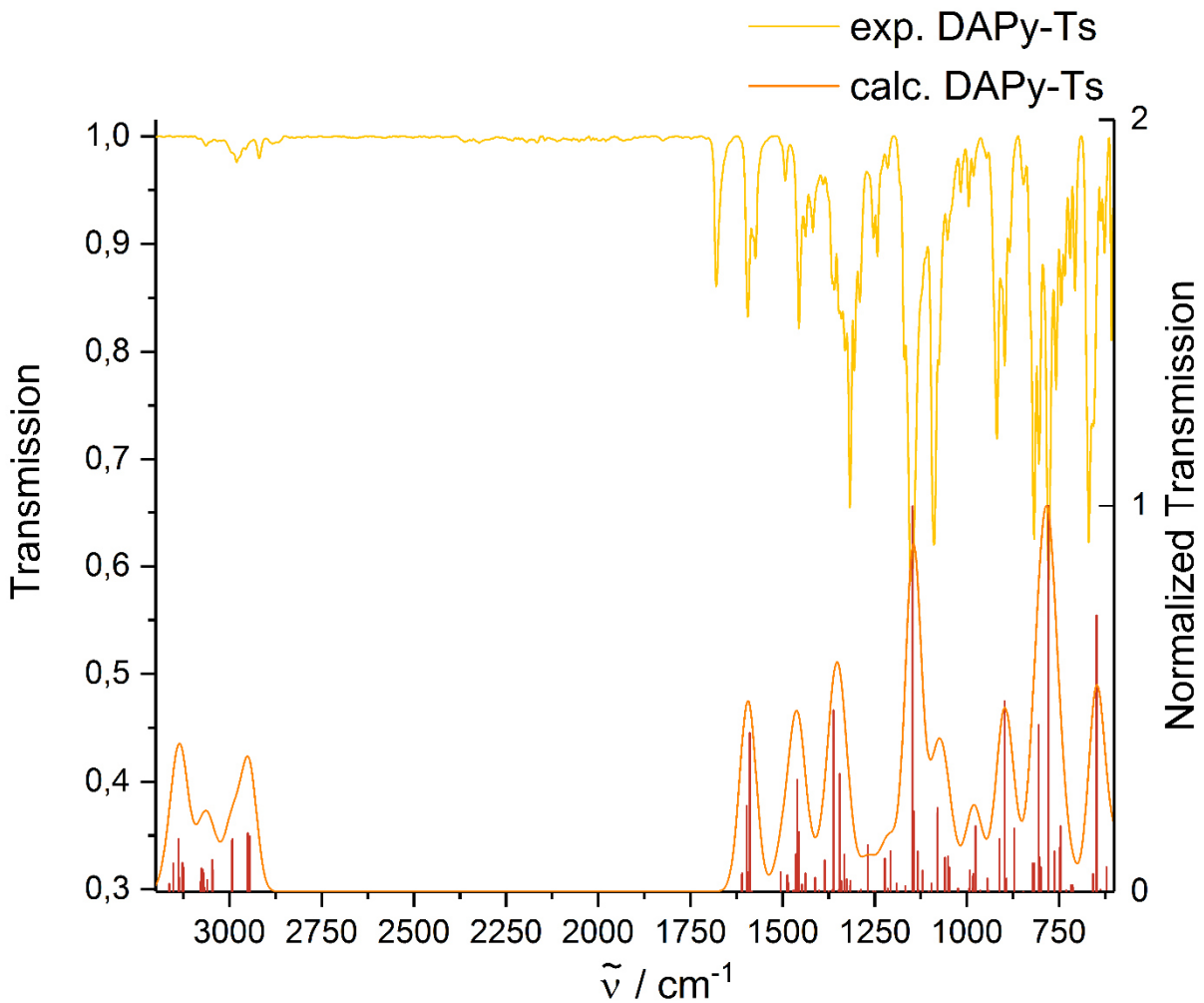

Figure 4-74: Experimental and calculated spectra of DAPy-Ts.

of C-H vibrations is merely weakly pronounced and smaller in terms of wavenumbers in the experimental spectrum than it is in the calculated one. All in all, the agreement of the theoretical and experimental spectra is especially in the harmonic area at low wavenumber satisfying.

A lower amount of signals are certainly assigned in the case of the complex **[Cu(DAPy-Ts)(MeCN)][BF_4]** IR spectra, because of significant differences of intensities and a broad signal between 920 cm^{-1} and 1140 cm^{-1} in the experimental spectrum. Comparable to the ligand spectra, the transitions until 1020 cm^{-1} are mainly characterized by combined framework vibrations. Except a Cu-N stretch vibration at 954 cm^{-1} in the calculated spectrum, which has a too low transition dipole moment to gain significant intensity. The peak at 1146 cm^{-1} shows the SO_2 stretch vibration. A wagging vibration of the pyridine methyl moieties is correlated with the signals at 1334 cm^{-1} and 1356 cm^{-1}, while a bending vibration of the same atoms and a rocking vibration of the pyridine hydrogens are visible at 1468 cm^{-1}. The in-plane stretch vibrations of pyridine und tosyl functions are visible at 1577 cm^{-1} and 1609 cm^{-1}, respectively. Very weak Intensity has also the C≡N stretch vibration at 2318 cm^{-1}, which is not clearly visible in the experimental spectrum. The signals in the range of between 2960 cm^{-1} and 3182 cm^{-1} are the result of C-H vibrations of the methyl groups located within the pyridinophane cycle and aromatic C-H vibrations, respectively. To summarize, only the peaks above 2970 cm^{-1} are significantly shifted in comparison with the experimental data, while the assigned signals are in sufficient agreement.

Comparing the calculated spectra of **DAPy-Ts** and **[Cu(DAPy-Ts)(MeCN)][BF_4]**, two points are striking. First, the weak but visible signal of the MeCN ligand at 2318 cm^{-1} and second the loss of the vibration at 2948 cm^{-1}, which is assigned to a C-H valence stretch vibration of two diagonal located hydrogens of the pyridine methyl moiety. A minor shift (about. 20 cm^{-1}) to lower wavenumbers from 777 cm^{-1} to 756 cm^{-1} is observable, when comparing the ligand spectrum with the one of the complex. Additionally, a peak at 897 cm^{-1}, which is attributed to a ligand framework vibration, is not visible in the spectrum of the complex.

In the experimental complex spectrum broad signals due to superposition of vibrations are visible between 935 cm^{-1} and 1140 cm^{-1} and 680 cm^{-1} and 837 cm^{-1}, which was not predicted by DFT calculation. Shifted signals are not shifted into one direction, so that no systematic consideration can be done. Furthermore, no MeCN vibration is observed, which could be an indicator for the formation of the complex. In contrast the predicted signal loss at 918 cm^{-1}, which is related to a ligand framework vibration, is reproduced by experimental data. To conclude, this data indicates also the formation of the complex, although IR spectra are not a stand-alone solution.

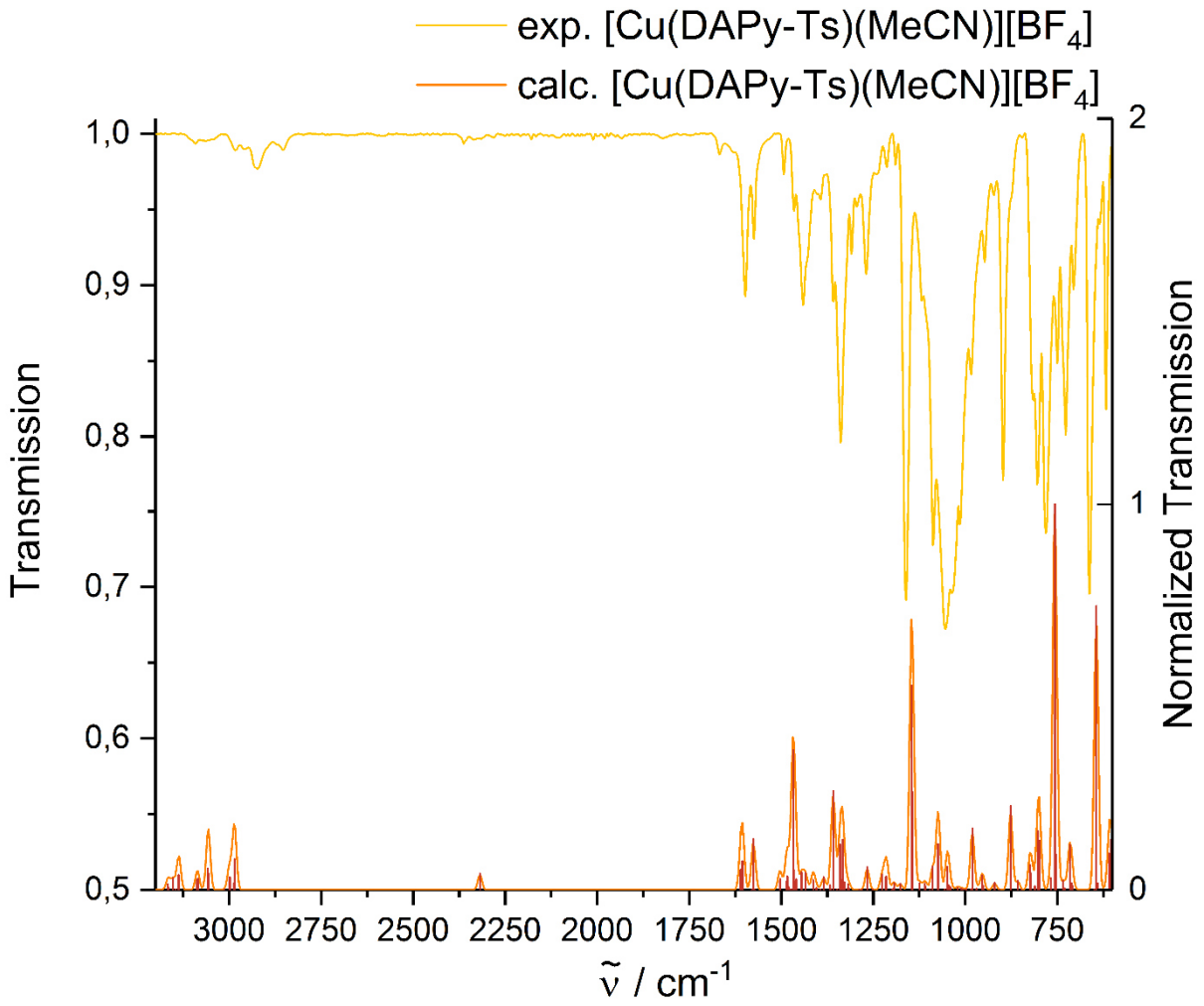

Figure 4-75: Experimental and calculated IR spectra of macrocyclic copper(I) complex [Cu(DAPy-Ts)(MeCN)][BF4].

In order to analyze the electronic structure of **[Cu(DAPy-Ts)(MeCN)][BF4]** a single point calculation was processed in AOMix by partitioning fragments as shown in figure 4-76. The atom orbital contributions to the molecular orbitals and the interaction between the fragments was then analyzed. The density of states plot shows a HOMO-

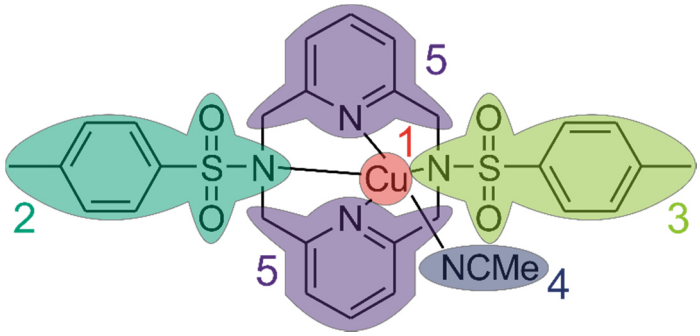

Figure 4-76: Fragment definition for DFT calculations.

LUMO gap between -6.2 and -5.7 eV, which is framed by mainly copper base MOs from HOMO-4 to HOMO on the one side and unoccupied pyridine states on the other side.

Table 4-20: Copper AO contribution to HOMOs.

State	Energy [eV]	Total contribution of copper fragment	Geometry of fragment orbitals
HOMO-4	-7.76	96.0 %	dx^2y^2
HOMO-3	-7.73	89.3 %	dxy
HOMO-2	-7.62	84.1 %	dxz, dyz
HOMO-1	-7.00	75.6 %	dz^2, dxy
HOMO	-6.79	71.6 %	dxz, dyz

The MeCN fragment contributes only to the LUMO+8 and LUMO+9 with about 85 % significantly and can therefore be neglected within this consideration. Both tosyl fragments show a comparable density-of-states plot although fragment 3 is shifted to lower energies.

Table 4-21: Pyridine and Tosyl AO contributions to LUMOs.

State	Energy [eV]	Total contribution of pyridine fragment (5)	Total contribution of tos. fragment (2)	Total contribution of tos. fragment (3)
LUMO	-5.13	93.9 %	0.3 %	0.3 %
LUMO-1	-4.75	97.1 %	1.6 %	0.9 %
LUMO-2	-4.46	97.2 %	1.2 %	1.0 %
LUMO-3	-4.03	33.9 %	0.4 %	65.7 %
LUMO-4	-3.97	65.4 %	1.0 %	33.5 %

The spectroscopic results for **[Cu(DAPy-Ts)(MeCN)][BF_4]** were shown in term of cyclic voltammetry, UV/VIS, steady state luminescence, X-ray absorption and IR spectroscopy. XAS supports the X-ray diffraction data in distances and oxidation state. Optical spectroscopy revealed no detectable MLCT population and poor luminescence behavior. These facts and irreversible CV behavior led to the conclusion, that this

compound is not suitable as photosensitizer due to its decomposition tendencies and poor optical properties. Therefore this route was not further investigated.

4.4 Copper(II) Water Oxidation Catalysts

4.4.1 Copper(II) complexes of DMP, Phen and bpy

In general, copper complexes of the type $[Cu(NN)(OH)_2]$ are considered to be active as water oxidation catalysts[75,231] as underlined by theoretical calculations[232]. The first approach was to reproduce complexes based on literature, where $[Cu(bpy)(OH)_2]$ was a reasonable starting point, since this the most investigated system by means of several methods.[75]

Since the synthesis of $[Cu(bpy)(OH)_2]$ is realized by a two-step procedure with $[Cu_2\text{-bis}(\mu\text{-OH})(bpy)_2][Cl]_2$ as an intermediate described in 1968[233], a comparable approach was followed at first. $CuSO_4$ was converted with 1 eq. bpy in water resulting in a blue solution and a precipitate, which is dissolvable in MeOH. Blue crystals were obtained from this solution and were confirmed as **$[Cu_2\text{-bis}(\mu\text{-}SO_4)(bpy)_2(MeOH)_2]$**, as depicted in figure 4-77. The general coordination core of this crystal structure is known by literature.[234] Both copper centers are coordinated in a tetragonal pyramidal manner in which one sulfate oxygen is located 0.5 Å out of plane towards the complex´s center. The distance between the two parallel ligand planes is 2.66°Å. During the work a mononuclear complex could not be isolated from this intermediate, but based on this work higher dilutions and chloride with lesser bridging properties were implemented in the synthetic route.

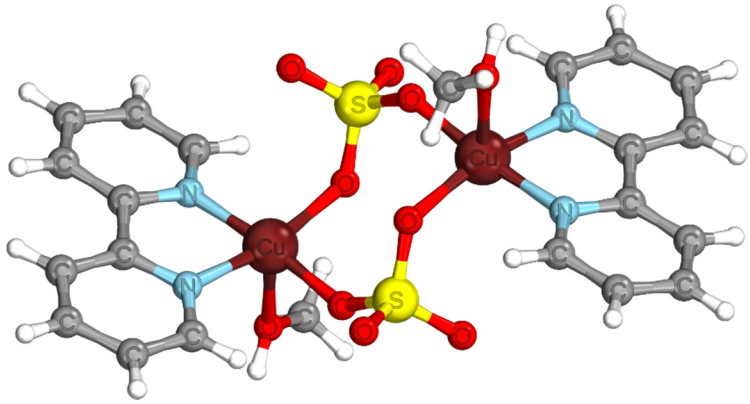

Figure 4-77: Representation of dinuclear $[Cu_2\text{-bis}(\mu\text{-}SO_4)(bpy)_2(MeOH)_2]$ from crystal structure.

In a more direct route to realize the synthesis of a bis-hydroxo species, $CuCl_2$ was used as copper precursor and converted with one equivalent bidentate (ligand, to give $[Cu(NN)(Cl)_2]$. In a subsequent step, this type of compound is treated with an excess

KOH in order to force a ligand exchange of chloride with hydroxide. In a preliminary test, **DMP** was dissolved in water under conversion with HCl to its hydrochloride and added to an aqueous $CuCl_2$ solution. A bright green solid precipitated spontaneously, while the solution were colorless at the end of addition. The heterogeneous solution was alkalized with 1 M KOH, resulted in an increasing dark green solution. When pH = 7 was reached, a turquoise coloration was locally observed during addition. At pH = 9-10 completely turned blue-turquoise and became significantly less turbid, although precipitate was still present at pH = 14. The blue-turquoise solid, which turned greenish brown when dried, was filtered off and a yellowish filtrate was obtained. Fine red crystals precipitated out of the filtrate (figure 4-78, left), which could not be analyzed by X-ray diffraction and was considered as an undesired byproduct since crystals with such coloration were so far found to be either Cu(I) or halogen-bridged dinuclear complexes. In addition, the crystals were only minor amount of the total mass. The mass of the dried greenish main solid corresponds to 72 % of the used reactants. When the solid was treated with 1 M HCl, it became pale turquoise, nearly colorless. Intriguingly, the solid exhibits solvent dependent different colors. In DCM a yellow solution and brightening, even partly orange coloring of the solid is observable. In MeCN the formation of a yellow solution is consistent, while the remaining solid exhibited a red-orange coloration. A crystallization approach of the aqueous solution of the greenish solid with 1,4-dioxane as antisolvent giving polycrystalline green material. As described in 4.2.2, when a solvent of lower polarity is used, here DCM, brown crystals of the dinuclear **[Cu_2-bis(μ-Cl)$(DMP)_2(Cl)_2$]** are formed.

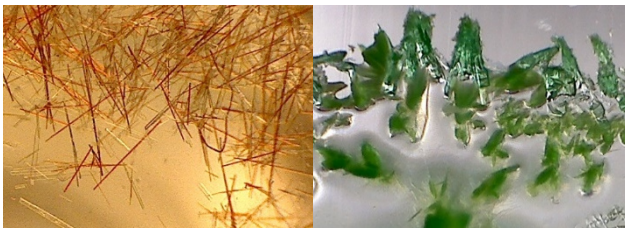

Figure 4-78: Synthesis of [$Cu(DMP)(OH)_2$]. Red crystals from aqueous filtrate (left) and greenish polycrystalline from H_2O/1,4-dioxane crystallization approach (right).

To potentially increase solubility, the same reaction as performed with **phen** as ligand. When the *in situ* gained **phen** hydrochloride was added to the copper salt solution, initially a bluish solid was formed, which dissolved under stirring and a permanent green precipitated was observed at the end of the transfer. Although not fully dissolved, 1 M KOH was added turning the mixture increasingly darker green. A bright blue precipitate appeared at approximately pH = 4 under dissolution of the dark green solid.

When pH = 14 was reached the suspension was filtered gaining a bright blue solid, which is solubilized by 1 M KOH and water to a dark blue solution. An analogue methanolic solution is colored green. Green crystals out of the latter solution were too poor in quality for X-ray diffraction.

IR spectra of at a pH value of 14 precipitated blue solid, blue crystals crystallized from the subsequent filtrate and **phen** were recorded and are shown in figure 4-79. Since NMR spectroscopy and ESI mass spectrometry are not accessible due to its paramagnetic character as d^9 ion and a reduction of copper(II) ions during ionization, respectively. It was anticipated that the δ Cu-OH bending mode below 1200 cm^{-1}, the ν Cu-O between 900 cm^{-1} and 300 cm^{-1} or a signal for a bridging OH function around 950 cm^{-1} could be observable for the dried blue solid.[235]

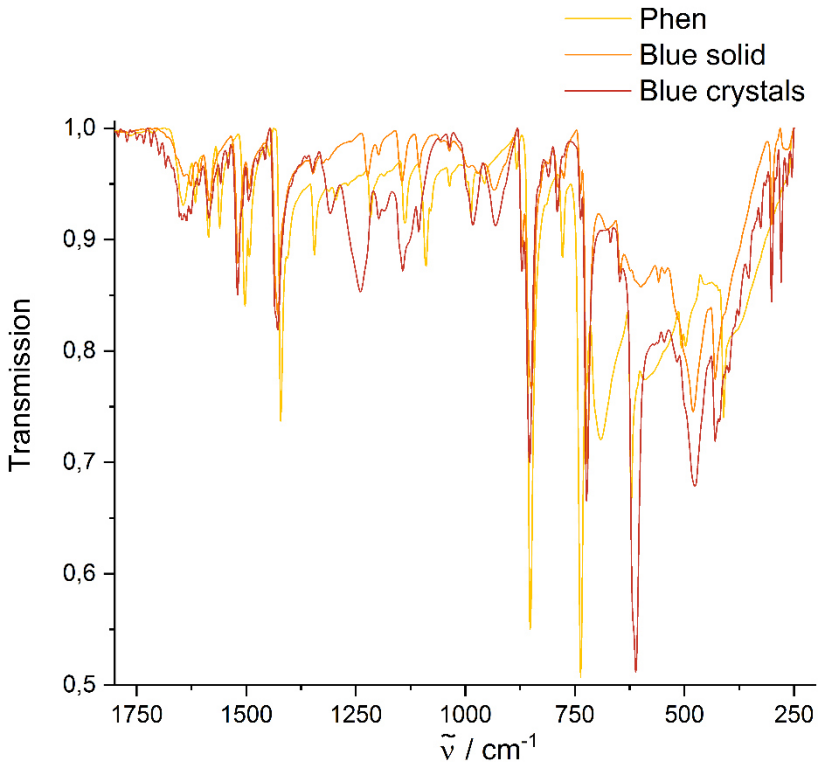

Figure 4-79: IR spectra of phen, blue solid and blue crystals obtained from the reaction of phen with $CuCl_2$ and aq. KOH.

No significant difference can be seen in additional acquired spectra of aqueous 1 M KOH solution with a saturated solution of the blue solid in aqueous 1 M KOH (not shown), because of the water and KOH vibrations resulting in three broad peaks. Compared to the **Phen** spectrum, the blue solid exhibits a comparable signals set although slightly shifted and weaker in absorption, except for an new signal at 933 cm^{-1}, which could fit to the bending mode of a bridging OH function.[235] Signals at

852 cm^{-1} and 738 cm^{-1} are likely modes of water, since the **phen** monohydrate was used to reference and assign water related signals. This results were ambiguous, since no hard evidence for hydroxo species were found, but at least it could be stated that the ligand seems to be altered, most likely complexed.

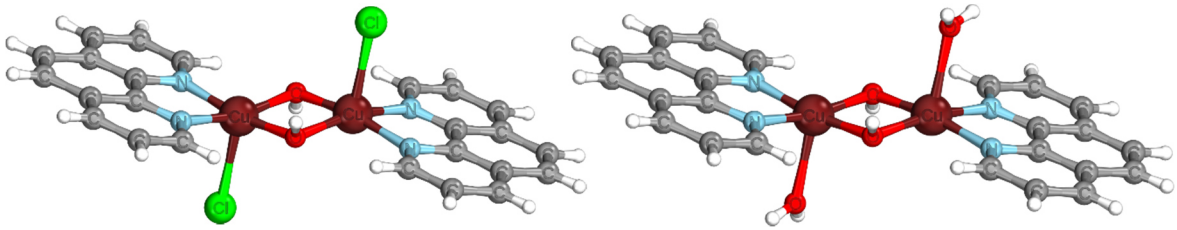

Figure 4-80: Representations of [Cu_2-bis(μ-OH)$(Phen)_2(Cl)_2$] (left) and [Cu_2-bis(μ-OH)$(Phen)_2(H_2O)_2$][Cl]$_2$ (right) from crystal structure.

Dark blue single crystals could be obtained out of a aqueous solution revealing two different copper complexes within the asymmetric unit, **[Cu_2-bis(μ-OH)$(phen)_2(Cl)_2$]** and **[Cu_2-bis(μ-OH)$(Phen)_2(H_2O)_2$][Cl]$_2$** (figure 4-80). The IR spectrum of the crystals is also shown in figure 4-79. Significant differences can be seen in comparison to the blue precipitate, since several signals were detected in the range 1900 cm^{-1} – 2400 cm^{-1}. All other signals were reproduced although the absorption between 1330 cm^{-1} – 1070 cm^{-1} is increased. In addition, the signal at 1643 cm^{-1} is broadened, which can indicate a δ HOH mode.[235,236] According to literature[235,236], the broad signal at ca. 1030 cm^{-1} can be assigned as δ Cu-bis(μ-OH)-Cu.

Both complexes exhibit the same coordination geometry differing only in bond length. The central Cu-bis(μ-OH)-Cu unit can be described as a parallelogram with two opposing sets of Cu-O bond lengths. This structural motive is slightly tilted opening to parallel **phen** planes, which were separated by 0.83 Å and 0.79 Å for the chlorido and the aquo complex, respectively. Cu-(μ-OH) bond lengths in the aquo species are decreased by approximately 0.01 Å. A possible explanation excluding packing effect is, that a lower electron density on the copper ion is caused by weaker electron donating properties of water resulting in increasing bond length to compensate the deficiency. The Cu-Cu distances are both 2.93 Å, just 0.13 Å larger than the doubled van-der-Waals radius of copper.[224] The formation of this co-crystal was already published[237] at neutral pH and similar structures[238] were reported in MeCN/H_2O at pH 10 or 13 giving evidence for its pH stability.

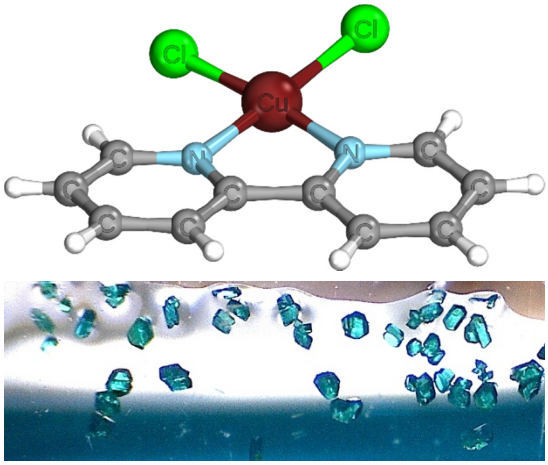

Figure 4-81: Representation of $[Cu(bpy)(Cl)_2]$ from crystal structure and crystal habitus.

Since the poor solubility was a key problem, the more polar **bpy** and copper(II) acetate, as better water dissolvable compound, was converted in the before discussed procedure. The resulting mixture was dark blue and alkalized to pH = 9-10, where a blue solid precipitated. Further addition of water had no effect. Overnight, a small amount of a red-brown solid precipitated and the solution darkened not having changed the pH value. An aliquot of the suspension was further alkalized resulting in a complete dissolution of the solid. By filtration of the remaining suspension about 25 % the initial mass of bpy and copper(II) salt were obtained as blue solid, while the filtrate was also blue. Blue crystals were gained from letting the aqueous solution evaporate. Interestingly, **$[Cu(bpy)(Cl)_2]$** was determined as the blue crystals with chlorides originating from the conversion to bpy hydrochloride. This species could also be crystalized from an acidic pH = 1 solution showing its stability over a broad pH range. The bpy rings of this complex (figure 4-81) are twisted against each other by 7.2 ° and one chloride is elevated from the N-Cu-N coordination plane by 0.34 Å. A direct synthesis with 1 eq. bpy in a $MeOH/H_2O$ mixture gave crystals of **$[Cu(bpy)(Cl)_2]$** as main product in 67 % yield. A minor fraction was identified as **$[Cu(bpy)_2(Cl)][Cl]$**.

In addition, a hydroxo-bridged tetranuclear complex – consisting of two $[Cu_2\text{-bis}(\mu\text{-}OH)(bpy)_2(Cl)]^+$ units connected by two additional Cu-OH coordinative bonds – was obtained, which can be seen in figure 4-82 and was initially published in 2002.[239]

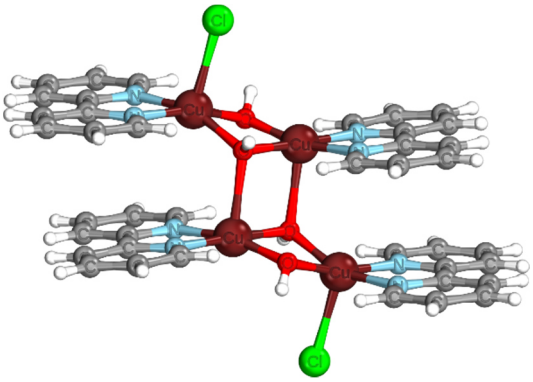

Figure 4-82: Representation of tetranuclear $[Cu_2\text{-bis}(\mu\text{-}OH)(bpy)_2(Cl)]_2^{2+}$ from crystal structure.

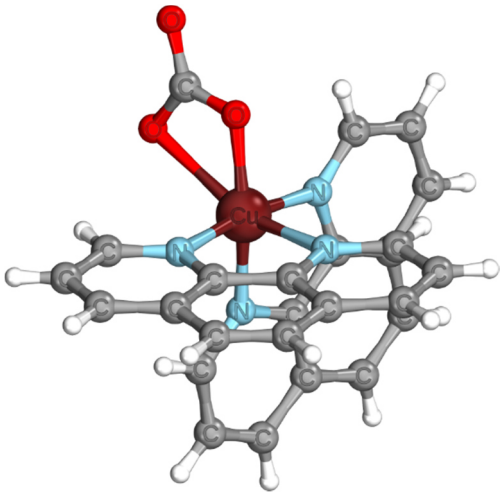

Figure 4-83: Representation of $[Cu(Phen)_2(CO_3)]$ from crystal structure.

Due to the success of synthesizing a mononuclear copper complex with two chloro ligands as potentially good cleavage groups, the reaction was repeated with **phen** as ligand. The reaction solution was colored blue, similar to the aforementioned conversion. A blue precipitate was observed after 30 min, and fully redissolved by adding water. An aliquot was transferred into another vessel and was let to evaporate the water leading a green crystals at pH = 3. In the unit cell two pairs of identical complexes were found. Beside the already discussed **$[Cu_2$-bis(μ-OH)$(Phen)_2(H_2O)_2][Cl]_2$**, **$[Cu(Phen)_2(CO_3)]$** was refined (figure 4-83), showing one example of the less common unbridged, mononuclear carbonato copper compounds. Only a few other complexes of this type are known by literature[240,241], among are the synthesized species.[240,242] The carbonate ions were most likely introduced by water and are coordinating the copper ions in a symmetrical bidentate manner at 1.95 Å and 2.52 Å. The vertical N-N-N-O alignment is nearly planar making this structure a distorted octahedron, because the axial oxygen atom is deviated by 26 °.

When starting to alkalize the initial reaction mixture, a bright blue suspension with a large amount of blue precipitate was obtained at pH = 7. Whether tuning the pH to 9-10 nor addition of water had an effect on the flocculent blue solid. Phases separated overnight leading to a flocculent blue precipitate on the vessel´s bottom, a green transparent gel like layer – which could not be separated by a syringe because both phases behave like one gel – and a pale blue aqueous layer. A sample of this three phasic mixture was successfully dissolved by adding more aqueous NaOH resulting in a homogenous dark blue solution. The remaining suspension was filtrated giving a significant amount blue solid and a pale blue filtrate. All crystallization approaches of the solid and the filtrate in different solvent and with different techniques were delivering blue, non-analyzable crystals.

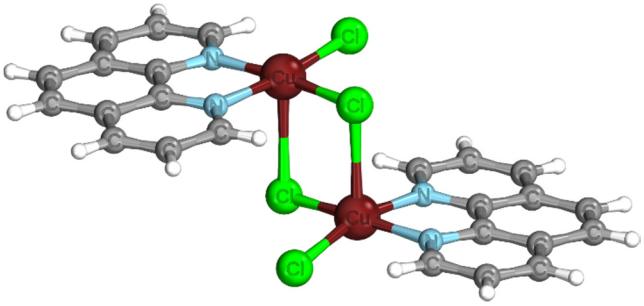

Figure 4-84: Representation of [Cu_2-bis(μ-Cl)$(phen)_2(Cl)_2$] from crystal structure.

The same reaction was performed in an up-scaled approach resulted in a bright green solution, which may be an effect of slightly lower amount of conc. HCl solution and/or a higher dilution, since no other parameters were varied. After addition of several drops, a more than half of the initially reagent weight was precipitated as right green solid. Green single crystals were obtained from the filtrate and could be identified as dinuclear dimer **[Cu_2-bis(μ-Cl)$(phen)_2(Cl)_2$]** (figure 4-84) of the desired species. The central Cu-Cl-Cu-Cl motive forms a nearly planar rectangle, since the Cu-Cl distances of axial bridging chloride ligands were longer. Both copper atoms were coordinated in a geometry close to square planar, the **phen** ligands were bend by ca. 4.0 ° and these were tilted against each other by 6.1 °.

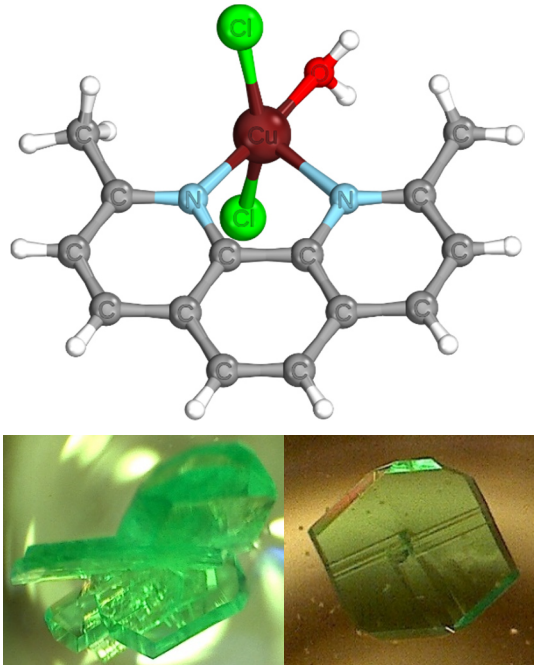

Figure 4-85: Representation of [Cu(DMP)$(Cl)_2(H_2O)$] from crystal structure and crystal habitus.

The same reaction with **DMP** as ligand was performed and a green solid precipitated, which could be dissolved by more water. Upon changing pH to 8, a significant amount of flocculent, olive solid precipitated from the green solution. The solid is not soluble in more aqueous NaOH. Interestingly, a small amount of fine red needles were grown in the filtrate as observed before. Green crystals were grown from the green filtrate. These have been refined as literature known[243] **[Cu(DMP)$(Cl)_2(H_2O)$]**. The copper ion is asymmetrically coordinated forming an O-N-N based distorted trigonal bipyramid, where a nearly rectangular triangle (O-N-N angle at 79.5 °) is the base. The distortion is most likely introduced by the asymmetric ligand coordination. In addition, the copper lies on the hypotenuse on the N-Cu-O line (171.6 °) and is elevated by 0.14 Å. The axial positions are slightly oriented away from the aquo ligand in a Cl-Cu-Cl angle of 155.3 °.

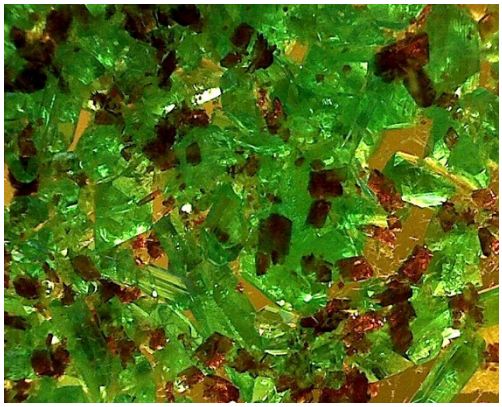

Figure 4-86: Crystal habitus of $[Cu(DMP)(Cl)_2(H_2O)]$ (green) and $[Cu_2\text{-bis}(\mu\text{-}Cl)(DMP)_2(Cl)_2]$ (brown).

$[Cu(DMP)(Cl)_2(H_2O)]$ was then synthesized target-oriented in a larger scale by dissolving DMP in water and a very small amount hydrochloric acid and adding this to a solution of $CuCl_2$ in water. Larger amounts of this compound was obtained in a direct crystallization of the acidic mixture in 84 % yield as green crystalline plates of **$[Cu(DMP)(Cl)_2(H_2O)]$**. Associated IR spectra are discussed in chapter 4.4.1.1. Intriguingly, ether diffusion crystallization of a higher diluted reaction resulted in a parallel formation of **$[Cu_2\text{-bis}(\mu\text{-}Cl)(DMP)_2(Cl)_2]$** and **$[Cu(DMP)(Cl)_2(H_2O)]$**, as depicted in figure 4-86.

One way to favor mononuclear species is to increase the polarity and dilution of the reaction solvent, which functions as additional ligand hindering a coordination of another copper ion. In this case, it prevents the formation of **$[Cu_2\text{-bis}(\mu\text{-}Cl)(DMP)_2(Cl)_2]$**. This strategy was successful performed in all further synthesis. Recrystallization in DCM resulted in **$[Cu_2\text{-bis}(\mu\text{-}Cl)(DMP)_2(Cl)_2]$** verifying the dependence on polarity as discussed before.

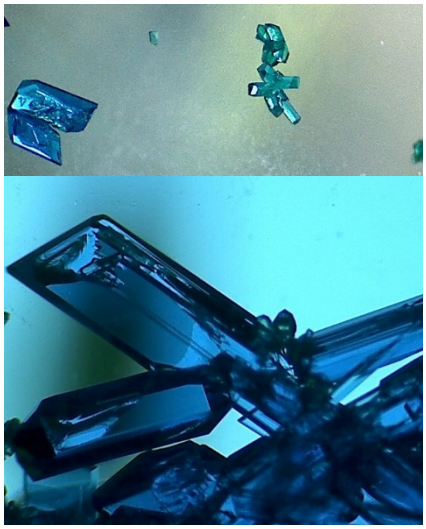

Figure 4-87: Crystals of $[Cu(bpy)(Cl)_2]$ (turquoise) and $[Cu(bpy)_2(Cl)][Cl]$ (blue).

The homoleptic $[Cu(NN)_2(Cl)]^+$ complexes of **bpy**, **phen** and **DMP** were synthesized to compare the analytical data and potential catalytic activity to the $[Cu(NN)(Cl)_2]$ species. Starting with complex **$[Cu(bpy)_2(Cl)][Cl]$**, the direct conversion of 2.1 eq. **bpy** wit 1 eq. $CuCl_2$ in MeOH resulted in a dark blue solution, which underwent a diethyl ether diffusion to gain blue and turquoise crystals of **$[Cu(bpy)_2(Cl)][Cl]$** and **$[Cu(bpy)(Cl)_2]$**, respectively. IR analysis of both species are discussed in chapter 4.4.1.1. The ligand planes angle is 67.8 °, while the coordinating chloride lays on the angle bisecting plane. Ca. 76 % overall yield was reached. When separated the crystals manually by means of a light microscope, the blue crystals became fissured and pale fast owing to the evaporating co-crystalized

MeOH. Since both complexes are dissolvable in water, water splitting in water without any additional auxiliary solvent is possible.

When $CuCl_2$ was added dropwise to 2.1 eq. of **phen** in methanol, the solution turned pale yellow first, than pale green, after that it turned dark leaf green and nearly before the addition ended a small amount bright green solid precipitated corresponding to about 5 % of the total reagents weight. Two different crystal structures were obtained from the filtrate, although the crystals are made up out of **[Cu(phen)(Cl)][Cl]**, the same copper complex. The difference is, that blue crystals were densely packaged, while the turquoise ones exhibit a layer structure which is induced by non-coordinated ligands., as can be seen in figure 4-88, which shows a direct comparison of the crystal structure about 2.6 times the unit cell. The shortest layer distance between the MeOH is 7.98 Å, while the Cu-Cu distance is 21.77 Å. All layers consist out of a two complex building block represented by the asymmetric unit.

Since both species tend to be dependent on the ratio between copper precursors and phenanthroline ligand, a small deficit in ligand substance should favor the densely packed blue species, while an excess should favor the mononuclear **[Cu(phen)$(Cl)_2$]** compound. Such an approach with 1 eq. **phen** resulted in the bright green crystals of dimer **[Cu_2-bis(μ-Cl)$(phen)_2(Cl)_2$]** (figure 4-84) only, a before described structure.

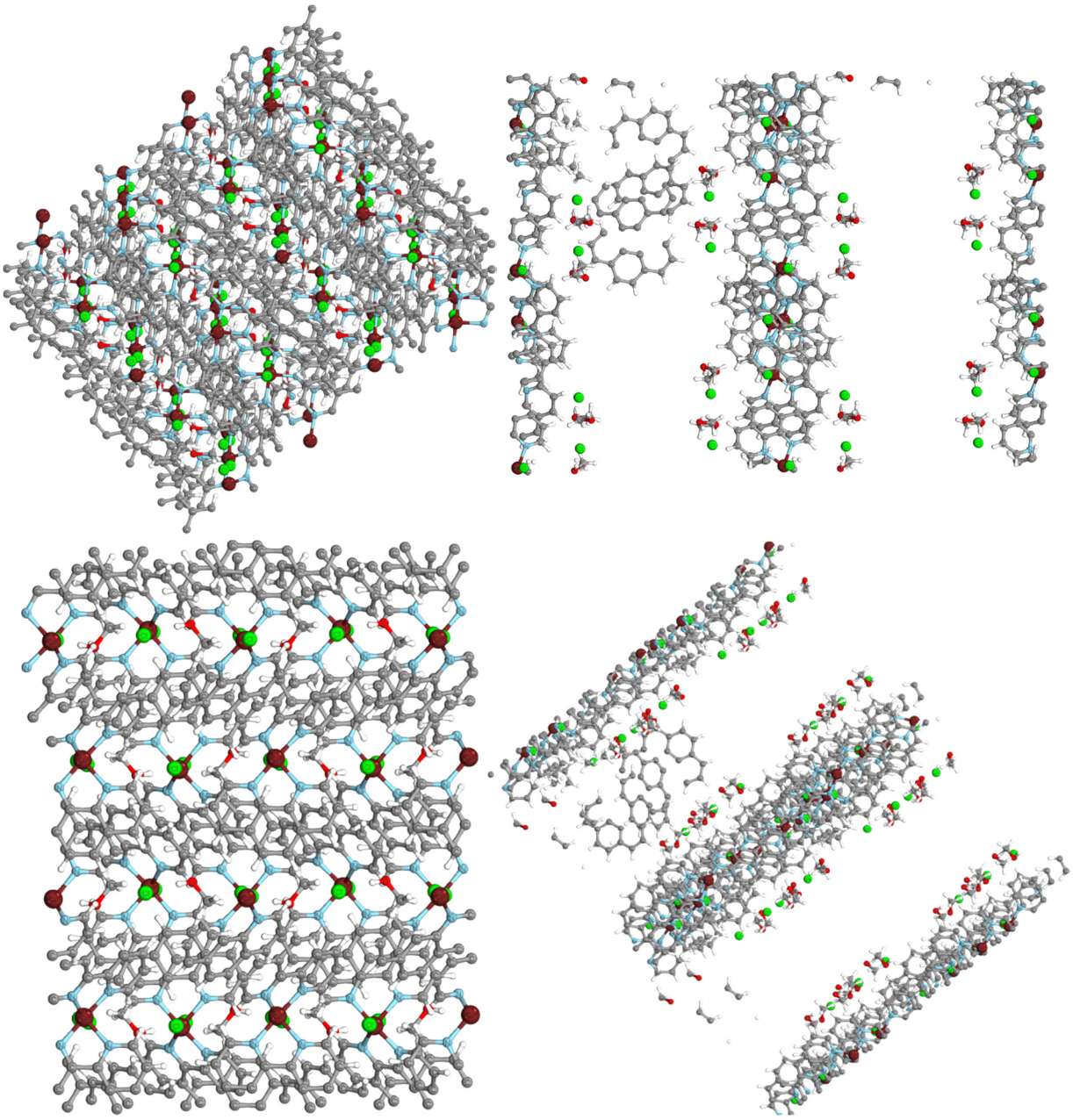

Figure 4-88: Representation of [Cu(phen)$_2$(Cl)][Cl] as blue crystals (left) and turquoise crystals (right), each horizontal figures are shown from the identical crystal axis.

UV/VIS spectra in MeOH at two different concentrations (figure 4-89) were conducted in order to identify the origin of the coloration difference. Single crystals of each sort were used as sample and the molecular weight determined by X-ray diffraction was used to calculate the molar attenuation coefficient. UV/VIS spectra of both dissolved crystal species, reveal no significant difference whether in signal shape nor in intensity indicating, that the coloration could mainly be a solid state phenomenon.

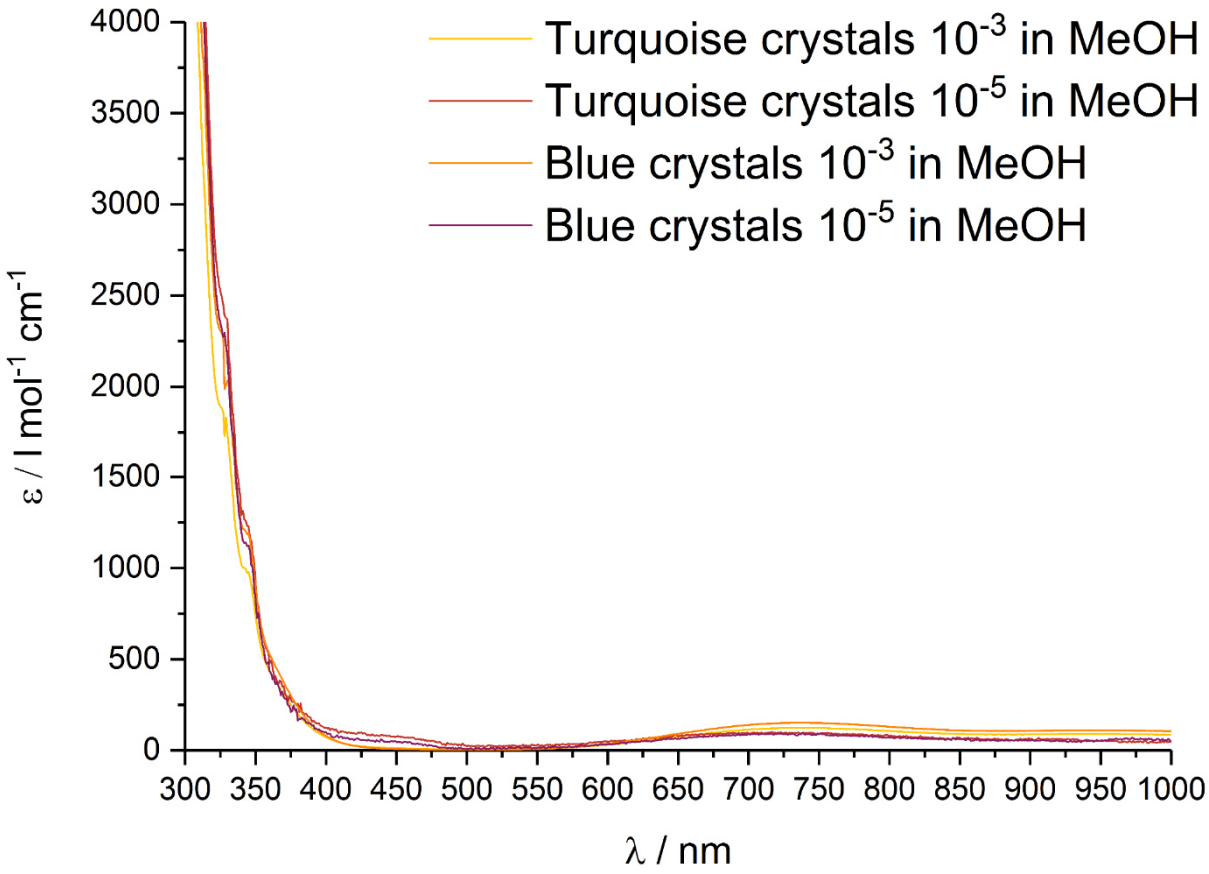

Figure 4-89: UV/VIS absorption spectra of blue and turquoise crystals in methanolic solution.

Since the steady state UV/VIS spectra were inconclusive, the colored solids were directly probed by DRUVS. The spectra were area normalized to ensure a better comparability. As can be seen in figure 4-90, the phen ligand does only exhibit significant absorption in the UV region, while $CuCl_2$ dihydrate– a blue green solid – is absorbing light in two main areas from the UV region to 400 nm and from ca. 550 nm to the end of the spectrum. In order to verify the proposed source of the different coloration, especially the correlation between pestled and dried material is interesting. Here can be seen, that pattern and intensity of blue and turquoise species are very similar. The assumed higher intensity at both ends of the spectra are most likely induced by the more pronounced intensity drop at 500 nm. The crystalline material was directly transferred from mother liquor to the sample holder. While the turquoise crystals exhibit a in general similar optical behavior compared to the dried samples, the blue crystals show at least two signals at 482 nm and 522 nm, where no significant signal is detected in all other spectra. Due to the area normalization, the intensity in the UV and the near-IR range is consequently lowered. These results underline the

before proposed thesis, that the layered structure and/or solvent molecules being the origin of the different coloration.

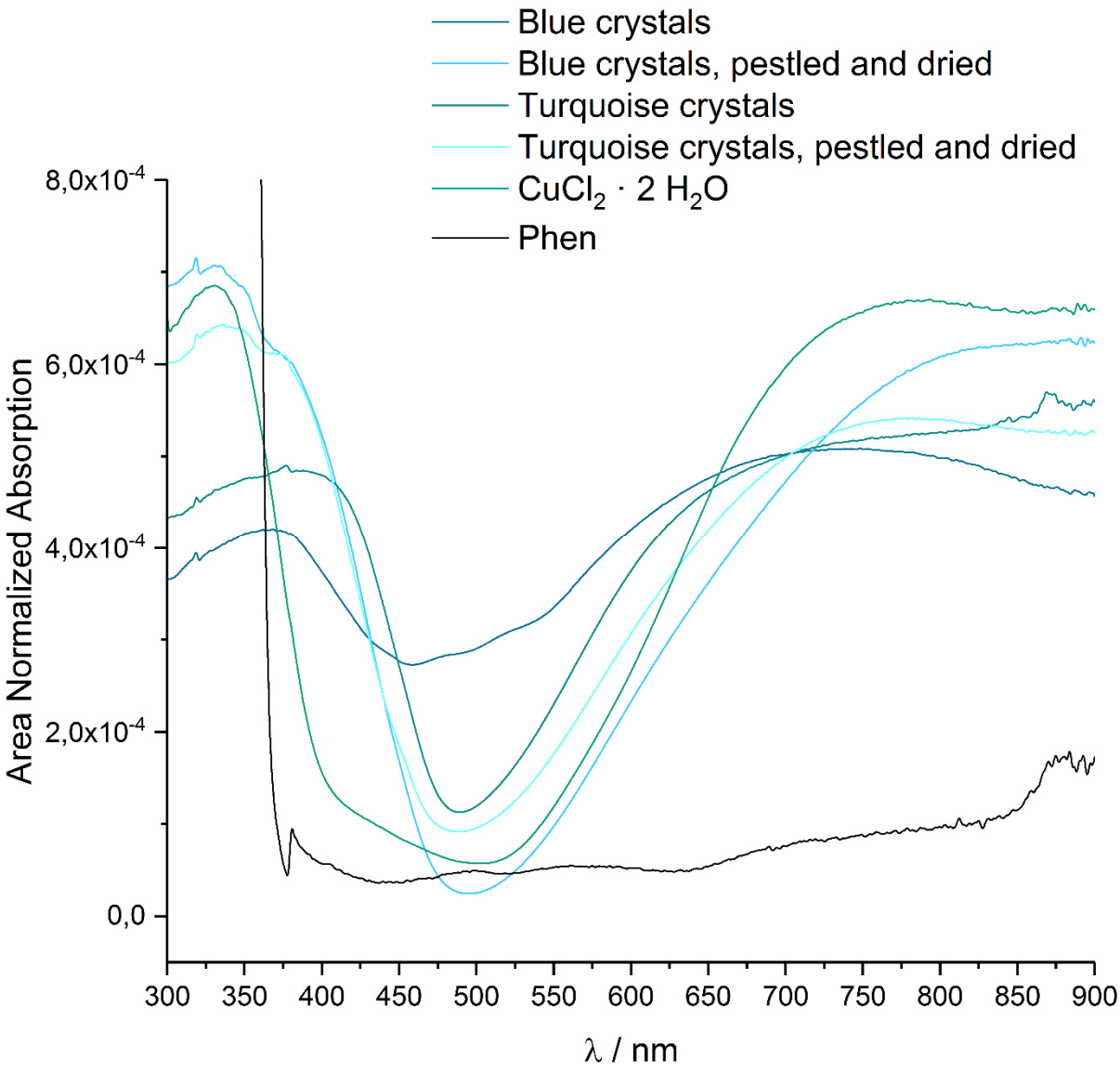

Figure 4-90: Area normalized diffuse reflectance UV/VIS spectra of blue and turquoise species as crystals and as dried solid with copper precursor and ligand as reference.

The analogue addition of $CuCl_2$ to 2.1 eq. **DMP** resulted in a green solution and slow evaporation of the methanolic solvent give in also green crystals of **[Cu(DMP)$_2$(Cl)]-[Cl]**, which is the same type as shown in the **phen** case. Two different colored crystal species were not found.

In the following, chloride-free synthesis were performed to prevent the subsequent halide complexes, which could be blocking the coordination sites from a hydroxyl attack, and directly obtain $[Cu(NN)(OH)_2]$ complexes. Therefor BF_4 was chosen as anion because of its weakly coordinating properties.

During the conversion of bpy with $Cu(BF_4)$ in water under addition of 1 M aqueous KOH, a fine blue precipitated out of a blue solution. When filtered, a brown solid remained and dark blue filtrate was obtained. Out of this filtrate, long blue prisms were grown, which were refined as **$[(Cu(bpy)_2O)_3\text{-}C][BF_4]_4$**. Again this carbonated ions were probably introduced by the used water. All three copper ions are lying in a plane with the central CO_3 unit and are each copper is exhibiting two different Cu-O contacts (1.97 Å/ 2.70 Å, 2.01 Å / 2.71 Å, 1.95 Å / 3.20 Å). The rings of one ligand per copper ion are significantly tilted against each other (10.9 ° and 8.2 °), where the highest torsion is found for one bpy at the copper center with the largest second oxygen coordination (3.20 Å). No other single crystal material could be obtained by crystallization.

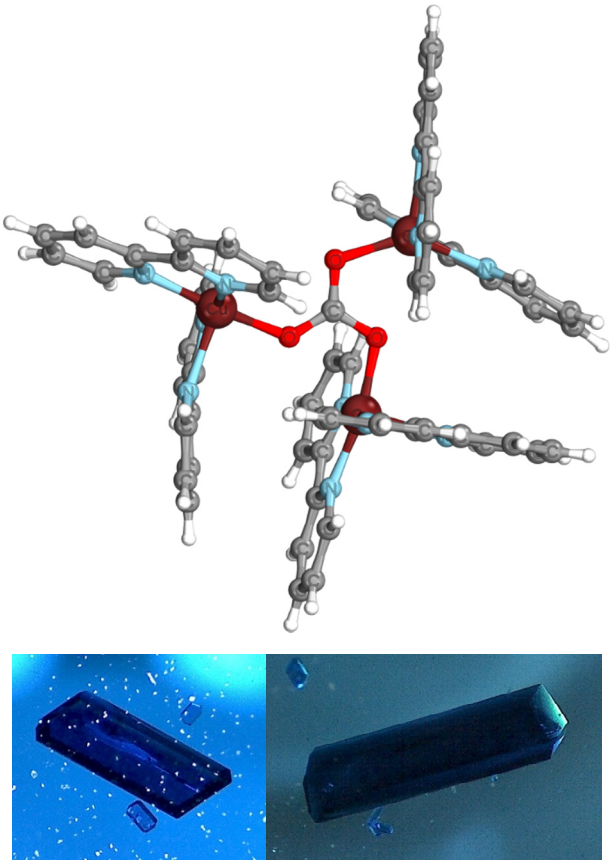

Figure 4-91: Representation and crystals of $[(Cu(bpy)_2O)_3\text{-}C][BF_4]_4$.

Several interesting copper(II) species – each differing in structure – were obtained by complexation with commercial available ligands. The bis(µ-halide) motive is as common in copper chemistry as bis(µ-OH), which is especially pursued, when oxygen activation is investigated. Furthermore, rare carbonate-containing species like **$[Cu(Phen)_2(CO_3)]$** and **$[(Cu(bpy)_2O)_3\text{-}C][BF_4]_4$** are investigated as temporary CO_2 storage substance.

For water oxidation catalysis pursued in this work, the mononuclear species **[Cu(bpy)(Cl)$_2$]** and **[Cu(DMP)(Cl)$_2$(H$_2$O)]** are of interest, because these enable a ligand exchange chloride to open a coordination site for catalysis. Analogue complexes with **phen** could not be obtained, but in an excess ligand two different crystal types were grown differing in color. It was shown that higher order arrangements in layers give rise to the coloration.

4.4.1.1 IR spectroscopy of DMP-, phen-, and bpy-based copper(II) complexes.

Since the synthesized copper(II) complexes are not identifiable by NMR spectroscopy and mass spectrometry, IR spectra of crystalline material was conducted to verify the structure of all crystals gained from subsequent reactions. As handled before, the assigned calculated signals are denoted in brackets.

[Cu(bpy)(Cl)$_2$] and **[Cu(bpy)(Cl)][Cl]** can be differentiated by IR spectroscopy with ease.

General C=C ring-based vibration are detected at 1566.0 cm^{-1} (1635.1 cm^{-1}, two signals and 1566.0 cm^{-1} (1608.1 cm^{-1}, two signals), followed by several rocking and scissoring C-H modes between 1157.2 cm^{-1} and 1496.6 cm^{-1} (1191.0 cm^{-1} and 1499.4 cm^{-1}). Ring breathing vibrations can be assigned to signals between 1014.4 cm^{-1} and 1056.9 cm^{-1} (1023.2 cm^{-1} and 1077.4 cm^{-1}). At 727.1 cm^{-1} (777.8 cm^{-1}) and 773.4 cm^{-1} (780.1 cm^{-1}) δ C-H modes are observed. In-plane and out-

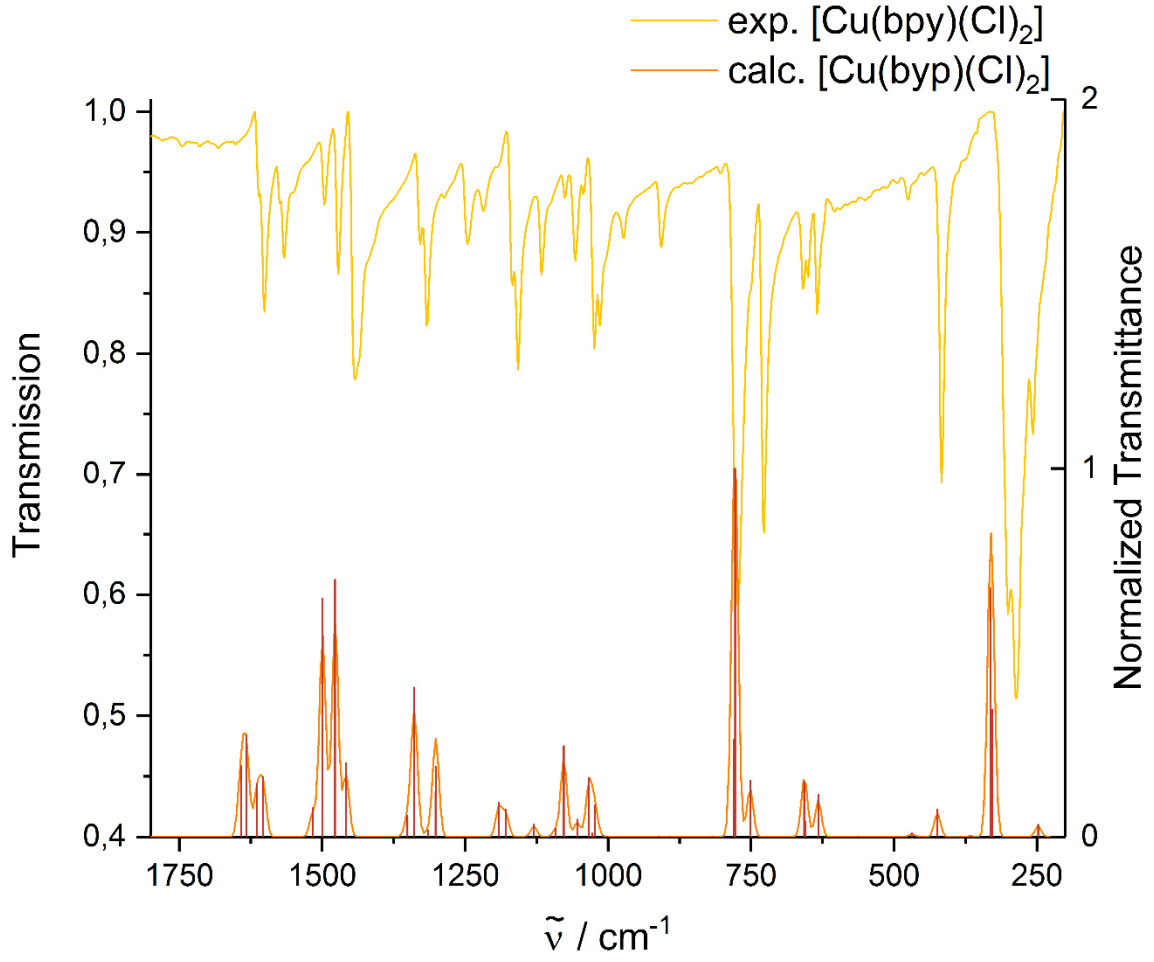

Figure 4-92: Experimental and calculated IR spectra of [Cu(bpy)(Cl)$_2$].

of-plane ring vibration give rise to signals at 416.6 cm^{-1} (424.2 cm^{-1}), 634.5 cm^{-1} (632.4 cm^{-1}) and 655.4 cm^{-1} (two signals) (656.0 cm^{-1}, two signals). Finally, the most characteristic signals are observed at 287.4 cm^{-1} and 300.9 cm^{-1} (330.3 cm^{-1}, two vibrations) and represent ν_{as} and ν_{sym} Cl-Cu-Cl stretching vibrations. This species is therefore identifiable due to this unique signal set in the fingerprint range.

This vibrations are not observable in the IR spectrum of **[Cu(bpy)$_2$(Cl)][Cl]**, since the signal for ν Cu-Cl is located at 291.2 cm^{-1} (322.6 cm^{-1})

According to the calculations, the intense signal to highest energy at 231.4 cm^{-1} (282.0 cm^{-1}) is a vibration of the copper ion between the two ligands under torsion of both aryl moieties of the **bpy**. The other **bpy** signals are not significantly altered und consistent with the before described discussion.

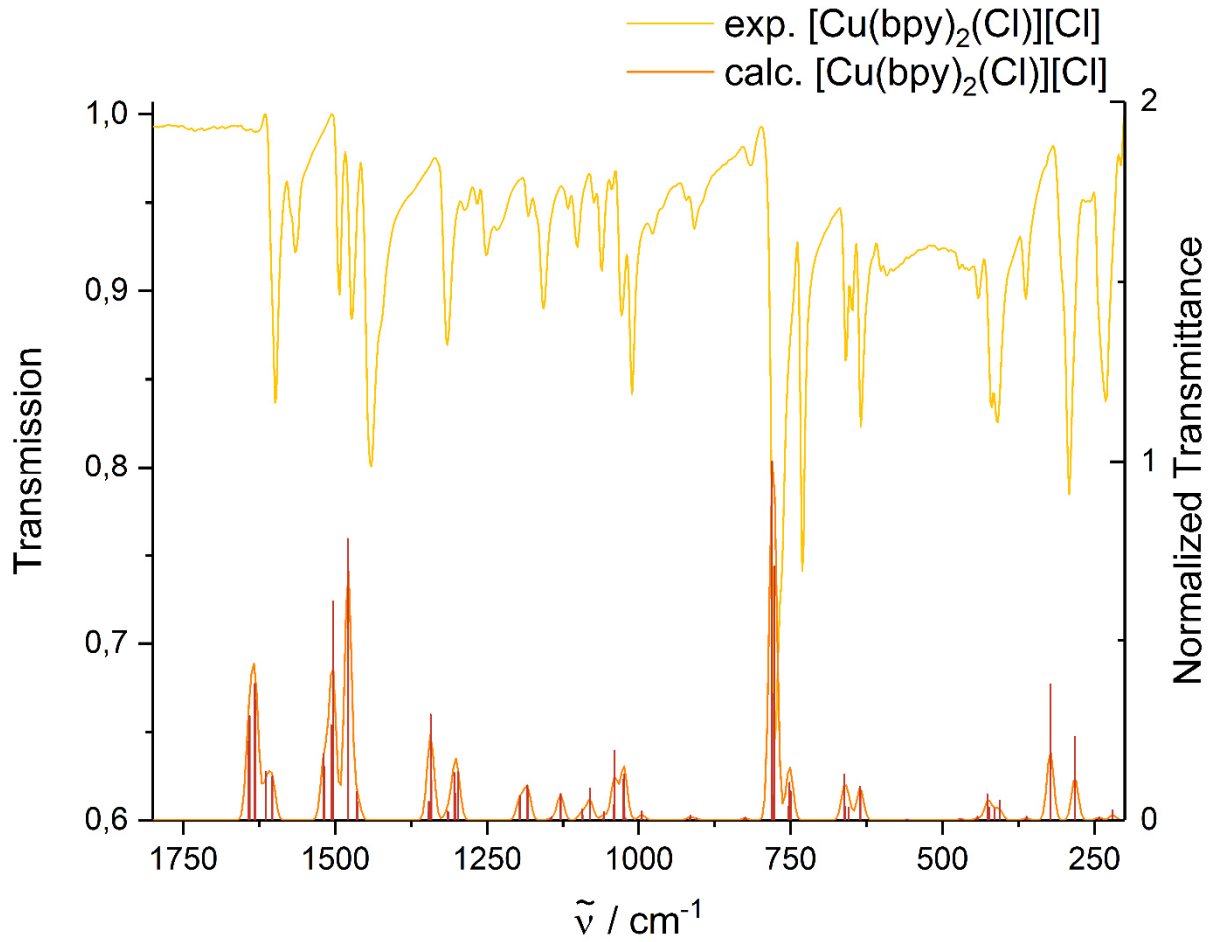

Figure 4-93: Experimental and calculated IR spectra of [Cu(bpy)$_2$(Cl)][Cl].

The IR spectra of **[Cu(DMP)(Cl)$_2$(H$_2$O)]** are shown in figure 4-94, where two experimental spectra are depicted. The first spectrum was obtained by isolating the crystals out of the mother liquor and remove the residual liquid by touching a filter paper. Exposing the pestled solid to air for 6 h resulted in the second spectra. Another

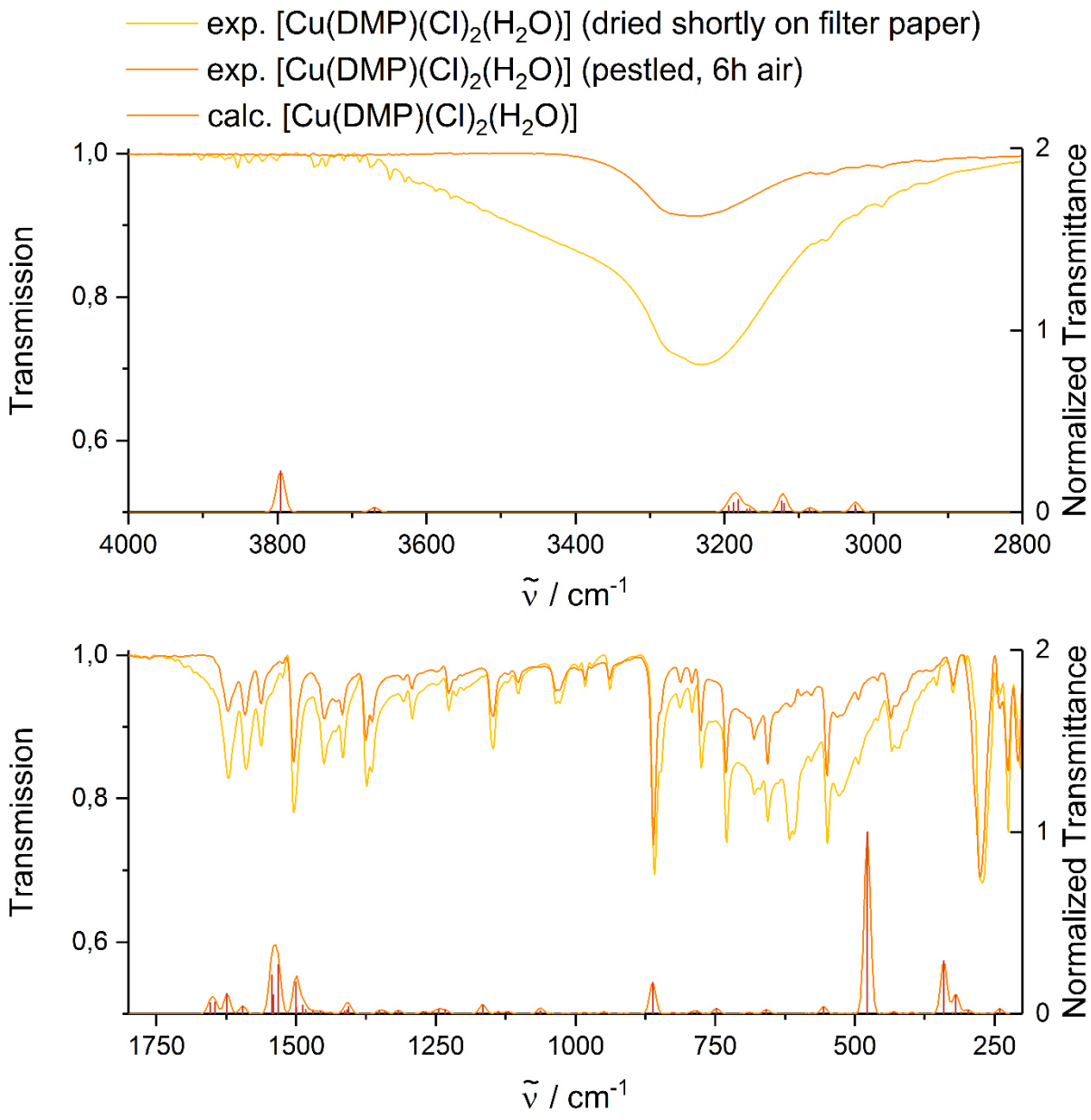

Figure 4-94: Experimental and calculated IR spectra of [Cu(DMP)(Cl)$_2$(H$_2$O)] at different drying stages.

acquisition after 16 h reveals no significant changes.For **[Cu(DMP)(Cl)$_2$(H$_2$O)]** the analogue characteristic ν_{as} Cu-Cl vibration is located at 275.8 cm^{-1} (340.8 cm^{-1}) and includes a H-O-H wagging. Since the literature expects a large transition dipole moment as proofed by calculated vibration and ν_{as} and ν_{sym} Cl-Cu-Cl stretching vibrations in **[Cu(bpy)(Cl)$_2$]**, the suitable signal at 275.8 cm^{-1} is assigned despite of the

large deviation (65 cm^{-1}) from the calculated signals, although the residual assignments exhibit a high comparability. Additionally, the vibrational mode at 225.6 cm^{-1} (240.7 cm^{-1}) is assigned to a v_{sym} Cl-Cu-Cl under participation of the ligand and the water oxygen atom due to the equatorial deflection of the copper ion. Consequently, 324.0 cm^{-1} (319.4 cm^{-1}) is a mainly a v Cu-O (H_2O), which causes axial compensations movements of the chloro ligands and bending of **DMP**, which´s range is additionally is consistent with literature.[235]

Calculations indicate the wagging vibration of water at 477.7 cm^{-1}, which cannot be assigned to a distinct signal in the experimental spectrum, since the broad signals at 433.9 cm^{-1}, 493.7 cm^{-1}, 528.4 cm^{-1} and 549.7 cm^{-1}. Due to the broad signal and the shift in comparison to literature, 528.4 cm^{-1} is likely to be the mentioned vibration. 549.7 cm^{-1} (555.8 cm^{-1}) is assigned to rocking distortions of methyl hydrogen atom. The isolated water scissoring vibration is detected at 1504.3 cm^{-1} (1532.5 cm^{-1}), the following C=C vibrations are contaminated with a percentage of that mode. Calculations indicate two modes of v_{as} H-O-H at 3669.8 cm^{-1} and 3795.8 cm^{-1}. In the experimental IR spectrum of the shortly dried complex are two low intense signals, barely evolved out of the baseline at 3741.3 cm^{-1} and 3853.2 cm^{-1}, which could be the previously described vibrations.

The IR spectra are in good accordance with calculations enabling a precise assignment of signals. Some uncertainties remained only in the case of **[Cu(DMP)$(Cl)_2$(H_2O)]**, due to the complex results of water coordination.

4.4.2 Copper(II) complexes of DMP-OH and DMP-OOH

Hydroxyl and carboxyl containing ligand open the opportunity to stabilize higher oxidation states due to their even more non-innocent character, which is especially important for catalytic applications, where the copper center need to be oxidized and ligands are needed to accommodate electrons.[231,244,245,246,247] Octahedral oxygen coordinating copper complexes with aromatic N donor ligands are only known as bridged bipyridine compounds. For the first time copper(II) complexes of more rigid,

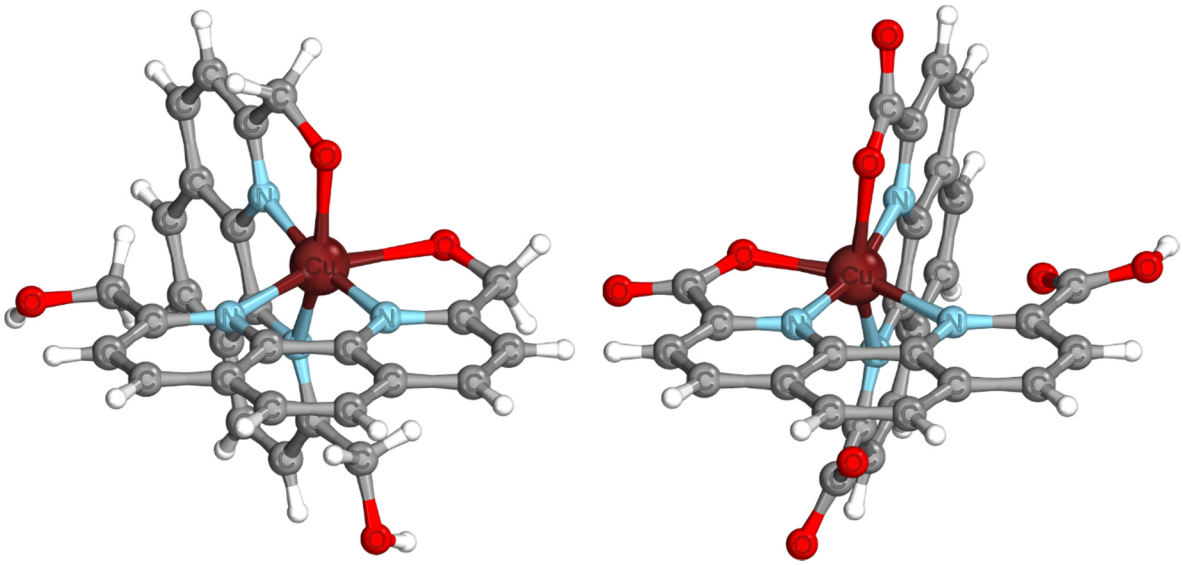

Figure 4-95: Representation of $[Cu(DMP\text{-}OH)_2]^{2+}$ (left) and $[Cu(DMP\text{-}OOH)_2]$ (right) from crystal structures. (Hydrogen atoms of the coordinates OH groups could not be resolved.)

oxygen containing DMP-based were used, in the case of **$[Cu(DMP\text{-}OOH)_2]$** without using a proton-transfer compound as in literature.[248,249]

Explicitly, **DMP-OH** was converted with $Cu(BF_2)$ in MeOH resulting in a yellow solution and subsequently in yellow-green crystals, as depicted in table 4-22. Despite the poor crystals quality, the structure of **$[Cu(DMP\text{-}OH)_2][BF_4]_2$** (figure 4-95, left) could be revealed. Although the hydrogens on the coordinating oxygen atoms could not be resolved, a Cu(IV) complex can be excluded, since these complexes are very instable and – beside the harsh conditions for synthesis[250] – these substances are strong oxidants itself.[218] In addition, the only confirmed Cu(IV) complex has been successfully synthesized recently.[251]

In a distorted octahedral geometry, the copper ion is coordinated equatorial by all three N donor functions and one hydroxyl group. The O-Cu-N angle of the opposing functions on the base is smaller (157 °) than the idealized 180 ° for a squared base. This is nearly the same case for the axial coordination delivering an angle of 155 °. The coordination of only one oxygen per ligand is most likely favored because the distance between two hydroxyl functions is as large as approximately 4.5 Å when the oxygen atoms atom would be oriented to each other, while the N-N distance is only ca. 2.7 Å and additionally only 2.6 Å to the neighboring oxygen atom. Due to that, it is geometrically favored to coordinate in an N-N-O manner. In any other case only two donor functions would be coordinated resulting in a thermodynamically unfavorable state, not considering the steric overload of the copper center. This is also verified by a nearly rectangular torsion angle between both ligands.

A comparable coordination geometry is observed for **[Cu(DMP-OOH)$_2$][BF$_4$]$_2$**, which is even more distorted octahedral than the complex mentioned before (figure 4-95, right). The significant difference is a partial deprotonation of the carboxylic acids, which is most likely resulting in tetrafluoroboric acid as a byproduct, since no anions were present in the crystal and two equivalents BF_4 anions with respect to the copper center were used. A drawback is that the only effective solvent to dissolve **DMP-OOH** is DMSO, which is built into the crystal causing distortions and complicating the further processing of this compound.

The solubility of this compound needed to be improved in order to substitute DMSO as a solvent. Proton transfer reagents – based on Brønsted-Lowry acid-base principle – as applied in literature are considered to be a viable method for increasing the solubility.[248,249] Consequently, **DMP-OOH** was converted with 2,6-diaminopyridine in refluxing ethanol. Upon cooling down a very small amount of black precipitate was filtered off. A brown precipitate was obtained by a crystallization approach of the filtrate. ^{1}H-NMR spectroscopy confirms a phenanthroline signals set an additional aromatic signals. Since no accessible standard analytic is capable of verifying the adduct formation – most likely IR spectroscopy is also not able to do so, because of dynamic peak broadening effects. Consequently, the precipitate is used without further analysis. The complexation reaction was performed in MeOH and MeCN, which both turned into a yellow solution. Later the MeCN solution turned green. A green-brown solid was precipitating out of the crystallization approach.

Since the homoleptic copper(II) complexes of **DMP-OH** and **DMP-OOH** were synthesized, heteroleptic complexes were interesting because of possible synergistic effects. Therefore 1 eq. **DMP-OOH** was suspended in MeOH resulting in a bright yellow solution and a methanolic solution of 1 eq. $Cu(BF_4)_2$ was added dropwise resulting in a more intense yellow solution. Then 1 eq. **DMP-OH** was added, which turned the solution green. A crystallization approaches resulted in a pale yellow precipitate.

Table 4-22: $[Cu(DMP\text{-}OH)_2][BF_4]_2$ and $[Cu(DMP\text{-}OOH)_2][BF_4]_2$.

Complex	Crystals	Additional ligand	Torsion angle	Cu-N bond length
$[Cu(DMP\text{-}OH)_2][BF_4]_2$		OH Cu-O 2.140(4) Å 2.297(4) Å	89.8 °	1.928(4) Å 1.968(5) Å 2.140(4) Å 2.235(4) Å
$[Cu(DMP\text{-}OOH_2)][BF_4]_2$	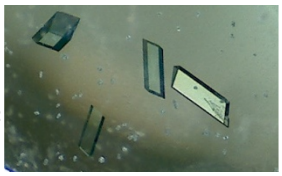	COO Cu-O 2.0724(16) Å 2.2571(15) Å	87.3 °	1.916(2) Å 1.966(2) Å 2.3121(19) Å 2.3402(18) Å

The coordination of only one of these ligands should open at least the two axial sites for catalytic reactions. Therefore the synthetic procedure was adapted accordingly. First, **DMP-OOH** is dissolved with $CuCl_2$ in water to give a yellow-brown solution and a brown precipitate, which was filtered off and is redissolvable in water resulting in a solution of the same color.

In order to synthesize the deprotonated neutral complex **[Cu(DMP-OO)]** basic conditions were established to ensure a deprotonation of the carboxyl functions by adding 2 eq. $NaCO_3$ per acid function to the reaction mixture of 1 eq. **DMP-OOH** and 1 eq. $CuCl_2$, which did not lead to crystalline material., **DMP-OOH** was dissolved in a aqueous 0.2 M NaOH solution to give a yellow to bright orange solution. Afterwards 1 eq. $CuCl_2$ was added turning the solution via a turbid green solution to a turquoise turbid solution. Crystallization approaches remained unsuccessful.

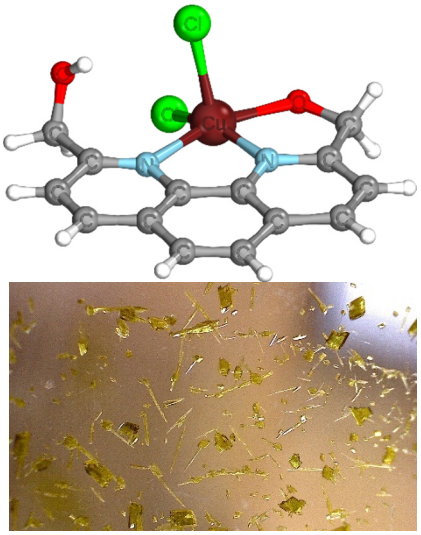

Figure 4-96: Representation and crystal habitus of $[Cu(DMP\text{-}OH)(Cl)_2]$.

1 eq. **DMP-OH** was converted 1 eq. $CuCl_2$ in MeOH to give a yellow solution. A subsequent ether diffusion results in yellow crystals (figure 4-96), which exhibited poor quality. Despite of that, X-ray diffraction was able to confirm **$[Cu(DMP\text{-}OH)(Cl)_2]$**, although the proton of the coordinating alcohol group could not be determined due to the poor data set. A plane is spanned by nitrogen atoms, copper ion and the coordinating oxygen atom. One chlorine is position in a 96 ° angle to this plane, while the other one is merely deviating 0.95 Å from the plane on the other plane´s side. The resolved alcoholic hydrogen exhibits a contact with a chloride at a 2.57 Å distance within the van-der-Waals radii.[224]

Crystal structures of **$[Cu(DMP\text{-}OH)_2][BF_4]_2$** and **$[Cu(DMP\text{-}OOH)_2]$** as well as **$[Cu(DMP\text{-}OH)(Cl)_2]$** were obtained. In particular the latter is interesting for water oxidation catalysis because of the easily achievable ligand exchange.

4.4.3 Water oxidation catalysis

4.4.3.1 Chemical water oxidation catalysis

In literature, most of the water oxidation research is conducted by means of electrochemical methods. Here, diammonium cerium(IV) nitrate – $(NH_4)_2Ce(NO_3)_6$ – (CAN) was applied as chemical sacrificial one-electron donor, as established in a variety of chemical water oxidation reactions, including oxidation of organic compounds.[252] CAN is a strong oxidant with an redox potential of ca. + 1.7 V vs. NHE[253] and does not decompose in aqueous and even acidic aqueous solution, which is mandatory in water oxidation catalysis.[254] A drawback is the ability of the nitrate anion to transfer oxygen atoms. This can influence the actual water splitting process resulting in oxygen gas originating from nitrate.[255] The water and CAN (99 %) was analyzed qualitatively by TR-XRF showing traces of calcium, iron and chlorine and calcium, silver and caesium, respectively. Since iron complexes can catalyze water oxidation the results have to be interpreted critically.[247,256] A homogenous catalytic activity of calcium or silver is not known in literature, yet.[145]

In a general catalysis approach as described in chapter 6.2.12, the water oxidation catalyst was dissolved in 15 ml of a reaction solvent. CAN exhibits a high solubility in polar aqueous solvents, thus only 5 ml of the solvent was necessary resulting in a characteristic yellow-orange color.

The first catalysis run started with a 100 µM of **[Cu(bpy)(Cl)$_2$]** and 500 eq. CAN regarding to the catalyst in a 0.1 M aqueous trifluoromethanesulfonic acid solution. [Cu(NN)(Cl)$_2$] type species are considered to undergo ligand exchange reactions for the chloride anions, especially in stabilizing polar environments, opening up to two coordination sites for catalytic reactions. Therefore these complexes were investigated first. The maximal oxygen volume evolving would be ca. 5.6 ml, since four equivalents CAN are needed to generate one oxygen molecule. To ensure, that every gas evolution is measured, a dropping funnel was installed and loaded with the CAN solution. After dropping the CAN solution into the copper catalyst solution, which was initially blue, the measurement was started. The combined liquid was turned dark green as expected for a mixture of yellow-orange and a blue solution. Vapor pressure was let to equilibrate for 10 min, before adding the CAN solution into the copper catalyst solution. After 15 h

no significant volume was generated and the solution turned yellow indicating a possible degradation of the blue copper compound or formation of another species absorbing visible light.

Frequently, the stability of the WOC is limiting the systems efficiency, because the active species decomposes under the harsh reaction conditions.[257] In order to investigate if this is the case, a saturated solution of the WOC concentration was increased by factor 518 to 0.05 M. Due to solubility reasons the amount of CAN was only doubled resulting in a 1:1 WOC/CAN ratio, which ideally would account for ca. 11 ml oxygen gas. This solution exhibited the same coloration than before, but more intense. The analysis of the catalysis revealed also no significant gas evolution indicating that this system is most likely not catalyzing water oxidation at all. One possibility is, that the assumed ligand exchange did not take place, which seems not very likely, since this kind of chloride exchange – even by water – is literature-known[218] and was confirmed by use of coordinating ligands in this work.

To investigate if the catalysis run in a basic medium, an analogue reaction was performed in 0.1 M NaOH/0.1 NaOAc, in which a saturated solution of **[Cu(bpy)(Cl)$_2$]** was prepared. Under alkaline conditions the subsequent hydroxide complex should be formed readily, as shown in adapted literature.[75,218] The solubility was about one order of magnitude poorer than in the acidic solution giving an overall concertation of 0.07 M. But the same amount of CAN was used correlating to 10 eq. regarding to the WOC in this case. Still the observed coloration was comparable to the runs before and no gas was evolved.

Copper(II) complex based on the **DMP-OH** was also tested for chemical water oxidation purposes under basic conditions in order to favor the coordination of alkoxy groups, which then may forces a chloride to disengage stabilizing higher oxidation states by donation of electron density. A water molecule can then attack the central ion to give a copper hydoxo species under reduction of the alkoxide to the alcohol or preservation of the former. This pathway leads then likely to the active copper bis-hydroxo compound. Crystals of **[Cu(DMP-OH)(Cl)$_2$]** were dissolved in an aqueous 0.1 M NaOH/0.1 NaOAc solution to reach a reaction concentration of 0.005 M. A 20 eq. CAN containing solution was prepared, which would give rise to ca. 11 ml oxygen, when fully converted. Initially both solutions formed two phases becoming a

homogenous green solution after 45 s. Consistent with the results before, no gas evolution could be detected.

Under the performed conditions, the tested systems were not found to be significantly active in terms of gas evolution. The abstraction of chloride atoms opening coordination sites may not take place or the activity of the resulting hydroxo species is way too low for detection with this set-up. Of course, concurring coordination processes by anionic Lewis bases – especially by chloride and nitride – may also lower the activity to an undetectable amount, as indicated by literature in a comparable case.[61]

4.4.3.2 Electrochemical water oxidation catalysis

Electrochemical tests were conducted on **[Cu(DMP)$_2$(Cl)][Cl]**, **[Cu(bpy)(Cl)$_2$]** and **[Cu(DMP-OH)(Cl)$_2$]**. A basic reaction media was chosen to establish comparable conditions to afore mentioned chemical water splitting approaches.

Unfortunately **[Cu(DMP)$_2$(Cl)][Cl]** is not dissolvable in aqueous media and was therefore investigated in MeCN and in a MeCN/H_2O mixture, which makes a comparison to the other two compounds in basic reaction media not possible. In addition, the catalytic activity should be weak due to the two coordinating **DMP** ligands shielding the catalytic center. When performing cyclic voltammetry of a 1 mM **[Cu(DMP)$_2$(Cl)][Cl]** a dynamical behavior was observed upon anodic scanning. Two features are observed when performing the measurement at 50 mV/s and 800 mV/s, as depicted in figure 4-97. Both exhibits a hardly reversible redox wave at 0.61 V vs. Ag/AgCl, which could be assigned to an one-electron charge transfer of Cu^{III}/Cu^{II}.[258] In addition, an irreversible peak is observed at 1.26 V vs. Ag/AgCl, which corresponds to an analogue literature known[75] catalytic wave. This is observable in any cycle, but its current decreases with increasing number of cycles. As for the waves of the redox reaction, the catalytic waves are shifting to higher potentials with increasing scan rates. This may indicate a kinetic control of the reactions, since no change of the electrode surface was observed.

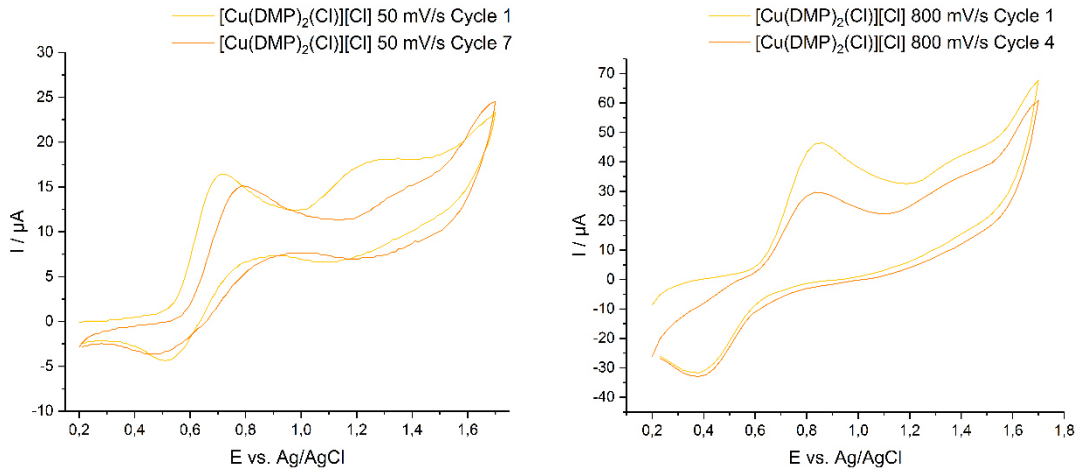

Figure 4-97: Cyclic voltammogram of 1 mM [Cu(DMP)$_2$(Cl)][Cl] in 0.1 M TBA[PF]$_6$/MeCN at 50 mV/s (left) and 800 mV/s (right).

After these scans, a small amount of water was added to approach water splitting conditions. When scanning the same potential range with 800 mV/s, the comparison

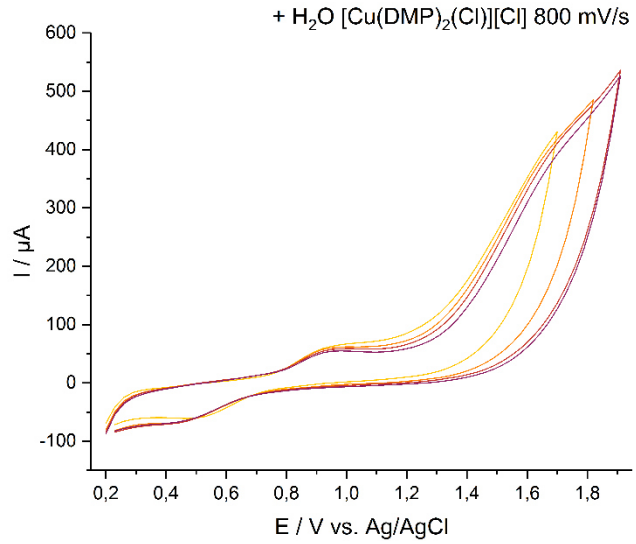

Figure 4-98: Cyclic voltammograms of 1mM [Cu(DMP)$_2$(Cl)][Cl] in 0.1 M TBA[PF]$_6$ /MeCN with water added at 800 mV/s.

of the catalytic current at 1.7 V vs. Ag/AgCl reveals a 6.4 time increase indicating a diffusion or substrate controlled behavior, as expected. The only parameter changed in the scans in figure 4-98 were the maximal anodic potential. During cycling, a significant amount of gas bubbles was visible on the working electrode indicating a successful evolution of oxygen.

The samples of **[Cu(DMP-OH)(Cl)$_2$]** and **[Cu(bpy)(Cl$_2$)]** have been prepared in an identical manner in aqueous 0.1 M NaOH to compare the catalytic currents of both species under water oxidation (figure 4-99). Again, a significant gas evolvement was visible. At 1.7 V vs. Ag/AgCl the current in the case of **[Cu(bpy)(Cl$_2$)]** is ca. 17 % than that of **[Cu(DMP-OH)(Cl)$_2$]** indicating a higher activity. Interestingly, no redox signals at 0.61 V vs. Ag/AgCl are observable.

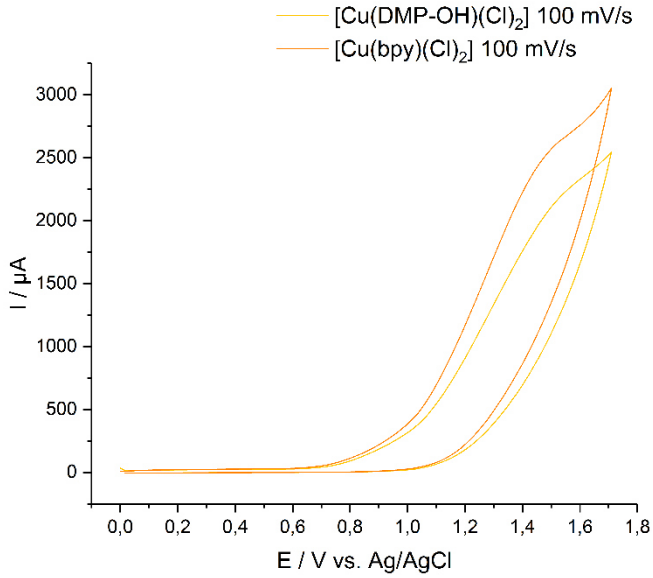

Figure 4-99: Cyclic voltammograms of [Cu(DMP-OH)(Cl)$_2$] and [Cu(bpy)(Cl$_2$)] in 0.1 M NaOH/H$_2$O at 100 mV/s.

This findings indicate a catalytic activity of the synthesized species under water splitting electrochemical conditions. Despite the before formulated thesis of increasing activity based on auxiliary coordination abilities of the **DMP-OH** ligand, the results show, that the opposite is most likely the case, at least when apply electrochemical methods.

Although several electrochemically investigated copper(II)-based systems are known in literature[75–77,231,244,246,259], a direct comparison of catalytic performance is not possible because of differing set-ups, solvents or electrodes. To support classifying

the tested substances, the electrochemical measurements should be extended to other species and thorough rinse test should be conducted in addition to varying the workings electrode, since the surface and material may have an crucial impact on the performance.

5 **Summary and Outlook**

Within importance and necessity of sustainable and resource-saving processes of energy generation, copper-based water splitting systems driven by solar light exhibit promising development in research towards real-life implementation. This work reports a thorough spectroscopic investigation of a photoactive [Cu(DMP-X)2][BF4] type series and reveals deep insights into the underlying photo-physical behavior. Based on these fact, conclusions were stated to further improve complexes in this field. In addition, fundamental research in the field of water oxidations catalysts with copper as central metal were conducted. The obtained target molecular motives were discussed and analyzed with regard to their properties. A variety of different complexes were synthesized by chance, during these complexation reactions.

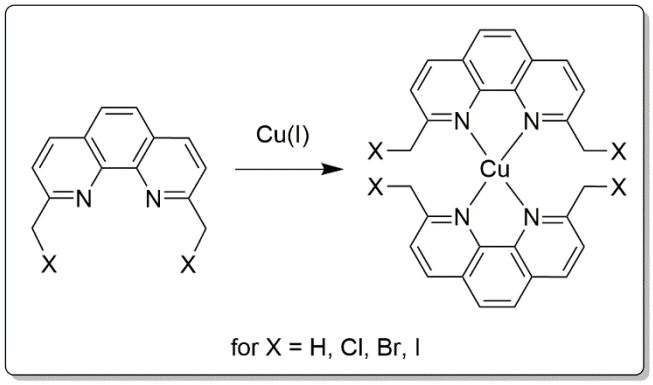

Figure 5-1: [Cu(DMP-X)$_2$][BF$_4$] series.

A series of [Cu(DMP-X)$_2$][BF$_4$] type complexes (figure 5-1) was synthesized to elucidate the optical properties as photosensitizer. As shown before, steric influences change the photoexcitation behavior crucially, which is why the increasing diameter of the halogens are used. These complexes can then be compared to the well-investigated [Cu(DMP)$_2$][BF$_4$]. The result of this series is also depending on electronic properties, but for bromine and chlorine the difference is rather small according to their electronegativity. Furthermore, no significant difference was found for the whole halogenated series taking the steric aspect into foreground. The desired process of photoexcitation – MLCT transitions under oxidation of copper – has been verified by optical and X-ray spectroscopy. Unfortunately, the complexes of halogenated ligands exhibit an inferior ability to population MLCT states, which was also indicated by steady state luminescence spectroscopy. The photo-oxidation was mimicked by electrochemical means while conduction X-ray absorption and UV/VIS spectroscopy to identify electronic property changes.

Although the targeted cyclic phenanthrolines could not be obtained, they remain a very interesting ligand class due to their coordinationally tensed structure regarding to the

entatic principle. Based on the results in the field of diazapyridinophanes, the N donor function should be in a normal Cu-N bonding distance (ca 2.0 Å) to provide a sufficient stability. **[Cu(DAPy-Ts)(MeCN)][BF$_4$]** was synthesized and characterized under inert gas atmosphere. The complex was determined by X-ray single crystal analysis and X-ray absorption spectroscopy underlining the coordination geometry and the oxidation state. The complex is oxidation stable against atmosphere as solid, but tends to build bis(μ^2-hydroxo)-Cu$_2$ complexes in solution under exposure of atmosphere for several days implicating a possible reactivity towards oxygen activation. which has to be further elucidated. Furthermore, the Cu(II) complex **[Cu(DAPy-NH)(Cl)$_2$]** could be obtained by reaction with the solvent DCM presumably and has there be performed once again with a non-halogen containing solvent. Additionally, a low temperature syntheses may have a positive influence on gaining the corresponding Cu(I) complex. Due to the found instability and the poor optical properties, the aim must be to configure the steric properties of the secondary nitrogen donors to prevent a Lewis base attack under generation of an exciplex complex spatially and the implementation of better electron donor introducing a higher electron density to the copper would lead to higher stability. This could be achieved on the one hand by ensuring a shorter Cu-N distance and on the other hand by electron-donating groups.

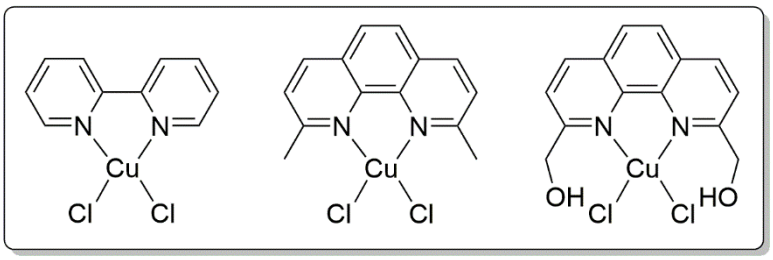

Figure 5-2: Synthesized copper(II) water oxidation catalyst precursors.

The implementation of copper(II) species as water oxidation catalysts was pursued with commercially available and synthesized potentially non-innocent oxygen-based ligands. A remarkable diversity of structural motives was obtained during the synthetic route to suitable copper(II) water oxidation catalysts and copper(II) species without coordination Lewis bases – like anions or solvent molecules – for spectroscopic purposes. Within well-known structures like **[Cu(NN)$_2$(X)][X]** and **[Cu$_2$-bis(μ-X)(NN)$_2$(X)$_2$]**, a **phen**-based reaction system was investigated, which delivered blue and turquoise crystals both consisting of the same complex **[Cu(phen)$_2$(Cl)][Cl]**, but differing in higher order, since the turquoise crystals show a layered structured spanned by uncoordinated ligands. The different coloration was

investigated by DRUVS indicating the layers and/or incorporated solvent molecules to be key factor for this behavior. Hydroxo bridged dinuclear copper(II) complexes, like the synthesized **[Cu_2-bis(μ-OH)$(phen)_2(Cl)_2$]** and **[Cu_2-bis(μ-OH)$(phen)_2(H_2O)_2$]$[Cl]_2$**, are investigated for its oxygen activation abilities. Rare CO_3coordinated copper(II) complexes **[Cu$(phen)_2(CO_3)$]** and **[$(Cu(bpy)_2O)_3$-C]$[BF_4]_4$** were obtained, which are in general subject to investigations concerning the temporary fixation of CO_2 in order to decrease to atmospheric CO_2 levels. Mononuclear [Cu(NN)$(Cl)_2$] type complexes **[Cu(bpy)$(Cl)_2$]** and **[Cu(DMP)$(Cl)_2(H_2O)$]** could be synthesized, as assumed water oxidation catalyst precursors. Although no gas evolution was observed in chemical water splitting experiments, electrochemical approaches show an observable activity.

The structural diversity of copper chemistry lead to a variety of application possibilities in particular in the field of water splitting. Copper(I) photosensitizer are relatively well-investigated and are able to outperformed established noble metal-based systems. Especially water oxidation with copper(II) complexes is an emerging area, where fundamental research still needs to be conducted. Hopefully, efficient water splitting systems will be implemented in the future on a large scale to replace fossil and nuclear energy resources in order to contribute to the energy mix.

6 **Experimental Section**

6.1 Working Techniques

All air and moisture sensitive synthesis and substances, like copper(I) salts, were handled under anaerobic and water-free conditions using the Schlenk technique (vacuum gas manifold) with nitrogen (5.0) or argon (5.0) as inert gas. Both gases have previously been dried by a column of phosphorus pentoxide with moisture indicator. The glass-ware were at least three times heated *in vacuo* by a heat gun and a rotary vane pump over several minutes to minimize the amount of surface absorbed water. Additionally, the glass-ware was filled with inert gas after each heating/*in vacuo* step. Liquids were measured and transferred by single-use syringes. Dried diethyl ether and dried MeCN were dried by an *MBraun SPS-800* solvent dying system and additionally stored of mole sieve. All other solvents were dried manually an stored over mole sieve.

Crystallization approaches were conducted by weather a diethyl ether diffusion into the vessel of the dissolved target substance, which is especially the case for the copper(I) compounds. In addition, some crystals were obtained by slow solvent evaporation of the target species containing solution into a antisolvent, which were in general chosen according to literature.[260]

In denoted cases the MPLC system *CombiFlash® Rf+* from *Teledyne Isco* was used as flash chromatographic device using original RediSep Rf prepacked columns only. *n*-hexane/EtAc and DCM/methanol were used as standard solvent couples. The software suggested gradient programs for each column was used as starting point, which was adapted the particular separation problem. When detecting a peak, the system automatically initiates the isocratic hold of the solvent mixture. The detection of each fraction within the eluate is realized through UV absorption between 200 nm and 400 nm. A suitable eluent was determined by thin-layer chromatography (*Kieselgel 60 F254* from *VWR*) before using the MPLC device.

All crystal pictures were obtained by a *dnt® DigiMicro 2.0 Scale* digital microscope with 2 million pixel CMOS image sensor and 20x to 200x magnification. The provided Software was used to measure the crystals size in order to select crystals for X-ray diffractometry.

6.2 Analytic and Spectroscopic Techniques

6.2.1 Nuclear Magnetic Resonance Spectroscopy

The nuclear magnetic resonance measurements were performed on a *Bruker Avance 500*. ^{1}H (500 MHz), ^{13}C (125 MHz), ^{15}N (50.7 MHz) and ^{31}P (202.4 MHz) spectra were collected at 30 °C, unless otherwise stated. Additionally a *Bruker Avance 300* was used for ^{1}H and ^{13}C spectra at room temperature. The deuterated solvents are denoted for each substance. All chemical shifts refer to the δ scale and were indicated in ppm.

TMS is used as reference substance (δ = 0 ppm) for ^{1}H and ^{13}C spectra. The calibration of ^{1}H spectra was arranged by the non-deuterated part of the used sol-vent in comparison to the position of TMS in the spectra. In case of the ^{13}C NMR measurements, the calibration was done by means of the deuterated solvent part referred to TMS. Ammonia and an 85% aqueous solution of phosphoric acid were used as reference substances (δ = 0 ppm) for ^{15}N and ^{31}P spectra, respectively. Two-dimensional NMR spectra, like COSY, HMBC and HMQC were used to ensure correct nuclei correlations.

All NMR spectra were plotted with the *Bruker TOPSPIN 2.1 Plot Editor*.

Multiplicities were abbreviated as follows: s (singlet), d (doublet), t (triplet), q (quartet), quin (quintet), m (multiplet), dd (doublet of doublets), dt (doublet of triplets).

6.2.2 X-Ray Crystallography

Intensity data were collected on a *Bruker AXS SMART APEX* diffractometer with graphite monochromated MoK radiation (λ = 0.71073 Å) at 120(2) K. Data reduction and absorption correction were performed with SAINT[261] and SADABS[262]. The structures were solved with direct and conventional Fourier methods. All non-hydrogen atoms were refined anisotropically with full-matrix least-squares procedures based on F^2 by SHELXL.[263] Hydrogen atom positions were derived from different Fourier maps and then refined at idealized positions, riding on their parent C or N atoms with isotropic displacement parameters $U_{iso}(H) = 1.2\ U_{eg}(C/N)$ and $1.5\ U_{eq}$(C methyl). In denoted cases of severely disordered small molecules *SQEEZE* from the *PLATON* program package was used.[264]

6.2.3 Mass Spectroscopy

ESI spectra were measured by a *Water Synapt G2* quadrupole – time of flight (Q-ToF) spectrometer. The solvent used is denoted for every substance.

Mass spectra with EI as ionization method were performed at 200 °C source temperature and 70 eV electron impact energy in connection with a *Thermo Scientific DFS* sector field mass spectrometer. In special denoted cases, high resolution mass spectra were obtained.

The GC-MS unit contains a *Thermo Scientific Focus GC* and *DSQ II quadrupol MS*. Unless otherwise stated, temperature program was 80°C, 1 min; 10°C/min; 300°C.

6.2.4 Elemental Analysis

The elemental analysis was performed on a *vario MIRCOCube* from *elementar* with WO_3 as additive.

6.2.5 Infrared Spectroscopy

The IR spectra were recorded on a *Bruker Vertex 70* FTIR spectrometer (HeNe-Laser, λ=633 nm) using the ATR sampling technique with a diamond crystal. The samples were measured directly after purification and drying. The data is stated as transmission with a resolution of 4 cm^{-1} in the range of 600 to 4500 cm^{-1}. All spectra were baseline corrected by the software *OPUS* from *Bruker*.[265]

Signal intensities were abbreviated as follows: vs (very strong), s (strong), m (middle), w (weak), br (broad).

6.2.6 X-Ray Absorption and Emission Spectroscopy

XAS experiments were performed at the XAS beamline at ANKA– Angstrømquelle Karlsruhe – (maximum beam current 200 mA with an energy of 2.5 GeV) in Karlsruhe

(Germany), at PetraIII-P65 beamline at DESY – Deutsches Elektronen Synchrotron – (maximum beam current 100 mA) in Hamburg (Germany) and at BM25a at ESRF – European Synchrotron Radiation Facility – (maximum beam current 200 mA with an energy of 6 GeV) in Grenoble (France). The acquisition of XES spectra were also conducted at ID26 at ESRF.

All solid samples were pestled with cellulose to pellets in order to avoid self-absorption effects and were measured at ambient temperature.

For XAS (XANES and EXAFS) measurements at the copper K-edge (8979 eV) a Si(111) double-crystal monochromator was used. HERFD-XANES spectra were acquired by an Si(311) double-crystal monochromator set-up. A Si(111) double-crystal monochromator was used for the emission measurement. The solid samples for these measurements were cooled down to 30 K in a closed cycle helium cryostat. The Cu(I) samples were additionally prepared under inert atmosphere in a glove box. The spectrometer was kept under helium atmosphere to reduce the absorption of the luminescence radiation. No signs of radiation damage could be detected in any sample within the acquisition time and measurements were carried out on multiple spots.

In the first step of data analysis the background of the spectrum was removed by subtracting a Victoreen-type polynomial.[266] Due to the very differing shapes of the absorption edges of the samples and the used references, the first inflection point of the first derivative of the corresponding spectrum was defined as energy E_0. Afterwards the first inflection point was taken as energy E_0. A piecewise polynomial was used to determine the smooth part of the spectrum and was adjusted in a way that the low-R components of the resulting Fourier transform were minimal. The background subtracted spectrum was divided by its smoothed part and the photon energy was converted to photoelectron wave number *k*. For evaluation of the EXAFS spectra the resulting functions were weighted with k^3 and calculated with EXCURVE98, which works based on the EXAFS function and according to a formulation in terms of radial distribution functions[267,268]:

$$\chi(k) = \sum_j S_0^2(k) \frac{N_j}{kr_j^2} F_j(k) e^{-2\sigma_j^2 k^2} e^{-\frac{2rj}{\lambda(k)}} \sin\left[2kr_j + \varphi_{ij}(k)\right] \qquad \textbf{(6-1)}$$

The number of independent points N_{ind} was calculated according to information theory to determine the degree of overdeterminacy[267]:

$$N_{ind} = \frac{2\Delta k \Delta R}{\pi} \quad \textbf{(6-2)}$$

Here, Δk describes the range in *k*-space used for data analysis and ΔR corresponds to the distance range in the Fourier filtering process. For the analysis a Δ*k*-range of 10 and a Δ*R*-range of 3 was used, which yielded a number of independent points of 19.1. The quality of a fit was determined using two methods. The reduced χ^2_{red} considers the degree of overdeterminacy of the system and the number of fitted parameters *p*. It therefore allows a direct comparison of different models[269]:

$$\chi^2_{red} = \frac{\left({N_{ind}}/{N}\right)}{N_{ind} - p} \sum_i \left(\frac{k_i^n}{\sum_j k_j^n \left| \chi_j^{exp}(k_j) \right|} \right)^2 \left(\chi^{exp}(k_i) - \chi^{theo}(k_i) \right)^2 \quad \textbf{(6-3)}$$

The R-factor, which represents the percentage disagreement between experiment and adjusted function and takes into account both systematic and random errors according to the equation[269]:

$$R = \sum_i \frac{k_i^n}{\sum_j k_j^n \left| \chi_j^{exp}(k_j) \right|} \left| \chi^{exp}(k_i) - \chi^{theo}(k_i) \right| \cdot 100\% \quad \textbf{(6-4)}$$

The accuracy of the determined distances is 1 %, of the Debye-Waller-like factor 10 % and of the coordination numbers depending of the distance 5-15 %.[270] The amplitude reducing factor was iterated free in every fit.

6.2.7 UV/VIS Spectroscopy and Diffuse Reflectance UV/VIS Spectroscopy

A *Varian Cary 50* and a *Perkin-Elmer Lambda 45 (double beam spectrometer)* device were used to record the UV/VIS spectra under exclusion of oxygen at room temperature. The molar attenuation coefficient was determined by the Beer-Lambert law. Quartz cuvettes with an optical pathway of 10 mm from *Hellma* were used. The

samples were prepared using spectroscopy grade *SPECTRONORM* acetonitrile from *VWR chemicals* and performing at least three freeze-pump-thaw cycles to remove dissolved gases. All cuvettes were treated with a solution of *Hellmanex® III* from *Hellma Analytics* in pure water with a low conductivity (≥ 8.0 µS/cm at 20 °C) for at least 2 h. Subsequently, the cuvettes were cleaned by rinsing with pure water (≥ 8.0 µS/cm at 20 °C), acetone (p.a.)and the desired sample solvent and were finally dried.

The diffuse reflectance UV/VIS spectra were recorded by Dr. C. Wilhelm at University Kaiserslautern. *A Perkin Elmer Lambda 18* spectrometer with an diffuse reflectance sample holder system. All spectra were recorded with identical measurement parameters: Measurement range: 300 nm – 900 nm, data interval: 0.25 nm, measurement rate: 120 nm/min and smoothing: 4 nm.

6.2.8 Total Reflection X-Ray Fluorescence spectroscopy

For element detection, a total reflection X-ray fluorescence spectrometer *S2 PICOFOX automatic* from *Bruker Nano GmbH* was used, which delivers an element detection limit as low as 2 pg Ni give rise to a concentration range from ppb to 100 %. A 50 W molybdenum containing metal-ceramic at max. 50 kV and 1 mA is implemented as X-ray source. The detector is a Peltier-cooled *XFlash* Silicon Drift Detector with an energy resolution < 149 eV at 100 kcps for the Mo k_α source. A 1 µg As sample was used as gain correction. All samples were prepared on single-use acrylic glass carriers.

6.2.9 Steady State Luminescence spectroscopy

The luminescence spectra were recorded on a *Jasco FP-8300* luminescence spectrometer at room temperature. Quartz cuvettes with an optical pathway of 10 mm from *Hellma* were used. The samples were prepared using spectroscopy grade solvents and performing at least three freeze-pump-thaw cycles to remove dissolved gases. All cuvettes were prepared as described in chapter 6.2.7.

6.2.10 Time Correlated Single Photon Counting

Decay curves and TRES spectra were obtained by the modular luminescence-lifetime-system *Ultima-01-DD* from *HORIBA Yvon IBH Ltd* using the TCSPC technique. All cuvettes were prepared as described in chapter 6.2.7.

The maximal time resolution with FluoroHubA+ and PPD detection module under usage of appropriate light sources with small pulse width is about 25 ps to 30 ps. This TC-SPC setting is equipped with four exchangeable diodes with 256 nm, 280 nm, 346 nm and 374 nm wavelength build by the same company. The three first mentioned diodes are based on LED technique, while the last one is a LASER diode. In this system, the time resolution of the LED diodes is determined as 100 ps and 30 ps for the LASER technique based diode. The bandpass filter was adjusted to 32 nm.

The acquisitions were performed in the reverse mode using 16384 channels.

Excitation wavelength, solvents and other relevant parameters are explicitly mentioned for each spectrum. All decay curves were processed with the analysis software *DAS6* (version 6.8.13) and fitted by multiple fits with different parametrized exponential functions as shown in equation ((6-5).

$$f(t) = A + \sum_{i=1}^{i} B_i + \exp\left(-\frac{t}{\tau_i}\right) \qquad \textbf{(6-5)}$$

The goodness of data fit was evaluated by several parameters. First, the X^2 value is below 1.2 and does not improve significantly upon adding an additional decay component. Residuals are randomly distributed, lifetimes are in accordance with literature and other measurement of a comparable substance type, meaning an inherently consistence. Lifetime value below 0.01 ns are to be seen critical, since scattered excitation light may be responsible for the results. Large standard deviations, negative or large shifts within more than three channels are also an indicator for a bad fit. Negative pre-exponential components may indicate an excited state process and are not automatically an indicative of the fit quality.

TRES spectra were sliced within the *DataStation* (version 2.7.7) software over the information containing area. Slicing information were given for each dataset

separately. The start point of the slicing area is represented by the begin of the decay curve. After slicing the generated spectra were area normalized in order to gain TRANES spectra.[271] Wavelength regions of the original TRES spectra are shown in the resulting TRANES spectra. For clarity, the mean time of the sliced spectrum after the beginning of the decay curve is indicated instead of the sliced time region.

As investigating the TC-SPC system with pure, spectroscopic grade solvents with the 256 nm diode, luminescence in the range of 480 nm – 560 nm and 750 nm – 800 nm were found, which correlates to non-linear optics effects[272] of frequency doubling and frequency tripling by generation of the second and third harmonic, respectively. This effect does not have an effect on time correlation measurements like single decays or TRES spectra or TRANES spectra, since the lifetime is the harmonics are identical. Scattering reference spectra as system response function were measured to account for this issues. The steady state luminescence spectra are corrupted by these higher harmonics, which were therefore consequently rejected. The signal of the incident light is detected up to 307 nm and a Raman signal is observable in the range between 307 nm and 382 nm for a MeCN solvent sample.

6.2.11 Electrochemistry

Cyclic voltammetry and square-wave voltammetry experiments were performed on two different systems:

- *Metrohm-Autolab PGSTAT 101* potentiostat with the software *NOVA* 1.10.5 from *Metrohm*. Three electrode system: Pt or glassy carbon working electrode (1 mm diameter), Pt wire counter electrode and Ag/0.01 M $AgNO_3$ reference electrode.
- *Ivium Technologies CompactStat* with the software *IviumSoft* 2.698. This electrode setting is identical to the before mentioned, except the 3 mm diameter of the working electrode.

The acquisitions were performed in a continuously argon flushed electrochemical cell at room temperature. The working electrode material is denoted for every measurement. Ferrocenium/Ferrocene (Fc+/Fc) was used as internal standard and

added to the sample solution after the measurements. The samples were prepared under argon atmosphere. The solvents and scan rates as well as sample and conducting salt concentration is mentioned in each case. Normally the latter are in the range of 0.001 M for samples and 0.1 M for the conducting salt and MeCN as solvent. For organic solvents TBA[PF]$_6$ was used as conducting salt.

6.2.12 Water splitting catalysis

All water splitting reaction were performed with apparatus, in whose construction the author contributed as well as Maike Amen. The main contribution in maintenance and construction was done by Peter Zimmer.[273,274] The system consists of an automatic gas burette, a sun light simulator, a reaction vessel and a cryostat as described in the following. This system allows a time-depended, isobaric measurement of evolving gas under simulated sun light, as can schematically be seen in figure 6-1 and figure 6-2.[273,274]

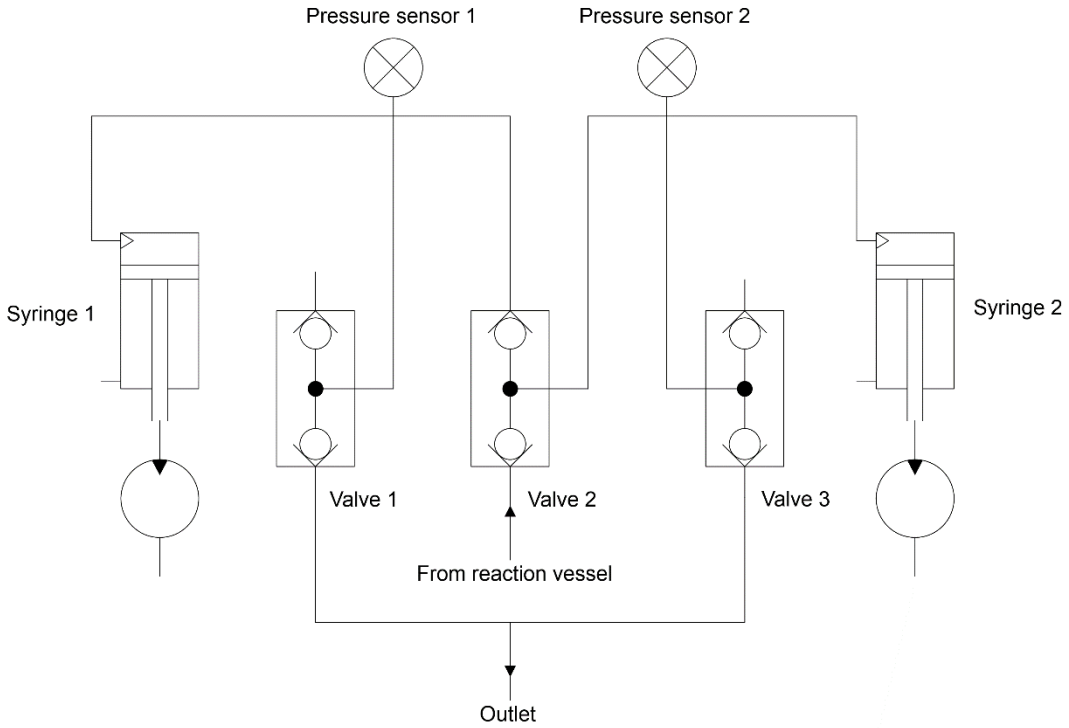

Figure 6-1: Function scheme of the automatic gas burette. Figure adapted from Peter Zimmer.

Set-Up

The automatic gas burette *MesSen Nord GASMESS-5-CONT* operates isobar and adjusts the interior pressure upon gas evolution by two 100 ml syringes, which are

working alternating to ensure a continuously operation. The movement of the plunger is recorded and after a pressure correction plotted against time with the software *GasMess* (version 5.2.8) from *LIKAT Rostock* + *MesSen Nord GmbH*. As shown in figure 6-1, the evolved gas passes valve 3 to get either to syringe 1 or syringe 2. When the addressed plunge has reached its maximal deflection, valve 3 switches and the other syringe starts collecting the gas. After the maximal volume is collected, the plunges pushes the gas through valve 1 or 3 out of the system leaving the plunges back in the initial state. The pressure sensors 1 and 2 are ensuring that the active plunge move sufficiently to hold the pressure.

To perform a temperature depended volume correction, the room temperature is acquired during catalysis by *TFA USB Temp Control* (version 2.9.2) from *TFA Dorstmann* with a precision if 0.5 °C and a resolution of 0.0625 °C, which was calibrated to 0.2 °C. The burette is connected with the reaction vessel by tubing and then glassware.

Tubing is isolated by foam material and al glassware is tempered at 25°°C by a cryostat *Ministat 230* with *Pilot ONE* from *Peter Huber Kältemaschinenbau GmbH* exhibiting a temperature precision of ± 0.02 °C and 2000 W power drain. Silicon oil *Huber M40.165/220.10*(6164)* was used as medium.

The sun simulator *LOT-QuantumDesign LS0400* consist of a 300 W xenon arc lamp with an AM-1.5 global filter from, which emits middle-european sun light. The filter used simulates the path length through 1.5 times the atmosphere allowing for the sun light to be tilted. The light is emitted through a fiber optic cable to a lens, which exhibits a light intensity of 100 W/cm², when placed in a distance of 20 cm simulating the sun intensity. This setup is forming a spot of 15 mm in diameter, which is too focused to illuminate a most of the reaction solution. The lens was removed resulting in a broader light cone. A shutter was used to start the illumination at any given point of time.

The reactor vessel is a custom product with four NS14/23 glass joints and a vacuum and gas tight SVG thread with shell. The optic cable is mounted in this shell aligned to illuminate the solution homogenously. Before any catalysis run, the vessel was always cleaned by *aqua regia* and organic solvents.

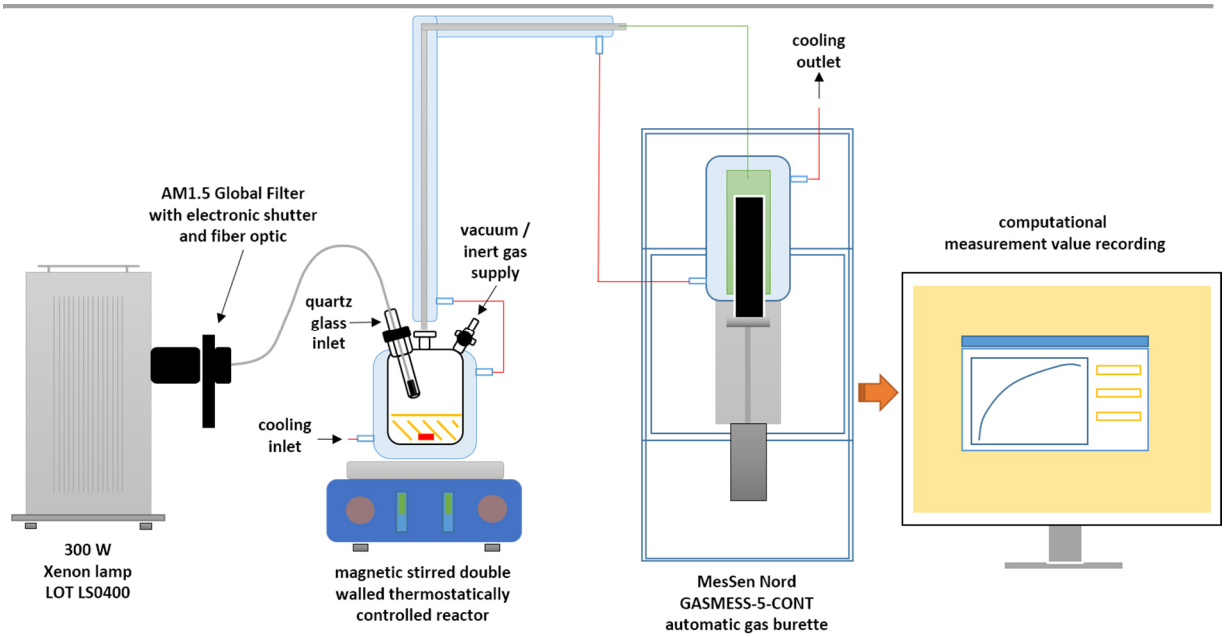

Figure 6-2: Schematic representation of the gas evolution measurement system. Figure by Peter Zimmer.

Performing a water splitting catalysis reaction

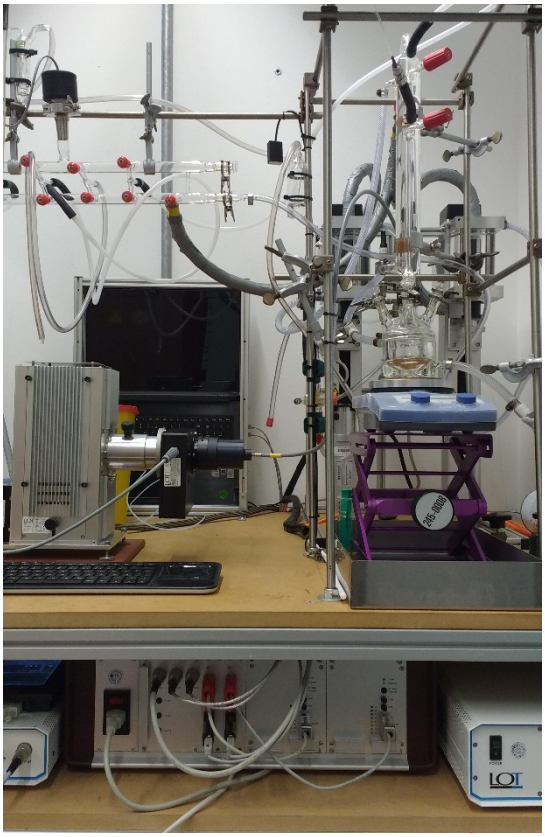

Figure 6-3: Set-Up of the gas measuring system.

The tightness of the gas burette was ensured before every run by holding an increased pressure over time. After that the total inner volume was measured and 20 ml was subtracted from that value because this is the later added reaction volume.

All samples were prepared under anaerobe and water-free condition by means of a fully equipped Schlenk line with a pressure relief valve, which can be seen in the middleground of figure 6-3. The reached vacuum pressure by the *Vacuubrand RZ 2.5* is displayed by a *Vacuubrand VSP 3000* manometer and a *DCP 3000* display. Therefore, the reaction vessel and the attached glassware was inertized by three vacuum pump – nitrogen purge cycles. Since, the residue part of the gas burette is not capable to resist vacuum und is only purged with nitrogen. Cryostat and

lights source were switched on at least two hours before starting the run in order to reach a steady temperature state.

The solids were used as single crystals to exclude any impurities. These were inertized in crimp sealed vials with septum by three vacuum pump – nitrogen purge cycles. Deionized pure water with a low conductivity (≥ 8.0 µS/cm at 20 °C) was applied as reactant. After that solvents degassed by three freeze-pump-thaw cycles were added through the septum under maintained overpressure. The homogenous solutions were transferred into the reaction vessel by syringe in argon counter flow. Then the vessel is closed and the stirring at 300 rpm is switched on. To ensure that the vapor pressure is not causing a wrong gas volume, the light and the measuring is started ten minutes after addition later. This time was chosen based on analyzing blind runs, where the volume was constant after 10 min. Additionally, the vessel was wrapped in aluminum foil to reflect not absorbed light back into the solution.

Every run consists of an actual catalysis reaction and a blind measurement, where no photosensitizer was added.

Temperature and blind correction

Due to the dependence between temperature and pressure as described in the ideal gas law, a temperature correction is necessary to prevent an erroneous impact on the measured gas volume. This was realized by constantly measuring the room temperature and smoothing the curve by a Savitzky-Golay filter. This filter generates a polynomial regression, which is manipulable by choosing the window size and the degree of polynomial.

The volume at each measuring point is corrected by applying equation ((6-10) derived from the ideal gas law.[273] Originating from the ideal gas law in equation ((6-6), a term for $n(t)$ is formed (equation ((6-8)) and inserted into the ideal gas law resulting in equation ((6-9). The final correction term is shown in ((6-10), where equation ((6-9) is integrated. In addition, a weighing factor a was implemented for the temperature correction and the blind volume is subtracted from the measured volume for each data point.

$$p \cdot V = n \cdot R \cdot T \implies \frac{V}{T} = \frac{n \cdot R}{p} \quad \textbf{(6-6)}$$

$$\Delta V(t) = \frac{n \cdot R}{p} \cdot \Delta T(t) = \frac{n(t) \cdot R}{p} \cdot \Delta T(t) \Longrightarrow n(t) = \frac{V(t)_{measured} \cdot p}{T(t)_{measured} \cdot R} \quad \textbf{(6-7)}$$

$$\Delta V(t) = \frac{n(t) \cdot R}{p} \cdot \Delta T(t) = \frac{V(t)_{measured} \cdot p \cdot R}{T(t)_{measured} \cdot R \cdot p} \cdot \Delta T(t) = \frac{V(t)_{measured}}{T(t)_{measured}} \cdot \Delta T(t) \quad \textbf{(6-8)}$$

$$\Delta V(t) = \frac{V(t)_{measured}}{T(t)_{measured}} \cdot \Delta T(t) \quad \textbf{(6-9)}$$

$$V = V_{measured} - a \cdot \frac{\left(T_{measured} - T_{reference}\right)(V_{measured} + V_{reactor})}{T_{measured}} - V_{blind} \quad \textbf{(6-10)}$$

For the automatic correction of the data a script was used within the *Python(x,y)* distribution[275], which loads the temperature and volume plot of the catalytic reaction and the blind measurement as well as processing parameters. The last mentioned includes start times of the measurements for synchronization of catalysis and blind runs, weighing factor (default: 0.5), reactor vessel volume, smoothing window size (default: 1001) and degree of polynomial (default: 3).

6.2.13 Computational Chemistry

All calculations were performed on the *OCuLUS Cluster* within the *High Performance Computing System* of the *Paderborn Center for Parallel Computing (PC²)*[276] using the *ORCA* 3.0.3. program package[277].

All frequency calculations and geometry optimizations were performed on a TPSS[278,279]/def-TZVP[280–282] level of theory for ligands and a TPSSh[279]/ def2-TZVP[280–282] level of theory for complexes applying atom-pairwise dispersion correction with the Becke-Johnson damping scheme[283]. TPSSh is considered as the functional of choice for copper based systems and has been proven to describe structural and vibrational properties of copper complexes.[284] UV/VIS absorption spectra were also calculated by means of TD-DFT on a TPSSh[279]/def2-TZVP[280–282] level of theory including triplet transitions, but without taking solvent effects into consideration, since test calculations with the continuum solvation model SMD[285]

delivered no significant improvement. In all cases the cation coordinates of single-crystal data were applied as input. The spectra were generated by orca_mapspc as implemented in ORCA with 8000 points and a line width of 1000 cm^{-1}.

To consider relativistic effect from heavier atoms and halogen the zeroth order regular approximation (ZORA) was utilized.[286]

Copper K-edge spectra were calculated using the time-dependent DFT (TD-DFT) approach as implemented in ORCA 3.0.3..[287] In these calculations the core properties were described by triple-ζ basis sets CP(PPP)[288] for Cu and Ahlrich's all electron TZVP[280–282] for all other atoms.

HERFD-XANES and VtC emission spectra have been calculated for the crystal structure. The hybrid XC-functional TPSSh[279] was used for the absorption and the non-hybrid version TPSS[278,279] has been utilized in case of the VtC spectra. The RIJCOSX[142] approximation was utilized as implemented in ORCA to speed up calculations. A special DFT grid of seven was set for copper. The tight convergence criterion was imposed on all calculations. The calculated spectra have all been shifted to match the experiment. A shift of 0.5-0.8 eV was required for the HERFD-XANES spectra, while for VtC emission the required shift was 20 eV. In addition to the shift, all spectra have been normalized to the intensity of a characteristic peak (in case of Cu(II) the prepeak). The discrete single energy transitions have been subjected to Gaussian broadening with a FWHM linearly rising with increasing excitation energy.

MOAnalyzer was used analyze the calculation results.[289]

Other applied functionals, basis sets and additional calculation parameters are denoted for each calculation.

The electronic structure was analyzed using the *AO-Mix* program[290], while the calculated IR spectra has been plotted by the *ORCA* utility program orca_mapspc applying the default settings with Gaussian lineshapes except for the line width (FHHW: 13 cm^{-1}). Afterwards the spectra has been normalized.

Orbitals were plotted by IboView[291] with an iso-surface value of 80 %.

6.3 Chemicals

Unless otherwise stated, all water-free solvents were received from the solvent drying device *MBraun MB-SPS-800* and are transferred under nitrogen inert gas on molecular sieve.

Chemical	Purity	Supplier	Remarks
1,10-Phenanthroline	99 %	Alfa Aesar	
1,2-Phenylene-diamine	99 %	Merck	
1,3-Dibromopropane	98 %	Alfa Aesar	
1,4-Dioxane	technical	UPB	
2,6-Bis(bromomethyl)pyridine	98 %	Sigma Aldrich	
2,6-Pyridinedicarboxylic acid	> 98 %	Merck	
2,9-Dimethyl-1,10-phenanthroline hemihydrate	99 +%	Acros Organics	
2,9-Dimethyl-1,10-phenanthroline hemihydrate	98 +%	Alfa Aesar	
2-Fluoropyridine	98 %	Acros Organics	
2-Methylpyridine	98 %	Sigma Aldrich	
Acetone	technical	UPB	
Acetone	p.a.	UPB	Cuvette cleaning
Acetonitrile	Spectronorm > 99.9 %	VWR	Spectroscopic solvent
Acetonitrile	technical	UPB	
Ammonium chloride	99.8 %, p.a.	Merck	
Benzaldehyde	> 99.5 %	Sigma Aldrich	

Bromine	99 %	Acros Organics	
Chlorobenzene	technical	Riedel-de Häen	Distilled before use
Chloroform	technical	UPB	Refluxed over $CaCl_2$, distilled under inter gas and stored over 4 Å molecular sieve, when necessary
Copper(I) chloride	99.995 +%	Sigma Aldrich	Stored under inert gas and light exclusion
Copper(II) chloride dihydrate	99.999 +%	Sigma Aldrich	
Copper(II) bromide	99.999 %	Sigma Aldrich	
Copper(II) perchlorate hexahydrate	98 %	Sigma Aldrich	
Copper(II) nitrate trihydrate	puriss. p.a. 99.0 – 104 %	Fluka	
Deuterated solvents		Deutero	
Di(2-pyridyl)ketone	> 98 %	TCI	
Diammonium cerium(IV) nitrate	99.5 % REacton	Alfa Aesar	Sacrificial oxidant
Dichloromethane	technical	UPB	Dried over 4 Å molecular sieve, when necessary
Dichloromethane	Spectronorm > 99.9 %	VWR	Spectroscopic solvent
Diethylether	technical	UPB	
Diiodomethane	99 %	Sigma Aldrich	Copper as stabilizer

Ethanol	technical	UPB	Dried over sodium, distilled under inert gas, stored over 3 Å molecular sieve
Ethyl acetate	technical	UPB	
n-Hexane	technical	UPB	
Hydrazine monohydrate	98 %	TCI	64 % to 65 % of hydrazine w/w
Hydrobromic acid	technical	Riedel-de Häen	Approx. 48 %
Hydrochloric acid	technical	UPB	37 % w/w
Hydroiodic acid	technical	Janssen Chimica	57 % w/w, stabilized with 0.5 % H_2PO_3
Lithium aluminum hydride		UPB	
Lithium bis(trimethylsilyl)amide		Sigma Aldrich	1 M in THF
Lithium diisopropyl amide		Acros Organics	2 M in THF/n-pentane/ethylbenzene
Magnesium sulfate	technical	UPB	
Magnesium, turning	99.9 +%	Acros Organics	
Manganese(IV) oxide	98 %	Alfa Aesar	
Methanol	technical	UPB	
Methanol	technical	UPB	Dried over sodium, distilled off and stored over 4 Å, when necessary
Methyllithium		Acros Organics	1.6 M in diethyl ether, ± 5 % w/v
n-Butyllithium		Acros Organics	1.6 M in hexane
Nitric acid	technical	UPB	65 % w/w

n-Pentane	technical	UPB	
Phosphorus oxybromide	>97 %	Alfa Aesar	
Phosphorus pentoxide	> 99 %	Carl Roth	
Phosphorus tribromide	97 %	Sigma Aldrich / Self-synthesis	
Phosphorus trichloride	97 %	Sigma Aldrich	
Phosphorus, red	97 %	Sigma Aldrich	Dried over phosphorus pentoxide *in vacuo*
Potassium hydroxide	technical	UPB	
Potassium iodide	> 99 %, p.a.	Merck	
Potassium tert-butoxide	> 98 %	Sigma Aldrich	
Potassium tetrachloroplatinate(II)	99.9 % (metals basis)	Alfa Aesar	Water reduction catalyst precursor
Propyl amine	99 +%	Acros Organics	
p-Toluenesulfonamide	> 98 %	TCI	
Selenium dioxide	99.4 %	Alfa Aesar	
Silica gel 60, fine	0.063 – 0.040 mm	UPB	
Sodium		Merck	Rods
Sodium borohydride	96 %	Merck	
Sodium carbonate	technical	UPB	
Sodium chloride	technical	UPB	
Sodium hydrogen carbonate	technical	UPB	
Sodium hydroxide	technical	UPB	
Sodium sulfate	water free	UPB	
Sodium sulfate	technical	UPB	

Sulfuric acid	technical	UPB	96 % solution
tert-Butanol	technical	UPB	Dried over sodium, afterwards distilled and stored 4 Å molecular sieve before use
Tetrakis(acetonitrile)copper(I) tetrafluoroborate	97 %	Sigma Aldrich	
THF	technical	UPB	Pre-dried over KOH, then dried over sodium, afterwards distilled and stored 4 Å molecular sieve before use, when necessary
Thionyl chloride	99.7 %	Acros Organics	
Titanium(IV) chloride	99 %	Fluka	
Toluene	technical	UPB	
Triethylamine	99%, pure	Acros Organics	
Trimethyl borate	99 %	abcr	
Water	deionized, ultrafiltrated, low conductivity	UPB	Cuvette cleaning
Water	deionized	UPB	

All chemicals labelled with “UPB” were purchased from the central chemical distribution of Paderborn University.

6.4 Synthesis and Characterization

6.4.1 Synthesis of Phosphorus bromide compounds

6.4.1.1 Phosphorus tribromide

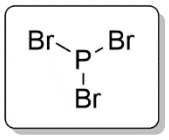

Phosphorus tribromide was synthesized based on literature.[292] Over phosphorus pentoxide *in vacuo* dried red phosphorus (0.83 eq., 0.83 mol, 26.6 g) was suspended in phosphorus tribromide (0.058 mol, 5.5 ml) and heated to 70 °C. Thereafter bromine (1 eq., 1.00 mol, 51.8 ml) was added dropwise. Finally, the reaction solution was boiled for several minutes. Phosphorus tribromide was then distilled as a colorless liquid.

Yield: 186 g, 0.69 mol, 82 %.

^{31}P-NMR (50.7 MHz, $CDCl_3$ in capillary): δ (ppm) = 226.8 ppm (s, 1P).

6.4.1.2 Phosphorus pentabromide

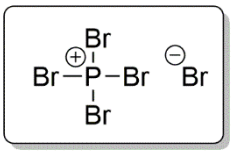

Method 1: from phosphorus tribromide:

Phosphorus tribromide (1 eq., 0.1 mol, 13 ml) was added to dry chloroform (15 ml) under stirring. Then bromine (1 eq., 0.1 mol, 5.18 ml) was added dropwise into the ice bath cooled first solution, so that temperature is not exceed 30 °C. 15 minutes after complete addition the solvent was evaporated resulting in a homogenous yellow solid.

Yield: 40.3 g, 0.09 mol, 94 %.

Method 2: from red phosphorus:

Bromine (2.5 eq., 0.35 mol, 18 ml) was added to a solution of red phosphorus (1 eq., 0.14 mol, 4.44 g) and dry DCM (385 ml) dropwise while using an ice bath to cool the reaction bulb. The temperature did not exceed 30 °C. A yellow solid was obtained.

Yield: 59.8 g, 0.14 mol, 100 %.

6.4.1.3 Phosphoryl bromide

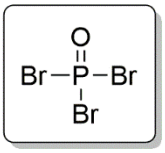

According to literature[293], phosphorus pentabromide was synthesize firstly to react with phosphorus pentoxide.

Bromine (1 eq., 52.2 mmol, 2.7 ml) was slowly added to phosphorus tribromide (1 eq., 51.7 mmol, 7 ml), while cooling with an ice bath. The generated yellow solid was well broken and phosphorus pentoxide (0.36 eq., 26.9 mmol, 1.68 ml) was added and mixed with the first mentioned solid. The mixture was heated to 35 °C in 30 minutes and 3 h later to 40 °C for 2 h. At this stadium only a small amount of liquid was formed, instead an orange mixture was visible. The temperature was increased to 55 °C for 6 resulting in bromine gas, red solution and a grey solid. The distillation approach was neither at room atmosphere and 150 °C nor at 200 mbar and 180 °C successful.

6.4.2 Azapyridinophane ligands

The following synthesis in this chapter were to a large amount performed by *Anke Hillebrand* under the author´s guidance during her master thesis in 2015.[133]

6.4.2.1 Sodium *p*-toluenesulfonamide

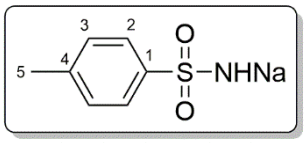

Based on literature[133–135], sodium (1.1 eq., 88.0 mmol, 2.02 g) was dissolved in dry EtOH (95 ml) in small portions. *p*-Toluenesulfonamide (1.0 eq., 79.8 mmol, 13.95 g) was added and the mixture was heated for two hours at 78°C. Colorless needles were precipitating, filtered off and washed with small amounts of cold EtOH. The product was dried and stored under argon.

Yield: 14.6 g, 75.8 mmol, 95%

^{1}H-NMR (500 MHz, DMSO-d_6): δ (ppm) = 2.29 (s, 3H, H-5), 7.09-7.12 (m, 2H, H-3), 7.56-7.58 (m, 2H, H-2).

^{13}C-NMR (125 MHz, DMSO-d_6): δ (ppm) = 21.21 (s, CH3, 1C, C-5), 125.54 (s, CH, 2C, C-2), 128.41 (s, CH, 2C, C-3), 137.57 (s, C_q, 1C, C-1), 149.99 (s, C_q, 1C, C-4).

Elemental Analysis: calcd. for $C_7H_8NNaO_2S$ (%): C 43.52, H 4.17, N 7.25, S 16.60; found: C 43.64, H 4.18 N 7.34, S 16.65.

ATR-IR ($\tilde{\nu}$ [cm^{-1}]) (transmission [%])):662 (61), 808 (57), 982 (55), 1103 (41), 1148 (59), 1205 (78), 1217 (79), 1377 (94), 1394 (95), 1452-1440 (96), 1492 (91), 1597 (93), 2860 (96), 2914 (94), 3018 (96), 3209 (89).

6.4.2.2 Dimethyl pyridine-2,6-dicarboxylate

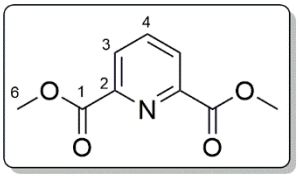

According to literature[133,136], thionyl chloride (10 eq., 60 mmol, 30 ml) was added dropwise to 2,6-pyridinedicarboxylic acid (1 eq., 6.0 mmol, 1.01 g) under cooling with an ice bath. Afterwards the resulting suspension was heated at 70°C for 45 minutes and excess thionyl chloride was distilled off under slightly reduced pressure (850-900 mbar). Dry methanol (30 ml) was added to the colorless residue after cooling the solid. The resulting mixture was heated to reflux for 45 min and the solvent was

evaporated. The colorless precipitate was solved in saturated sodium carbonate solution (100 ml) and extracted with DCM (4 x 15 ml). After drying the combined organic layers with sodium sulfate and filtering subsequently, the solvent was evaporated resulting in an off-white powder.

Yield: 1.1 g, 5.66 mmol, 95%

^{1}H-NMR (500 MHz, $CDCl_3$): δ (ppm) = 3.98 (s, 6H, H-6), 7.99 (t, $^{3}J_{HH}$=7.8 Hz, 1H, H4), 8.27 (d, $^{3}J_{HH}$=7.8 Hz, 2H, H-3).

^{13}C-NMR (125 MHz, $CDCl_3$): δ (ppm) = 53.12 (s, CH_3, 2C, C-6), 127.98 (s, CH, 2C, C3), 138.32 (s, CH, 1C, C-4), 148.24 (s, C_q, 2C, C-2), 165.02 (s, C_q, 2C, C-1).

ESI-MS (pos) (m/z (%) in MeOH): 136.04 (0.4) [M-COOMe], 164.04 (1) [M-CH_3O], 196.06 (1.7) [M+H], 218.05 (100) [M+Na].

Elemental Analysis: calcd. for $C_9H_9NO_4$(%): C 55.39, H 4.65, N 7.18; found: C 55.46., H 4.70, N 7.18.

6.4.2.3 Pyridine-2,6-diyldimethanol

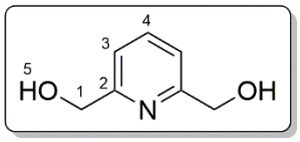

Based on literature[133,141], sodium borohydride (4.5 eq., 216 mmol, 8.15 g) was added in four portions over 30 minutes to a solution of dimethyl pyridine-2,6-dicarboxylate (1 eq., 47.9 mmol, 9.35 g) in dry EtOH (350 ml). After stirred for 3 h at r.t., the mixture was heated to reflux for 18 h. The colorless solid, which remained from evaporating the solvent, was stirred with saturated sodium hydrogen carbonate solution (80 ml) and refluxed for 5 min. Then water (100 ml) was added and the flask was stored at 5 °C overnight. The resulting colorless precipitate was filtered off and washed with cold water. When evaporating half of the solvent and storing at 5 °C another night, a second product fraction was obtained. The combined solids were extracted with acetone (6 x 300 ml) for 4 – 12 h each time. The combined organic layers were dried over sodium sulfate, filtrated and the solvent was evaporated resulting in a colorless solid.

Yield: 6.17 g, 44.3 mmol, 93%

^{1}H-NMR (500 MHz, $CDCl_3$): δ (ppm) = 3.29 (s, 2H, H-5), 3.98 (s, 6H, H-1), 7.99 (t, $^{3}J_{HH}$=7.8 Hz, 1H, H-4), 8.27 (d, $^{3}J_{HH}$=7.8 Hz, 2H, H-3).

^{13}C-NMR (125 MHz, $CDCl_3$): δ (ppm) = 53.12 (C_6), 127.98 (C_3), 138.32 (C_4), 148.24 (C_2), 165.02 (C_5).

ESI-MS (pos) (m/z (%) in MeOH/H_2O): 162.06 (17.5) [M^++Na], 154.09 (7.1), 140.07 (100) [M^++H], 122.06 (43.9)[M^+-OH], 79.05(10.0) [Pyridine$^+$], 77.04 (2.2).

Elemental Analysis: calcd. for $C_7H_9NO_2$(%): C 60.42, H 6.52, N 10.07; found: C 60.49, H 6.52, N 10.09.

6.4.2.4 2,6-Bis(bromomethyl)pyridine

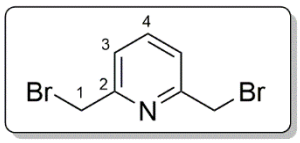

According to literature[133,142,143], pyridine-2,6-diyldimethanol (1 eq., 58.6 mmol, 8.15 g) was dissolved in dry DMF (125 ml). The solution was cooled down to 0 °C and phosphorus tribromide (2.3 eq., 135.0 mmol, 12.7 ml) was added dropwise which induced a color change to orange, while a dark solid precipitated. The reactions mixture was allowed to warm up to r.t. and was stirred for 42 h. Then water (150 ml) was added, after the solution was cooled to 0 °C again, whereupon the precipitate dissolved. The aqueous phase was extracted with diethyl ether (3 x 130 ml), the combined ether fractions were washed with water (150 ml) and brine (150 ml). Pale yellow needles were obtained by drying with magnesium sulfate, filtering and solvent evaporation.

Yield: 11.8 g, 44.5 mmol, 76%

^{1}H-NMR (500 MHz, $CDCl_3$): δ (ppm) = 4.65 (s, 4H, H-1), 7.36 (d, $^3J_{HH}$=7.8 Hz, 2H, H3), 7.70 (t, $^3J_{HH}$=7.8 Hz, 1H, H-4).

^{13}C-NMR (125 MHz, $CDCl_3$): δ (ppm) = 33.42 (s, CH_2, 2C, C-1), 122.73 (s, CH, 2C, C3), 138.06 (s, CH, 1C, C-4), 156.73 (s, C_q, 2C, C-2).

ESI-MS (pos) (m/z (%) in MeCN/Formic acid): 106.07 (1.1) [M-2Br+2H], 184.98 (6.3) [M-Br], 265.90 (100) [M+H].

Elemental Analysis: calcd. for $C_7H_7NBr_2$(%): C 31.73, H 2.66, N 5.29; found: C 31.69, H 2.73, N 5.33

6.4.2.5 Dipropyl Diazapyridinophanes (DAPy-Propyl)

Firstly, the ring closure was performed according to *Chi-Ming Che* et al.[294], which was executed as follows.

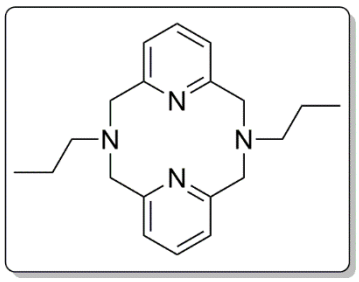

A 2,6-bis(bromomethyl)pyridine (1 eq., 1.00 mmol, 0.27 g) in toluene (6.25 ml) was added to a refluxing mixture of propylamine (2.5 eq., 2.5 mmol, 0.21 ml) in aqueous sodium carbonate solution (2.5 ml, 10 5 aqueous solution) within 1 h. the solution was held at reflux conditions for 6 h, additionally. After it was let cool to r.t. and the organic phase was washed with water (5 ml). Evaporating the solvent led to a colorless solid (0.13 g), which exhibits three pyridine signal sets in ^{1}H- and ^{31}C-NMR spectra with an 1:1 propyl-pyridine ratio. Sublimation delivered a separation of the compound, while distillation did not. ESI MS spectra of the sublimed colorless crystals – unsuitable for X-ray diffraction – revealed trimeric and dimeric species in an 1:1 propyl-pyridine ratio and additional not assignable signals, which indicate similar heavier fragments. *Miyahara* et al.[295] confirmed the erroneous route as well with the same result. Due to the resulting product mixture, this reaction approach was rejected.

ESI-MS (pos) (m/z (%) in MeCN): 244.18 (2) [Trimer+2H], 266.68 (12) [], 325.24 (2) [Dimer+H], 368.43 (100) [], 404.68 (32) [], 487.36 (53) [Trimer+H].

6.4.2.6 Ditosyl Diazapyridinophane (DAPy-Ts)

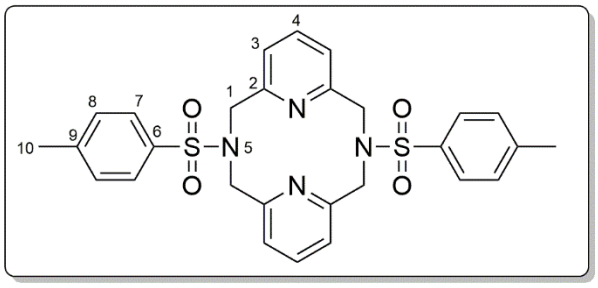

The second ring closure approach based on the denoted literature[133–135,296], *p*-toluenesulfonamide sodium salt (1 eq., 6.1 mmol, 1.18 g) was dissolved in 80 °C hot DMF (100 ml). 2,6-Bis(bromo-methyl)pyridine (1 eq., 6.0 mmol, 1.62 g) in DMF (20 ml) was added dropwise over 20 minutes. The reaction mixture was heated at 80 °C for 40 minutes, when the second equivalent *p*-toluenesulfonamide sodium salt (1 eq., 6.1 mmol, 1.18 g) was added in one portion. The orange solution was stirred at 80 °C for 4 h. Thereafter the solvent was evaporated and the brown solid was washed

with water (100 ml), MeOH (80 ml), EtOH (80 ml) and finally with acetone (20 ml) resulting in a pale brown powder.

Yield: 0.89 g, 1.6 mmol, 54%

^{1}H-NMR (500 MHz, $CDCl_3$): δ (ppm)= 2.42 (s, 6H, H-10), 4.28 (s, 8H, H-1), 7.11 (d, $^{3}J_{HH}$=7.7 Hz, 4H, H-3), 7.26 (dd, $^{3}J_{HH}$=8.2 Hz, $^{4}J_{HH}$=0.5 Hz, 4H, H-8), 7.40 (t, $^{3}J_{HH}$=7.7 Hz, 2H, H-4), 7.64 (dd, $^{3}J_{HH}$=8.2 Hz, $^{4}J_{HH}$=0.5 Hz, 4H, H-7).

^{13}C-NMR (125 MHz, $CDCl_3$): δ (ppm)= 21.41 (s, CH_3, 2C, C-10), 54.12 (s, CH_2, 4C, C1), 121.03 (s, CH, 4C, C-3),127.29 (s, CH, 4C, C-7), 129.64 (s, CH, 4C, C-8), 136.11 (s, C_q, 2C, C-6), 136.80 (s, CH, 2C, C-4), 143.50 (s, C_q, 2C, C-9), 155.65 (s, C_q, 4C, C-2).

^{15}N-NMR (50.7 MHz, $CDCl_3$): δ (ppm) = 98.64 (s, 2N, N-5), 308.55 (s, 2N, N-pyridine).

ESI-MS (pos) (m/z (%) in MeOH/H_2O): 239.13 (3) [M^{+}-$2S_2C_7H_7$], 393.13 (4) [M-$S_2C_7H_7$], 468.10 (7) [M-C_7H_7N+Na+2H], 549.17 (100) [M+H], 571.15 (7) [M+Na], 697.26 (8.5).

ATR-IR ($\tilde{\nu}$ [cm^{-1}] (transmission [%])):608 (81), 669 (62), 758 (77), 779 (58), 804 (70), 818 (63), 918 (72), 1090 (62), 1151 (59), 1242 (89), 1317 (65), 1437 (91), 1456 (82), 1493 (96), 1595 (83), 1680 (86), 2883 (99), 2919 (98), 2980 (98), 3065 (99).

6.4.2.7 Unsubstituted Diazapyridinophane (DAPy-NH)

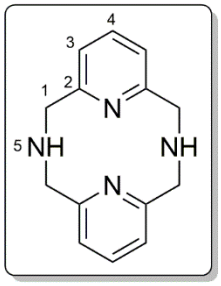

According to literature[133,135], ditosyl diazapyridinophane (0.84 mmol, 0.46 g) was dissolved in H_2SO_4 solution (5 ml. 90°% aqueous solution) and heated at 110°C for two hours. After the solution reached r.t., it was added to an excess of a sodium hydroxide solution (20% aqueous solution) under stirring inducing a precipitation if a pale brown solid, which was filtered off and washed with chloroform (5 x 50 ml). The filtrate was dried over magnesium sulfate, which was filtered off afterwards and the solvent was evaporated to obtain a pale yellow solid.

Yield: 0.06 g, 0.25 mmol, 30%

^{1}H-NMR (500 MHz, $CDCl_3$): δ (ppm) = 3.6 (s, 2H, H-5), 3.39 (s, 8H, H-1), 6.48 (d, $^{3}J_{HH}$=7.6 Hz, 4H, H-3), 7.06 (t, $^{3}J_{HH}$=7.6 Hz, 2H, H-4).

^{13}C-NMR (125 MHz, $CDCl_3$): δ (ppm) = 56.02 (s, CH_2, 4C, C-1), 119.75 (s, CH, 4C, C3), 135.69 (s, CH, 2C, C-4), 159.47 (s, C_q, 4C, C-2).

^{15}N-NMR (50.7 MHz, $CDCl_3$): δ (ppm) = 31.29 (s, 2N, N-5), 314.49 (s, 2N, N-pyridine).

ESI-MS (pos) (m/z (%) in MeCN/H_2O/Formic acid): 121.07 (3) $[M+H]^{2+}$, 136.08 (3) [$C_7H_{10}N_3$], 241.14 (100) [M+H], 263.12(24) [M+Na], 361.21 (1), 383.19 (6), 485.40 (2), 549.15 (2.3) [DAPy-Ts].

6.4.2.8 Dibenzyl diazapyridinophane (DAPy-Bz)

Referring to Leuckart-Wallach reactions[297], the reaction principle was applied on the unsubstituted Diazapyridinophane.

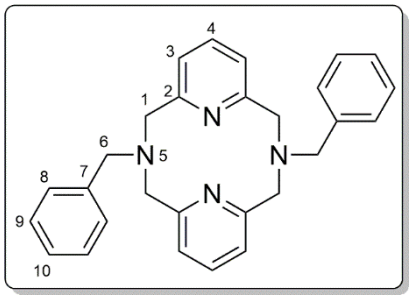

Unsubstituted Diazapyridinophane (1 eq., 0.5 mmol, 0.25 g) and benzaldehyde (4 eq., 2 mmol, 0.2 ml) were dissolved in dried EtOH (9 ml) the resulting mixture was heated to 50 °C for 2 h. After cooling back to r.t., sodium borohydride (9 eq., 4.5 mmol, 0.17 g) was added in small portions and the solution was heated to 50 °C for 2 h again. The solvent was evaporated and the residue was dissolved in sodium hydroxide solution (50 ml, 1 M). The aqueous phase was extracted with DCM (3 x 75 ml), the combined organic phases were washed with sodium hydroxide solution (150 ml, 1 M) and afterwards dried over sodium sulfate. Afterwards the solvent was evaporated and the crude product remains as a solid.

ESI-MS (pos) (m/z (%) in MeOH): 241.14 (12) [DAPy-NH], 331.19 (16) [M-C_7H_7+2H], 421.24 (100) [M+H].

6.4.2.9 Dicarbaldehyde Diazapyridinophane (DAPy-O)

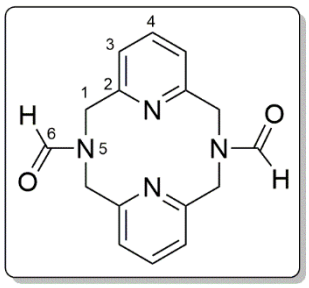

With the intention to synthesize Dimethyl Diazapyridinophane the reaction was designed according to literature.[135,298]

Unsubstituted Diazapyridinophane (1 eq., 1.0 mmol, 0.24 g) was dissolved in formic acid (20 ml) and benzaldehyde (2.4 eq., 2.4 mmol, 0.24 ml). The reaction mixture was heated at 100 °C for 22 h. Hydrochloric acid (5 ml, 37 % aqueous solution) was added to r.t. cooled initial solution and the volatile species were evaporated. The resulting brown solid was dissolved in ice cold water (30 ml) and the solution was neutralized to pH 8 by adding sodium hydroxide solution (20 % aqueous solution). The aqueous phase was extracted with DCM (3 x 30 ml), the combined organic phases were dried over sodium sulfate and the drying agent was filtered off. A greenish solid (0.277 g) remained after evaporation as a crude product.

ESI-MS (pos) (m/z (%) in MeCN): 269.14 (4) [M-CO+2H], 297.14 (100) [M+H], 319.12 (4) [M+Na].

6.4.3 DMP-X-based ligands

6.4.3.1 2,9-Dimethyl-1,10-phenanthroline (DMP)

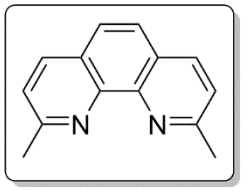

This synthesis is based on *Sauvage* et al..[299]

Dry 1,10-phenanthroline (1 eq., 1 mmol, 0.18 g) was suspended in abs. THF (3.5 ml) and the resulting solution was cooled to 0 °C to give a dark brown solution. Methyllithium (4 eq., 4 mmol, 2.5 ml related to a 1.6 M solution) was added over 50 minutes. After 3 h of stirring, water (5 ml) was added giving a bright yellow solution under gas evolution. The phases were separated and the solvent of the THF phase was evaporated to give a yellow solid (0.11 g). The aqueous phase was four times extracted with chloroform (40 ml in sum) and manganese(IV) oxide (10 g) was added to the organic phase. Additionally, it was dried with magnesium sulphate. The suspension was filtered and the solvent was evaporated. NMR spectra revealed a variety of different 1,10-phenanthroline-like species and the target molecule.

Manual column chromatography (0.1 g substance, 2 g silica, gradient eluation starting with EtAc/*n*-Pentane 25:75) provided still a mixture of species.

Amber colored crystals could be obtained out of the bulb, where the chloroform extract was collected. X-ray crystallography revealed a manganese(II) complex with two mono-methylated 1,10-phenanthrolines and two hydrogen carbonates as ligands as can be seen in the appendix.

6.4.3.2 1,10-Phenanthroline-2,9-dicarbaldehyde (DMP-O)

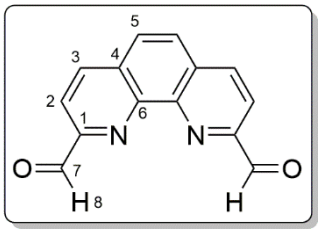

Based on literature[149] the synthetic procedure was adapted from *Ruiz-Azuara* et al..[150] SeO_2 (2.5 eq., 50.4 mmol, 5.65 g) was added to a solution of 1,4-Dioxane (147 ml) and deionized water (8.6 ml). After heating to reflux, a solution of DMP (1 eq., 20 mmol, 4.61 g) in 1,4-Dioxane (90 ml) was added dropwise into the first solution over ca. 35 min. The colorless reaction solution darkened increasingly over an orange coloration until a reddish brown color with black precipitate is reached. The reaction remained under reflux for 2 h. The mixture was

filtered while hot, washed with warm 1,4-Dioxane and the filtrate was left to cool. The precipitated yellowish solid was collected by filtering, washed with warm 1,4-Dioxane. This solid has about 12 % impurities according to ^{1}H NMR spectra in DMSO-d_6, but was used without further purification for further synthetic purposes.

Yield: 4.16 g, 17.6 mmol, 88 %.

Purification by flash chromatographic devices resulted as expected in ca. 10 % less yield than obtained unpurified as a beige colorless crystalline solid.

^{1}H-NMR (500 MHz, DMSO-d_6): δ (ppm) = 8.28 (s, 2H, H-5), 8.32 (d, $^{3}J_{HH}$=8.2 Hz, 2H, H-2), 8.80 (dd, $^{5}J_{HH}$=0.8 Hz, $^{3}J_{HH}$=8.3 Hz, 2H, H-3), 10.37 (d, $^{5}J_{HH}$=0.8 Hz, 2H, H-8).

^{13}C-NMR (125 MHz, DMSO-d_6): δ (ppm) = 120.6 (s, CH, 2C, C-2), 129.7 (s, CH, 2C, C-5), 131.9 (s, C_q, 2C, C-4), 138.9 (s, CH, 2C, C-3), 145.7 (s, C_q, 2C, C-6), 152.7 (s, C_q, 2C, C-1), 194.2 (s, CH, 2C, C-7).

^{15}N-NMR (50.7 MHz, $CDCl_3$): δ (ppm) = 316.2 (s, 2N).

ESI-MS (pos) (m/z (%) in MeOH): 207.06 (0.1) [M-2·=O+H], 223.09 (10) [M-=O+H], 237.07 (30) [M+H], 251.08 (73) [M+CH_3], 259.05 (100) [M+Na], 291.07 (30) [M+MeOH+Na], 323.10 (26) [Me+2MeOH+H], 383.19 (3), 527.07 (4) [2M+Na+MeOH].

Elemental Analysis: calcd. for $C_{14}H_8N_2O_2$ (%): C 71.18, H 3.41, N 11.86; found: C 70.93, H 3.79, N 11.65.

Crystal structure is located in the appendix.

6.4.3.3 (1,10-Phenanthroline-2,9-diyl)dimethanol (DMP-OH)

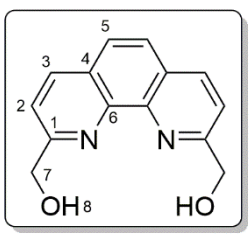

According to literature[149], dry 1,10-phenanthroline-2,9-dicarbaldehyde (1 eq., 21.7 mmol, 5.13 g) was suspended in previously dried ethanol (220 ml). After that sodium borohydride (2.22 eq., 48.2 mmol, 1.82 g) was added. The reaction mixture was refluxed for 1.5 h after the gas evolution has decreased. The solvent was evaporated and the resulting material was suspended in water. The subsequently

extraction with ethyl acetate at least 20-times (100 ml each) resulted in a beige solid which was used without purification for further synthetic reactions.

Yield: 3.94 g, 16.4 mmol, 76 %.

^{1}H-NMR (500 MHz, DMSO-d_6): δ (ppm) = 4.90 (s, 4H, H-7), 5.67 (s, 2H, H-8), 7.88 (d, $^{3}J_{HH}$=8.3 Hz, 2H, H-2), 7.94 (s, 2H, H-5), 8.48 (d, $^{3}J_{HH}$=8.3 Hz, 2H, H-3).

^{13}C-NMR (125 MHz, DMSO-d_6): δ (ppm) = 65.3 (s, CH_2, 2C, C-7), 120.8 (s, CH, 2C, C-2), 126.4 (s, CH, 2C, C-5), 127.9 (s, C_q, 2C, C-4), 137.3 (s, CH, 2C, C-3), 144.7 (s, C_q, 2C, C-6), 162.5 (s, C_q, 2C, C-1).

^{15}N-NMR (50.7 MHz, DMSO-d_6, obtained by ^{15}N-^{1}H-HMBC): δ (ppm) = 298.8 (s, 2N).

ESI-MS (pos) (m/z (%) in MeOH/H_2O): 241.10 (100) [M+H], 263.08 (24) [M+Na], 295.02 (2) [M+MeOH+Na].

6.4.3.4 1,10-Phenanthroline-2,9-dicarboxylic acid (DMP-OOH)

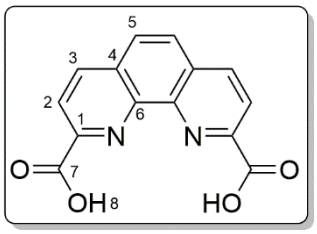

Although a comparable direct way from 1,10-phenanthroline-2,9-dicarbaldehyde to the corresponding dicarboxylic acid exists[149,151], this synthesis was performed with the dialcohol compound.

(1,10-Phenanthroline-2,9-diyl)dimethanol (8.55 mmol, 2.05 g) was solved in nitric acid (41.1 ml, 65 % nitric acid solution) and heated to reflux for 2 h. The reaction mixture was cooled to r.t. and poured in ice (45 g) under precipitating of a colorless solid, which was used without further purification.

Yield: 1.67 g, 6.26 mmol, 73 %.

^{1}H-NMR (500 MHz, DMSO-d_6): δ (ppm) = 8.22 (s, 2H, H-5), 8.43 (d, $^{3}J_{HH}$=8.3 Hz, 2H, H-2), 8.75 (d, $^{3}J_{HH}$=8.3 Hz, 2H, H-3).

^{13}C-NMR (125 MHz, DMSO-d_6): δ (ppm) = 123.9 (s, CH, 2C, C-2), 128.9 (s, CH, 2C, C-5), 131.0 (s, C_q, 2C, C-4), 145.2 (s, C_q, 2C, C-6), 148.7 (s, C_q, 2C, C-1), 166.7 (s, C_q, 2C, C-7).

ESI-MS (neg) (m/z (%) in MeOH): 179.06 (20) [M-2COOH-H], 223.05 (100) [M-COOH], 251.05 (2) [M-OH], 267.04 (9) [M-H], 268.04 (8) [M], 573.03 (7), 288.00 (5), 513.03 (7), 588.00 (5).

Crystal structure is located in the appendix.

6.4.3.5 2,9-Bis(chloromethyl)-1,10-phenanthroline (DMP-Cl)

Two approaches were carried out to synthesize 2,9-Bis(chloromethyl)-1,10-phenanthroline.[148]

Approach 1:

First, 2,9-Bis(trichloromethyl)-1,10-phenanthroline was obtained by reaction described in chapter 6.4.3.6. Adapted from literature[149,152], 2,9-bis(trichloromethyl)-1,10-phenanthroline (1 eq., 3.50 mmol, 1.452 g) was subsequently dissolved in dry toluene (50 ml). After that tributyltin hydride (4 eq., 14.00 mmol, 4.08 g) and azobis-isobutyronitrile (0.1 eq., 0.35 mmol, 0.057 g) was added. The reaction mixture was heated to 85 °C for 2.5 h, when the end was verified by TLC. During heating the yellow solution turned orange-brown. The toluene phase was extracted with $CHCl_3$ (6 · 50 ml), which was subsequently dried over $MgSO_4$. After removing the solvent, the crude product was purified by manual column chromatography (SiO_2, *n*-Hexane/Ethyl acetate). 2,9-bis(chloromethyl)-1,10-phenanthroline was obtained as a slightly yellowish solid.

Yield: 0.29 g, 1.05 mmol, 30 %

Approach 2:

The following procedure is based on literature.[152] (1,10-Phenanthroline-2,9-diyl)dimethanol (1 eq., 2 mmol, 0.48 g) was suspended in $CHCl_3$ (350 ml) under inert gas atmosphere. Then PCl_3 (11 eq., 22 mmol, 1.92 ml) was added dropwise resulting in a flocculent precipitation. This suspension was refluxed for one hour. Afterward the solvent was removed by distillation. The orange residue was treated with saturated $NaCO_3$ solution until pH 9 was reached. The solid was filtrated off and washed with water. A green crude product was obtained.

The crude product was purified by flash chromatography with *n*-pentane and ethyl acetate as eluents. The product was obtained as short, colorless needles.

Yield: 0.01 g, 0.36 mmol, 18 %.

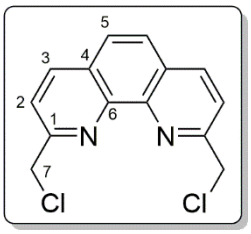

^{1}H-NMR (500 MHz, $CDCl_3$): δ (ppm) = 5.11 (s, 4H, H-7), 7.84 (s, 2H, H-5), 7.95 (d, $^{3}J_{HH}$ = 8.3 Hz, 2H, H-2), 8.33 (d, $^{3}J_{HH}$ = 8.3 Hz, 2H, H-3).

^{13}C-NMR (125 MHz, $CDCl_3$): δ (ppm) = 47.7 (s, CH_2, 2C, C-7), 122.7 (s, CH, 2C, C-2), 126.8 (s, CH, 2C, C-5), 128.5 (s, C_q, 2C, C-4), 137.6 (s, CH, 2C, C-3), 144.9 (s, C_q, 2C, C-6), 157.7 (s, C_q, 2C, C-1).

^{15}N-NMR (50.7 MHz, $CDCl_3$, obtained by ^{15}N-^{1}H-HMBC): δ (ppm) = 298.8 (s, 2N).

ESI-MS (pos) (m/z (%) in MeCN): 277.03 (100) [M+H], 299.01 (96) [M+Na], 124.09 (6) [].

Elemental Analysis: calcd. for $C_{14}H_{10}N_2Cl_2 \cdot 0.5\ H_2O$ (%):C 58.76, H 3.87, N 9.79; found: C 58.49, H 4.58, N 9.52.

6.4.3.6 2,9-Bis(trichloromethyl)-1,10-phenanthroline (DMP-Cl_3)

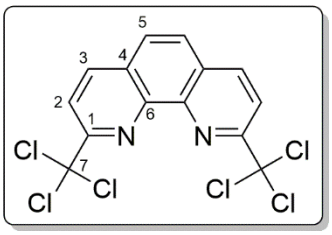

In a literature adapted[149,152] procedure, 2,9-dimethyl-1,10-phenanthroline (1 eq., 5.0 mmol, 1.109 g) was dissolved in $CHCl_3$ (50 ml) and *N*-chlorosuccinimide (15 eq., 75.0 mmol, 10.015 g) was added with additional $CHCl_3$ (50 ml) resulting in a suspension. When heating to reflux for 7 h, the suspension clears up and becomes temporary green and in the end yellow. During cooling to r.t. a large amount of colorless solid precipitates, which was filtered off. The solvent of the filtrate was evaporated obtaining a yellow solid. The precipitate was treated with saturated $NaCO_3$ solution (200 ml) and filtered off afterwards. $CHCl_3$ (200 ml) was used to extract the yellow solid, the organic phase was dried over $MgSO_4$ and the solvent was evaporated. The yellow crude product was purified by MPLC (*n*-Hexane/Ethyl acetate; gradient) and 2,9-bis(trichloromethyl)-1,10-phenanthroline was obtained as a colorless solid.

Yield: 1.66 g, 3.99 mmol, 80 %

^{1}H-NMR (500 MHz, $CDCl_3$): δ (ppm) = 7.96 (s, 2H, H-5), 8.33 (d, $^{3}J_{HH}$ = 8.6 Hz, 2H, H-2), 8.33 (d, $^{3}J_{HH}$ = 8.6 Hz, 2H, H-3).

^{13}C-NMR (125 MHz, $CDCl_3$): δ (ppm) = 98.4 (s, CH_2, 2C, C-7), 120.6 (s, CH, 2C, C-2), 127.7 (s, CH, 2C, C-5), 129.4 (s, C_q, 2C, C-4), 138.3 (s, CH, 2C, C-3), 143.5 (s, C_q, 2C, C-6), 158.2 (s, C_q, 2C, C-1).

6.4.3.7 2,9-Bis(bromomethyl)-1,10-phenanthroline (DMP-Br)

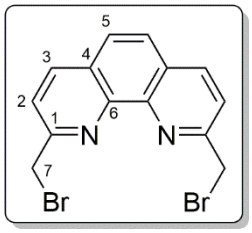

According to literature[149,151], (1,10-phenanthroline-2,9-diyl)-dimethanol (3.33 mmol, 0.80 g) was dissolved in hydrobromic acid (58.1 ml, 48 % hydrobromic acid solution) to a yellow solution and refluxed with a sand bath for 2 h. Afterwards the solution was neutralized with saturated aqueous sodium carbonate solution to pH 9 resulting in a rose coloration. Filtration of the precipitated solid gives a pale rose solid.

Yield: 1.16 g, 3.14 mmol, 94 %.

^{1}H-NMR (500 MHz, $CDCl_3$): δ (ppm) = 4.97 (s, 4H, H-7), 7.81 (s, 2H, H-5), 7.91 (d, $^{3}J_{HH}$ = 8.3 Hz, 2H, H-2), 8.28 (d, $^{3}J_{HH}$ = 8.3 Hz, 2H, H-3).

^{13}C-NMR (125 MHz, $CDCl_3$): δ (ppm) = 35.0 (s, CH_2, 2C, C-7), 124.0 (s, CH, 2C, C-2), 127.1 (s, CH, 2C, C-5), 128.6 (s, C_q, 2C, C-4), 137.8 (s, CH, 2C, C-3), 145.2 (s, C_q, 2C, C-6), 157.9 (s, C_q, 2C, C-1).

^{15}N-NMR (50.7 MHz, $CDCl_3$, obtained by ^{15}N-^{1}H-HMBC): δ (ppm) = 299.5 (s, 2N).

EI MS (m/z (%)): 103.08 (44), 149.08 (11), 178.12 (15), 206.15 (100) [M-2Br-H], 207.16 (65) [M-2Br], 285.08 (97) [M-Br], 366.01 (39) [M].

ESI-MS (pos) (m/z (%) in MeOH): 287.02 (2) [M-Br+2H], 325.00 (3) [M-Br+Na+OH], 366.93 (100) [M+H], 388.91 (29) [M+Na], 754.83 (4) [2M+Na].

Elemental Analysis: calcd. for $C_{14}H_{10}N_2Br_2$ (%): C 44.30, H 3.05, N 7.38; found: C 44.35, H 3.36, N 7.26.

6.4.3.8 2,9-Bis(iodomethyl)-1,10-phenanthroline (DMP-I)

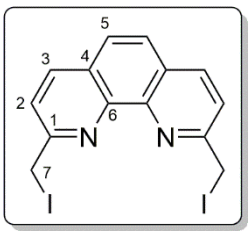

In the context of a *Finkelstein* reaction[155], potassium iodide (10 eq., 8 mmol, 1.33 g) was dissolved in acetone (200 ml) und afterwards 2,9-Bis(bromomethyl)-1,10-phenanthroline (1 eq., 0.8 mmol, 0.29 g) was added portion wise. The reaction mixture turned yellow and a colorless fine precipitate was formed. After heating 2 h at 50 °C, the solvent was removed.[148]

The residue was washed with water und the crude product was obtained as grey solid, which was purified by flash chromatography with *n*-Hexane and ethyl acetate as eluents. The product was obtained as brownish solid and was used for the complexation step despite the impurities.

Yield: 0.19 g, 0.42 mmol, 53%.

^{1}H-NMR (500 MHz, d_3-MeCN): δ (ppm) = 4.85 (s, 4H, H-7), 7.82 (d, $^{3}J_{HH}$ = 8.3 Hz, 2H, H-2), 7.87 (s, 2H, H-5), 8.33 (d, $^{3}J_{HH}$ = 8.3 Hz, 2H, H-3).

^{13}C-NMR (125 MHz, d_3-MeCN): δ (ppm) = 7.0 (s, CH_2, 2C, C-7), 123.0 (s, CH, 2C, C-2); 126.7 (s, CH, 2C, C-5), 128.1 (s, C_q, 2C, C-4), 137.6 (s, CH, 2C, C-3), 144.9 (s, C_q, 2C, C-6); 159.0 (s, C_q, 2C, C-1).

^{15}N-NMR (50.7 MHz, d_3-MeCN, obtained by ^{15}N-^{1}H-HMBC): δ (ppm) = 302.4 (s, 2N).

ESI-MS (pos) (m/z (%) in MeCN): 124.09 (20) [], 208.10 (57) [M-2I], 225.10 (33) [], 247.08 (14) [M-2I+2H+K], 327.28 (32) [], 335.00 (100) [M-I+2H], 351.00 (22) [], 372.98 (29) [M-I+H+K], 460.90 (95) [M+H], 482.88 (20) [M+Na].

6.4.3.9 2,2'-((1,10-phenanthroline-2,9-diyl)bis(methylene))bis(isoindoline-1,3-dione) (DMP-Phthalimide)

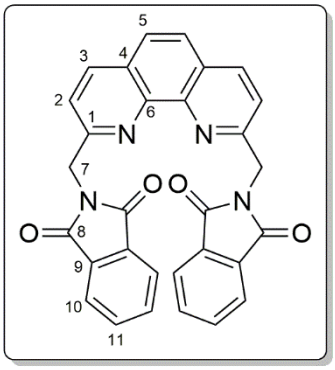

DMP-Br (1 eq., 0.5 mmol, 0.18 g) and potassium phthalimide (2 eq., 1.0 mmol, 0.19 g) were dissolved in DMF (33.5 ml) and heated for 22 h at 100 °C. The reaction mixture was allowed to cool down too room temperature. The precipitated was filtered off and the filtrate´s solvent was evaporated. The resulting yellow solid was purified by chromatography (*n*-hexane/EtAc), where fine, colorless crystals were obtained.

Yield: 0.19 g, 0.38 mmol, 76 %.

^{1}H-NMR (500 MHz, $CDCl_3$): δ (ppm) = 5.38 (s, 4H, H-7), 7.47 (d, $^{3}J_{HH}$ = 8.3 Hz, 2H, H-2), 7.71 (s, 2H, H-5), 7.79 – 7.76 (m, 4H, H-10), 7.96 – 7.93 (m, 4H, H-11), 8.16 (d, $^{3}J_{HH}$ = 8.3 Hz, 2H, H-3).

^{13}C-NMR (125 MHz, $CDCl_3$): δ (ppm) = 44.3 (s, CH_2, 2C, C-7), 120.2 (s, CH, 2C, C-2), 123.7 (s, CH, 4C, C-10), 126.3 (s, CH, 2C, C-5), 132.5 (s, C_q, 2C, C-4), 134.3 (s, CH, 4C, C-11), 137.1 (s, CH, 2C, C-3), 145.7 (s, C_q, 2C, C-6), 156.3 (s, C_q, 2C, C-1), 168.4 (s, CO, 4C, C-8).

ESI-MS (pos) (m/z (%) in MeCN): 124.09 (20) [], 208.10 (57) [M-2I], 225.10 (33) [], 247.08 (14) [M-2I+2H+K], 327.28 (32) [], 335.00 (100) [M-I+2H], 351.00 (22) [], 372.98 (29) [M-I+H+K], 460.90 (95) [M+H], 482.88 (20) [M+Na].

6.4.4 Macrocyclic phen-based ligands

6.4.4.1 5,6,7,8,9,14,15,16,17,18-decahydrodibenzo[b,i][1,4,8,11]tetraazacyclotetradecine (BenzeneNH_2Propyl$_2$)

Approach 1:

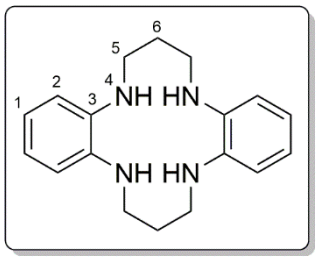

o-Phenylendiamine (1 eq., 1.0 mmol, 0.11 g) was dissolved in chloroform at 65 °C. 1,3-Dibromopropane (1 eq., 1.0 mmol, 0.10 ml) was added dropwise and the reaction mixture was heated to reflux for 6 h, while a colorless solid precipitated, which was dissolved by adding 3 ml chloroform. The reaction was filtered resulting in a pale pink solid and a bright yellow filtrate.

^{1}H NMR spectra and EI MS analysis revealed a mixture of reagents, target molecule, one side connected species and some heavier compounds, which could not be assigned.

EI MS (m/z (%)): 108.04 (25) [benzene-1,2-diamine], 119.03 (100), 148.08 (76), 161.09 (47), 187.11 (62), 256.16 (41) [N^1,$N^{1'}$-(propane-1,3-diyl)bis(benzene-1,2-diamine)], 296.16 (66) [M], 404.24 (57).

Approach 2:

Based on to literature[178] a template route was chosen.

Copper(II) chloride dihydrate (1 eq., 0.5 mmol, 87 mg) was dissolved in MeOH (3 ml), which generates a green coloration. Then *o*-Phenylendiamine (2 eq., 1.0 mmol, 0.11 g) in MeOH (5 ml) was added dropwise resulting in a dark green turbid solution. After adding more MeOH (10 ml), 1,3-Dibromopropane (1 eq., 1.0 mmol, 0.10 ml) was added dropwise and the mixture was started to heat to 75 °C for 6 h. The dark solid was filtered off and washed with MeOH (10 ml). The solvent of the filtrate was evaporated.

Both EI and ESI mass spectra show no signals, which could be assigned to the target species.

Approach 3:

This synthesis was performed under anaerobic and inert gas conditions. To a solution of sodium methoxide made out of dry MeOH (5 ml) and sodium (4 eq., 2 mmol, 46 mg) was added dropwise a solution of *o*-Phenylendiamine (2 eq., 1.0 mmol, 0.11 g) in MeOH (3 ml). Dry copper(II) chloride (1 eq., 0.5 mmol, 67 mg) was dissolved in MeOH (3 ml) and added resulting in a black, precipitating solid. Additional MeOH (10 ml) was transferred into the reaction bulb. Then 1,3-Dibromopropane (1 eq., 1.0 mmol, 0.10 ml) was added dropwise and after 20 min of stirring, the mixture was heated to reflux for 8 h resulting in a brown solution and a black solid.

EI and ESI mass spectra revealed a large amount of different signals, which are not assignable.

6.4.4.2 Di(pyridin-2-yl)methane

Approach 1:

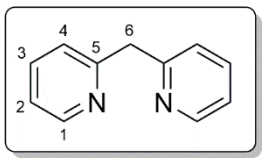

A Wolff-Kishner reduction was performed according to literature.[300] Di(2-pyridyl)ketone (1 eq., 1 mmol, 0.18 g), hydrazine (140 eq., 140 mmol, 6.9 ml) and sodium hydroxide (6.5 eq., 6.5 mmol, 0.26 g) was added under stirring to Ethylene glycol (39 ml).After stirring at 100 °C for 2 h, water was distilled off. Then the reaction mixture was heated at 160 °C for 6 h. Water (26 ml) was added and the pink liquid was extracted with toluene several times resulting in a discoloration of the aqueous phase to a pale yellowish green, while the organic phase became yellow. Finally, it was extracted DCM gaining a black solid after evaporation of the solvent. The toluene phase included beside the target species a large amount of heavier ions.

EI MS (m/z (%)): 65.04 (11) [C_5H_5], 78.08 (19) [pyridine-H], 108.12 (9) [2-ethylpyridine+H], 141.14 (10), 168.15 (56) [M-2H], 169.16 (100) [M-H], 170.17 (85) [M].

ESI MS (pos) (m/z (%) in MeCN): 171.09 (100) [M+H], 185.07 (1) [reagent+H], 199.10 (13) [M+2CH_3+H], 224.12 (58) [M+CH_2+MeCN], 239.13 (31), 287.12 (56), 365.15 (50).

Approach 2:

An addition of two pyridine compound based on literature was performed.[301] A solution of 2-methylpyridine (1 eq., 2 mmol, 0.02 ml) in dry THF (3 ml) was cooled to -78 °C. *n*-Butyllithium (1 eq., 2 mmol, 1.25 ml related to a 1.6 M solution) was added resulting in a bright orange solution. After stirring for 45 min at -78 °C and then warming up to – 20 °C 2-Fluoropyridine (0.5 eq., 1 mmol, 0.01 ml) was added. The reaction mixture was heated to reflux for 25 min and hydrolyzed with ice (1.86 g). The aqueous layer was extracted three times with DCM (3 x 2 ml), and the combined organic layers were dried over $NaSO_4$. The solvent was evaporated. GC/MS analysis with EI shows no sign of the target molecule.

6.4.4.3 5H-6,7-Dihydro[1,4]diazepino[1,2,3,4-lmn][1,10]phenanthrolinium dibromide (Phen-Pr)

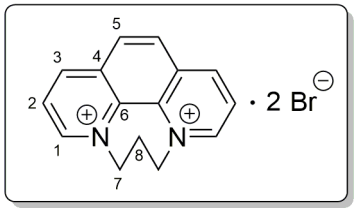

This synthesis was performed according to literature.[174] 1,10-Phenantholine (100 mmol, 18.2 g) was dissolved in chlorobenzene (158 ml) in a and heated at 70 °C under stirring.1,3-dibromopropane (500 mmol, 51.8 ml) was added dropwise to the colorless solution over 30 minutes. The resulting solution was stirred for 4 h at 120 °C and allowed to cool to room temperature. A yellow solid was precipitated, which is separated from the filtrate, washed with pentane (about 35 ml) and dried *in vacuo*.

Yield: 37.6 g, 98.4 mmol, 98 %.

^{1}H-NMR (500 MHz, D_2O): δ (ppm) = 3.45 (quin, $^3J_{HH}$=7.0 Hz, 2H, H-8), 5.17 (t, $^3J_{HH}$=7.0 Hz, 4H,H-7), 8.56 (dd, $^3J_{HH}$=8.4 Hz, $^3J_{HH}$=5.8 Hz, 2H, H-2), 8.61 (s, 2H,H-5), 9.47 (d, $^3J_{HH}$=8.4 Hz, 2H,H-3) 9.68 (d, $^3J_{HH}$=5.8 Hz, 2H, H-1).

^{13}C-NMR (125 MHz, D_2O): δ (ppm) = 30.0 (s, CH_2, 1C,C-8), 60.6 (s, CH_2, 2C, C-7), 127.5 (s, CH, 2C, C-2), 130.4 (s, CH, 2C, C-5), 133.6 (s, C_q, 2C, C-6), 134.3 (s, C_q, 2C, C-4), 147.5 (s, CH, 2C, C-3), 151.0 (s, CH, 2C, C-1).

^{15}N-NMR (50.7 MHz, D_2O): δ (ppm) = 198.6 (s, 2N).

ESI-MS (pos) (m/z (%) in H_2O): 181.08 (100) [M-C3H6+H], 221.11 (61) [M-H], 239.1192 (26) [M-H+H_2O].

Elemental analysis: calc. (found) for $C_{15}H_{14}Br_2N_2$ (%): C 47.15 (46.67), H 3.69 (3.98), N 7.33 (7.27)

6.4.4.4 5H-6,7-Dihydro[1,4]diazepino[1,2,3,4-lmn][1,10]phenanthroline-3,9-dione (Phen-Pr-Ox)

This synthesis was performed according to literature[174] with small modifications.

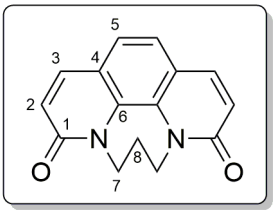

5H-6,7-Dihydro[1,4]diazepino[1,2,3,4-lmn][1,10]phenanthrolinium dibromide (1 mmol, 0.38 g) was suspended in abs. tert-butanol (4 ml) and degassed by purging nitrogen through the solution over 20 minutes. After the resulting solution has reached 40 °C, potassium *tert*-butoxide (4 mmol, 0.45 g) in degassed *tert*-butanol (4 ml) was added. Four hours later, the solution was allowed to cool down to room temperature and the brown precipitate was collected. The solid was dissolved in water (5 ml) and the solution was extracted with chloroform (4 x 3ml). Subsequently, the combined extract were dried over sodium sulfate and evaporated.

The gained brownish solid has an impurity grade between 5 % and 30 % according to ^{1}H NMR analysis.

Yield: 0.18 g, 0.72 mmol, 72 %

Chromatographic separation by hand with a DCM/Methanol gradient elution resulted in a distribution of all species over the whole column. Flash chromatography gave three fractions. The first fraction was gained at a solvent composition of *n*-Hexane/EtAc 10:90 which was free of impurities and contained 12.6 % of the used solid. It was followed by an approximately 50 % pure substance mixture in 16 % yield regarding to the used solid by application of 100 % DCM as eluent. The third fraction contained mostly impurities, although the target species could be seen in the ^{1}H-NMR spectra. This fraction was collected with a DCM/Methanol (75/25) mixture and included 40% of the initially deployed solid.

^{1}H-NMR (500 MHz, $CDCl_3$): δ (ppm) = 2.45 (quin, $^{3}J_{HH}$=6.5 Hz, 2H, H-8), 4.31 (s, 4H, H-7), 6.79 (d, $^{3}J_{HH}$=9.5 Hz, 2H, H-2), 7.35 (s, 2H, H-5), 7.71 (d, $^{3}J_{HH}$=9.5 Hz, 2H, H-3).

^{13}C-NMR (125 MHz, $CDCl_3$): δ (ppm) = 25.7 (s, CH_2, 1C, C-8), 45.7 (s, CH_2, 2C, C-7), 122.7 (s, CH, 2C, C-2), 122.8 (s, C_q, 2C, C-4), 123.1 (s, CH, 2C, C-5), 132.1 (s, C_q, 2C, C-6), 138.8 (s, CH, 2C, C-3), 162.6 (s, CO, 2C, C-1).

^{15}N-NMR (50.7 MHz, $CDCl_3$, obtained by ^{15}N-^{1}H-HMBC): δ (ppm) = 148.5 (s, 2N).

ESI-MS (pos) (m/z (%) in MeOH/Formic acid): 223.10 (7) [M-2=O-H], 237.10 (28) [M-=O-H], 239.16 (100) [M-=O+H], 309.20 (11) [M-=O+2H], 453.78 (76) [M+H], 661.57 (11).

6.4.4.5 2,9-dibromo-1,10-phenanthroline (Phen-Br)

This synthesis was performed according to literature.[174]

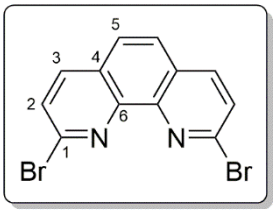

Phosphorus oxybromide (14.7 eq., 70.5 mmol, 20.6 g) and phosphorus pentabromide (2 eq., 9.6 mmol, 4.13 g) were added to 5H-6,7-Dihydro[1,4]diazepino[1,2,3,4-lmn][1,10] phenanthroline-3,9-dione (1 eq., 4.8 mmol, 1.21 g) and heated at 110 °C for 5 hours. Afterwards the phosphorus oxibromide was regained by distillation at reduced pressure at 90 °C.

The brown solid residue was decomposed on ice and neutralized to pH 8 with aqueous ammonia solution (30 %). The suspension was filtered and a brown solid was obtained a crude product.

Yield crude product: 1.45 g, 4.29 mmol, 90%.

A reaction in dry chloroform was not leading to the target molecule. Small scale neat reactions (< 0.15 mmol) between 5H-6,7-Dihydro[1,4]diazepino[1,2,3,4-lmn][1,10] phenanthroline-3,9-dione with 2.22 eq. phosphorus pentabromide resulted in yield around 30 % in high purity. For higher scale reactions the resulting solid contained a large amount of impurities. Despite of the flash chromatographic treatment just one fraction with about 10 % yield of the pure substance was obtained. All other fractions were contaminated with impurities.

^{1}H-NMR (500 MHz, DMSO-d_6): δ (ppm) = 7.94 (d, $^3J_{HH}$=8.4 Hz, 2H, H-2), 8.03 (s, 2H, H-5), 8.42 (d, $^3J_{HH}$=8.4 Hz, 2H, H-3).

6.4.4.6 1,10-Phenanthroline-2,9-dimagnesium bromide

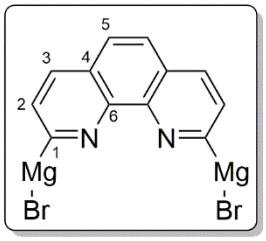

Magnesium (10.7 eq., 4.3 mmol, 0.1 g) was well heated out under thorough stirring. THF (0.3 ml), a small amount of iodine and 2,9-dibromo-1,10-phenanthroline (8 mg) was added and heated to reflux for 1 h. After no reaction took place the whole amount of 2,9-dibromo-1,10-phenanthroline (1 eq., 0.4 mmol, 0.14 g) was added together with another small amount of iodine. The heating was stopped after 3 h and a TLC showed only reagent.

Other similar approaches remained not successful.

6.4.4.7 Di(1,10-phenanthrolin-2-yl)methane by coupling with Diiodomethane

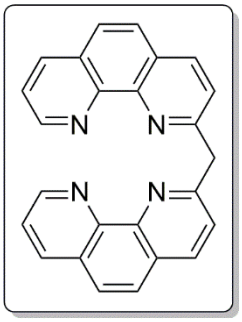

Based on comparable literature dealing with 2,9-dimethyl-1,10-phenanthroline[175], dried 1,10-phenanthroline (1 eq., 4.1 mmol, 0.75 g) was suspended in abs. THF (1m ml) to a beige muddy solution, which was subsequently cooled to – 40 °C. Then LDA (2 eq., 8.1 mmol, 4.1 ml related to a 2 M solution) was added dropwise over 10 minutes at – 45 °C resulting in a dark red solution. The solution was warmed up under stirring to – 10 °C in 2.5 h and afterwards cooled again to – 45 °C. NMR spectra of this solution under inert gas conditions revealed no reactant, but at least two different phenanthroline species.

Thereafter a solution of diiodomethane (0.3 eq., 1.1 mmol, 0.09 ml) in abs. THF (3.5 ml) was added dropwise over 20 minutes. The darkened red solution was allowed to warm up until r.t. was reached. A brown solid precipitated.

The reaction mixture was quenched with NH_4Cl solution (9.8 %, 69 ml) and the aqueous phase including the brown solid was extracted with DCM (3 x 34 ml). The DCM phase was further extracted with a diluted HCl solution (0.25 % v/v, 3 x 25ml) in order to gain more product. Another extraction with diluted HCl solution (5.00 % v/v,

6 x 34ml) was performed resulting in an orange solution. Neutralization gave 0.034 g of a solid.

ESI-MS spectra showed the $[M+H]^+$ peak besides a highly intense reactant signal, as depicted in the appendix, while the NMR spectra were not clearly assignable and the target molecule could not be isolated.

6.4.4.8 PhenMe$_2$Phen by coupling DMP with Phen-Br

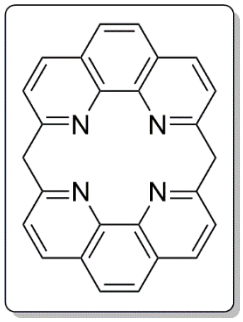

Based on the literature[177], DMP (1 eq., 1 mmol, 0.21 g) Phen-Br (1 eq., 1 mmol, 0.34 g) was pestled thoroughly in a mortar and added into a Schlenk tube, which has been prepared according to inert gas procedures with argon. After drying *in vacuo*, a pre-heated sand bath at 245 °C was installed. The mixture was immediately molten. The sand bath was removed after 5 h and the resulting substances were let to cool to r.t. under argon atmosphere. A brownish black porous solid was obtained and washed with acetone (32 ml) resulting in a yellow filtrate.

EI and ESI mass spectra showed a large amount of reactants and not the target molecule, although an acidic gas was detected during the reaction.

6.4.4.9 Deuteration approaches in 2,9 position

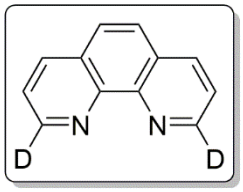

A screening of deprotonation and deuteration reaction was done in order to investigate the possibility of deuteration and the substitution positions. The following exemplary procedure was executed with LDA, *n*-BuLi, potassium *t*-butoxide and lithium bis(trimethylsilyl)amide:

Dry THF was added to dry 1,10-phenanthroline (1 eq., 0.05 mmol, 0.091 g) resulting in a clear solution, which was cooled to ca. - 80 °C. Then the deprotonation agent (2 eq., 1 mmol) was added dropwise. In the case of potassium *t*-butoxide, a suspension in THF (1 ml) was used. After three hours of stirring D_2O (0.2 ml) was added. The solvent was evaporated, water (2 ml) was added and the aqueous phase was extracted with DCM (4 x 2ml).

^{1}H and ^{13}C NMR spectra for LDA and *n*-BuLi revealed a diversity of aromatic species including a large amount of undeuterised 1,10-phenanthroline. In the case of potassium *t*-butoxide and pure undeuterised 1,10-phenanthroline was obtained. In total no deuterium coupling was visible.

6.4.4.10 Deuteration approaches in 2,9 position

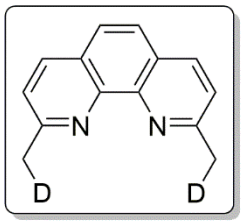

A screening of deprotonation and deuteration reaction was done in order to investigate the possibility of deuteration and the substitution positions. The following exemplary procedure was executed with LDA, *n*-BuLi, potassium *t*-butoxide and lithium bis(trimethylsilyl)amide:

Dry THF was added to dry DMP (1 eq., 0.05 mmol, 0.11 g) resulting in a clear solution, which was cooled to ca. - 80 °C. Then the deprotonation agent (2 eq., 1 mmol) was added dropwise. In the case of potassium *t*-butoxide, a suspension in THF (3 ml) was used. After three hours of stirring D_2O (0.2 ml) was added. The solvent was evaporated, water (2 ml) was added and the aqueous phase was extracted with DCM (3 x 2ml).

^{1}H and ^{13}C NMR spectra revealed only undeuterised DMP without a large amount of by-products.

6.4.4.11 1,2-Bis(9-methyl-1,10-phenanthrolin-2-yl)ethane

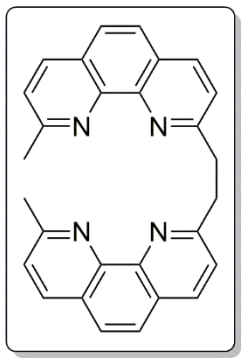

Based on literature[176], dry 2,9-Dimethyl-1,10-phenanthroline (1 eq., 1.63 mmol, 0.34 g) was dissolved in degassed and dried THF (80 ml) to give a beige solution and cooled down to – 80 °C. LDA (1 eq., 1.63 mol, 0.82 ml related to a 2 M solution) was added dropwise within 1 min. After 4 hours the solution was treated with bromine (1 eq., 1.63 mol, 0.08 ml) in dry THF (8 ml) resulting in a bright brown solution. 30 min later, the reaction was cooled with an ice bath, while quenching by water addition (3.2 ml) under precipitating of a brownish solid. THF was evaporated and the aqueous phase was extracted with DCM (6 x 17 ml) giving a reddish brown organic phase.

ESI MS analysis of the organic phase revealed that the target molecule was synthesized beside a high intense reactant peak. The mass spectra of fractions obtained by manual column chromatography with DCM/MeOH gradient showed no sign of the desired substance.

6.4.4.12 (2Z,5Z)-1,4(2,9)-diphenanthrolinacyclohexaphane-2,5-diene

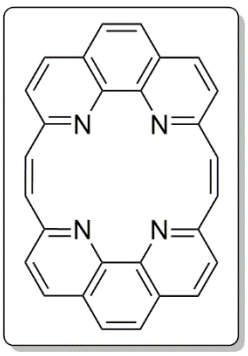

Dry 1,10-Phenanthroline-2,9-dicarbaldehyde (1 eq., 0.50 mmol, 0.12 g) was dissolved in dry THF (120 ml) and heated to 80 °C. Titanium(IV) chloride (4.5 eq., 2.25 mmol, 0.25 ml) was added to dry THF (15 ml) followed by addition of lithium aluminum hydride (2.6 eq., 1.28 mmol, 0.05 g) resulting in a black solid and a slightly red solution, which was heated to 80 °C, too. Then the first solution was transferred into the second, which induced the color to change to grey. After three hours the TLC was indicating no reagent, the solution was let cool to r.t. and afterwards aqueous sodium carbonate solution (20 %). The last-mentioned causes the solution to clear off under precipitation of the black solid follow by color changes from dark brown over green to blue. Both blue aqueous phase and slightly green organic phase were filtered with a glass frit and additional silica gel on top, which retained a brown solid. The solvent of the filtrate was evaporated. Water (50 ml) was added and the aqueous phase was extracted with DCM (6 x 40ml) resulting in slightly yellow-brown solid after evaporation of the solvent. Extraction with pentane (3 x 40 ml) and ethyl acetate (3 x 40 ml) led to the same colored solid.

Characterization of the obtained solids showed no signs of the target molecule.

6.4.4.13 ((1,10-Phenanthroline-2,9-diyl)bis(methylene))diboronic acid

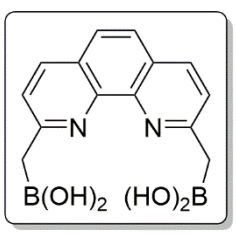

According to literature[302], dried 2,9-Dimethyl-1,10-phenanthroline (1 eq., 2.00 mmol, 0.42 g) was dispersed in dry THF (0.9 ml) and then cooled down to – 80 °C. *n*-BuLi (2 eq., 4.00 mmol, 2.5 ml related to a 1.6 M solution) was added dropwise giving a red solution. The dropwise addition of trimethyl borate (2 eq., 4.00 mmol, 0.45 ml) was performed after 1 h of stirring und resulted in no further color

change. 40 min later the cooling bath was removed and it was stirred overnight. The solvent was evaporated and the residue material was treated with water (10 ml) and extracted with chloroform (8 ml) resulting in a brownish beige aqueous phase and a nearly black organic phase, which resulted in a reddish brown oil with a large diversity of signals in the ^{1}H NMR spectra.

6.4.4.14 PhenC(O)OC$_2$Phen

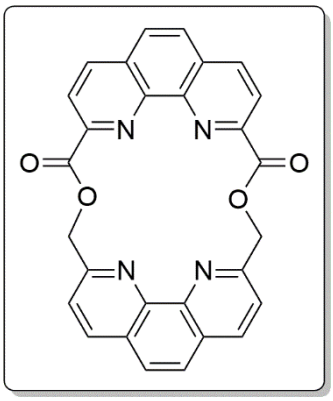

Adapted from literature[298], in the first step the diacyl chloride is generated out of dry 1,10-phenanthroline-2,9-dicarboxylic acid (1 eq., 1 mmol, 0.27 g) in an excess thionyl chloride (789 eq., 789 mmol, 57.8 ml) to give an homogenous beige solution. After 3.5 h at 80 °C a pale green solution was observed and the excess thionyl chlorides was distilled off under reduced pressure. A yellow solid remained was dissolved in dry THF (35 ml). Dry (1,10-Phenanthroline-2,9-diyl)dimethanol (1 eq, 1 mmol, 0.24 g) was suspended in THF/MeCN (160 ml/160 ml) and added to the former solution slowly by a syringe pump at 3.43 ml/min. The color turned orange during addition. After stirring over night, the suspension was filtered resulting in an orange-red solid and after evaporation of the filtrate´s solvent another orange-red solid was obtained.

Although ESI mass spectroscopy could detect the coupling product all purification approaches remained unsuccessful. In addition, product separation by complexation with [Cu(MeCN)$_4$][BF$_4$] and CuCl$_2$ were also not successful.

6.4.5 DMP-X-based Cu(I) complexes

6.4.5.1 [Cu(2,9-dimethyl-1,10-phenanthroline)$_2$][BF_4]

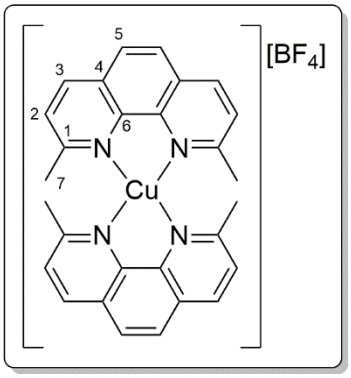

2,9-Dimethyl-1,10-phenanthroline (2.1 eq., 2.1 mmol, 0.47 g) and [Cu($MeCN_4$)][BF_4] (1 eq., 1.0 mmol, 0.32 g) were dissolved in DCM (65 ml) resulting in an immediate orange-red coloration. The solution was filtered and an ether diffusion. The formed dark red crystals were washed with diethyl ether and were obtained as the target complex with one DCM molecule per formula unit.

Yield: 0.59 g, 0.90 mmol, 90%.

^{1}H-NMR (500 MHz, $CDCl_3$): δ (ppm) = 4.42 (s, 8H, H-7), 7.79 (d, $^3J_{HH}$ = 8.3 Hz, 4H, H-2), 8.03 (s, 4H, H-5), 8.51 (d, $^3J_{HH}$ = 8.3 Hz, 4H, H-3).

^{13}C-NMR (125 MHz, $CDCl_3$): δ (ppm) = 26.0 (s, CH_2, 4C, C-7), 125.8 (s, CH, 4C, C-2), 126.3 (s, CH, 4C, C-5), 127.8 (s, C_q, 4C, C-4), 137.5 (s, CH, 4C, C-3), 143.3 (s, C_q, 4C, C-6), 157.9 (s, C_q, 4C, C-1).

^{15}N-NMR (50.7 MHz, $CDCl_3$, obtained by ^{15}N-^{1}H-HMBC): δ (ppm) = 254.2 (s, 4N).

ESI MS (pos) (m/z (%) in MeCN + Formic Acid): 207.09 (51) [L-2I+H], 334.00 (98) [L-I+H], 395.92 (9) [M-L-I], 460.90 (98) [L+H], 522.82 (75) [M-L], 856.82 (6) [M-I+H], 982.71 (100) [M].

UV-VIS (λ_{max} [nm] (ε [L mol^{-1} cm^{-1}]) in MeCN): 203 (80600), 226 (109300), 273 (87100), 456 (9500).

Crystal structure is located in the appendix.

6.4.5.2 [Cu(2,9-bis(chloromethyl)-1,10-phenanthroline)$_2$][BF_4]

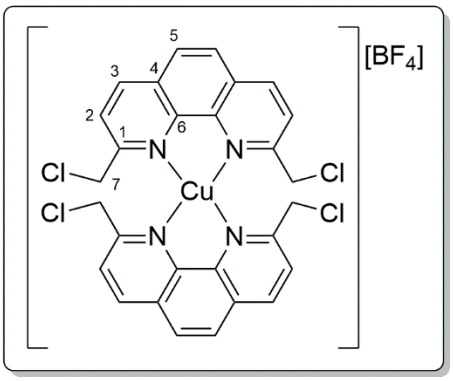

2,9-Bis(chloromethyl)-1,10-phenanthroline (2.2 eq., 0.43 mmol, 0.12 g) and [Cu($MeCN_4$)][BF_4] (1 eq., 0.2 mmol, 0.06 g) were dissolved in DCM (5 ml) and the resulting solution turned immediately red. After 30 minutes of stirring, the solution was filtrated under inert gas atmosphere und an ether diffusion was used to gain crystals red crystals.[148]

Yield: 0.11 g, 0.15 mmol, 75%.

^{1}H-NMR (500 MHz, MeCN-d_3): δ (ppm) = 4.61 (s, 8H, H-7), 8.12 (d, $^3J_{HH}$ = 8.2 Hz, 4H, H-2), 8.25 (s, 4H, H-5), 8.80 (d, $^3J_{HH}$ = 8.2 Hz, 4H, H-3).

^{13}C-NMR (125 MHz, MeCN-d_3): δ (ppm) = 47.1 (s, CH_2, 4C, C-7), 122.7 (s, CH, 4C, C-2), 127.3 (s, CH, 4C, C-5), 129.4 (s, C_q, 4C, C-4), 139.2 (s, CH, 4C, C-3), 143.3 (s, C_q, 4C, C-6), 155.9 (s, C_q, 4C, C-1).

^{15}N-NMR (50.7 MHz, MeCN-d_3, obtained by ^{15}N-^{1}H-HMBC): δ (ppm) = 254.6 (s, 4N).

ESI MS (pos) (m/z (%) in MeCN): 243.08 (15) [L-Cl+H]$^+$, 259.07 (15) []$^+$, 277.03 (82) [L+H]$^+$, 340.95 (16) [M-L], 549.05 (7) [M-2Cl+2H], 583.01 (56) [M-Cl+H]$^+$, 616.97 (100) [M].

UV-VIS (λ_{max} [nm] (ε [L mol^{-1} cm^{-1}]) in MeCN): 207 (44600), 233 (92600), 274 (64000), 400- 425 (790).

Crystal structure is located in the appendix.

6.4.5.3 [Cu(2,9-bis(bromomethyl)-1,10-phenanthroline)$_2$][BF_4]

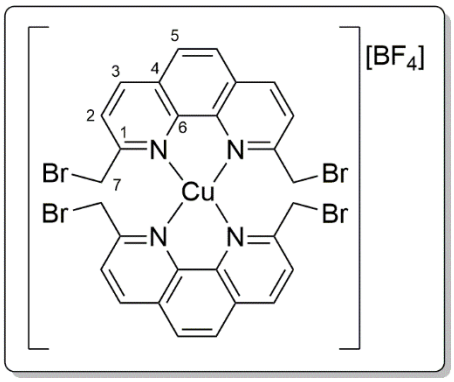

2,9-Bis(bromomethyl)-1,10-phenanthroline (2.0 eq., 0.47 mmol, 0.19 g) and [Cu($MeCN_4$)][BF_4] (1 eq., 0.24 mmol, 0.074 g) were dissolved in DCM (60 ml) and the resulting solution turned immediately orange-red. After 30 minutes of stirring, the solution was filtrated under inert gas atmosphere und an ether diffusion was used to gain red-orange crystals.

Yield: 0.028 g, 0.03 mmol, 14 %.

^{1}H-NMR (500 MHz, MeCN-d_3): δ (ppm) = 4.54 (s, 8H, H-7), 8.10 (d, $^3J_{HH}$ = 8.3 Hz, 4H, H-2), 8.24 (s, 4H, H-5), 8.77 (d, $^3J_{HH}$ = 8.3 Hz, 4H, H-3).

^{13}C-NMR (125 MHz, MeCN-d_3): = 34.0 (s, CH_2, 4C, C-7), 125.9 (s, CH, 4C, C-2), 127.3 (s, CH, 4C, C-5), 129.2 (s, Cq, 4C, C-4), 139.1 (s, CH, 4C, C-3), 143.3 (s, Cq, 4C, C-6), 156.4 (s, Cq, 4C, C-1).

^{15}N-NMR (50.7 MHz, MeCN-d_3, obtained by ^{15}N-^{1}H-HMBC): δ = 255.1 (s, 4N).

ESI MS (pos) (m/z (%) in MeCN): 103.96 (1) [Cu+MeCN], 124.09 (2) [], 164.12 (2) [], 303.01 (12) [M-L-2Br+2OH], 325.00 (8) [L-Br+OH+Na], 366.93 (42) [M-L-Br+OH], 388.90 (10) [L+Na], 428.85 (34) [M-L], 652.94 (2) [M-2Br+H_2O], 668.94 (2) [M-2Br+2OH], 716.86 (5) [M-Br+OH], 732.85 (35) [M-Br+OH], 794.77 (100) [M].

UV-VIS (λ_{max} [nm] (ε [L mol^{-1} cm^{-1}]) in MeCN): 207 (64600), 236 (92400), 280 (67900), 449 (3400).

Crystal structure is located in the appendix.

6.4.5.4 [Cu(2,9-bis(iodomethyl)-1,10-phenanthroline)$_2$][BF_4]

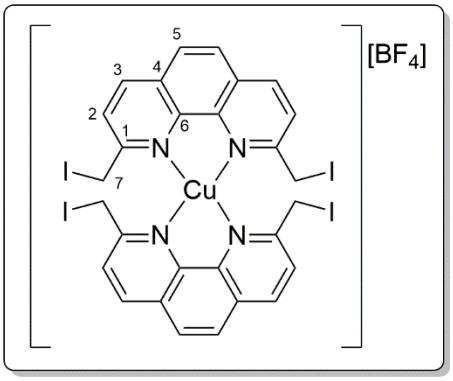

2,9-bis(iodomethyl)-1,10-phenanthroline (2.1 eq., 0.42 mmol, 0.19 g) and [Cu($MeCN_4$)][BF_4] (1 eq., 0.20 mmol, 0.06 g) were dissolved in MeCN (8 ml) and the resulting solution turned immediately red. After 1 h of stirring, the solution was filtrated under inert gas atmosphere revealing a red solid, which was identified as amorphous target compound. In addition, the filtrate was exposed to an ether diffusion to obtain red crystals.[148]

Amorphous solid yield: 0.077 g, 0.07 mmol, 35 %

Crystalline solid yield: 0.052 g, 0.05 mmol, 24 %

Total yield: 0.129 g, 0.12 mmol, 59 %

^{1}H-NMR (500 MHz, MeCN-d_3): δ (ppm) = 4.55 (s, 8H, H-7), 8.05 (d, $^3J_{HH}$ = 8.3 Hz, 4H, H-2), 8.20 (s, 4H, H-5), 8.69 (d, $^3J_{HH}$ = 8.3 Hz, 4H, H-3).

^{13}C-NMR (125 MHz, MeCN-d_3): δ (ppm) = 46.2 (s, CH_2, 4C, C-7), 125.7 (s, CH, 4C, C-2), 127.0 (s, CH, 4C, C-5), 129.4 (s, C_q, 4C, C-4), 139.2 (s, CH, 4C, C-3), 143.3 (s, C_q, 4C, C-6), 158.5 (s, C_q, 4C, C-1).

^{15}N-NMR (50.7 MHz, MeCN-d_3, obtained by ^{15}N-^{1}H-HMBC): δ (ppm) = 251.6 (s, 4N).

ESI MS (pos) (m/z (%) in MeCN + Formic acid): 207.09 (51) [4-2I+H]$^+$, 334.00 (98) [4-I+H]$^+$, 395.92 (9) [M-2-I]$^+$, 460.90 (98) [4+H]$^+$, 522.82 (75) [Cu(4)]$^+$, 856.82 (6) [Cu(4)$_2$-I+H]$^+$, 982.71 (100)

ESI MS (pos) (m/z (%) in MeCN): 103.96 (1) [Cu+MeCN], 124.09 (5) [], 144.98 (1) [Cu+2MeCN], 164.12 (4) [], 207.09 (2) [L-2I+H], 333.00 (9) [L-I+H], 460.90 (80) [L+H], 482.88 (2) [L+Na], 522.82 (40) [M-L], 856.82 (8) [M-I+H], 872.81 (2) [M-I+OH], 982.71 (100) [M].

UV-VIS (λ_{max} [nm] (ε [L mol^{-1} cm^{-1}]) in MeCN): 207 (71600), 241 (74400), 281 (57300), 456 (2200).

Crystal structure is located in the appendix.

6.4.5.5 [Cu(2,9-bis(trichloromethyl)-1,10-phenanthroline)$_2$][BF_4]

2,9-bis(trichloromethyl)-1,10-phenanthroline (2.0 eq., 0.40 mmol, 0.17 g) and [Cu($MeCN_4$)][BF_4] (1.0 eq., 0.20 mmol, 0.06 g) were dissolved in DCM (10 ml) and the resulting solution turned to yellow-orange. After the solution was filtrated under inert gas atmosphere, an ether diffusion was used to gain crystals, but about 15 min later the solution became turbid.

6.4.6 DMP-based Cu(II) complexes as models for the excited state

Not all yields were determined, since most of the complexes were not of further interest.

6.4.6.1 [Cu(2,9-dimethyl-1,10-phenanthroline)$_2$(Cl)][Cl]

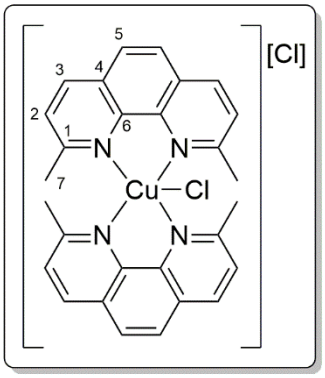

Copper(II) chloride dihydrate (1 eq., 0.10 mmol, 0.02 g) was dissolved in methanol (1 ml) resulting in a pale green solution. Afterwards a solution of 2,9-dimethyl-1,10-phenanthroline (2.1 eq., 0.21 mmol, 0.05 g) in methanol (2 ml) was added to the first solution, which turned bright green. After 30 minutes, crystalline green needles were formed. Recrystallization approaches in DCM with diethyl ether led to orange plates as the target molecule with one methanol per formula unit.

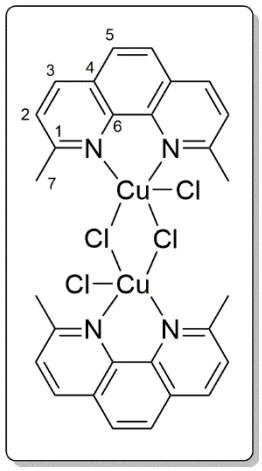

Note: Green plates were obtained by crystallization of the methanol solution with diethyl ether. This compound is the bis(µ-chlorido) species of the target molecule.

Crystal structures are located in the appendix.

6.4.6.2 [Cu(DMP)$_2$(MeOH)][ClO$_4$]$_2$

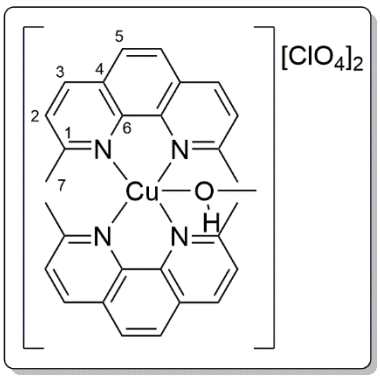

Copper(II) perchlorate hexahydrate (1 eq., 0.10 mmol, 0.04 g) and 2,9-dimethyl-1,10-phenanthroline (2.1 eq., 0.21 mmol, 0.05 g) were dissolved in MeOH (total 3 ml). The copper salt containing solution was added dropwise to the ligand solution resulting in a bright green color, which turned dark green immediately. Green crystals were grown out of this solution, which were identified as [Cu(DMP)$_2$(MeOH)][ClO$_4$].

Crystal structure is located in the appendix.

6.4.6.3 [Cu(DMP)$_2$(NO$_3$)][NO$_3$]

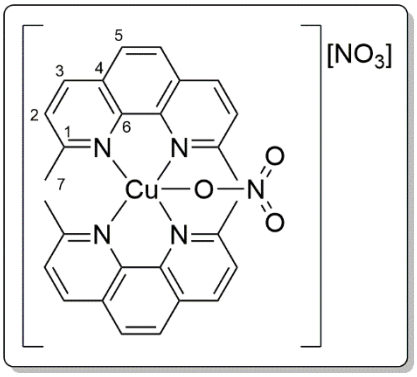

Copper(II) nitrate trihydrate (1 eq., 0.10 mmol, 0.02 g) and 2,9-dimethyl-1,10-phenanthroline (2.1 eq., 0.21 mmol, 0.05 g) were dissolved in MeOH (total 3 ml). The copper salt containing solution was added dropwise to the ligand solution resulting in a bright green color and an precipitation of an bright green, polycrystalline solid. The precipitated was dissolved in MeOH giving a red solution. Green crystals of [Cu(DMP)$_2$(NO$_3$)][NO$_3$] were obtained by ether diffusion.

Crystal structure is located in the appendix.

6.4.6.4 [Cu(DMP)$_2$(MeCN)][BF$_4$]$_2$

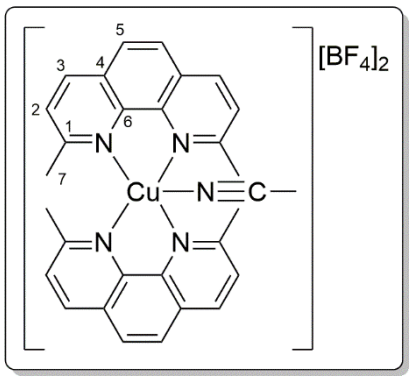

Copper(II) tetrafluoroborate 4.04 hydrate (1.0 eq., 1.05 mmol, 0.33 g) was dissolved in methanol (5 ml). Afterwards a solution of 2,9-dimethyl-1,10-phenanthroline (2.0 eq., 2.10 mmol, 0.47 g) in methanol (45 ml) was added to the first solution, which became bright green and darkened turned dark green immediately. After four days, green and brown crystals were obtained. The green crystals were identified as the target complex.

Crystal structure is located in the appendix.

6.4.6.5 [Cu(DMP)$_2$(BF$_4$)][BF$_4$]

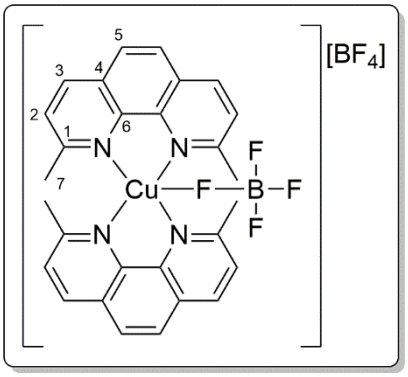

Copper(II) tetrafluoroborate 4.04 hydrate (1.2 eq., 0.12 mmol, 0.04 g) was dissolved in methanol (1 ml). Afterwards a solution of 2,9-dimethyl-1,10-phenanthroline (2.0 eq., 0.20 mmol, 0.04 g) in methanol (2 ml) was added to the first solution, which turned bright green. After four days, green and brown

crystals were obtained. The green needles were identified as the target compound.

Crystal structure is located in the appendix.

6.4.6.6 [Cu(DMP)$_2$][BF$_4$]$_2$

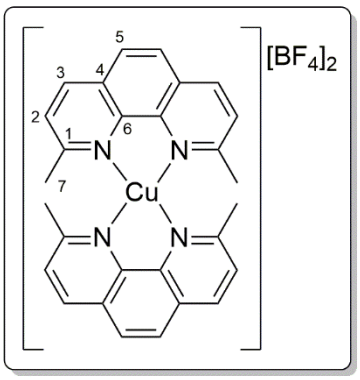

Copper(II) tetrafluoroborate 4.04 hydrate (1.0 eq., 0.5 mmol, 0.16 g) was dissolved in methanol (5 ml). Then a solution of 2,9-dimethyl-1,10-phenanthroline (0.9 eq., 0.47 mmol, 0.10 g) in a methanol/water mixture (3 ml/0.3 ml) was added to the first solution, which turned bright green. Green (unidentified coordination polymer), brown crystals and colorless (DMP) crystals were obtained. The brown crystals were identified as the target compound.

Yield: 0.062 g, 0.09 mmol, 18 %.

Crystal structure is located in the appendix.

6.4.7 Copper(I) DMP complexes obtained by contaminated Cu(II) precursors

6.4.7.1 [Cu(DMP)$_2$][BF$_4$]

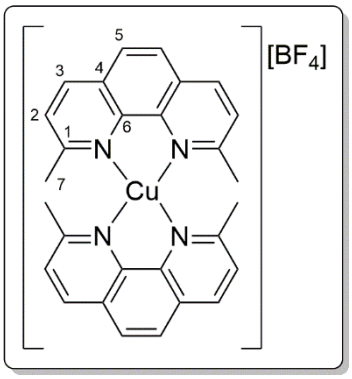

Copper(II) tetrafluoroborate 4.04 hydrate (1.0 eq., 1.0 mmol, 0.31 g) was dissolved in methanol. Then a solution of 2,9-dimethyl-1,10-phenanthroline (2.0 eq., 2.0 mmol, 0.44 g) in a methanol was added to the first solution, which turned bright green and darkened afterwards. Diffusion of diethyl ether into this solution resulted in red, octahedral crystals of the target complex.

Crystal structure is located in the appendix.

6.4.7.2 [Cu(DMP)$_2$][Br]

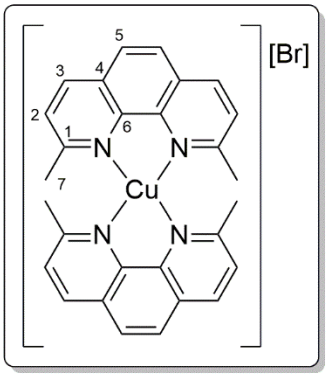

Copper(II) bromide (1.1 eq., 0.10 mmol, 0.02 g) and 2,9-dimethyl-1,10-phenanthroline (2.1 eq., 0.21 mmol, 0.05 g) were dissolved in MeOH (total 3 ml). The copper salt containing solution was added dropwise to the ligand solution resulting in a bright green color and an precipitation of an bright green, polycrystalline solid. The precipitated was dissolved in DCM and a crystallization by diethyl ether diffusion was performed resulting in orange ([Cu(DMP)(Br)]), red ([Cu$_2$-bis(μ-Br)(DMP)$_2$]) and brown crystals. The last mentioned were identified as the target compound.

Crystal structure is located in the appendix.

6.4.7.3 [Cu(DMP)$_2$(H$_2$O)][Br]

Copper(II) bromide (1.0 eq., 1.0 mmol, 0.22 g) and 2,9-dimethyl-1,10-phenanthroline (2.1 eq., 2.1 mmol, 0.45 g) were dissolved in acetone (total 80 ml). The copper salt containing solution was added dropwise to the ligand solution resulting in a red-orange solution and a flocculent beige, slightly red-brown precipitate, which was filtered off.

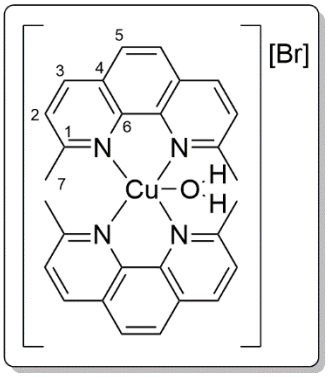

Red crystals were obtained as the target compound by diethyl ether diffusion into the filtrate.

Yield: 0.177 g, 0.316 mmol, 31 %.

Crystal structure is located in the appendix.

6.4.7.4 [Cu(DMP)$_2$][CF$_3$SO$_3$]

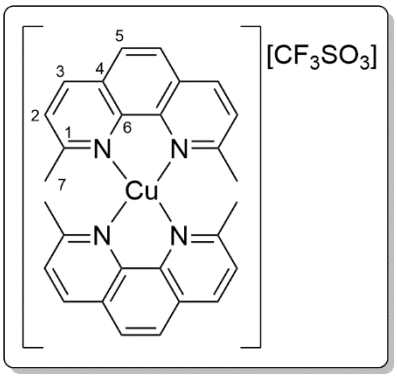

Copper(II) triflate (1.0 eq., 0.1 mmol, 0.04 g) was dissolved in MeOH (1 ml) resulting in a green solution. Afterwards a solution of 2,9-dimethyl-1,10-phenanthroline (2.1 eq., 0.48 mmol, 0.10 g) in MeOH (2 ml) was added to the first solution, which turned bright green und then darkened. Slow evaporation of the solvent led to orange-red crystals , which was identified as the product.

Crystal structure is located in the appendix.

6.4.7.5 [Cu(DMP)(Br)]

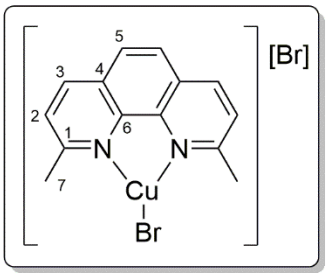

Copper(II) bromide (1.1 eq., 0.10 mmol, 0.02 g) and 2,9-dimethyl-1,10-phenanthroline (2.1 eq., 0.21 mmol, 0.05 g) were dissolved in MeOH (total 3 ml). The copper salt containing solution was added dropwise to the ligand solution resulting in a bright green color and an precipitation of an bright green, polycrystalline solid. The precipitated was dissolved in DCM and a crystallization by diethyl ether diffusion was performed resulting in brown ([Cu(DMP)$_2$][Br]), red ([Cu$_2$-bis(μ-Br)(DMP)$_2$]) and orange crystals. The last mentioned were identified as the target compound.

Crystal structure is located in the appendix.

6.4.7.6 [Cu_2-bis(μ-Br)($DMP)_2$]

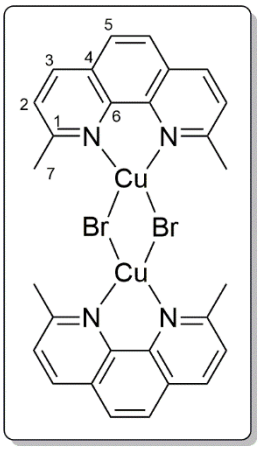

Copper(II) bromide (1.1 eq., 0.10 mmol, 0.02 g) and 2,9-dimethyl-1,10-phenanthroline (2.1 eq., 0.21 mmol, 0.05 g) were dissolved in MeOH (total 3 ml). The copper salt containing solution was added dropwise to the ligand solution resulting in a bright green color and an precipitation of an bright green, polycrystalline solid. The precipitated was dissolved in DCM and a crystallization by diethyl ether diffusion was performed resulting in brown ([Cu($DMP)_2$][Br]), orange ([Cu(DMP)(Br)]) and red crystals. The last mentioned were identified as the target compound.

Crystal structure is located in the appendix.

6.4.7.7 [Cu(DMP-$Br)_2$][Br]

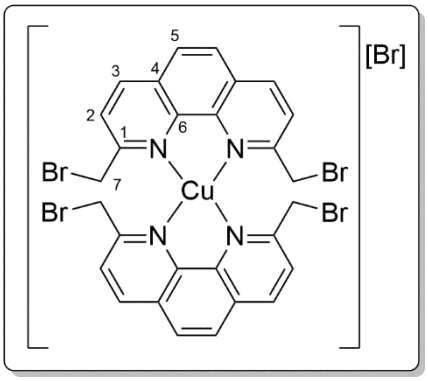

Copper(II) bromide (1.0 eq., 0.005 mmol, 1.1 mg) and DMP-Br (2.1 eq., 0.001 mmol, 4.3 mg) were dissolved a methanol resulting in a yellow-orange suspension. The solid was filtered off. Diffusion of diethyl ether into the filtrate resulted in red-orange crystals of the target complex.

Crystal structure is located in the appendix.

6.4.7.8 [Cu(DMP-$Br)_2$][ClO_4]

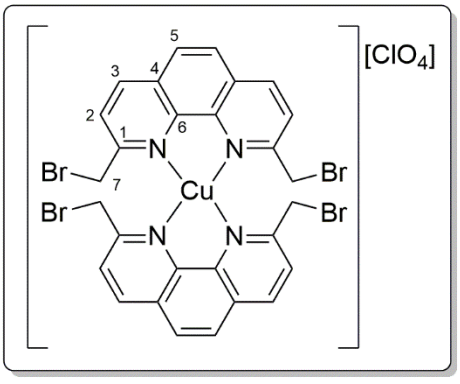

Copper(II) perchlorate hexahydrate (1.0 eq., 0.3 mmol, 0.11 g) and DMP-Br (2.5 eq., 0.75mmol, 0.31 g) were dissolved in methanol (70 ml) resulting in a brown-orange suspension. The precipitate was filtered off and homogeneously dissolved in DCM. Diffusion of diethyl ether into this solution resulted in orange-red crystals of the target complex.

Crystal structure is located in the appendix.

6.4.8 Complexes of Azapyrinidophane ligands

6.4.8.1 [Cu(DAPy-Ts)MeCN][BF_4]

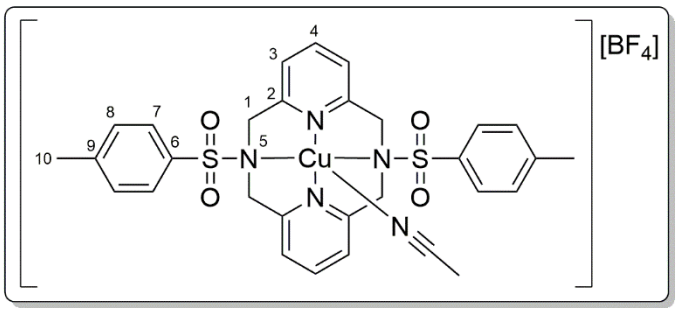

Ditosyl diazapyridinophane (1 eq., 0.27 mmol, 150 mg) and [$Cu(MeCN)_4$][BF_4] (1 eq., 0.27 mmol, 86.2 mg) were dissolved in abs. DCM (5 mL) and stirred for 15 min. The yellow reaction mixture was filtered under inert gas atmosphere and the complex was crystallized by ether vapor diffusion overnight. Yellow crystals were obtained and dried *in vacuo*. It could be observed that the solution turned blue-green, when atmosphere entered the flask resulting in blue crystals which were identified by X-Ray structure analysis as the analogous bis(μ-hydroxo) copper(II) complex.

^{1}H-NMR (500 MHz, DMSO-d_6): δ (ppm) = 2.56 (s, 6H, H-10), 3.04 (s, 8H, H-1), 8.02 (d, $^3J_{HH}$=8.1 Hz, 4H, H-8), 8.18 (d, $^3J_{HH}$=7.9 Hz, 4H, H-3), 8.32 (d, $^3J_{HH}$=7.9 Hz, 4H, H-7), 8.75 (t, $^3J_{HH}$=7.8 Hz, 4H, H-4).

^{13}C-NMR (125 MHz, DMSO-d_6): δ (ppm) = 21.6 (s, CH_3, 2C, C-10), 54.5 (s, CH_2, 4C, C-1), 123.9 (s, CH, 4C, C-3), 128.6 (s, CH, 4C, C-7), 131.2 (s, CH, 4C, C-8), 135.3 (s, C_q, 2C, C-6), 144.1 (s, CH, 2C, C-4), 146.2 (s, C_q, 2C, C-9), 156.7 (s, C_q, 4C, C-2).

ESI-MS (pos) (m/z (%) in MeCN): 549.16 (82) [M-Cu+H], 571.15 (4) [M-Cu+Na], 611.08 (100) [M].

ATR-IR ($\tilde{\nu}$ [cm^{-1}] (transmission [%])): 617 (82), 663 (70), 727 (80), 781 (74), 804 (77), 897 (77), 1161-1047 (67), 1269 (91), 1338 (80), 1418 (91), 1441(89), 1493 (97), 1574 (93), 1597 (89), 2854 (99), 2924 (98), 2957 (99), 2984 (99), 3092 (99), 3564-3594 (99).

Crystal structure is located in the appendix.

6.4.8.2 [Cu(DAPy-NH)Cl_2]

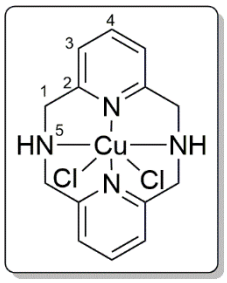

Unsubstituted Diazapyridinophane (1.2 eq., 0.32 mmol, 77 mg) and [Cu(MeCN)$_4$][BF_4] (1 eq., 0.28 mmol, 60 mg) were dissolved in abs. DCM (5 mL) and stirred for 50 minutes. The solution turned dark red, was filtered and colorless crystals (probably Cu(I)-species) precipitated after ether vapor diffusion overnight. After further 48 hours the solution became green, brown solid and green needles could be observed. The green needles could be identified as the complex.

ESI-MS (pos) (m/z (%) in MeCN): 241.14 (30) [M-2Cl-Cu+H], 246.14 (6), 252.13 (6), 269.14 (6), 275.05 (44) [M-CH_2N], 289.06 (8), 302.06 (100) [M-2Cl+H], 329.07 (25), 338.04 (28) [M-Cl], 361.22 (13) [M-Cl+Na], 381.18 (5), 423.13 (3).

Crystal structure is located in the appendix.

6.4.9 Phen-based homoleptic Cu(II) complexes

6.4.9.1 [Cu(phen)$_2$(Cl)][Cl]

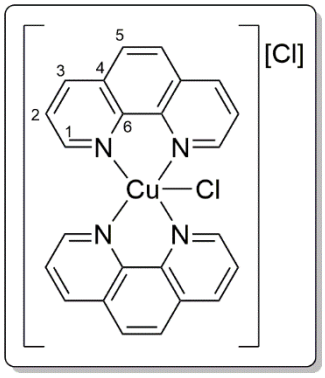

Copper(II) chloride dihydrate (1 eq., 0.5 mmol, 0.09 g) was dissolved in MeOH (4.4 ml) resulting in a green solution. Then Phen (2.1 eq., 1.1 mmol, 0.19 g) was dissolved in MeOH (4.4 ml) and was added to the first solution, which turned green and darkened. A small amount of bright green solid precipitated, which was filtered off and a diffusion of diethyl ether into the filtrate was conducted. Blue and turquoise crystals were obtained with the same complex but differently aligned. When increasing the amount of Phen, the formation of turquoise crystals are favored.

Crystal structures are located in the appendix.

6.4.9.2 [Cu(phen)$_2$(Br)][Br]

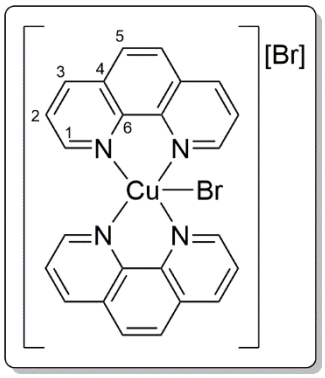

Copper(II) bromide (1.0 eq., 0.1 mmol, 0.02 g) and Phen (2.1 eq., 0.2 mmol, 0.04 g) were dissolved a methanol resulting in a dark green solution. Crystals of the target complex were formed after 10 min.

Crystal structure is located in the appendix.

6.4.9.3 [Cu(phen)$_2$(NO$_3$)][NO$_3$]

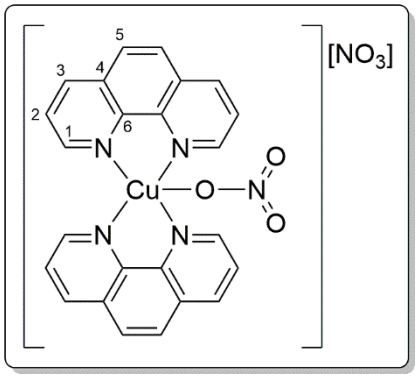

Copper(II) nitrate trihydrate (1.0 eq., 0.1 mmol, 0.02 g) was dissolved in MeOH resulting in a green solution. Then a solution of Phen (2.1 eq., 0.2 mmol, 0.04 g) in MeOH was added to the first solution, which turned turquoise. Slow evaporation of the solvent led to blue crystals, which was identified as the product.

Crystal structure is located in the appendix.

6.4.9.4 [Cu(phen)$_2$(CF$_3$SO$_3$)][CF$_3$SO$_3$]

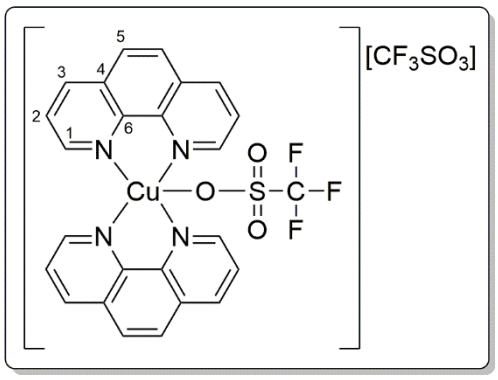

Copper(II) triflate (1.0 eq., 0.1 mmol, 0.04 g) was dissolved in MeOH resulting in a green solution. Then a solution of Phen (2.2 eq., 0.22 mmol, 0.04 g) in MeOH was added to the first solution, which turned turquoise. Slow evaporation of the solvent led to turquoise-blue crystals, which was identified as the product.

Crystal structure is located in the appendix.

6.4.9.5 [Cu(phen)3(ClO$_4$)][ClO$_4$]

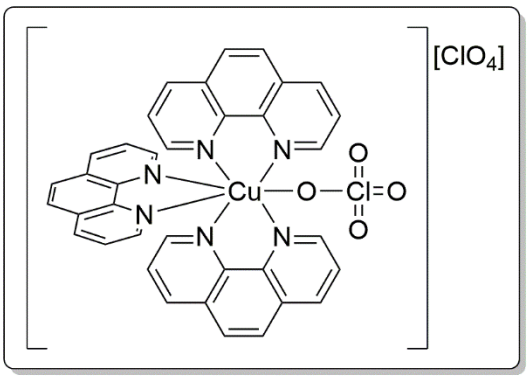

Copper(II) perchlorate hexahydrate (1.0 eq., 0.1 mmol, 0.04 g) and phen (2.1 eq., 0.21 mmol, 0.04 g) were separately dissolved in methanol. The Copper salt solution was added dropwise to the ligand solution resulting in bluish crystalline precipitate. Diffusion of diethyl ether into the filtrate resulted in blue crystals of the target complex.

Crystal structure is located in the appendix.

6.4.9.6 [Cu_2-bis(μ-OH)(phen)$_4$][BF_4]$_3$

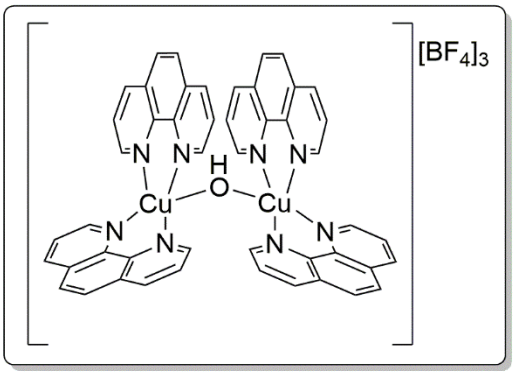

Copper(II) tetrafluoroborate 4.04 hydrate (1.0 eq., 0.1 mmol, 0.03 g) was dissolved in methanol (10 ml). Then a solution of Phen (2.0 eq., 0.2 mmol, 0.03 g) in a methanol (10 ml) was dropwise added to the first solution, which turned blue. Diffusion of diethyl ether into this solution resulted in blue crystals of the target complex.

Crystal structure is located in the appendix.

6.4.10 Copper(II) complexes of DMP, phen and bpy

6.4.10.1 [Cu_2-bis(μ-SO_4)(bpy)$_2$($MeOH$)$_2$]

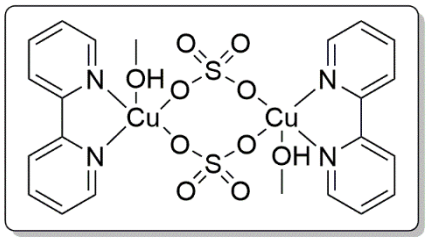

Copper(II) sulfate (1.0 eq., 0.75 mmol, 0.12 g) was dissolved in water. Then a solution of bpy (1.0 eq., 0.75 mmol, 0.12 g) in water was dropwise added to the first solution, which turned blue. The precipitate was dissolved by addition of MeOH. Diffusion of diethyl ether into this solution resulted in blue crystals of the target compound.

Crystal structure is located in the appendix.

6.4.10.2 [Cu_2-bis(μ-Cl)(DMP)$_2$(Cl)$_2$]

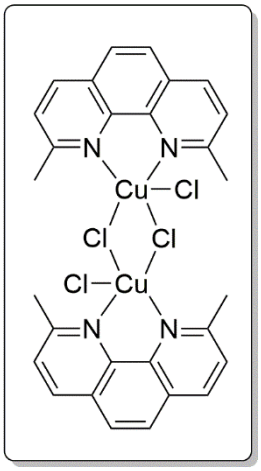

Copper(II) chloride dihydrate (1.0 eq., 0.35 mmol, 0.06 g) was dissolved in water (2 ml). Then a solution of DMP (1.0 eq., 0.35 mmol, 0.08 g) was dissolved in MeOH (2 ml) and three droplets of HCl (37 %). The ligand solution was added dropwise to the copper salt solution. A bright green solid precipitated and a colorless solution remained. After filtration, the solid was dissolved in DCM and a diffusion of diethyl ether into this solution was conducted to obtain red crystals, which was identified as the target compound.

Crystal structure is located in the appendix.

6.4.10.3 [Cu_2-bis(μ-OH)($phen)_2(Cl)_2$]/[Cu_2-bis(μ-OH)($phen)_2(H_2O)_2$][$Cl]_2$

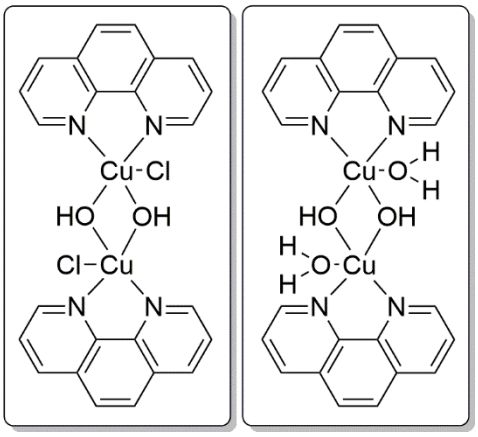

Copper(II) chloride dihydrate (1.0 eq., 0.35 mmol, 0.06 g) was dissolved in water (2 ml). Then a solution of DMP (1.0 eq., 0.35 mmol, 0.08 g) was dissolved in MeOH (2 ml) and three droplets of HCl (37 %). The ligand solution was added dropwise to the copper salt solution. A small amount of a bright green solid precipitated, while a blue solution was observed. It was alkalized to pH = 14 with a aqueous 1 M KOH solution. The precipitated blue solid was dried and dissolved in water. Slow evaporation of the solvent led to the designated co-crystal.

Crystal structure is located in the appendix.

6.4.10.4 [Cu(bpy)($Cl)_2$]

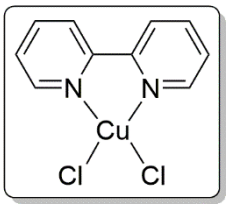

Copper(II) chloride dihydrate (1.0 eq., 5.0 mmol, 0.87 g) was dissolved in MeOH (27.5 ml). Then a solution of bpy (1.0 eq., 5.0 mmol, 0.78 g) in MeOH/H_2O (167 ml/75 ml) was very slowly added to the first solution, which turned blue. Diffusion of diethyl ether into this solution resulted in turquoise crystals of the target compound.

Yield: 0.966 g, 3.33 mmol, 67 %.

Crystal structure is located in the appendix.

6.4.10.5 [Cu(bpy)$_2$(Cl)][Cl]

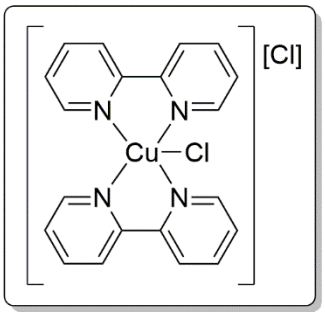

Copper(II) chloride dihydrate (1.0 eq., 0.5 mmol, 0.09 g) was dissolved in MeOH (4.4 ml). Then a solution of bpy (2.1 eq., 1.0 mmol, 0.17 g) in MeOH (4.4 ml) was very slowly added to the first solution, which turned dark blue. Diffusion of diethyl ether into this solution resulted in turquoise ([Cu(bpy)(Cl)$_2$], 0.03 g, 0.12 mmol, 23%) and blue crystals, which were identified as the target compound.

Yield: 0.17 g, 0.38 mmol, 76 %.

Crystal structure is located in the appendix.

6.4.10.6 [Cu$_2$-bis(μ-OH)(bpy)$_2$(Cl)$_2$][Cl]$_2$

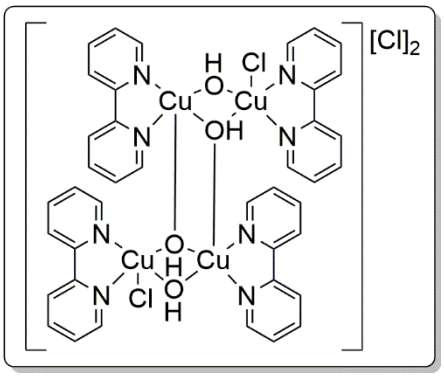

Copper(II) acetate monohydrate (1.0 eq., 0.3 mmol, 0.06 g) was dissolved in water (4 ml). Then a solution of bpy (1.0 eq., 0.3 mmol, 0.05 g) was dissolved in water (2 ml) and three droplets of HCl (37 %). The ligand solution was added dropwise to the copper salt solution. A dark blue solution was obtained, which was alkalized by an 1 M aqueous NaOH solution, which resulted in a blue precipitate. The precipitate was filtered off, dissolved in water and the solvent was allowed to evaporate slowly causing the formation of blue crystals of the target complex.

Crystal structure is located in the appendix.

6.4.10.7 [Cu(phen)$_2$(CO$_3$)]/[Cu$_2$-bis(μ-OH)(phen)$_2$(H$_2$O)$_2$][OH]$_2$

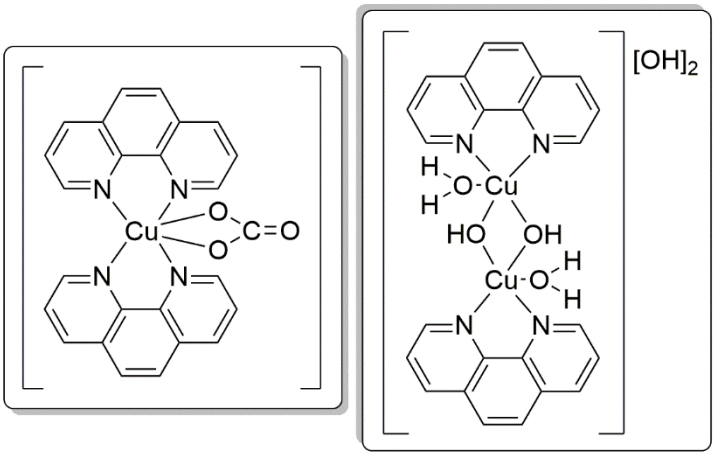

Copper(II) acetate monohydrate (1.0 eq., 0.3 mmol, 0.06 g) was dissolved in water (4 ml). Then a solution of bpy (1.0 eq., 0.3 mmol, 0.05 g) was dissolved in water (2 ml) and three droplets of HCl (37 %). The ligand solution was added dropwise to the copper salt solution. A dark blue solution pf pH = 2-3 was obtained. The solvent was allowed to evaporate slowly giving green crystals of the target co-crystals.

Crystal structure is located in the appendix.

6.4.10.8 [Cu$_2$-bis(μ-Cl)(phen)$_2$(Cl)$_2$]

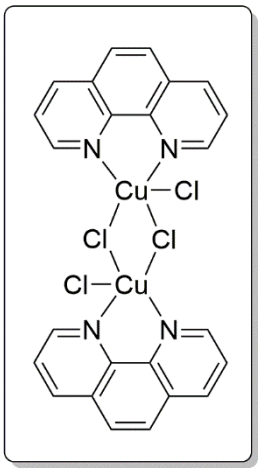

Copper(II) chloride dihydrate (1 eq., 1 mmol, 0.17 g) was dissolved in MeOH (24 ml). Then a solution of 2,9-dimethyl-1,10-phenanthroline (0.9 eq., 0.9 mmol, 0.16 g) was dissolved in MeOH/water (122 ml/20 ml) and added dropwise first solution. A subsequent diffusion of diethyl ether into the solution resulted in turquoise crystals, which was identified as the target compound.

Yield: 0.495 g, 0.50 mmol, 79 %.

Crystal structure is located in the appendix.

6.4.10.9 [Cu(DMP)(Cl)$_2$(H$_2$O)]

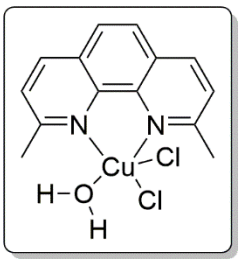

Copper(II) chloride dihydrate (1.0 eq., 1.0 mmol, 0.17 g) was dissolved in water (8 ml). Then a solution of DMP (1.0 eq., 1.0 mmol, 0.22 g) was dissolved in water (8 ml) and seven droplets of HCl (37 %). The ligand solution was added dropwise to the copper salt solution. A dark green solid precipitated and a pale bright blue solution remained after filtration. Green plates formed after solvent

evaporation at room temperature. The yield is referring to the precipitated solid, which was also identified as the target compound.

Yield: 0.287 g, 0.84 mmol, 84 %.

Crystal structure is located in the appendix.

6.4.10.10 [(Cu(bpy)$_2$O)$_3$-C][BF$_4$]$_4$

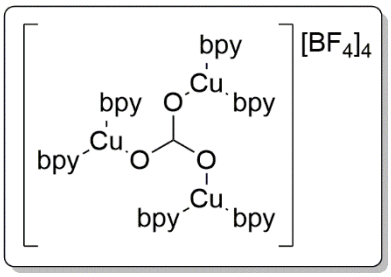

An 1 M aqueous KOH solution (2 ml) and water (7 ml) were added to Copper(II) tetrafluoroborate 4.04 hydrate (1.0 eq., 0.5 mmol, 0.16 g) and bpy (1.0 eq., 0.5 mmol, 0.08 g) resulting in a blue suspension with an fine blue precipitate. Small blue crystals were obtained by slow evaporation of the solvent.

Crystal structure is located in the appendix.

6.4.10.11 [Cu(DMP-OH)$_2$][BF$_4$]$_2$

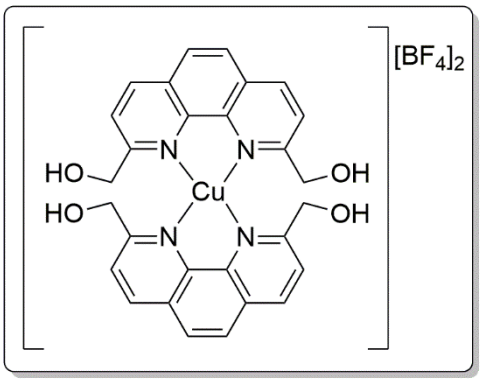

Copper(II) tetrafluoroborate 4.04 hydrate (1.0 eq., 0.1 mmol, 0.03 g) was dissolved in methanol (1 ml). Then a solution of DMP-OH (2.0 eq., 0.2 mmol, 0.05 g) in a methanol (14 ml) was dropwise added to the first solution, which turned bright yellow. Diffusion of diethyl ether into this solution resulted in yellowish crystals of the target complex.

Crystal structure is located in the appendix.

6.4.10.12 [Cu(DMP-OOH)$_2$]

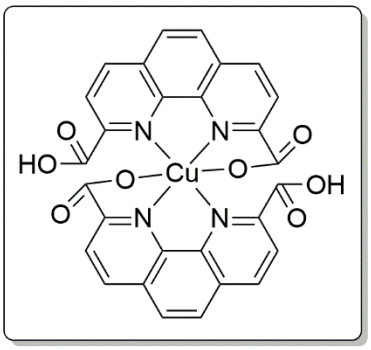

Copper(II) tetrafluoroborate 4.04 hydrate (1.0 eq., 0.1 mmol, 0.03 g) was dissolved in methanol (1 ml). Then a solution of DMP-OOH (2.0 eq., 0.2 mmol, 0.05 g) in a DMSO (4 ml) was dropwise added to the first solution, which turned green. Diffusion of diethyl ether into this solution resulted in turquoise crystals of the target complex.

Crystal structure is located in the appendix.

6.4.10.13 [Cu(DMP-OH)(Cl)$_2$]

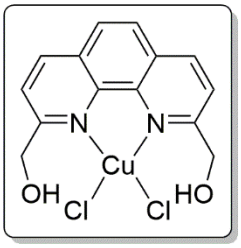

Copper(II) chloride dihydrate (1.0 eq., 0.25 mmol, 0.04 g) was dissolved in MeOH (2 ml). Then a solution of DMP-OH (1.0 eq., 0.25 mmol, 0.06 g) was dissolved in MeOH (20 ml). The ligand solution was added dropwise to the copper salt solution, which resulted in a pale yellow solution. Diffusion of diethyl ether into this solution resulted in green crystals of the target compound.

Crystal structure is located in the appendix.

7 List of References

[1] P. D. Frischmann, K. Mahata, F. Würthner, *Chem. Soc. Rev.* **2013**, *42*, 1847.

[2] United Nations Development Program, *World Energy Assessment: Overview - 2004 Update*, United Nations, New York, **2004**.

[3] N. S. Lewis, D. G. Nocera, *Proc. Natl. Acad. Sci.* **2006**, *103*, 15729.

[4] T. M. L. Wigley, R. Richels, J. A. Edmonds, *Nature* **1996**, *379*, 240.

[5] E. Maier-Reimer, K. Hasselmann, *Climate Dynamics* **1987**, *2*, 63.

[6] a) U. Siegenthaler, T. F. Stocker, E. Monnin, D. Lüthi, J. Schwander, B. Stauffer, D. Raynaud, J.-M. Barnola, H. Fischer, V. Masson-Delmotte et al., *Science (New York, N.Y.)* **2005**, *310*, 1313; b) J. R. Petit, J. Jouzel, D. Raynaud, N. I. Barkov, J.-M. Barnola, I. Basile, M. Bender, J. Chappellaz, M. Davis, G. Delaygue et al., *Nature* **1999**, *399*, 429.

[7] Gesellschaft Deutscher Chemiker e.V., Gesellschaft für Chemische Technik und Biotechnologie e.V., Deutsche Wissenschaftliche Gesellschaft für Erdöl, Erdgas und Kohle e.V., Verband der Chemischen Industrie, W. Keim, M. Röper, "Rohstoffbasis im Wandel. Positionspapier", can be found under https://dechema.de/dechema_media/Positionspapier_Rohstoffbasis+im+Wandel-p-3094-view_image-1-called_by-dechema-original_site-dechema_eV-original_page-124930.pdf, **2010**.

[8] International Energy Agency, *Key World Energy Statistics*, http://www.iea.org/publications/freepublications/publication/KeyWorld_Statistics_2015.pdf, **2015**.

[9] a) N. Muradov, T. Veziroglu, *Int. J. Hydrog. Energy* **2008**, *33*, 6804; b) J. O. Bockris, *Int. J. Hydrog. Energy* **2013**, *38*, 2579; c) O. V. Marchenko, S. V. Solomin, *Int. J. Hydrog. Energy* **2015**, *40*, 3801.

[10] a) J. M. Ogden, *Annu. Rev. Energy. Environ.* **1999**, *24*, 227; b) D. G. Nocera, *Inorg. Chem.* **2009**, *48*, 10001.

[11] O. Edenhofer, R. Pichs Madruga, Y. Sokona, *Renewable energy sources and climate change mitigation*. *Special report of the Intergovernmental Panel on Climate Change*, Cambridge University Press, New York, **2012**.

[12] C. Philibert, *Solar energy perspectives*, OECD/IEA, Paris, **2011**.

[13] N. S. Lewis, *Science (New York, N.Y.)* **2007**, *315*, 798.

[14] a) L. Vergani, C. Colombo, G. Gobbi, F. M. Bolzoni, G. Fumagalli, *Procedia Engineering* **2014**, *74*, 468; b) M. B. Djukic, G. M. Bakic, V. S. Zeravcic, A. Sedmak,

B. Rajicic, *Corrosion* **2016**, *72*, 943; c) W. Zhong, Y. Cai, D. Tománek, *Nature* **1993**, *362*, 435.

[15] a) C. Fink, S. Katsyuba, G. Laurenczy, *Phys. Chem. Chem. Phys.* **2016**, *18*, 10764; b) D. Mellmann, E. Barsch, M. Bauer, K. Grabow, A. Boddien, A. Kammer, P. Sponholz, U. Bentrup, R. Jackstell, H. Junge et al., *Chemistry* **2014**, *20*, 13589; c) Y. Hartadi, D. Widmann, R. J. Behm, *Phys. Chem. Chem. Phys.* **2016**, *18*, 10781.

[16] R. Baum, *Chem. Eng. News* **1982**, *60*, 27.

[17] L. L. Tinker, N. D. McDaniel, S. Bernhard, *J. Mater. Chem.* **2009**, *19*, 3328.

[18] Web of Science®, "Citation report of search key terms "Water Reduction", "Water Oxidation", "Water Splitting" and "Artificial Photosynthesis" between 1900 and 2016.", can be found under http://apps.webofknowledge.com, **2017**.

[19] J. K. Hurst, *Science (New York, N.Y.)* **2010**, *328*, 315.

[20] T. J. Meyer, *Acc. Chem. Res.* **1989**, *22*, 163.

[21] a) S. H. Ahn, A. Manthiram, *J. Mater. Chem. A* **2017**, *5*, 2496; b) S. Anantharaj, S. R. Ede, K. Sakthikumar, K. Karthick, S. Mishra, S. Kundu, *ACS Catal.* **2016**, *6*, 8069; c) M. P. Browne, S. Stafford, M. O'Brien, H. Nolan, N. C. Berner, G. S. Duesberg, P. E. Colavita, Lyons, Michael E. G., *J. Mater. Chem. A* **2016**, *4*, 11397; d) P. Ganesan, A. Sivanantham, S. Shanmugam, *ACS Appl. Mater. Interfaces* **2017**, *9*, 12416; e) M. Y. Gao, C. Yang, Q. B. Zhang, J. R. Zeng, X. T. Li, Y. X. Hua, C. Y. Xu, P. Dong, *J. Mater. Chem. A* **2017**, *5*, 5797; f) X. Gao, H. Zhang, Q. Li, X. Yu, Z. Hong, X. Zhang, C. Liang, Z. Lin, *Angew. Chem. Int. Ed.* **2016**, *55*, 6290; g) Y. Tan, H. Wang, P. Liu, Y. Shen, C. Cheng, A. Hirata, T. Fujita, Z. Tang, M. Chen, *Energy Environ. Sci.* **2016**, *9*, 2257.

[22] a) J. W. Ager, M. R. Shaner, K. A. Walczak, I. D. Sharp, S. Ardo, *Energy Environ. Sci.* **2015**, *8*, 2811; b) J.-P. Becker, B. Turan, V. Smirnov, K. Welter, F. Urbain, J. Wolff, S. Haas, F. Finger, *J. Mater. Chem. A* **2017**, *5*, 4818; c) N. Bidin, S. R. Azni, M. A. Abu Bakar, A. R. Johari, D. H. F. Abdul Munap, M. F. Salebi, S. N. Abd. Razak, N. S. Sahidan, S. N. A. Sulaiman, *Int. J. Hydrog. Energy* **2017**, *42*, 133; d) S. Y. Chae, S. J. Park, O.-S. Joo, B. K. Min, Y. J. Hwang, *Solar Energy* **2016**, *135*, 821; e) A. Eftekhari, V. J. Babu, S. Ramakrishna, *Int. J. Hydrog. Energy* **2017**, *42*, 11078; f) M. Hansen, S. Troppmann, B. König, *Chem. Eur. J.* **2016**, *22*, 58; g) D. Kang, T. W. Kim, S. R. Kubota, A. C. Cardiel, H. G. Cha, K.-S. Choi, *Chem. Rev.* **2015**, *115*, 12839; h) A. Kudo, Y. Miseki, *Chem. Soc. Rev.* **2009**, *38*, 253; i) X. Li,

J. Yu, M. Jaroniec, *Chem. Soc. Rev.* **2016**, *45*, 2603; j) K. D. Malviya, H. Dotan, D. Shlenkevich, A. Tsyganok, H. Mor, A. Rothschild, *J. Mater. Chem. A* **2016**, *4*, 3091; k) S. Murcia-López, C. Fàbrega, D. Monllor-Satoca, M. D. Hernández-Alonso, G. Penelas-Pérez, A. Morata, J. R. Morante, T. Andreu, *ACS Appl. Mater. Interfaces* **2016**, *8*, 4076; l) C. Xiang, A. Z. Weber, S. Ardo, A. Berger, Y. Chen, R. Coridan, K. T. Fountaine, S. Haussener, S. Hu, R. Liu et al., *Angew. Chem. Int. Ed.* **2016**, *55*, 12974.

[23] S. Wang, P. Chen, J.-H. Yun, Y. Hu, L. Wang, *Angew. Chem. Int. Ed.* **2017**, *56*, 8500.

[24] a) S. B. Betzler, F. Podjaski, M. Beetz, K. Handloser, A. Wisnet, M. Handloser, A. Hartschuh, B. V. Lotsch, C. Scheu, *Chem. Mater.* **2016**, *28*, 7666; b) C.-F. Fu, Q. Luo, X. Li, J. Yang, *J. Mater. Chem. A* **2016**, *4*, 18892; c) T. Grewe, H. Tüysüz, *J. Mater. Chem. A* **2016**, *4*, 3007; d) A. M. Huerta-Flores, L. M. Torres-Martínez, E. Moctezuma, *Int. J. Hydrog. Energy* **2017**; e) S. Kamimura, M. Higashi, R. Abe, T. Ohno, *J. Mater. Chem. A* **2016**, *4*, 6116; f) J. H. Kim, H. Kaneko, T. Minegishi, J. Kubota, K. Domen, J. S. Lee, *ChemSusChem* **2016**, *9*, 61; g) G. Ma, S. Chen, Y. Kuang, S. Akiyama, T. Hisatomi, M. Nakabayashi, N. Shibata, M. Katayama, T. Minegishi, K. Domen, *J. Phys. Chem. Lett.* **2016**, *7*, 3892; h) S. Okamoto, M. Deguchi, S. Yotsuhashi, *J. Phys. Chem. C* **2017**, *121*, 1393; i) B. D. Sherman, M. V. Sheridan, K.-R. Wee, S. L. Marquard, D. Wang, L. Alibabaei, D. L. Ashford, T. J. Meyer, *J. Am. Chem. Soc.* **2016**, *138*, 16745; j) H. Shi, H. Liang, F. Ming, Z. Wang, *Angew. Chem. Int. Ed.* **2016**; k) D. Tang, Rettie, Alexander J. E., O. Mabayoje, B. R. Wygant, Y. Lai, Y. Liu, C. B. Mullins, *J. Mater. Chem. A* **2016**, *4*, 3034; l) B. J. Trześniewski, W. A. Smith, *J. Mater. Chem. A* **2016**, *4*, 2919; m) J. A. Vigil, T. N. Lambert, B. T. Christensen, *J. Mater. Chem. A* **2016**, *4*, 7549.

[25] a) Y. Hao, L. Li, J. Zhang, H. Luo, X. Zhang, E. Chen, *Int. J. Hydrog. Energy* **2017**, *42*, 5916; b) T.-F. Hou, R. Boppella, A. Shanmugasundaram, D. H. Kim, D.-W. Lee, *Int. J. Hydrog. Energy* **2017**, *42*, 15126; c) Y. Hou, M. Qiu, T. Zhang, J. Ma, S. Liu, X. Zhuang, C. Yuan, X. Feng, *Adv. Mater.* **2016**; d) Y. Jin, X. Yue, C. Shu, S. Huang, P. K. Shen, *J. Mater. Chem. A* **2017**, *5*, 2508; e) I. Khan, A. Abdalla, A. Qurashi, *Int. J. Hydrog. Energy* **2017**, *42*, 3431; f) I. H. Kwak, H. S. Im, D. M. Jang, Y. W. Kim, K. Park, Y. R. Lim, E. H. Cha, J. Park, *ACS Appl. Mater. Interfaces* **2016**, *8*, 5327; g) M. Ledendecker, J. S. Mondschein, O. Kasian, S. Geiger, D. Göhl, M. Schalenbach, A. Zeradjanin, S. Cherevko, R. E. Schaak, K. Mayrhofer,

Angew. Chem. Int. Ed. **2017**, *56*, 9767; h) J. Li, J. Li, X. Zhou, Z. Xia, W. Gao, Y. Ma, Y. Qu, *ACS Appl. Mater. Interfaces* **2016**, *8*, 10826; i) P. F. Liu, S. Yang, B. Zhang, H. G. Yang, *ACS Appl. Mater. Interfaces* **2016**, *8*, 34474; j) S. Sharma, S. Singh, N. Khare, *Int. J. Hydrog. Energy* **2016**, *41*, 21088; k) J. Wang, W. Yang, J. Liu, *J. Mater. Chem. A* **2016**, *4*, 4686; l) W. Wang, H. Wang, Q. Zhu, W. Qin, G. Han, J.-R. Shen, X. Zong, C. Li, *Angew. Chem. Int. Ed.* **2016**, *55*, 9229; m) Y. Wang, F. Li, X. Zhou, F. Yu, J. Du, L. Bai, L. Sun, *Angew. Chem. Int. Ed.* **2017**, *56*, 6911; n) F. Yan, Y. Wang, K. Li, C. Zhu, P. Gao, C. Li, X. Zhang, Y. Chen, *Chem. Eur. J.* **2017**, *23*, 10187; o) X. Yan, K. Li, L. Lyu, F. Song, J. He, D. Niu, L. Liu, X. Hu, X. Chen, *ACS Appl. Mater. Interfaces* **2016**, *8*, 3208; p) Y. Yan, B. Y. Xia, X. Ge, Z. Liu, A. Fisher, X. Wang, *Chem. Eur. J.* **2015**; q) Y. Yan, B. Y. Xia, B. Zhao, X. Wang, *J. Mater. Chem. A* **2016**, *4*, 17587; r) Y. Jia, L. Zhang, G. Gao, H. Chen, B. Wang, J. Zhou, M. T. Soo, M. Hong, X. Yan, G. Qian et al., *Adv. Mater.* **2017**, *29*, 1700017; s) J. Y. Kim, D. H. Youn, K. Kang, J. S. Lee, *Angew. Chem. Int. Ed.* **2016**, *55*, 10854.

[26] a) A. Annamalai, P. S. Shinde, T. H. Jeon, H. H. Lee, H. G. Kim, W. Choi, J. S. Jang, *Sol. Energy Mater. Sol. Cells* **2016**, *144*, 247; b) V. Artero, M. Fontecave, *Comptes Rendus Chimie* **2011**, *14*, 799; c) H. Chen, M. Lyu, G. Liu, L. Wang, *Chemistry* **2016**, *22*, 4802; d) X. Gao, J. Li, R. Du, J. Zhou, M.-Y. Huang, R. Liu, J. Li, Z. Xie, L.-Z. Wu, Z. Liu et al., *Adv. Mater.* **2017**, *29*, 1605308; e) A. T. Garcia-Esparza, T. Shinagawa, S. Ould-Chikh, M. Qureshi, X. Peng, N. Wei, D. H. Anjum, A. Clo, T.-C. Weng, D. Nordlund et al., *Angew. Chem. Int. Ed.* **2017**, *56*, 5780; f) D. A. Grave, H. Dotan, Y. Levy, Y. Piekner, B. Scherrer, K. D. Malviya, A. Rothschild, *J. Mater. Chem. A* **2016**, *4*, 3052; g) F. Guo, J. Chen, M. Zhang, B. Gao, B. Lin, Y. Chen, *J. Mater. Chem. A* **2016**, *4*, 10806; h) Y. Ham, T. Hisatomi, Y. Goto, Y. Moriya, Y. Sakata, A. Yamakata, J. Kubota, K. Domen, *J. Mater. Chem. A* **2016**, *4*, 3027; i) A. Han, H. Zhang, R. Yuan, H. Ji, P. Du, *ACS Appl. Mater. Interfaces* **2017**, *9*, 2240; j) C. Han, L. Yan, W. Zhao, Z. Liu, *Int. J. Hydrog. Energy* **2017**, *42*, 12276; k) L. Han, S. Dong, E. Wang, *Adv. Mater.* **2016**, *28*, 9266.

[27] Z. Li, W. Wang, C. Ding, Z. Wang, S. Liao, C. Li, *Energy Environ. Sci.* **2017**, *10*, 765.

[28] D. M. Fabian, S. Hu, N. Singh, F. A. Houle, T. Hisatomi, K. Domen, F. E. Osterloh, S. Ardo, *Energy Environ. Sci.* **2015**, *8*, 2825.

[29] a) Q. Dong, Y. Fang, Y. Shao, P. Mulligan, J. Qiu, L. Cao, J. Huang, *Science (New York, N.Y.)* **2015**, *347*, 967; b) M.-S. Balogun, W. Qiu, H. Yang, W. Fan, Y. Huang, P. Fang, G. Li, H. Ji, Y. Tong, *Energy Environ. Sci.* **2016**, *9*, 3411.

[30] G. Ciamician, *Science* **1912**, *36*, 385.

[31] a) H. Yoneyama, H. Sakamoto, H. Tamura, *Electrochim. Acta* **1975**, *20*, 341; b) A. J. Nozik, *Appl. Phys. Lett.* **1976**, *29*, 150; c) K. Ohashi, J. McCann, J. O. Bockris, *Nature* **1977**, *266*, 610.

[32] M. Graetzel, *Acc. Chem. Res.* **1981**, *14*, 376.

[33] a) V. Balzani, L. Moggi, M. F. Manfrin, F. Bolletta, M. Gleria, *Science* **1975**, *189*, 852; b) J. R. Bolton, *Science* **1978**, *202*, 705; c) E. Borgarello, J. Kiwi, E. Pelizzetti, M. Visca, M. Grätzel, *Nature* **1981**, *289*, 158.

[34] a) K. Kalyanasundaram, J. Kiwi, M. Grätzel, *Helv. Chim. Acta* **1978**, *61*, 2720; b) N. Sutin, C. Creutz, *Pure Appl. Chem.* **1980**, *52*, 2717.

[35] G. M. Brown, B. S. Brunschwig, C. Creutz, J. F. Endicott, N. Sutin, *J. Am. Chem. Soc.* **1979**, *101*, 1298.

[36] a) K. Sayama, K. Mukasa, R. Abe, Y. Abe, H. Arakawa, *Chem. Commun.* **2001**, 2416; b) J. Ye, Z. Zou, H. Arakawa, M. Oshikiri, M. Shimoda, A. Matsushita, T. Shishido, *J. Photochem. Photobiol. A* **2002**, *148*, 79.

[37] M. Kirch, J.-M. Lehn, J.-P. Sauvage, *Helv. Chim. Acta* **1979**, *62*, 1345.

[38] H. Ozawa, K. Sakai, *Chem. Commun.* **2011**, *47*, 2227.

[39] K. Sakai, H. Ozawa, *Coord. Chem. Rev.* **2007**, *251*, 2753.

[40] S. Fukuzumi, Y. Yamada, T. Suenobu, K. Ohkubo, H. Kotani, *Energy Environ. Sci.* **2011**, *4*, 2754.

[41] P. Du, J. Schneider, P. Jarosz, R. Eisenberg, *J. Am. Chem. Soc.* **2006**, *128*, 7726.

[42] G. Ajayakumar, M. Kobayashi, S. Masaoka, K. Sakai, *Dalton Trans.* **2011**, *40*, 3955.

[43] L. L. Tinker, N. D. McDaniel, P. N. Curtin, C. K. Smith, M. J. Ireland, S. Bernhard, *Chem. Eur. J.* **2007**, *13*, 8726.

[44] E. Amouyal, *Sol. Energy Mater. Sol. Cells* **1995**, *38*, 249.

[45] a) L. H. Gade, J. Lewis, *Koordinationschemie*, Wiley-VCH, Weinheim [u.a.], **2010**; b) E. C. Constable, *Metals and ligand reactivity. An introduction to the organic chemistry of metal complexes*, VCH, Weinheim, New York, **1996**; c) R. H.

Crabtree, *The Organometallic Chemistry of the Transition Metals, 4th Edition*, John Wiley & Sons, **2005**.

[46] a) J. W. Peters, *Curr. Opin. Struct. Biol.* **1999**, *9*, 670; b) H. Beinert, R. H. Holm, E. Münck, *Science* **1997**, *277*, 653; c) D. E. Wilcox, *Chem. Rev.* **1996**, *96*, 2435; d) R. H. Holm, S. Ciurli, J. A. Weigel in *Progress in Inorganic Chemistry* (Ed.: S. J. Lippard), Wiley, New York, N.Y., **1984**, pp. 1–74; e) O. V. Ozerov, *Chem. Soc. Rev.* **2008**, *38*, 83; f) M. M. T. Khan, S. B. Halligudi, S. Shukla, *Angew. Chem. Int. Ed. Engl.* **1988**, *27*, 1735.

[47] A. J. Esswein, D. G. Nocera, *Chem. Rev.* **2007**, *107*, 4022.

[48] V. Artero, M. Fontecave, *Coord. Chem. Rev.* **2005**, *249*, 1518.

[49] W. T. Eckenhoff, R. Eisenberg, *Dalton Trans.* **2012**, *41*, 13004.

[50] a) W. Martin, M. Müller, *Nature* **1998**, *392*, 37; b) M. Y. Darensbourg, E. J. Lyon, J. J. Smee, *Coord. Chem. Rev.* **2000**, *206-207*, 533; c) J. W. Peters, N. L. Lanzilotta, B. J. Lemon, L. C. Seefeldt, *Science* **1998**, *282*, 1853.

[51] H. R. Pershad, J. L. Duff, H. A. Heering, E. C. Duin, S. P. Albracht, F. A. Armstrong, *Biochemistry* **1999**, *38*, 8992.

[52] a) J. C. Fontecilla-Camps, A. Volbeda, C. Cavazza, Y. Nicolet, *Chem. Rev.* **2007**, *107*, 4273; b) F. Gloaguen, T. B. Rauchfuss, *Chem. Soc. Rev.* **2009**, *38*, 100; c) L. Sun, B. Åkermark, S. Ott, *Coord. Chem. Rev.* **2005**, *249*, 1653; d) C. Tard, C. J. Pickett, *Chem. Rev.* **2009**, *109*, 2245; e) Y. Na, M. Wang, J. Pan, P. Zhang, B. Akermark, L. Sun, *Inorg. Chem.* **2008**, *47*, 2805; f) S. Ott, M. Kritikos, B. Akermark, L. Sun, *Angew. Chem. Int. Ed. Engl.* **2003**, *42*, 3285; g) W. Gao, J. Liu, B. Akermark, L. Sun, *Inorg. Chem.* **2006**, *45*, 9169; h) S. Ott, M. Kritikos, B. Akermark, L. Sun, R. Lomoth, *Angew. Chem. Int. Ed. Engl.* **2004**, *43*, 1006; i) A. Silakov, M. T. Olsen, S. Sproules, E. J. Reijerse, T. B. Rauchfuss, W. Lubitz, *Inorg. Chem.* **2012**, *51*, 8617.

[53] a) P. Du, J. Schneider, G. Luo, W. W. Brennessel, R. Eisenberg, *Inorg. Chem.* **2009**, *48*, 4952; b) S. Losse, J. G. Vos, S. Rau, *Coord. Chem. Rev.* **2010**, *254*, 2492; c) B. D. Stubbert, J. C. Peters, H. B. Gray, *J. Am. Chem. Soc.* **2011**, *133*, 18070; d) P. Zhang, M. Wang, F. Gloaguen, L. Chen, F. Quentel, L. Sun, *Chem. Commun.* **2013**, *49*, 9455.

[54] a) V. Artero, M. Chavarot-Kerlidou, M. Fontecave, *Angew. Chem. Int. Ed.* **2011**, *50*, 7238; b) D. Basu, S. Mazumder, X. Shi, R. J. Staples, H. B. Schlegel, C. N. Verani, *Angew. Chem. Int. Ed.* **2015**, *54*, 7139; c) V. Fourmond, P.-A. Jacques, M.

Fontecave, V. Artero, *Inorg. Chem.* **2010**, *49*, 10338; d) N. Kaeffer, M. Chavarot-Kerlidou, V. Artero, *Acc. Chem. Res.* **2015**, *48*, 1286; e) N. Kaeffer, A. Morozan, V. Artero, *J. Phys. Chem. B* **2015**, *119*, 13707; f) S. Losse, J. G. Vos, S. Rau, *Coord. Chem. Rev.* **2010**, *254*, 2492; g) G. Smolentsev, B. Cecconi, A. Guda, M. Chavarot-Kerlidou, van Bokhoven, Jeroen A, M. Nachtegaal, V. Artero, *Chem. Eur. J.* **2015**, *21*, 15158.

[55] M. D. Kärkäs, E. V. Johnston, O. Verho, B. Åkermark, *Acc. Chem. Res.* **2014**, *47*, 100.

[56] C. Herrero, B. Lassallekaiser, W. Leibl, A. Rutherford, A. Aukauloo, *Coord. Chem. Rev.* **2008**, *252*, 456.

[57] G. F. Manbeck, K. J. Brewer, *Coord. Chem. Rev.* **2013**, *257*, 1660.

[58] F. Gärtner, B. Sundararaju, A.-E. Surkus, A. Boddien, B. Loges, H. Junge, P. H. Dixneuf, M. Beller, *Angew. Chem. Int. Ed.* **2009**, *48*, 9962.

[59] M. Wang, Y. Na, M. Gorlov, L. Sun, *Dalton Trans.* **2009**, 6458.

[60] R. Eisenberg, H. B. Gray, *Inorg. Chem.* **2008**, *47*, 1697.

[61] X. Sala, I. Romero, M. Rodríguez, L. Escriche, A. Llobet, *Angew. Chem. Int. Ed. Engl.* **2009**, *48*, 2842.

[62] a) W. A. Caspari, *Z. Phys. Chem.* **1899**, *30U*; b) J. Tafel, *Z. Phys. Chem.* **1905**, *50U*; c) A. Hickling, S. Hill, *Discuss. Faraday Soc.* **1947**, *1*, 236.

[63] a) A. Harriman, M.-C. Richoux, P. A. Christensen, S. Mosseri, P. Neta, *J. Chem. Soc., Faraday Trans. 1* **1987**, *83*, 3001; b) X. Chen, G. Chen, P. L. Yue, *J. Phys. Chem. B* **2001**, *105*, 4623.

[64] J.-R. Shen, *Annu. Rev. Plant Biol.* **2015**, *66*, 23.

[65] a) K. N. Ferreira, T. M. Iverson, K. Maghlaoui, J. Barber, S. Iwata, *Science (New York, N.Y.)* **2004**, *303*, 1831; b) J. S. Vrettos, J. Limburg, G. W. Brudvig, *Biochim. Biophys. Acta* **2001**, *1503*, 229; c) P. E. Siegbahn, *Curr. Opin. Chem. Biol.* **2002**, *6*, 227; d) Siegbahn, Per E. M., R. H. Crabtree, *J. Am. Chem. Soc.* **1999**, *121*, 117.

[66] a) S. W. Gersten, G. J. Samuels, T. J. Meyer, *J. Am. Chem. Soc.* **1982**, *104*, 4029; b) J. A. Gilbert, D. S. Eggleston, W. R. Murphy, D. A. Geselowitz, S. W. Gersten, D. J. Hodgson, T. J. Meyer, *J. Am. Chem. Soc.* **1985**, *107*, 3855.

[67] *Cambridge Structural Database (Version 5.38)*. *Update February 2017*, Cambridge Crystallographic Data Centre - CCDC Refcode DAKXOC, CCDC Number 1135854, deposited on 22.04.1986, Cambridge, **2017**.

[68] A. Llobet, M. E. Curry, H. T. Evans, T. J. Meyer, *Inorg. Chem.* **1989**, *28*, 3131.

[69] J. P. Collin, J. P. Sauvage, *Inorg. Chem.* **1986**, *25*, 135.

[70] International Labour Organization, "Baseline Survey on Child and Adult Workers in Informal Gold and Fluorspar Mining", can be found under http://www.ilo.org/wcmsp5/groups/public/---asia/---ro-bangkok/---ilo-beijing/documents/publication/wcms_538141.pdf, **2006**.

[71] International Labour Organization, "Out of sight – girls in mining", can be found under http://www.ilo.org/global/about-the-ilo/newsroom/features/WCMS_084034/lang--en/index.htm, **2007**.

[72] International Labour Organization, Jakarta Office, International Programme on the Elimination of Child Labour, "Child labour in the informal mining sector in east Kalimantan. A rapid assessment", can be found under http://www.ilo.org/wcmsp5/groups/public/---asia/---ro-bangkok/---ilo-jakarta/documents/publication/wcms_123820.pdf, **2004**.

[73] M. S. Winkler, M. J. Divall, G. R. Krieger, M. Z. Balge, B. H. Singer, J. Utzinger, *Environmental Impact Assessment Review* **2010**, *30*, 52.

[74] T. Navch, T. Bolormaa, B. Enkhtsetseg, D. Khurelmaa, B. Munkhjargal, *Informal gold mining in Mongolia*. *A baseline survey report covering Bornuur and Zaamar Soums, Tuv Aimag*, ILO, Bangkok, **2006**.

[75] S. M. Barnett, K. I. Goldberg, J. M. Mayer, *Nature chemistry* **2012**, *4*, 498.

[76] Z. Chen, T. J. Meyer, *Angew. Chem. Int. Ed.* **2013**, *52*, 700.

[77] M.-T. Zhang, Z. Chen, P. Kang, T. J. Meyer, *J. Am. Chem. Soc.* **2013**, *135*, 2048.

[78] a) X. Yang, M. B. Hall, *J. Am. Chem. Soc.* **2010**, *132*, 120; b) Z. Chen, J. J. Concepcion, X. Hu, W. Yang, P. G. Hoertz, T. J. Meyer, *Proc. Natl. Acad. Sci.* **2010**, *107*, 7225; c) J. J. Concepcion, D. K. Zhong, D. J. Szalda, J. T. Muckerman, E. Fujita, *Chem. Commun.* **2015**, *51*, 4105; d) Z. Chen, J. J. Concepcion, H. Luo, J. F. Hull, A. Paul, T. J. Meyer, *J. Am. Chem. Soc.* **2010**, *132*, 17670; e) J. J. Concepcion, M.-K. Tsai, J. T. Muckerman, T. J. Meyer, *J. Am. Chem. Soc.* **2010**, *132*, 1545.

[79] a) J. D. Blakemore, N. D. Schley, D. Balcells, J. F. Hull, G. W. Olack, C. D. Incarvito, O. Eisenstein, G. W. Brudvig, R. H. Crabtree, *J. Am. Chem. Soc.* **2010**, *132*, 16017; b) J. F. Hull, D. Balcells, J. D. Blakemore, C. D. Incarvito, O. Eisenstein, G. W. Brudvig, R. H. Crabtree, *J. Am. Chem. Soc.* **2009**, *131*, 8730.

[80] J. K. Nørskov, T. Bligaard, A. Logadottir, J. R. Kitchin, J. G. Chen, S. Pandelov, U. Stimming, *J. Electrochem. Soc.* **2005**, *152*, J23.

[81] M. Zeng, Y. Li, *J. Mater. Chem. A* **2015**, *3*, 14942.

[82] a) R. Schoch, with friendly permission adapted from:, *Active species identification of iron-based homogeneously and heterogeneously catalyzed reactions*. *Dissertation.*, Paderborn University, Faculty of Natural Sciences, Department of Chemistry, Paderborn, **2017**; b) Stock Exchange Frankfurt (Börse Frankfurt), "Historic price developments of metals", can be found under http://www.boerse-frankfurt.de/rohstoffe, **2017**.

[83] a) P. D. Frischmann, K. Mahata, F. Würthner, *Chem. Soc. Rev.* **2013**, *42*, 1847; b) V. Artero, M. Fontecave, *Comptes Rendus Chimie* **2011**, *14*, 799; c) J. H. Alstrum-Acevedo, M. K. Brennaman, T. J. Meyer, *Inorg. Chem.* **2005**, *44*, 6802; d) A. J. Bard, M. A. Fox, *Acc. Chem. Res.* **1995**, *28*, 141; e) D. Gust, T. A. Moore, A. L. Moore, *Acc. Chem. Res.* **2009**, *42*, 1890; f) L. Sun, L. Hammarström, B. Åkermark, S. Styring, *Chem. Soc. Rev.* **2001**, *30*, 36; g) S. Fukuzumi, K. Ohkubo, T. Suenobu, *Acc. Chem. Res.* **2014**, *47*, 1455.

[84] D. G. Nocera, *Acc. Chem. Res.* **2012**, *45*, 767.

[85] R. Abe, *J. Photochem. Photobiol. C* **2010**, *11*, 179.

[86] *Special report on renewable energy sources and climate change mitigation*. *Summary for policymakers and technical summary*, Intergovernmental Panel on Climate change, Geneva, **2012**.

[87] S.-P. Luo, E. Mejía, A. Friedrich, A. Pazidis, H. Junge, A.-E. Surkus, R. Jackstell, S. Denurra, S. Gladiali, S. Lochbrunner et al., *Angew. Chem. Int. Ed.* **2013**, *52*, 419.

[88] Web of Science®, "Citation report of search key word "Ru(bpy)" shows 8630 hits.", can be found under http://apps.webofknowledge.com, **2015**.

[89] D. V. Scaltrito, D. W. Thompson, J. A. O'Callaghan, G. J. Meyer, *Coord. Chem. Rev.* **2000**, *208*, 243.

[90] F. H. Burstall, *J. Chem. Soc.* **1936**, 173.

[91] a) G. A. Crosby, W. G. Perkins, D. M. Klassen, *J. Chem. Phys.* **1965**, *43*, 1498; b) G. A. Crosby, R. J. Watts, D. H. Carstens, *Science (New York, N.Y.)* **1970**, *170*, 1195.

[92] H. D. Gafney, A. W. Adamson, *J. Am. Chem. Soc.* **1972**, *94*, 8238.

[93] C. Creutz, N. Sutin, *Proc. Natl. Acad. Sci.* **1975**, *72*, 2858.

[94] a) B. Durham, J. V. Caspar, J. K. Nagle, T. J. Meyer, *J. Am. Chem. Soc.* **1982**, *104*, 4803; b) A. Juris, V. Balzani, F. Barigelletti, S. Campagna, P. Belser, A. von Zelewsky, *Coord. Chem. Rev.* **1988**, *84*, 85.

[95] M.-S. Chan, A. C. Wahl, *J. Phys. Chem.* **1978**, *82*, 2542.

[96] C. R. Bock, J. A. Connor, A. R. Gutierrez, T. J. Meyer, D. G. Whitten, B. P. Sullivan, J. K. Nagle, *J. Am. Chem. Soc.* **1979**, *101*, 4815.

[97] V. Balzani, G. Bergamini, F. Marchioni, P. Ceroni, *Coord. Chem. Rev.* **2006**, *250*, 1254.

[98] R. S. Khnayzer, C. E. McCusker, B. S. Olaiya, F. N. Castellano, *J. Am. Chem. Soc.* **2013**, *135*, 14068.

[99] D. R. Lide, *CRC Handbook of Chemistry and Physics*. *A ready-reference book of chemical and physical data*, CRC Press, Boca Raton, Fla, **2009**.

[100] C. Kutal, *Coord. Chem. Rev.* **1990**, *99*, 213.

[101] a) O. Horváth, *Coord. Chem. Rev.* **1994**, *135-136*, 303; b) M. Ruthkosky, C. A. Kelly, F. N. Castellano, G. J. Meyer, *Coord. Chem. Rev.* **1998**, *171*, 309.

[102] B. L. Vallee, Williams, R. J. P., *Proc. Natl. Acad. Sci.* **1968**, *59*, 498.

[103] a) R. Williams, *Inorg. Chim. Acta Rev.* **1971**, *5*, 137; b) Williams, Robert J. P., *Eur. J. Biochem. (European Journal of Biochemistry)* **1995**, *234*, 363; c) P. Comba, V. Müller, R. Remenyi, *J. Inorg. Biochem.* **2004**, *98*, 896.

[104] J. J. Warren, K. M. Lancaster, J. H. Richards, H. B. Gray, *J. Inorg. Biochem.* **2012**, *115*, 119.

[105] Olsson, Mats H. M., U. Ryde, B. O. Roos, K. Pierloot, *J. Biol. Inorg. Chem.* **1998**, *3*, 109.

[106] P. Comba, *Coord. Chem. Rev.* **2000**, *200-202*, 217.

[107] P. Comba, *Coord. Chem. Rev.* **1999**, *182*, 343.

[108] a) P. Comba, *Coord. Chem. Rev.* **2003**, *238-239*, 21; b) G. Chaka, J. L. Sonnenberg, H. B. Schlegel, M. J. Heeg, G. Jaeger, T. J. Nelson, L. A. Ochrymowycz, D. B. Rorabacher, *J. Am. Chem. Soc.* **2007**, *129*, 5217; c) L. Yang, D. R. Powell, R. P. Houser, *Dalton Trans.* **2007**, 955.

[109] A. Hoffmann, S. Binder, A. Jesser, R. Haase, U. Flörke, M. Gnida, M. Salomone Stagni, W. Meyer-Klaucke, B. Lebsanft, L. E. Grünig et al., *Angew. Chem. Int. Ed.* **2014**, *53*, 299.

[110] E. C. Riesgo, X. Jin, R. P. Thummel, *J. Org. Chem.* **1996**, *61*, 3017.

[111] F. A. Cotton, *Advanced inorganic chemistry*, Wiley, New York, **1999**.

[112] a) V. S. Bryantsev, M. S. Diallo, W. A. Goddard, *J Phys Chem A* **2009**, *113*, 9559; b) U. Ryde, Olsson, Mats H. M., B. O. Roos, A. C. Borin, *Theor. Chem. Acc.* **2001**, *105*, 452.

[113] C. T. Cunningham, Cunningham, Kurstan L. H., J. F. Michalec, D. R. McMillin, *Inorg. Chem.* **1999**, *38*, 4388.

[114] a) K. M. Lancaster, M.-E. Zaballa, S. Sproules, M. Sundararajan, S. DeBeer, J. H. Richards, A. J. Vila, F. Neese, H. B. Gray, *J. Am. Chem. Soc.* **2012**, *134*, 8241; b) K. M. Lancaster, S. D. George, K. Yokoyama, J. H. Richards, H. B. Gray, *Nature Chem* **2009**, *1*, 711; c) K. M. Lancaster, O. Farver, S. Wherland, E. J. Crane, J. H. Richards, I. Pecht, H. B. Gray, *J. Am. Chem. Soc.* **2011**, *133*, 4865; d) B. E. Bursten, *J. Am. Chem. Soc.* **1982**, *104*, 1299.

[115] K. L. Cunningham, C. R. Hecker, D. R. McMillin, *Inorg. Chim. Acta* **1996**, *242*, 143.

[116] R. E. Gamache, R. A. Rader, D. R. McMillin, *J. Am. Chem. Soc.* **1985**, *107*, 1141.

[117] M. K. Eggleston, D. R. McMillin, K. S. Koenig, A. J. Pallenberg, *Inorg. Chem.* **1997**, *36*, 172.

[118] D. R. McMillin, J. R. Kirchhoff, K. V. Goodwin, *Coord. Chem. Rev.* **1985**, *64*, 83.

[119] J. Windisch, M. Orazietti, P. Hamm, R. Alberto, B. Probst, *ChemSusChem* **2016**, *9*, 1719.

[120] N. Armaroli, *Chem. Soc. Rev.* **2001**, *30*, 113.

[121] D. R. McMillin, K. M. McNett, *Chem. Rev.* **1998**, *98*, 1201.

[122] R. M. Everly, R. Ziessel, J. Suffert, D. R. McMillin, *Inorg. Chem.* **1991**, *30*, 559.

[123] Palmer, Cynthia E. A., D. R. McMillin, C. Kirmaier, D. Holten, *Inorg. Chem.* **1987**, *26*, 3167.

[124] T. Bessho, E. C. Constable, M. Graetzel, A. Hernandez Redondo, C. E. Housecroft, W. Kylberg, M. K. Nazeeruddin, M. Neuburger, S. Schaffner, *Chem. Commun.* **2008**, 3717.

[125] S.-M. Kuang, D. G. Cuttell, D. R. McMillin, P. E. Fanwick, R. A. Walton, *Inorg. Chem.* **2002**, *41*, 3313.

[126] B. R. James, Williams, R. J. P., *J. Chem. Soc.* **1961**, 2007.

[127] V. Artero, M. Fontecave, *Chem. Soc. Rev.* **2013**, *42*, 2338.

[128] D. G. Cuttell, S.-M. Kuang, P. E. Fanwick, D. R. McMillin, R. A. Walton, *J. Am. Chem. Soc.* **2002**, *124*, 6.

[129] a) R. A. Rader, D. R. McMillin, M. T. Buckner, T. G. Matthews, D. J. Casadonte, R. K. Lengel, S. B. Whittaker, L. M. Darmon, F. E. Lytle, *J. Am. Chem. Soc.* **1981**, *103*, 5906; b) P. A. Breddels, Berdowski, Peter A. M., G. Blasse, D. R. McMillin, *J. Chem. Soc., Faraday Trans. 2* **1982**, *78*, 595.

[130] M. Ruthkosky, F. N. Castellano, G. J. Meyer, *Inorg. Chem.* **1996**, *35*, 6406.

[131] M. Heberle, S. Tschierlei, N. Rockstroh, M. Ringenberg, W. Frey, H. Junge, M. Beller, S. Lochbrunner, M. Karnahl, *Chem. Eur. J.* **2016**.

[132] E. Mejía, S.-P. Luo, M. Karnahl, A. Friedrich, S. Tschierlei, A.-E. Surkus, H. Junge, S. Gladiali, S. Lochbrunner, M. Beller, *Chem. Eur. J.* **2013**, *19*, 15972.

[133] A. Hillebrand, *Synthesis and Characterization of Different Substituted Diazapyridinaphanes and their Copper(I) Complexes*. *Master Thesis*, Paderborn University, Faculty of Natural Sciences, Department of Chemistry, Paderborn, **2015**.

[134] S. Pappalardo, F. Bottino, M. Di Grazia, P. Finocchiaro, A. Mamo, *Heterocycles* **1985**, *23*, 1881.

[135] F. Bottino, M. Di Grazia, P. Finocchiaro, F. R. Fronczek, A. Mamo, S. Pappalardo, *J. Org. Chem.* **1988**, *53*, 3521.

[136] M. Polasek, P. Caravan, *Inorg. Chem.* **2013**, *52*, 4084.

[137] M. Newcomb, J. M. Timko, D. M. Walba, D. J. Cram, *J. Am. Chem. Soc.* **1977**, *99*, 6392.

[138] W. Q. Ong, H. Zhao, X. Fang, S. Woen, F. Zhou, W. Yap, H. Su, Li, Sam F Y, H. Zeng, *Org. Lett.* **2011**, *13*, 3194.

[139] N. W. Alcock, G. Clarkson, P. B. Glover, G. A. Lawrance, P. Moore, M. Napitupulu, *Dalton Trans.* **2005**, 518.

[140] S.-s. Jew, B.-s. Park, D.-y. Lim, M. G. Kim, I. K. Chung, J. H. Kim, C. I. Hong, J.-K. Kim, H.-J. Park, J.-H. Lee et al., *Bioorganic Med. Chem. Lett.* **2003**, *13*, 609.

[141] X.-M. Gan, R. T. Paine, E. N. Duesler, H. Nöth, *Dalton Trans.* **2003**, 153.

[142] S. Abada, A. Lecointre, M. Elhabiri, L. J. Charbonnière, *Dalton Trans.* **2010**, *39*, 9055.

[143] T. Cheisson, A. Auffrant, *Dalton Trans.* **2014**, *43*, 13399.

[144] a) B. Tuemmler, G. Maass, E. Weber, W. Wehner, F. Voegtle, *J. Am. Chem. Soc.* **1977**, *99*, 4683; b) H. Takemura, H. Nakamichi, R. Nogita, T. Iwanaga, M. Yasutake, T. Shinmyozu, *Tetrahedron Lett.* **2003**, *44*, 5087; c) H. Takemura, T. Inazu, *J. Syn. Org. Chem., Jpn.* **1998**, *56*, 604.

[145] American Abstracts Service, *SciFinder*. *Search August 2017*, American Chemical Society, **2017**.

[146] *Cambridge Structural Database (Version 5.38)*. *Update February 2017*, Cambridge Crystallographic Data Centre, Cambridge, **2017**.

[147] G. Gros, J. Hasserodt, *Eur. J. Org. Chem.* **2015**, *2015*, 183.

[148] P. Dierks, *Synthese und Charakterisierung von 2,9-Bis(halogenmethyl)-1,10-phenanthrolinen und deren Cu(I)-Komplexe zur Verwendung als Photosensibilisatoren*. *Bachelor Thesis*, Paderborn University, Faculty of Natural Sciences, Department of Chemistry, Paderborn, **2016**.

[149] C. J. Chandler, L. W. Deady, J. A. Reiss, *J. Heterocyclic Chem.* **1981**, *18*, 599.

[150] J. C. García-Ramos, Y. Toledano-Magaña, L. G. Talavera-Contreras, M. Flores-Álamo, V. Ramírez-Delgado, E. Morales-León, L. Ortiz-Frade, A. G. Gutiérrez, A. Vázquez-Aguirre, C. Mejía et al., *Dalton Trans.* **2012**, *41*, 10164.

[151] T. Higashi, K. Inami, M. Mochizuki, *J. Heterocyclic Chem.* **2008**, *45*, 1889.

[152] G. R. Newkome, G. E. Kiefer, W. E. Puckett, T. Vreeland, *J. Org. Chem.* **1983**, *48*, 5112.

[153] J. Clayden, N. Greeves, S. G. Warren, *Organische Chemie*, Springer, Berlin, **2013**.

[154] H. Fakhraian, A. Mirzaei, *Org. Process Res. Dev.* **2004**, *8*, 401.

[155] H. Finkelstein, *Ber. Dtsch. Chem. Ges.* **1910**, *43*, 1528.

[156] M. J. Shapiro, *J. Org. Chem.* **1976**, *41*, 3197.

[157] J. B. Lambert, E. P. Mazzola, *Nuclear Magnetic Resonance Spectroscopy*. *An Introduction to Principles, Applications, and Experimental Methods*, Prentice Hall, Upper Saddle River, N.J., London, **2002**.

[158] E. Breitmaier, *Structure Elucidation by NMR in Organic Chemistry*, John Wiley & Sons, Ltd, Chichester, UK, **2002**.

[159] G. Schulze, J. Simon, *Massanalyse*. *Theorie und Praxis der Titrationen mit chemischen und physikalischen Indikationen*, De Gruyter, Berlin, **2009**.

[160] P. Dierks, *Synthese von 2,9-bis((diphenylphosphanyl)methyl)-1,10-phenanthrolin*. *Research Report from Advanced Inorganic Chemistry Pratical Course*, Paderborn University, Faculty of Natural Sciences, Department of Chemistry, Paderborn, **2016**.

[161] R. Ziessel, *Tetrahedron Lett.* **1989**, *30*, 463.

[162] a) A. A. Borisenko, N. M. Sergeyev, Y. Ustynyuk, *Mol. Phys.* **2006**, *22*, 715; b) C. Scriban, I. Kovacik, D. S. Glueck, *Organometallics* **2005**, *24*, 4871; c) J. C. Tebby, *CRC Handbook of phosphorus-31 nuclear magnetic resonance data*, CRC Press, Boca Raton, Fl., **1991**.

[163] W. Chen, X. Tang, W. Dou, Z. Ju, B. Xu, W. Xu, W. Liu, *Chem. Commun.* **2016**, *52*, 5124.

[164] M. I. Velasco, C. O. Kinen, R. Hoyos de Rossi, L. I. Rossi, *Dyes and Pigments* **2011**, *90*, 259.

[165] S. Berger, S. Braun, H.-O. Kalinowski (Eds.) *NMR-Spektroskopie von Nichtmetallen*, */ Stefan Berger; Siegmar Braun; Hans-Otto Kalinowski ; Bd. 3*, Thieme, Stuttgart [u.a.], **1993**.

[166] M. Hesse, H. Meier, B. Zeeh, *Spektroskopische Methoden in der organischen Chemie*, Thieme, Stuttgart, New York, **2005**.

[167] a) R. Dick, *Synthese und Reaktivität von 3,5-Bis-(diphenylphosphino)-substutuierten Pyrazoliumsalzen*. *Bachelor Thesis*, Paderborn University, Faculty of Natural Sciences, Department of Chemistry, Paderborn, **2011**; b) A. Klöpping, *Darstellung und Reaktivität von 3,5-disubstituierten Pyrazoliumsalzen*. *Dissertation*, Paderborn University, Faculty of Natural Sciences, Department of Chemistry, Paderborn, **2017**; c) K. Stührenberg, *Neuartige β-Diketiminate*. *Bachelor Thesis*, Paderborn University, Faculty of Natural Sciences, Department of Chemistry, Paderborn, **2012**.

[168] a) N. Armaroli, L. D. Cola, V. Balzani, J.-P. Sauvage, C. O. Dietrich-Buchecker, J.-M. Kern, *Faraday Trans.* **1992**, *88*, 553; b) M. S. Henry, M. Z. Hoffman, *J. Phys. Chem.* **1979**, *83*, 618; c) M. A. West, K. J. McCallum, R. J. Woods, S. J. Formosinho, *Trans. Faraday Soc.* **1970**, *66*, 2135.

[169] G. M. Badger, I. S. Walker, *J. Chem. Soc.* **1956**, *0*, 122.

[170] B. N. Bandyopadhyay, A. Harriman, *J. Chem. Soc., Faraday Trans. 1* **1977**, *73*, 663.

[171] S. G. Shulman, *Fluorescence News* **1973**, *7*, 33.

[172] H. Günzler, H.-U. Gremlich, *IR-Spektroskopie*. *Eine Einführung*, Wiley-VCH, Weinheim, **op. 2003**.

[173] P. J. Larkin, *Infrared and Raman spectroscopy*. *Principles and spectral interpretation*, Elsevier, Amsterdam [u.a.], **2011**.

[174] H. C. Guo, R. H. Zheng, H. J. Jiang, *Org. Prep. Proc. Int.* **2012**, *44*, 392.

[175] S. Bernhard, K. Takada, D. Jenkins, H. D. Abruña, *Inorg. Chem.* **2002**, *41*, 765.

[176] J.-M. Lehn, R. Ziessel, *Helv. Chim. Acta* **1988**, *71*, 1511.

[177] S. Ogawa, *J. Chem. Soc., Perkin Trans. 1* **1977**, 214.

[178] T. A. Khan, S. S. Ghani, *Polish J. Chem.* **2005**, *79*, 817.

[179] M. V. Nandakumar, S. Ghosh, C. Schneider, *Eur. J. Org. Chem.* **2009**, *2009*, 6393.

[180] a) K. P. C. Vollhardt, H. Butenschön, B. Elvers, N. E. Schore, *Organische Chemie*, Wiley-VCH, Weinheim, **2009**; b) R. Brückner, *Reaktionsmechanismen. Organische Reaktionen, Stereochemie, moderne Synthesemethoden*, Spektrum, Akad. Verl., Berlin, Heidelberg, **2011**; c) C.-L. Xiao, C.-Z. Wang, L.-Y. Yuan, B. Li, H. He, S. Wang, Y.-L. Zhao, Z.-F. Chai, W.-Q. Shi, *Inorg. Chem.* **2014**, *53*, 1712; d) D. Manna, S. Mula, A. Bhattacharyya, S. Chattopadhyay, T. K. Ghanty, *Dalton Trans.* **2015**, *44*, 1332; e) C. J. Chandler, L. W. Deady, J. A. Reiss, V. Tzimos, *J. Heterocyclic Chem.* **1982**, *19*, 1017.

[181] a) N. Armaroli, G. Accorsi, F. Cardinali, A. Listorti in *Topics in current chemistry*, *280-281* (Eds.: V. Balzani, S. Campagna, G. Accorsi), Springer, Berlin, New York, **2007**, pp. 69–115; b) S. Garakyaraghi, E. O. Danilov, C. E. McCusker, F. N. Castellano, *J. Phys. Chem. A* **2015**, *119*, 3181; c) S. Garakyaraghi, P. Koutnik, F. N. Castellano, *Phys. Chem. Chem. Phys.* **2017**, *19*, 16662; d) M. Iwamura, S. Takeuchi, T. Tahara, *Phys. Chem. Chem. Phys.* **2014**, *16*, 4143; e) L. Hua, M. Iwamura, S. Takeuchi, T. Tahara, *Phys. Chem. Chem. Phys.* **2015**, *17*, 2067; f) M. Iwamura, S. Takeuchi, T. Tahara, *Acc. Chem. Res.* **2015**, *48*, 782; g) M. Iwamura, H. Watanabe, K. Ishii, S. Takeuchi, T. Tahara, *J. Am. Chem. Soc.* **2011**, *133*, 7728; h) A. Barbieri, G. Accorsi, N. Armaroli, *Chem. Commun.* **2008**, 2185.

[182] G. Capano, M. Chergui, U. Rothlisberger, I. Tavernelli, T. J. Penfold, *J. Phys. Chem. A* **2014**, *118*, 9861.

[183] N. E. Jacobsen, *Understanding nuclear magnetic resonance spectroscopy. A practical guide*, Wiley; John Wiley [distributor], Hoboken, N.J., Chichester, **2007**.

[184] J. Keeler, *Understanding NMR spectroscopy*, Wiley, Chichester, **2009**.

[185] a) A. J. Blake, S. J. Hill, P. Hubberstey, W.-S. Li, *J. Chem. Soc., Dalton Trans.* **1998**, 909; b) A. Y. Kovalevsky, M. Gembicky, I. V. Novozhilova, P. Coppens, *Inorg. Chem.* **2003**, *42*, 8794; c) S. P. Watton, *Acta Cryst. Sect. E* **2010**, *66*, m1449.

[186] A. D. Laurent, D. Jacquemin, *Int. J. Quantum Chem.* **2013**, *113*, 2019.

[187] F. Neese, *J. Biol. Inorg. Chem.* **2006**, *11*, 702.

[188] M. E. Casida, M. Huix-Rotllant, *Annual review of physical chemistry* **2012**, *63*, 287.

[189] A. C. Tsipis, *RSC Adv.* **2014**, *4*, 32504.

[190] M. S. Lazorski, F. N. Castellano, *Polyhedron* **2014**, *82*, 57.

[191] A. K. Ichinaga, J. R. Kirchhoff, D. R. McMillin, C. O. Dietrich-Buchecker, P. A. Marnot, J. P. Sauvage, *Inorg. Chem.* **1987**, *26*, 4290.

[192] N. A. Gothard, M. W. Mara, J. Huang, J. M. Szarko, B. Rolczynski, J. V. Lockard, L. X. Chen, *J. Phys. Chem. A* **2012**, *116*, 1984.

[193] B. A. Gandhi, O. Green, J. N. Burstyn, *Inorg. Chem.* **2007**, *46*, 3816.

[194] O. Green, B. A. Gandhi, J. N. Burstyn, *Inorg. Chem.* **2009**, *48*, 5704.

[195] M. W. Mara, K. A. Fransted, L. X. Chen, *Coord. Chem. Rev.* **2015**, *282-283*, 2.

[196] M. Z. Zgierski, *J. Chem. Phys.* **2003**, *118*, 4045.

[197] M. W. Mara, N. E. Jackson, J. Huang, A. B. Stickrath, X. Zhang, N. A. Gothard, M. A. Ratner, L. X. Chen, *J. Phys. Chem. B* **2013**, *117*, 1921.

[198] M. W. Blaskie, D. R. McMillin, *Inorg. Chem.* **1980**, *19*, 3519.

[199] J. R. Lakowicz, C. D. Geddes, *Topics in Fluorescence Spectroscopy*. *Volume 4 - Probe Design and Chemical Sensing*, Plenum Press, New York, **1991-2005**.

[200] T. J. Penfold, S. Karlsson, G. Capano, F. A. Lima, J. Rittmann, M. Reinhard, M. H. Rittmann-Frank, O. Braem, E. Baranoff, R. Abela et al., *J. Phys. Chem. A* **2013**, *117*, 4591.

[201] E. Gumienna-Kontecka, Y. Rio, C. Bourgogne, M. Elhabiri, R. Louis, A.-M. Albrecht-Gary, J.-F. Nierengarten, *Inorg. Chem.* **2004**, *43*, 3200.

[202] a) C. E. McCusker, F. N. Castellano, *Inorg. Chem.* **2013**, *52*, 8114; b) S. Garakyaraghi, P. D. Crapps, C. E. McCusker, F. N. Castellano, *Inorg. Chem.* **2016**, *55*, 10628.

[203] R. Holze, R. Börnstein, H. Landolt, W. Martienssen, *Electrochemical thermodynamics and kinetics*. *Group IV: Physical Chemistry; Volume 9: Electrochemistry; Subvolume A Electrochemical Thermodynamics and Kinetics*, Springer, Berlin, **2007**.

[204] I. M. Kolthoff, J. F. Coetzee, *J. Am. Chem. Soc.* **1957**, *79*, 1852.

[205] A. I. Popov, D. H. Geske, *J. Am. Chem. Soc.* **1958**, *80*, 1340.

[206] F. Baucke, R. Bertram, K. Cruse, *J. Electroanal. Chem.* **1971**, *32*, 247.

[207] C. V. Krishnan, C. Creutz, H. A. Schwarz, N. Sutin, *J. Am. Chem. Soc.* **1983**, *105*, 5617.

[208] S. E. Braslavsky, *Pure Appl. Chem.* **2007**, *79*, 359.

[209] R. F. Winter in *Spectroelectrochemistry* (Eds.: W. Kaim, A. Klein), Royal Society of Chemistry, Cambridge, **op. 2008**, pp. 145–206.

[210] a) P. Du, J. Schneider, P. Jarosz, J. Zhang, W. W. Brennessel, R. Eisenberg, *J. Phys. Chem. B* **2007**, *111*, 6887; b) M. Kobayashi, S. Masaoka, K. Sakai, *Angew. Chem. Int. Ed.* **2012**, *51*, 7431; c) D. Miller, G. McLendon, *Inorg. Chem.* **1981**, *20*, 950.

[211] J. Kiwi, M. Grätzel, *Nature* **1979**, *281*, 657.

[212] S. Fischer, D. Hollmann, S. Tschierlei, M. Karnahl, N. Rockstroh, E. Barsch, P. Schwarzbach, S.-P. Luo, H. Junge, M. Beller et al., *ACS Catal.* **2014**, 1845.

[213] E. Mejía, S.-P. Luo, M. Karnahl, A. Friedrich, S. Tschierlei, A.-E. Surkus, H. Junge, S. Gladiali, S. Lochbrunner, M. Beller, *Chem. Eur. J.* **2013**, *19*, 15972.

[214] L. Lemus, J. Guerrero, J. Costamagna, G. Estiu, G. Ferraudi, A. G. Lappin, A. Oliver, B. C. Noll, *Inorg. Chem.* **2010**, *49*, 4023.

[215] R. Devi, E. Burkholder, J. Zubieta, *Inorg. Chim. Acta* **2003**, *348*, 150.

[216] R. E. Marsh, *Acta Cryst. Sect. B* **1997**, *53*, 317.

[217] S. P. Watton, *Acta Cryst. Sect. E* **2009**, *65*, m585-6.

[218] N. Wiberg, *Lehrbuch der anorganischen Chemie*. *[mit 188 Tabellen]*, De Gruyter, Berlin [u.a.], **2007**.

[219] P. D. Boyd, J. Hope, R. L. Martin, *Inorg. Chim. Acta* **1980**, *44*, L291-L294.

[220] P. C. Healy, C. Pakawatchai, A. H. White, *J. Chem. Soc., Dalton Trans.* **1985**, 2531.

[221] T. W. Hambley, C. L. Raston, A. H. White, *Aust. J. Chem.* **1977**, *30*, 1965.

[222] D. Boys, C. Escobar, S. Martínez-Carrera, *Acta Cryst. Sect. B* **1981**, *37*, 351.

[223] a) F. M. Shen, S. F. Lush, *Acta Cryst. Sect. E* **2016**, *72*, 1577; b) S. J. Hill, P. Hubberstey, W.-S. Li, *Polyhedron* **1997**, *16*, 2447; c) C. J. Simmons, K. Seff, F. Clifford, B. J. Hathaway, *Acta Cryst. Sect. C* **1983**, *39*, 1360.

[224] A. Bondi, *J. Phys. Chem.* **1964**, *68*, 441.

[225] O. P. Anderson, *J. Chem. Soc., Dalton Trans.* **1973**, 1237.

[226] a) L. Wang, X.-M. Gu, D.-D. Ye, W.-L. Zhang, L. Ni; b) M. S. Haddad, S. R. Wilson, D. J. Hodgson, D. N. Hendrickson, *J. Am. Chem. Soc.* **1981**, *103*, 384.

[227] J. R. Khusnutdinova, J. Luo, N. P. Rath, L. M. Mirica, *Inorg. Chem.* **2013**, *52*, 3920.

[228] a) R. R. Jacobson, Z. Tyeklár, K. D. Karlin, *Inorg. Chim. Acta* **1991**, *181*, 111; b) A. W. Maverick, M. L. Ivie, F. R. Fronczek, *J. Coord. Chem.* **1990**, *21*, 315; c) O. A. Varzatskii, S. V. Shul'ga, A. S. Belov, V. V. Novikov, A. V. Dolganov, A. V. Vologzhanina, Y. Z. Voloshin, *Dalton Trans.* **2014**, *43*, 17934.

[229] A. B. Ene, M. Bauer, T. Archipov, E. Roduner, *Phys. Chem. Chem. Phys.* **2010**, *12*, 6520.

[230] N. E. Tokel-Takvoryan, R. E. Hemingway, A. J. Bard, *J. Am. Chem. Soc.* **1973**, *95*, 6582.

[231] T. Zhang, C. Wang, S. Liu, J.-L. Wang, W. Lin, *J. Am. Chem. Soc.* **2014**, *136*, 273.

[232] a) J. M. de Ruiter, F. Buda, *Phys. Chem. Chem. Phys.* **2017**, *19*, 4208; b) S. G. Winikoff, C. J. Cramer, *Catal. Sci. Technol.* **2014**, *4*, 2484.

[233] C. M. Harris, E. Sinn, W. R. Walker, P. R. Woolliams, *Aust. J. Chem.* **1968**, 631.

[234] a) Y.-K. He, Z.-B. Han, *Acta Cryst. Sect. E* **2006**, *62*, m2676-m2677; b) N. Alvarez, N. Veiga, S. Iglesias, M. H. Torre, G. Facchin, *Polyhedron* **2014**, *68*, 295; c) C.-B. Liu, J. Chen, H.-Y. Bai, S.-T. Wang, Q.-W. Wang, G.-B. Che, *Cambridge Crystallographic Data Centre* **2013**, *CCDC 859709*.

[235] K. Nakamoto, *Infrared and Raman Spectra of Inorganic and Coordination Compounds*, John Wiley & Sons, Inc, Hoboken, NJ, USA, **2008**.

[236] E. A. Evsei, V. R. Pupkevich, A. M. Kirillov, E. A. Telushchenko, M. N. Kopylovich, A. K. Baev, *J. Appl. Spectrosc.* **2001**, *68*, 736.

[237] L. Lu, M.-L. Zhu, P. Yang, *J. Inorg. Biochem.* **2003**, *95*, 31.

[238] a) Y.-Q. Zheng, J.-L. Lin, J. Sun, *Z. Anorg. Allg. Chem.* **2001**, *627*, 1647; b) Y.-Q. Zheng, J. Sun, J.-L. Lin, *Z. Anorg. Allg. Chem. (Zeitschrift für anorganische und allgemeine Chemie)* **2000**, *626*, 613; c) Y.-Q. Zheng, J.-L. Lin, J. Sun, *Z. Kristallogr. - New Cryst. Struct.* **2001**, *216*.

[239] Y.-Q. Zheng, J.-L. Lin, *Z. Anorg. Allg. Chem.* **2002**, *628*, 203.

[240] Z.-W. Mao, F. W. Heinemann, G. Liehr, R. van Eldik, *J. Chem. Soc., Dalton Trans.* **2001**, 3652.

[241] a) C. Roy Choudhury, S. K. Dey, S. Mitra, V. Gramlich, *Dalton Trans.* **2003**, 1059; b) R. D. Maples, A. N. Cain, B. P. Burke, J. D. Silversides, R. E. Mewis, T. D'huys, D. Schols, D. P. Linder, S. J. Archibald, T. J. Hubin, *Chem. Eur. J.* **2016**, *22*, 12916.

[242] Z.-W. Mao, G. Liehr, R. van Eldik, *J. Am. Chem. Soc.* **2000**, *122*, 4839.

[243] H. S. Preston, C. H. L. Kennard, *J. Chem. Soc., A* **1969**, *0*, 2955.

[244] P. Garrido-Barros, I. Funes-Ardoiz, S. Drouet, J. Benet-Buchholz, F. Maseras, A. Llobet, *J. Am. Chem. Soc.* **2015**, *137*, 6758.

[245] a) J. L. Boyer, J. Rochford, M.-K. Tsai, J. T. Muckerman, E. Fujita, *Coord. Chem. Rev.* **2010**, *254*, 309; b) J. T. Muckerman, D. E. Polyansky, T. Wada, K. Tanaka, E. Fujita, *Inorg. Chem.* **2008**, *47*, 1787; c) P. J. Chirik, K. Wieghardt, *Science (New York, N.Y.)* **2010**, *327*, 794; d) M. M. R. Choudhuri, W. Kaim, B. Sarkar, R. J. Crutchley, *Inorg. Chem.* **2013**, *52*, 11060; e) D. W. Shaffer, Y. Xie, D. J. Szalda, J. J. Concepcion, *Inorg. Chem.* **2016**, *55*, 12024.

[246] D. L. Gerlach, S. Bhagan, A. A. Cruce, D. B. Burks, I. Nieto, H. T. Truong, S. P. Kelley, C. J. Herbst-Gervasoni, K. L. Jernigan, M. K. Bowman et al., *Inorg. Chem.* **2014**, *53*, 12689.

[247] M. D. Kärkäs, O. Verho, E. V. Johnston, B. Åkermark, *Chem. Rev.* **2014**, *114*, 11863.

[248] A. Moghimi, R. Alizadeh, A. Shokrollahi, H. Aghabozorg, M. Shamsipur, A. Shockravi, *Inorg. Chem.* **2003**, *42*, 1616.

[249] A. Moghimi, R. Alizadeh, H. Aghabozorg, A. Shockravi, M. C. Aragoni, F. Demartin, F. Isaia, V. Lippolis, A. Harrison, A. Shokrollahi et al., *J. Mol. Struct.* **2005**, *750*, 166.

[250] W. Harnischmacher, R. Hoppe, *Angew. Chem. Int. Ed. Engl.* **1973**, *12*, 582.

[251] W. Sinha, M. G. Sommer, N. Deibel, F. Ehret, M. Bauer, B. Sarkar, S. Kar, *Angew. Chem. Int. Ed.* **2015**, *54*, 13769.

[252] V. Nair, A. Deepthi, *Chem. Rev.* **2007**, *107*, 1862.

[253] E. Wadsworth, F. R. Duke, C. A. Goetz, *Anal. Chem.* **2012**, *29*, 1824.

[254] A. R. Parent, R. H. Crabtree, G. W. Brudvig, *Chem. Soc. Rev.* **2013**, *42*, 2247.

[255] A. Ikeda-Ohno, S. Tsushima, C. Hennig, T. Yaita, G. Bernhard, *Dalton Trans.* **2012**, *41*, 7190.

[256] a) M. K. Coggins, M.-T. Zhang, A. K. Vannucci, C. J. Dares, T. J. Meyer, *J. Am. Chem. Soc.* **2014**, *136*, 5531; b) G. Panchbhai, W. M. Singh, B. Das, R. T. Jane, A. Thapper, *Eur. J. Inorg. Chem.* **2016**, *2016*, 3262; c) W. C. Ellis, N. D. McDaniel, S. Bernhard, T. J. Collins, *J. Am. Chem. Soc.* **2010**, *132*, 10990.

[257] a) J. D. Blakemore, R. H. Crabtree, G. W. Brudvig, *Chem. Rev.* **2015**, *115*, 12974; b) P. Manna, J. Debgupta, S. Bose, S. K. Das, *Angew. Chem. Int. Ed.* **2016**;

c) H. Lv, Y. V. Geletii, C. Zhao, J. W. Vickers, G. Zhu, Z. Luo, J. Song, T. Lian, D. G. Musaev, C. L. Hill, *Chem Soc Rev* **2012**, *41*, 7572.

[258] E. Tas, M. Aslanoglu, A. Kilic, Z. Kara, *J. Coord. Chem.* **2006**, *59*, 861.

[259] a) K. J. Fisher, K. L. Materna, B. Q. Mercado, R. H. Crabtree, G. W. Brudvig, *ACS Catal.* **2017**, *7*, 3384; b) X.-J. Su, M. Gao, L. Jiao, R.-Z. Liao, Siegbahn, Per E. M., J.-P. Cheng, M.-T. Zhang, *Angew. Chem. Int. Ed.* **2015**, *54*, 4909; c) R.-J. Xiang, H.-Y. Wang, Z.-J. Xin, C.-B. Li, Y.-X. Lu, X.-W. Gao, H.-M. Sun, R. Cao, *Chem. Eur. J.* **2016**, *22*, 1602; d) W.-B. Yu, Q.-Y. He, X.-F. Ma, H.-T. Shi, X. Wei, *Dalton Trans.* **2015**, *44*, 351.

[260] B. Spingler, S. Schnidrig, T. Todorova, F. Wild, *CrystEngComm* **2012**, *14*, 751.

[261] Bruker AXS Inc., *SAINT (version 6.02)*, Madison, Wisconsin, USA, **2002**.

[262] G. M. Sheldrick, *SADABS*, University of Göttingen, Germany, **2004**.

[263] G. M. Sheldrick, *Acta crystallographica. Section A, Foundations of crystallography* **2008**, *64*, 112.

[264] A. L. Spek, *Acta crystallographica. Section D, Biological crystallography* **2009**, *65*, 148.

[265] Bruker Optik GmbH, *OPUS (version 7.2.139.1294)*. IR package, **2012**.

[266] a) T. S. Ertel, H. Bertagnolli, S. Hückmann, U. Kolb, D. Peter, *Appl. Spectrosc.* **1992**, *46*, 690; b) M. Newville, *J. Synchrotron Rad.* **2001**, *8*, 322; c) M. Newville, P. Līviņš, Y. Yacoby, J. J. Rehr, E. A. Stern, *Phys. Rev. B* **1993**, *47*, 14126; d) B. Ravel, M. Newville, *J. Synchrotron Rad.* **2005**, *12*, 537.

[267] N. Binsted, S. S. Hasnain, *EXCURV98 Manual*, Daresbury, UK.

[268] N. Binsted, S. S. Hasnain, *J. Synchrotron Rad.* **1996**, *3*, 185.

[269] M. Bauer, H. Bertagnolli, *J. Phys. Chem. B* **2007**, *111*, 13756.

[270] D. C. Koningsberger, B. L. Mojet, G. E. van Dorssen, D. E. Ramaker, *Topics in Catalysis* **2000**, *10*, 143.

[271] A. S. R. Koti, M. M. G. Krishna, N. Periasamy, *J. Phys. Chem. A* **2001**, *105*, 1767.

[272] a) W. Demtröder, *Experimentalphysik*. *Band 2 - Elektrizität und Wärme*, Springer, Berlin, Heidelberg, New York, **2004**; b) N. Tkachenko, *Optical Spectroscopy*. *Methods and Instrumentations*, Elsevier Science, San Diego, CA, USA, **2006**.

[273] P. Zimmer, *Temperature and Blind Correction for Water Splitting Catalysis*. Personal correspondence, **2016**, Paderborn.

[274] P. Zimmer, *Unpublished Dissertation*, Paderborn University, Faculty of Natural Sciences, Department of Chemistry, Paderborn, **2017**.

[275] P. Raybaut, G. Davar, *Python(x,y) (version 2.7.10.0). the scientific Python distribution.*, **2017**.

[276] *PC²* - *Paderborn Center for Parallel Computing*, Universität Paderborn, Paderborn, **2016**.

[277] F. Neese, *WIREs Comput Mol Sci* **2012**, *2*, 73.

[278] J. Tao, J. P. Perdew, V. N. Staroverov, G. E. Scuseria, *Phys. Rev. Lett.* **2003**, *91*.

[279] V. N. Staroverov, G. E. Scuseria, J. Tao, J. P. Perdew, *J. Chem. Phys.* **2003**, *119*, 12129.

[280] A. Schäfer, H. Horn, R. Ahlrichs, *J. Chem. Phys.* **1992**, *97*, 2571.

[281] A. Schäfer, C. Huber, R. Ahlrichs, *J. Chem. Phys.* **1994**, *100*, 5829.

[282] F. Weigend, R. Ahlrichs, *Phys. Chem. Chem. Phys.* **2005**, *7*, 3297.

[283] a) S. Grimme, J. Antony, S. Ehrlich, H. Krieg, *J. Chem. Phys.* **2010**, *132*, 154104; b) S. Grimme, S. Ehrlich, L. Goerigk, *J. Comput. Chem.* **2011**, *32*, 1456.

[284] a) A. Jesser, M. Rohrmüller, W. G. Schmidt, S. Herres-Pawlis, *J. Comput. Chem.* **2014**, *35*, 1; b) A. Hoffmann, R. Grunzke, S. Herres-Pawlis, *J Comput Chem* **2014**; c) A. Hoffmann, M. Rohrmüller, A. Jesser, I. dos Santos Vieira, W. G. Schmidt, S. Herres-Pawlis, *J. Comput. Chem.* **2014**, *35*, 2146; d) M. Witte, U. Gerstmann, A. Neuba, G. Henkel, W. G. Schmidt, *J. Comput. Chem.* **2016**.

[285] A. V. Marenich, C. J. Cramer, D. G. Truhlar, *J. Phys. Chem. B* **2009**, *113*, 6378.

[286] D. A. Pantazis, X.-Y. Chen, C. R. Landis, F. Neese, *J. Chem. Theory Comput.* **2008**, *4*, 908.

[287] a) S. DeBeer George, T. Petrenko, F. Neese, *Inorg. Chim. Acta* **2008**, *361*, 965; b) S. DeBeer George, F. Neese, *Inorg. Chem.* **2010**, *49*, 1849; c) S. DeBeer George, T. Petrenko, F. Neese, *J. Phys. Chem. A* **2008**, *112*, 12936.

[288] F. Neese, *Inorg. Chim. Acta* **2002**, *337*, 181.

[289] M. U. Delgado-Jaime, S. DeBeer, *J. Comput. Chem.* **2012**, *33*, 2180.

[290] S. I. Gorelsky, *AOMix: Program for Molecular Orbital Analysis; version 6.87*. http://www.sg-chem.net/, University of Ottawa, **2014**.

[291] G. Knizia, Klein, Johannes E M N, *Angew. Chem. Int. Ed.* **2015**, *54*, 5518.

[292] J. F. Gay, R. N. Maxson, J. Kleinberg, R. E. Haan in *Inorganic Syntheses*, *Vol. 2* (Ed.: W. C. Fernelius), John Wiley & Sons, Inc, Hoboken, NJ, USA, **1946**, pp. 147–151.

[293] M. Baudler, G. Brauer, *Handbuch der präparativen anorganischen Chemie in drei Bänden*, Ferdinand Enke, Stuttgart, **1975-1981**.

[294] C.-M. Che, Z.-Y. Li, K.-Y. Wong, C.-K. Poon, T. C. Mak, S.-M. Peng, *Polyhedron* **1994**, *13*, 771.

[295] G. Lee, Y. Miyahara, T. Inazu, *Chem. Lett.* **1996**, 873.

[296] W.-T. Lee, S. Xu, D. A. Dickie, J. M. Smith, *Eur. J. Inorg. Chem.* **2013**, *2013*, 3867.

[297] P. L. deBenneville, J. H. Macartney, *J. Am. Chem. Soc.* **1950**, *72*, 3073.

[298] Becker, Heinz G. O, *Organikum*, Wiley-VCH, Weinheim, **2001**.

[299] C. O. Dietrick-Buchecker, P. A. Marnot, J. P. Sauvage, *Tetrahedron Lett.* **1982**, *23*, 5291.

[300] a) H. Wolpher, O. Johansson, M. Abrahamsson, M. Kritikos, L. Sun, B. Åkermark, *Inorg. Chem. Commun.* **2004**, *7*, 337; b) O. Andell, J. Maaranen, J. Hoikka, T. Vanne, S. Rautio, WO0216374 (A1), **2001**.

[301] G. Dyker, O. Muth, *Eur. J. Org. Chem.* **2004**, *2004*, 4319.

[302] O. E. Alawode, V. K. Naganaboina, T. Liyanage, J. Desper, S. Rayat, *Org. Lett.* **2014**, *16*, 1494.

8 List of Figures

9 **List of Tables**

9 List of Tables

10 **Appendix**

10.1 NMR and mass spectra

10.1.1 Phosphorus tribromide

^{31}P-NMR

(50.7 MHz, $CDCl_3$ in capillary)

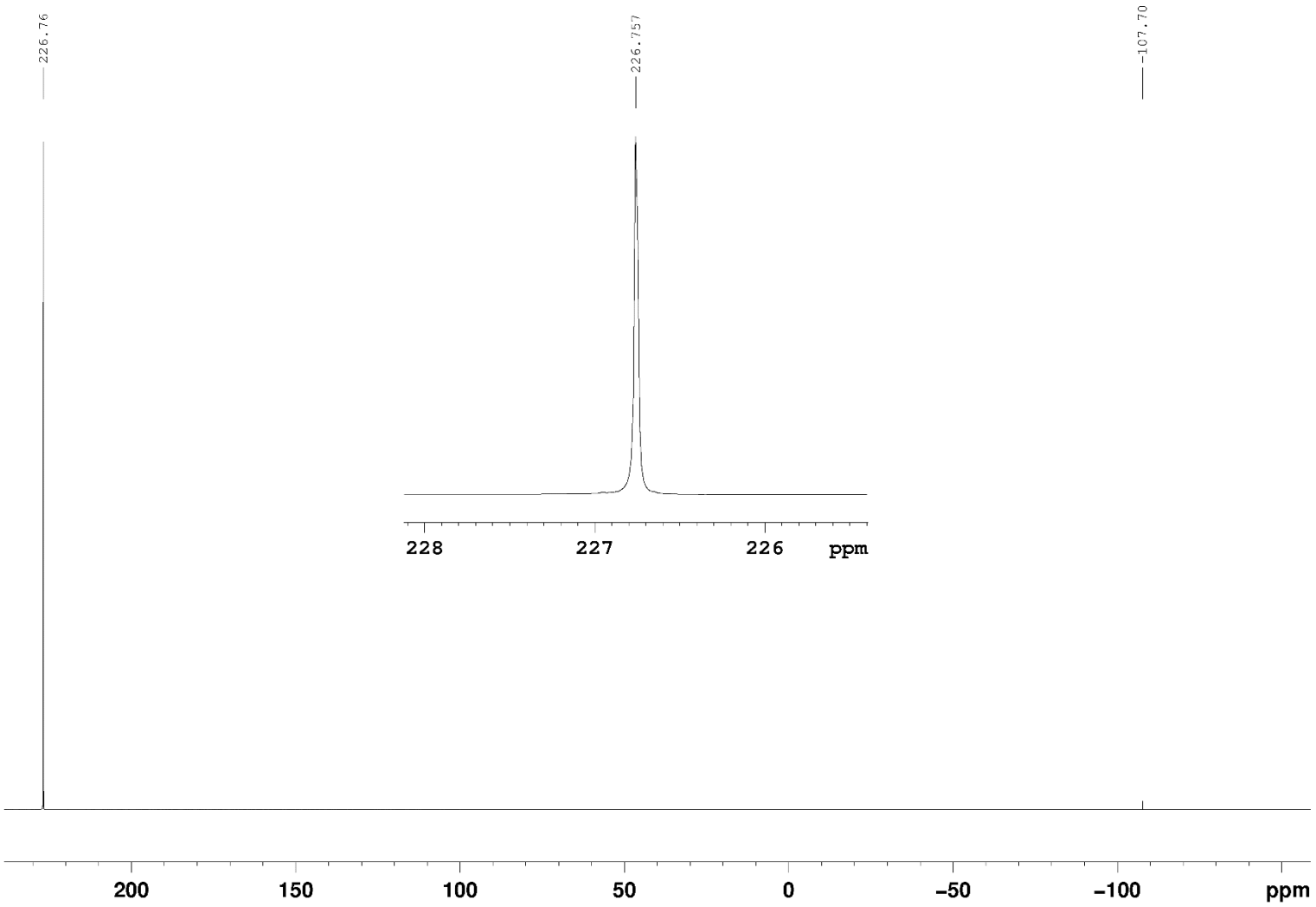

10.1.2 5H-6,7-Dihydro[1,4]diazepino[1,2,3,4-lmn][1,10]phenanthrolinium dibromide (Phen-Pr)

^{1}H-NMR

(500 MHz, D_2O)

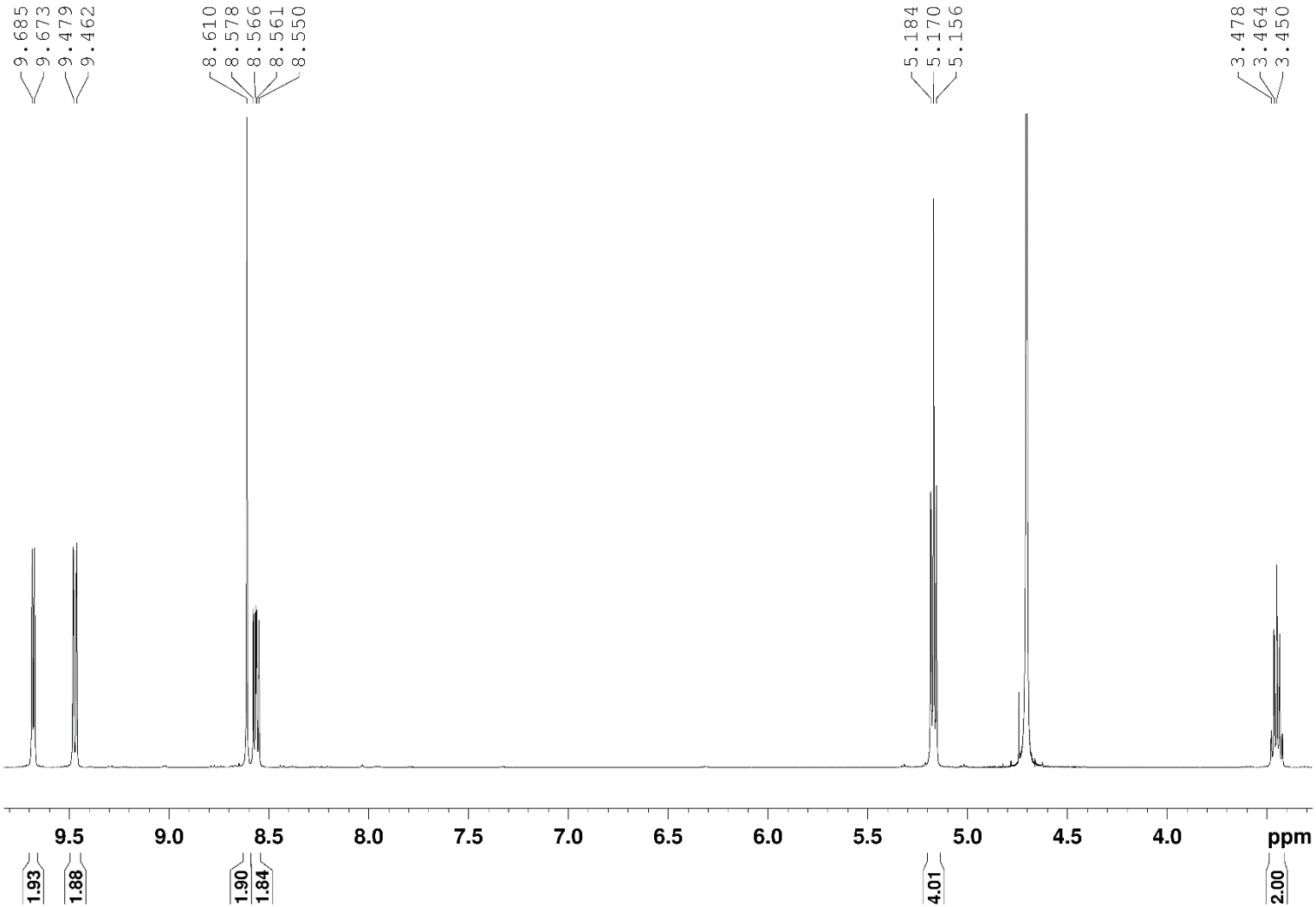

^{13}C-NMR

(125 MHz, D_2O)

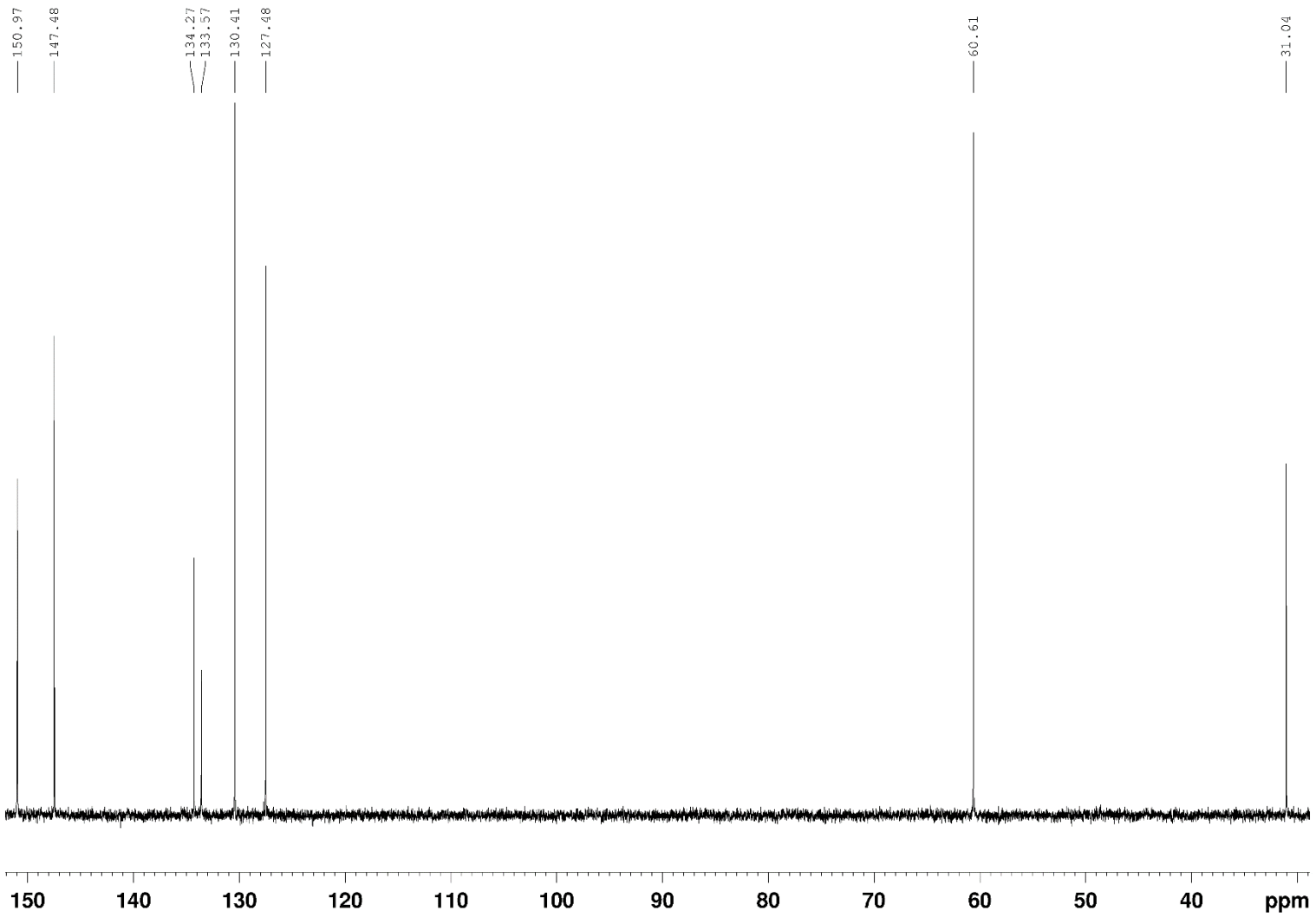

^{15}N-NMR

(50.7 MHz, D_2O)

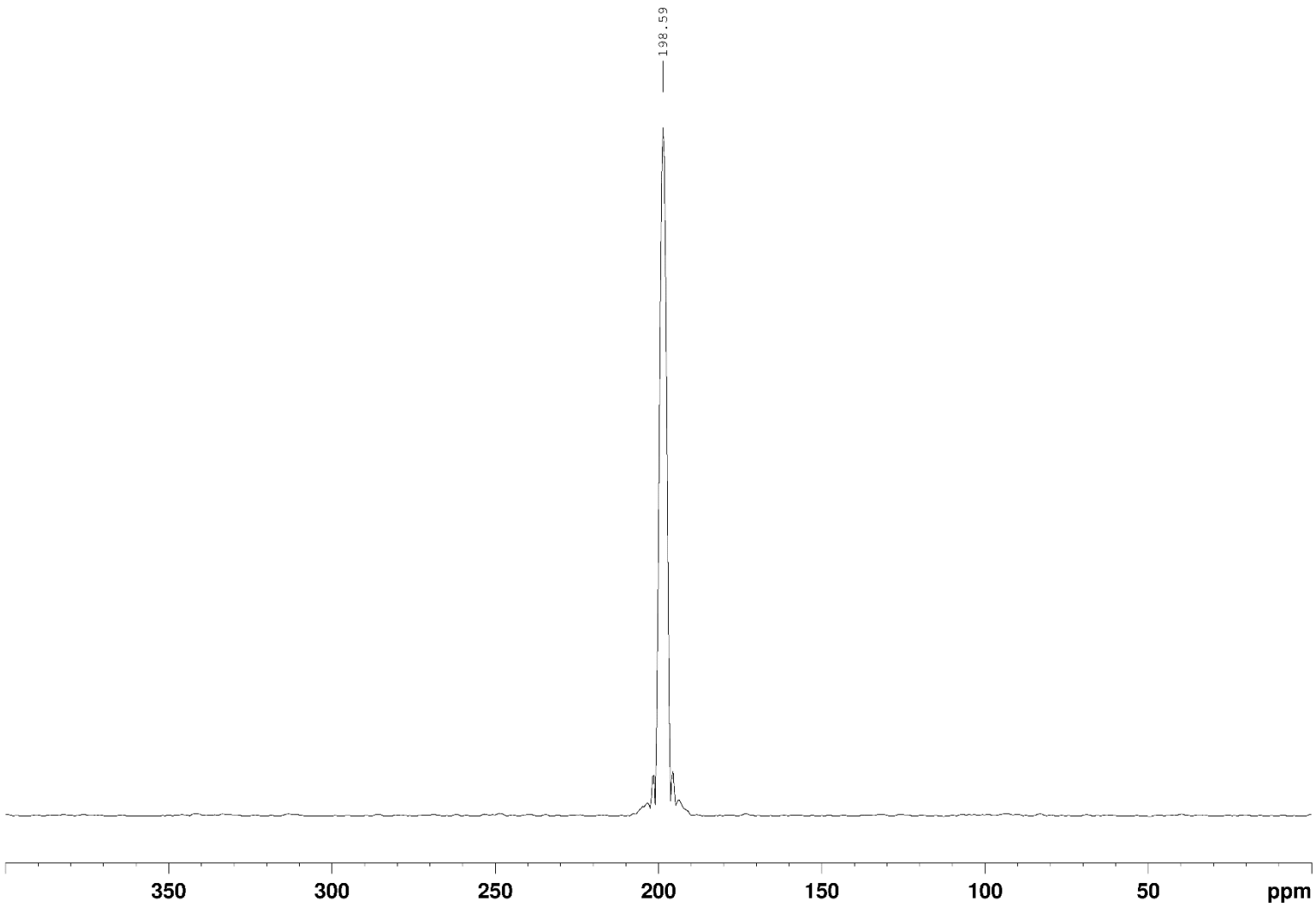

ESI-MS (pos)

(in H_2O)

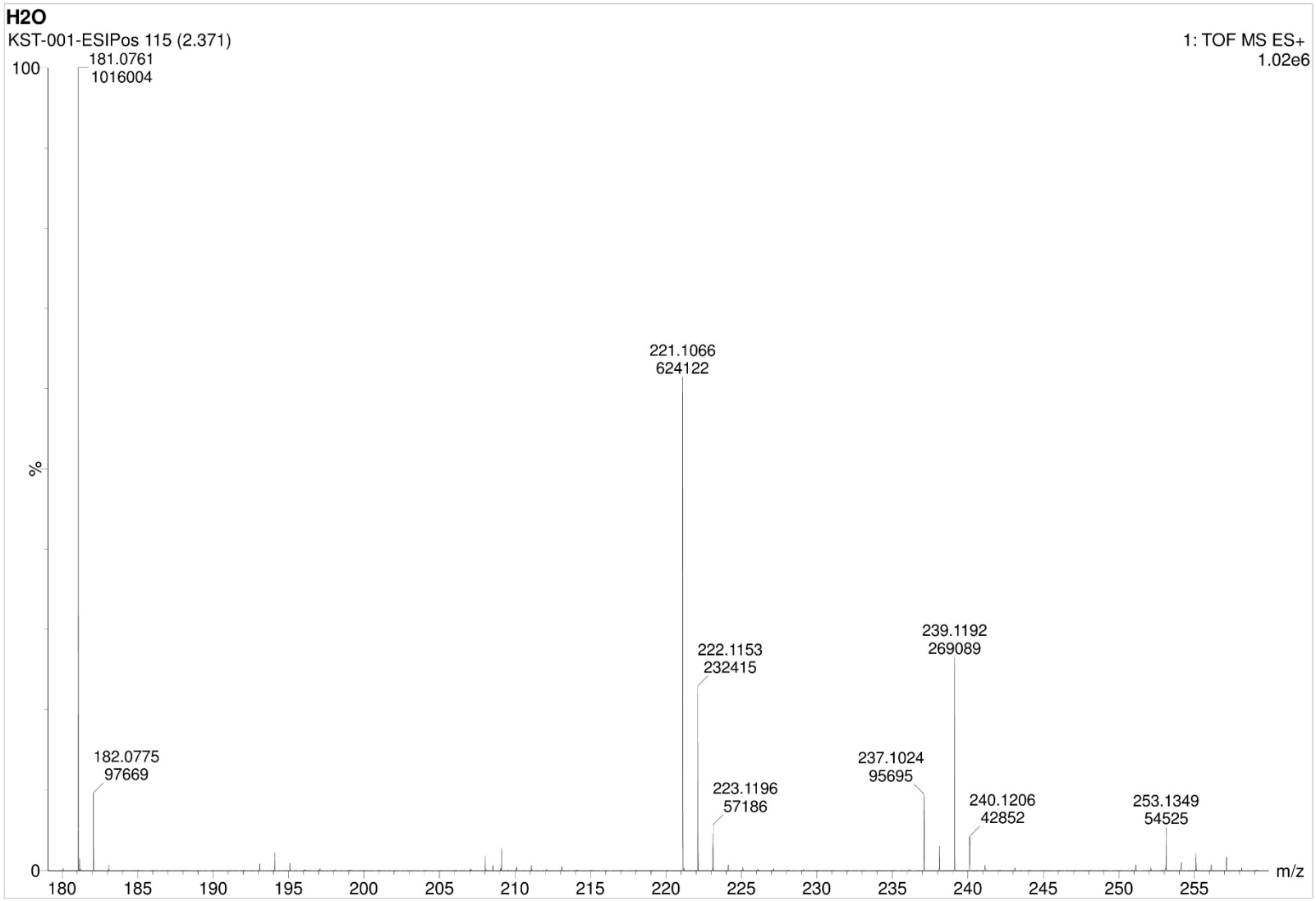

10.1.3 5H-6,7-Dihydro[1,4]diazepino[1,2,3,4-lmn][1,10]phenanthroline-3,9-dione (Phen-Pr-Ox)

^{1}H-NMR

(500 MHz, $CDCl_3$)

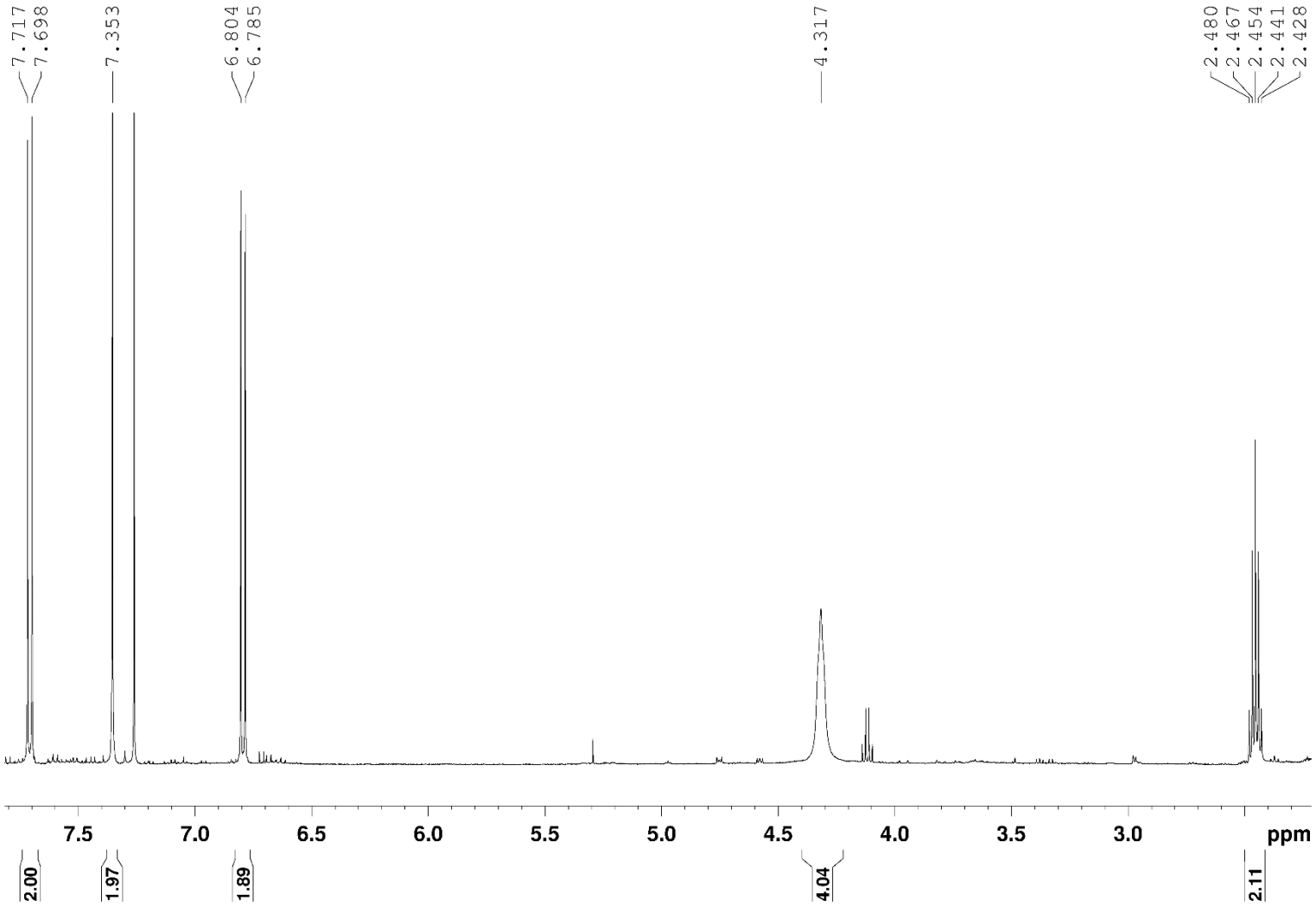

^{13}C-NMR

(125 MHz, $CDCl_3$)

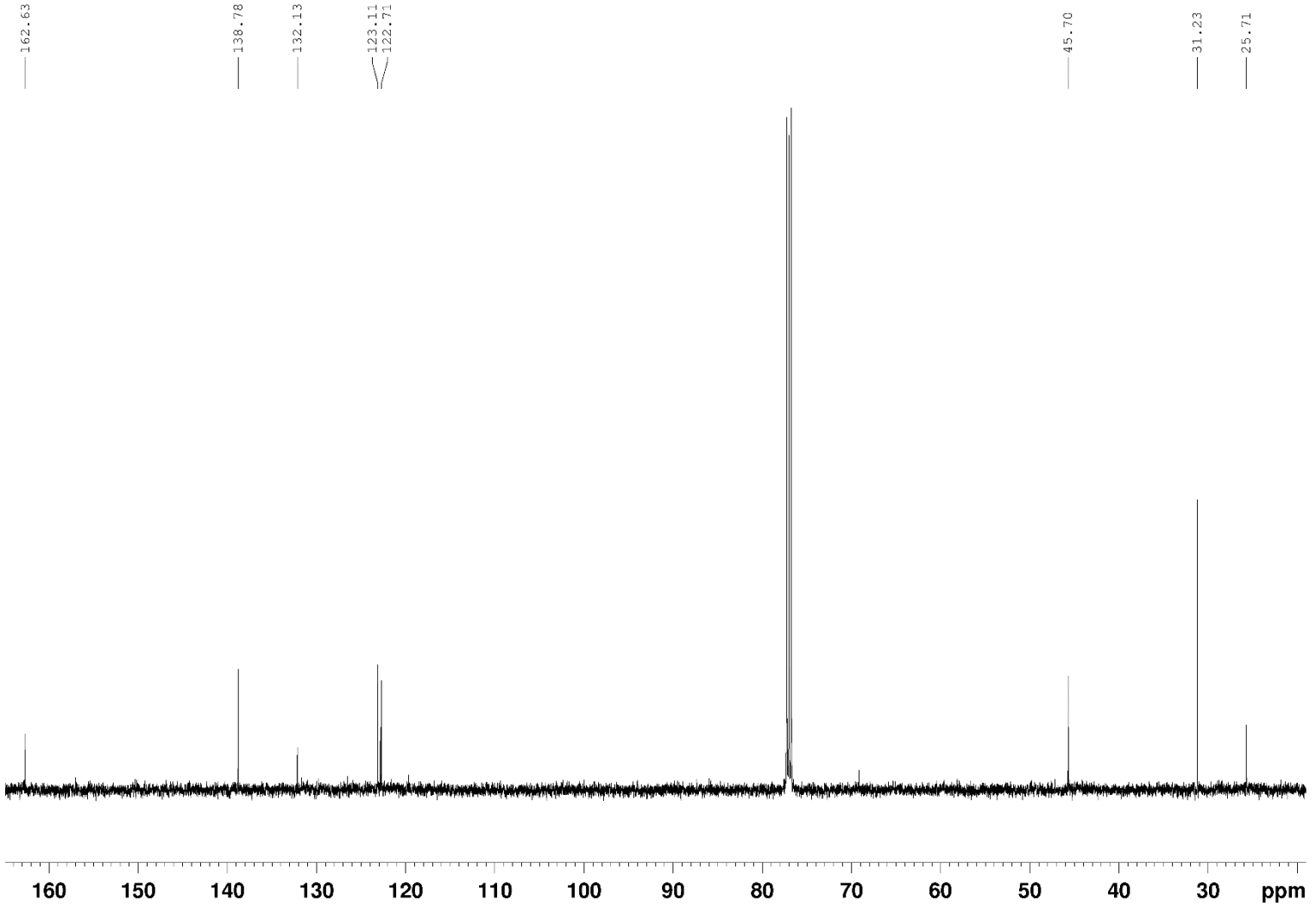

^{15}N-NMR

(50.7 MHz, $CDCl_3$, obtained by ^{15}N-^{1}H-HBMC)

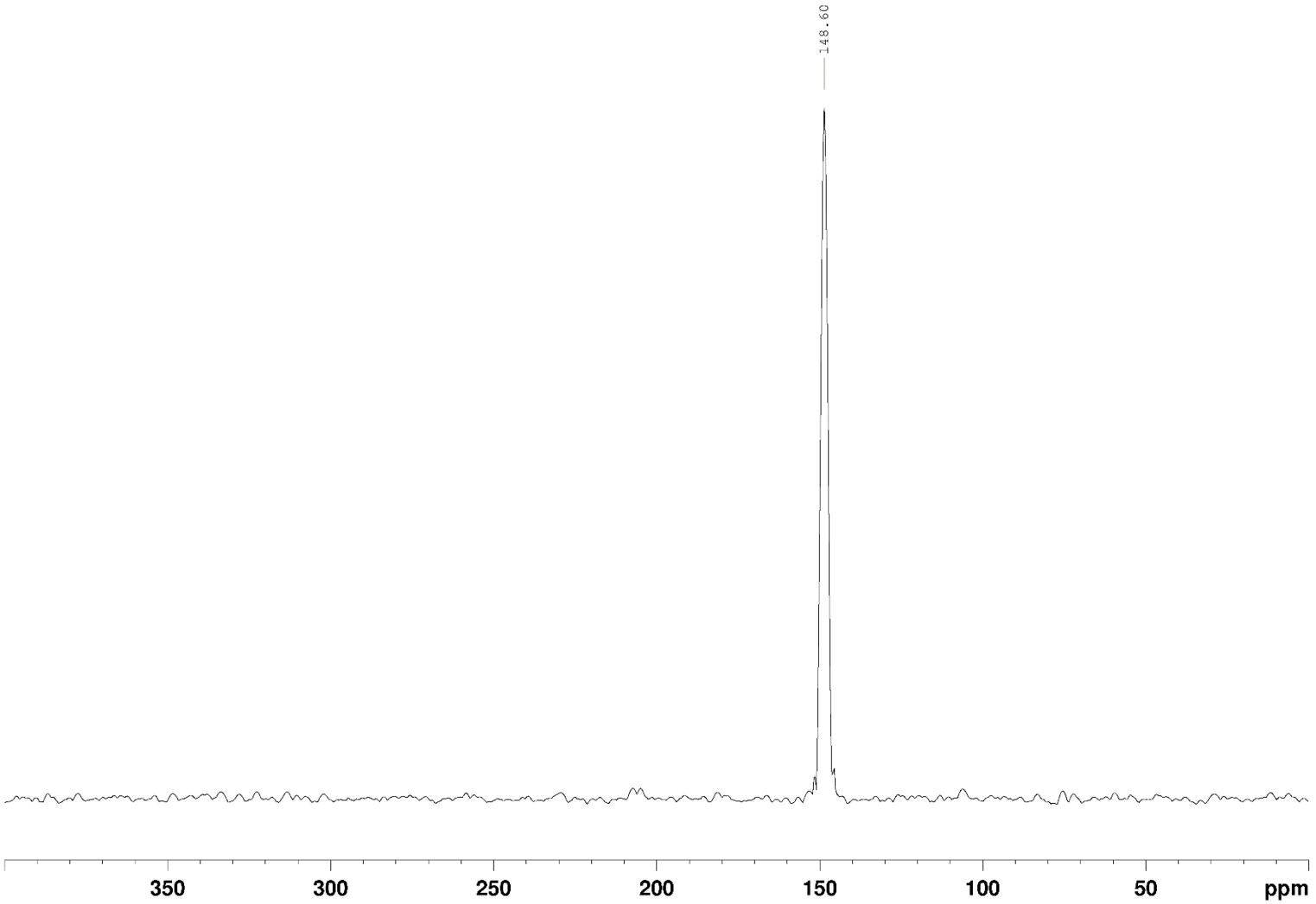

ESI-MS (pos)

(in MeOH/Formic acid)

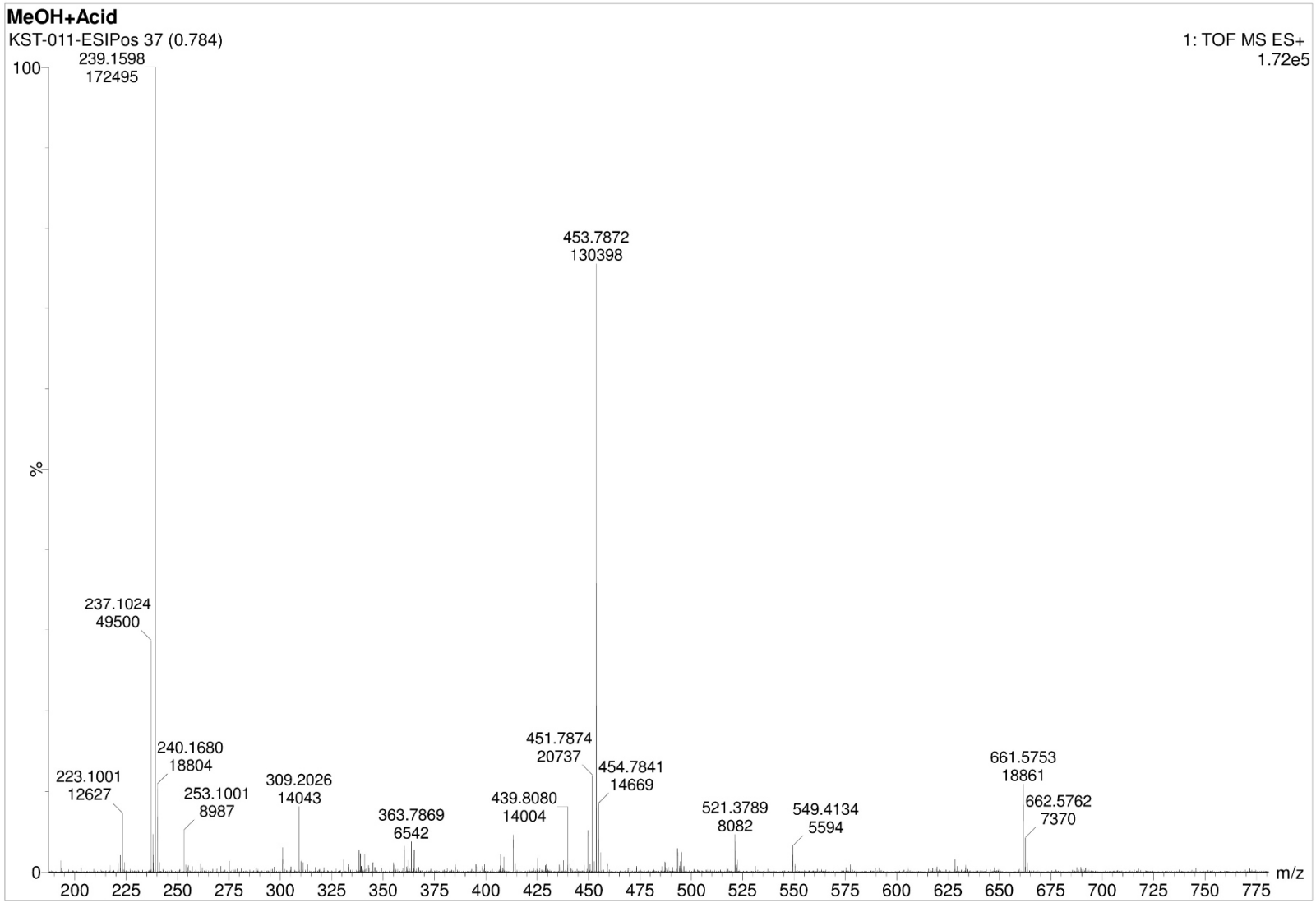

10.1.4 Di(1,10-phenanthrolin-2-yl)methane by coupling with Diiodomethane

ESI-MS (pos)

(in MeCN/H_2O/ Formic acid)

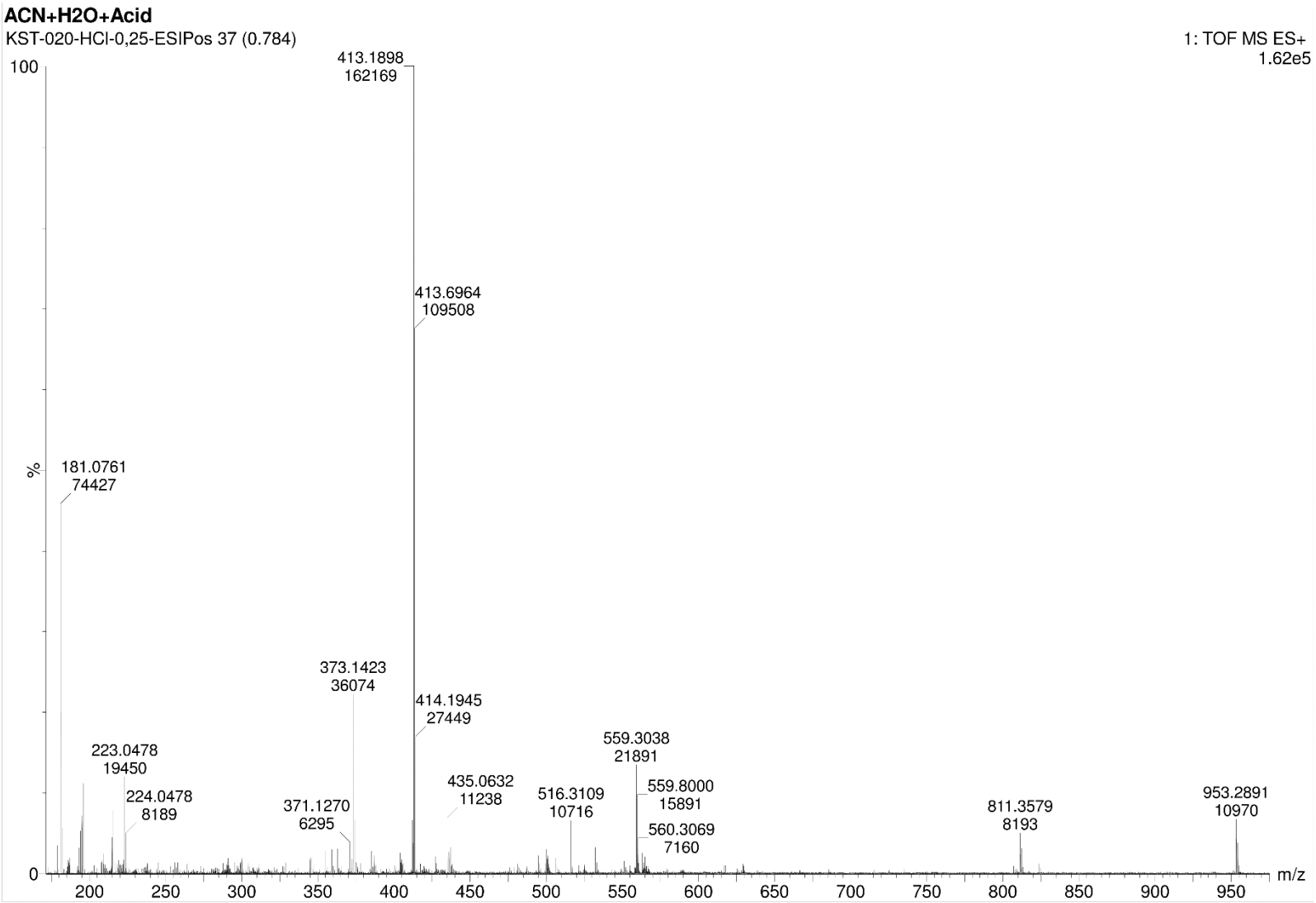

10.1.5 2,9-dibromo-1,10-phenanthroline (Phen-Br)

^{1}H-NMR

(500 MHz, DMSO-d_6)

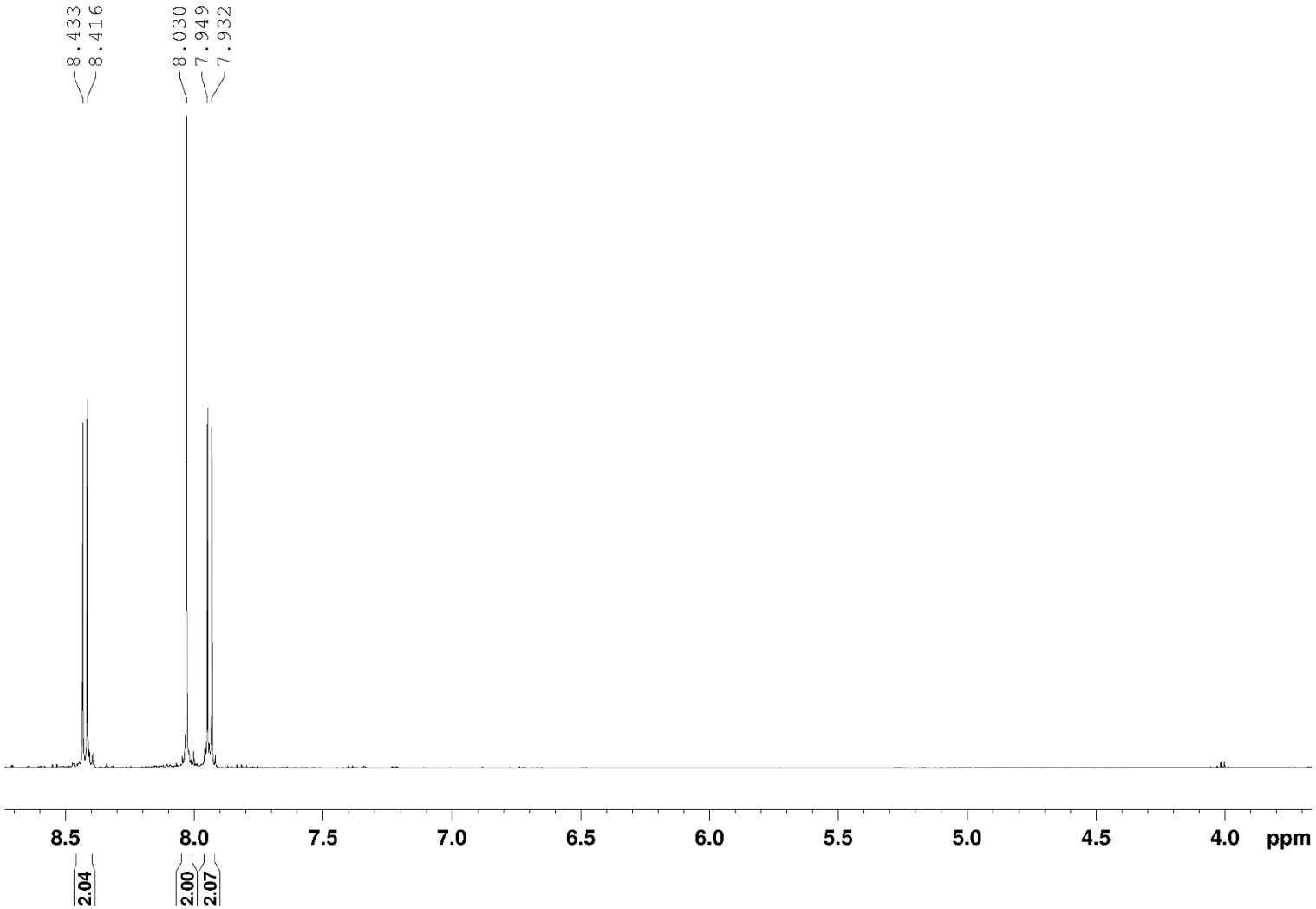

10.1.6 1,10-Phenanthroline-2,9-dicarbaldehyde (DMP-O)

^{1}H-NMR

(500 MHz, DMSO-d_6)

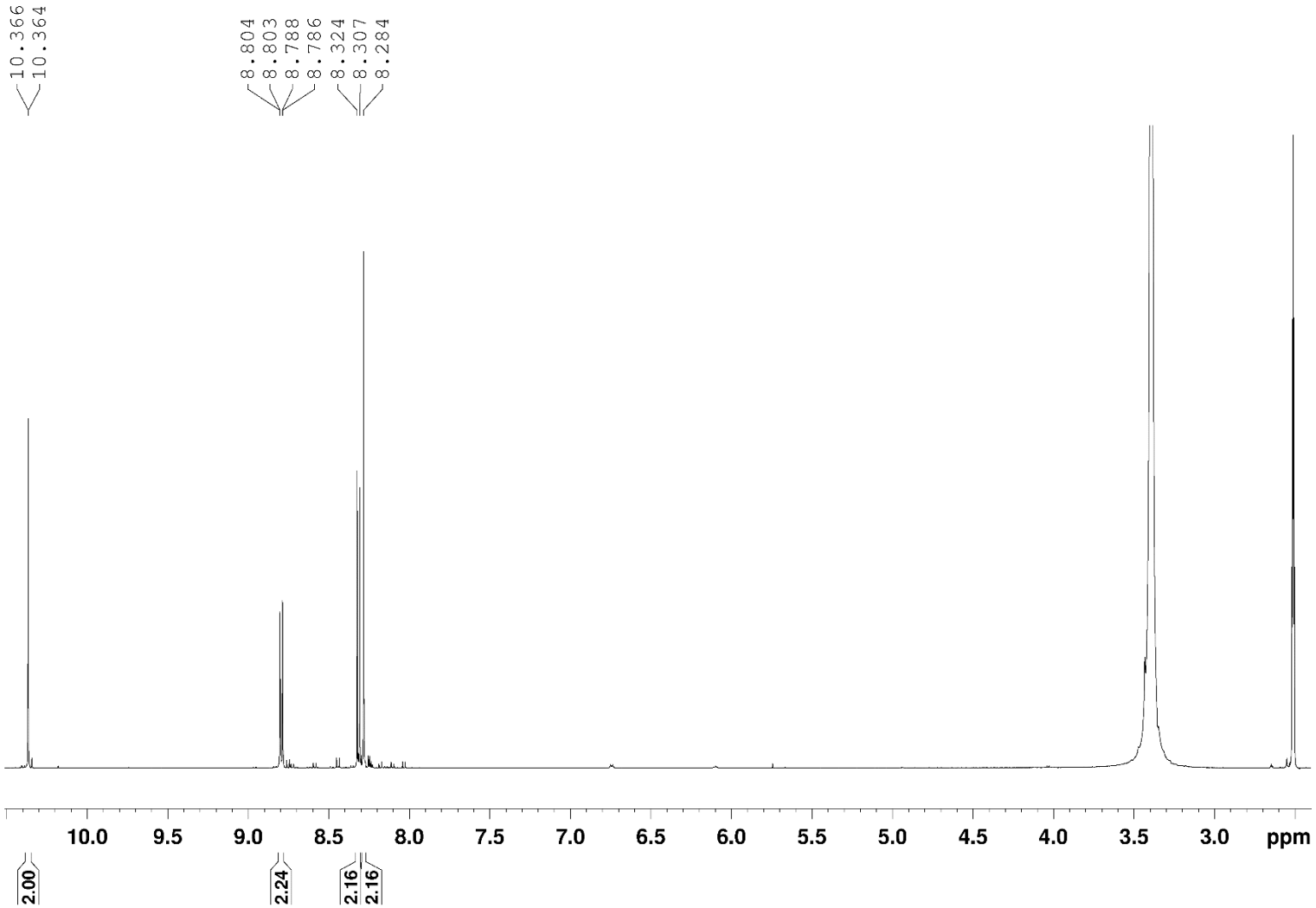

^{13}C-NMR

(125 MHz, DMSO-d_6)

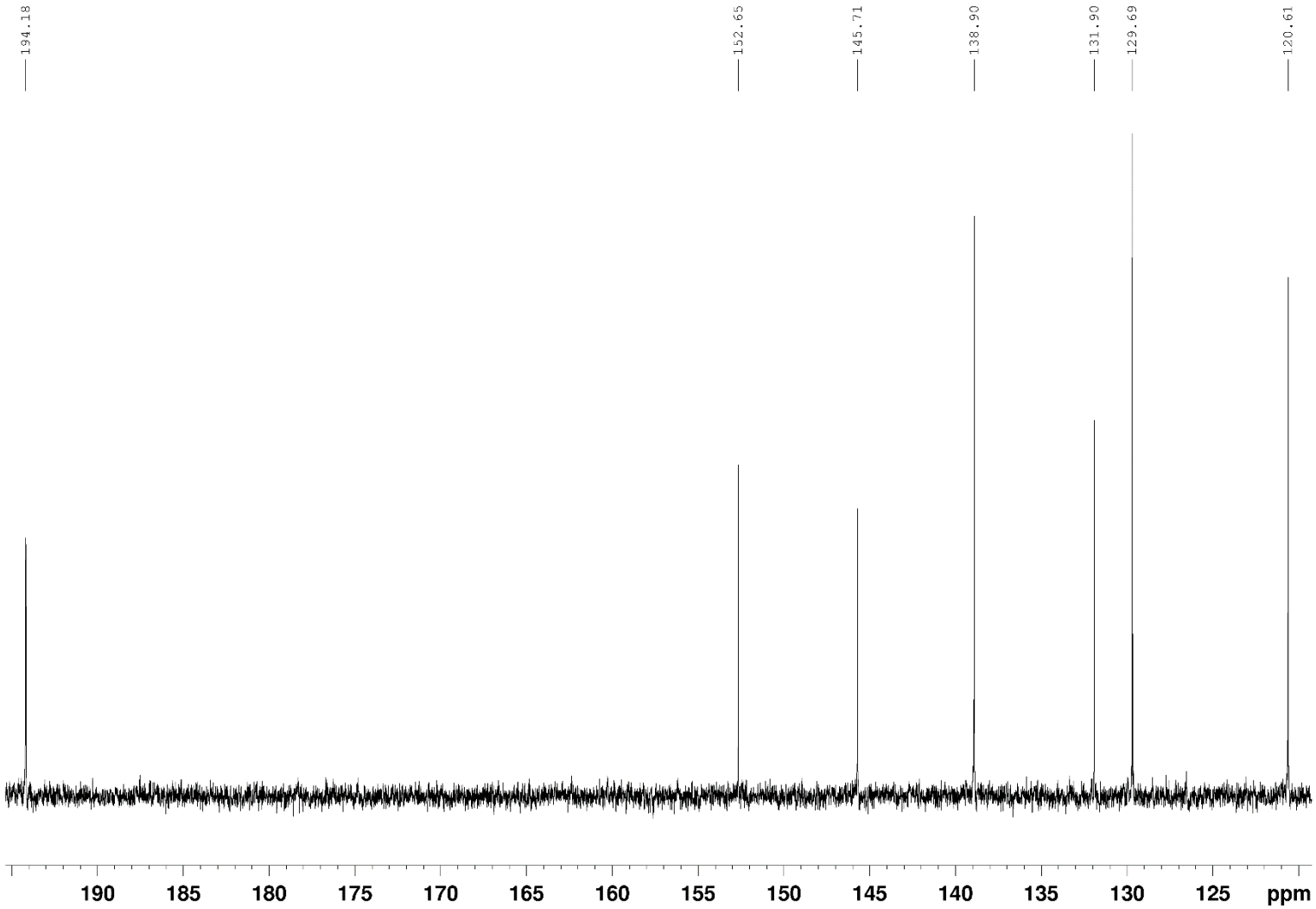

ESI-MS (pos)

(m/z in MeOH)

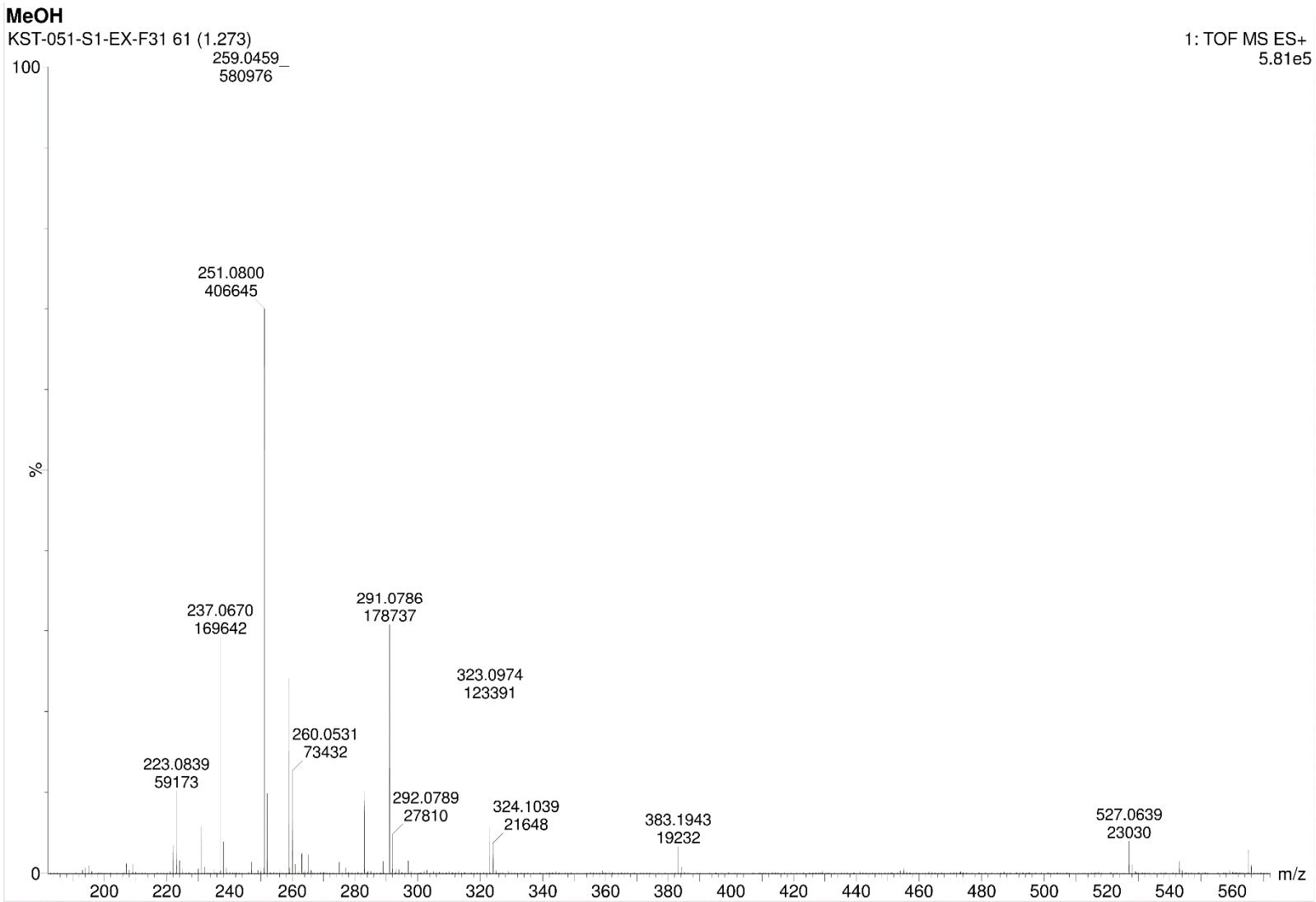

10.1.7 (1,10-Phenanthroline-2,9-diyl)dimethanol (DMP-OH)

^{1}H-NMR

(500 MHz, DMSO-d_6)

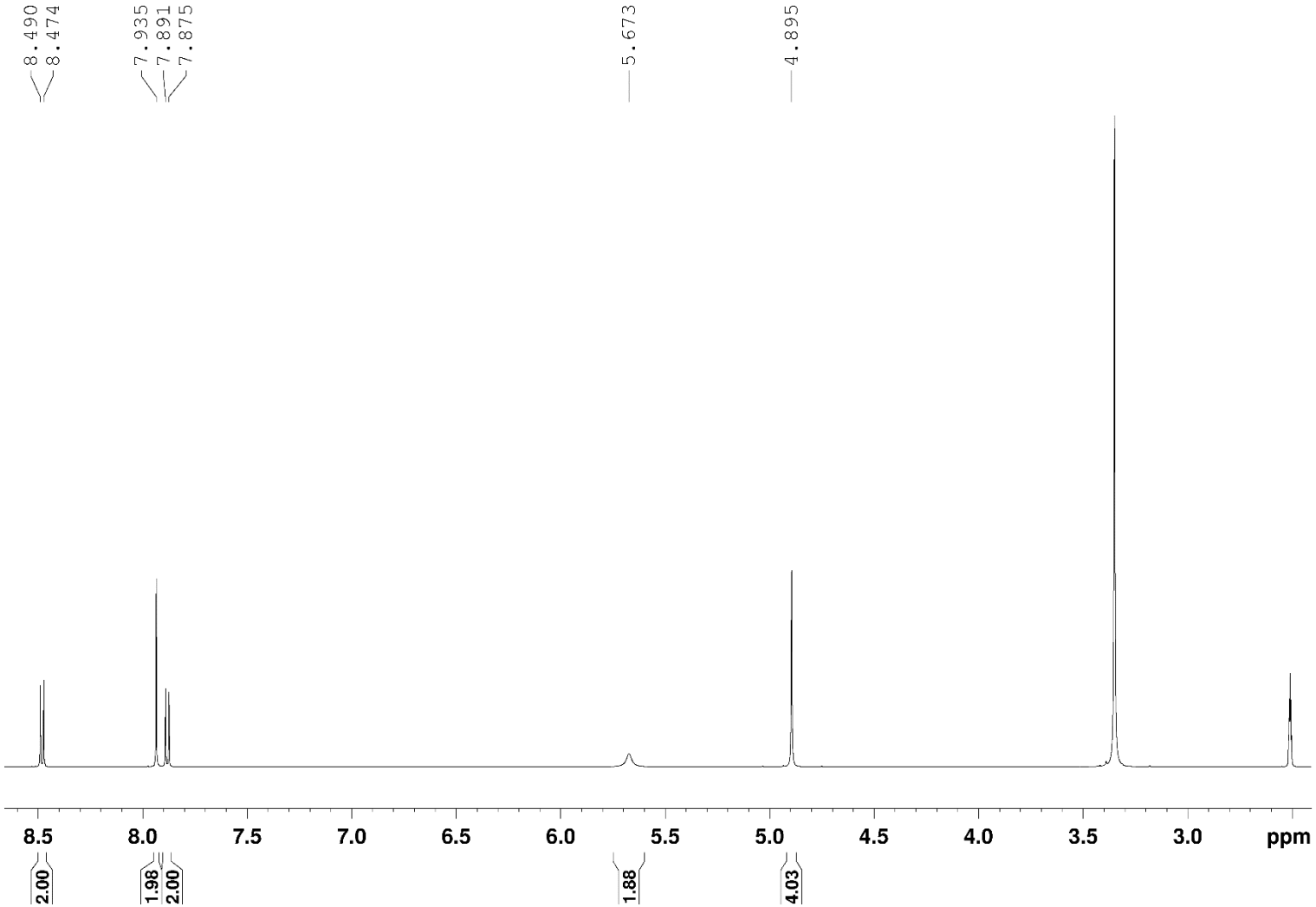

^{13}C-NMR

(125 MHz, DMSO-d_6)

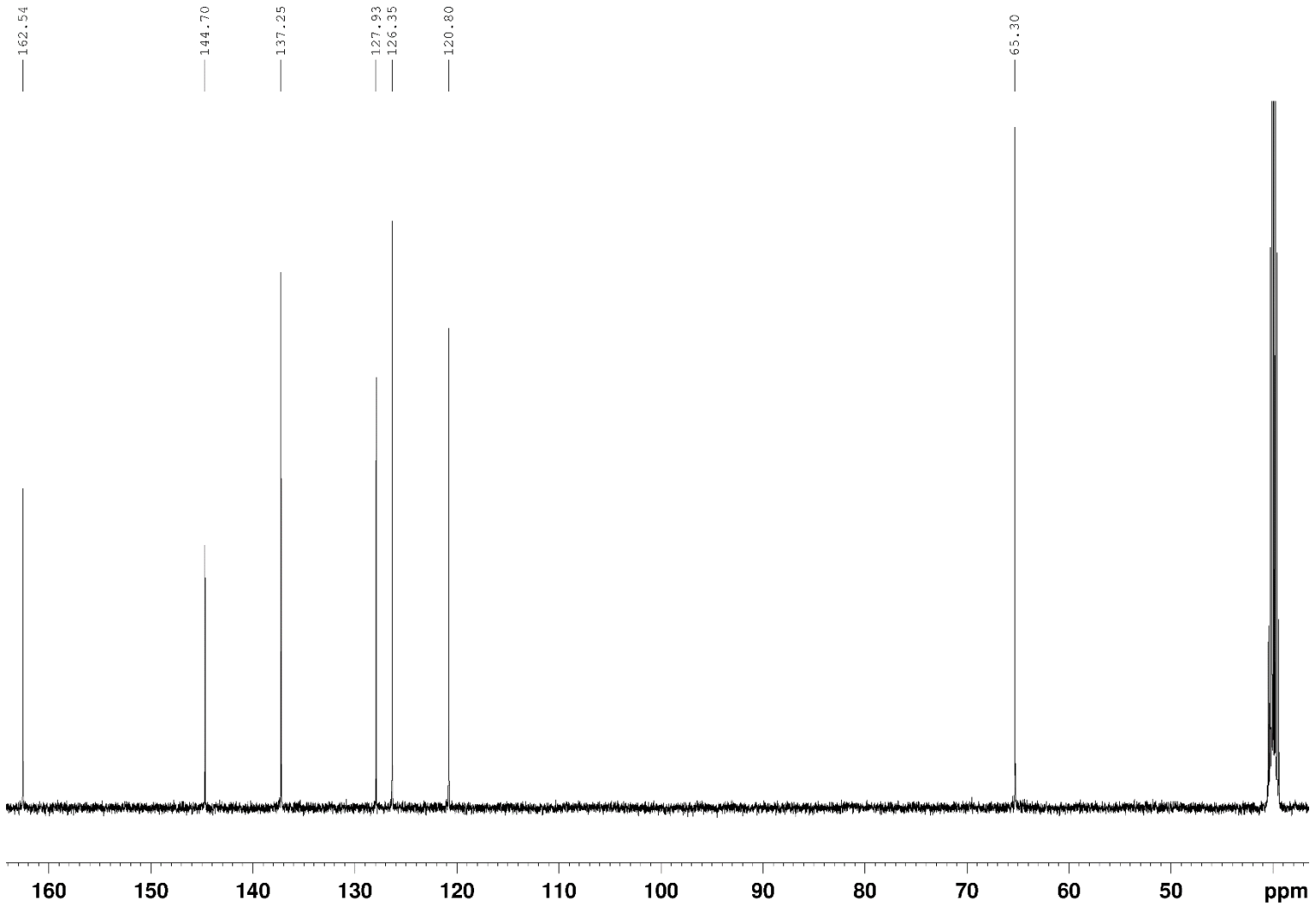

^{15}N-NMR

(50.7 MHz, DMSO-d_6, obtained by ^{15}N-^{1}H-HMBC)

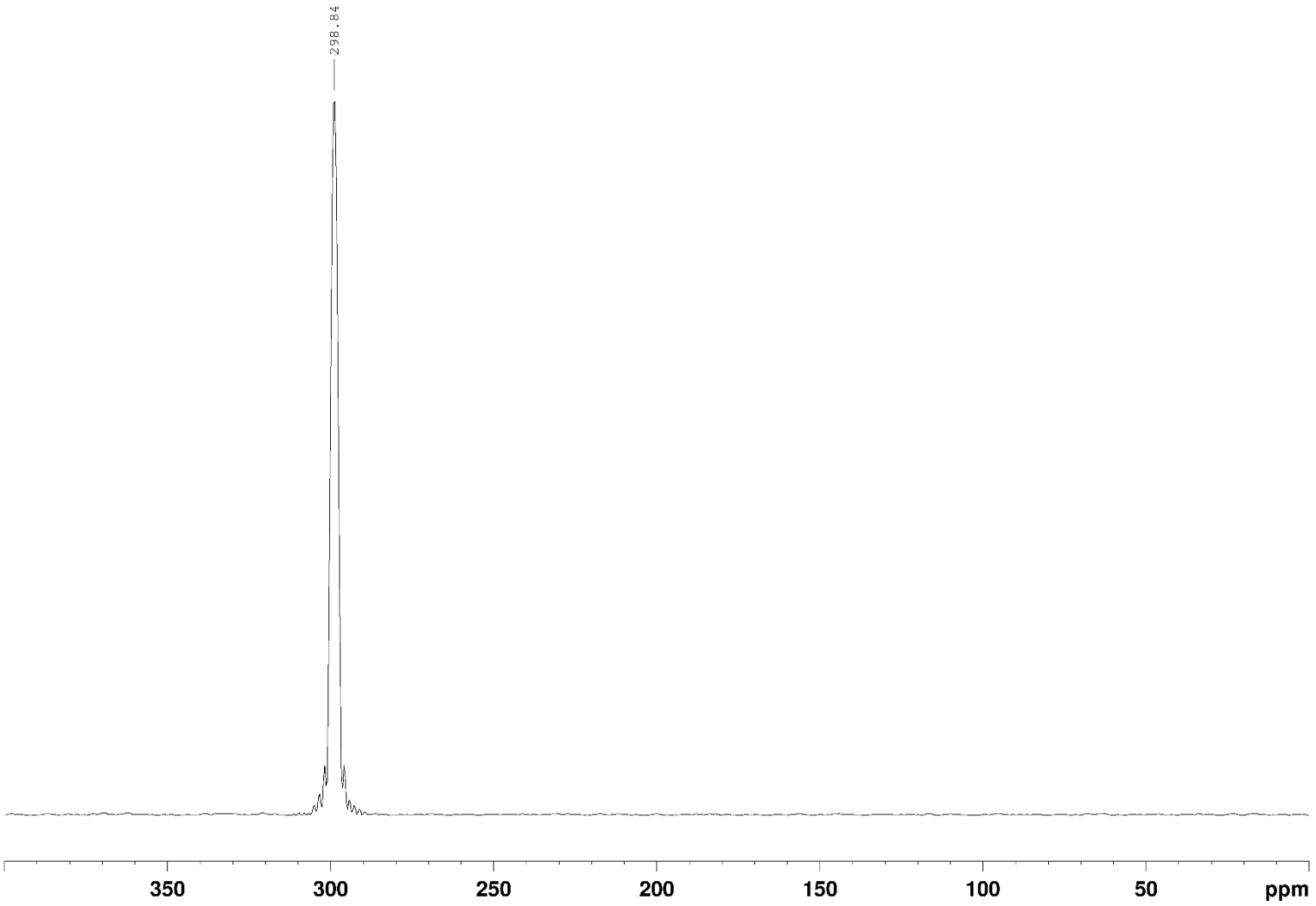

ESI-MS (pos)

(m/z in MeOH/H_2O)

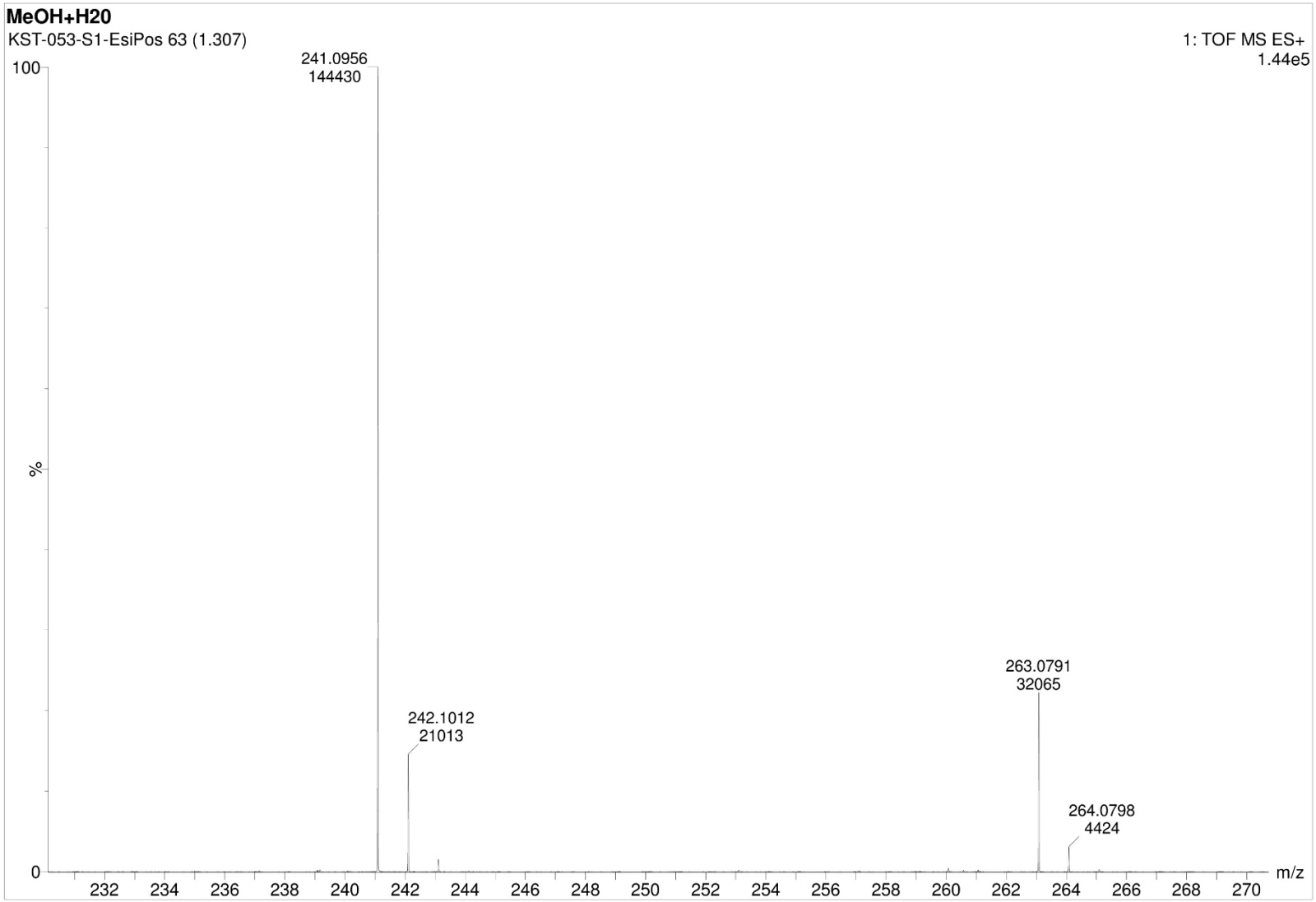

10.1.8 1,10-Phenanthroline-2,9-dicarboxylic acid (DMP-OOH)

^{1}H-NMR

(500 MHz, DMSO-d_6)

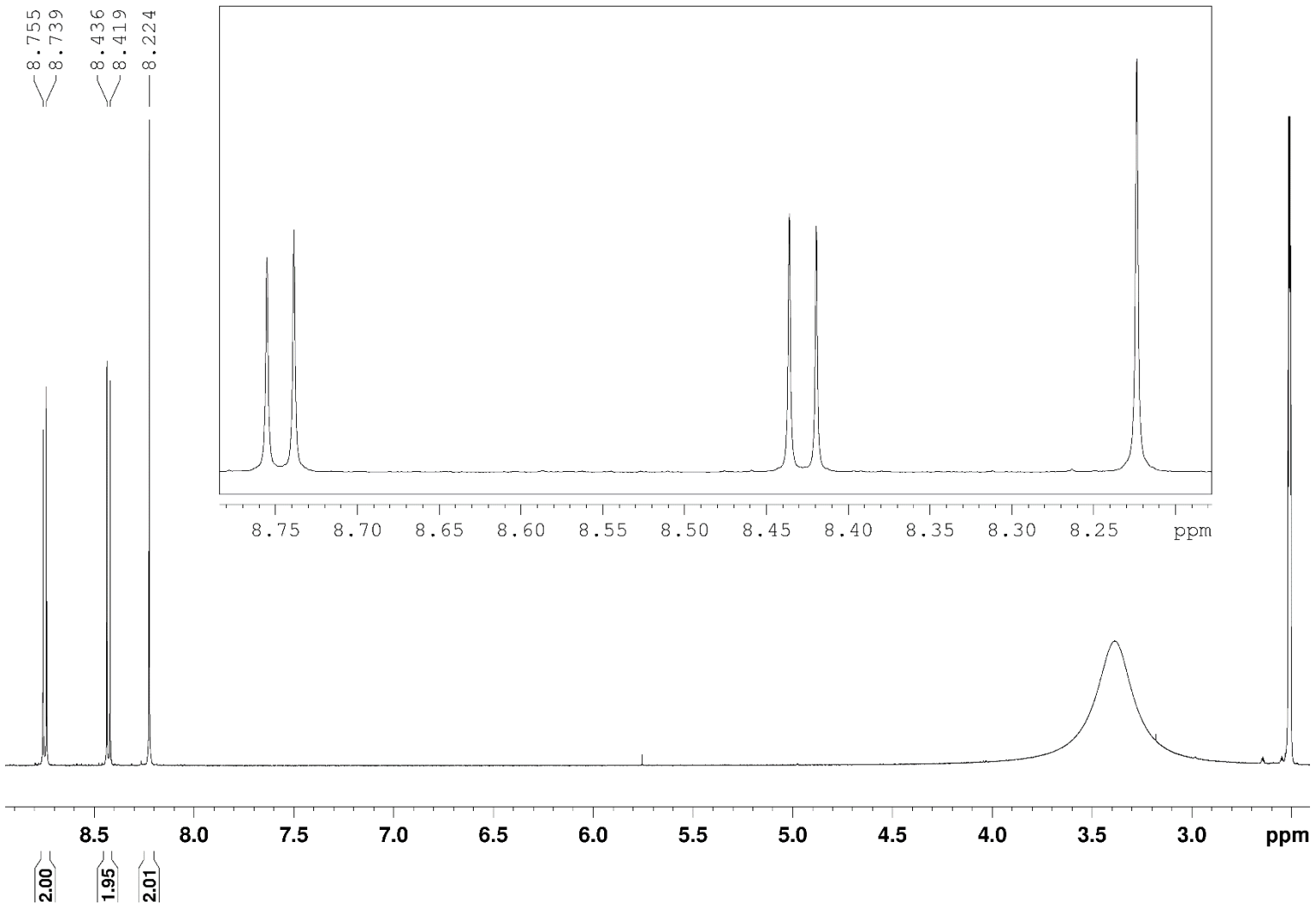

^{13}C-NMR

(125 MHz, DMSO-d_6)

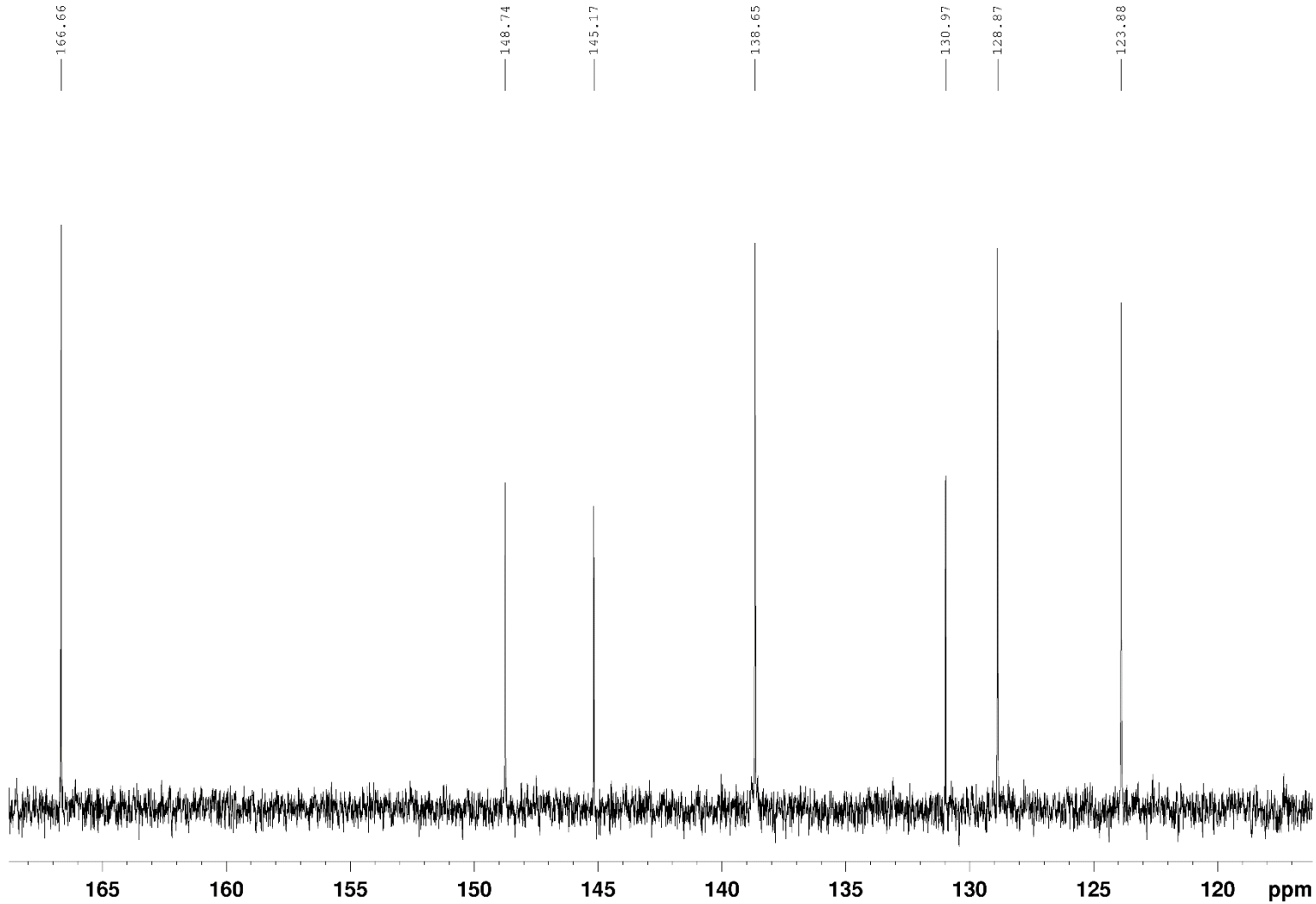

ESI-MS (neg)

(m/z in MeOH)

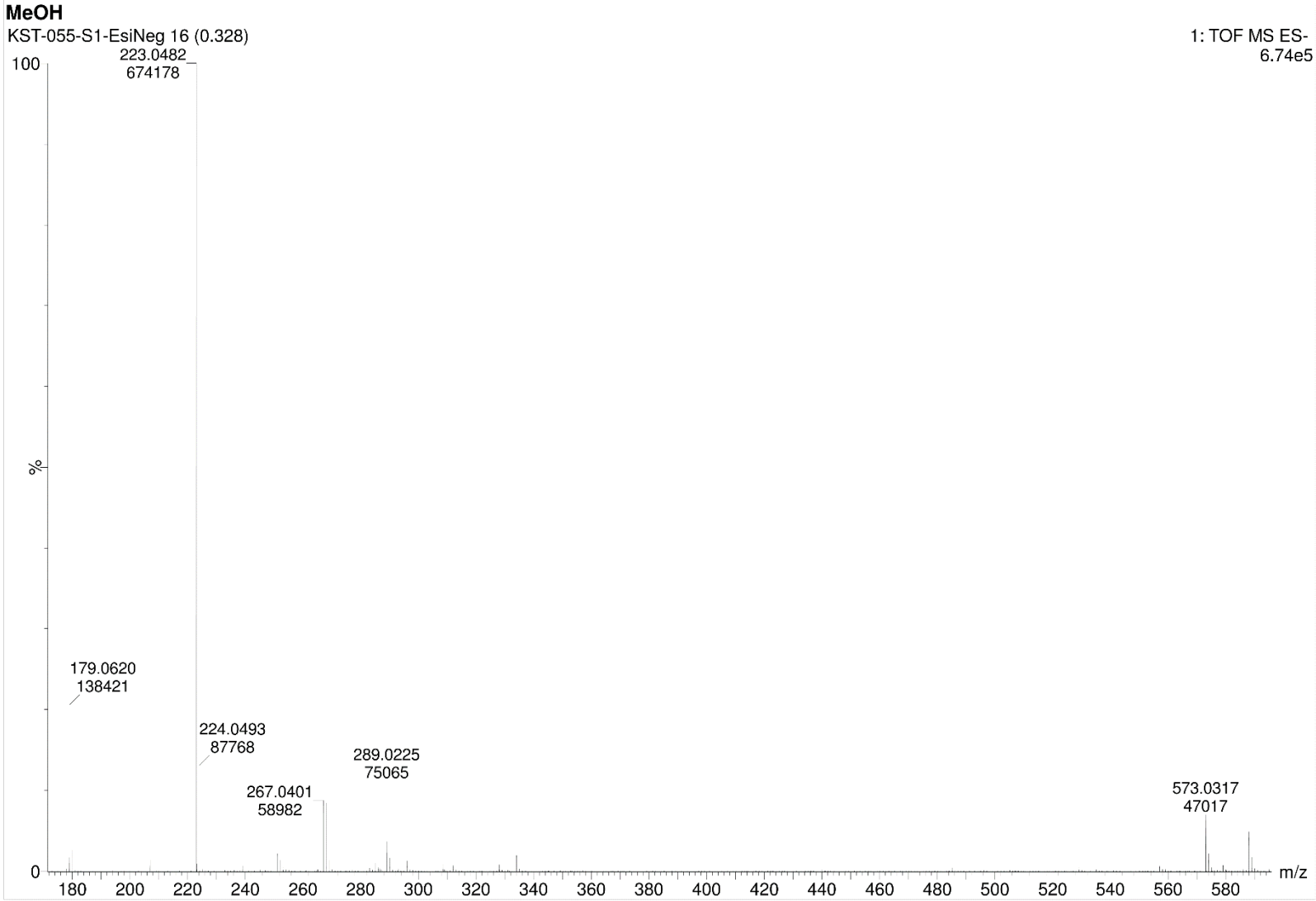

10.1.9 2,9-Bis(chloromethyl)-1,10-phenanthroline (DMP-Cl)

^{1}H-NMR

(500 MHz, $CDCl_3$)

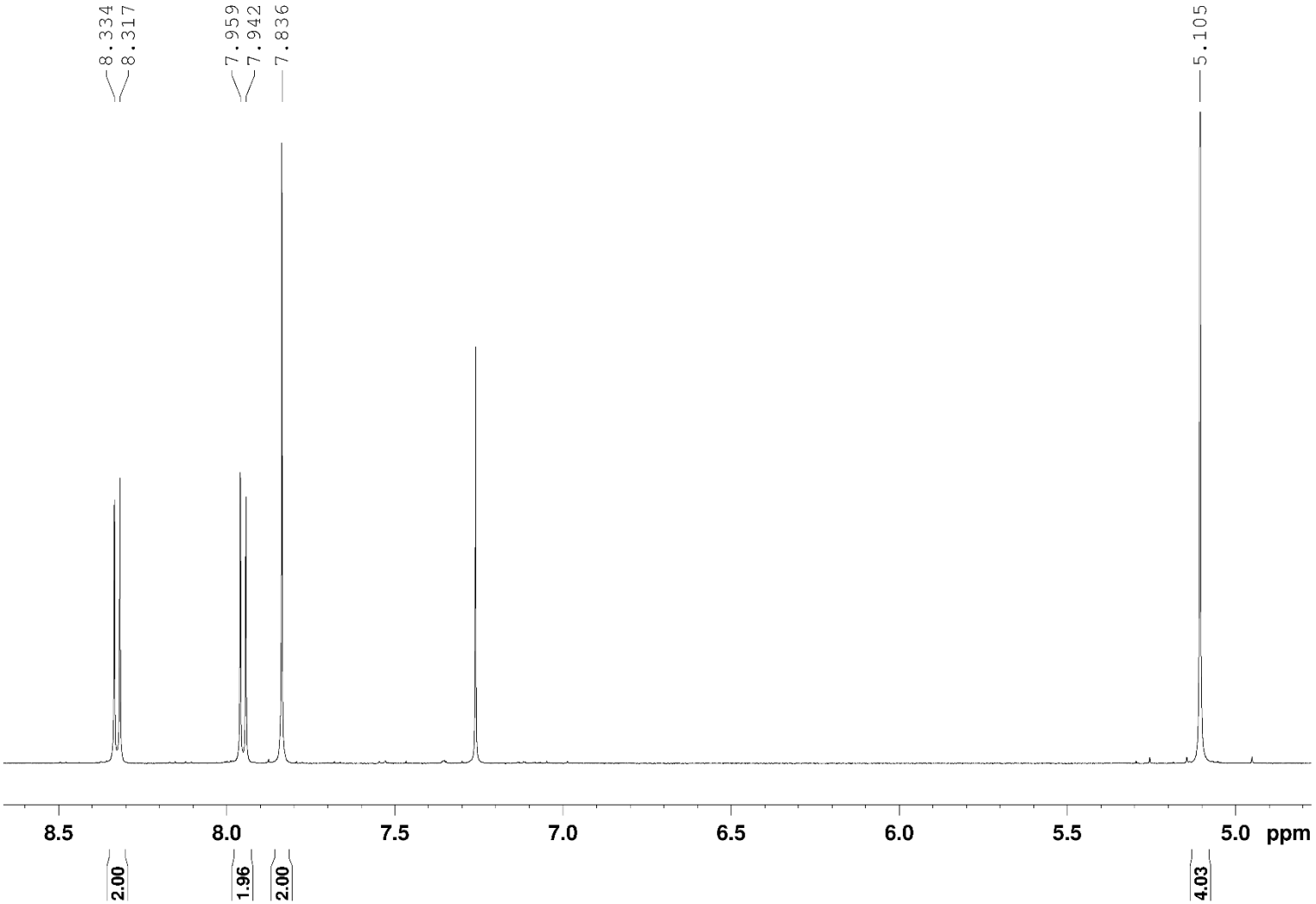

^{13}C-NMR

(125 MHz, $CDCl_3$)

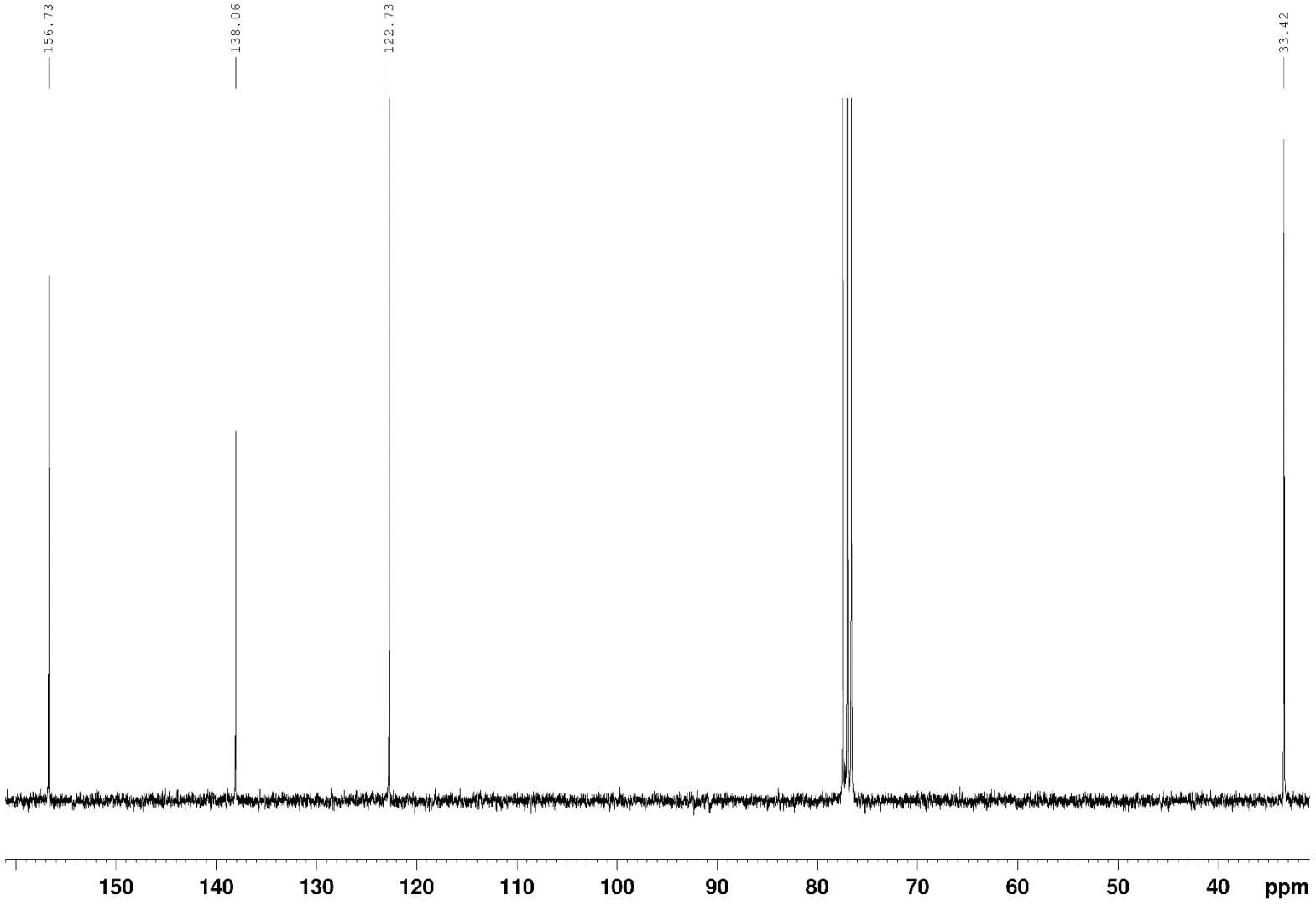

^{15}N-NMR

(50.7 MHz, $CDCl_3$, obtained by ^{15}N-^{1}H-HMBC)

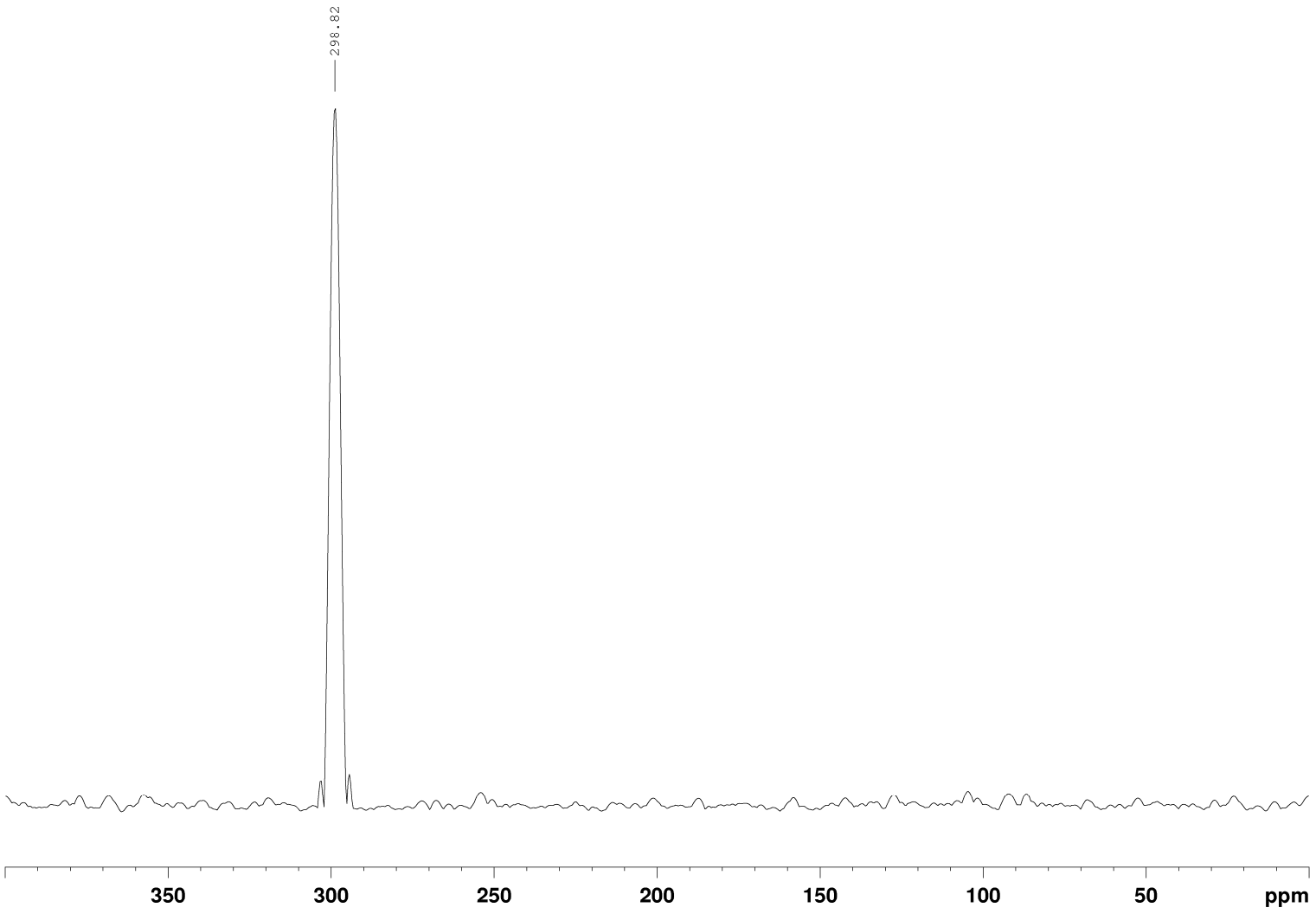

10.1.10 2,9-Bis(trichloromethyl)-1,10-phenanthroline (DMP-Cl_3)

^{1}H-NMR

(500 MHz, $CDCl_3$)

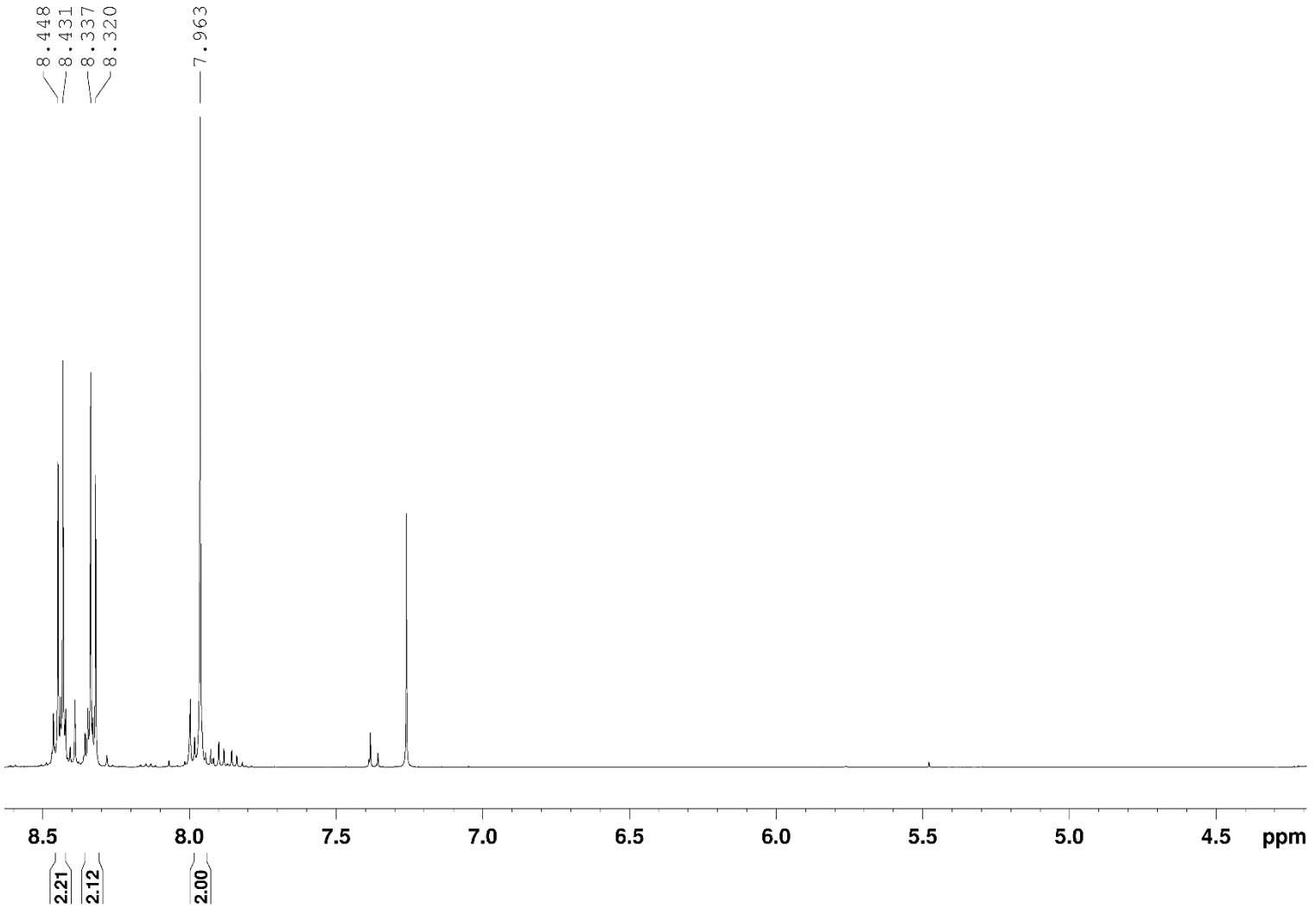

^{13}C-NMR

(125 MHz, $CDCl_3$)

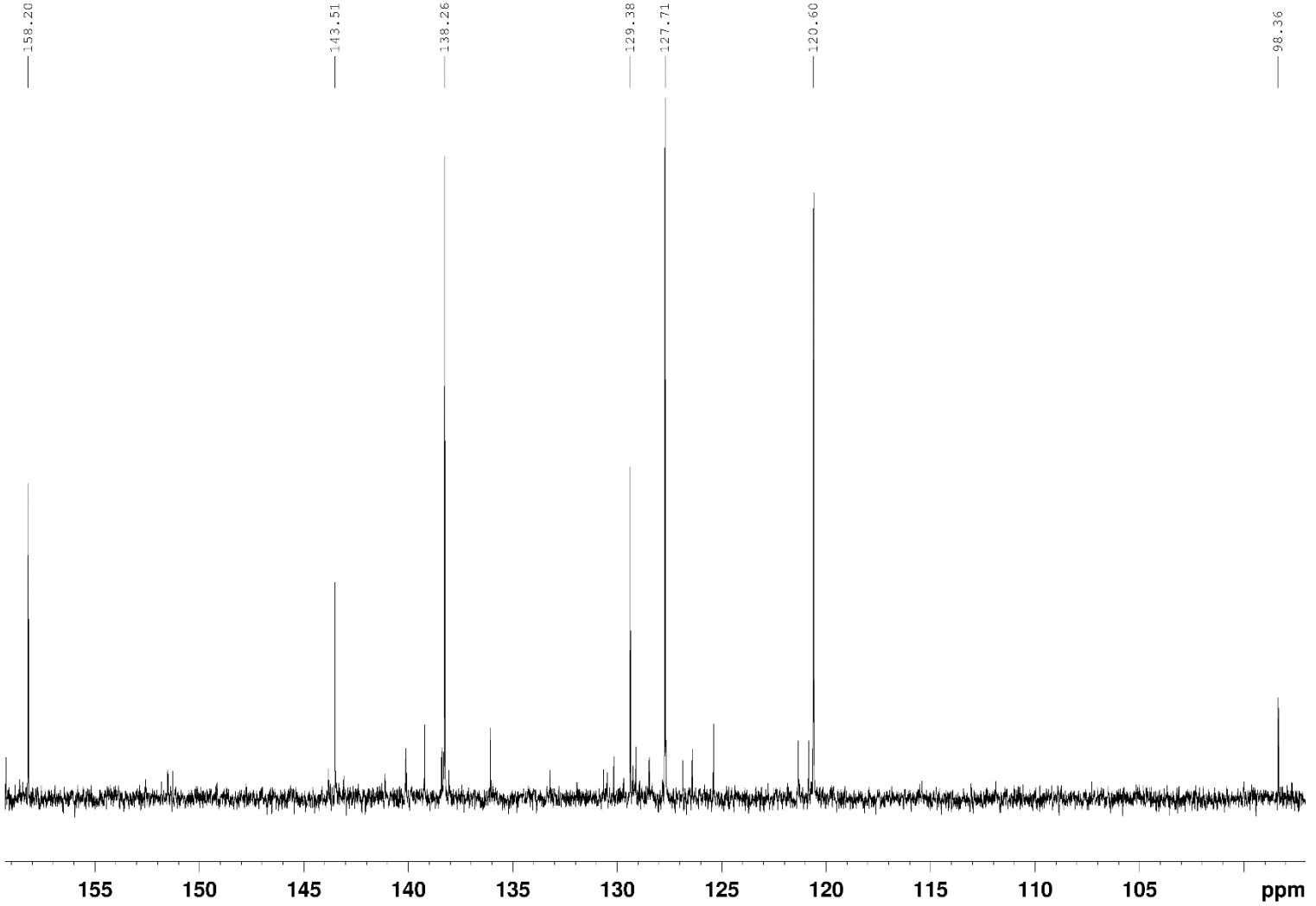

10.1.11 2,9-Bis(bromomethyl)-1,10-phenanthroline (DMP-Br)

^{1}H-NMR

(500 MHz, $CDCl_3$)

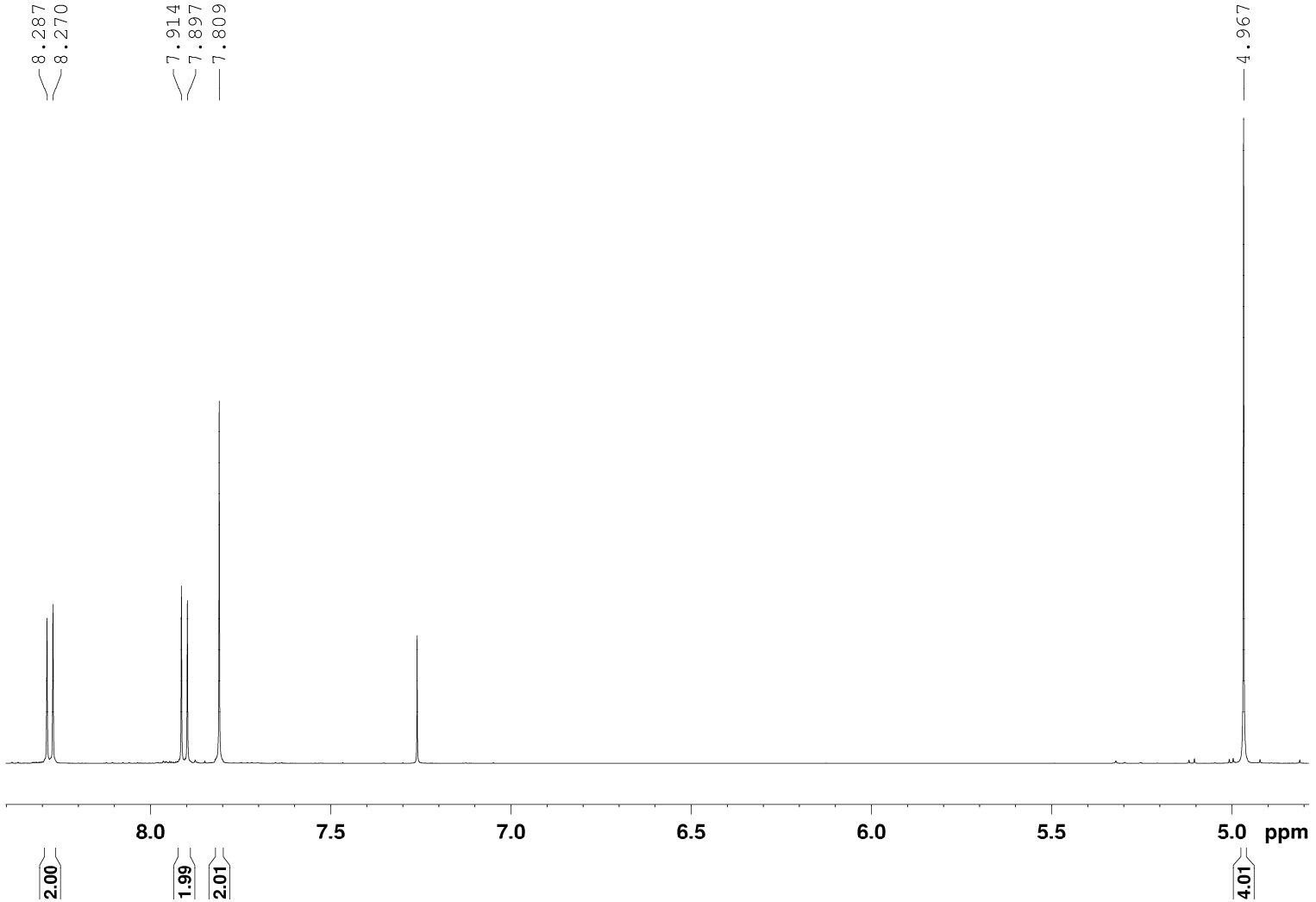

^{13}C-NMR

(125 MHz, $CDCl_3$)

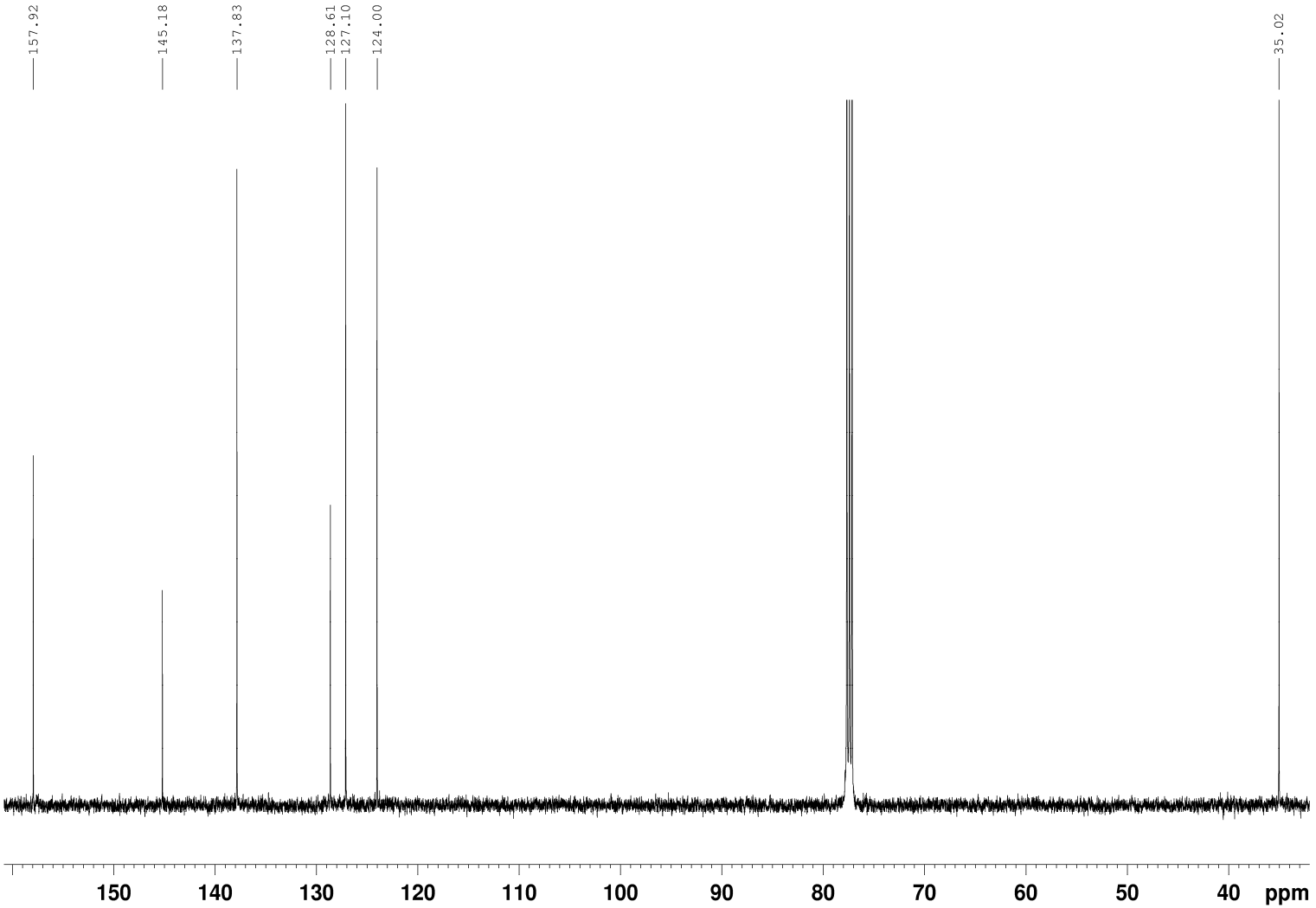

^{15}N-NMR

(50.7 MHz,
$CDCl_3$, obtained
by ^{15}N-^{1}H-HMBC)

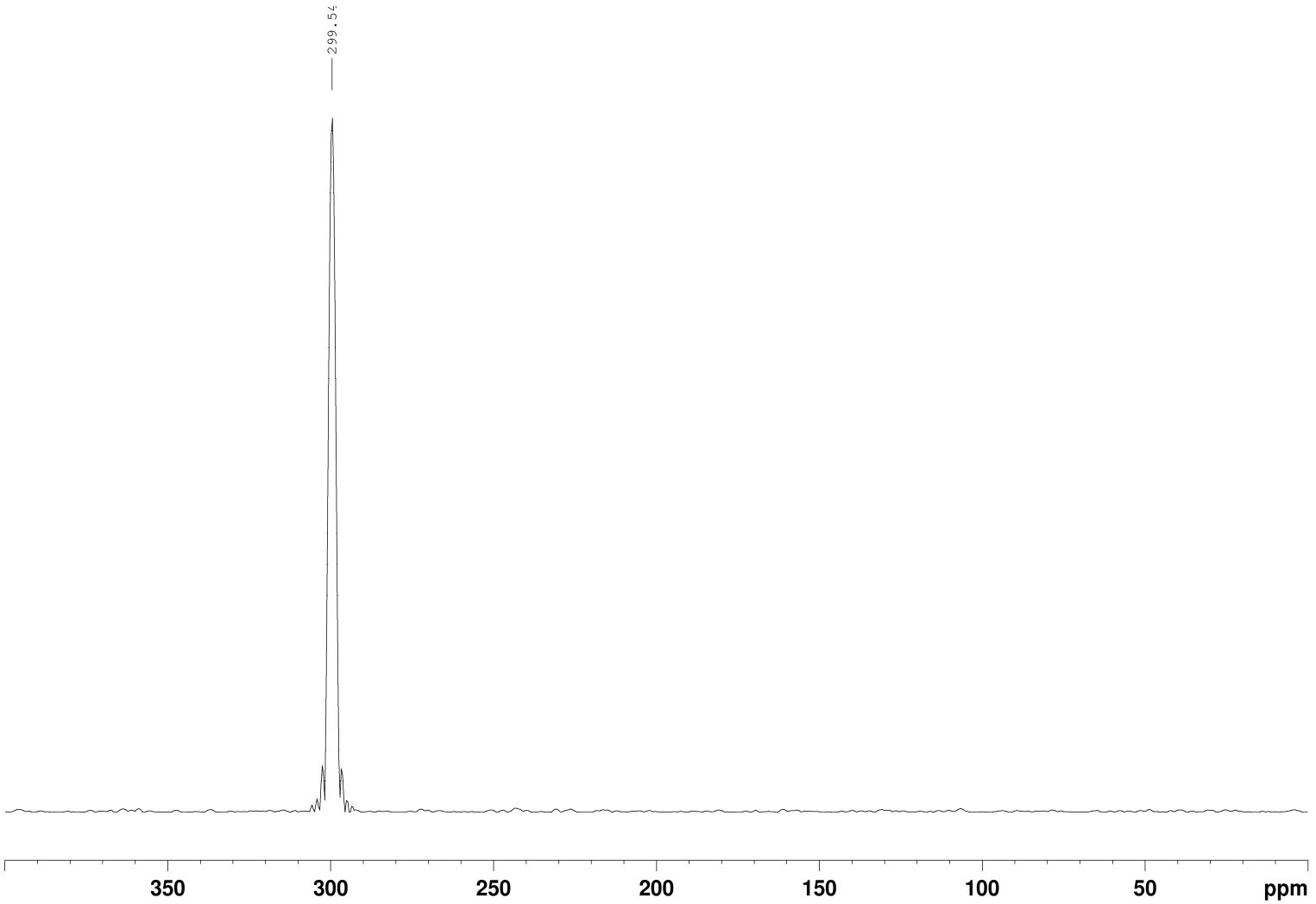

EI-MS

(m/z)

D:\Kai Stührenberg\...\KST-061-S1-EI 16.09.2015 11:57:18 KST-061-S1
EI, R=1200, 70 eV, 200 " C
KST-061-S1-EI #21 RT: 2,14 AV: 1 NL: 1,17E8
T: + c EI Full ms [34,50-600,50]

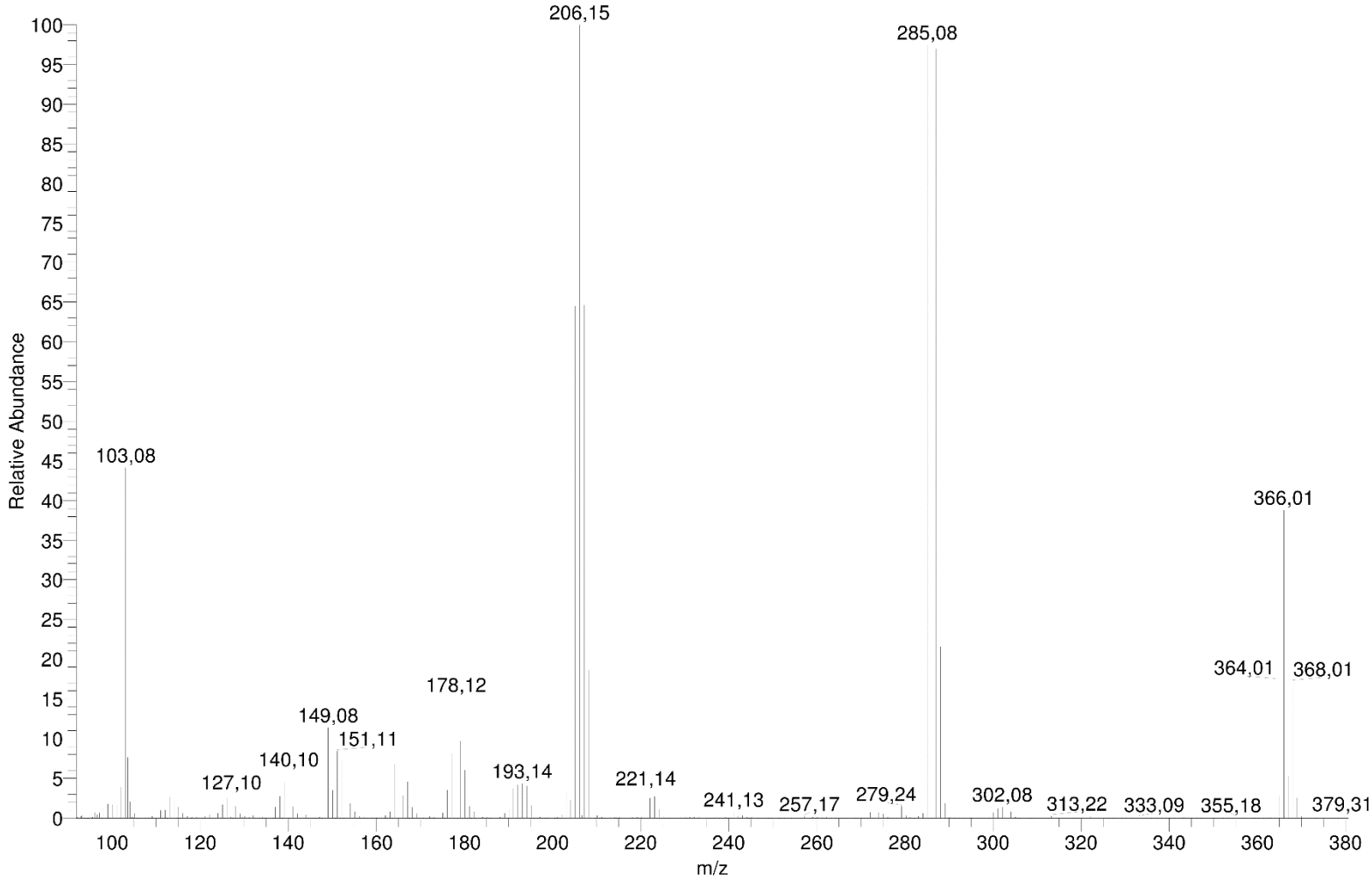

ESI-MS (pos)

(m/z in MeOH)

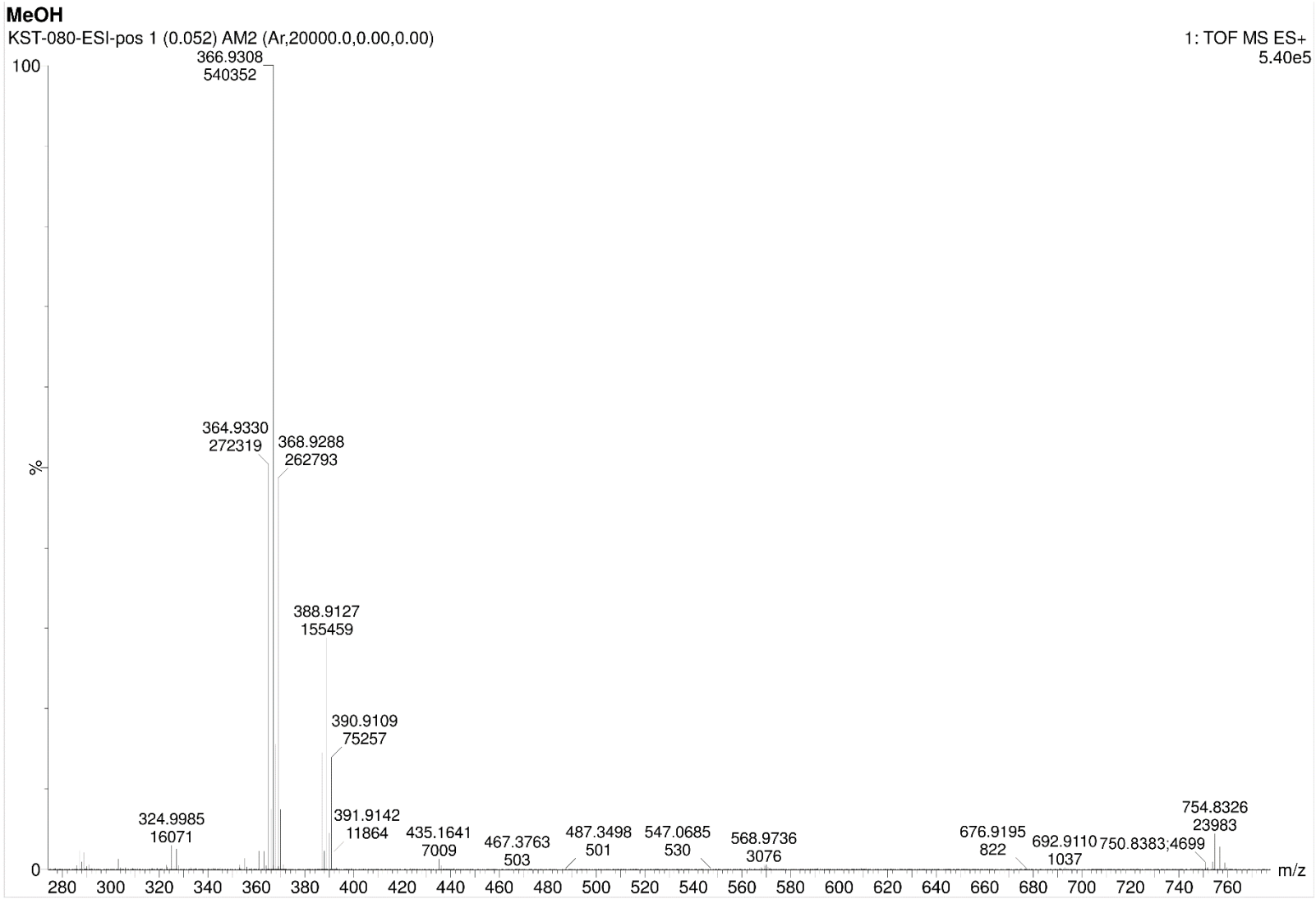

10.1.12 2,9-Bis(iodomethyl)-1,10-phenanthroline (DMP-I)

^{1}H-NMR

(500 MHz, MeCN-d_3)

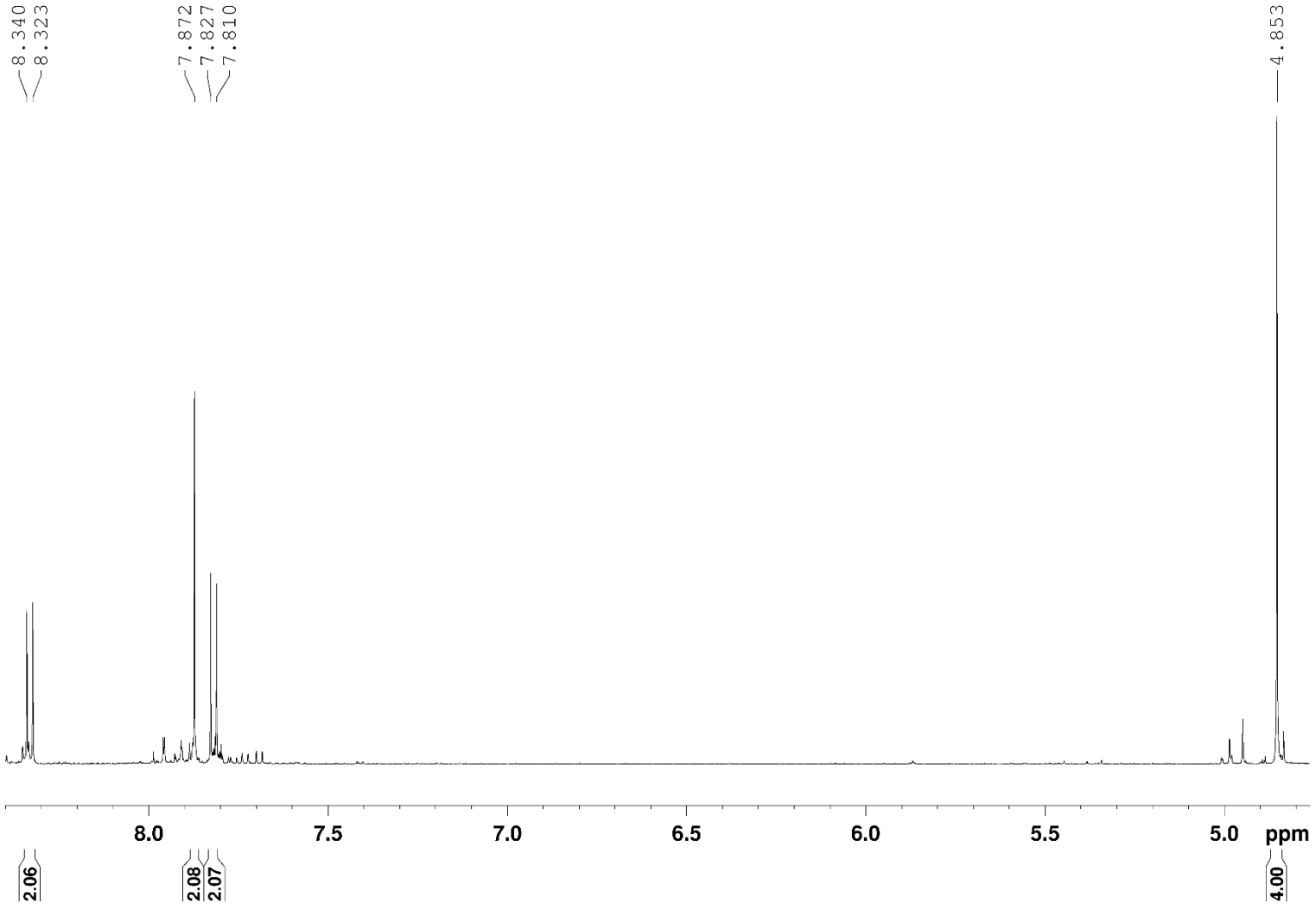

^{13}C-NMR

(125 MHz, MeCN-d_3)

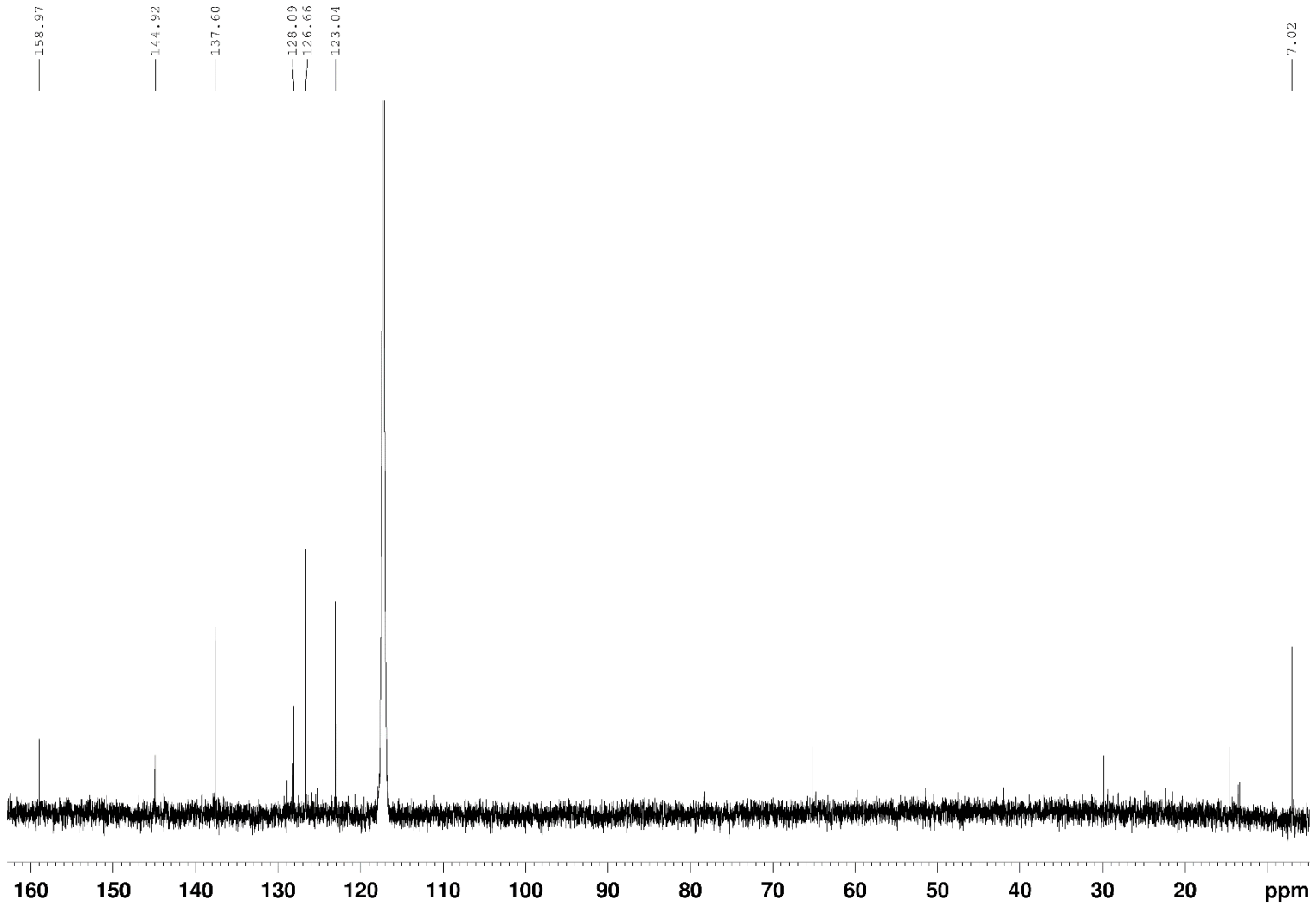

ESI-MS (pos)

(m/z in MeCN)

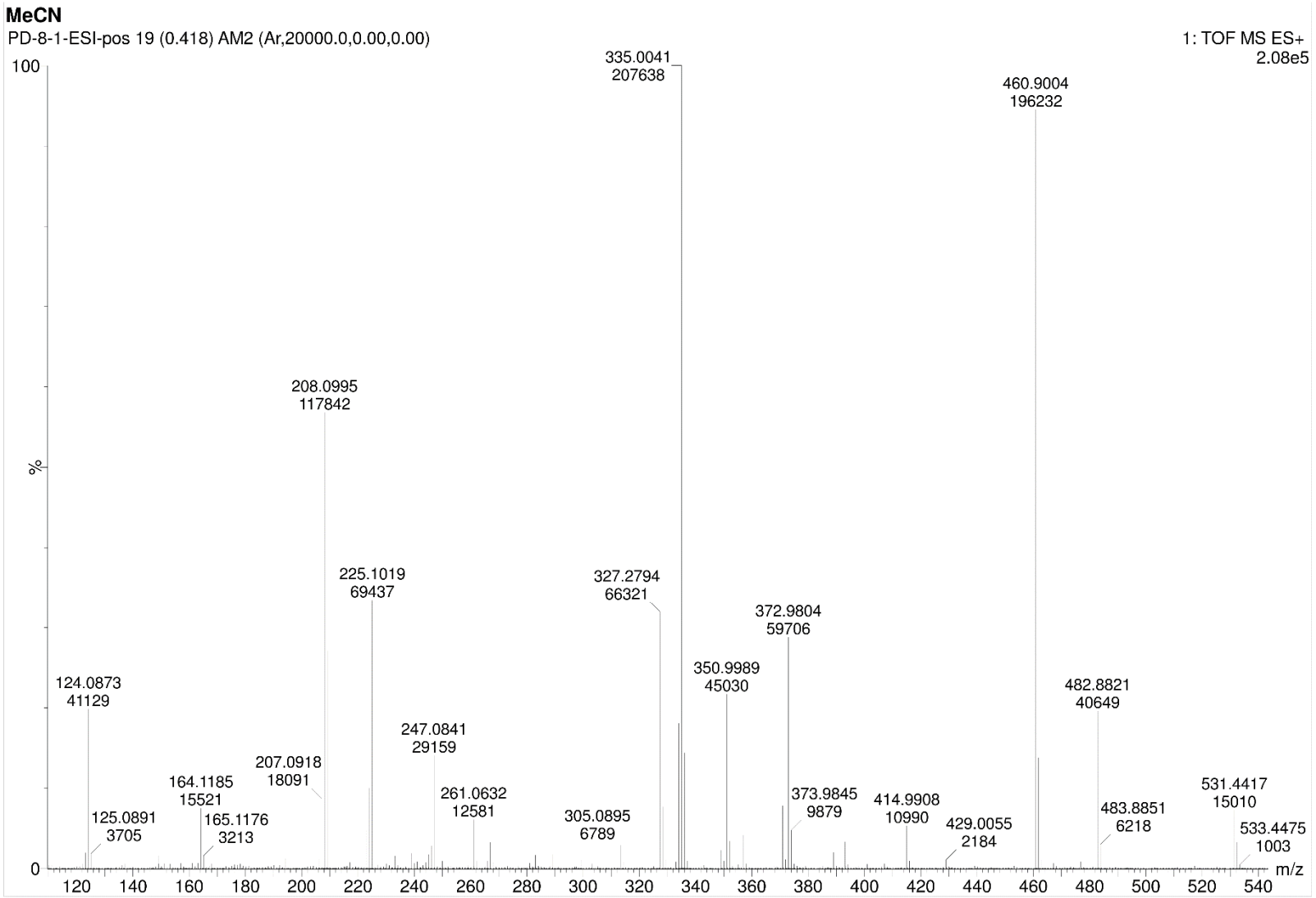

10.1.13 2,2'-((1,10-phenanthroline-2,9-diyl)bis(methylene))bis(isoindoline-1,3-dione) (DMP-Phthalimide)

^{1}H-NMR

(500 MHz, $CDCl_3$)

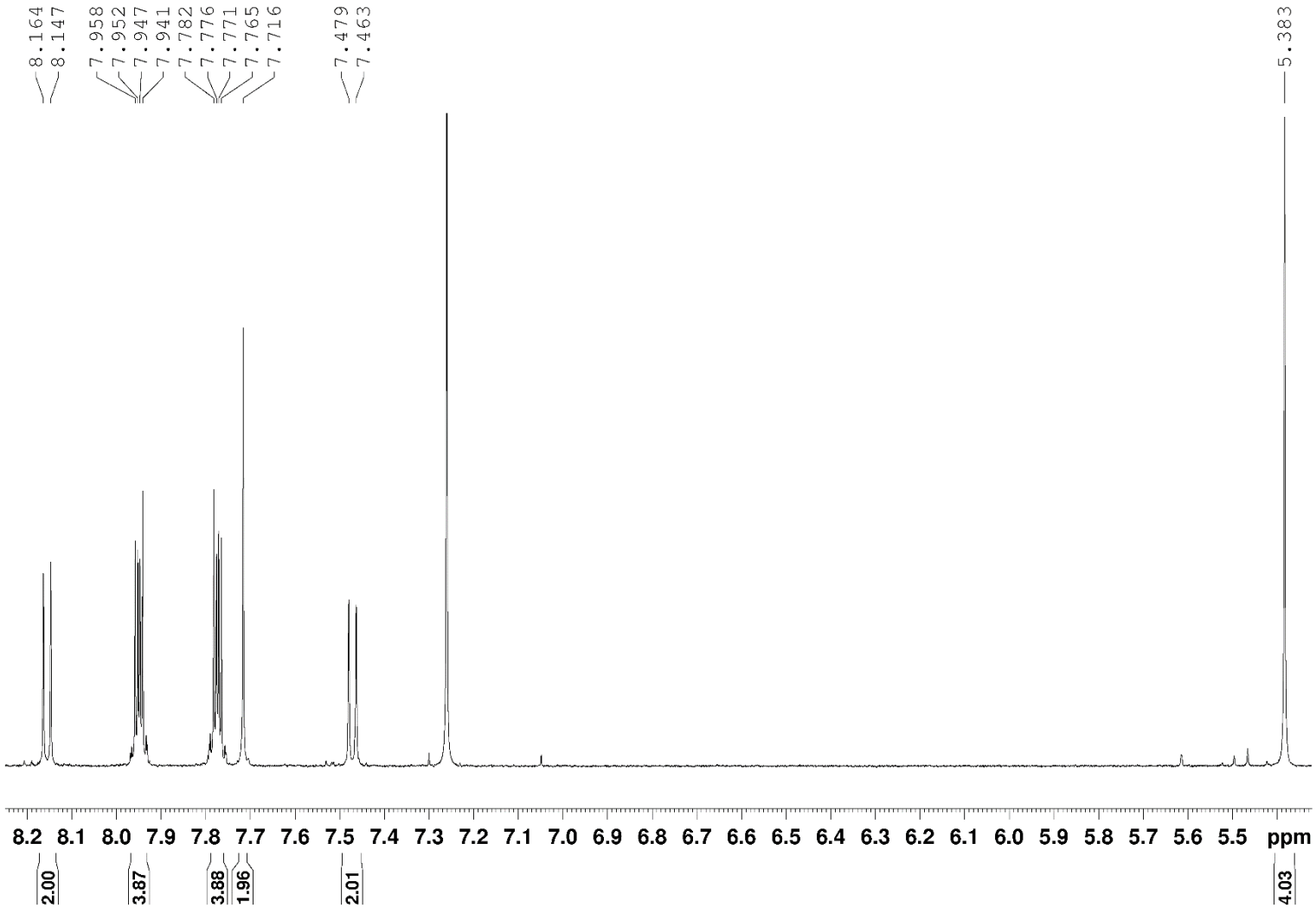

^{13}C-NMR

(125 MHz, $CDCl_3$)

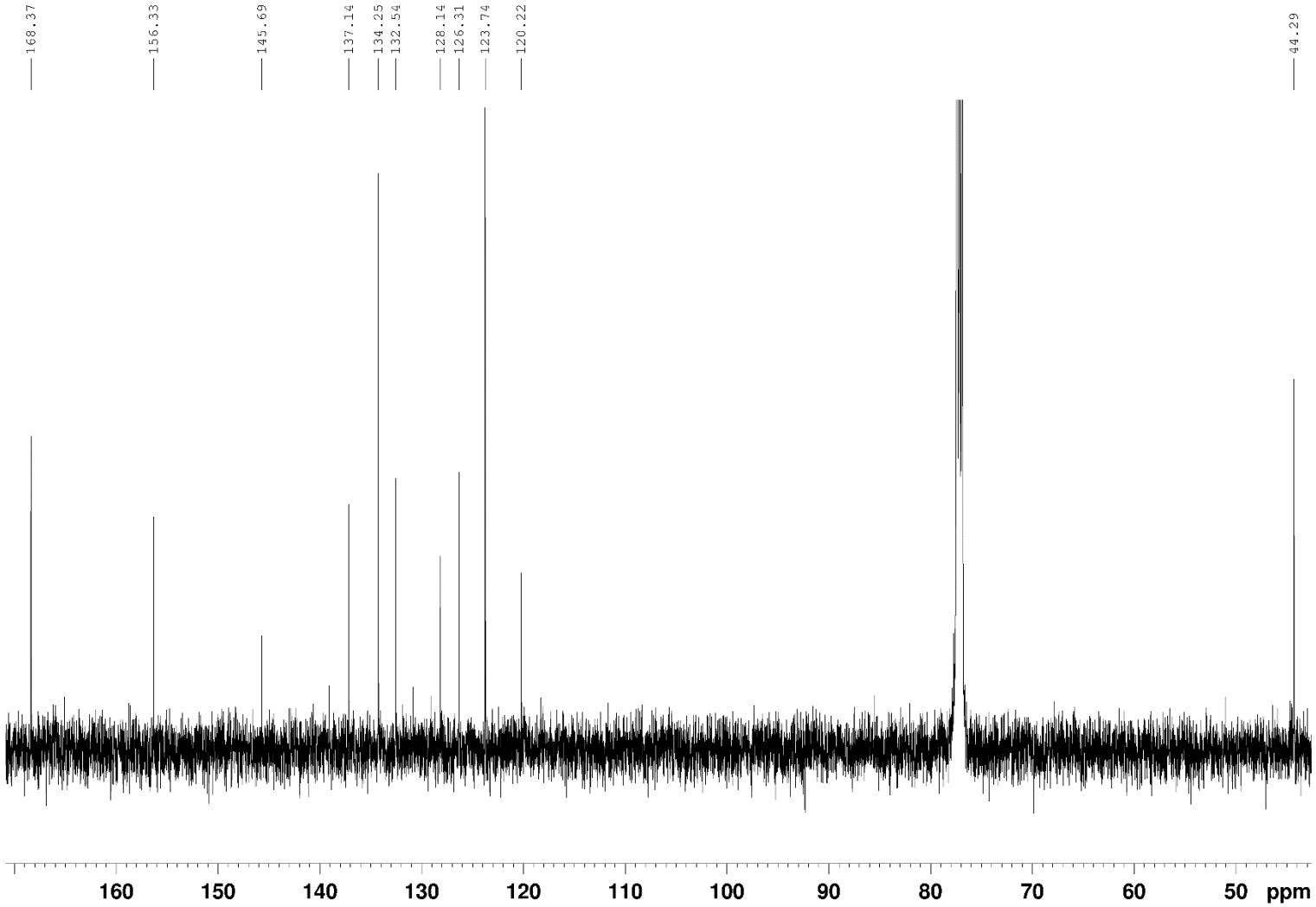

EI-MS

(m/z)

D:\Kai Stührenberg\...\KST-168-neu-EI 15.11.2016 09:52:31 KST-168-neu
EI, R=1200, 70eV, 200 " C
KST-168-neu-EI #41 RT: 4,28 AV: 1 NL: 6,93E6
T: + c EI Full ms [34,50-600,50]

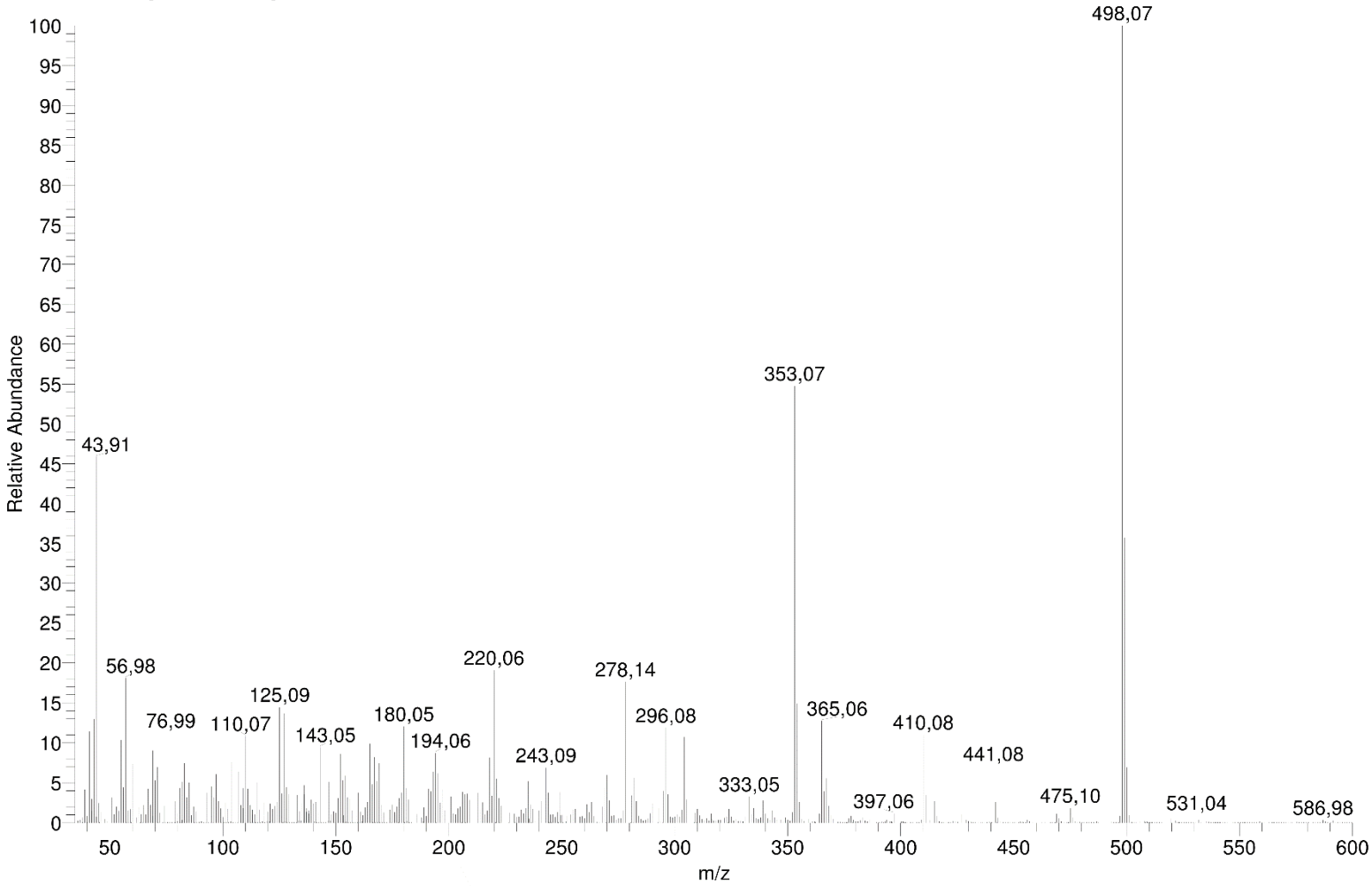

10.1.14 Di(pyridin-2-yl)methane

EI MS

(m/z)

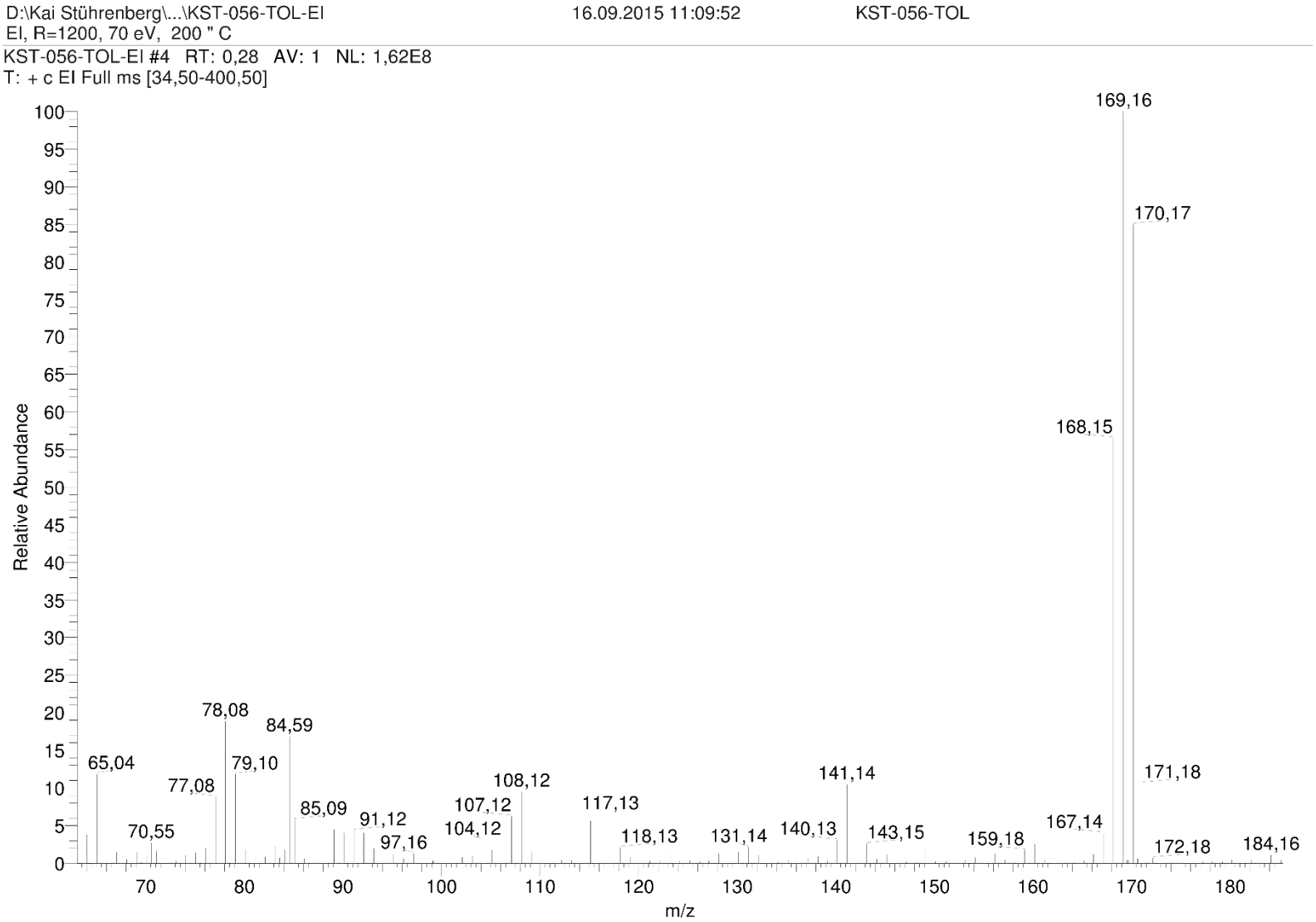

ESI-MS (pos)

(m/z in acetonitrile/ MeOH/Formic acid)

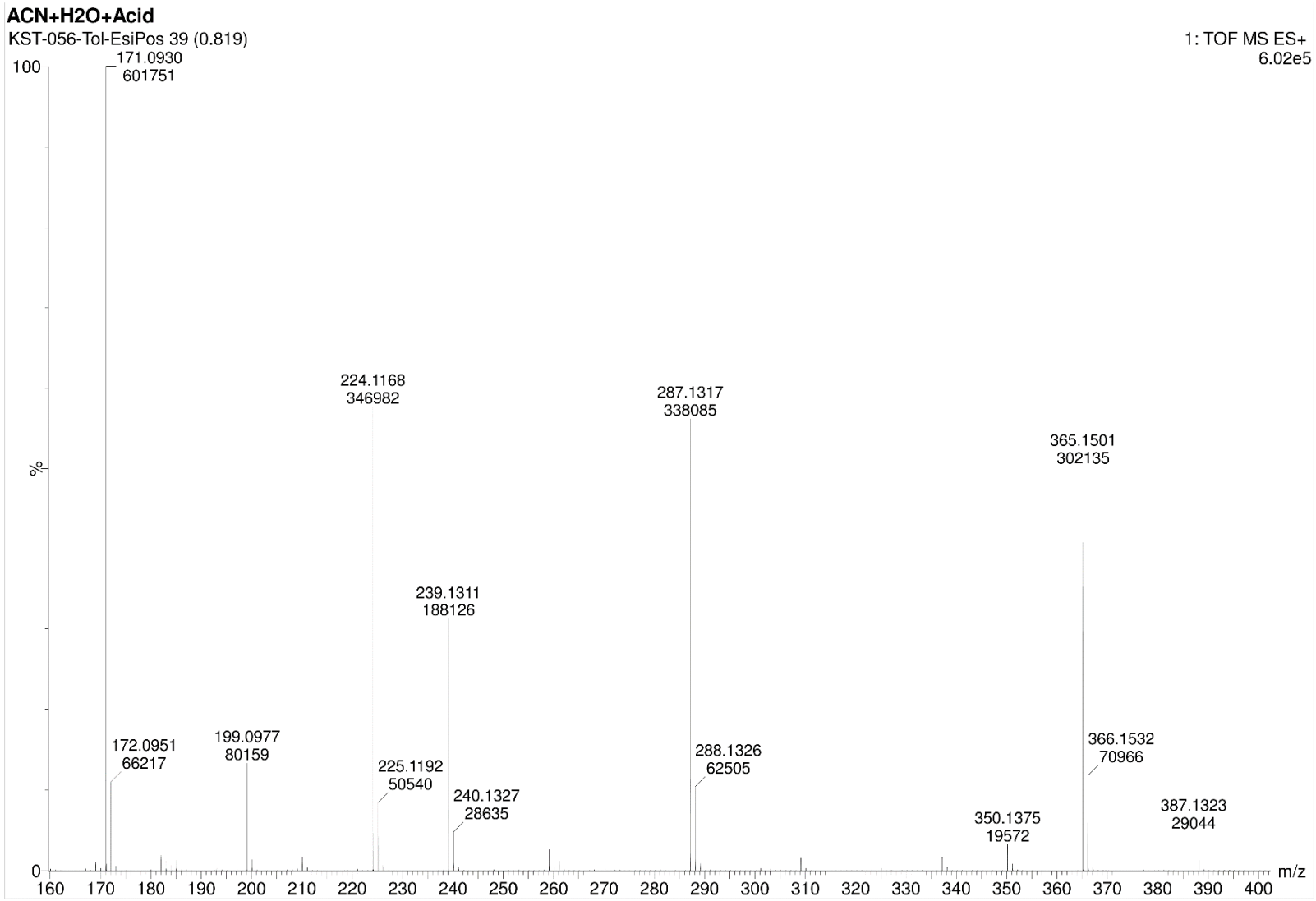

10.1.15 5,6,7,8,9,14,15,16,17,18-decahydrodibenzo[b,i][1,4,8,11]tetraazacyclotetradecine (BenzeneNH$_2$Propyl$_2$)

EI MS

(m/z)

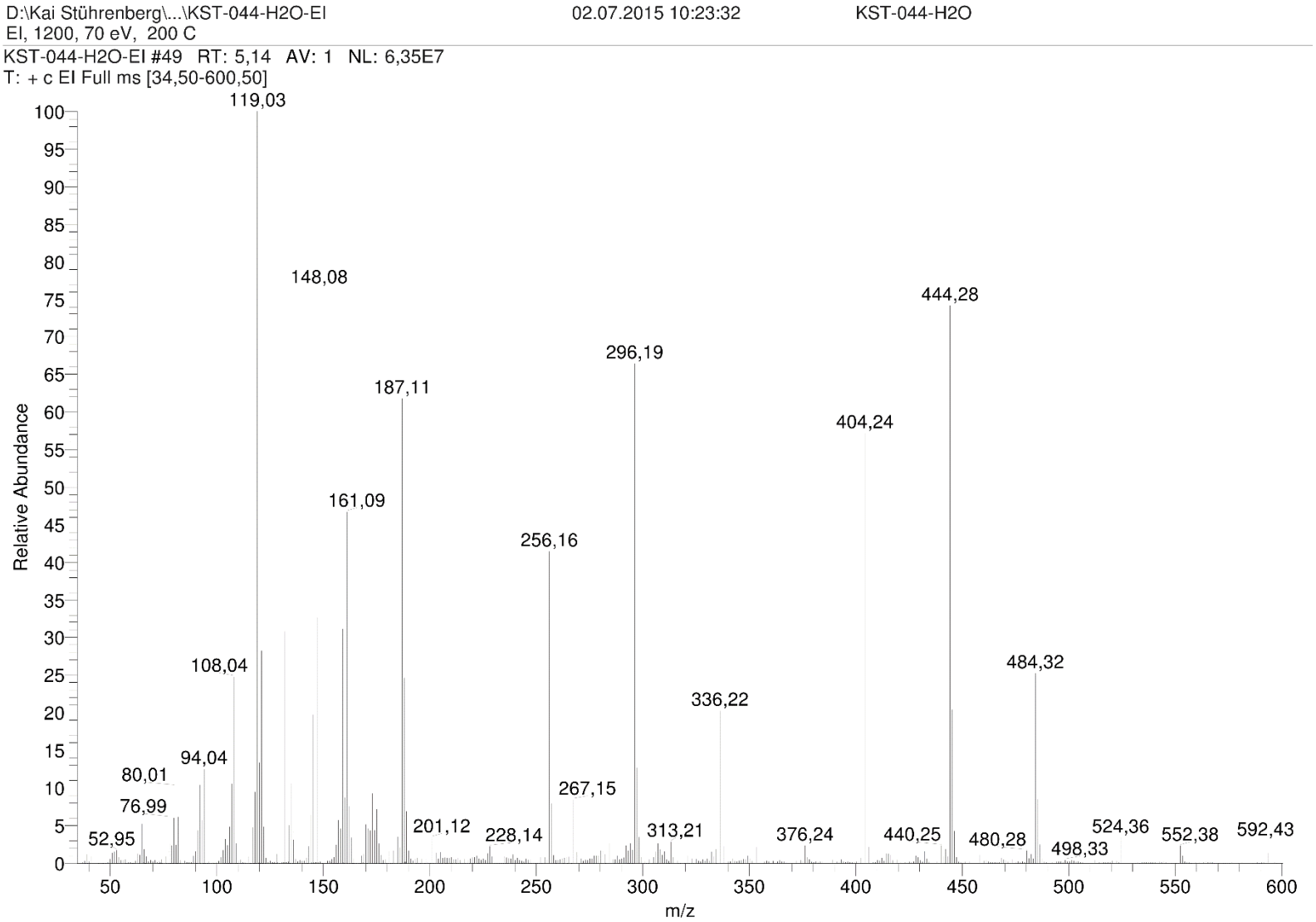

10.1.16 3,7-dipropyl-3,7-diaza-1,5(2,6)-dipyridinacyclooctaphane (DAPy-Propyl)

ESI-MS (pos)

(m/z in MeCN)

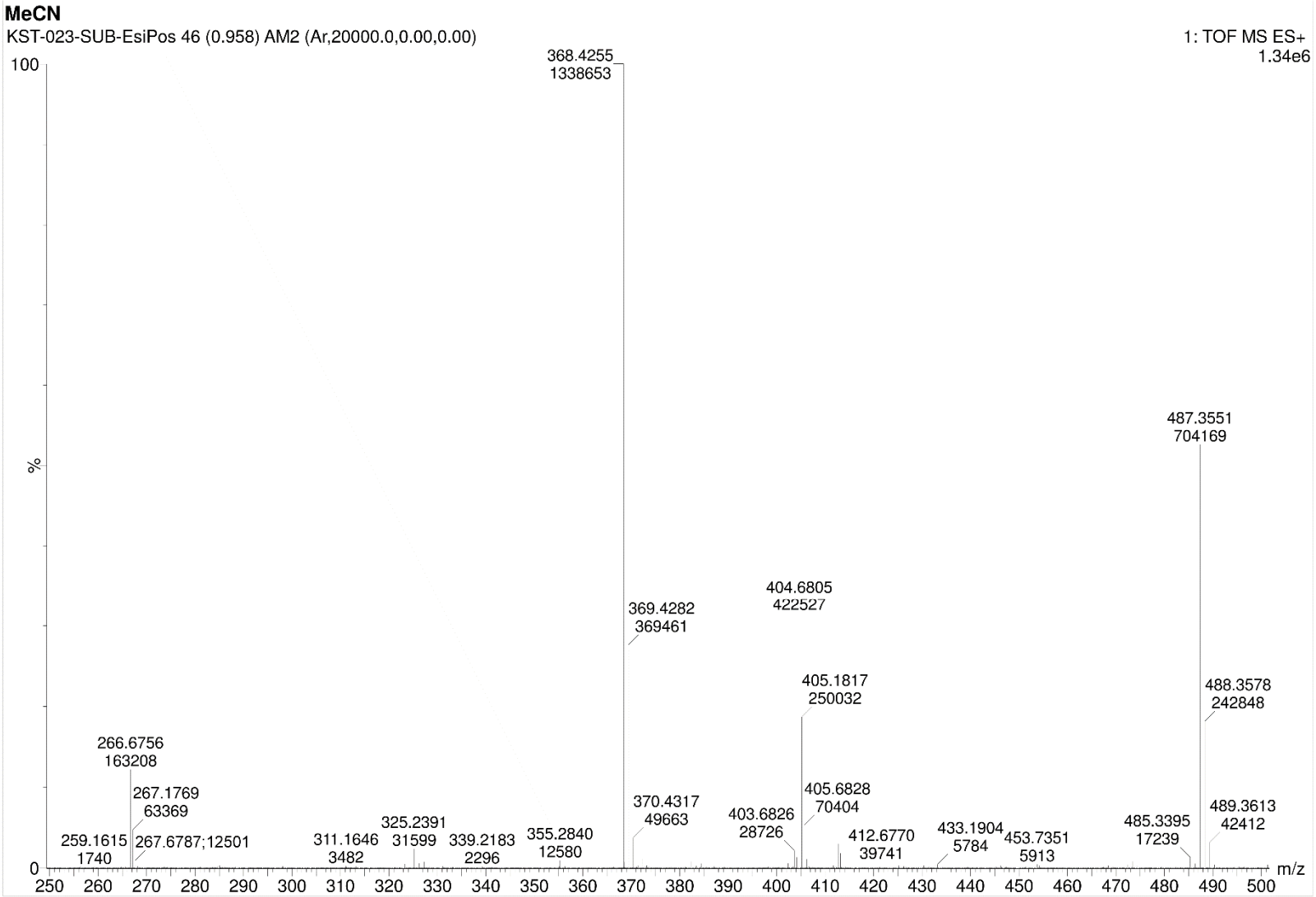

10.1.17 *p*-Toluenesulfonamide sodium salt

^{1}H-NMR

(500 MHz, DMSO-d_6)

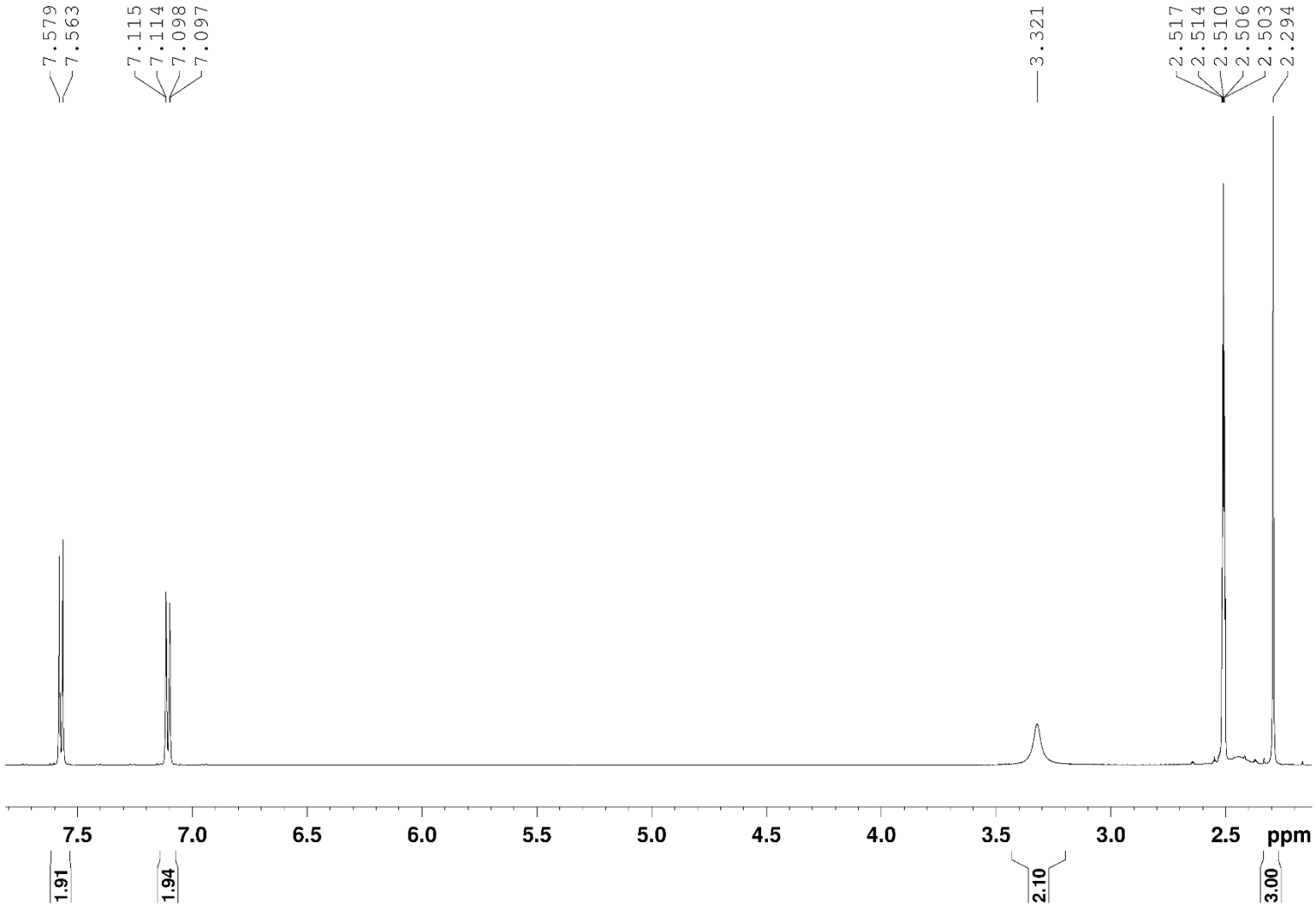

^{13}C-NMR

(125 MHz, DMSO-d_6)

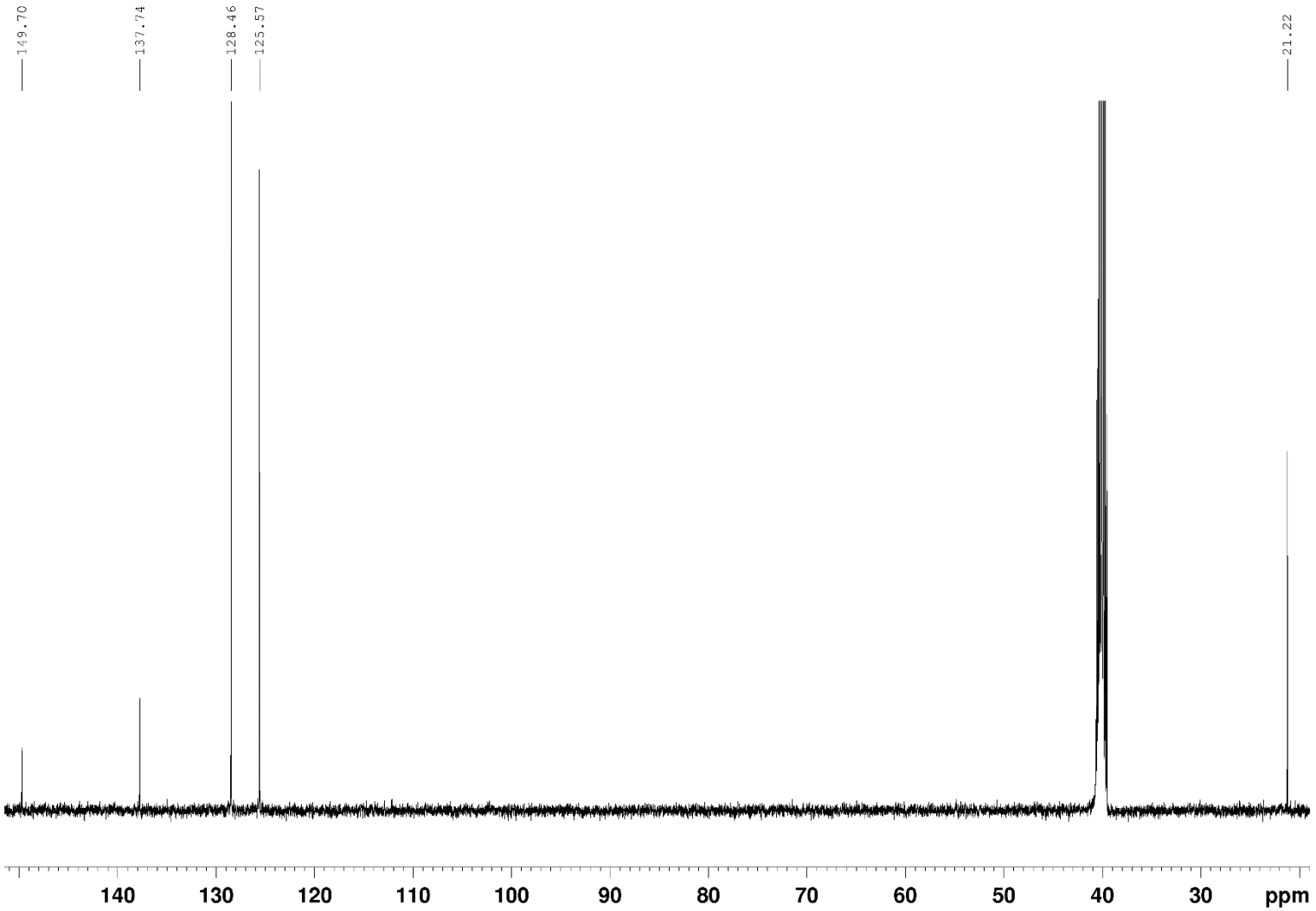

10.1.18 Dimethyl pyridine-2,6-dicarboxylate (DMPy-OOH)

^{1}H-NMR

(500 MHz, $CDCl_3$)

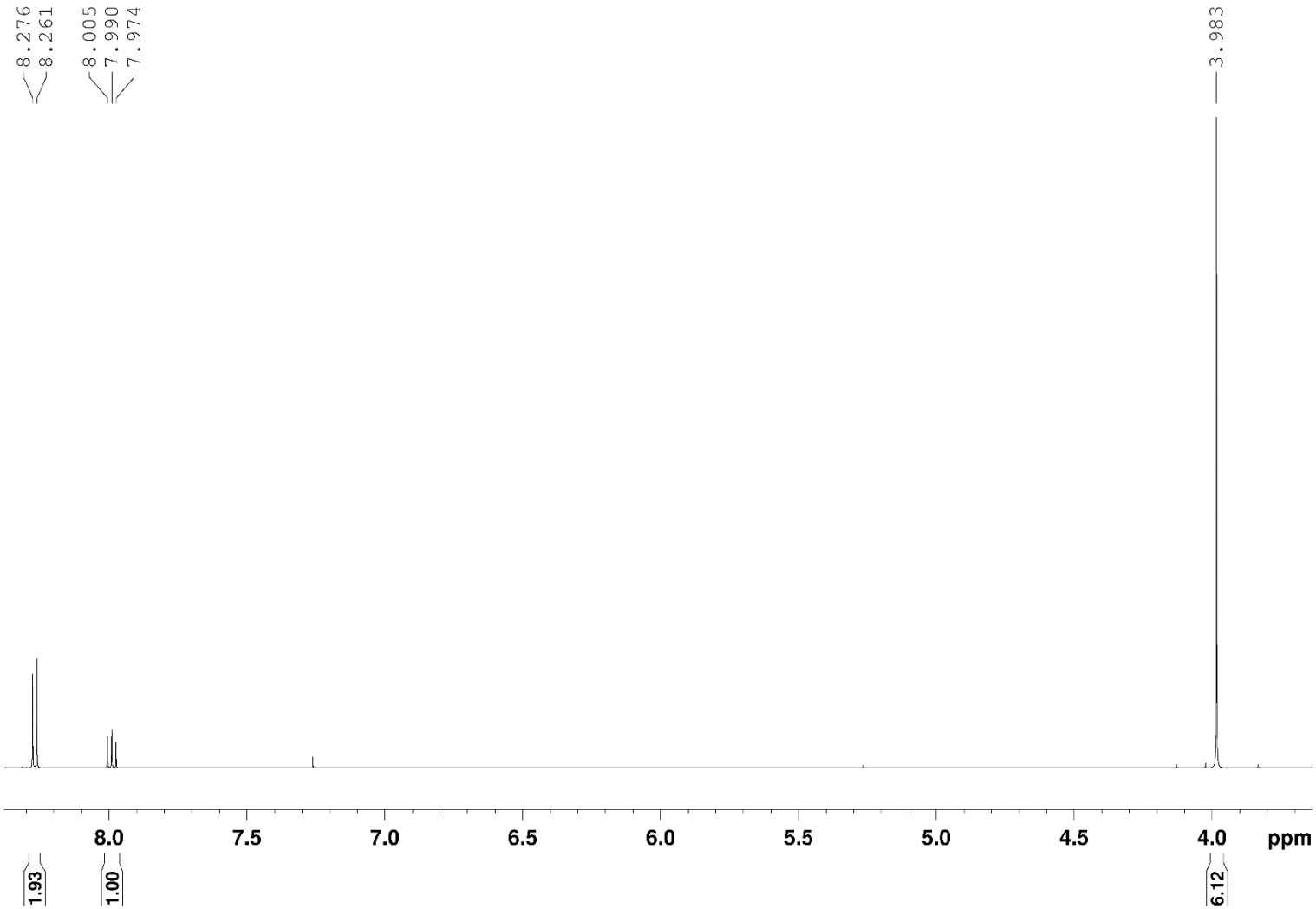

^{13}C-NMR

(125 MHz, $CDCl_3$)

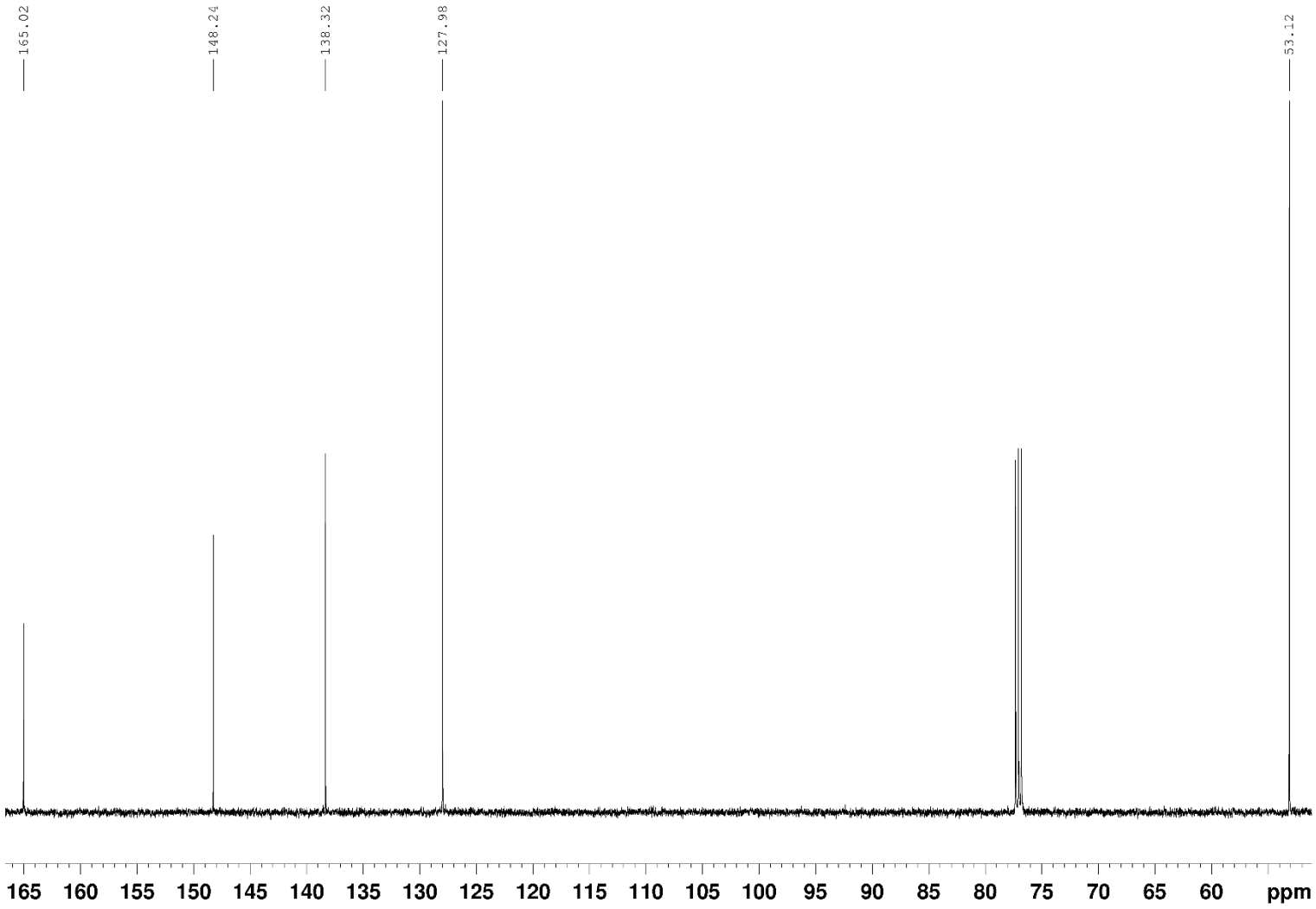

ESI-MS (pos)

(m/z (%) in MeOH)

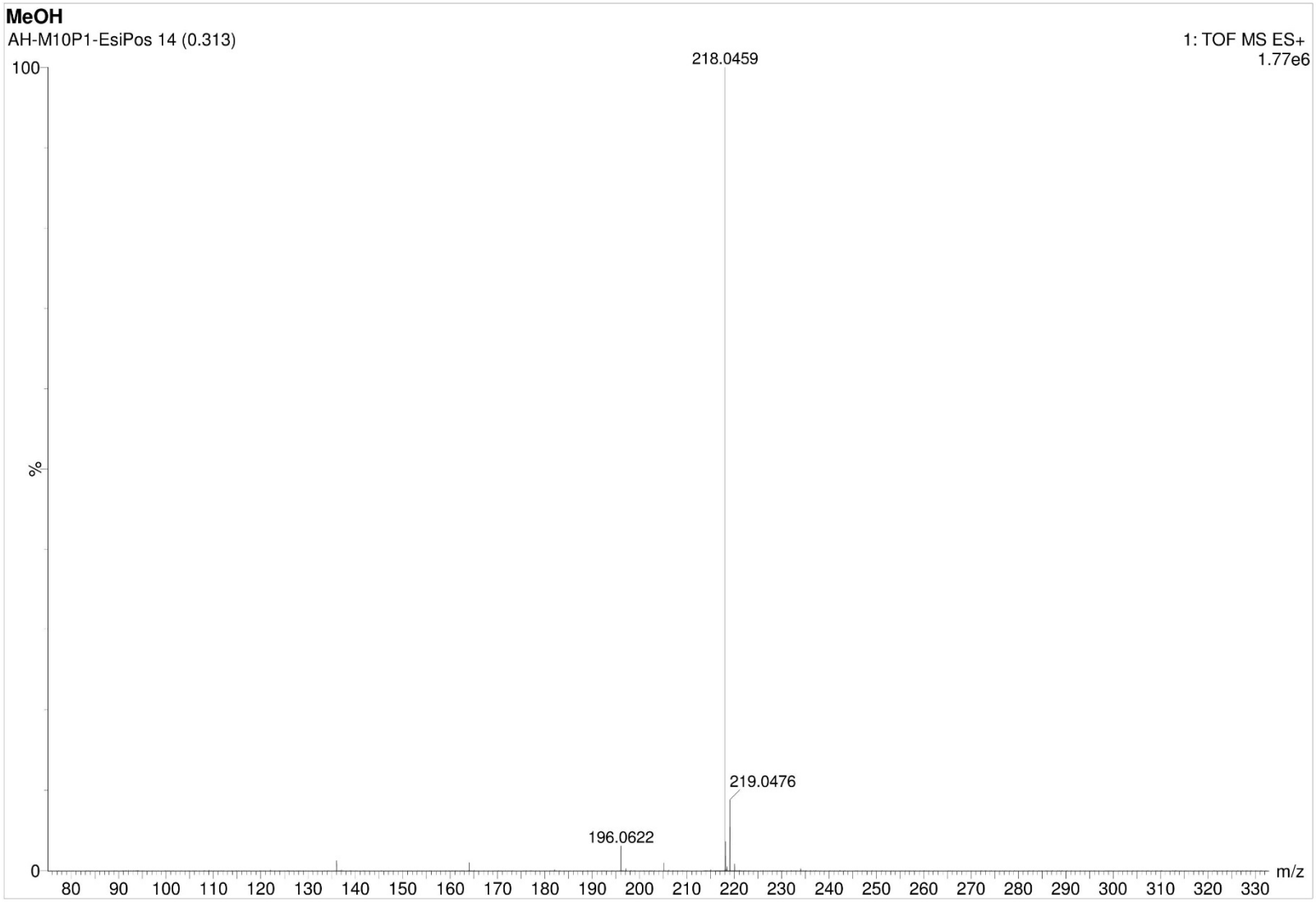

10.1.19 Pyridine-2,6-diyldimethanol (DMPy-OH)

^{1}H-NMR

(500 MHz, $CDCl_3$)

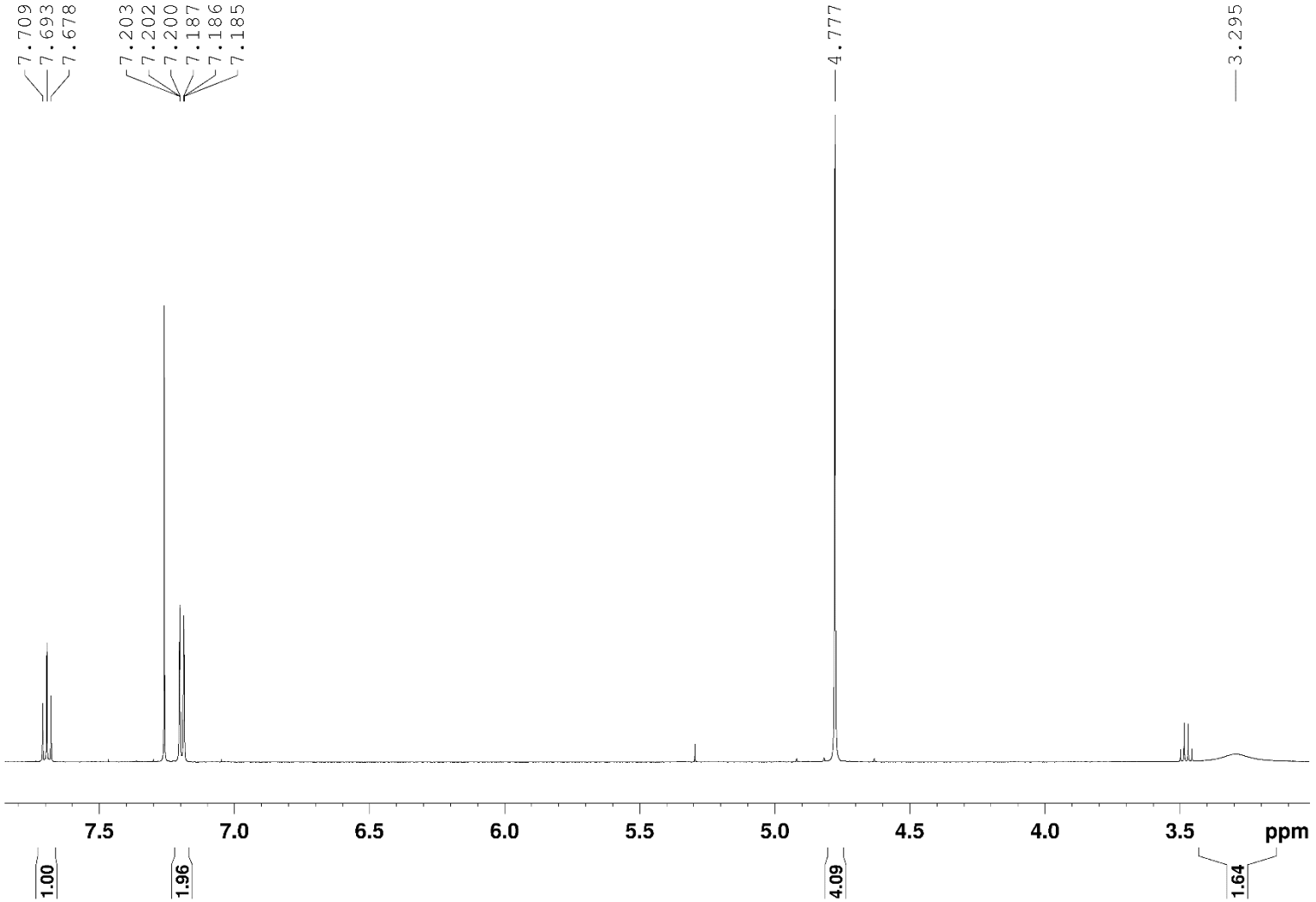

^{13}C-NMR

(125 MHz, $CDCl_3$)

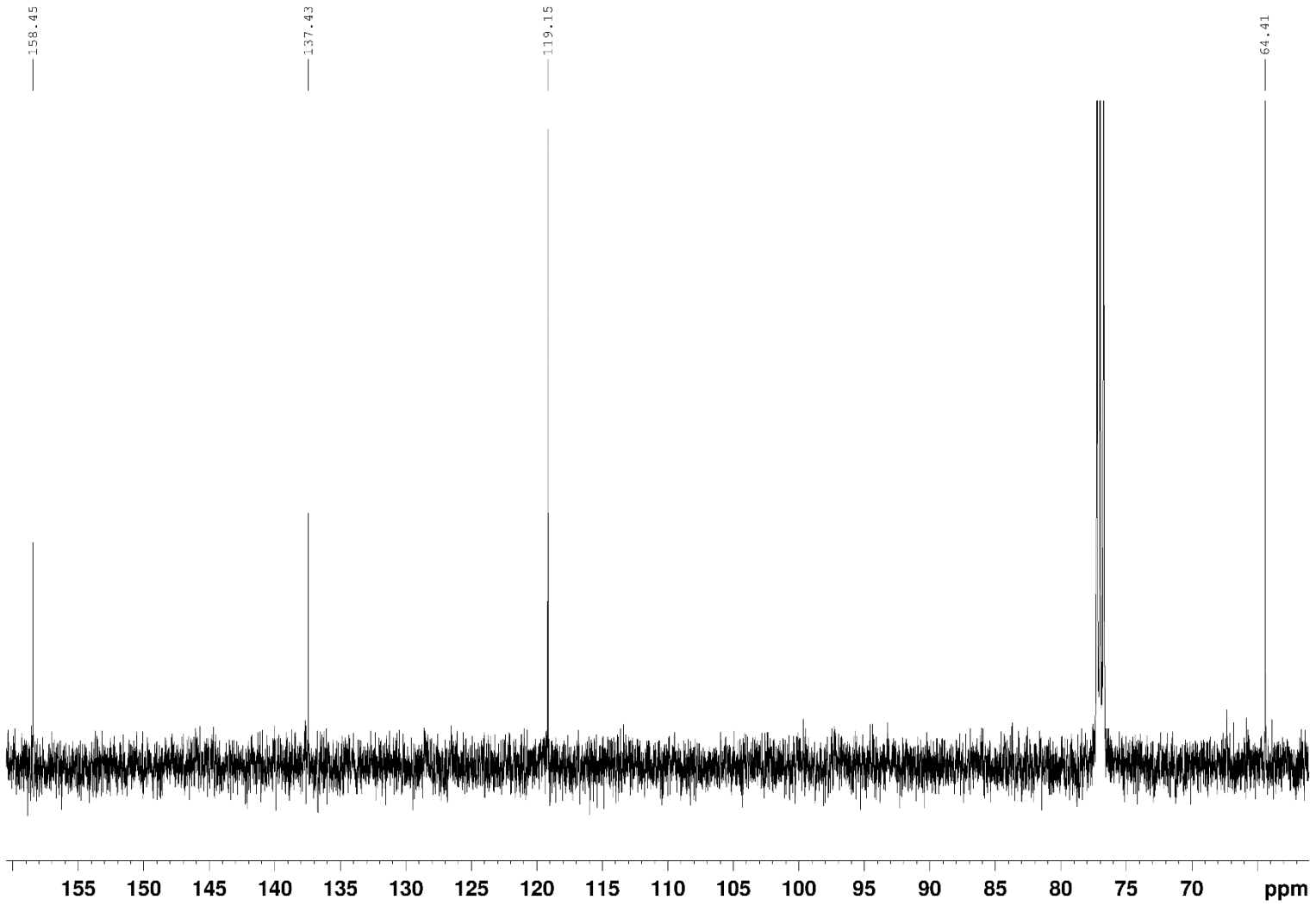

ESI-MS (pos)

(m/z (%) in MeOH/H_2O)

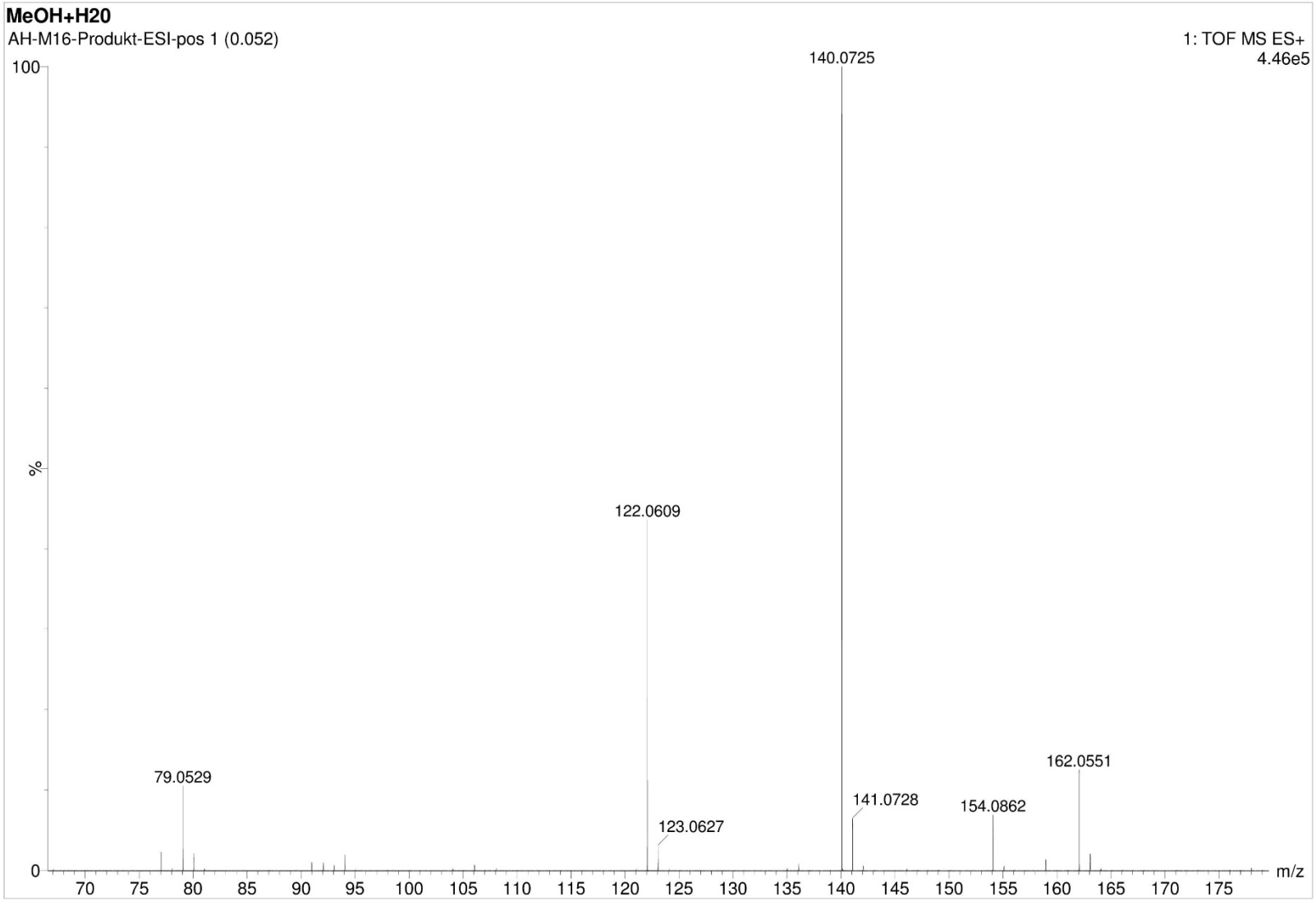

10.1.20 2,6-Bis(bromomethyl)pyridine (DMPy-Br)

^{1}H-NMR

(500 MHz, $CDCl_3$)

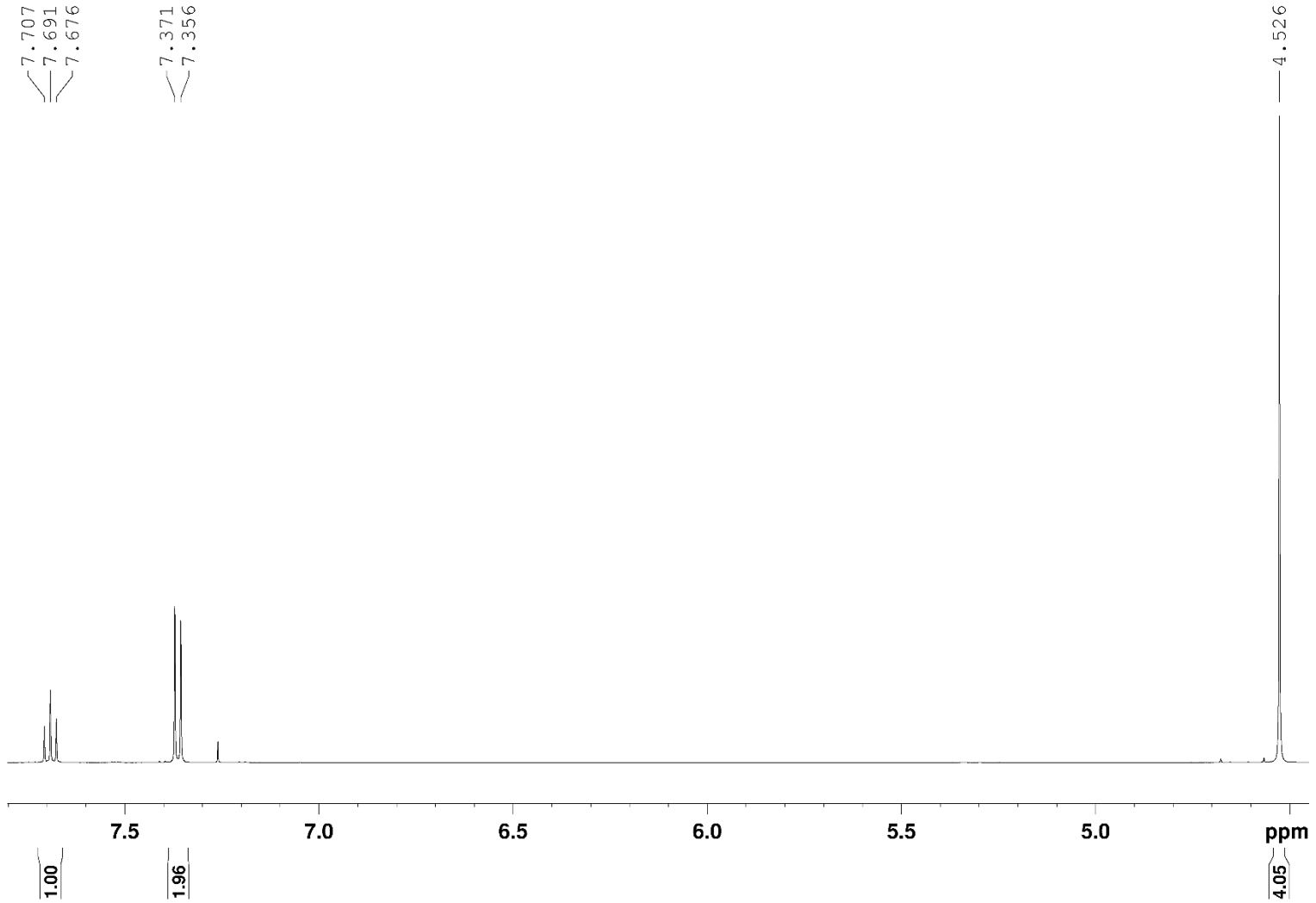

^{13}C-NMR

(125 MHz, $CDCl_3$)

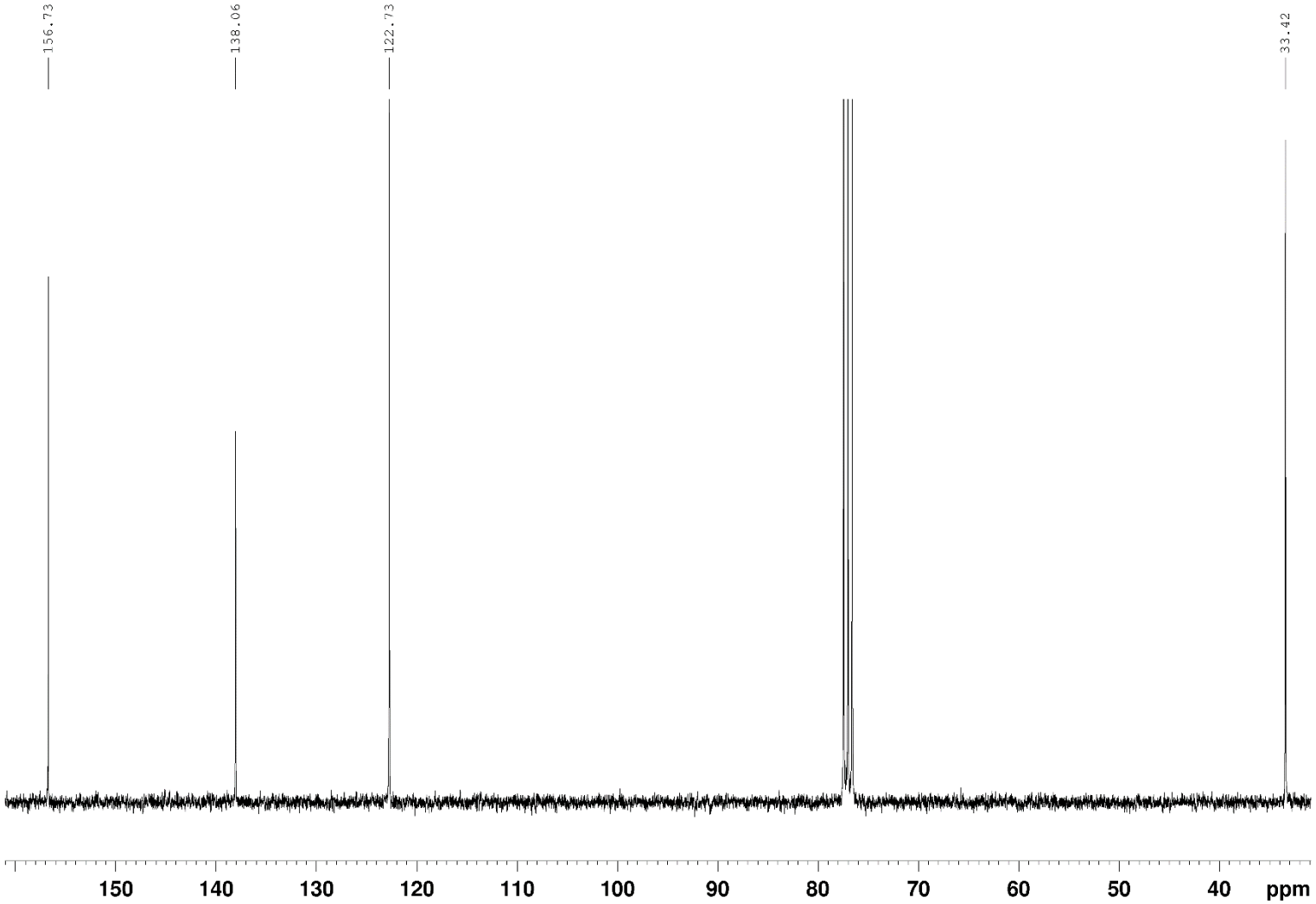

ESI-MS (pos)

(m/z (%) in MeCN/Formic acid)

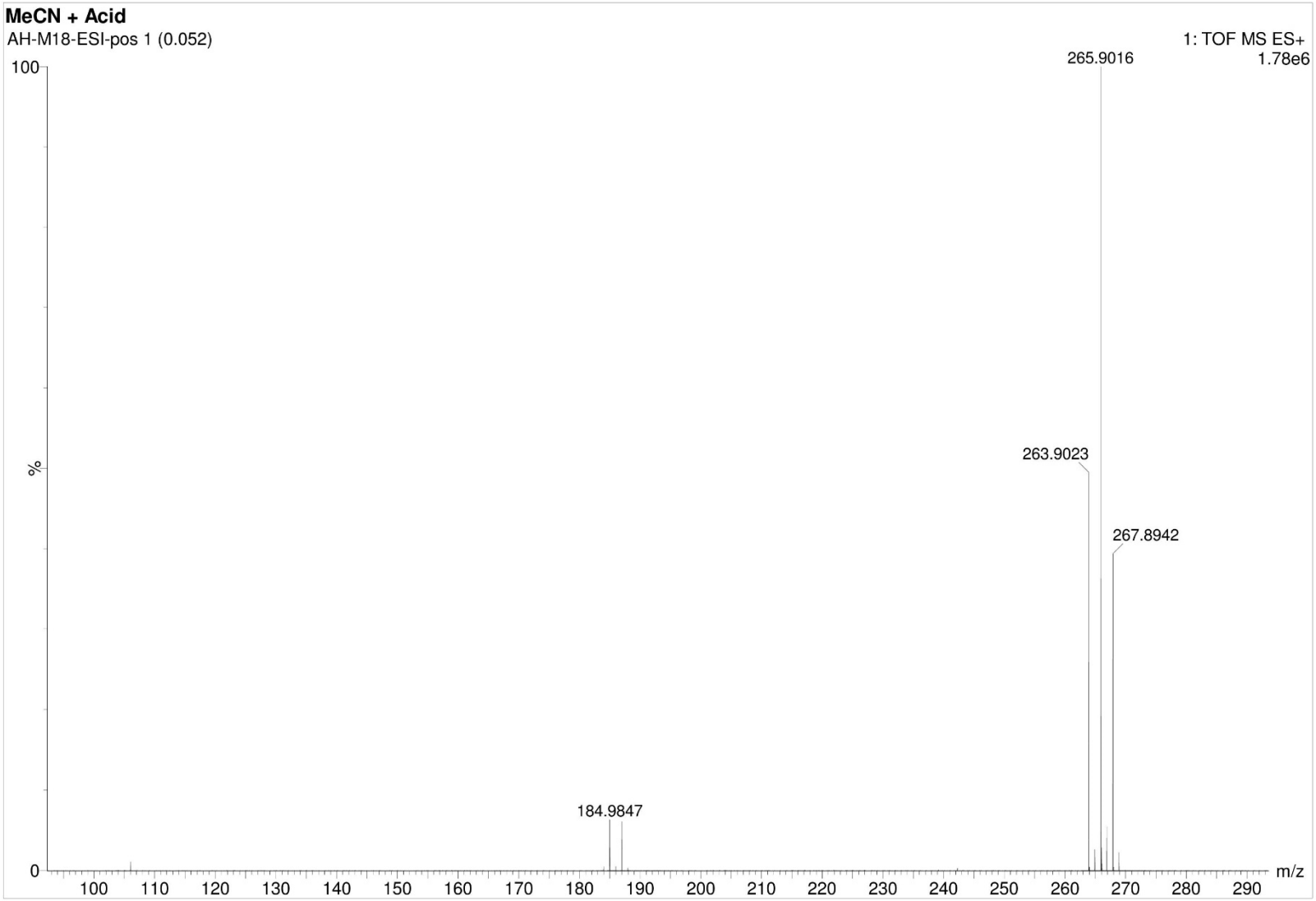

10.1.21 Ditosyl Diazapyridinophane (DAPy-Ts)

^{1}H-NMR

(500 MHz, $CDCl_3$)

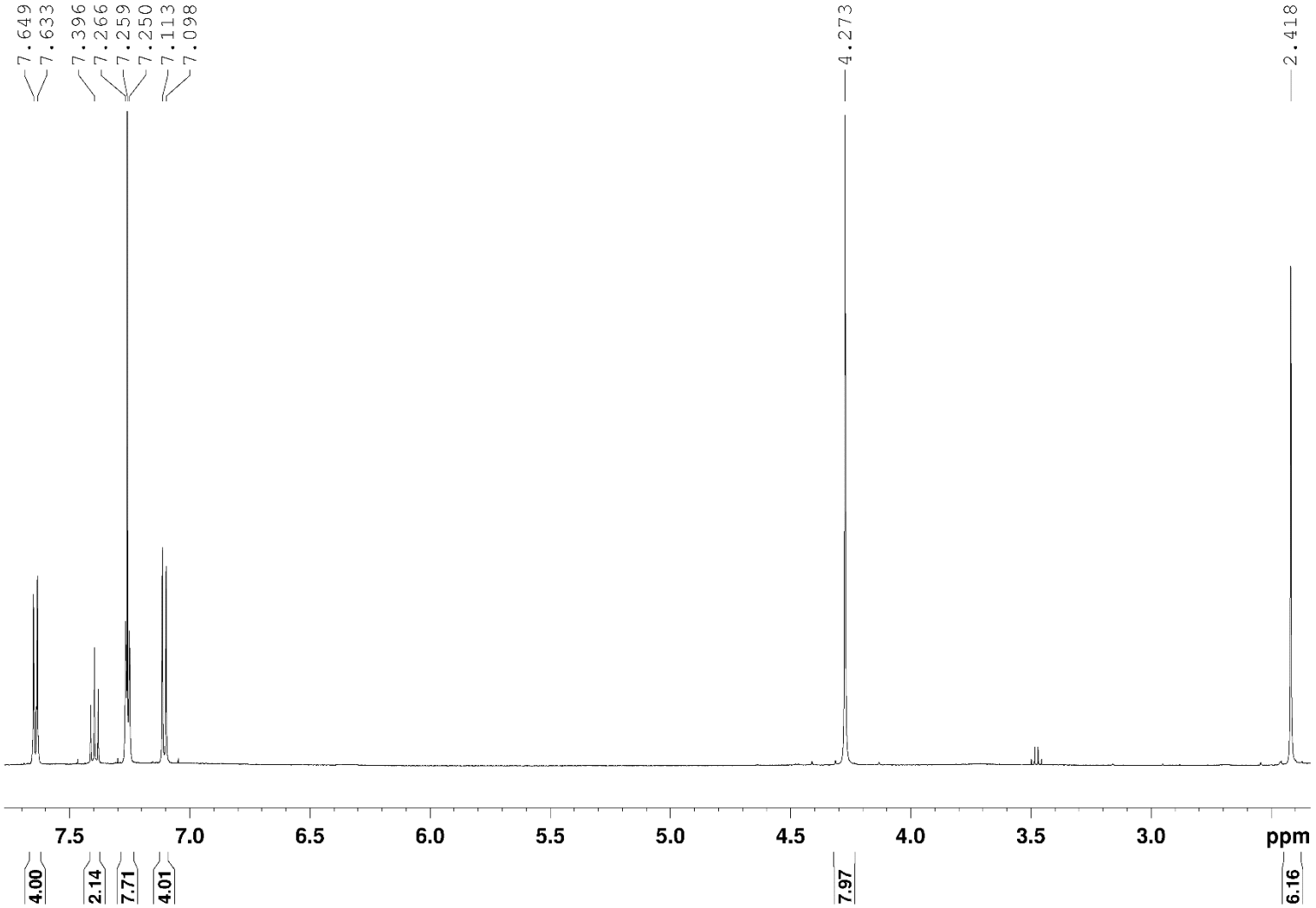

^{13}C-NMR

(125 MHz, $CDCl_3$)

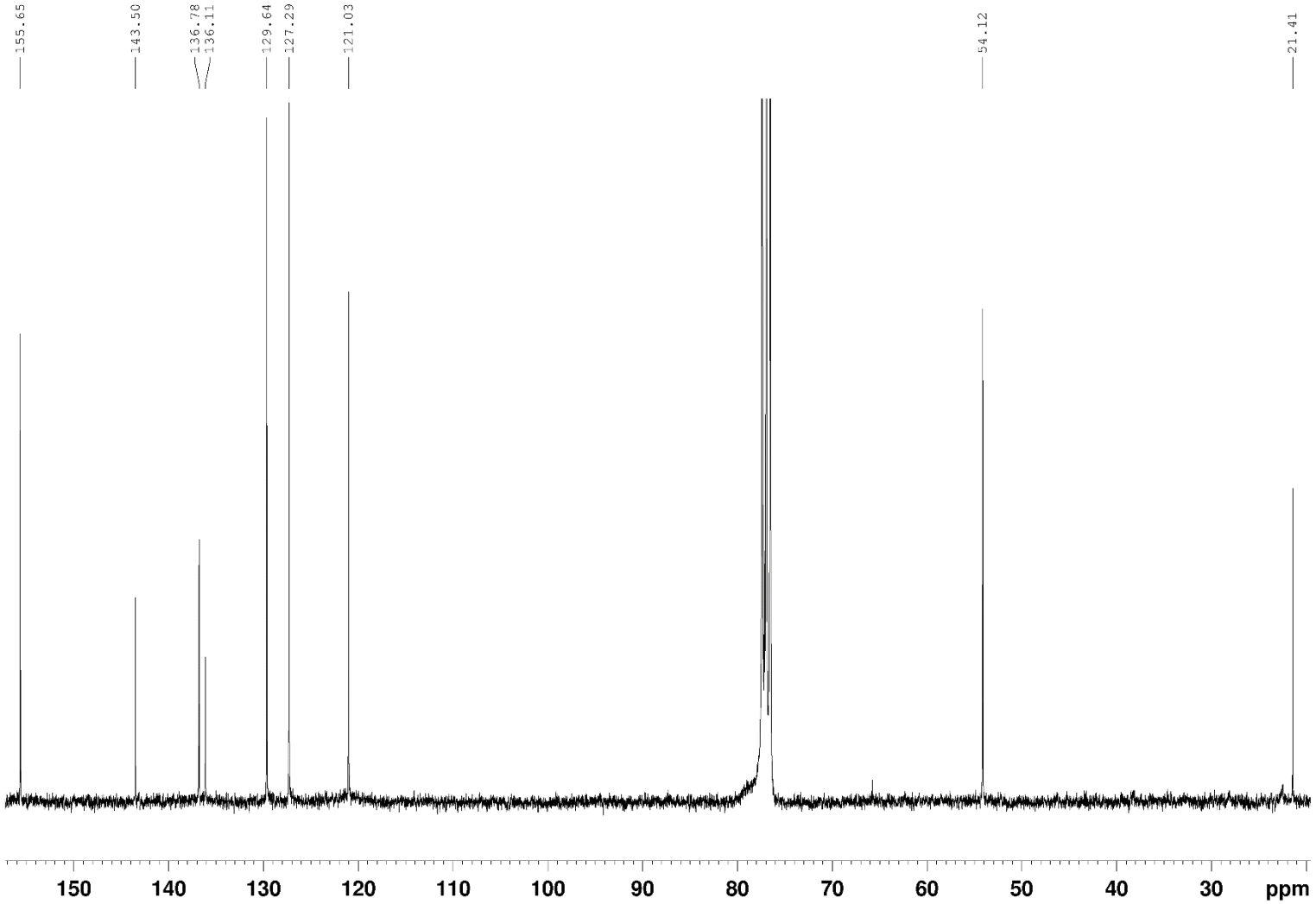

ESI-MS (pos)

(m/z (%) in MeOH/H_2O)

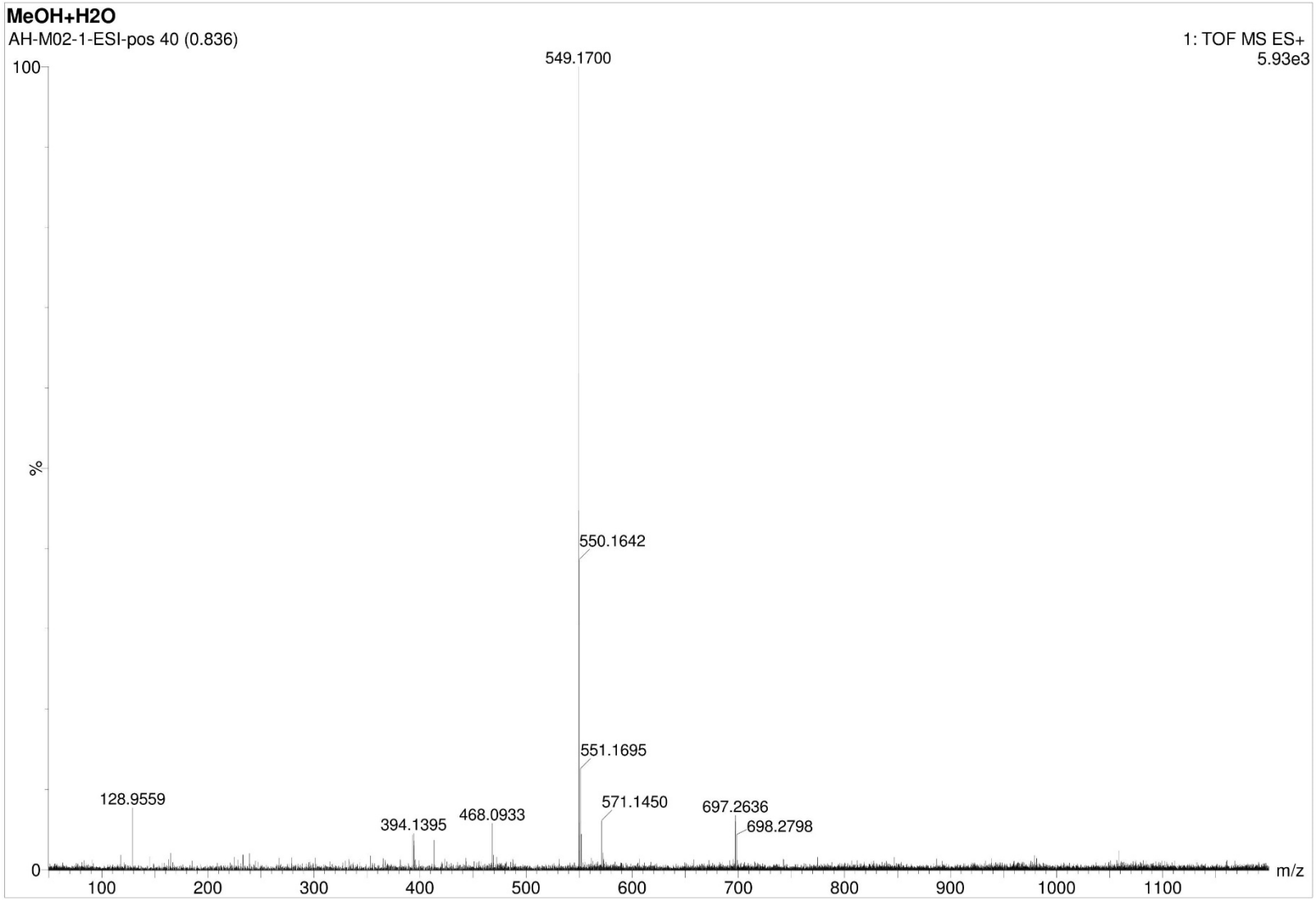

IR spectrum

(ATR)

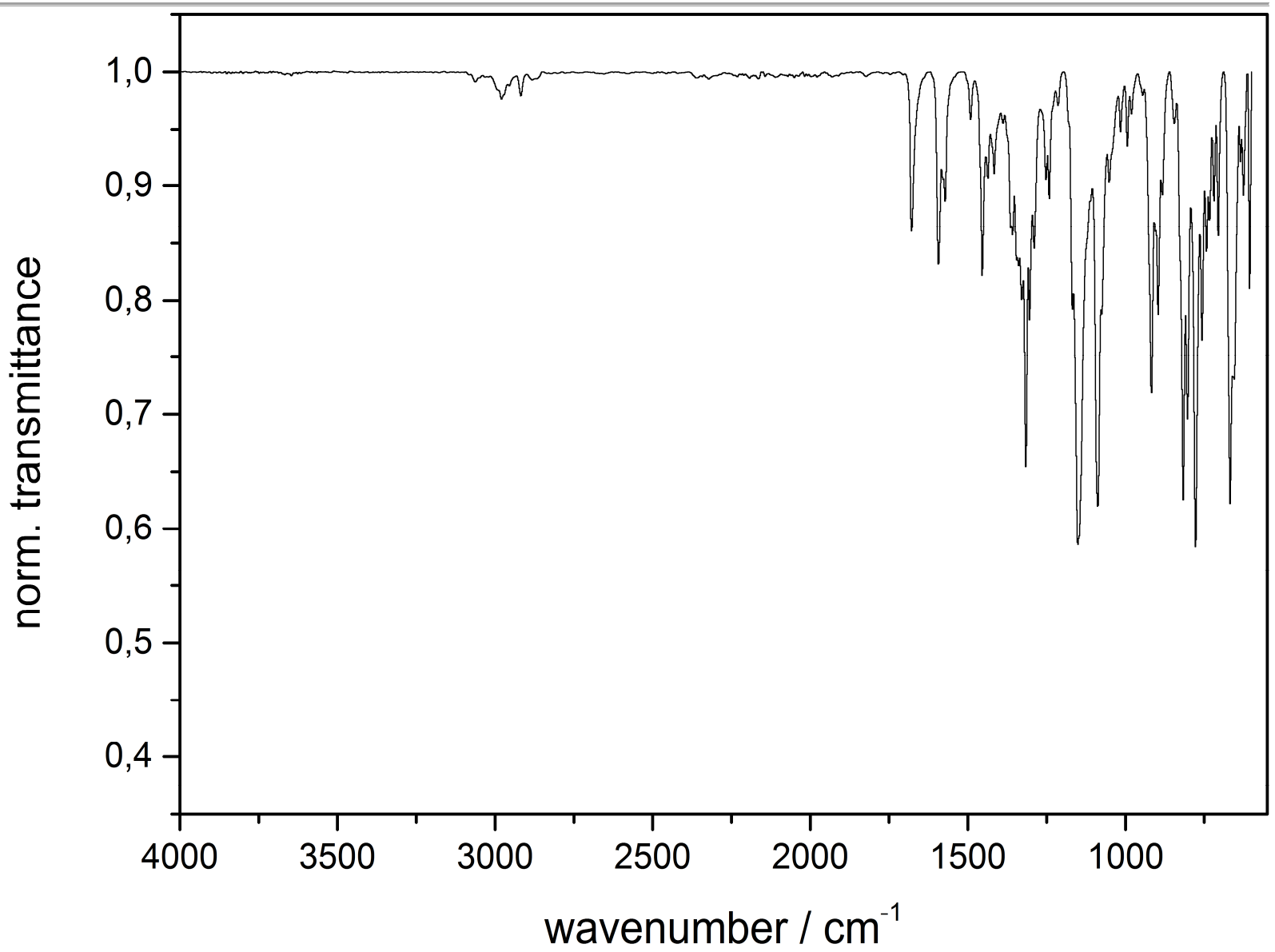

10.1.22 Unsubstituted Diazapyridinophane (DAPy-NH)

^{1}H-NMR

(500 MHz, $CDCl_3$)

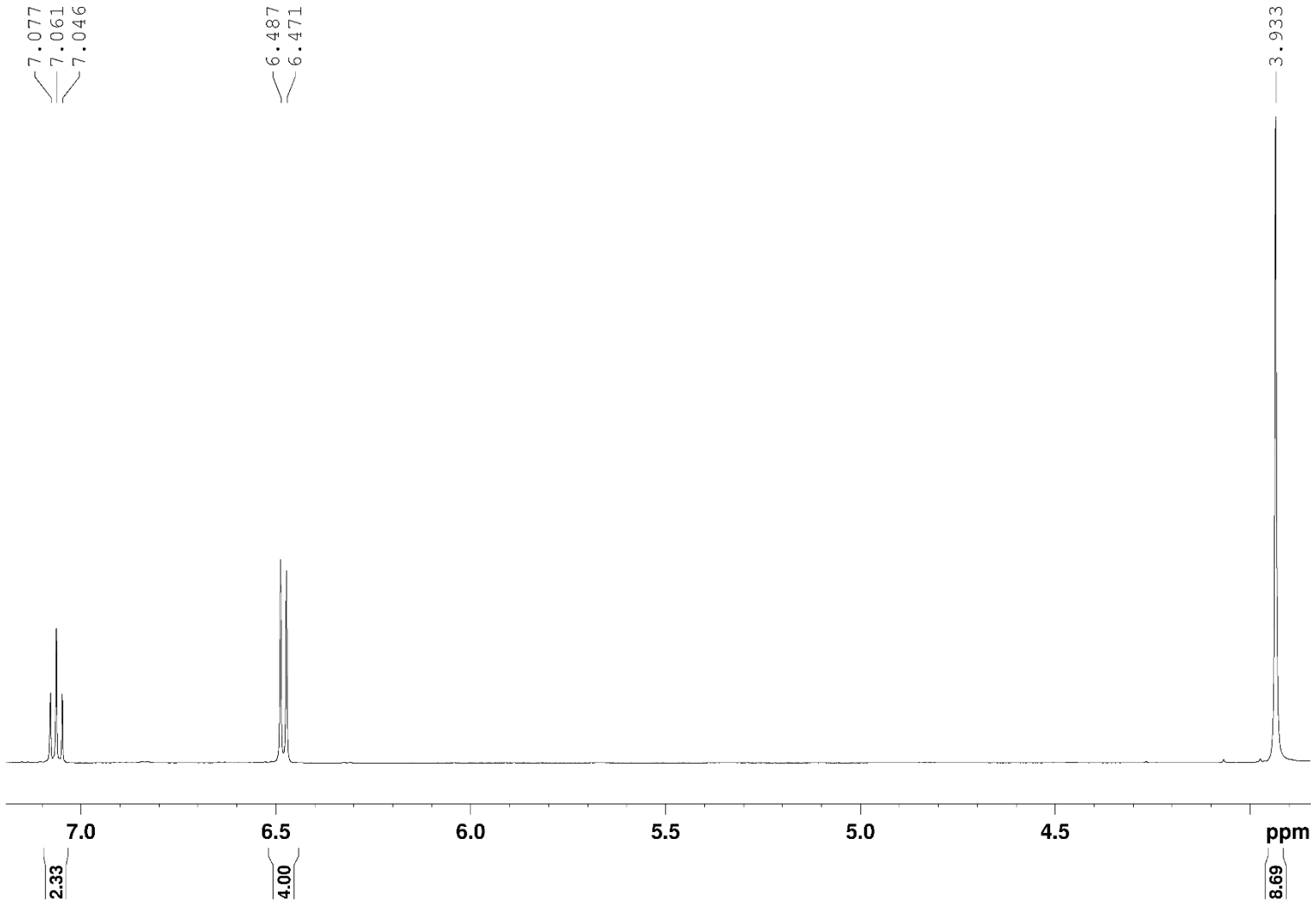

^{13}C-NMR

(125 MHz, $CDCl_3$)

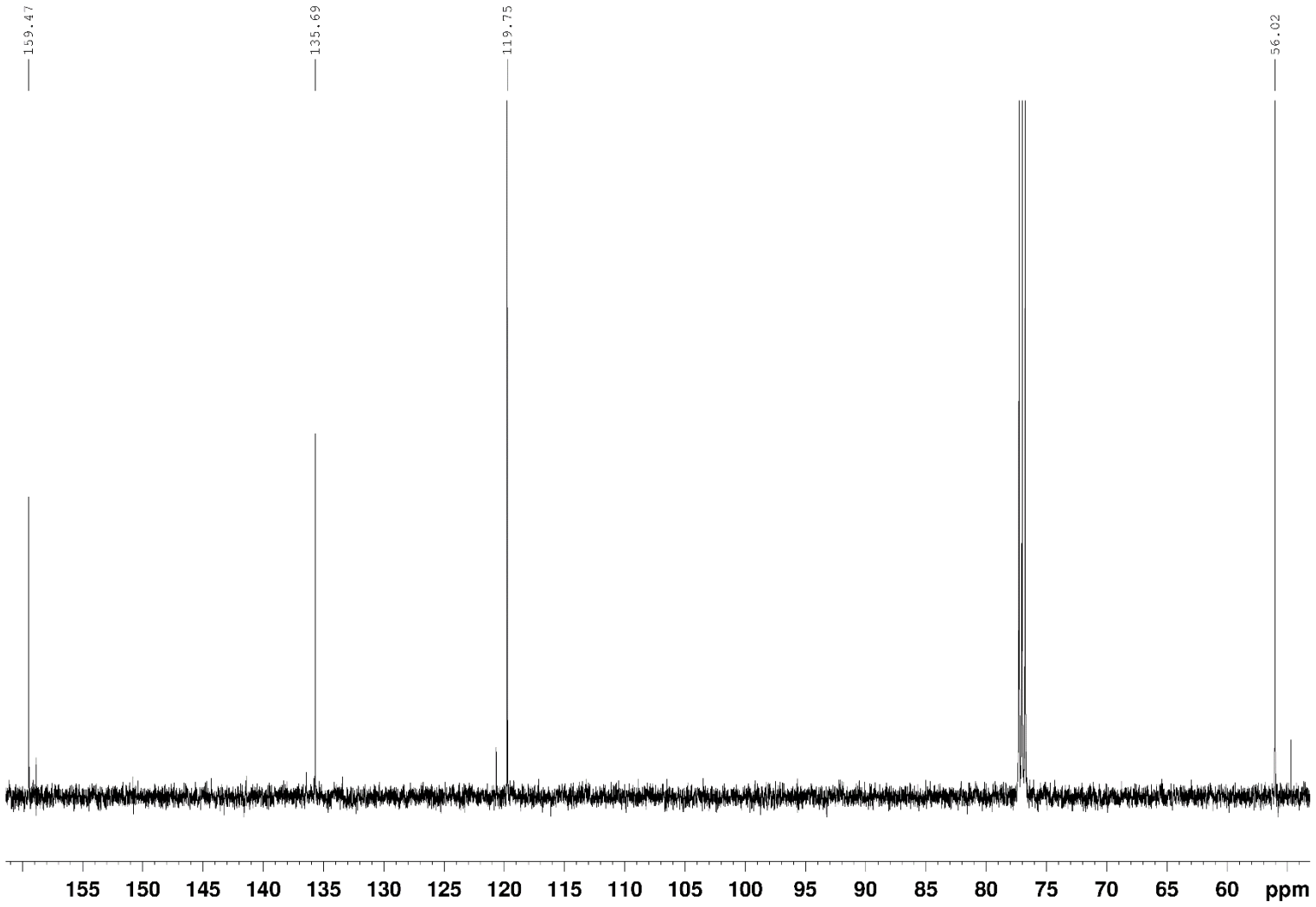

^{15}N-NMR

(50.7 MHz, $CDCl_3$, obtained by ^{15}N-^{1}H-HBMC)

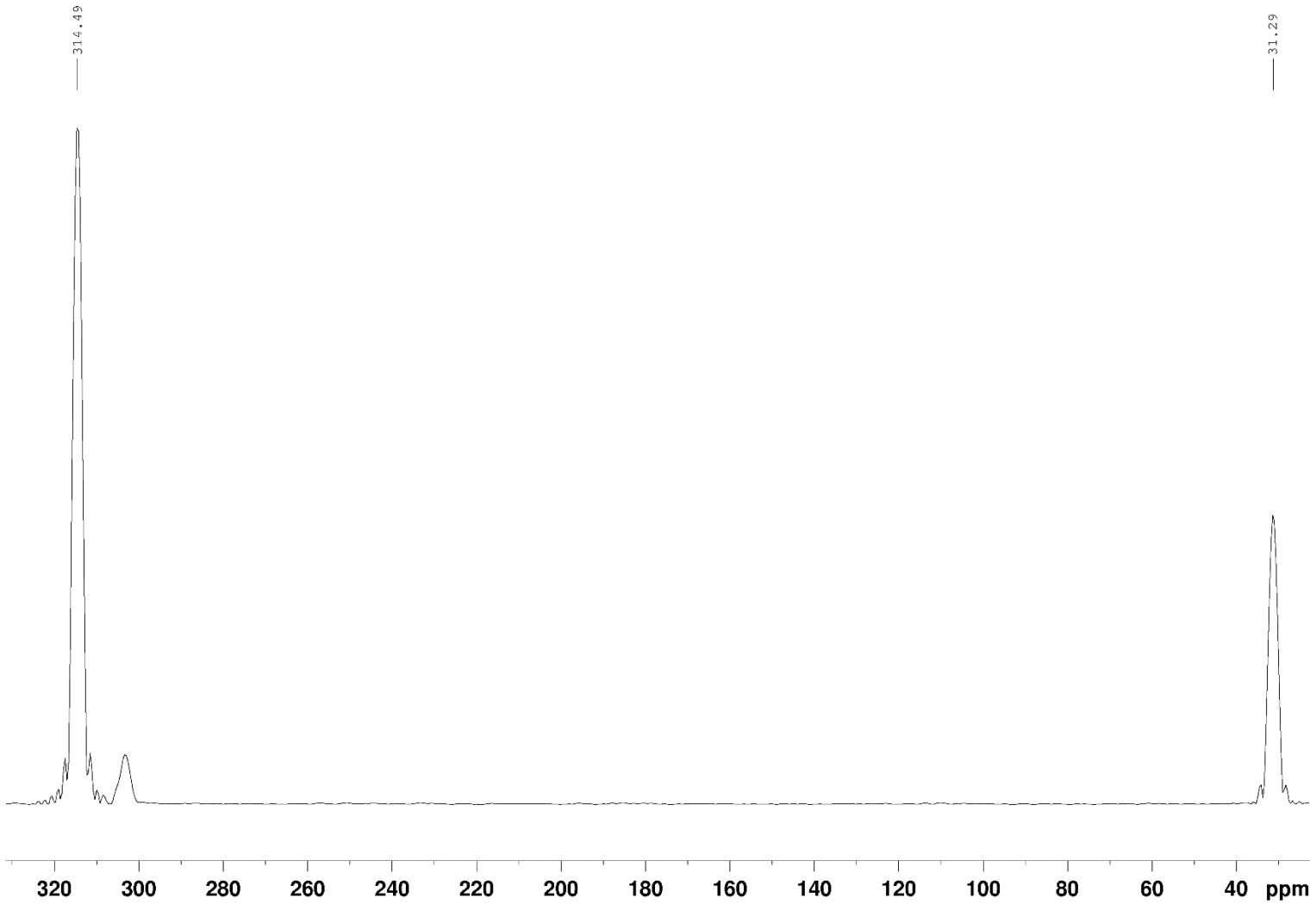

ESI-MS (pos)

(m/z (%) in MeOH/H_2O/Formic acid)

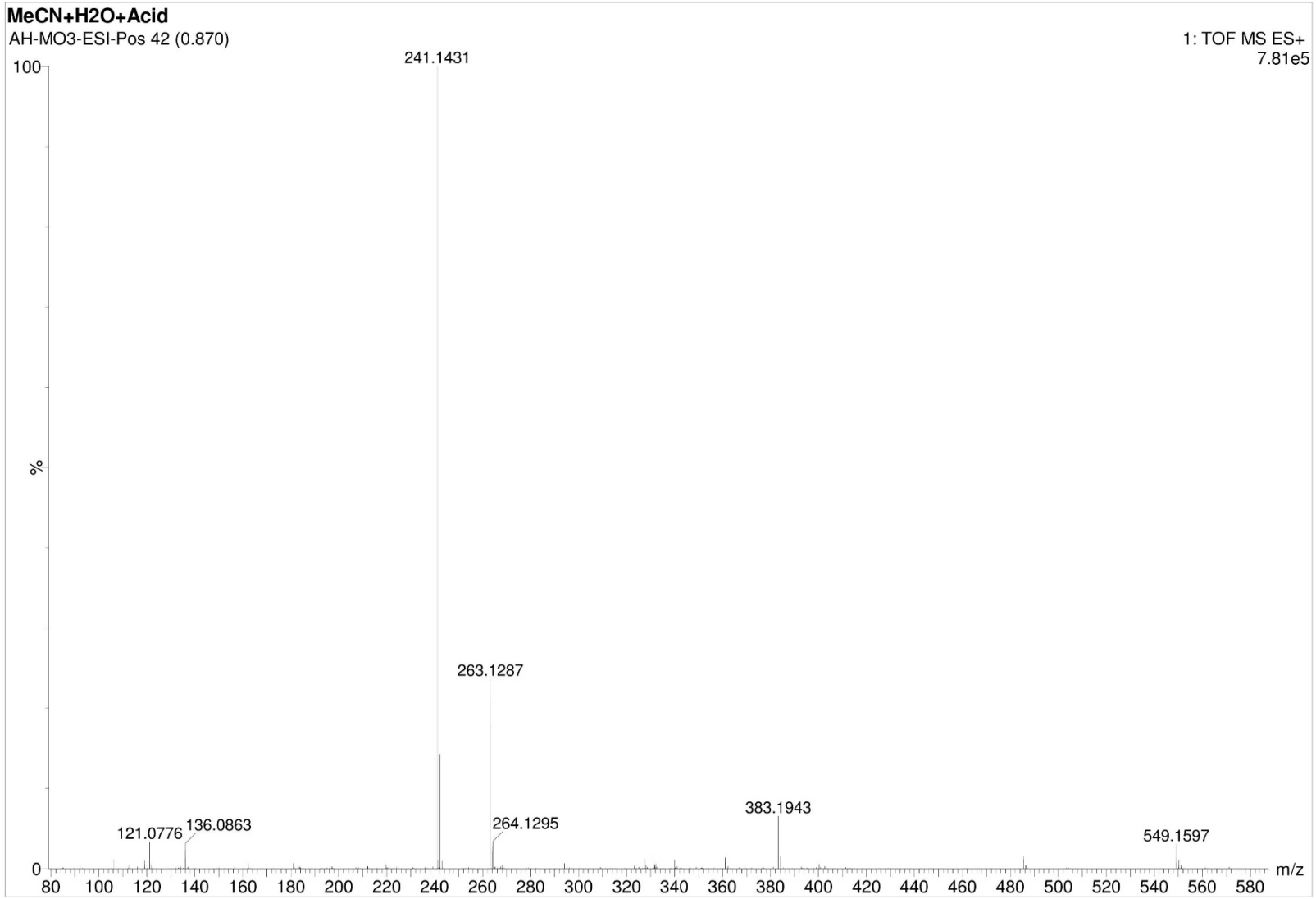

10.1.23 Dibenzyl diazapyridinophane ($N_4Benzyl_2$)

ESI-MS (pos)

(m/z (%) in MeOH)

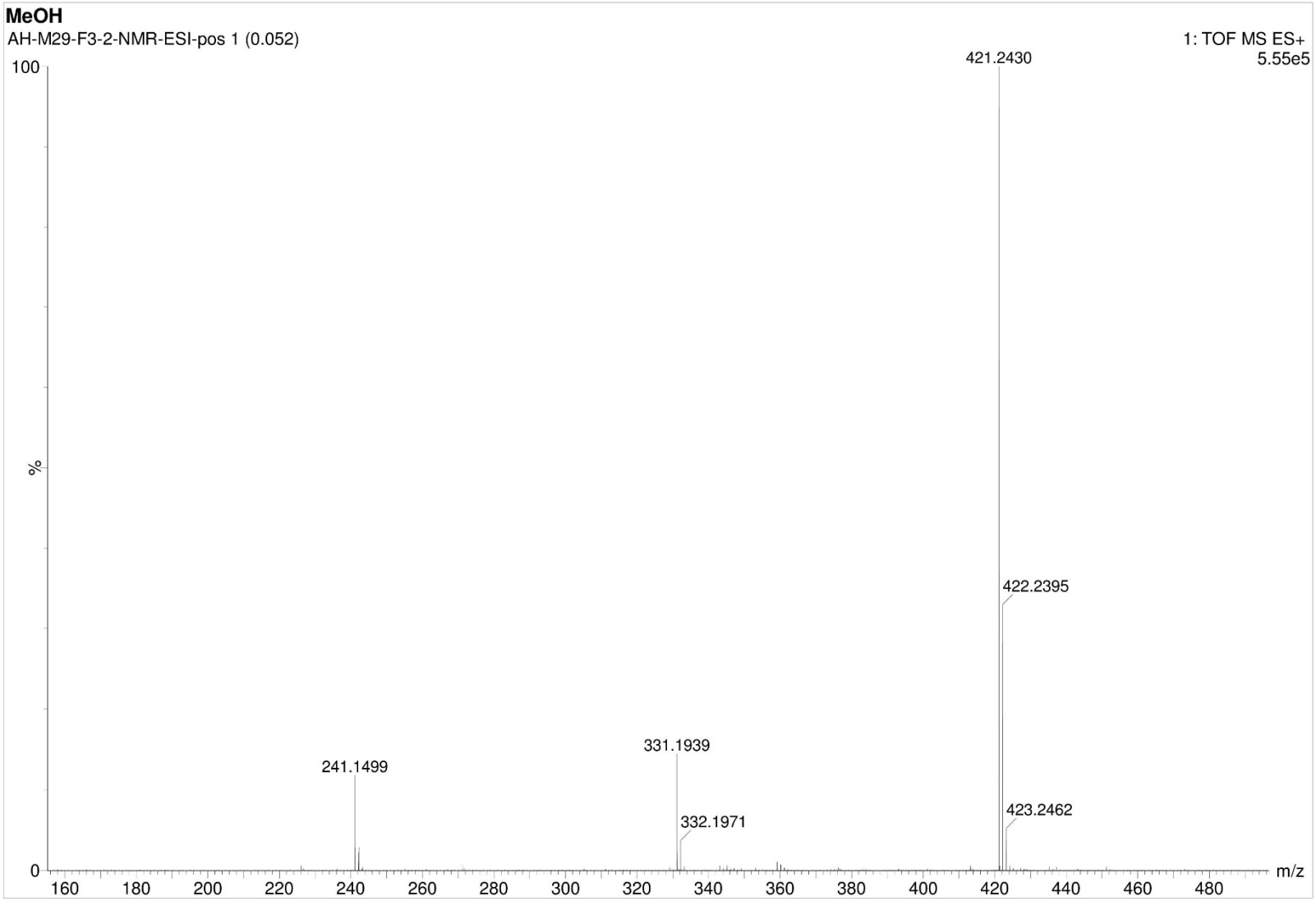

10.1.24 Dicarbaldehyde Diazapyridinophane (N_4COH_2)

ESI-MS (pos)

(m/z (%) in MeCN)

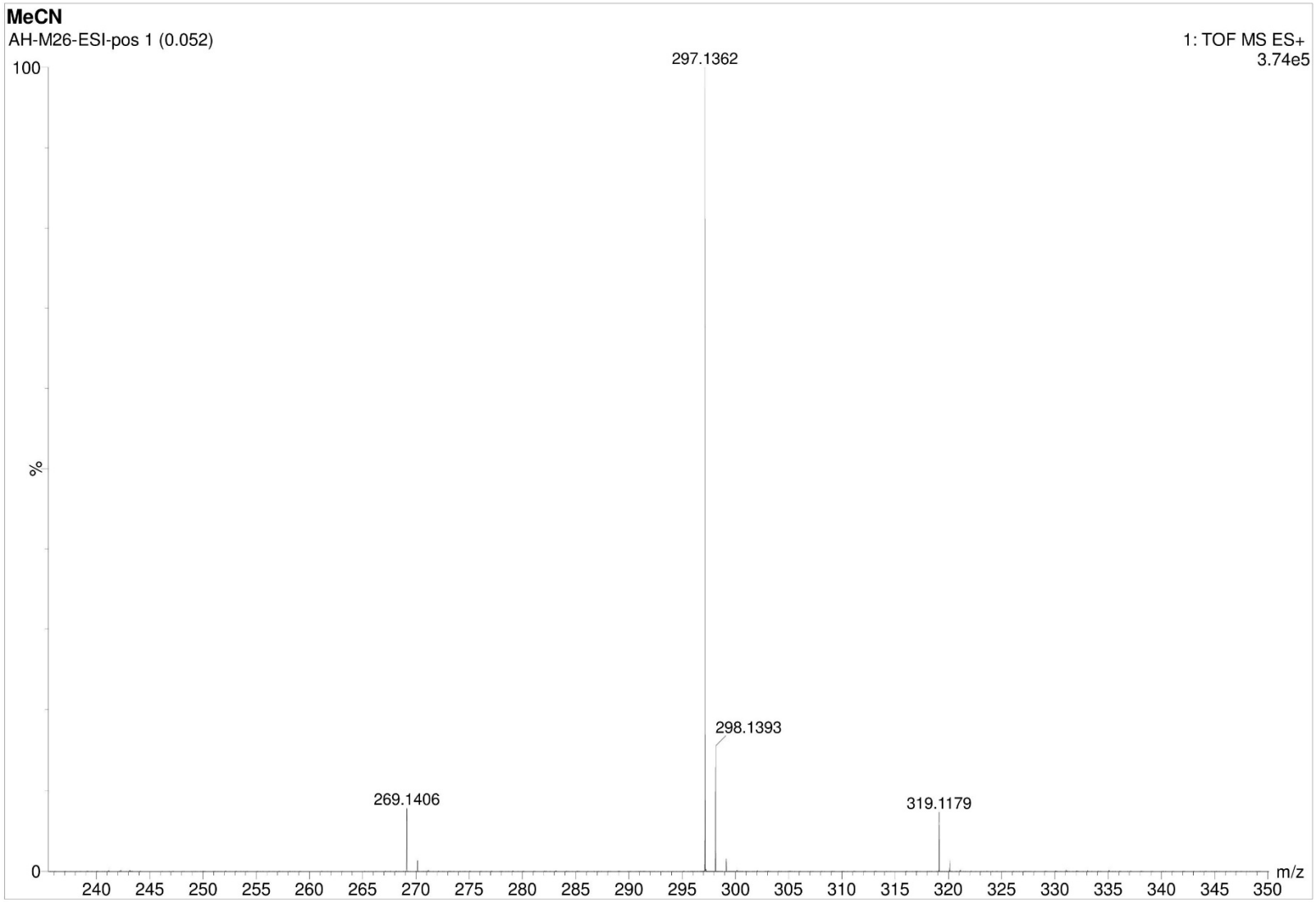

10.1.25 [Cu(2,9-dimethyl-1,10-phenanthroline)$_2$][BF$_4$]

^{1}H-NMR

(500 MHz, $CDCl_3$)

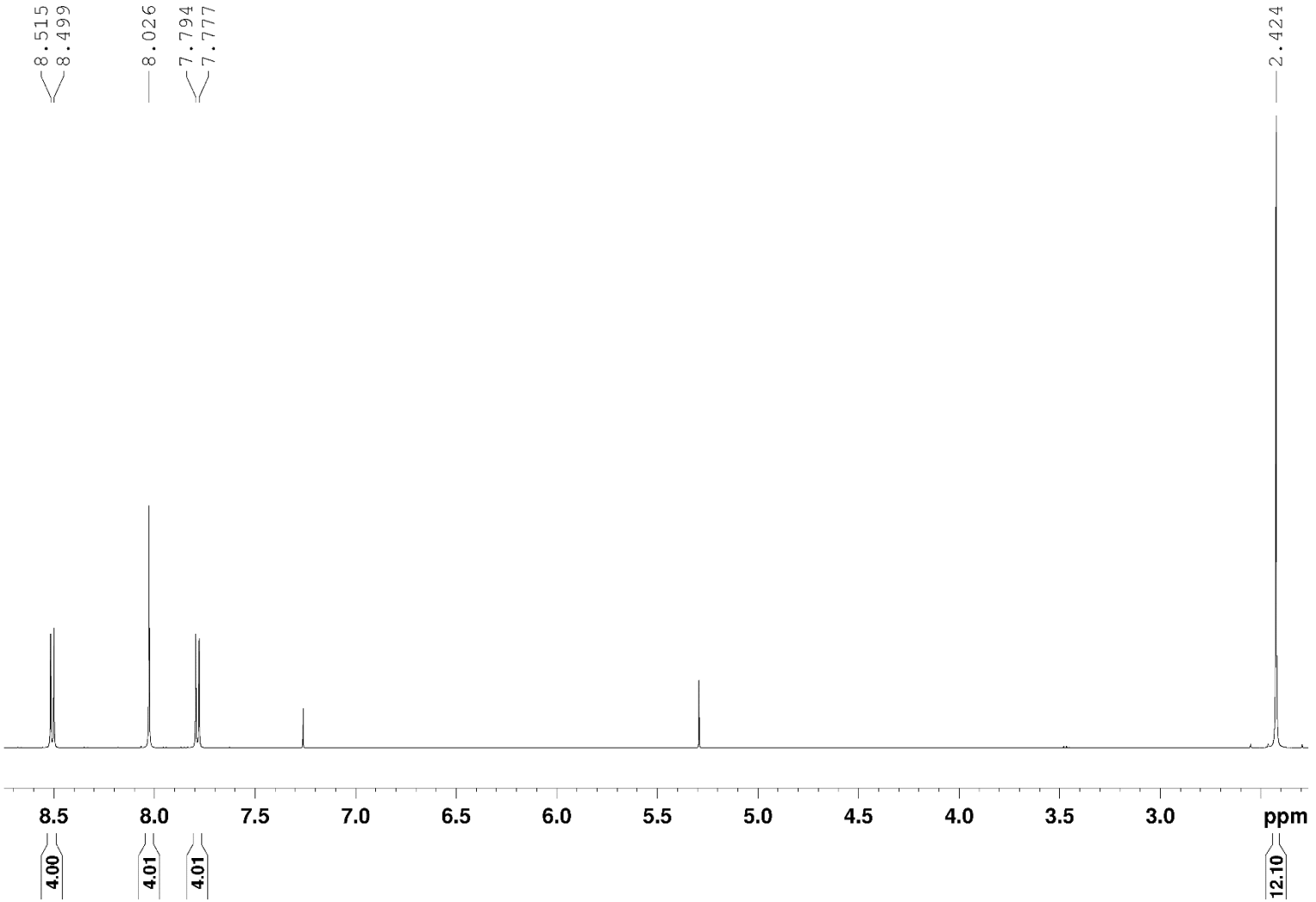

^{13}C-NMR

(125 MHz, $CDCl_3$)

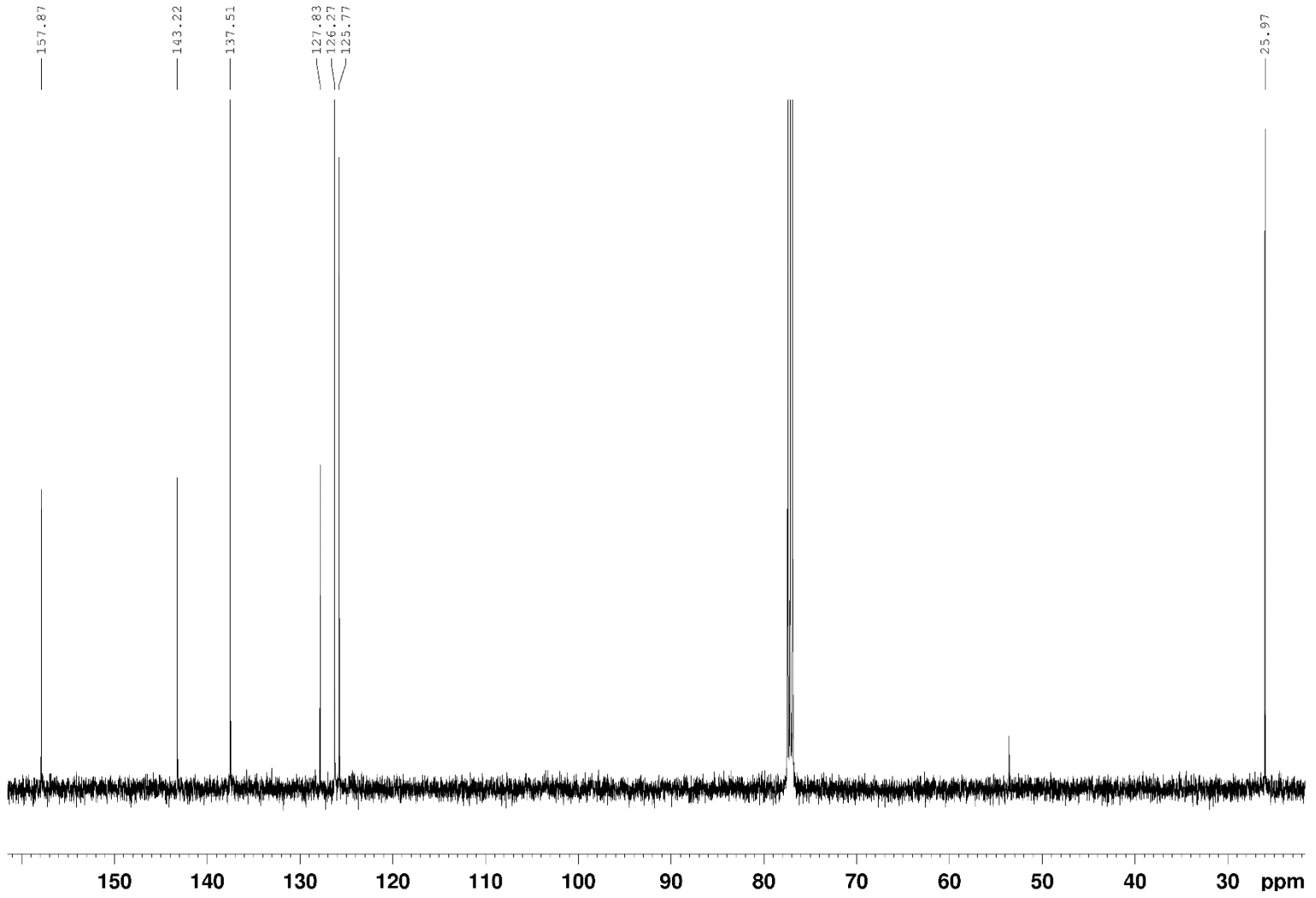

^{15}N-NMR

(50.7 MHz, $CDCl_3$, obtained by ^{15}N-^{1}H-HBMC)

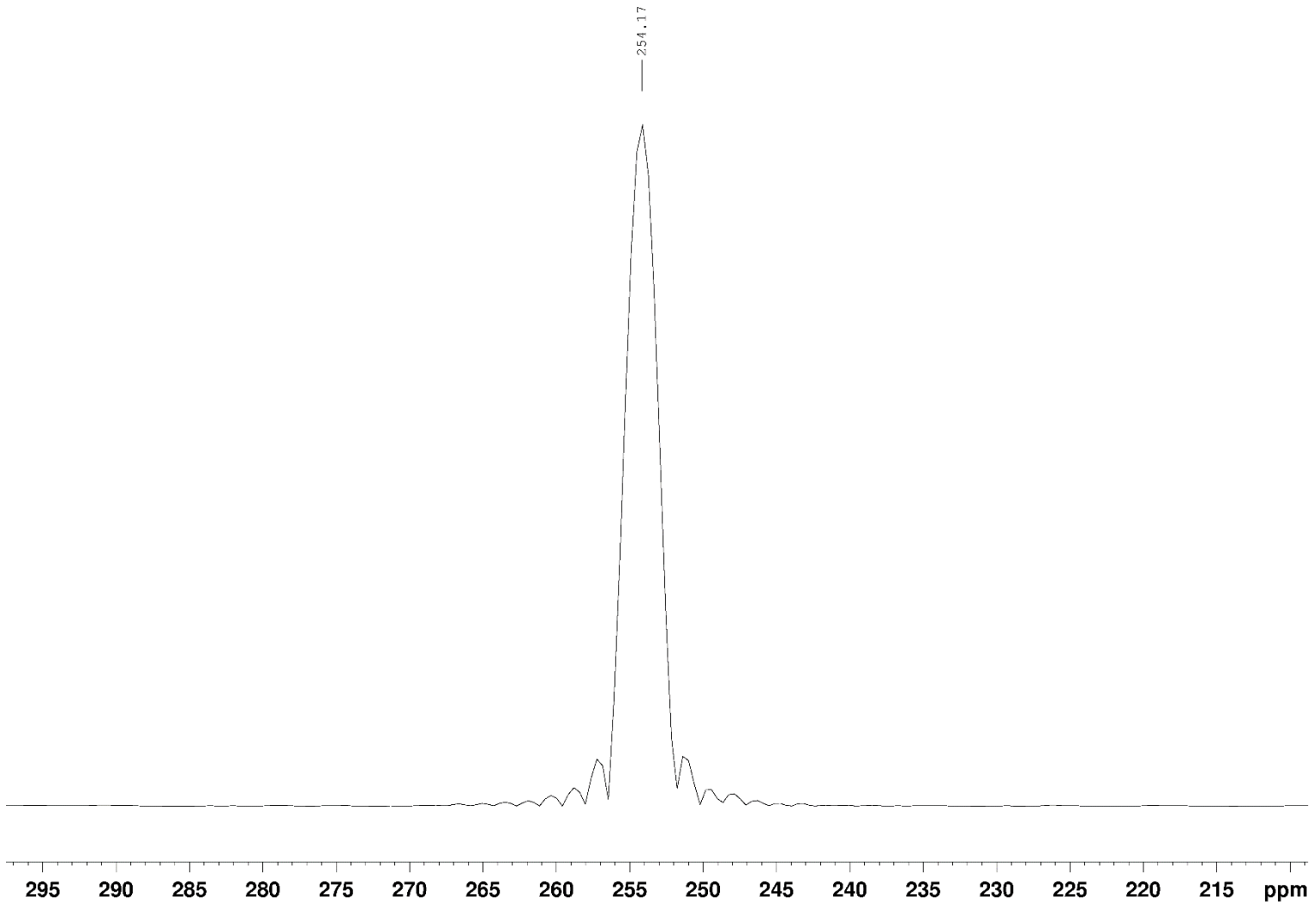

ESI-MS (pos)

(m/z (%) in MeCN)

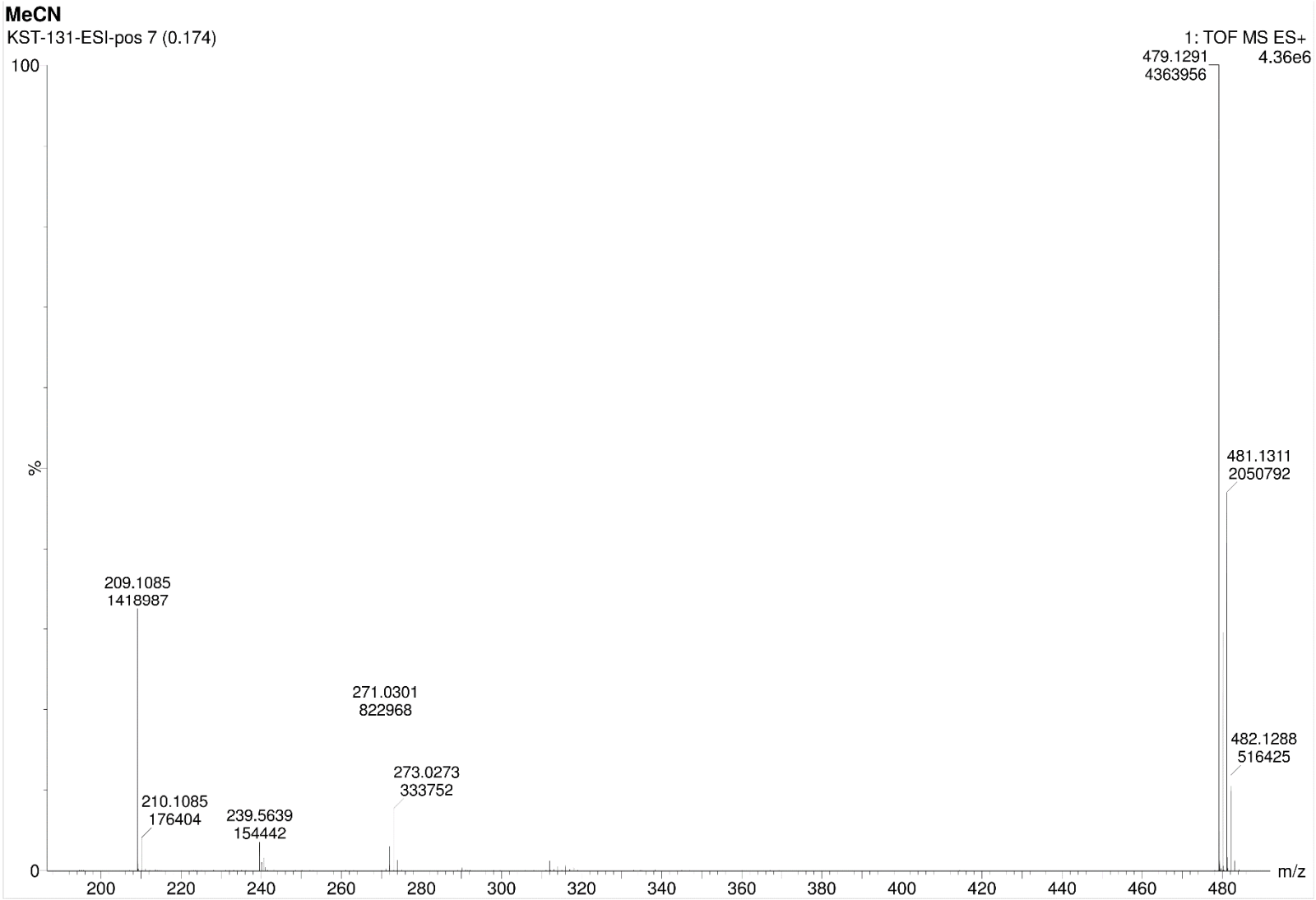

10.1.26 [Cu(2,9-bis(chloromethyl)-1,10-phenanthroline)$_2$][BF_4]

^{1}H-NMR

(500 MHz, MeCN-d_3)

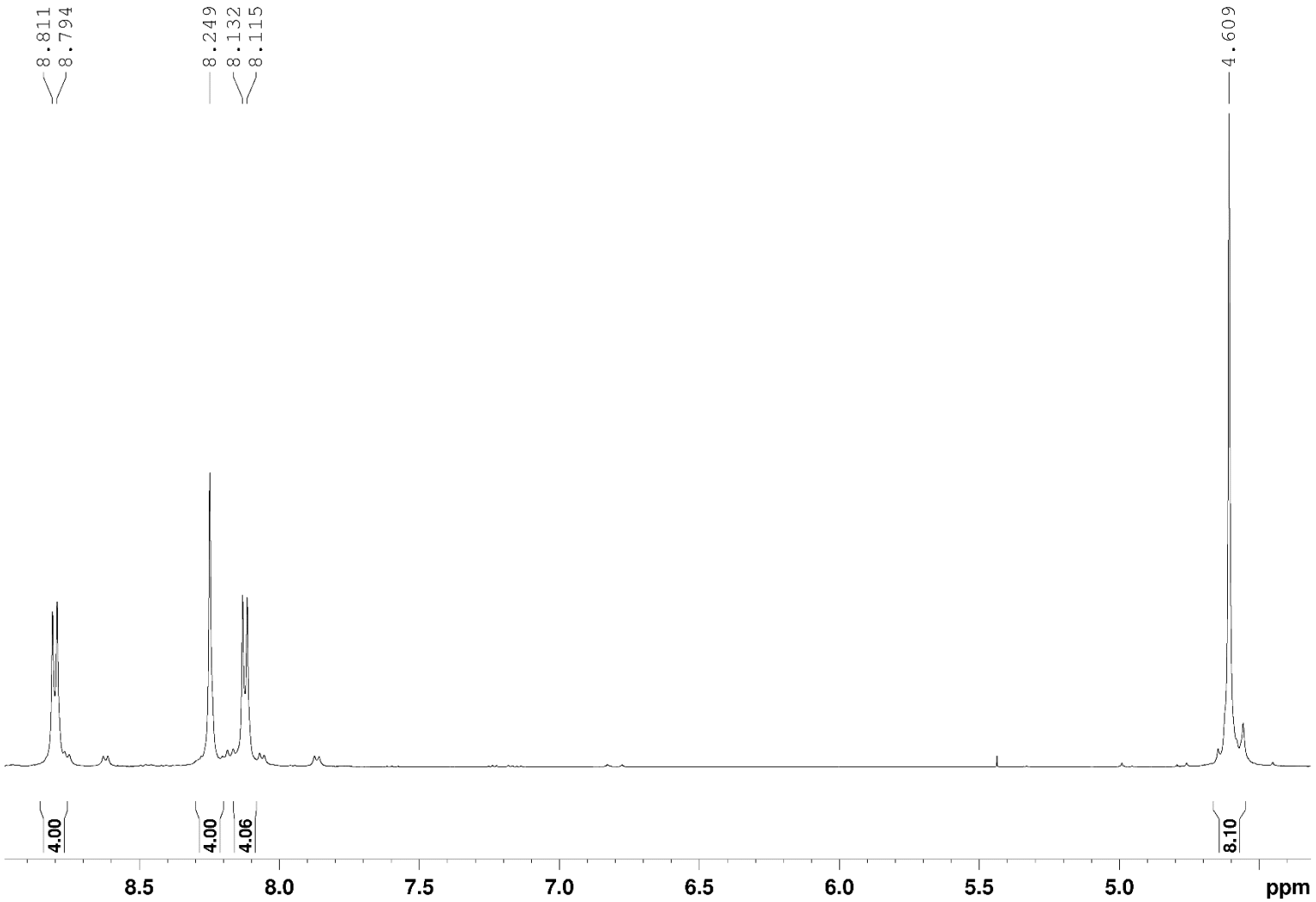

^{13}C-NMR

(125 MHz, MeCN-d_3)

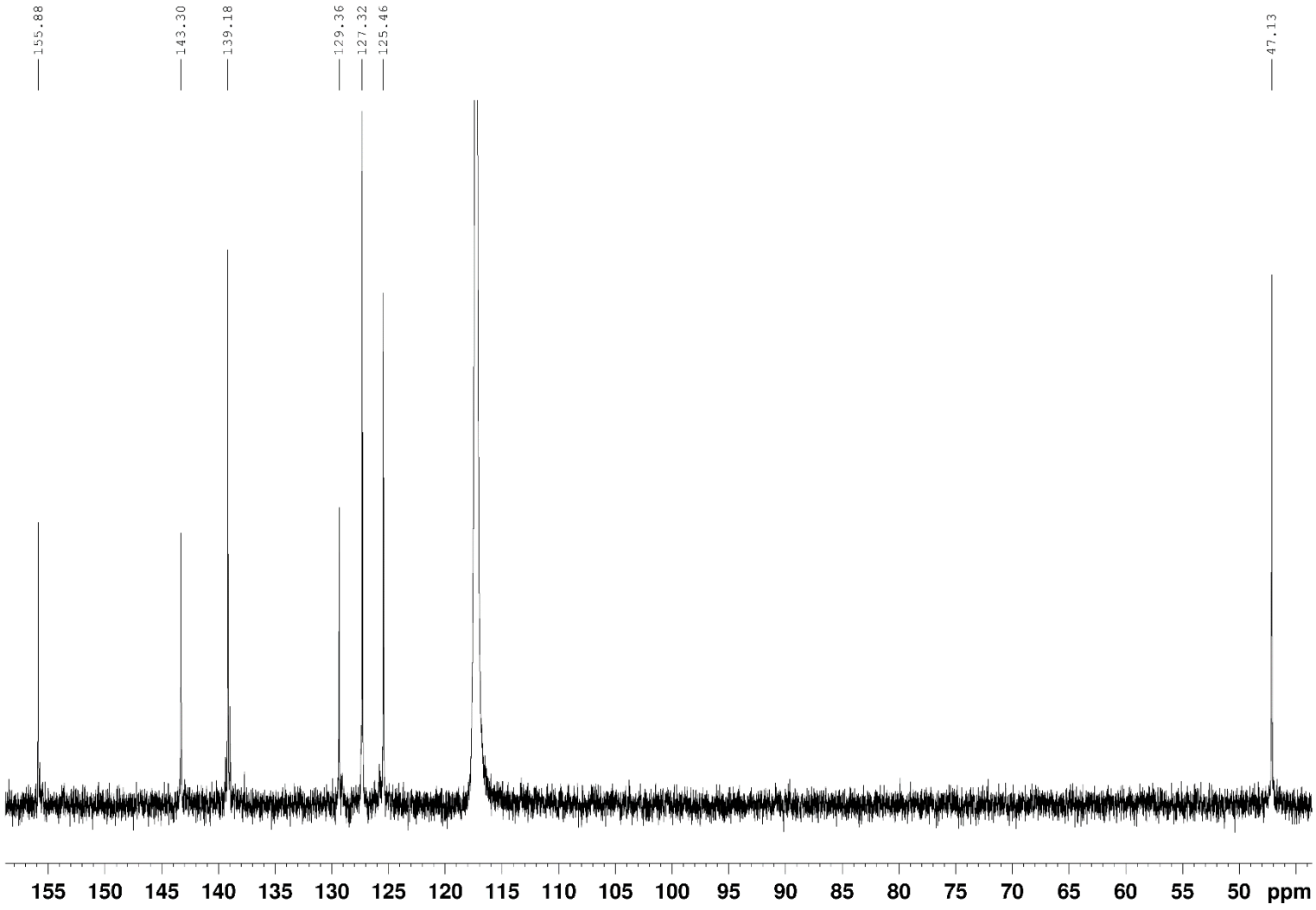

^{15}N-NMR

(50.7 MHz, MeCN-d_3, obtained by ^{15}N-^{1}H-HBMC)

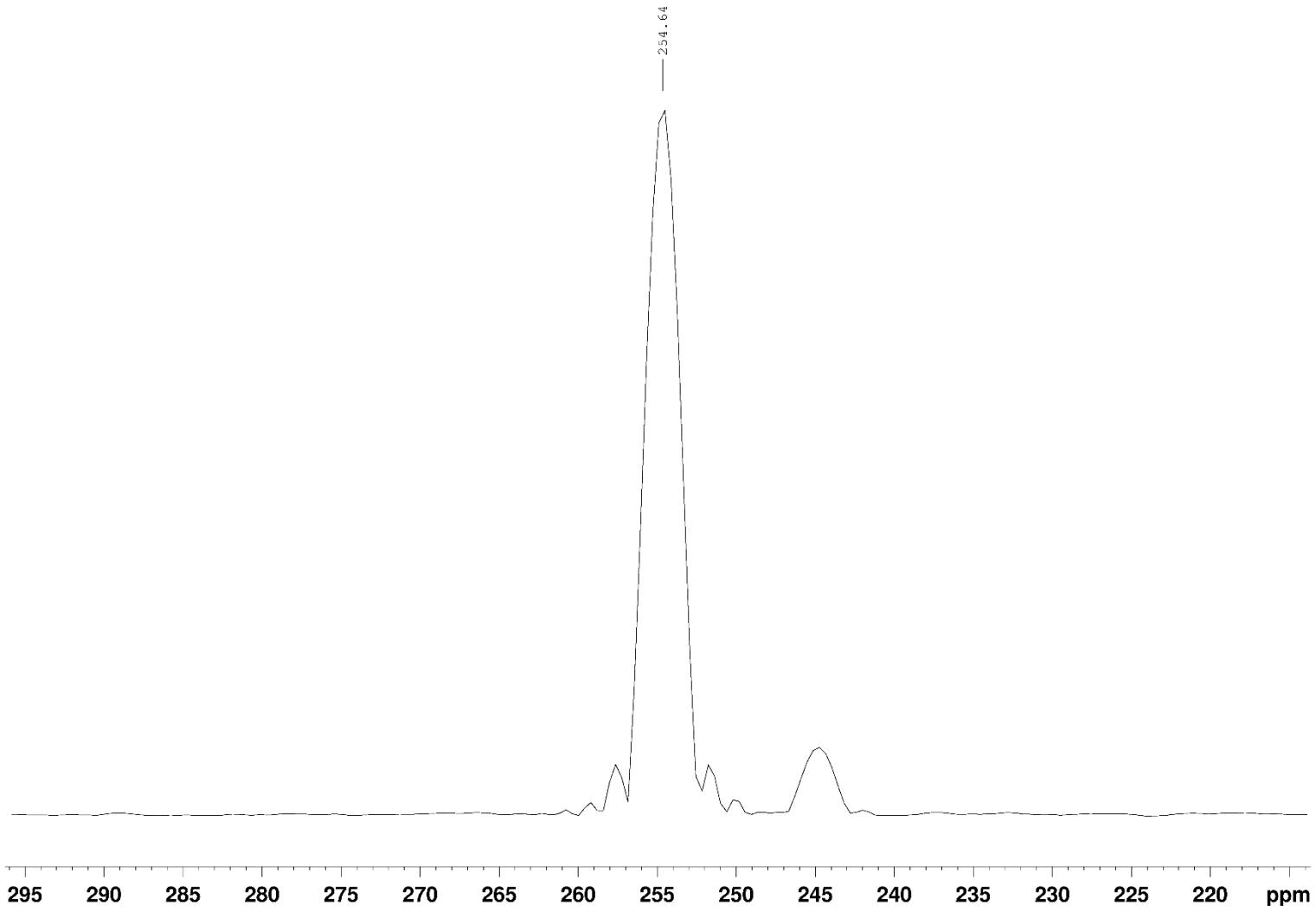

ESI-MS (pos)

(m/z (%) in MeCN)

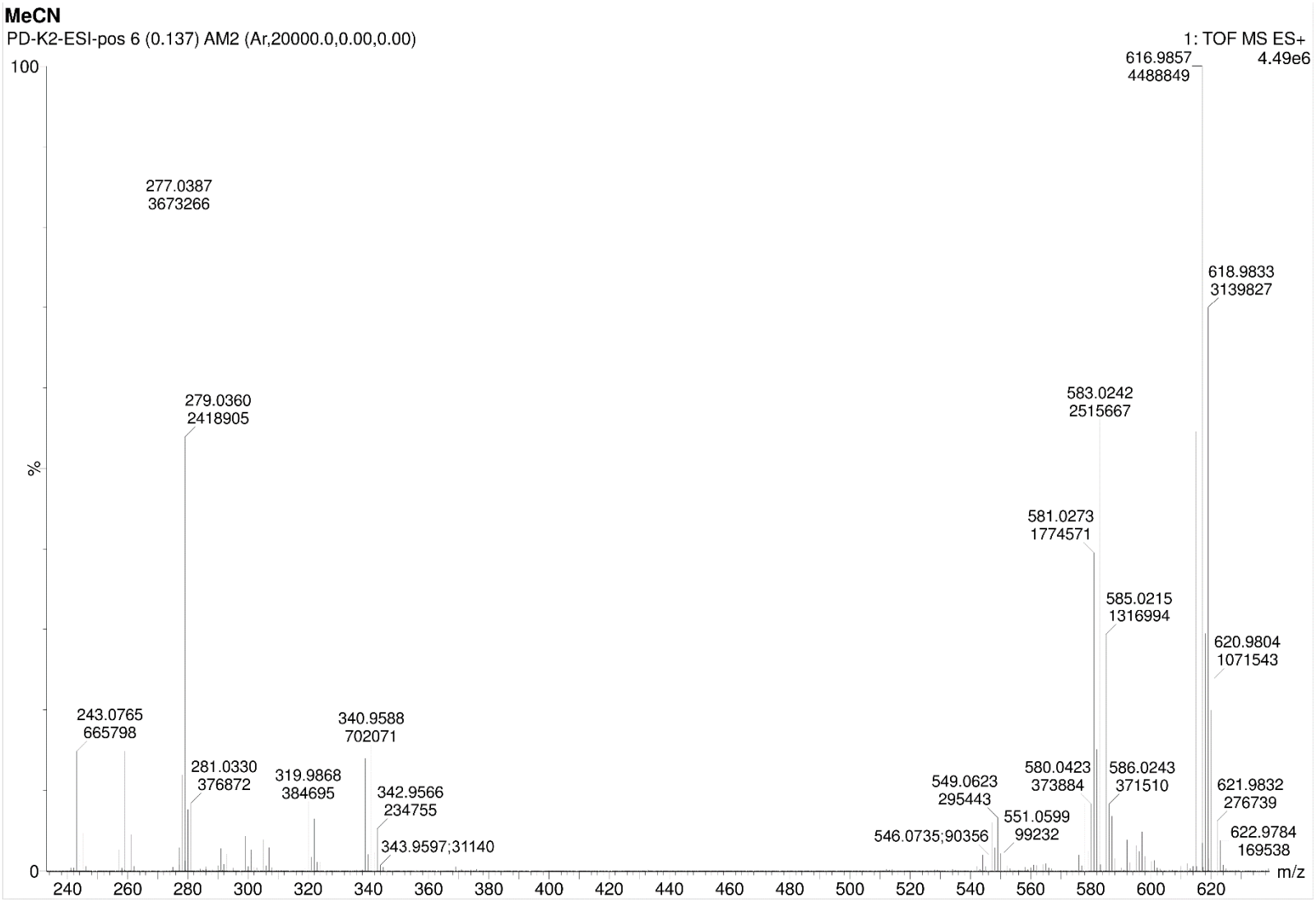

10.1.27 [Cu(2,9-bis(bromomethyl)-1,10-phenanthroline)$_2$[BF$_4$]

^{1}H-NMR

(500 MHz, MeCN-d_3)

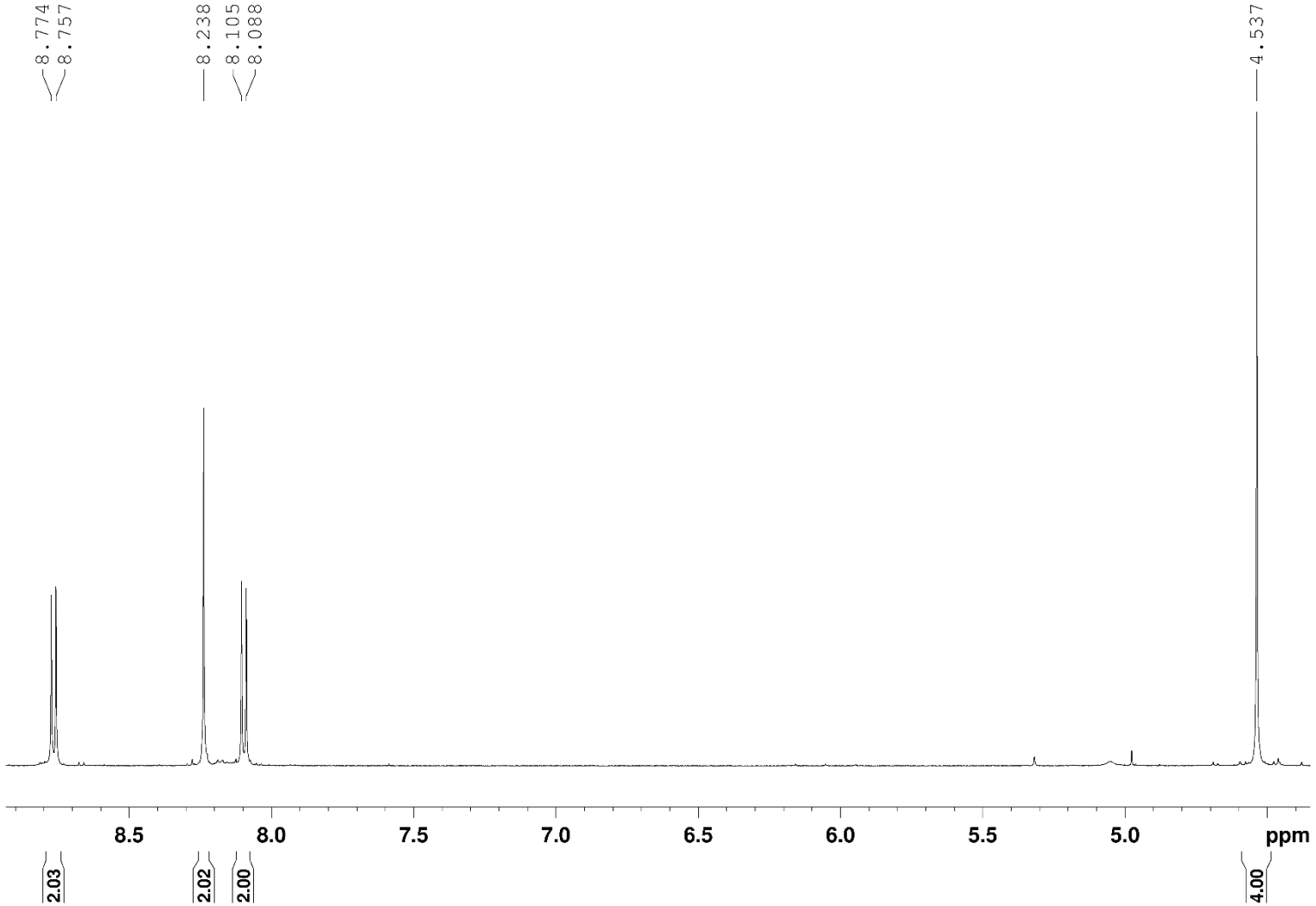

^{13}C-NMR

(125 MHz, MeCN-d_3)

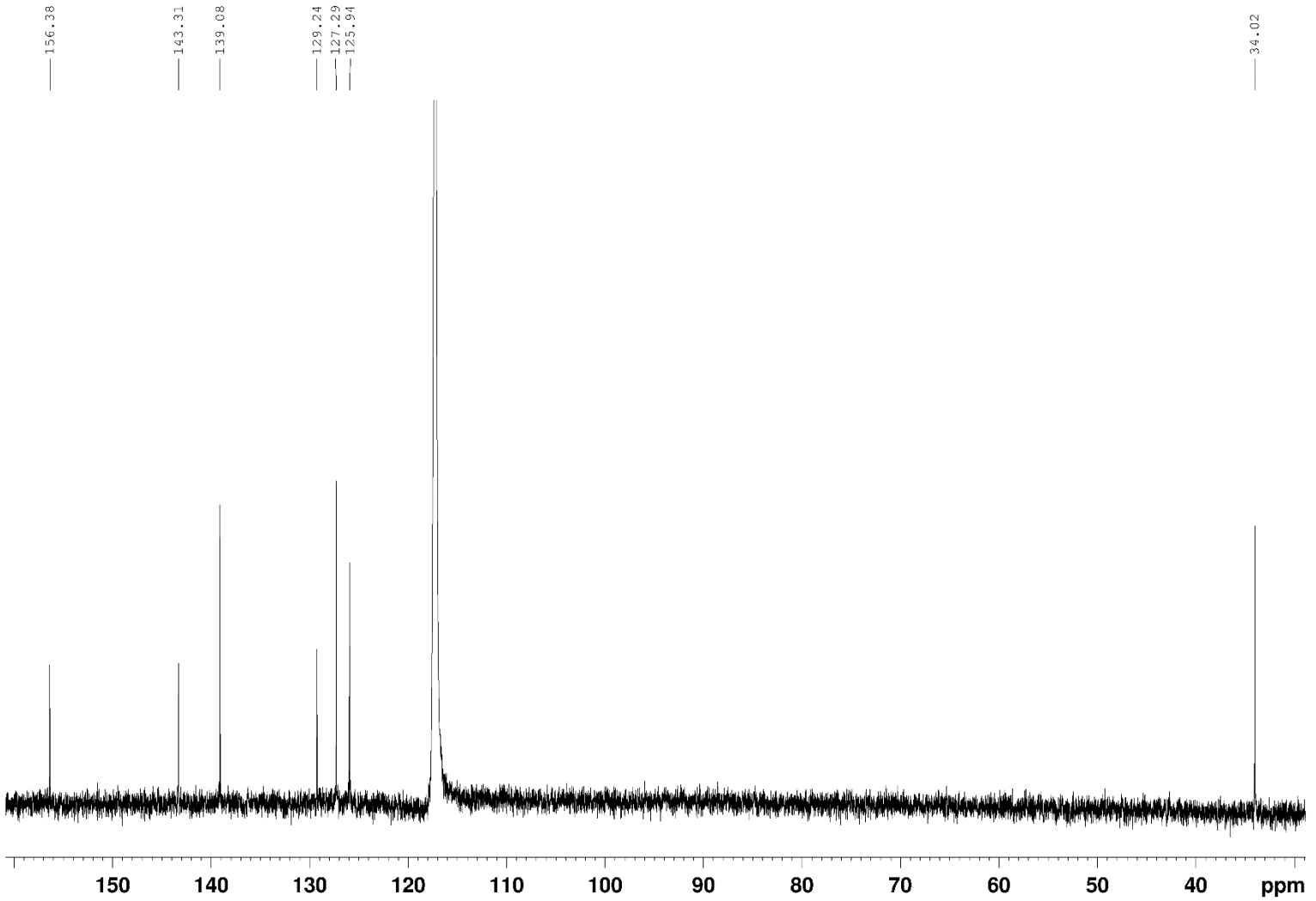

^{15}N-NMR

(50.7 MHz, MeCN-d_3, obtained by ^{15}N-^{1}H-HBMC)

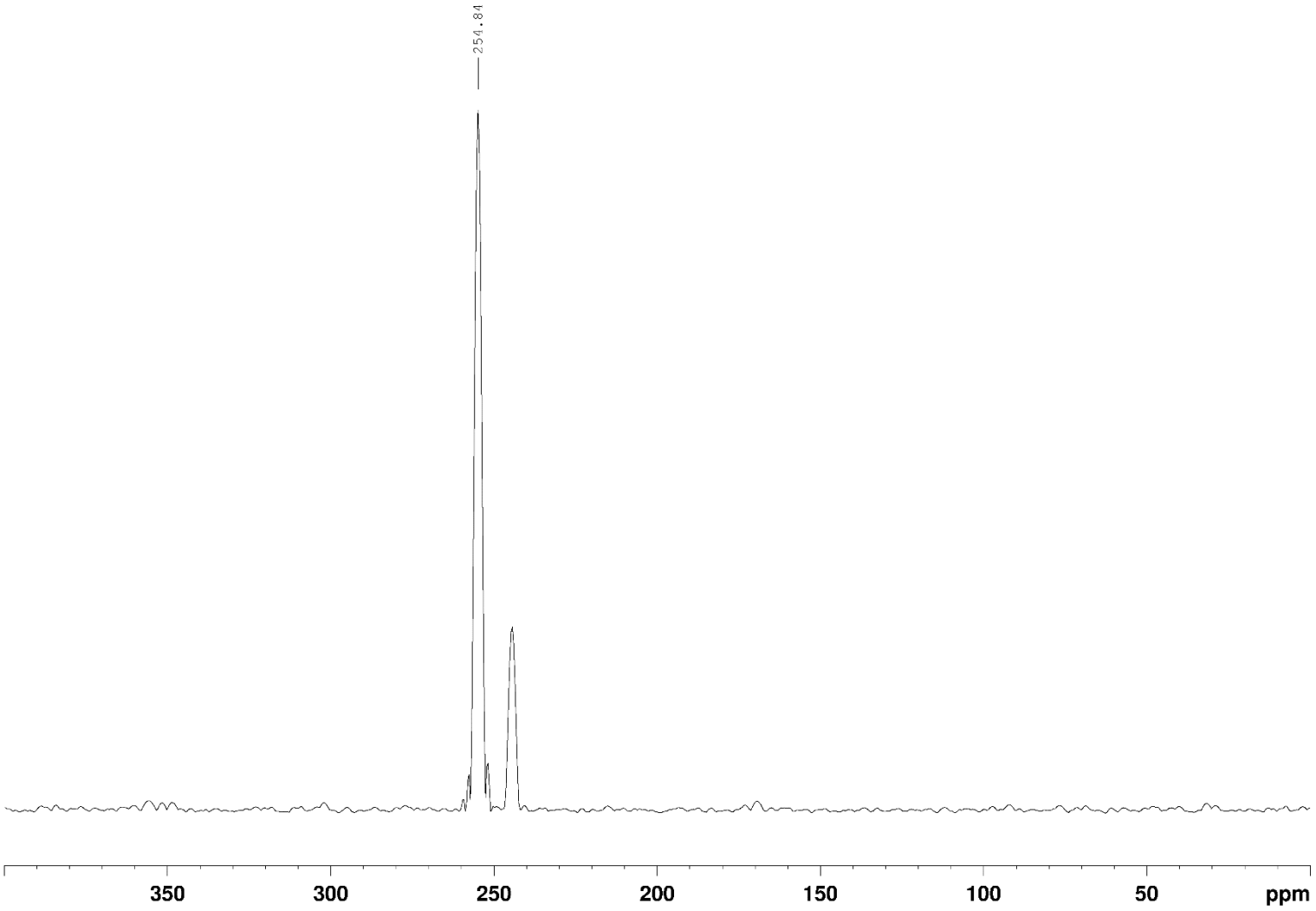

ESI-MS (pos)

(m/z (%) in MeCN)

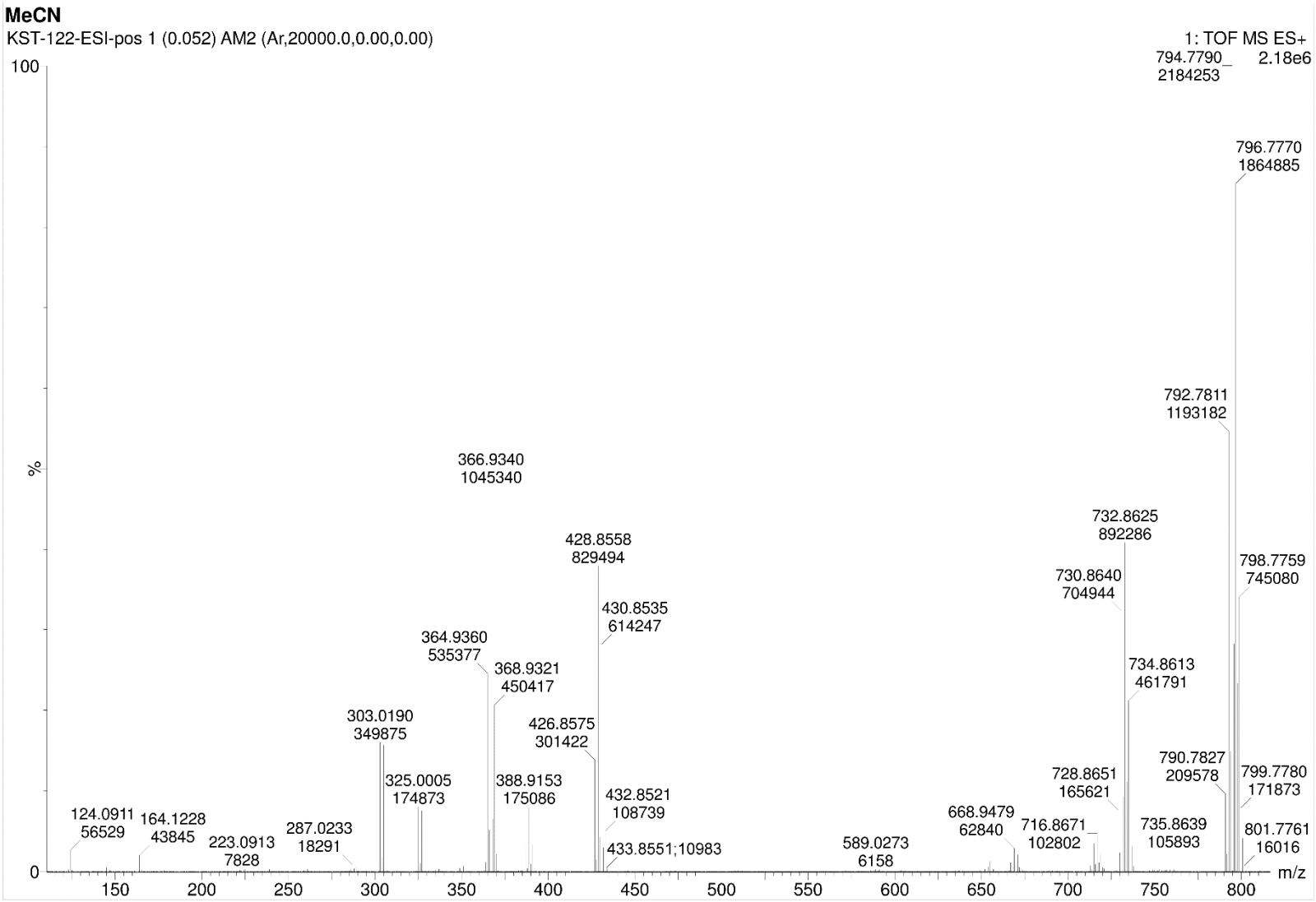

10.1.28 [Cu(2,9-bis(iodomethyl)-1,10-phenanthroline)$_2$[BF$_4$]

^{1}H-NMR

(500 MHz, MeCN-d_3)

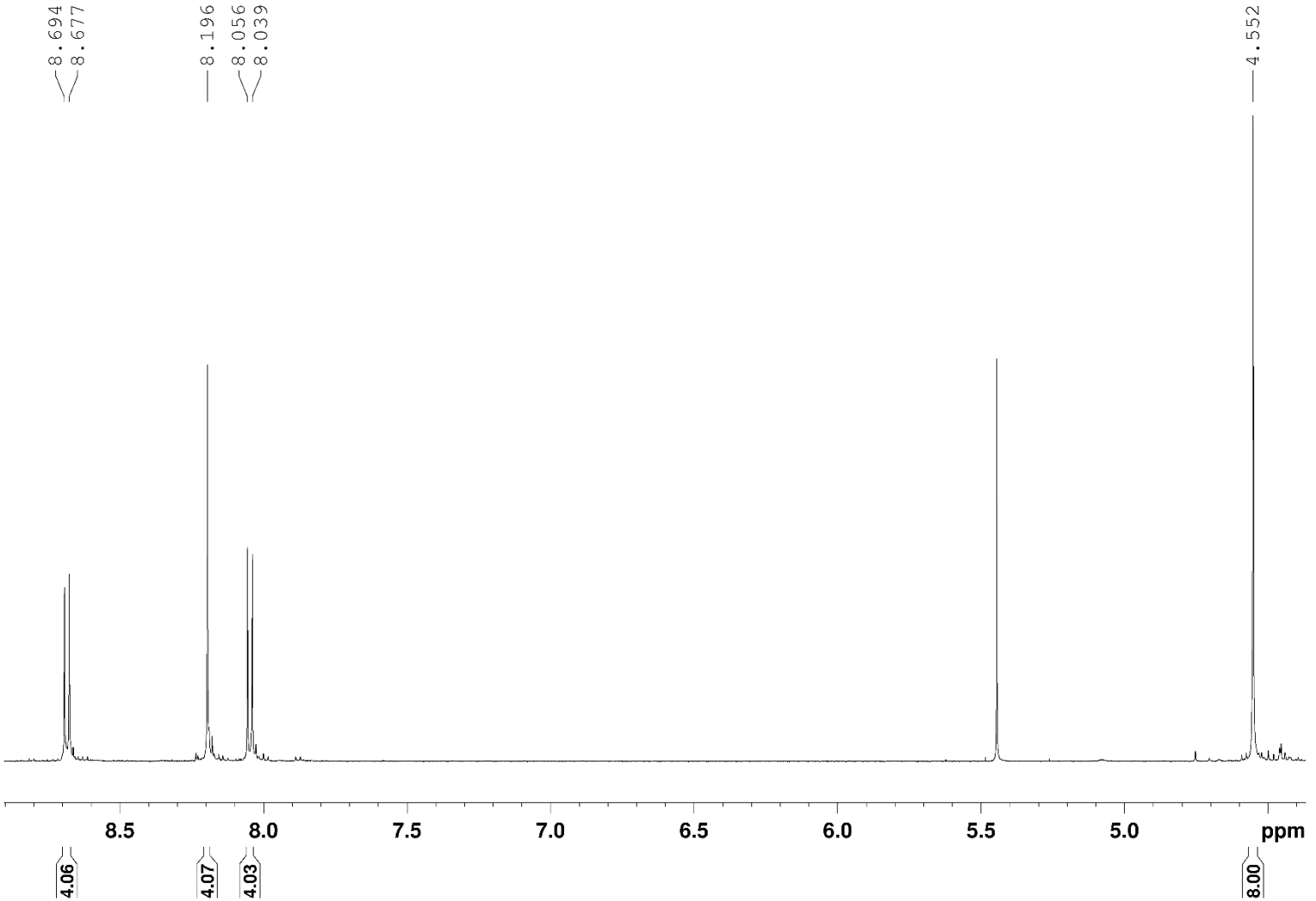

^{13}C-NMR

(125 MHz, MeCN-d_3)

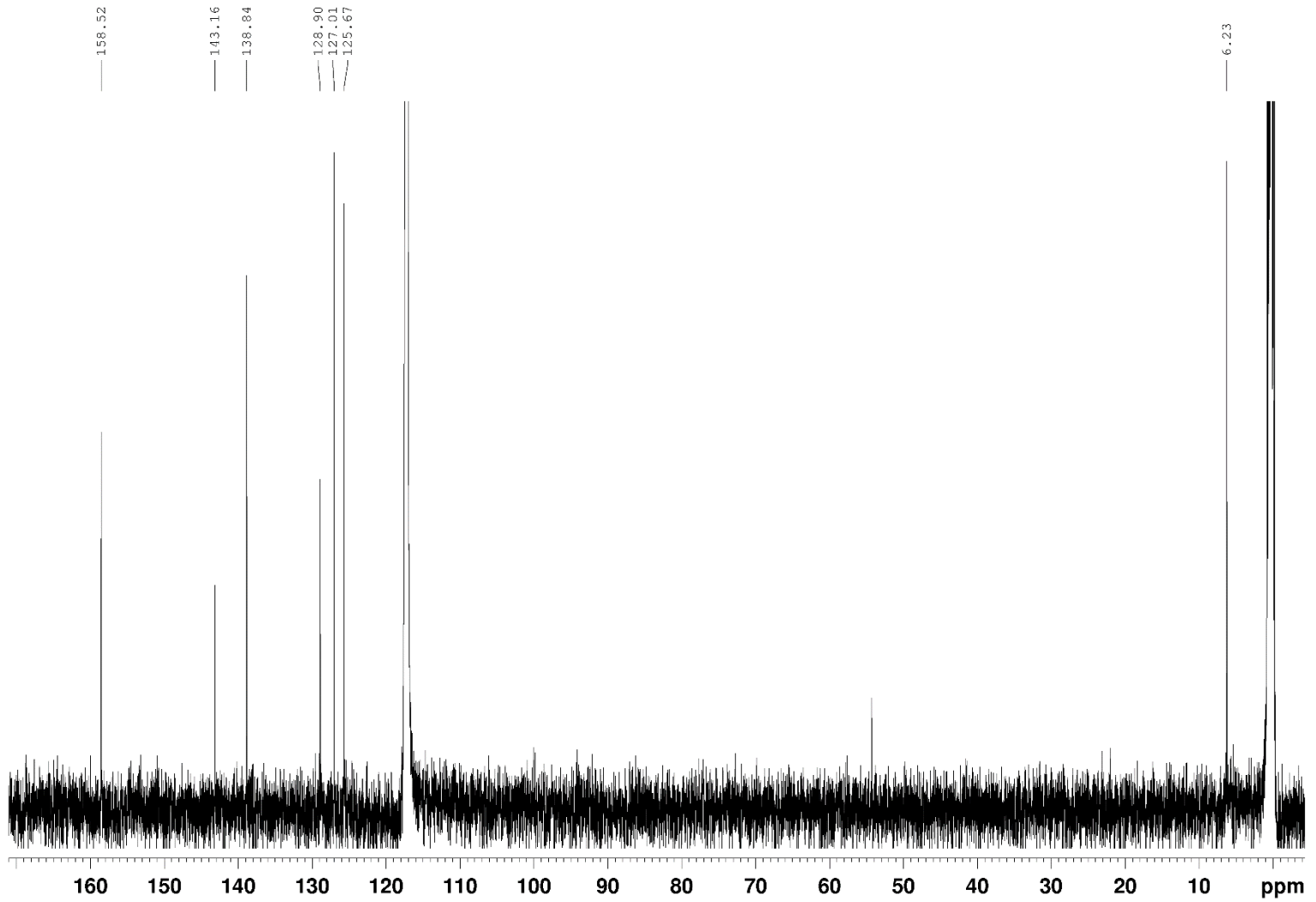

^{15}N-NMR

(50.7 MHz, MeCN-d_3, obtained by ^{15}N-^{1}H-HBMC)

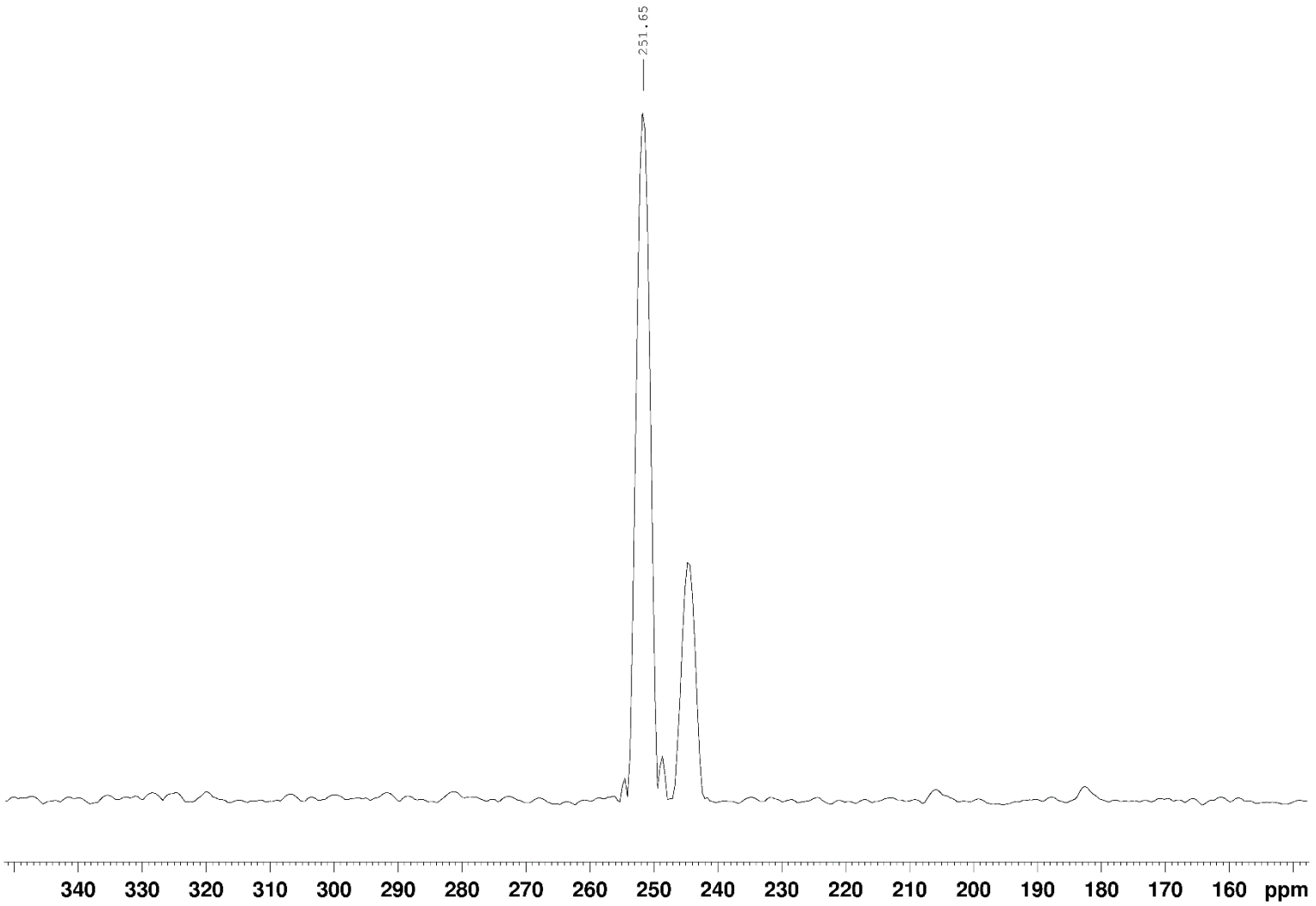

ESI-MS (pos)

(m/z (%) in MeCN + Formic acid)

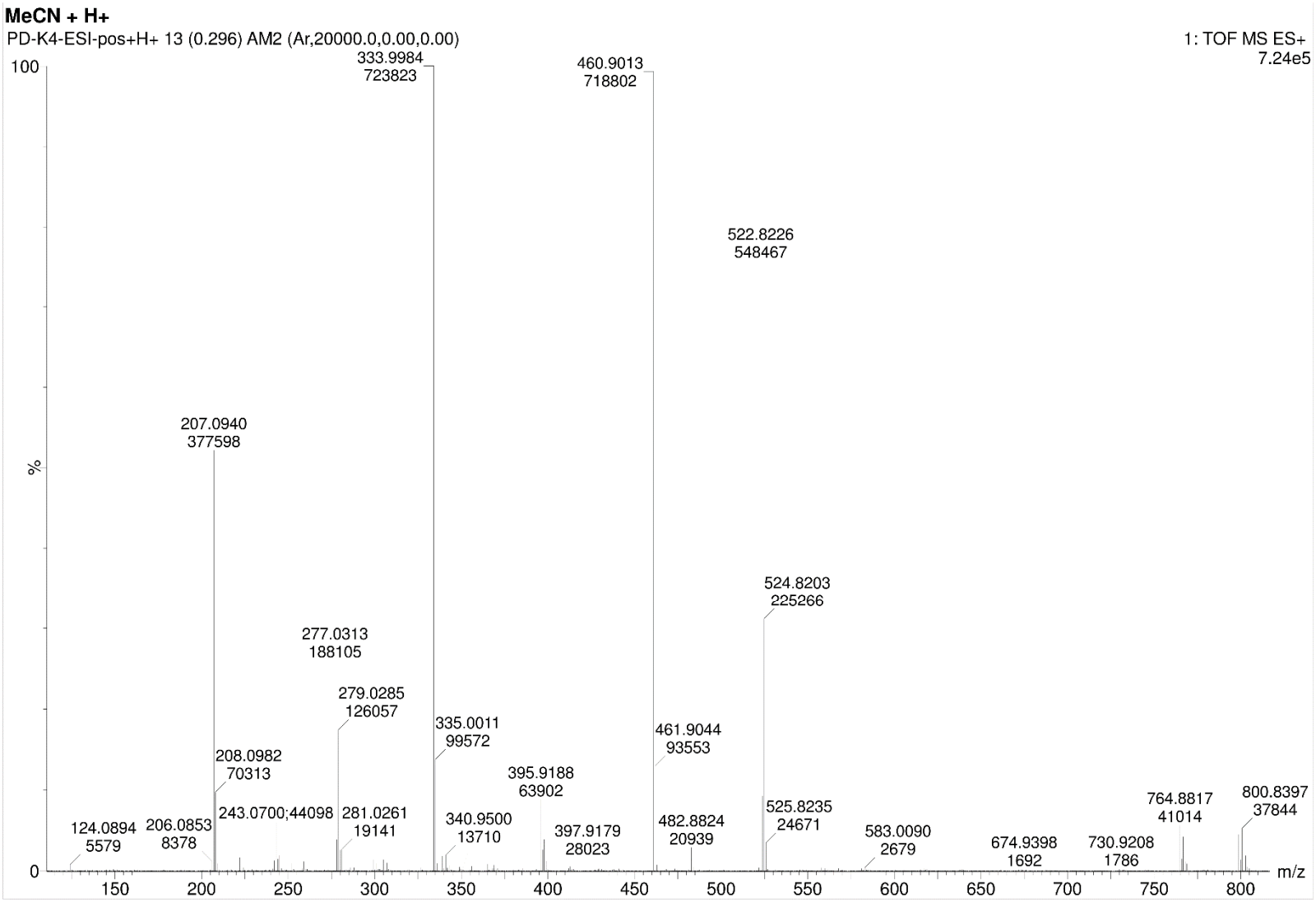

ESI-MS (pos)

(m/z (%) in MeCN)

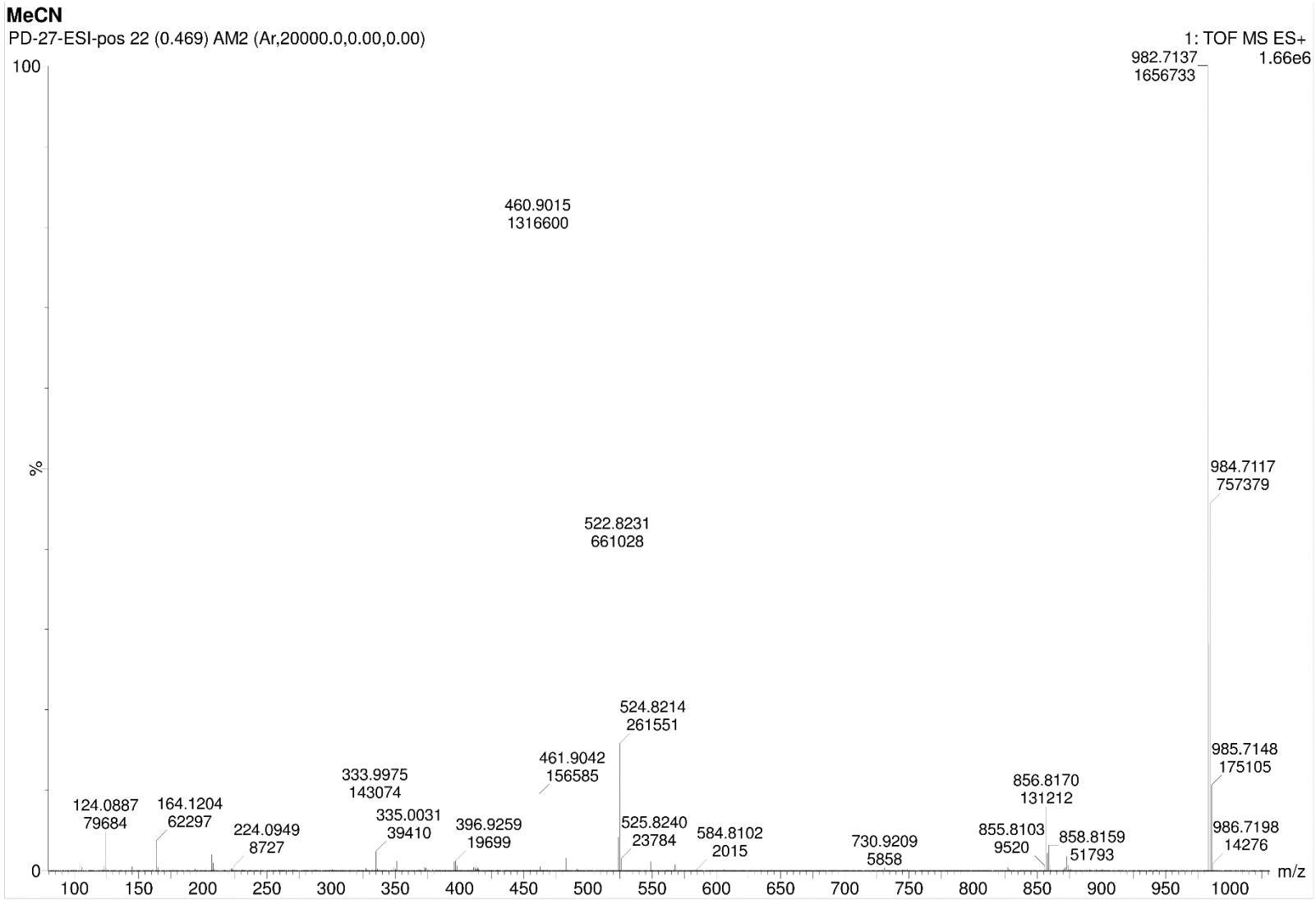

^{1}H-NMR

(500 MHz, $CDCl_3$)

^{13}C-NMR

(125 MHz, $CDCl_3$)

^{15}N-NMR

(50.7 MHz, $CDCl_3$, obtained by ^{15}N-^{1}H-HBMC)

ESI-MS (pos)

(m/z (%) in MeCN)

10.1.29 [Cu(DAPy-Ts)MeCN][BF_4]

^{1}H-NMR

(500 MHz, DMSO-d_6)

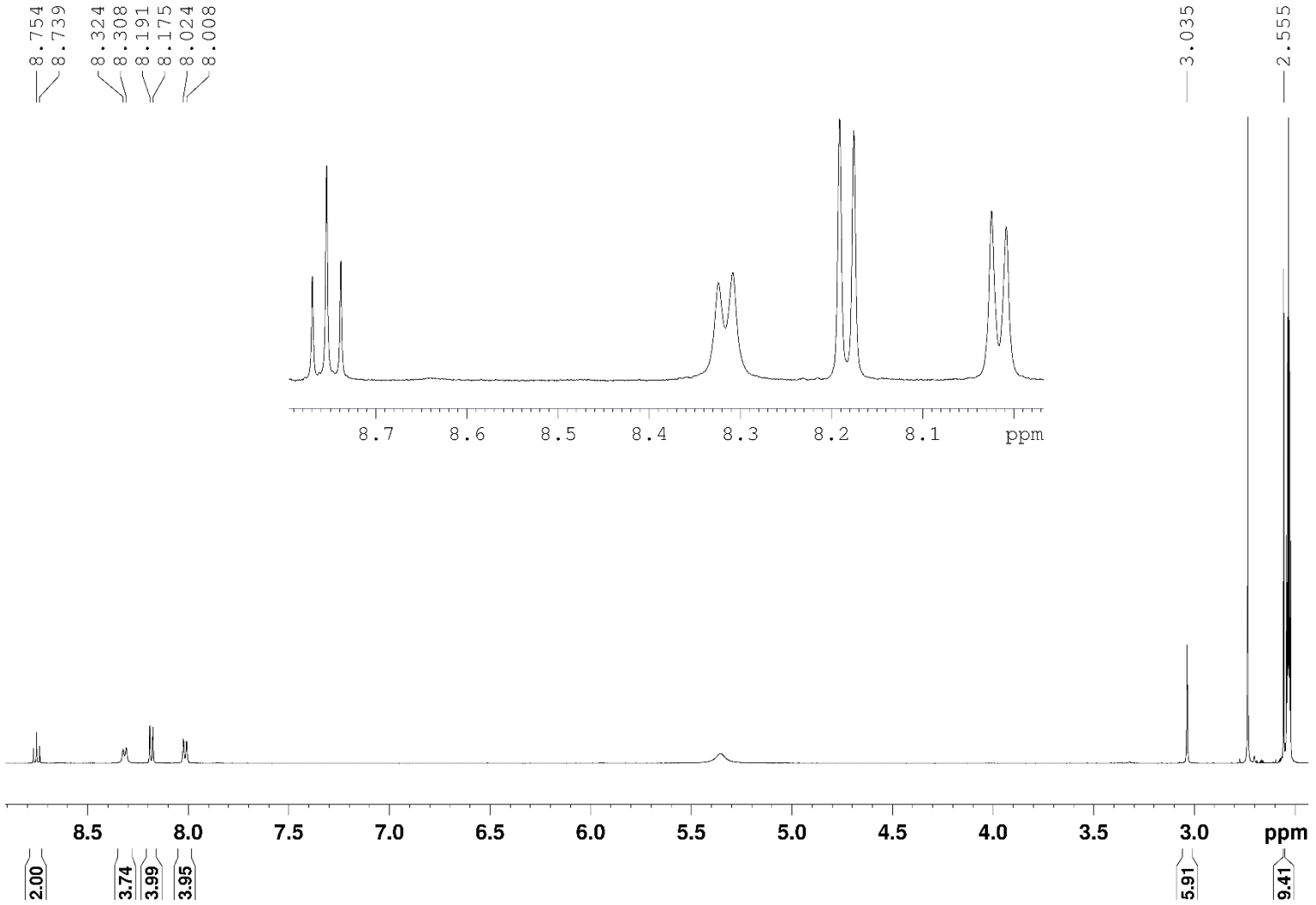

^{13}C-NMR

(125 MHz, $CDCl_3$)

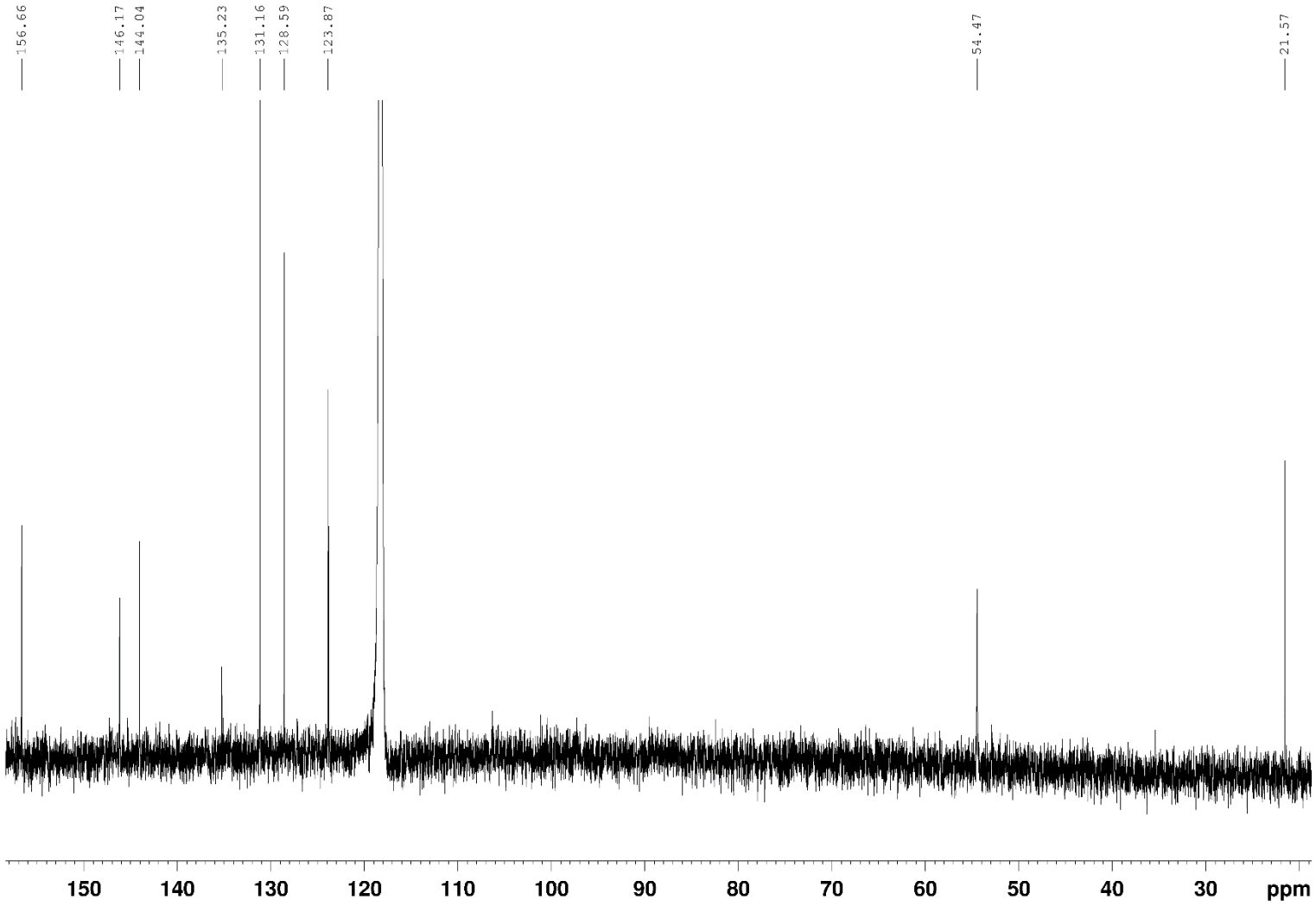

ESI-MS (pos)

(m/z (%) in MeCN)

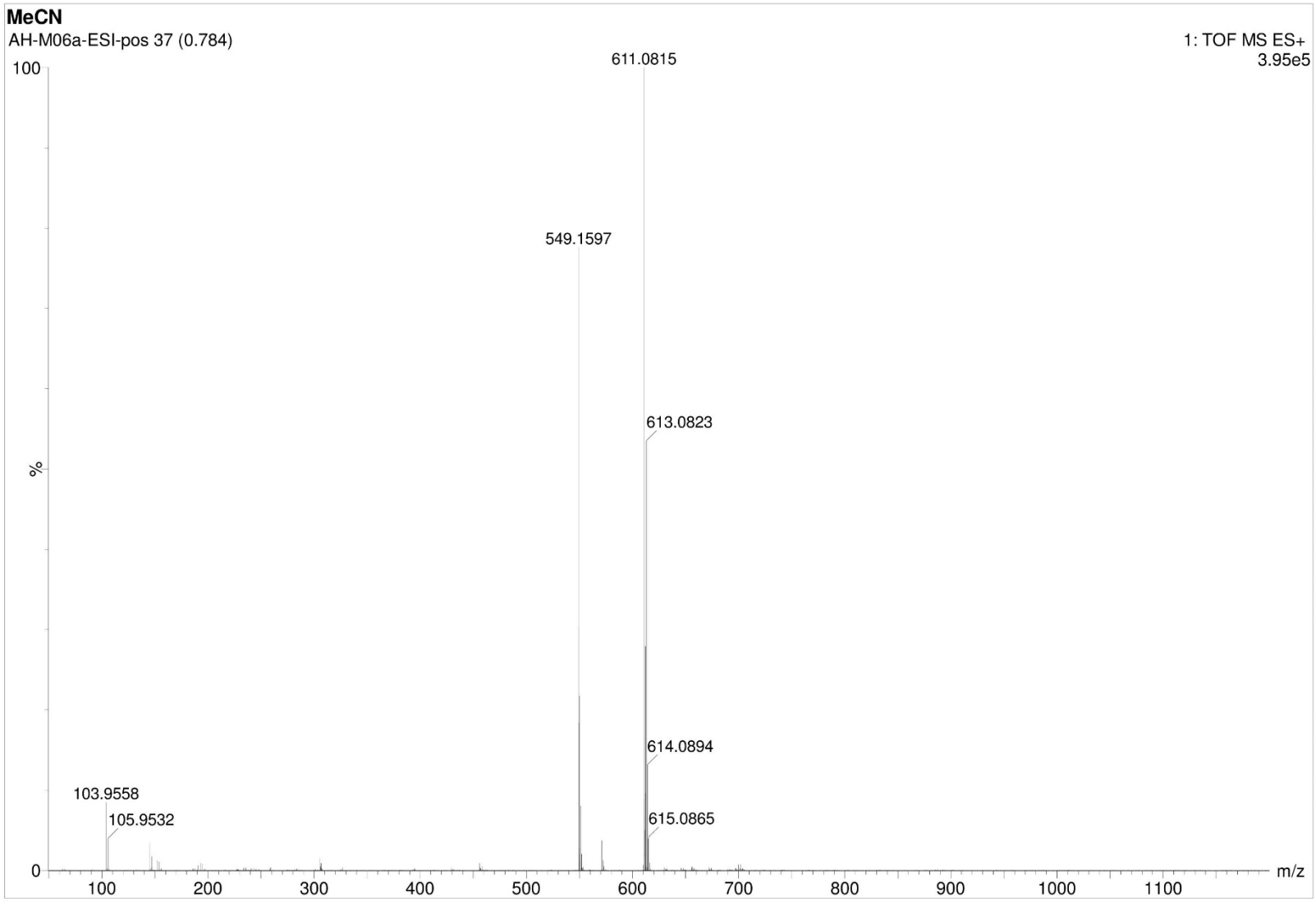

IR spectrum

(ATR)

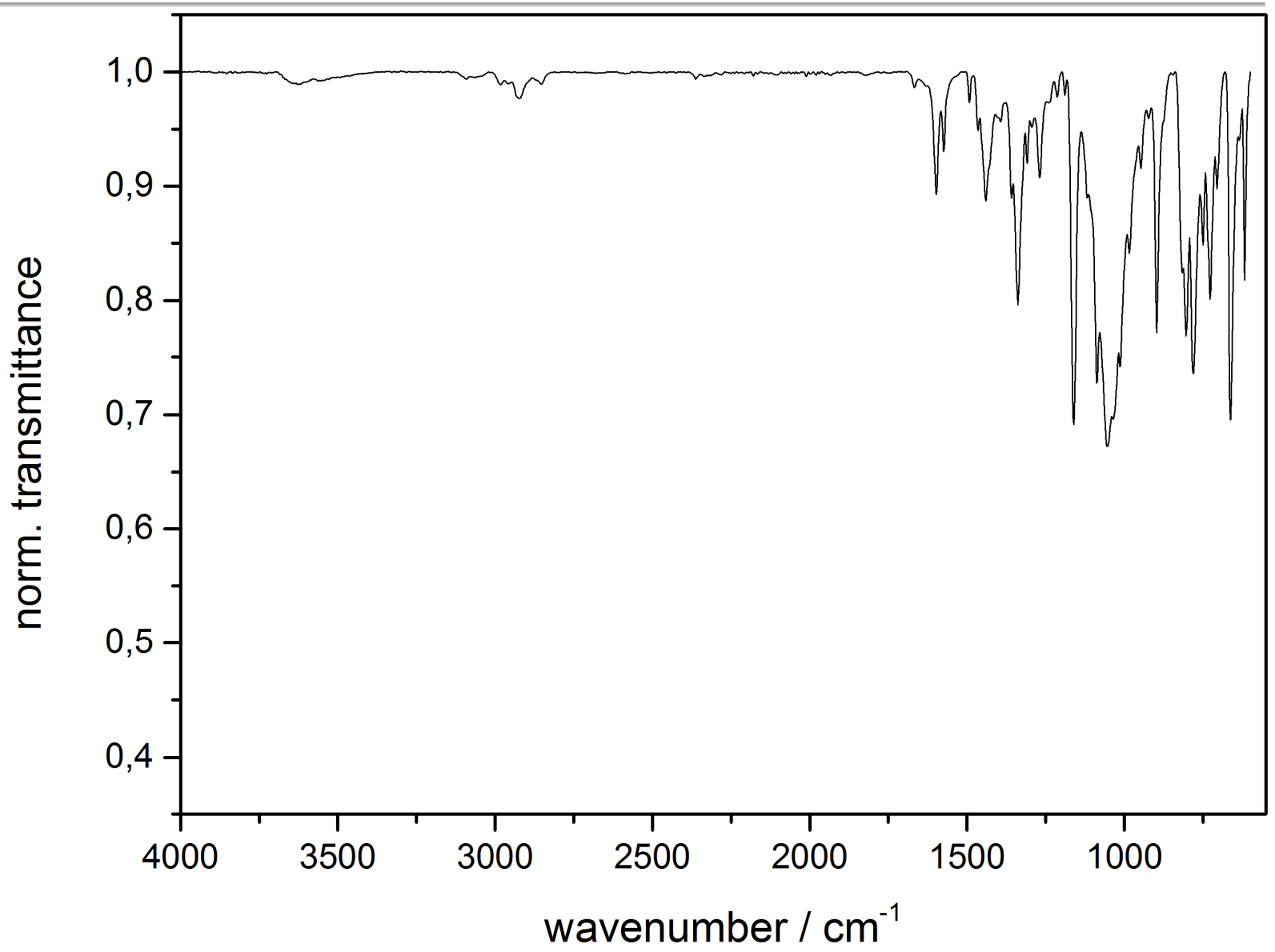

10.1.30 [Cu(DAPy-NH)Cl_2]

ESI-MS (pos)

(m/z (%) in MeCN)

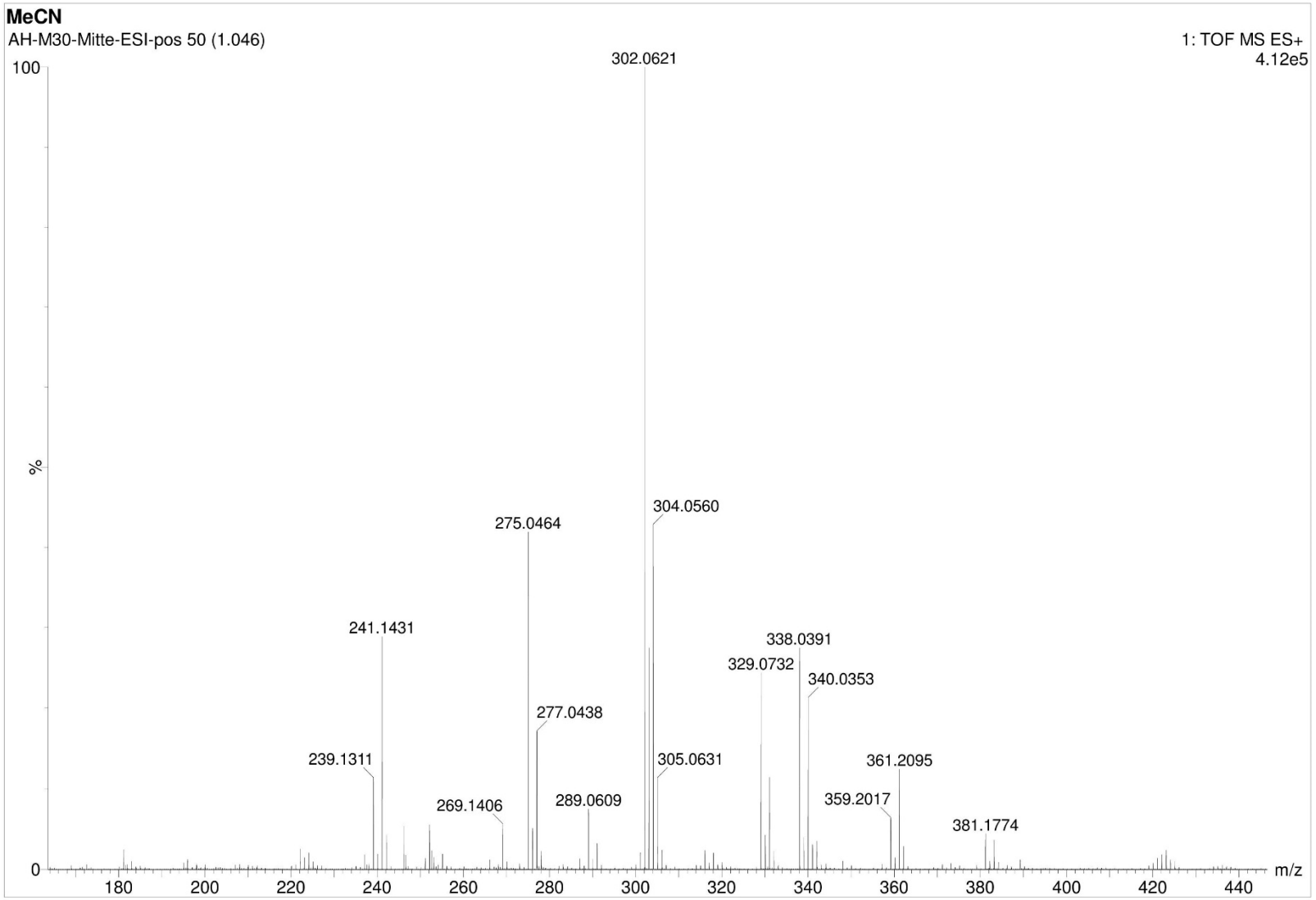

10.2 Crystal structures of precursors

10.2.1 5H-6,7-Dihydro[1,4]diazepino[1,2,3,4-lmn][1,10]phenanthrolinium dibromide

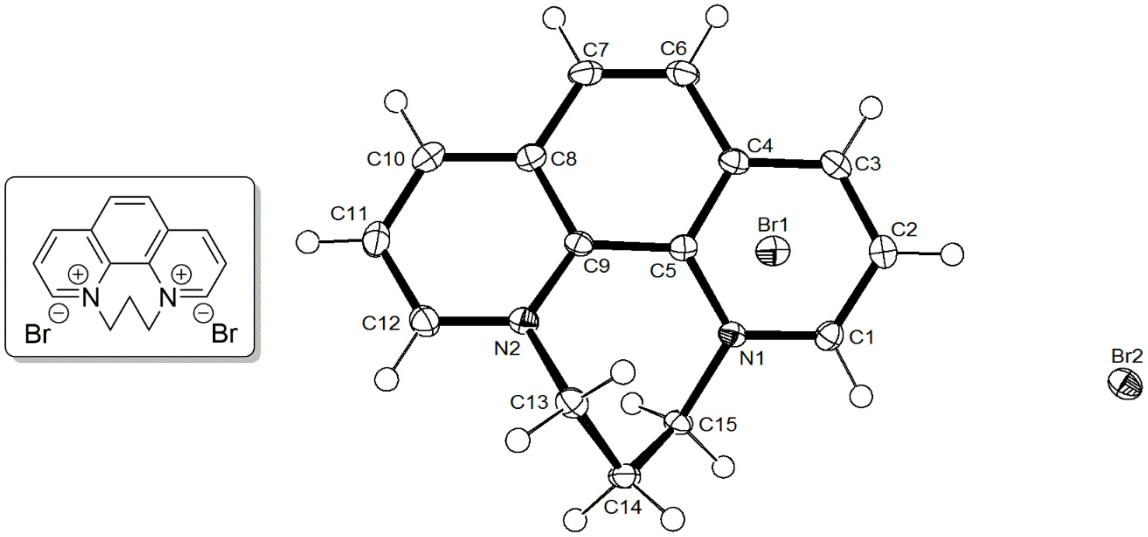

Figure 10-1: ORTEP plot of 5H-6,7-Dihydro[1,4]diazepino[1,2,3,4-lmn] [1,10] phenanthrolinium dibromide at 50 % probability level of thermal ellipsoids.

Table 10-1: Crystal data and structure refinement for 5H-6,7-Dihydro[1,4]diazepino[1,2,3,4-lmn][1,10]phenanthrolinium dibromide.

Identification code	s2442	
Empirical formula	C15 H14 Br2 N2	
Formula weight	382.10	
Temperature	130(2) K	
Wavelength	0.71073 Å	
Crystal system	Monoclinic	
Space group	P2(1)/n	
Unit cell dimensions	a = 10.9427(14) Å	α= 90°.
	b = 7.1896(9) Å	β= 106.562(2)°.
	c = 18.366(2) Å	γ = 90°.
Volume	1385.0(3) $Å^3$	
Z	4	
Density (calculated)	1.833 Mg/m^3	
Absorption coefficient	5.840 mm^{-1}	
F(000)	752	
Crystal size	0.39 x 0.19 x 0.05 mm^3	
Theta range for data collection	1.96 to 27.88°.	
Index ranges	-13<=h<=14, -9<=k<=9, -24<=l<=24	
Reflections collected	12478	
Independent reflections	3303 [R(int) = 0.0331]	
Completeness to theta = 27.88°	99.9 %	
Absorption correction	Semi-empirical from equivalents	
Max. and min. transmission	0.7589 and 0.2091	
Refinement method	Full-matrix least-squares on F^2	
Data / restraints / parameters	3303 / 0 / 172	
Goodness-of-fit on F^2	1.034	
Final R indices [I>2sigma(I)]	R1 = 0.0242, wR2 = 0.0551	
R indices (all data)	R1 = 0.0312, wR2 = 0.0573	
Largest diff. peak and hole	0.551 and -0.316 e.$Å^{-3}$	

10.2.2 1,10-Phenanthroline-2,9-dicarbaldehyde

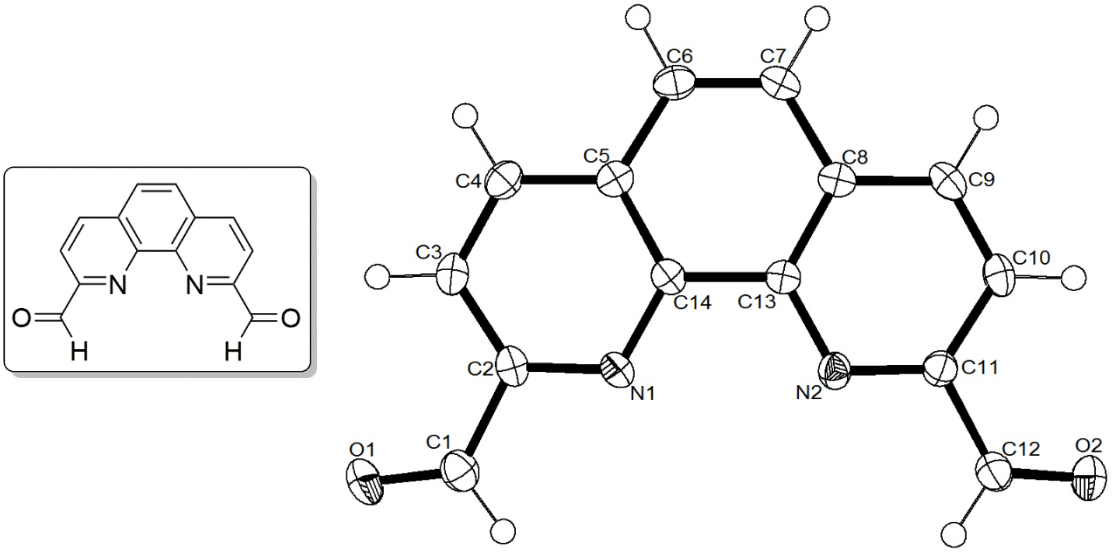

Figure 10-2: ORTEP plot of 1,10-Phenanthroline-2,9-dicarbaldehyde at 50 % probability level of thermal ellipsoids.

Table 10-2: Crystal data and structure refinement for 1,10-Phenanthroline-2,9-dicarbaldehyde.

Identification code	s2646	
Empirical formula	C14 H8 N2 O2	
Formula weight	236.22	
Temperature	130(2) K	
Wavelength	0.71073 Å	
Crystal system	Monoclinic	
Space group	P2(1)	
Unit cell dimensions	a = 9.9486(19) Å	α= 90°.
	b = 3.8105(7) Å	β= 107.610(4)°.
	c = 14.486(3) Å	γ = 90°.
Volume	523.42(18) $Å^3$	
Z	2	
Density (calculated)	1.499 Mg/m^3	
Absorption coefficient	0.103 mm^{-1}	
F(000)	244	
Crystal size	0.49 x 0.08 x 0.07 mm^3	
Theta range for data collection	2.15 to 27.88°.	
Index ranges	-13<=h<=13, -4<=k<=5, -17<=l<=19	
Reflections collected	4943	
Independent reflections	1411 [R(int) = 0.0551]	
Completeness to theta = 27.88°	99.6 %	
Absorption correction	Semi-empirical from equivalents	
Max. and min. transmission	0.9928 and 0.9512	
Refinement method	Full-matrix least-squares on F^2	
Data / restraints / parameters	1411 / 1 / 163	
Goodness-of-fit on F^2	0.945	
Final R indices [I>2sigma(I)]	R1 = 0.0433, wR2 = 0.0681	
R indices (all data)	R1 = 0.0692, wR2 = 0.0754	
Absolute structure parameter	1(2)	
Largest diff. peak and hole	0.249 and -0.179 e.$Å^{-3}$	

10.2.3 1,10-Phenanthroline-2,9-dicarboxylic acid

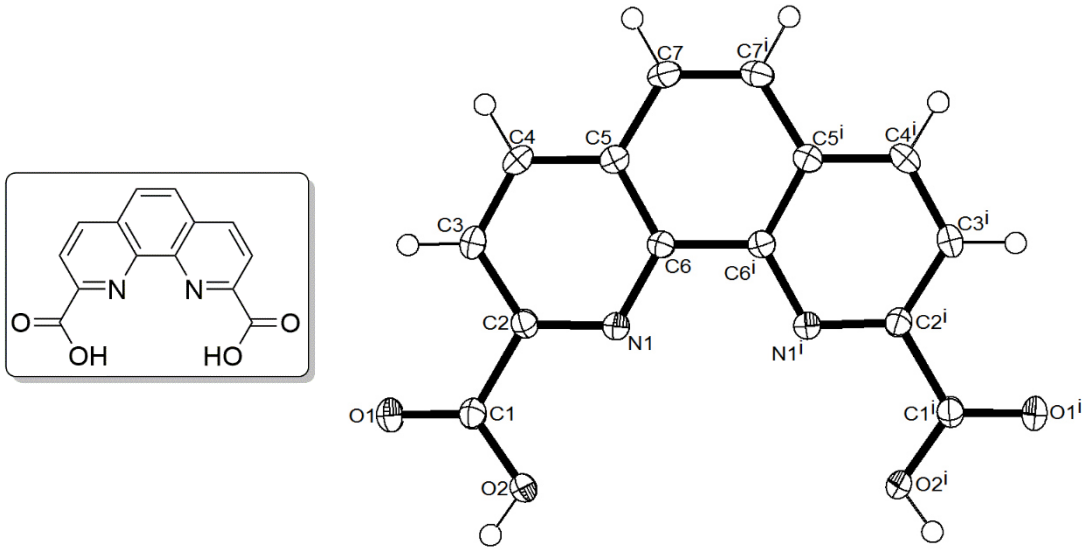

Figure 10-3: ORTEP plot of 1,10-Phenanthroline-2,9-dicarboxylic acid at 50 % probability level of thermal ellipsoids.

Table 10-3: Crystal data and structure refinement for 1,10-Phenanthroline-2,9-dicarboxylic acid.

Identification code	s2648	
Empirical formula	C18 H8 D12 N2 O6 S2	
Formula weight	436.55	
Temperature	130(2) K	
Wavelength	0.71073 Å	
Crystal system	Monoclinic	
Space group	C 2/c	
Unit cell dimensions	a = 14.225(3) Å	α= 90°.
	b = 9.936(2) Å	β= 102.128(5)°.
	c = 13.835(3) Å	γ = 90°.
Volume	1911.9(7) $Å^3$	
Z	4	
Density (calculated)	1.517 Mg/m^3	
Absorption coefficient	0.318 mm^{-1}	
F(000)	888	
Crystal size	0.370 x 0.250 x 0.200 mm^3	
Theta range for data collection	2.519 to 27.861°.	
Index ranges	-18<=h<=16, -13<=k<=13, -17<=l<=18	
Reflections collected	8965	
Independent reflections	2285 [R(int) = 0.0330]	
Completeness to theta = 25.242°	100.0 %	
Absorption correction	Semi-empirical from equivalents	
Max. and min. transmission	1.0000 and 0.8461	
Refinement method	Full-matrix least-squares on F^2	
Data / restraints / parameters	2285 / 0 / 130	
Goodness-of-fit on F^2	1.056	
Final R indices [I>2sigma(I)]	R1 = 0.0388, wR2 = 0.0958	
R indices (all data)	R1 = 0.0476, wR2 = 0.1026	
Extinction coefficient	n/a	
Largest diff. peak and hole	0.453 and -0.281 $e.Å^{-3}$	

10.2.4 Diphenylphosphinic acid

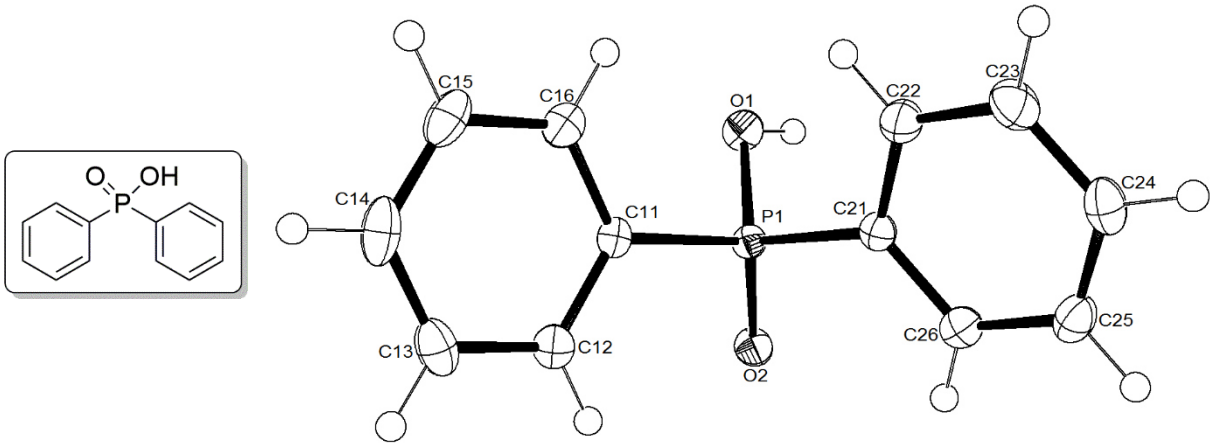

Figure 10-4: ORTEP plot of diphenylphosphinic acid at 50 % probability level of thermal ellipsoids.

Table 10-4: Crystal data and structure refinement for diphenylphosphinic acid.

Identification code	s2826	
Empirical formula	C12 H11 O2 P	
Formula weight	218.18	
Temperature	130(2) K	
Wavelength	0.71073 Å	
Crystal system	Monoclinic	
Space group	P 21/c	
Unit cell dimensions	a = 11.427(2) Å	α= 90°.
	b = 5.9487(11) Å	β= 100.155(4)°.
	c = 15.610(3) Å	γ = 90°.
Volume	1044.5(3) $Å^3$	
Z	4	
Density (calculated)	1.387 Mg/m^3	
Absorption coefficient	0.237 mm^{-1}	
F(000)	456	
Crystal size	0.390 x 0.220 x 0.210 mm^3	
Theta range for data collection	1.811 to 27.877°.	
Index ranges	-15<=h<=15, -7<=k<=7, -19<=l<=20	
Reflections collected	9358	
Independent reflections	2479 [R(int) = 0.0362]	
Completeness to theta = 25.242°	100.0 %	
Absorption correction	Semi-empirical from equivalents	
Max. and min. transmission	1.0000 and 0.7498	
Refinement method	Full-matrix least-squares on F^2	
Data / restraints / parameters	2479 / 0 / 137	
Goodness-of-fit on F^2	1.049	
Final R indices [I>2sigma(I)]	R1 = 0.0401, wR2 = 0.0979	
R indices (all data)	R1 = 0.0497, wR2 = 0.1040	
Extinction coefficient	n/a	
Largest diff. peak and hole	0.535 and -0.252 $e.Å^{-3}$	

10.2.5 [Mn(2-methyl-1,10-phenanthroline)$_2$(HCO$_3$)$_2$]

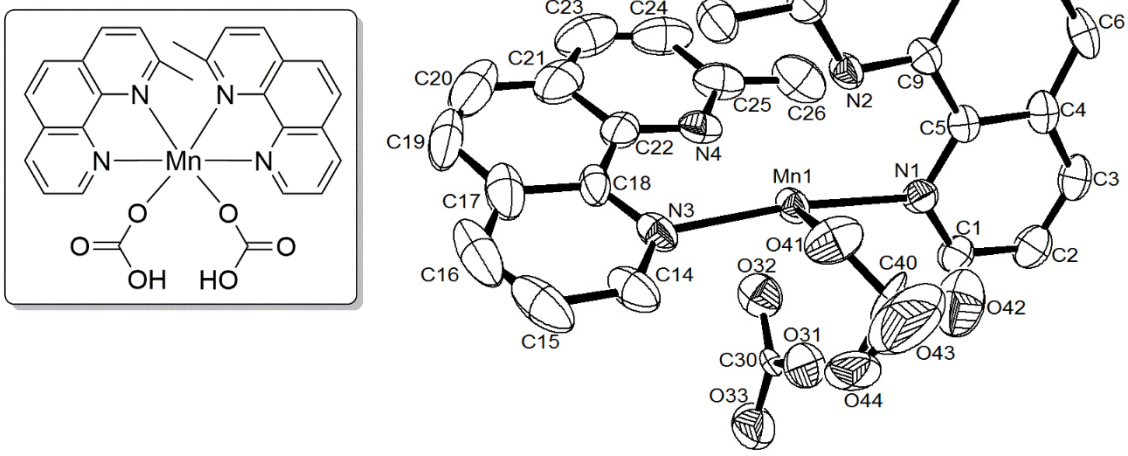

Figure 10-5: ORTEP plot of [Mn(2-methyl-1,10-phenanthroline)$_2$(HCO$_3$)$_2$] at 50 % probability level of thermal ellipsoids. (Hydrogens and two chloroform molecules were omitted.)

Remarks:

Two chloroform molecules per formula unit were detected, one of them was treated with SQUEEZE due to strong disorder. The hydrogens of the hydrogen carbonates could not be localized and one hydrogen carbonate exhibits a stronger disorder.

Table 10-5: Crystal data and structure refinement for [Mn(2-methyl-1,10-phenanthroline)$_2$(HCO$_3$)$_2$].

Identification code	s2441	
Empirical formula	C30 H24 Cl6 Mn N4 O6	
Formula weight	804.17	
Temperature	130(2) K	
Wavelength	0.71073 Å	
Crystal system	Triclinic	
Space group	P-1	
Unit cell dimensions	a = 11.715(3) Å	α= 111.864(5)°.
	b = 12.172(3) Å	β= 109.138(5)°.
	c = 13.870(3) Å	γ = 96.115(5)°.
Volume	1674.1(7) Å^3	
Z	2	
Density (calculated)	1.595 Mg/m^3	
Absorption coefficient	0.922 mm^{-1}	
F(000)	814	
Crystal size	0.37 x 0.25 x 0.21 mm^3	
Theta range for data collection	1.72 to 27.88°.	
Index ranges	-15<=h<=15, -16<=k<=15, -18<=l<=18	
Reflections collected	15796	
Independent reflections	7937 [R(int) = 0.0559]	
Completeness to theta = 27.88°	99.4 %	
Absorption correction	Semi-empirical from equivalents	
Max. and min. transmission	0.8299 and 0.7265	
Refinement method	Full-matrix least-squares on F^2	
Data / restraints / parameters	7937 / 0 / 401	
Goodness-of-fit on F^2	0.847	
Final R indices [I>2sigma(I)]	R1 = 0.0582, wR2 = 0.1300	
R indices (all data)	R1 = 0.0986, wR2 = 0.1421	
Largest diff. peak and hole	0.652 and -0.521 e.Å^{-3}	

10.3 Crystal structures of copper(I) phenanthroline complexes

10.3.1 [Cu(2,9-dimethyl-1,10-phenanthroline)$_2$][BF$_4$]

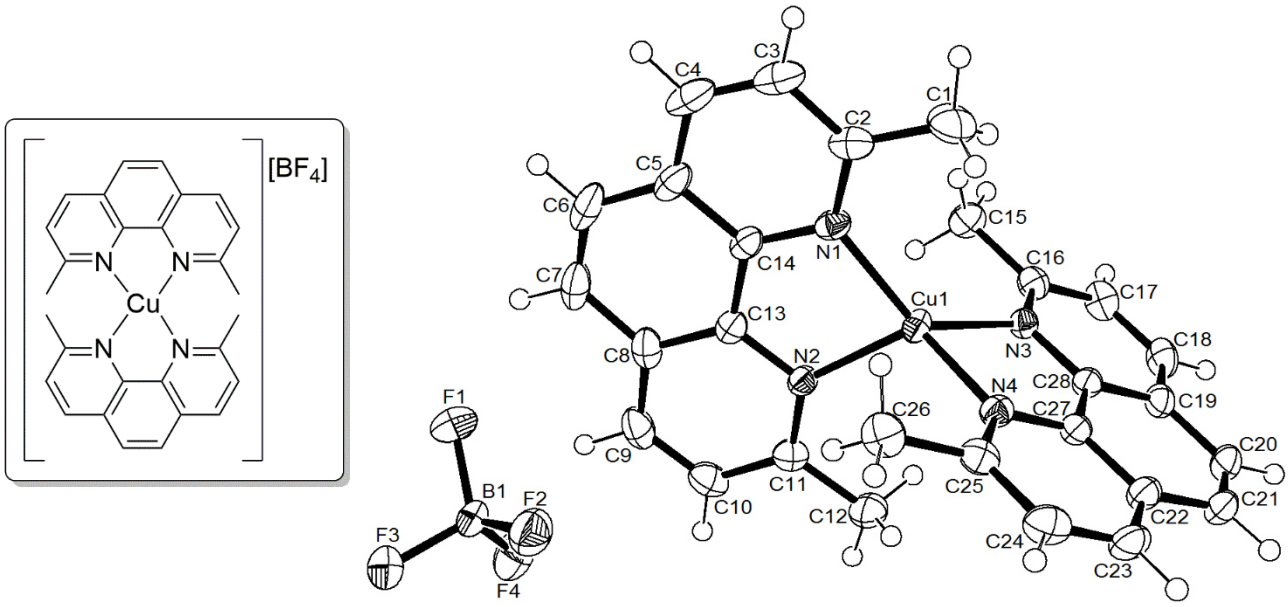

Figure 10-6: ORTEP plot of [Cu(2,9-dimethyl-1,10-phenanthroline)$_2$][BF$_4$] at 50 % probability level of thermal ellipsoids.

Table 10-6: Crystal data and structure refinement for [Cu(2,9-dimethyl-1,10-phenanthroline)$_2$][BF_4].

Identification code	s2825	
Empirical formula	C28 H24 B Cu F4 N4	
Formula weight	566.86	
Temperature	130(2) K	
Wavelength	0.71073 Å	
Crystal system	Orthorhombic	
Space group	P 21 21 21	
Unit cell dimensions	a = 11.7548(12) Å	α= 90°.
	b = 12.1538(12) Å	β= 90°.
	c = 18.0150(18) Å	γ = 90°.
Volume	2573.7(4) $Å^3$	
Z	4	
Density (calculated)	1.463 Mg/m^3	
Absorption coefficient	0.903 mm^{-1}	
F(000)	1160	
Crystal size	0.410 x 0.380 x 0.350 mm^3	
Theta range for data collection	2.021 to 27.874°.	
Index ranges	-15<=h<=15, -15<=k<=15, -23<=l<=23	
Reflections collected	24448	
Independent reflections	6143 [R(int) = 0.0343]	
Completeness to theta = 25.242°	100.0 %	
Absorption correction	Semi-empirical from equivalents	
Max. and min. transmission	1.0000 and 0.7611	
Refinement method	Full-matrix least-squares on F^2	
Data / restraints / parameters	6143 / 0 / 347	
Goodness-of-fit on F^2	1.079	
Final R indices [I>2sigma(I)]	R1 = 0.0330, wR2 = 0.0764	
R indices (all data)	R1 = 0.0374, wR2 = 0.0793	
Absolute structure parameter	-0.012(5)	
Extinction coefficient	n/a	
Largest diff. peak and hole	0.449 and -0.193 e.$Å^{-3}$	

10.3.2 [Cu(2,9-dimethyl-1,10-phenanthroline)$_2$][BF$_4$] · DCM

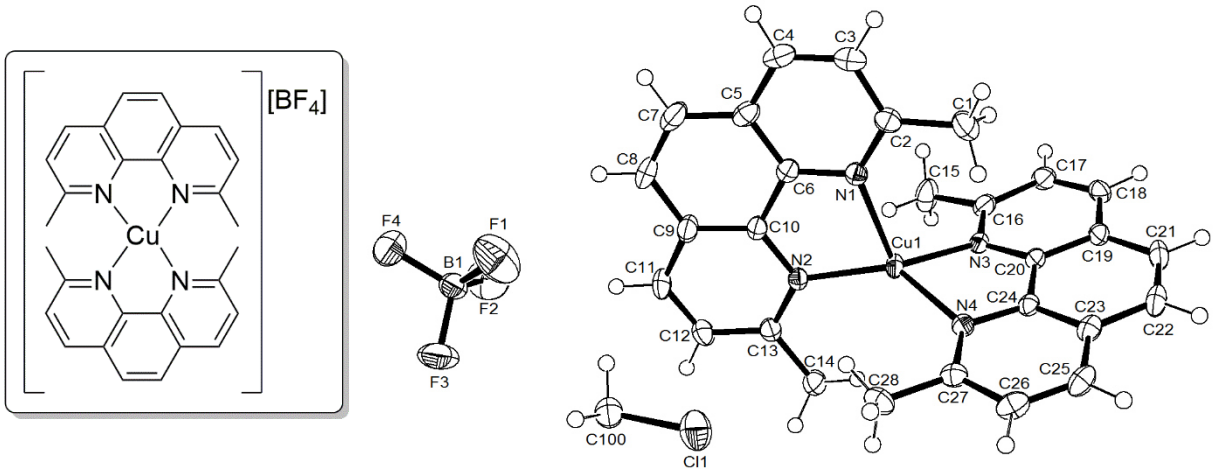

Figure 10-7: ORTEP plot of [Cu(2,9-dimethyl-1,10-phenanthroline)$_2$][BF$_4$] · DCM at 50 % probability level for thermal ellipsoids.

Remarks:

The foreground shows one DCM molecule and the tetrafluoroborate anion.

Table 10-7: Crystal data and structure refinement for [Cu(2,9-dimethyl-1,10-phenanthroline)$_2$][BF_4] · DCM.

Identification code	s2733	
Empirical formula	C28.50 H25 B Cl Cu F4 N4	
Formula weight	609.32	
Temperature	130(2) K	
Wavelength	0.71073 Å	
Crystal system	Triclinic	
Space group	P -1	
Unit cell dimensions	a = 10.4582(12) Å	α= 67.196(2)°.
	b = 11.1033(13) Å	β= 74.116(2)°.
	c = 12.8549(15) Å	γ = 73.091(2)°.
Volume	1294.4(3) $Å^3$	
Z	2	
Density (calculated)	1.563 Mg/m^3	
Absorption coefficient	1.003 mm^{-1}	
F(000)	622	
Crystal size	0.480 x 0.330 x 0.250 mm^3	
Theta range for data collection	1.748 to 27.876°.	
Index ranges	-13<=h<=13, -14<=k<=14, -16<=l<=16	
Reflections collected	12224	
Independent reflections	6126 [R(int) = 0.0202]	
Completeness to theta = 25.242°	99.8 %	
Absorption correction	Semi-empirical from equivalents	
Max. and min. transmission	1.0000 and 0.8095	
Refinement method	Full-matrix least-squares on F^2	
Data / restraints / parameters	6126 / 0 / 365	
Goodness-of-fit on F^2	1.023	
Final R indices [I>2sigma(I)]	R1 = 0.0371, wR2 = 0.0949	
R indices (all data)	R1 = 0.0406, wR2 = 0.0981	
Extinction coefficient	n/a	
Largest diff. peak and hole	0.754 and -0.461 e.$Å^{-3}$	

10.3.3 [Cu(2,9-bis(chloromethyl)-1,10-phenanthroline)$_2$][BF_4]

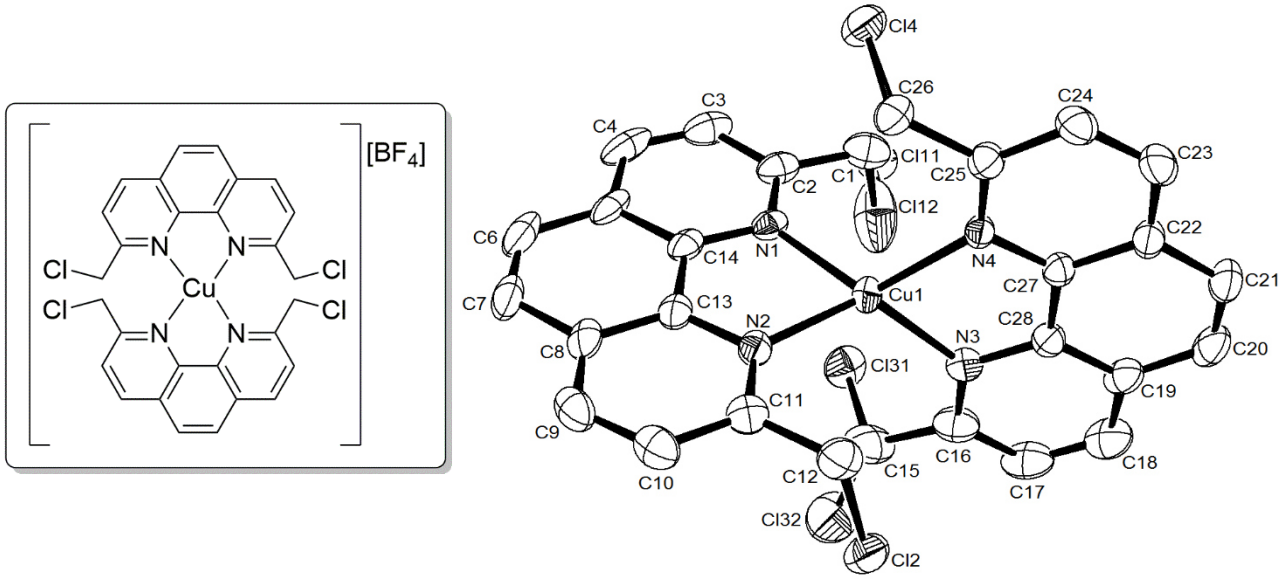

Figure 10-8: ORTEP plot of [Cu(2,9-bis(chloromethyl)-1,10-phenanthroline)$_2$][BF_4] at 50 % probability level for thermal ellipsoids. (The tetrafluoroborate anion is not depicted.)

Remarks:

The tetrafluoroborate anion was treated with SQUEEZE due to disorder. Two chlorine atoms are distorted over four positions.

Table 10-8: Crystal data and structure refinement for [Cu(2,9-bis(chloromethyl)-1,10-phenanthroline)$_2$][BF_4].

Identification code	d2747-sr	
Empirical formula	C28 H20 B Cl4 Cu F4 N4	
Formula weight	704.63	
Temperature	130(2) K	
Wavelength	0.71073 Å	
Crystal system	Monoclinic	
Space group	P 21/c	
Unit cell dimensions	a = 15.2771(18) Å	α= 90°.
	b = 17.852(2) Å	β= 95.589(3)°.
	c = 10.3591(13) Å	γ = 90°.
Volume	2811.9(6) Å^3	
Z	4	
Density (calculated)	1.664 Mg/m^3	
Absorption coefficient	1.212 mm^{-1}	
F(000)	1416	
Crystal size	0.490 x 0.210 x 0.100 mm^3	
Theta range for data collection	1.339 to 27.878°.	
Index ranges	-20<=h<=18, -23<=k<=23, -13<=l<=13	
Reflections collected	26116	
Independent reflections	6702 [R(int) = 0.0540]	
Completeness to theta = 25.242°	100.0 %	
Absorption correction	Semi-empirical from equivalents	
Max. and min. transmission	1.0000 and 0.7698	
Refinement method	Full-matrix least-squares on F^2	
Data / restraints / parameters	6702 / 2 / 355	
Goodness-of-fit on F^2	1.037	
Final R indices [I>2sigma(I)]	R1 = 0.0522, wR2 = 0.1199	
R indices (all data)	R1 = 0.0758, wR2 = 0.1296	
Extinction coefficient	n/a	
Largest diff. peak and hole	0.489 and -0.528 e.Å^{-3}	

10.3.4 [Cu(2,9-bis(bromomethyl)-1,10-phenanthroline)(MeCN)][BF_4]/Cu(2,9-bis(bromomethyl)-1,10-phenanthroline)(MeCN)$_2$][BF_4] 2:1 ratio · DCM

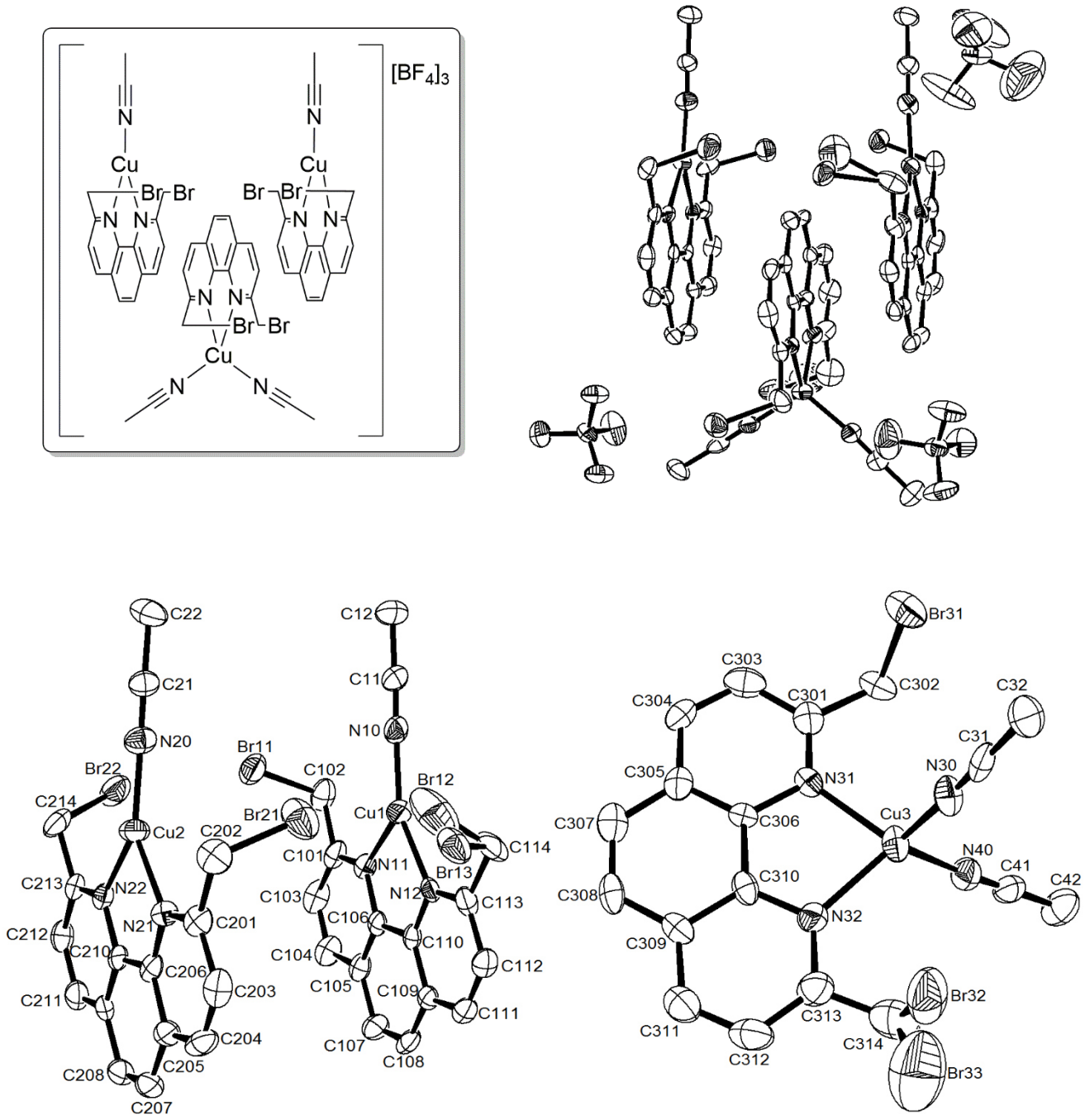

Figure 10-9: ORTEP plots of a cocrystal consisting of [Cu(2,9-bis(bromomethyl)-1,10-phenanthroline)(MeCN)][BF_4] and Cu(2,9-bis(bromomethyl)-1,10-phenanthroline)(MeCN)$_2$][BF_4] in a 2:1 ratio · DCM at 50 % probability level for thermal ellipsoids. (Hydrogens were omitted.)

Remarks:

The one DCM molecule per asymmetric unit has been treated with Squeeze.

Table 10-9: Crystal data and structure refinement for [Cu(2,9-bis(bromomethyl)-1,10-phenanthroline)(MeCN)][BF_4]/Cu(2,9-bis(bromomethyl)-1,10-phenanthroline)(MeCN)$_2$][BF_4] 2:1 ratio.

Identification code	s2695s	
Empirical formula	C51 H44 B3 Br6 Cl2 Cu3 F12 N10	
Formula weight	1798.37	
Temperature	130(2) K	
Wavelength	0.71073 Å	
Crystal system	Monoclinic	
Space group	P 21/n	
Unit cell dimensions	a = 16.508(3) Å	α= 90°.
	b = 21.015(4) Å	β= 97.182(5)°.
	c = 18.175(3) Å	γ = 90°.
Volume	6256(2) $Å^3$	
Z	4	
Density (calculated)	1.909 Mg/m^3	
Absorption coefficient	5.009 mm^{-1}	
F(000)	3496	
Crystal size	0.470 x 0.230 x 0.200 mm^3	
Theta range for data collection	1.572 to 27.876°.	
Index ranges	-21<=h<=21, -27<=k<=25, -23<=l<=23	
Reflections collected	56822	
Independent reflections	14894 [R(int) = 0.1267]	
Completeness to theta = 25.242°	100.0 %	
Absorption correction	Semi-empirical from equivalents	
Max. and min. transmission	1.0000 and 0.1940	
Refinement method	Full-matrix least-squares on F^2	
Data / restraints / parameters	14894 / 23 / 781	
Goodness-of-fit on F^2	0.837	
Final R indices [I>2sigma(I)]	R1 = 0.0667, wR2 = 0.1412	
R indices (all data)	R1 = 0.1512, wR2 = 0.1676	
Extinction coefficient	n/a	
Largest diff. peak and hole	1.824 and -0.934 $e.Å^{-3}$	

10.3.5 [Cu(2,9-bis(bromomethyl)-1,10-phenanthroline)$_2$][BF$_4$] · DCM-A

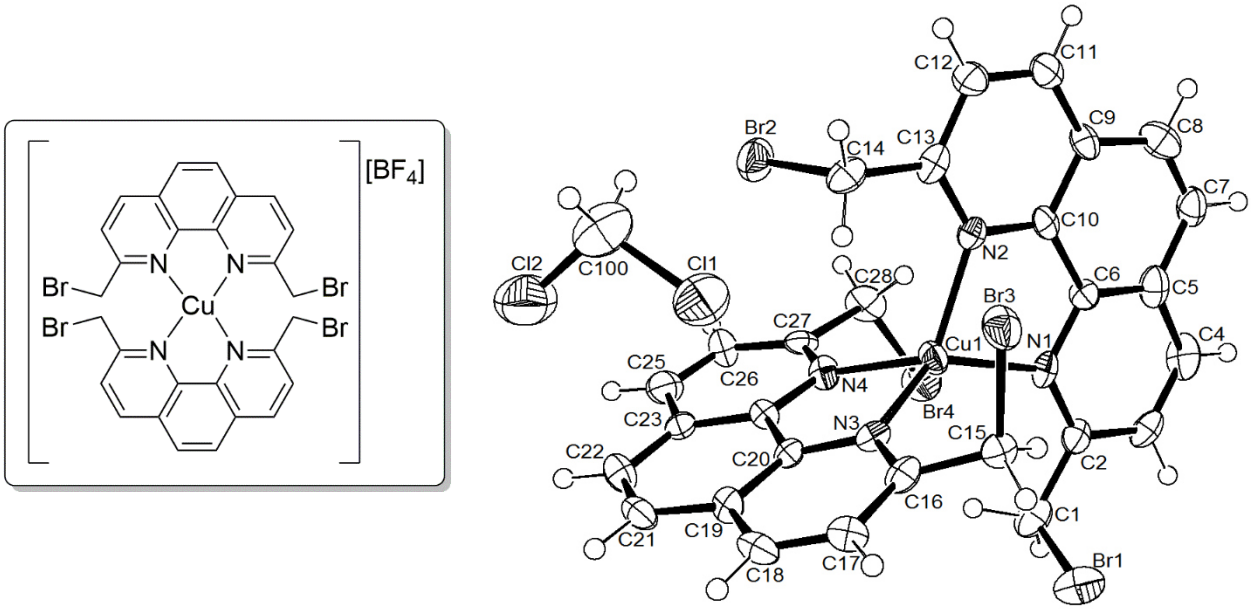

Figure 10-10: ORTEP plot of [Cu(2,9-bis(bromomethyl)-1,10-phenanthroline)$_2$][BF$_4$] at 50 % probability level for thermal ellipsoids.

Remarks:

The tetrafluoroborate anion was treated with Squeeze due to disorder.

Table 10-10: Crystal data and structure refinement for [Cu(2,9-bis(bromomethyl)-1,10-phenanthroline)$_2$][BF_4].

Identification code	s2709	
Empirical formula	C29 H22 B Br4 Cl2 Cu F4 N4	
Formula weight	967.40	
Temperature	130(2) K	
Wavelength	0.71073 Å	
Crystal system	Orthorhombic	
Space group	P2(1)2(1)2(1)	
Unit cell dimensions	a = 10.4951(19) Å	α= 90°.
	b = 12.719(2) Å	β= 90°.
	c = 24.714(5) Å	γ = 90°.
Volume	3299.0(10) Å^3	
Z	4	
Density (calculated)	1.948 Mg/m^3	
Absorption coefficient	5.720 mm^{-1}	
F(000)	1872	
Crystal size	0.20 x 0.11 x 0.08 mm^3	
Theta range for data collection	1.65 to 27.87°.	
Index ranges	-13<=h<=13, -16<=k<=16, -32<=l<=32	
Reflections collected	31633	
Independent reflections	7875 [R(int) = 0.1299]	
Completeness to theta = 27.87°	100.0 %	
Absorption correction	Semi-empirical from equivalents	
Max. and min. transmission	0.6576 and 0.3942	
Refinement method	Full-matrix least-squares on F^2	
Data / restraints / parameters	7875 / 0 / 361	
Goodness-of-fit on F^2	0.621	
Final R indices [I>2sigma(I)]	R1 = 0.0426, wR2 = 0.0670	
R indices (all data)	R1 = 0.0939, wR2 = 0.0787	
Absolute structure parameter	0.027(10)	
Largest diff. peak and hole	0.507 and -0.418 e.Å^{-3}	

10.3.6 [Cu(2,9-bis(bromomethyl)-1,10-phenanthroline)$_2$][BF_4]-B

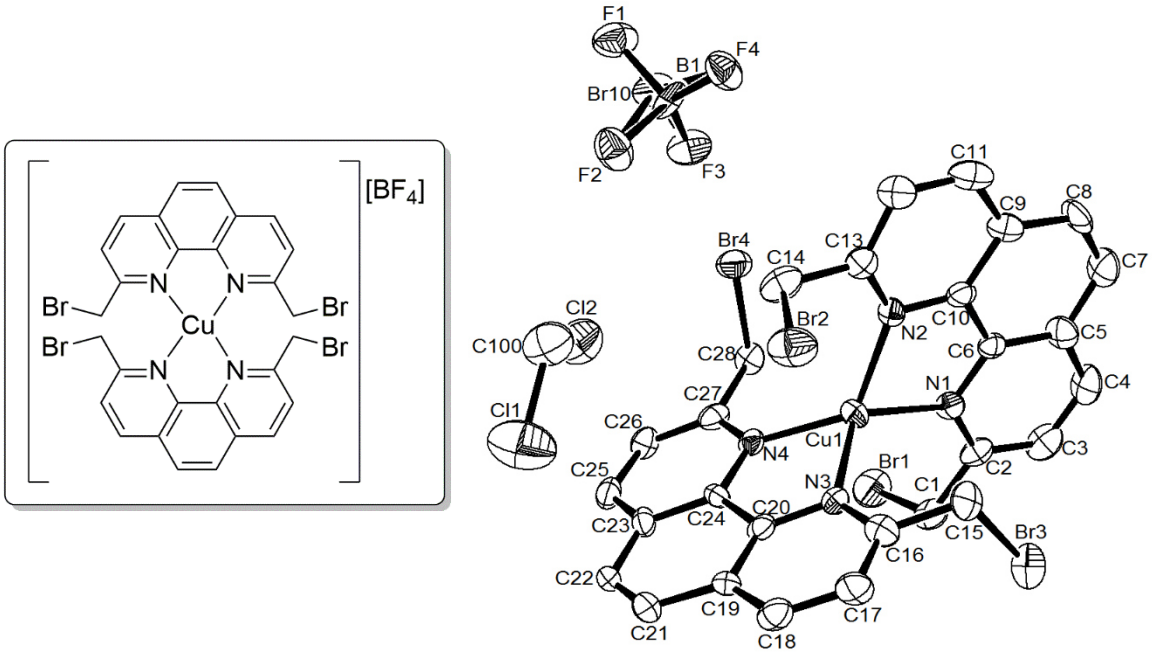

Figure 10-11: ORTEP plot of [Cu(2,9-bis(bromomethyl)-1,10-phenanthroline)$_2$][BF_4] at 50 % probability level for thermal ellipsoids. (Hydrogens were omitted. The anion disordered with 8.3 % Br and 91.7 % BF_4.)

Table 10-11: Crystal data and structure refinement for [Cu(2,9-bis(bromomethyl)-1,10-phenanthroline)$_2$][BF_4].

Identification code	s2726	
Empirical formula	C29 H22 B0.92 Br4.08 Cl2 Cu F3.68 N4	
Formula weight	966.84	
Temperature	130(2) K	
Wavelength	0.71073 Å	
Crystal system	Orthorhombic	
Space group	P 21 21 21	
Unit cell dimensions	a = 10.498(3) Å	α= 90°.
	b = 12.712(3) Å	β= 90°.
	c = 24.732(6) Å	γ = 90°.
Volume	3300.7(13) $Å^3$	
Z	4	
Density (calculated)	1.946 Mg/m^3	
Absorption coefficient	5.812 mm^{-1}	
F(000)	1870	
Crystal size	0.500 x 0.090 x 0.050 mm^3	
Theta range for data collection	1.647 to 27.878°.	
Index ranges	-13<=h<=13, -16<=k<=15, -32<=l<=32	
Reflections collected	31209	
Independent reflections	7891 [R(int) = 0.1282]	
Completeness to theta = 25.242°	100.0 %	
Absorption correction	Semi-empirical from equivalents	
Max. and min. transmission	1.0000 and 0.5353	
Refinement method	Full-matrix least-squares on F^2	
Data / restraints / parameters	7891 / 0 / 416	
Goodness-of-fit on F^2	0.786	
Final R indices [I>2sigma(I)]	R1 = 0.0473, wR2 = 0.0705	
R indices (all data)	R1 = 0.1154, wR2 = 0.0881	
Absolute structure parameter	0.009(10)	
Extinction coefficient	n/a	
Largest diff. peak and hole	0.506 and -0.496 e.$Å^{-3}$	

10.3.7 [Cu(2,9-bis(iodomethyl)-1,10-phenanthroline)$_2$][BF_4]

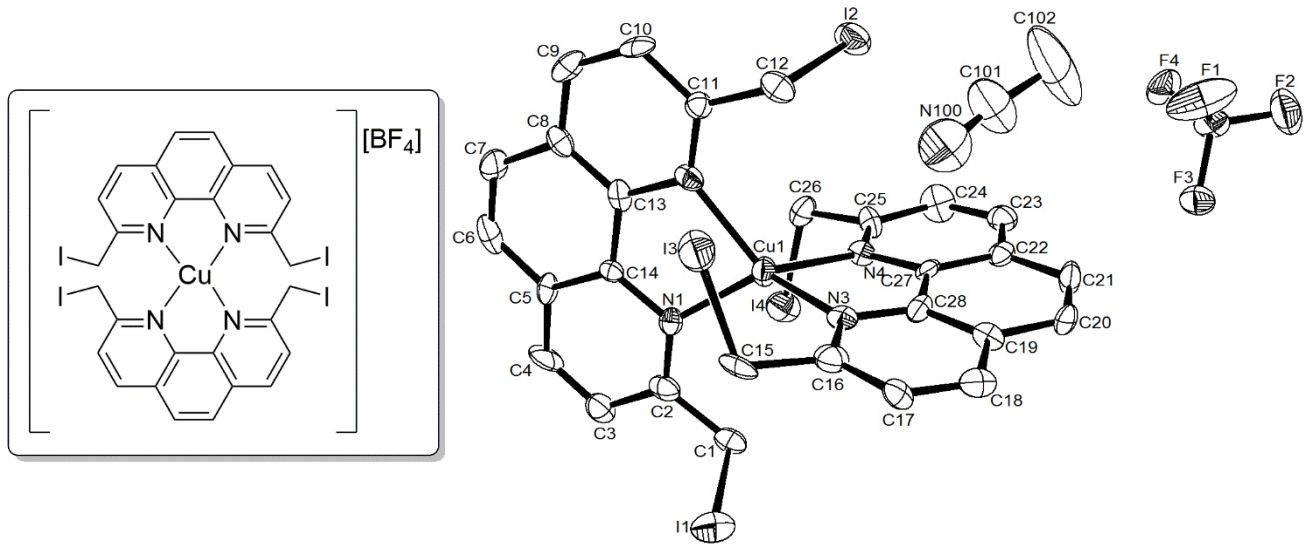

Figure 10-12: [Cu(2,9-bis(iodomethyl)-1,10-phenanthroline)$_2$][BF_4] at 50 % probability level for thermal ellipsoids. (Hydrogens were omitted. The anion is disordered with 3 % iodine and 97 % BF_4.)

Table 10-12: Crystal data and structure refinement for Cu(2,9-bis(iodomethyl)-1,10-phenanthroline)$_2$][BF$_4$].

Identification code	d2755	
Empirical formula	C30 H23 B0.98 Cu F3.91 I4.03 N5	
Formula weight	1112.58	
Temperature	130(2) K	
Wavelength	0.71073 Å	
Crystal system	Orthorhombic	
Space group	P 21 21 21	
Unit cell dimensions	a = 10.723(3) Å	α= 90°.
	b = 12.731(3) Å	β= 90°.
	c = 25.288(6) Å	γ = 90°.
Volume	3452.3(15) Å^3	
Z	4	
Density (calculated)	2.141 Mg/m^3	
Absorption coefficient	4.282 mm^{-1}	
F(000)	2081	
Crystal size	0.200 x 0.070 x 0.060 mm^3	
Theta range for data collection	1.611 to 27.874°.	
Index ranges	-14<=h<=14, -16<=k<=16, -33<=l<=33	
Reflections collected	31993	
Independent reflections	8224 [R(int) = 0.1555]	
Completeness to theta = 25.242°	100.0 %	
Absorption correction	Semi-empirical from equivalents	
Max. and min. transmission	1.0000 and 0.4172	
Refinement method	Full-matrix least-squares on F^2	
Data / restraints / parameters	8224 / 0 / 403	
Goodness-of-fit on F^2	0.667	
Final R indices [I>2sigma(I)]	R1 = 0.0469, wR2 = 0.0697	
R indices (all data)	R1 = 0.1092, wR2 = 0.0894	
Absolute structure parameter	-0.06(3)	
Extinction coefficient	n/a	
Largest diff. peak and hole	0.737 and -1.080 e.Å^{-3}	

10.3.8 [Cu(2,9-bis(bromomethyl)-1,10-phenanthroline)$_2$][ClO$_4$] · H$_2$O

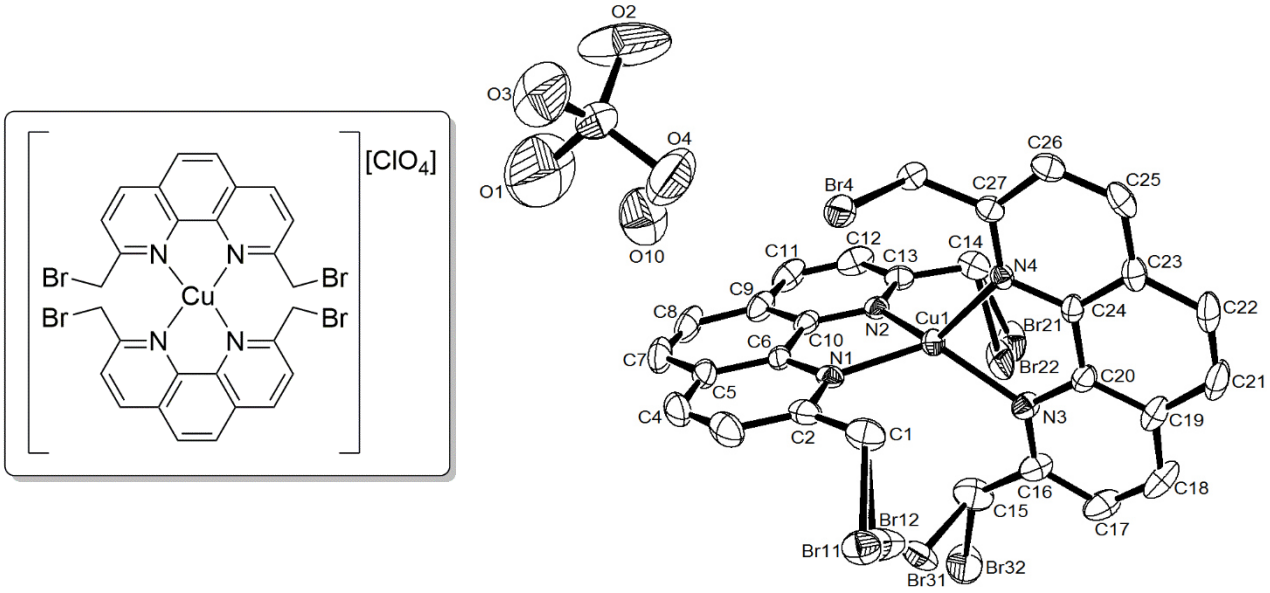

Figure 10-13: ORTEP plot of [Cu(2,9-bis(bromomethyl)-1,10-phenanthroline)$_2$][ClO$_4$] · H$_2$O at 50 % probability level for thermal ellipsoids. (Hydrogens were omitted. Three bromine atoms are disordered.)

Table 10-13: Crystal data and structure refinement for Cu(2,9-bis(bromomethyl)-1,10-phenanthroline)$_2$][ClO$_4$] · H$_2$O.

Identification code	s2727	
Empirical formula	C28 H22 Br4 Cl Cu N4 O5	
Formula weight	913.12	
Temperature	130(2) K	
Wavelength	0.71073 Å	
Crystal system	Monoclinic	
Space group	P 21/c	
Unit cell dimensions	a = 15.683(2) Å	α= 90°.
	b = 18.097(2) Å	β= 97.131(3)°.
	c = 10.7764(15) Å	γ = 90°.
Volume	3034.9(7) Å^3	
Z	4	
Density (calculated)	1.998 Mg/m^3	
Absorption coefficient	6.120 mm^{-1}	
F(000)	1776	
Crystal size	0.430 x 0.400 x 0.370 mm^3	
Theta range for data collection	1.726 to 27.877°.	
Index ranges	-20<=h<=16, -23<=k<=21, -14<=l<=14	
Reflections collected	28537	
Independent reflections	7232 [R(int) = 0.0458]	
Completeness to theta = 25.242°	100.0 %	
Absorption correction	Semi-empirical from equivalents	
Max. and min. transmission	1.0000 and 0.7533	
Refinement method	Full-matrix least-squares on F^2	
Data / restraints / parameters	7232 / 0 / 418	
Goodness-of-fit on F^2	1.033	
Final R indices [I>2sigma(I)]	R1 = 0.0458, wR2 = 0.1083	
R indices (all data)	R1 = 0.0685, wR2 = 0.1182	
Extinction coefficient	n/a	
Largest diff. peak and hole	1.620 and -0.672 e.Å^{-3}	

10.3.9 [Cu(2,9-bis(bromomethyl)-1,10-phenanthroline)$_2$][Br]

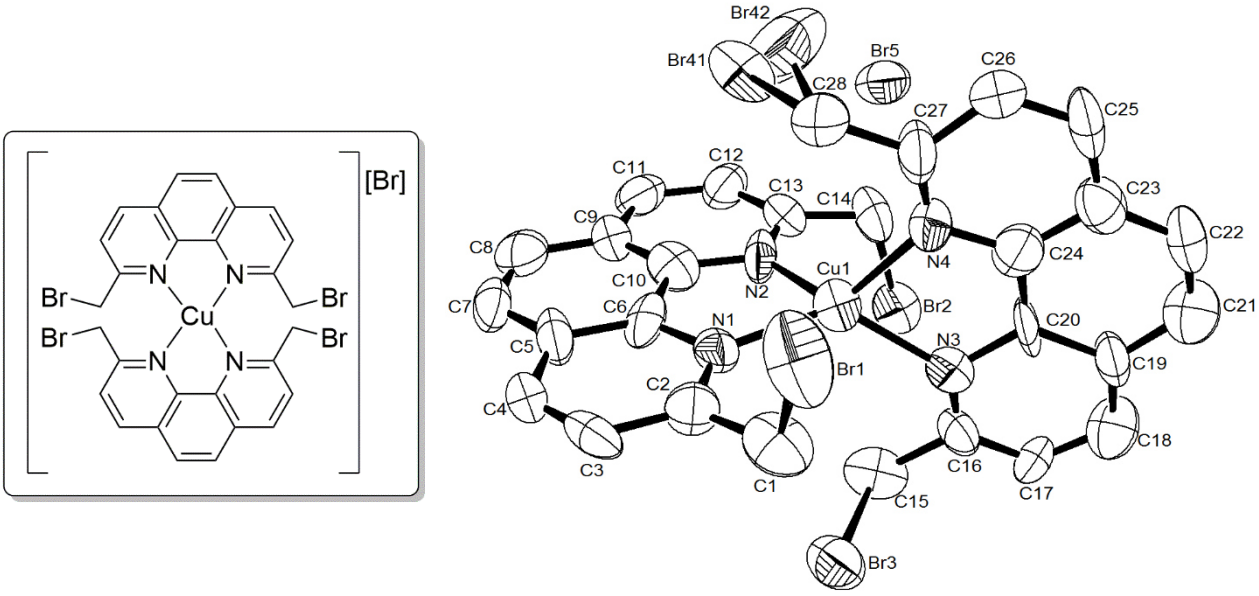

Figure 10-14: ORTEP plot of [Cu(2,9-bis(bromomethyl)-1,10-phenanthroline)$_2$][Br] at 50 % probability level for thermal ellipsoids. (Hydrogens were omitted. Two bromine atom are disordered.)

Table 10-14: Crystal data and structure refinement for [Cu(2,9-bis(bromomethyl)-1,10-phenanthroline)$_2$][Br].

Identification code	s2689	
Empirical formula	C28 H20 Br5 Cu N4	
Formula weight	875.57	
Temperature	130(2) K	
Wavelength	0.71073 Å	
Crystal system	Monoclinic	
Space group	P 21/c	
Unit cell dimensions	a = 15.193(19) Å	α= 90°.
	b = 10.827(14) Å	β= 127.77(6)°.
	c = 21.281(19) Å	γ = 90°.
Volume	2767(6) Å^3	
Z	4	
Density (calculated)	2.102 Mg/m^3	
Absorption coefficient	8.036 mm^{-1}	
F(000)	1680	
Crystal size	0.210 x 0.200 x 0.200 mm^3	
Theta range for data collection	1.696 to 27.877°.	
Index ranges	-19<=h<=19, -14<=k<=14, -27<=l<=21	
Reflections collected	25670	
Independent reflections	6597 [R(int) = 0.3783]	
Completeness to theta = 25.242°	100.0 %	
Absorption correction	Semi-empirical from equivalents	
Max. and min. transmission	1.0000 and 0.1564	
Refinement method	Full-matrix least-squares on F^2	
Data / restraints / parameters	6597 / 1 / 354	
Goodness-of-fit on F^2	0.789	
Final R indices [I>2sigma(I)]	R1 = 0.0887, wR2 = 0.1829	
R indices (all data)	R1 = 0.3359, wR2 = 0.2875	
Extinction coefficient	0.0041(5)	
Largest diff. peak and hole	1.022 and -1.109 e.Å^{-3}	

10.3.10 [Cu(2,9-dimethyl-1,10-phenanthroline)$_2$][Br] ·1.2 H_2O

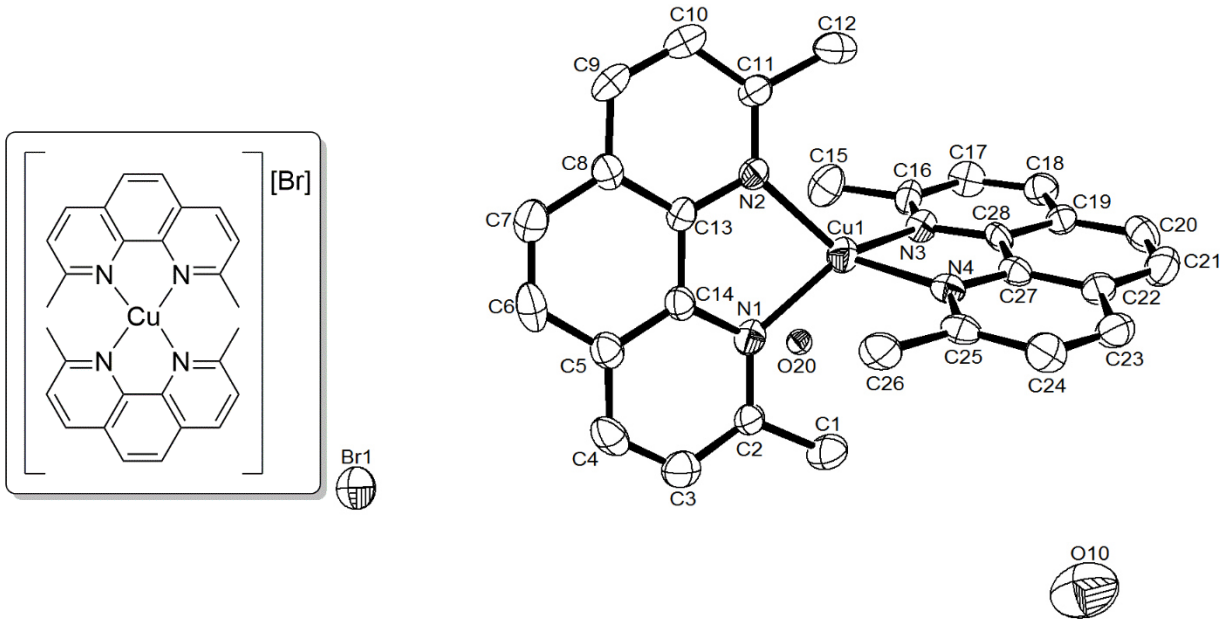

Figure 10-15: ORTEP plot of [Cu(2,9-dimethyl-1,10-phenanthroline)$_2$][Br] · 1.2 H_2O at 50 % probability level for thermal ellipsoids. (Hydrogens and water were omitted.)

Table 10-15: Crystal data and structure refinement for [Cu(2,9-dimethyl-1,10-phenanthroline)$_2$][Br] · 1.2 H_2O.

Identification code	s2738	
Empirical formula	C28 H26.40 Br Cu N4 O1.20	
Formula weight	581.58	
Temperature	130(2) K	
Wavelength	0.71073 Å	
Crystal system	Monoclinic	
Space group	P2(1)/c	
Unit cell dimensions	a = 13.798(5) Å	α= 90°.
	b = 17.724(7) Å	β= 90.190(9)°.
	c = 10.195(4) Å	γ = 90°.
Volume	2493.2(17) Å^3	
Z	4	
Density (calculated)	1.549 Mg/m^3	
Absorption coefficient	2.509 mm^{-1}	
F(000)	1184	
Crystal size	0.25 x 0.11 x 0.02 mm^3	
Theta range for data collection	1.48 to 27.88°.	
Index ranges	-18<=h<=18, -23<=k<=23, -12<=l<=13	
Reflections collected	23226	
Independent reflections	5961 [R(int) = 0.2237]	
Completeness to theta = 27.88°	99.9 %	
Absorption correction	Semi-empirical from equivalents	
Max. and min. transmission	0.9515 and 0.5728	
Refinement method	Full-matrix least-squares on F^2	
Data / restraints / parameters	5961 / 3 / 332	
Goodness-of-fit on F^2	0.768	
Final R indices [I>2sigma(I)]	R1 = 0.0617, wR2 = 0.0968	
R indices (all data)	R1 = 0.1915, wR2 = 0.1365	
Largest diff. peak and hole	0.670 and -0.738 e.Å^{-3}	

10.3.11 [Cu(2,9-dimethyl-1,10-phenanthroline)$_2$][Br]

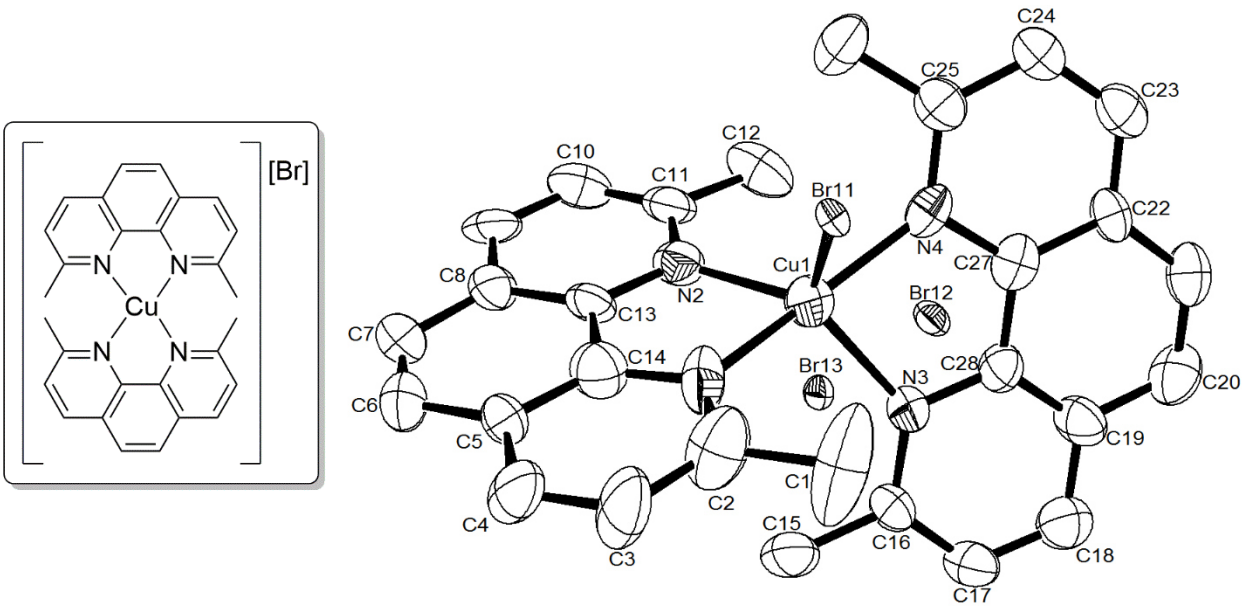

Figure 10-16: ORTEP plot of [Cu(2,9-dimethyl-1,10-phenanthroline)$_2$][Br] at 50 % probability level for thermal ellipsoids. (Hydrogens are omitted. The bromine atom is disordered over three positions.)

Remarks:

Due to the overlay of three different complex geometries is the copper center very anisotropic.

Table 10-16: Crystal data and structure refinement for [Cu(2,9-dimethyl-1,10-phenanthroline)$_2$][Br].

Identification code	s2805	
Empirical formula	C28 H24 Br Cu N4	
Formula weight	559.96	
Temperature	130(2) K	
Wavelength	0.71073 Å	
Crystal system	Monoclinic	
Space group	P 21/c	
Unit cell dimensions	a = 13.573(8) Å	α= 90°.
	b = 18.131(10) Å	β= 90.153(14)°.
	c = 10.050(6) Å	γ = 90°.
Volume	2473(2) Å^3	
Z	4	
Density (calculated)	1.504 Mg/m^3	
Absorption coefficient	2.522 mm^{-1}	
F(000)	1136	
Crystal size	0.210 x 0.170 x 0.050 mm^3	
Theta range for data collection	1.500 to 27.877°.	
Index ranges	-17<=h<=16, -23<=k<=23, -13<=l<=13	
Reflections collected	23131	
Independent reflections	5889 [R(int) = 0.3105]	
Completeness to theta = 25.242°	100.0 %	
Absorption correction	Semi-empirical from equivalents	
Max. and min. transmission	1.0000 and 0.0671	
Refinement method	Full-matrix least-squares on F^2	
Data / restraints / parameters	5889 / 1 / 333	
Goodness-of-fit on F^2	0.999	
Final R indices [I>2sigma(I)]	R1 = 0.0967, wR2 = 0.2037	
R indices (all data)	R1 = 0.2824, wR2 = 0.2625	
Extinction coefficient	0.0036(7)	
Largest diff. peak and hole	1.000 and -0.723 e.Å^{-3}	

10.3.12 [Cu(2,9-dimethyl-1,10-phenanthroline)$_2$][Br] · H_2O

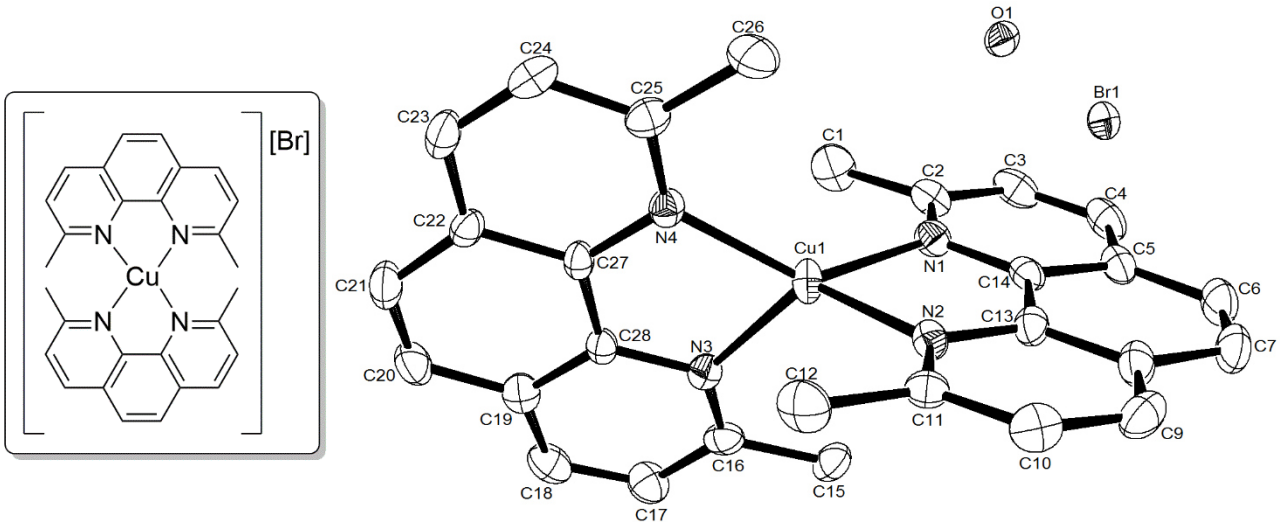

Figure 10-17: ORTEP plot of [Cu(2,9-dimethyl-1,10-phenanthroline)$_2$][Br] · H_2O at 50 % probability level for thermal ellipsoids. (Hydrogens were omitted.)

Table 10-17: Crystal data and structure refinement for [Cu(2,9-dimethyl-1,10-phenanthroline)$_2$][Br] · H_2O.

Identification code	s2867	
Empirical formula	C28 H26 Br Cu N4 O	
Formula weight	577.98	
Temperature	130(2) K	
Wavelength	0.71073 Å	
Crystal system	Monoclinic	
Space group	P 21/c	
Unit cell dimensions	a = 13.806(3) Å	α= 90°.
	b = 17.681(4) Å	β= 90.119(6)°.
	c = 10.194(2) Å	γ = 90°.
Volume	2488.4(10) $Å^3$	
Z	4	
Density (calculated)	1.543 Mg/m^3	
Absorption coefficient	2.512 mm^{-1}	
F(000)	1176	
Crystal size	0.430 x 0.150 x 0.130 mm^3	
Theta range for data collection	1.475 to 27.877°.	
Index ranges	-18<=h<=18, -23<=k<=22, -13<=l<=13	
Reflections collected	23473	
Independent reflections	5949 [R(int) = 0.0919]	
Completeness to theta = 25.242°	100.0 %	
Absorption correction	Semi-empirical from equivalents	
Max. and min. transmission	1.0000 and 0.6104	
Refinement method	Full-matrix least-squares on F^2	
Data / restraints / parameters	5949 / 3 / 328	
Goodness-of-fit on F^2	1.032	
Final R indices [I>2sigma(I)]	R1 = 0.0558, wR2 = 0.1084	
R indices (all data)	R1 = 0.0990, wR2 = 0.1263	
Extinction coefficient	n/a	
Largest diff. peak and hole	0.772 and -0.594 e.$Å^{-3}$	

10.3.13 [Cu(2,9-dimethyl-1,10-phenanthroline)(Br)]

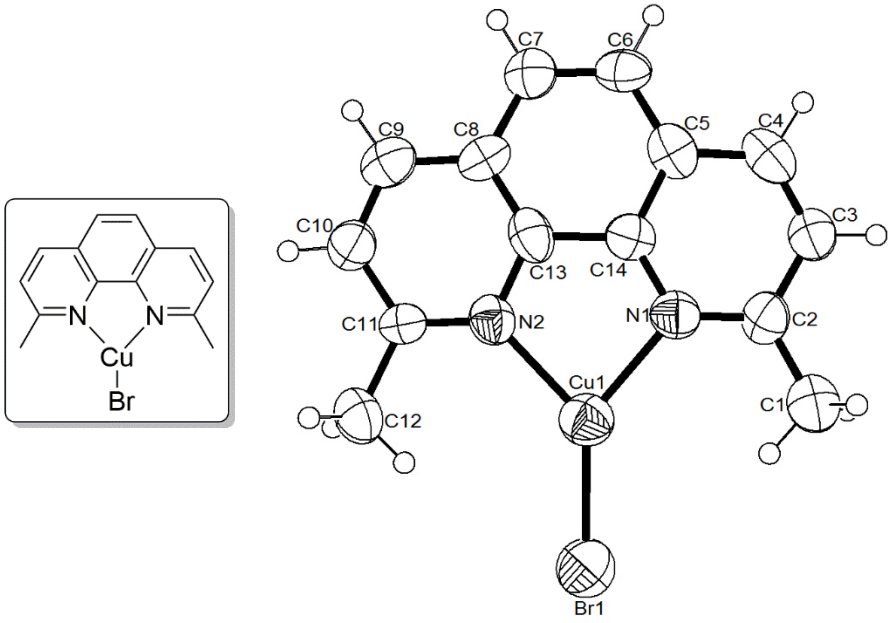

Figure 10-18: ORTEP plot of [Cu(2,9-dimethyl-1,10-phenanthroline)(Br)] at 50 % probability level for thermal ellipsoids.

Table 10-18: Crystal data and structure refinement for [Cu(2,9-dimethyl-1,10-phenanthroline)(Br)].

Identification code	s2804	
Empirical formula	C14 H12 Br Cu N2	
Formula weight	351.71	
Temperature	130(2) K	
Wavelength	0.71073 Å	
Crystal system	Monoclinic	
Space group	P 21/n	
Unit cell dimensions	a = 6.614(6) Å	α= 90°.
	b = 18.359(17) Å	β= 95.75(2)°.
	c = 10.186(10) Å	γ = 90°.
Volume	1231(2) $Å^3$	
Z	4	
Density (calculated)	1.898 Mg/m^3	
Absorption coefficient	5.002 mm^{-1}	
F(000)	696	
Crystal size	0.450 x 0.200 x 0.140 mm^3	
Theta range for data collection	2.219 to 27.873°.	
Index ranges	-8<=h<=8, -24<=k<=21, -13<=l<=13	
Reflections collected	11501	
Independent reflections	2925 [R(int) = 0.2429]	
Completeness to theta = 25.242°	100.0 %	
Absorption correction	Semi-empirical from equivalents	
Max. and min. transmission	1.0000 and 0.4616	
Refinement method	Full-matrix least-squares on F^2	
Data / restraints / parameters	2925 / 0 / 166	
Goodness-of-fit on F^2	0.888	
Final R indices [I>2sigma(I)]	R1 = 0.0981, wR2 = 0.2100	
R indices (all data)	R1 = 0.2464, wR2 = 0.2880	
Extinction coefficient	0.009(2)	
Largest diff. peak and hole	1.103 and -0.958 $e.Å^{-3}$	

10.3.14 [Cu_2(μ-Br)$_2$(2,9-dimethyl-1,10-phenanthroline)$_2$]

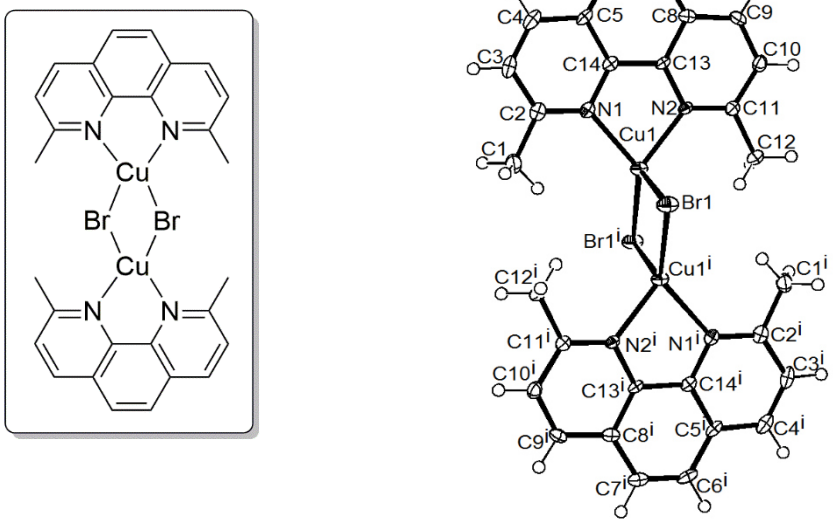

Figure 10-19: ORTEP plot of [Cu_2(μ-Br)$_2$(2,9-dimethyl-1,10-phenanthroline)$_2$] at 50 % probability level for thermal ellipsoids.

Table 10-19: Crystal data and structure refinement for [Cu_2(μ-Br)$_2$(2,9-dimethyl-1,10-phenanthroline)$_2$].

Identification code	s2806	
Empirical formula	C28 H24 Br2 Cu2 N4	
Formula weight	703.41	
Temperature	130(2) K	
Wavelength	0.71073 Å	
Crystal system	Monoclinic	
Space group	C 2/c	
Unit cell dimensions	a = 18.403(3) Å	α= 90°.
	b = 8.2921(16) Å	β= 110.173(4)°.
	c = 17.231(3) Å	γ = 90°.
Volume	2468.1(8) $Å^3$	
Z	4	
Density (calculated)	1.893 Mg/m^3	
Absorption coefficient	4.988 mm^{-1}	
F(000)	1392	
Crystal size	0.210 x 0.200 x 0.180 mm^3	
Theta range for data collection	2.358 to 27.868°.	
Index ranges	-22<=h<=24, -10<=k<=10, -22<=l<=22	
Reflections collected	11486	
Independent reflections	2948 [R(int) = 0.0500]	
Completeness to theta = 25.242°	100.0 %	
Absorption correction	Semi-empirical from equivalents	
Max. and min. transmission	1.0000 and 0.5984	
Refinement method	Full-matrix least-squares on F^2	
Data / restraints / parameters	2948 / 0 / 165	
Goodness-of-fit on F^2	1.076	
Final R indices [I>2sigma(I)]	R1 = 0.0414, wR2 = 0.0991	
R indices (all data)	R1 = 0.0562, wR2 = 0.1076	
Extinction coefficient	n/a	
Largest diff. peak and hole	0.817 and -0.591 e.$Å^{-3}$	

10.3.15 [Cu(2,9-dimethyl-1,10-phenanthroline)$_2$][CF_3SO_3]

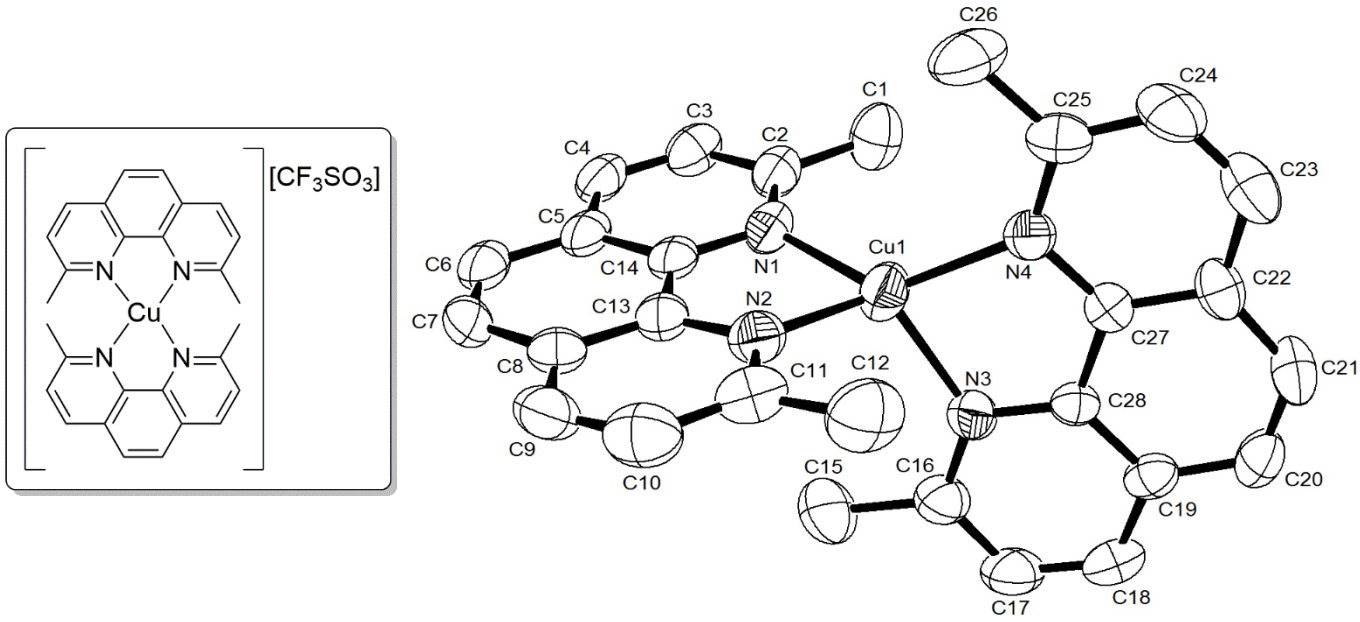

Figure 10-20: ORTEP plot of [Cu(2,9-dimethyl-1,10-phenanthroline)$_2$][CF_3SO_3] at 50 % probability level for thermal ellipsoids. (Hydrogens and anion are omitted.)

Remarks:

The triflate anion is strongly disordered and therefore treated with Squeeze.

Table 10-20: Crystal data and structure refinement for [Cu(2,9-dimethyl-1,10-phenanthroline)$_2$][CF_3SO_3].

Identification code	s2803s	
Empirical formula	C29 H24 Cu F3 N4 O3 S	
Formula weight	629.12	
Temperature	130(2) K	
Wavelength	0.71073 Å	
Crystal system	Monoclinic	
Space group	P 21/n	
Unit cell dimensions	a = 13.5010(16) Å	α= 90°.
	b = 11.0256(13) Å	β= 95.945(3)°.
	c = 18.272(2) Å	γ = 90°.
Volume	2705.3(6) $Å^3$	
Z	4	
Density (calculated)	1.545 Mg/m^3	
Absorption coefficient	0.945 mm^{-1}	
F(000)	1288	
Crystal size	0.490 x 0.260 x 0.200 mm^3	
Theta range for data collection	1.790 to 27.875°.	
Index ranges	-14<=h<=17, -14<=k<=14, -24<=l<=22	
Reflections collected	20661	
Independent reflections	6439 [R(int) = 0.0622]	
Completeness to theta = 25.242°	100.0 %	
Absorption correction	Semi-empirical from equivalents	
Max. and min. transmission	1.0000 and 0.3703	
Refinement method	Full-matrix least-squares on F^2	
Data / restraints / parameters	6439 / 0 / 302	
Goodness-of-fit on F^2	0.931	
Final R indices [I>2sigma(I)]	R1 = 0.0712, wR2 = 0.1669	
R indices (all data)	R1 = 0.1226, wR2 = 0.1911	
Extinction coefficient	n/a	
Largest diff. peak and hole	0.670 and -0.267 $e.Å^{-3}$	

10.3.16 [Cu(DAPy-Ts)MeCN][BF_4]

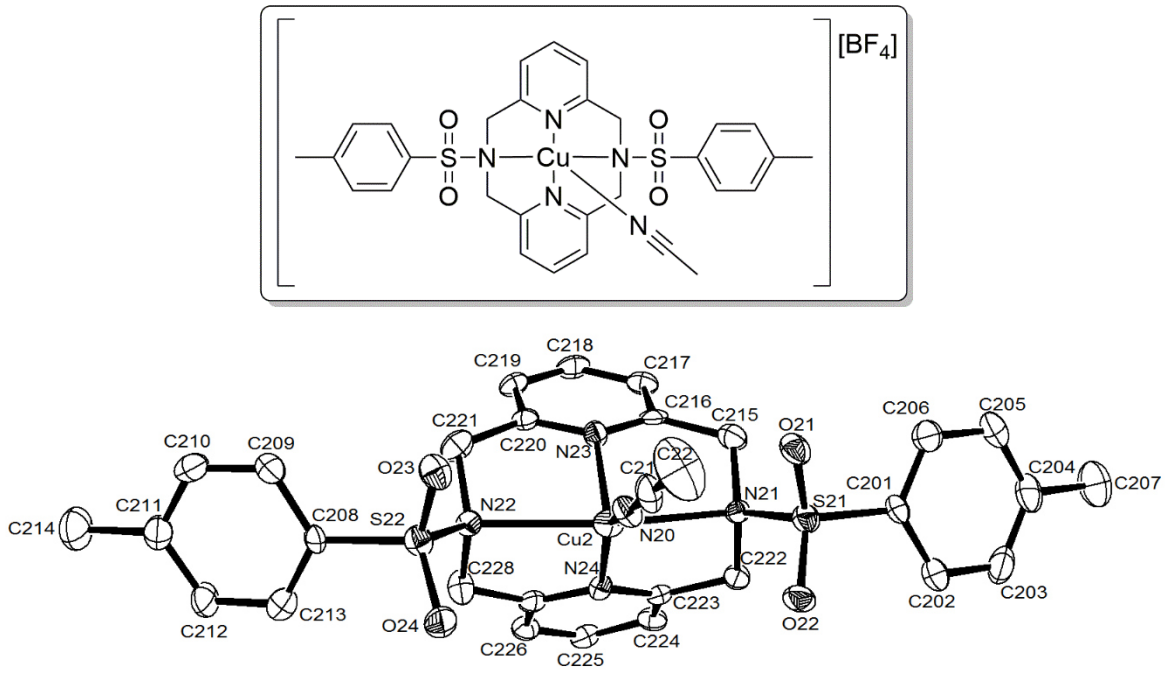

Figure 10-21: [Cu(DAPy-Ts)MeCN][BF_4] at 50 % probability level for thermal ellipsoids. (One DCM and 0.5 diethyl ether molecules was as well omitted for clarity as the tetrafluoroborate anion.).

Remarks:

One DCM and 0.5 diethyl ether are correlated with one cation/anion unit. The asymmetric unit consists of two stoichiometric units of the before mentioned system. One DCM molecule is disordered over two locations with a 53:47 ratio.

Table 10-21: Crystal data and structure refinement for [Cu(DAPy-Ts)MeCN][BF_4].

Identification code	h2551	
Empirical formula	C33 H38 B Cl2 Cu F4 N5 O4.50 S2	
Formula weight	862.05	
Temperature	130(2) K	
Wavelength	0.71073 Å	
Crystal system	Monoclinic	
Space group	P2(1)/n	
Unit cell dimensions	a = 27.550(4) Å	α= 90°.
	b = 8.8478(12) Å	β= 105.859(3)°.
	c = 30.709(4) Å	γ = 90°.
Volume	7200.5(17) $Å^3$	
Z	8	
Density (calculated)	1.590 Mg/m^3	
Absorption coefficient	0.940 mm^{-1}	
F(000)	3544	
Crystal size	0.47 x 0.10 x 0.08 mm^3	
Theta range for data collection	1.38 to 27.88°.	
Index ranges	-36<=h<=36, -11<=k<=11, -37<=l<=40	
Reflections collected	66675	
Independent reflections	17171 [R(int) = 0.1451]	
Completeness to theta = 27.88°	99.9 %	
Absorption correction	Semi-empirical from equivalents	
Max. and min. transmission	0.9286 and 0.6664	
Refinement method	Full-matrix least-squares on F^2	
Data / restraints / parameters	17171 / 6 / 926	
Goodness-of-fit on F^2	0.648	
Final R indices [I>2sigma(I)]	R1 = 0.0527, wR2 = 0.0734	
R indices (all data)	R1 = 0.1623, wR2 = 0.0903	
Largest diff. peak and hole	0.975 and -1.002 e.$Å^{-3}$	

10.4 Crystal structures of copper(II) phenanthroline complexes

10.4.1 [Cu(bpy)(Cl)$_2$]

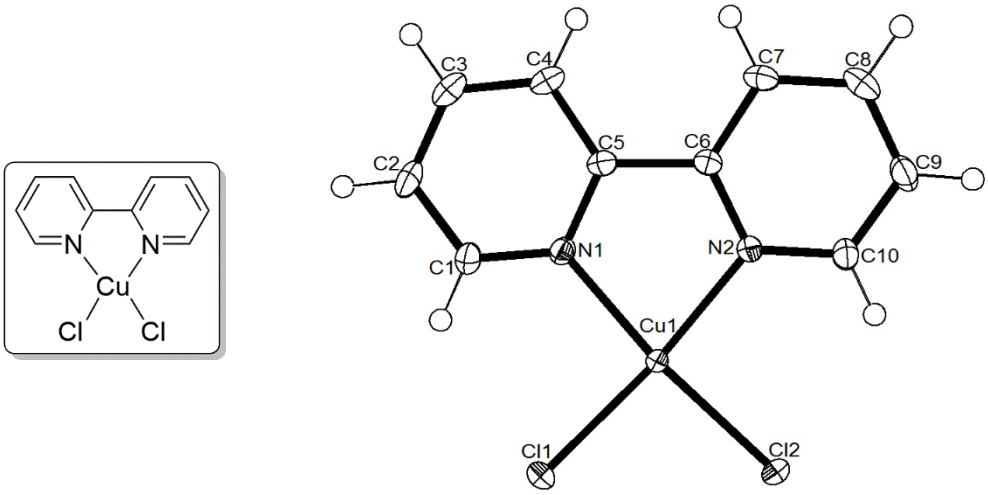

Figure 10-22: ORTEP plot of [Cu(bpy)(Cl)$_2$] at 50 % probability level for thermal ellipsoids.

Table 10-22: Crystal data and structure refinement for [Cu(bpy)(Cl)$_2$].

Identification code	s2871	
Empirical formula	C10 H8 Cl2 Cu N2	
Formula weight	290.62	
Temperature	130(2) K	
Wavelength	0.71073 Å	
Crystal system	Triclinic	
Space group	P -1	
Unit cell dimensions	a = 7.1893(11) Å	α= 114.898(2)°.
	b = 8.9674(13) Å	β= 106.821(3)°.
	c = 9.4009(14) Å	γ = 96.223(3)°.
Volume	507.38(13) Å^3	
Z	2	
Density (calculated)	1.902 Mg/m^3	
Absorption coefficient	2.639 mm^{-1}	
F(000)	290	
Crystal size	0.420 x 0.370 x 0.210 mm^3	
Theta range for data collection	2.573 to 27.876°.	
Index ranges	-9<=h<=9, -11<=k<=11, -12<=l<=12	
Reflections collected	4800	
Independent reflections	2405 [R(int) = 0.0194]	
Completeness to theta = 25.242°	99.5 %	
Absorption correction	Semi-empirical from equivalents	
Max. and min. transmission	1.0000 and 0.6104	
Refinement method	Full-matrix least-squares on F^2	
Data / restraints / parameters	2405 / 0 / 136	
Goodness-of-fit on F^2	1.069	
Final R indices [I>2sigma(I)]	R1 = 0.0344, wR2 = 0.0907	
R indices (all data)	R1 = 0.0359, wR2 = 0.0919	
Extinction coefficient	n/a	
Largest diff. peak and hole	0.960 and -0.744 e.Å^{-3}	

10.4.2 $[Cu(bpy)_2(Cl)][Cl] \cdot MeOH \cdot Et_2O$

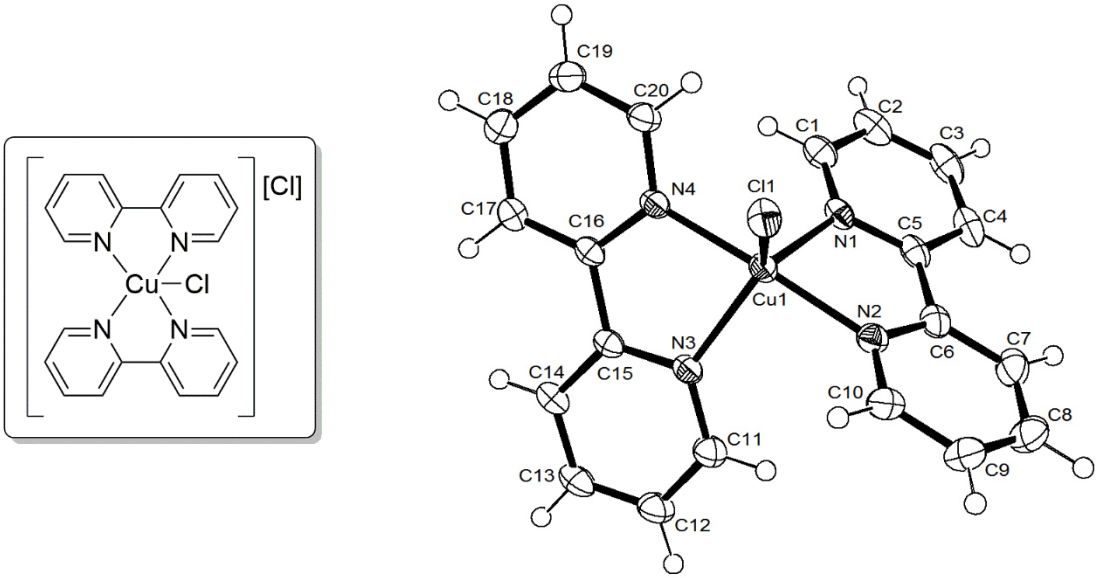

Figure 10-23: ORTEP plot of $[Cu(bpy)_2(Cl)][Cl] \cdot MeOH \cdot Et_2O$ at 50 % probability level for thermal ellipsoids. (One MeOH and one Et_2O molecule were omitted.)

Remarks: Et_2O was treated with SQUEEZE.

Table 10-23: Crystal data and structure refinement for $[Cu(bpy)_2(Cl)][Cl]$.

Identification code	s2875	
Empirical formula	C25 H30 Cl2 Cu N4 O2	
Formula weight	552.97	
Temperature	130(2) K	
Wavelength	0.71073 Å	
Crystal system	Triclinic	
Space group	P -1	
Unit cell dimensions	a = 8.0803(9) Å	α= 75.903(2)°.
	b = 11.7409(13) Å	β= 81.562(2)°.
	c = 12.7508(14) Å	γ = 77.764(2)°.
Volume	1140.8(2) $Å^3$	
Z	2	
Density (calculated)	1.610 Mg/m^3	
Absorption coefficient	1.225 mm^{-1}	
F(000)	574	
Crystal size	0.470 x 0.440 x 0.390 mm^3	
Theta range for data collection	1.655 to 27.877°.	
Index ranges	-10<=h<=10, -15<=k<=15, -16<=l<=16	
Reflections collected	10760	
Independent reflections	5423 [R(int) = 0.0213]	
Completeness to theta = 25.242°	100.0 %	
Absorption correction	Semi-empirical from equivalents	
Max. and min. transmission	1.0000 and 0.6783	
Refinement method	Full-matrix least-squares on F^2	
Data / restraints / parameters	5423 / 0 / 264	
Goodness-of-fit on F^2	1.059	
Final R indices [I>2sigma(I)]	R1 = 0.0385, wR2 = 0.0964	
R indices (all data)	R1 = 0.0451, wR2 = 0.1003	
Extinction coefficient	n/a	
Largest diff. peak and hole	1.067 and -0.497 $e.Å^{-3}$	

10.4.3 [Cu$_2$-bis(μ-OH)(bpy)$_2$(Cl)]$_2$[Cl]$_2$

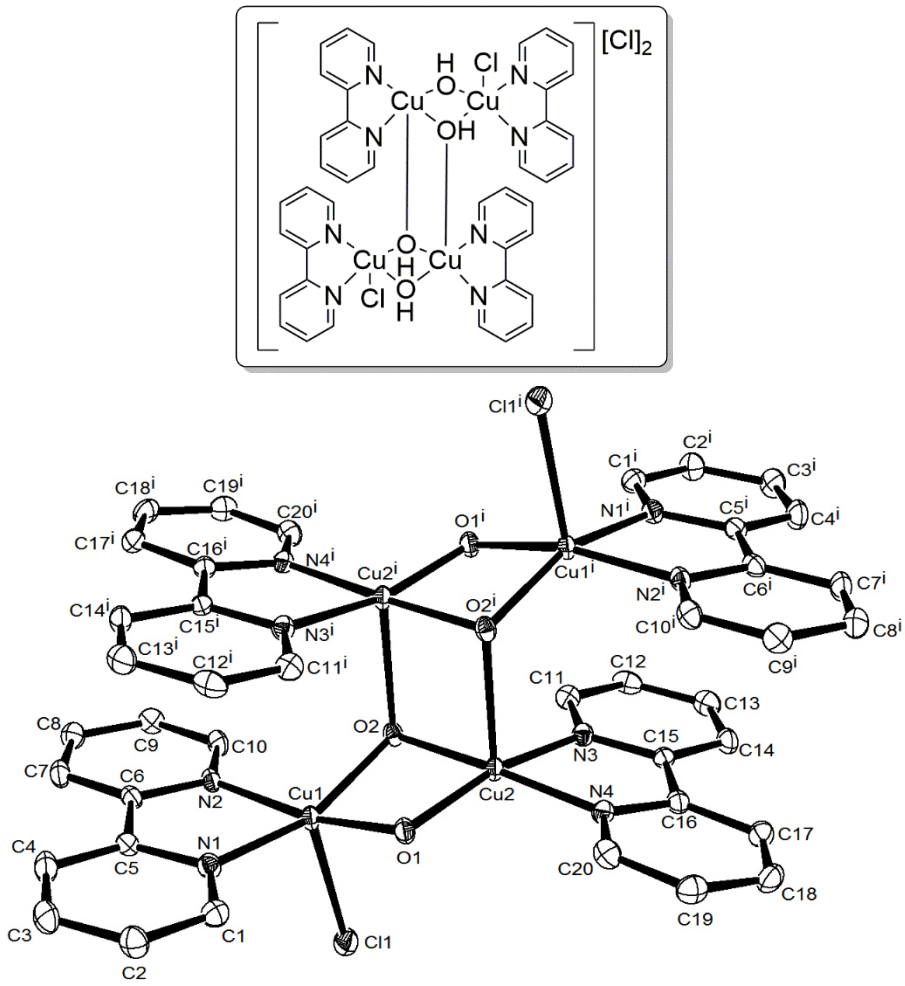

Figure 10-24: ORTEP plot of [Cu$_2$-bis(μ-OH)(bpy)$_2$(Cl)]$_2$[Cl]$_2$ at 50 % probability level for thermal ellipsoids. (Hydrogens, six water molecules and two anions are omitted.)

Table 10-24: Crystal data and structure refinement for $[Cu_2\text{-bis}(\mu\text{-OH})(bpy)_2(Cl)]_2[Cl]_2$.

Identification code	s2929	
Empirical formula	C40 H48 Cl4 Cu4 N8 O10	
Formula weight	1196.82	
Temperature	130(2) K	
Wavelength	0.71073 Å	
Crystal system	Triclinic	
Space group	P -1	
Unit cell dimensions	a = 9.1228(17) Å	α= 85.898(4)°.
	b = 10.293(2) Å	β= 75.512(4)°.
	c = 12.912(3) Å	γ = 73.174(4)°.
Volume	1123.6(4) $Å^3$	
Z	1	
Density (calculated)	1.769 Mg/m^3	
Absorption coefficient	2.172 mm^{-1}	
F(000)	608	
Crystal size	0.330 x 0.110 x 0.100 mm^3	
Theta range for data collection	1.629 to 27.877°.	
Index ranges	-12<=h<=11, -13<=k<=11, -16<=l<=16	
Reflections collected	10702	
Independent reflections	5317 [R(int) = 0.0296]	
Completeness to theta = 25.242°	100.0 %	
Absorption correction	Semi-empirical from equivalents	
Max. and min. transmission	1.0000 and 0.5981	
Refinement method	Full-matrix least-squares on F^2	
Data / restraints / parameters	5317 / 11 / 330	
Goodness-of-fit on F^2	1.027	
Final R indices [I>2sigma(I)]	R1 = 0.0364, wR2 = 0.0815	
R indices (all data)	R1 = 0.0483, wR2 = 0.0883	
Extinction coefficient	n/a	
Largest diff. peak and hole	0.575 and -0.416 $e.Å^{-3}$	

10.4.4 $[(Cu(bpy)_2O)_3\text{-}C][BF_4]_4 \cdot 5.5\ H_2O$

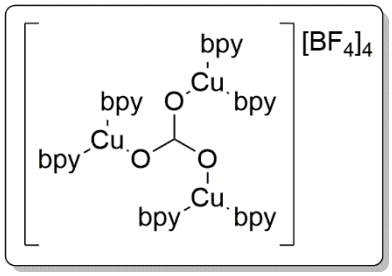

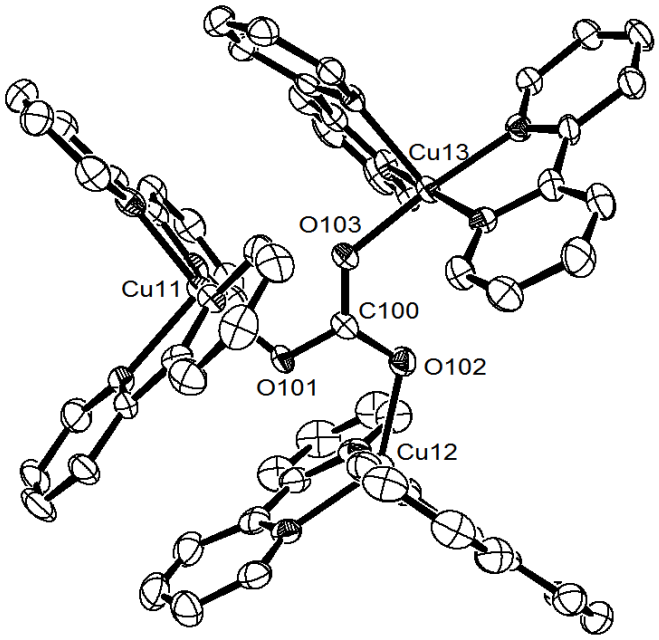

Figure 10-25: ORTEP plot of $[(Cu(bpy)_2O)_3\text{-}C][BF_4]_4 \cdot 5.5\ H_2O$ at 50 % probability level for thermal ellipsoids. (Hydrogens, 5.5 water molecules and four anions are omitted.)

Remarks:

Two full complexes in the asymmetric unit.

Table 10-25: Crystal data and structure refinement for $[(Cu(bpy)_2O)_3\text{-}C][BF_4]_4 \cdot 5.5\ H_2O$.

Identification code	s2900	
Empirical formula	C66 H57 B4 Cu3 F16 N13 O5.50	
Formula weight	1658.10	
Temperature	130(2) K	
Wavelength	0.71073 Å	
Crystal system	Triclinic	
Space group	P -1	
Unit cell dimensions	a = 12.7631(18) Å	α= 93.202(3)°.
	b = 23.431(3) Å	β= 90.442(3)°.
	c = 23.954(3) Å	γ = 104.957(3)°.
Volume	6908.2(16) $Å^3$	
Z	4	
Density (calculated)	1.594 Mg/m^3	
Absorption coefficient	1.020 mm^{-1}	
F(000)	3356	
Crystal size	0.450 x 0.370 x 0.200 mm^3	
Theta range for data collection	0.852 to 27.877°.	
Index ranges	-16<=h<=16, -30<=k<=30, -31<=l<=27	
Reflections collected	65690	
Independent reflections	32785 [R(int) = 0.0856]	
Completeness to theta = 25.242°	100.0 %	
Absorption correction	Semi-empirical from equivalents	
Max. and min. transmission	1.0000 and 0.4855	
Refinement method	Full-matrix least-squares on F^2	
Data / restraints / parameters	32785 / 0 / 1983	
Goodness-of-fit on F^2	0.991	
Final R indices [I>2sigma(I)]	R1 = 0.0794, wR2 = 0.1522	
R indices (all data)	R1 = 0.1707, wR2 = 0.1947	
Extinction coefficient	n/a	
Largest diff. peak and hole	1.181 and -0.706 $e.Å^{-3}$	

10.4.5 [Cu_2-bis(μ-SO_4)(bpy)$_2$(MeOH)$_2$]

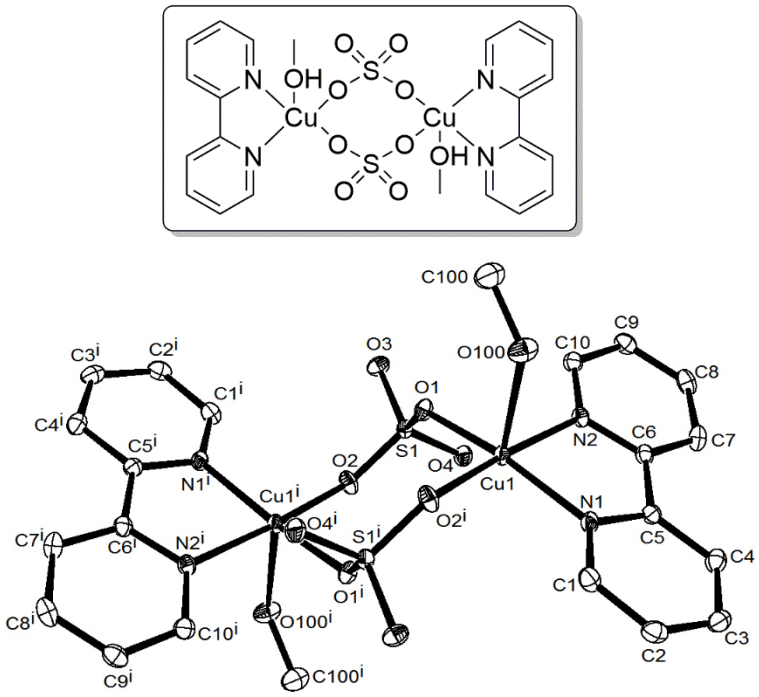

Figure 10-26: ORTEP plot of [Cu_2-bis(μ-SO_4)(bpy)$_2$(MeOH)$_2$] at 50 % probability level for thermal ellipsoids. (Hydrogens are omitted.)

Table 10-26: Crystal data and structure refinement for [Cu_2-bis(μ-SO_4)($bpy)_2$($MeOH)_2$].

Identification code	s2931	
Empirical formula	C22 H24 Cu2 N4 O10 S2	
Formula weight	695.65	
Temperature	130(2) K	
Wavelength	0.71073 Å	
Crystal system	Triclinic	
Space group	P -1	
Unit cell dimensions	a = 7.8823(12) Å	α= 76.534(3)°.
	b = 8.8184(13) Å	β= 83.615(3)°.
	c = 9.9123(15) Å	γ = 64.416(3)°.
Volume	604.31(16) $Å^3$	
Z	1	
Density (calculated)	1.912 Mg/m^3	
Absorption coefficient	2.002 mm^{-1}	
F(000)	354	
Crystal size	0.430 x 0.240 x 0.210 mm^3	
Theta range for data collection	2.113 to 27.875°.	
Index ranges	-10<=h<=10, -11<=k<=10, -13<=l<=13	
Reflections collected	5750	
Independent reflections	2877 [R(int) = 0.0220]	
Completeness to theta = 25.242°	100.0 %	
Absorption correction	Semi-empirical from equivalents	
Max. and min. transmission	1.0000 and 0.7147	
Refinement method	Full-matrix least-squares on F^2	
Data / restraints / parameters	2877 / 1 / 186	
Goodness-of-fit on F^2	1.052	
Final R indices [I>2sigma(I)]	R1 = 0.0314, wR2 = 0.0762	
R indices (all data)	R1 = 0.0358, wR2 = 0.0798	
Extinction coefficient	n/a	
Largest diff. peak and hole	0.589 and -0.366 e.$Å^{-3}$	

10.4.6 [Cu(DMP)(Cl_2)(H_2O)]

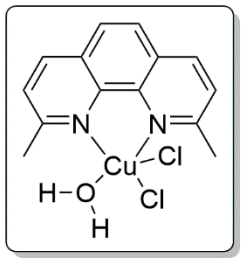

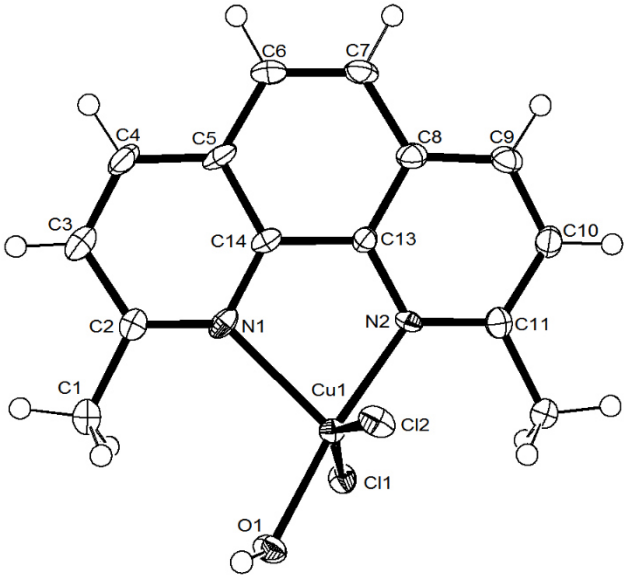

Figure 10-27: ORTEP plot of [Cu(DMP)$_2$(Cl)$_2$(H_2O)] at 50 % probability level for thermal ellipsoids.

Remarks: The second hydrogen atom of water could not be determined.

Table 10-27: Crystal data and structure refinement for [Cu(DMP)(Cl_2)(H_2O)].

Identification code	s2894	
Empirical formula	C14 H14 Cl2 Cu N2 O	
Formula weight	360.71	
Temperature	130(2) K	
Wavelength	0.71073 Å	
Crystal system	Monoclinic	
Space group	P 21	
Unit cell dimensions	a = 9.443(3) Å	α= 90°.
	b = 8.082(2) Å	β= 105.252(5)°.
	c = 9.813(3) Å	γ = 90°.
Volume	722.6(4) $Å^3$	
Z	2	
Density (calculated)	1.658 Mg/m^3	
Absorption coefficient	1.876 mm^{-1}	
F(000)	366	
Crystal size	0.350 x 0.270 x 0.220 mm^3	
Theta range for data collection	2.151 to 27.870°.	
Index ranges	-12<=h<=12, -10<=k<=10, -12<=l<=12	
Reflections collected	5791	
Independent reflections	3315 [R(int) = 0.0654]	
Completeness to theta = 25.242°	99.1 %	
Absorption correction	Semi-empirical from equivalents	
Max. and min. transmission	1.0000 and 0.3874	
Refinement method	Full-matrix least-squares on F^2	
Data / restraints / parameters	3315 / 2 / 187	
Goodness-of-fit on F^2	1.073	
Final R indices [I>2sigma(I)]	R1 = 0.0586, wR2 = 0.1618	
R indices (all data)	R1 = 0.0684, wR2 = 0.1750	
Absolute structure parameter	0.03(3)	
Extinction coefficient	n/a	
Largest diff. peak and hole	1.358 and -1.023 e.$Å^{-3}$	

10.4.7 [Cu(2,9-dimethyl-1,10-phenanthroline)$_2$][BF$_4$]$_2$ · 0.5 MeOH

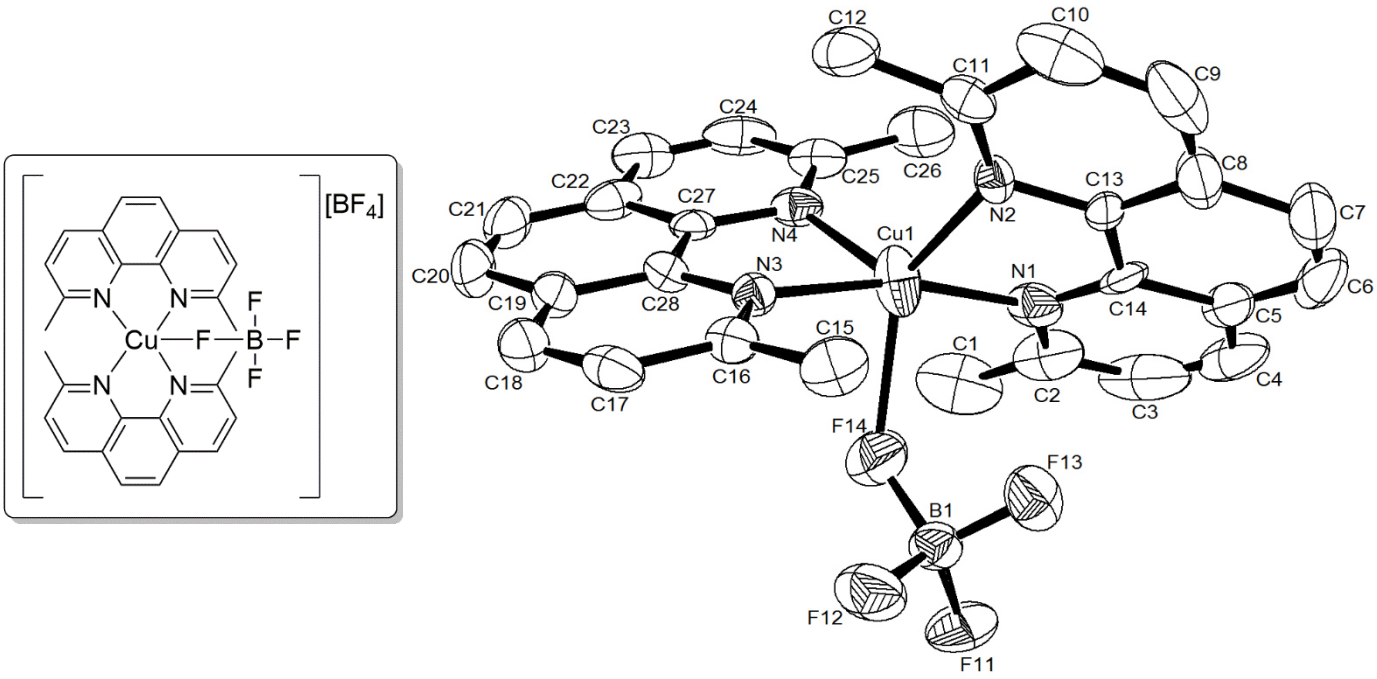

Figure 10-28: ORTEP plot of [Cu(2,9-dimethyl-1,10-phenanthroline)$_2$][BF$_4$]$_2$ · 0.5 MeOH at 50 % probability level for thermal ellipsoids. (Hydrogens, one anion and 0.5 MeOH were omitted.)

Remarks:

One anion and 0.5 MeOH per formula unit were treated with Squeeze due to strong disorder.

Table 10-28: Crystal data and structure refinement for [Cu(2,9-dimethyl-1,10-phenanthroline)$_2$][BF_4]$_2$ · 0.5 MeOH.

Identification code	s2813	
Empirical formula	C30 H29 B2 Cu F8 N4 O0.50	
Formula weight	690.73	
Temperature	130(2) K	
Wavelength	0.71073 Å	
Crystal system	Monoclinic	
Space group	P 21/n	
Unit cell dimensions	a = 17.003(6) Å	α= 90°.
	b = 10.643(3) Å	β= 108.620(9)°.
	c = 17.359(5) Å	γ = 90°.
Volume	2976.8(16) Å^3	
Z	4	
Density (calculated)	1.541 Mg/m^3	
Absorption coefficient	0.815 mm^{-1}	
F(000)	1408	
Crystal size	0.260 x 0.120 x 0.050 mm^3	
Theta range for data collection	1.460 to 27.877°.	
Index ranges	-22<=h<=22, -14<=k<=14, -19<=l<=22	
Reflections collected	27621	
Independent reflections	7101 [R(int) = 0.1200]	
Completeness to theta = 25.242°	100.0 %	
Absorption correction	Semi-empirical from equivalents	
Max. and min. transmission	1.0000 and 0.2412	
Refinement method	Full-matrix least-squares on F^2	
Data / restraints / parameters	7101 / 0 / 347	
Goodness-of-fit on F^2	0.920	
Final R indices [I>2sigma(I)]	R1 = 0.0819, wR2 = 0.1801	
R indices (all data)	R1 = 0.1654, wR2 = 0.2135	
Extinction coefficient	n/a	
Largest diff. peak and hole	1.272 and -1.050 e.Å^{-3}	

10.4.8 [Cu(2,9-dimethyl-1,10-phenanthroline)$_2$][BF$_4$]$_2$ · 0.5 Et$_2$O

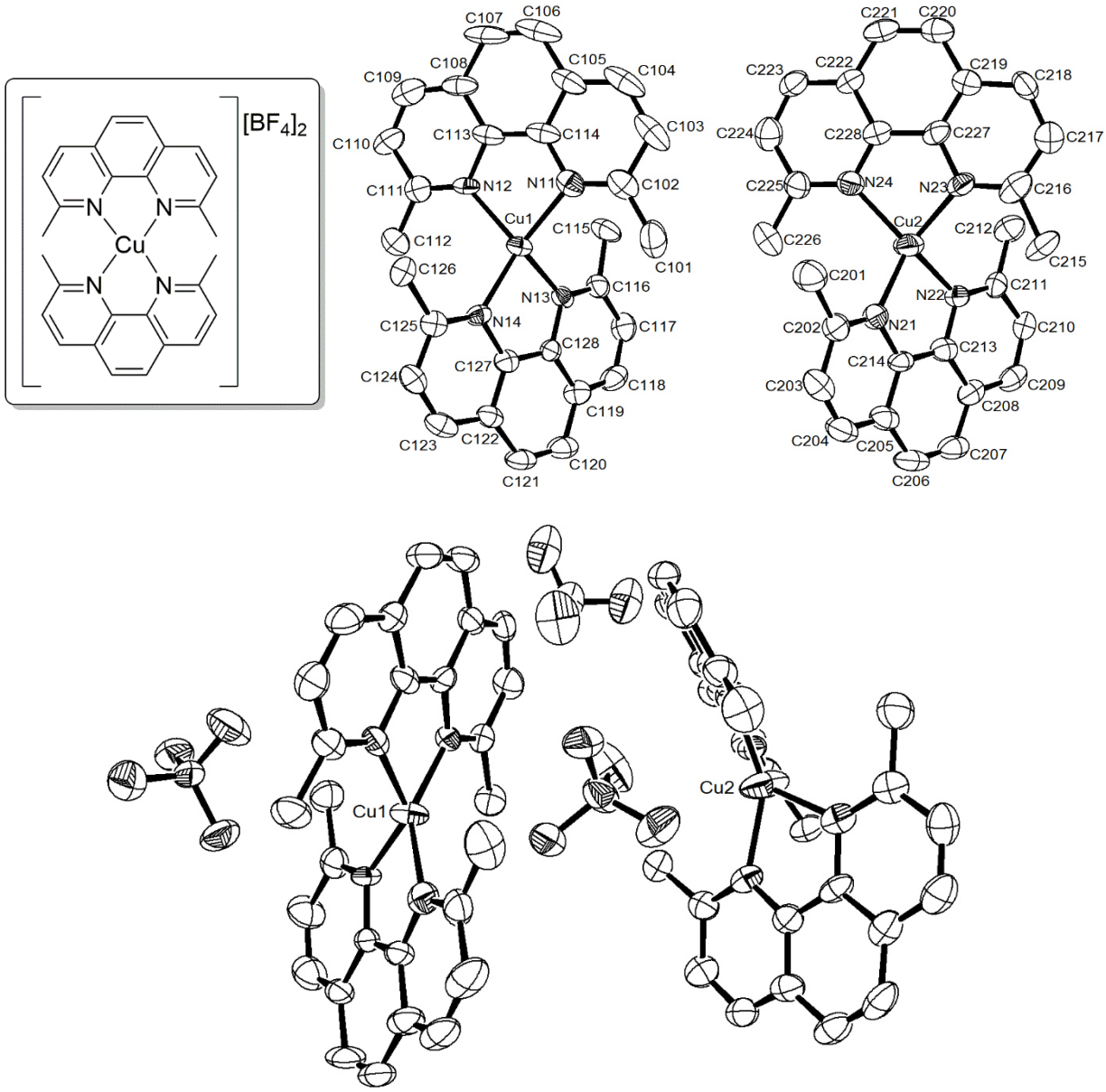

Figure 10-29: ORTEP plots of [Cu(2,9-dimethyl-1,10-phenanthroline)$_2$][BF$_4$]$_2$ · 0.5 Et$_2$O at 50 % probability level for thermal ellipsoids. (Hydrogens, anions and 0.5 Et$_2$O were omitted in the top left plots.)

Remarks:

Two formula unit per asymmetric unit. One diethyl ether molecule and anions were treated with Squeeze.

Table 10-29: Crystal data and structure refinement for [Cu(2,9-dimethyl-1,10-phenanthroline)$_2$][BF_4]$_2$ · 0.5 Et_2O.

Identification code	s2811	
Empirical formula	C30 H29 B2 Cu F8 N4 O0.50	
Formula weight	690.73	
Temperature	130(2) K	
Wavelength	0.71073 Å	
Crystal system	Monoclinic	
Space group	P 21/m	
Unit cell dimensions	a = 15.827(4) Å	α= 90°.
	b = 22.174(6) Å	β= 105.112(7)°.
	c = 18.176(5) Å	γ = 90°.
Volume	6158(3) $Å^3$	
Z	8	
Density (calculated)	1.490 Mg/m^3	
Absorption coefficient	0.788 mm^{-1}	
F(000)	2816	
Crystal size	0.370 x 0.220 x 0.170 mm^3	
Theta range for data collection	1.333 to 27.877°.	
Index ranges	-20<=h<=20, -29<=k<=27, -23<=l<=23	
Reflections collected	58916	
Independent reflections	15031 [R(int) = 0.1410]	
Completeness to theta = 25.242°	100.0 %	
Absorption correction	Semi-empirical from equivalents	
Max. and min. transmission	1.0000 and 0.2398	
Refinement method	Full-matrix least-squares on F^2	
Data / restraints / parameters	15031 / 0 / 720	
Goodness-of-fit on F^2	0.824	
Final R indices [I>2sigma(I)]	R1 = 0.0746, wR2 = 0.1515	
R indices (all data)	R1 = 0.1943, wR2 = 0.1911	
Extinction coefficient	n/a	
Largest diff. peak and hole	1.385 and -1.317 e.$Å^{-3}$	

10.4.9 [Cu(2,9-dimethyl-1,10-phenanthroline)$_2$(BF$_4$)][BF$_4$] · 0.25 Et$_2$O

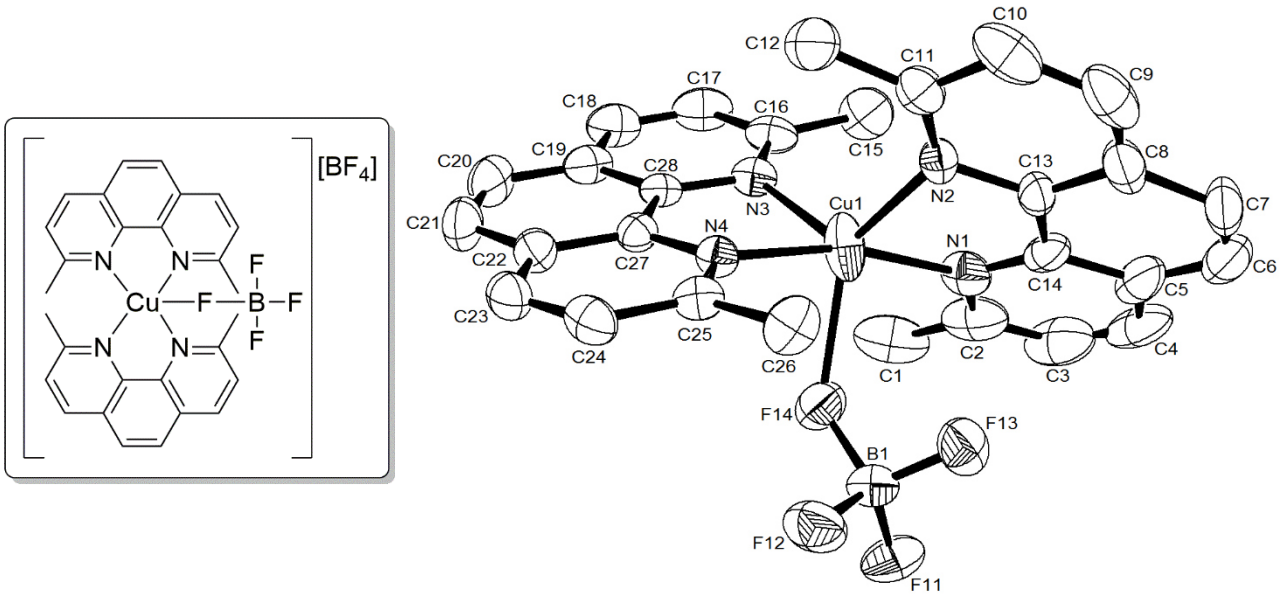

Figure 10-30: ORTEP plot of [Cu(2,9-dimethyl-1,10-phenanthroline)$_2$(BF$_4$)][BF$_4$] · 0.25 Et$_2$O at 50 % probability level for thermal ellipsoids. (Hydrogens, one anion and 0.25 Et$_2$O were omitted.)

Remarks:

The structure shows a large residue electron density. Additionally Et$_2$O is disordered.

Table 10-30: Crystal data and structure refinement for [Cu(2,9-dimethyl-1,10-phenanthroline)$_2$(BF$_4$)][BF$_4$] · 0.25 Et$_2$O.

Identification code	s2824	
Empirical formula	C29 H26.50 B2 Cu F8 N4 O0.25	
Formula weight	672.20	
Temperature	130(2) K	
Wavelength	0.71073 Å	
Crystal system	Monoclinic	
Space group	P 21/n	
Unit cell dimensions	a = 17.028(2) Å	α= 90°.
	b = 10.6692(14) Å	β= 108.645(3)°.
	c = 17.405(2) Å	γ = 90°.
Volume	2996.0(7) Å^3	
Z	4	
Density (calculated)	1.490 Mg/m^3	
Absorption coefficient	0.807 mm^{-1}	
F(000)	1366	
Crystal size	0.480 x 0.360 x 0.290 mm^3	
Theta range for data collection	1.456 to 27.874°.	
Index ranges	-22<=h<=22, -14<=k<=14, -22<=l<=22	
Reflections collected	27827	
Independent reflections	7140 [R(int) = 0.0651]	
Completeness to theta = 25.242°	100.0 %	
Absorption correction	Semi-empirical from equivalents	
Max. and min. transmission	1.0000 and 0.8111	
Refinement method	Full-matrix least-squares on F^2	
Data / restraints / parameters	7140 / 0 / 421	
Goodness-of-fit on F^2	2.218	
Final R indices [I>2sigma(I)]	R1 = 0.1150, wR2 = 0.3231	
R indices (all data)	R1 = 0.1328, wR2 = 0.3372	
Extinction coefficient	n/a	
Largest diff. peak and hole	3.258 and -2.258 e.Å^{-3}	

10.4.10 [Cu(2,9-dimethyl-1,10-phenanthroline)$_2$(MeCN)][BF$_4$]$_2$ · 2 MeCN

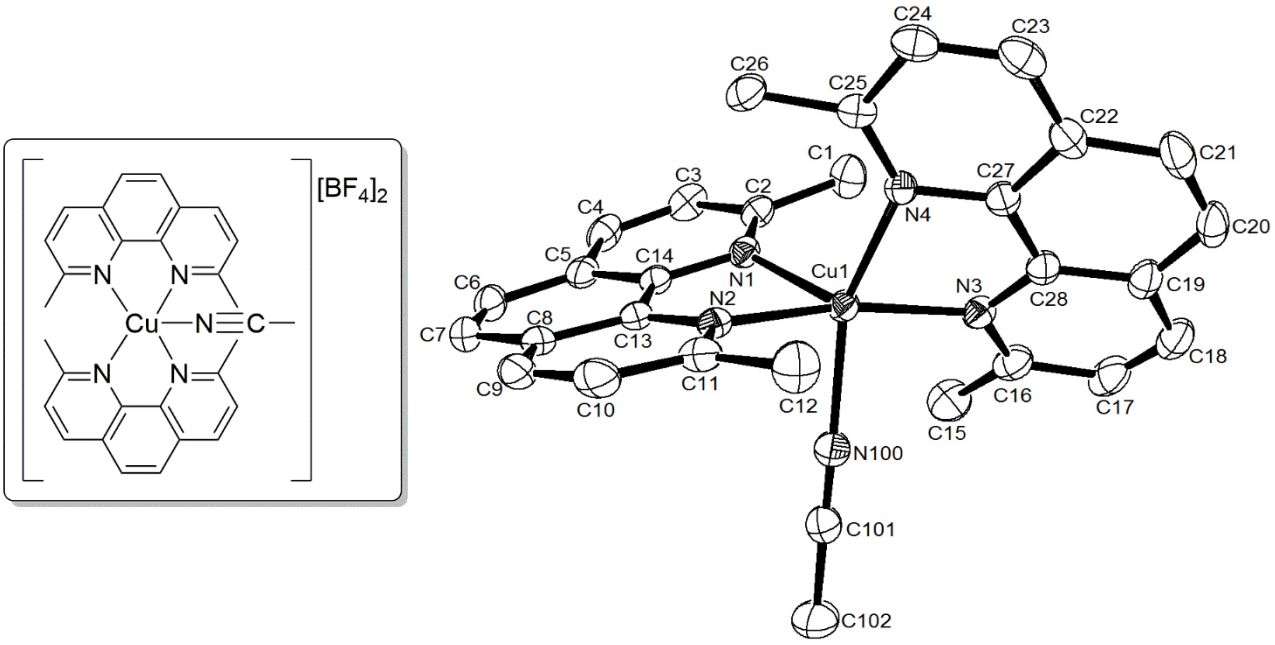

Figure 10-31: ORTEP plot of [Cu(2,9-dimethyl-1,10-phenanthroline)$_2$(MeCN)][BF$_4$]$_2$ · 2 MeCN at 50 % probability level for thermal ellipsoids. (Hydrogens, two anions and two MeCN were omitted.)

Table 10-31: Crystal data and structure refinement for [Cu(2,9-dimethyl-1,10-phenanthroline)$_2$(MeCN)][BF_4]$_2$ · 2 MeCN.

Identification code	s2847	
Empirical formula	C34 H33 B2 Cu F8 N7	
Formula weight	776.83	
Temperature	130(2) K	
Wavelength	0.71073 Å	
Crystal system	Triclinic	
Space group	P -1	
Unit cell dimensions	a = 11.287(3) Å	α= 72.850(5)°.
	b = 12.085(3) Å	β= 84.049(5)°.
	c = 13.777(3) Å	γ = 73.838(5)°.
Volume	1724.3(7) Å^3	
Z	2	
Density (calculated)	1.496 Mg/m^3	
Absorption coefficient	0.714 mm^{-1}	
F(000)	794	
Crystal size	0.430 x 0.350 x 0.220 mm^3	
Theta range for data collection	1.547 to 27.875°.	
Index ranges	-14<=h<=14, -15<=k<=15, -16<=l<=18	
Reflections collected	16485	
Independent reflections	8187 [R(int) = 0.0271]	
Completeness to theta = 25.242°	100.0 %	
Absorption correction	Semi-empirical from equivalents	
Max. and min. transmission	1.0000 and 0.7217	
Refinement method	Full-matrix least-squares on F^2	
Data / restraints / parameters	8187 / 21 / 504	
Goodness-of-fit on F^2	1.066	
Final R indices [I>2sigma(I)]	R1 = 0.0472, wR2 = 0.1112	
R indices (all data)	R1 = 0.0579, wR2 = 0.1192	
Extinction coefficient	n/a	
Largest diff. peak and hole	0.643 and -0.393 e.Å^{-3}	

10.4.11 [Cu(2,9-dimethyl-1,10-phenanthroline)$_2$][BF$_4$]$_2$/[Cu(2,9-dimethyl-1,10-phenanthroline)$_2$(???)][BF$_4$]$_2$ 1:1 ratio · 2 MeOH

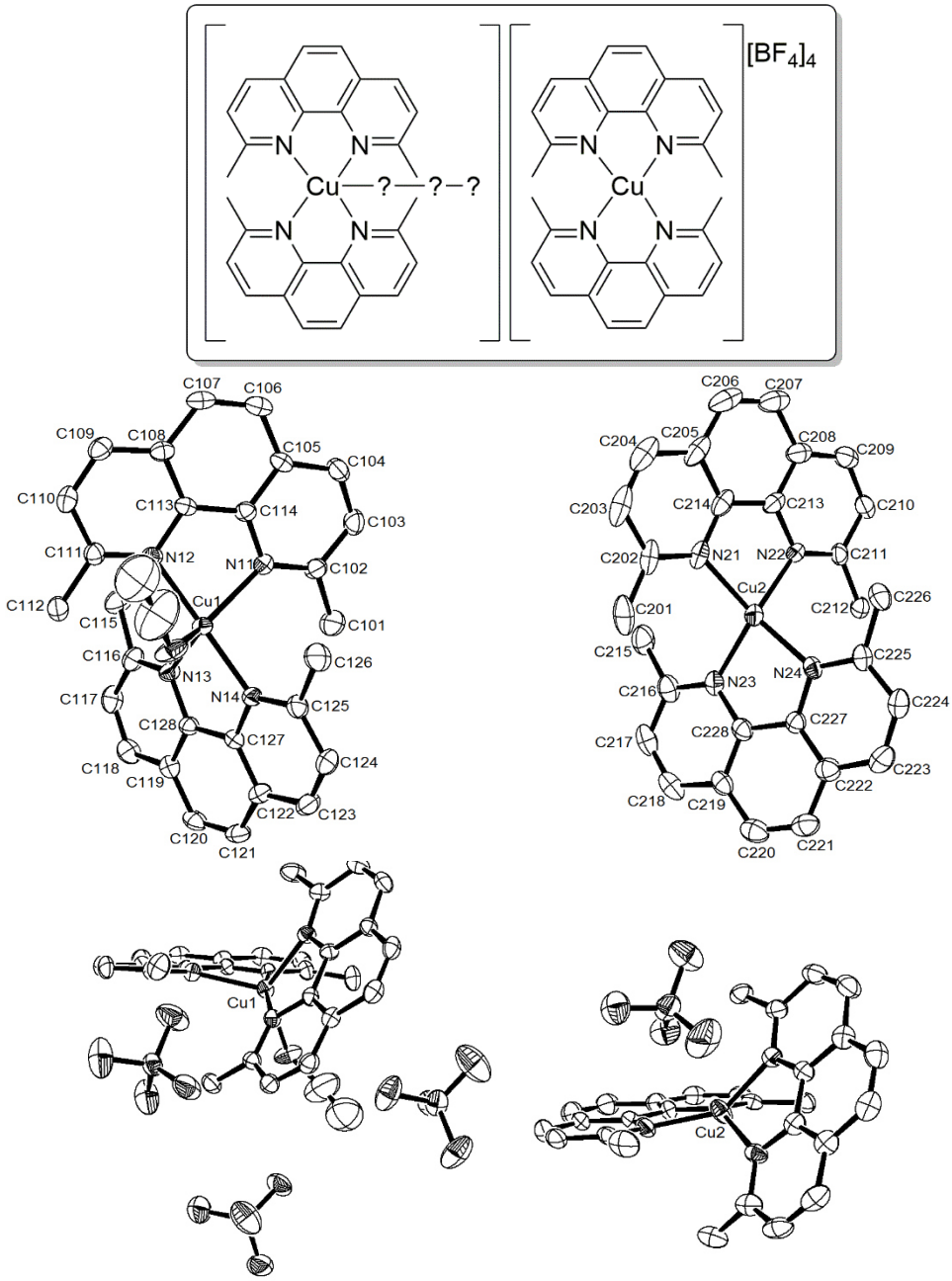

Figure 10-32: ORTEP plots of [Cu(2,9-dimethyl-1,10-phenanthroline)$_2$][BF$_4$]$_2$ / [Cu(2,9-dimethyl-1,10-phenanthroline)$_2$(???)][BF$_4$]$_2$ 1:1 ratio · 2 MeOH at 50 % probability level for thermal ellipsoids. (Hydrogens, anions and methanol molecules were omitted in the middle plots.)

Remarks:

The ligand depicted as ??? consists of three atom excluding possible hydrogen atoms and could be refined as ethynol, although this is not very likely due to the route of synthesis.

Table 10-32: Crystal data and structure refinement for [Cu(2,9-dimethyl-1,10-phenanthroline)$_2$][BF_4]$_2$ / [Cu(2,9-dimethyl-1,10-phenanthroline)$_2$(???)][BF_4]$_2$ 1:1 ratio · 2 MeOH.

Identification code	s2828	
Empirical formula	C57.83 H49.83 B4 Cu2 F16 N8 O0.90	
Formula weight	1345.50	
Temperature	130(2) K	
Wavelength	0.71073 Å	
Crystal system	Monoclinic	
Space group	P 21/c	
Unit cell dimensions	a = 19.709(3) Å	α= 90°.
	b = 17.348(3) Å	β= 116.471(3)°.
	c = 18.771(3) Å	γ = 90°.
Volume	5745.0(15) Å^3	
Z	4	
Density (calculated)	1.556 Mg/m^3	
Absorption coefficient	0.842 mm^{-1}	
F(000)	2728	
Crystal size	0.390 x 0.370 x 0.350 mm^3	
Theta range for data collection	1.154 to 27.877°.	
Index ranges	-25<=h<=25, -22<=k<=17, -24<=l<=24	
Reflections collected	53521	
Independent reflections	13706 [R(int) = 0.0990]	
Completeness to theta = 25.242°	100.0 %	
Absorption correction	Semi-empirical from equivalents	
Max. and min. transmission	1.0000 and 0.7219	
Refinement method	Full-matrix least-squares on F^2	
Data / restraints / parameters	13706 / 0 / 812	
Goodness-of-fit on F^2	1.028	
Final R indices [I>2sigma(I)]	R1 = 0.0649, wR2 = 0.1327	
R indices (all data)	R1 = 0.1262, wR2 = 0.1587	
Extinction coefficient	n/a	
Largest diff. peak and hole	1.120 and -0.473 e.Å^{-3}	

10.4.12 [Cu(2,9-dimethyl-1,10-phenanthroline)$_2$][BF$_4$]$_2$/[Cu(2,9-dimethyl-1,10-phenanthroline)$_2$(MeOH)][BF$_4$]$_2$ 1:1 ratio

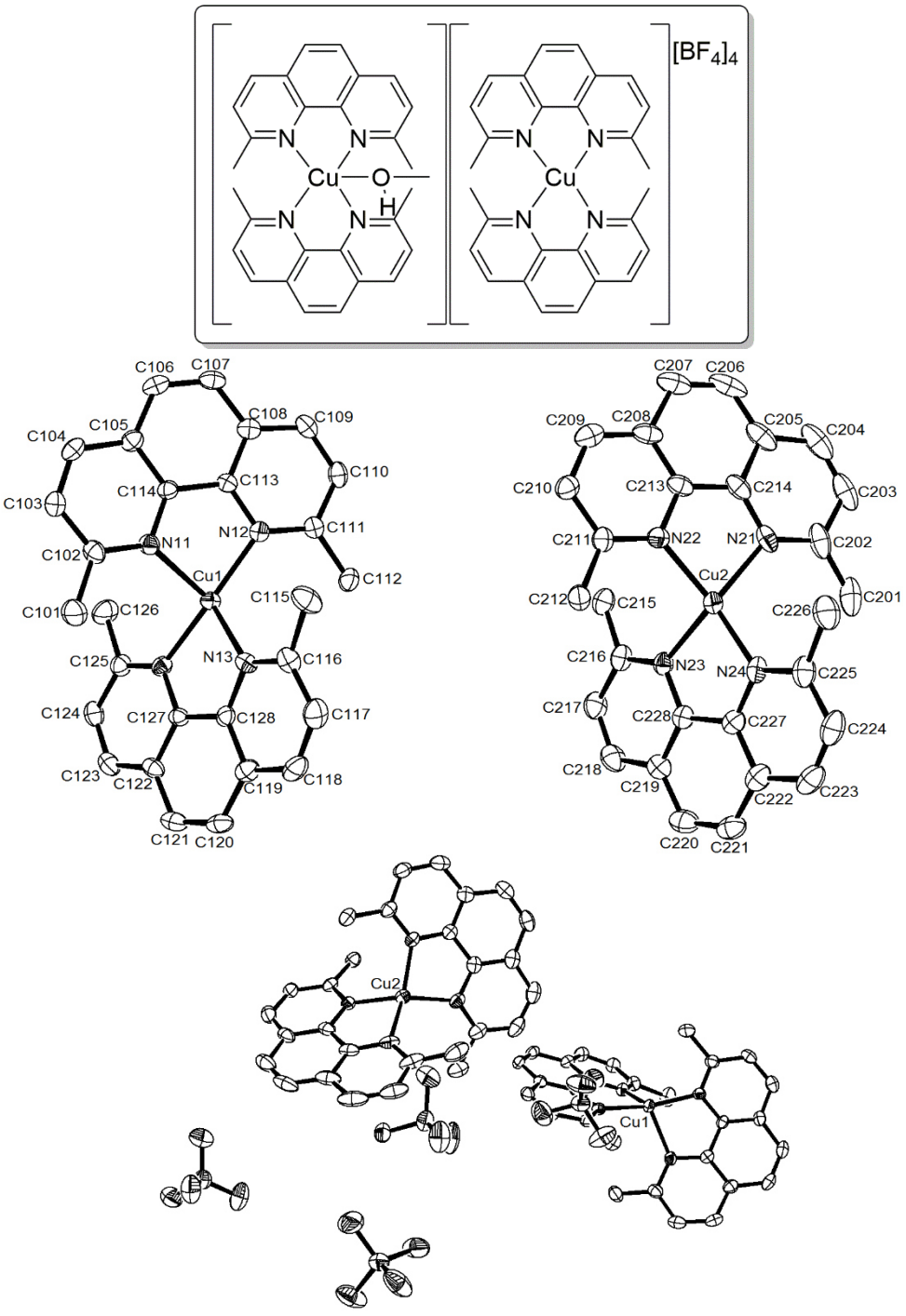

Figure 10-33: ORTEP plots of [Cu(2,9-dimethyl-1,10-phenanthroline)$_2$][BF$_4$]$_2$ / [Cu(2,9-dimethyl-1,10-phenanthroline)$_2$(MeOH)][BF$_4$]$_2$ 1:1 ratio at 50 % probability level for thermal ellipsoids. (Hydrogens, anions and methanol were omitted in the middle plots..)

Remarks:

MeOH is coordinating only Cu1 and is additionally disordered.

Table 10-33: Crystal data and structure refinement for [Cu(2,9-dimethyl-1,10-phenanthroline)$_2$][BF_4]$_2$ / [Cu(2,9-dimethyl-1,10-phenanthroline)$_2$(MeOH)][BF_4]$_2$ 1:1 ratio.

Identification code	s2866-sr	
Empirical formula	C28.50 H26 B2 Cu F8 N4 O0.50	
Formula weight	669.69	
Temperature	130(2) K	
Wavelength	0.71073 Å	
Crystal system	Monoclinic	
Space group	P 21/c	
Unit cell dimensions	a = 19.766(4) Å	α= 90°.
	b = 17.360(3) Å	β= 116.584(4)°.
	c = 18.803(3) Å	γ = 90°.
Volume	5769.8(18) Å^3	
Z	8	
Density (calculated)	1.542 Mg/m^3	
Absorption coefficient	0.838 mm^{-1}	
F(000)	2720	
Crystal size	0.410 x 0.230 x 0.160 mm^3	
Theta range for data collection	1.152 to 27.877°.	
Index ranges	-25<=h<=24, -22<=k<=22, -21<=l<=24	
Reflections collected	54463	
Independent reflections	13763 [R(int) = 0.0806]	
Completeness to theta = 25.242°	100.0 %	
Absorption correction	Semi-empirical from equivalents	
Max. and min. transmission	1.0000 and 0.7508	
Refinement method	Full-matrix least-squares on F^2	
Data / restraints / parameters	13763 / 0 / 783	
Goodness-of-fit on F^2	1.015	
Final R indices [I>2sigma(I)]	R1 = 0.0657, wR2 = 0.1438	
R indices (all data)	R1 = 0.1044, wR2 = 0.1612	
Extinction coefficient	n/a	
Largest diff. peak and hole	1.078 and -0.568 e.Å^{-3}	

10.4.13 [Cu(DMP)$_2$(Cl)][Cl]

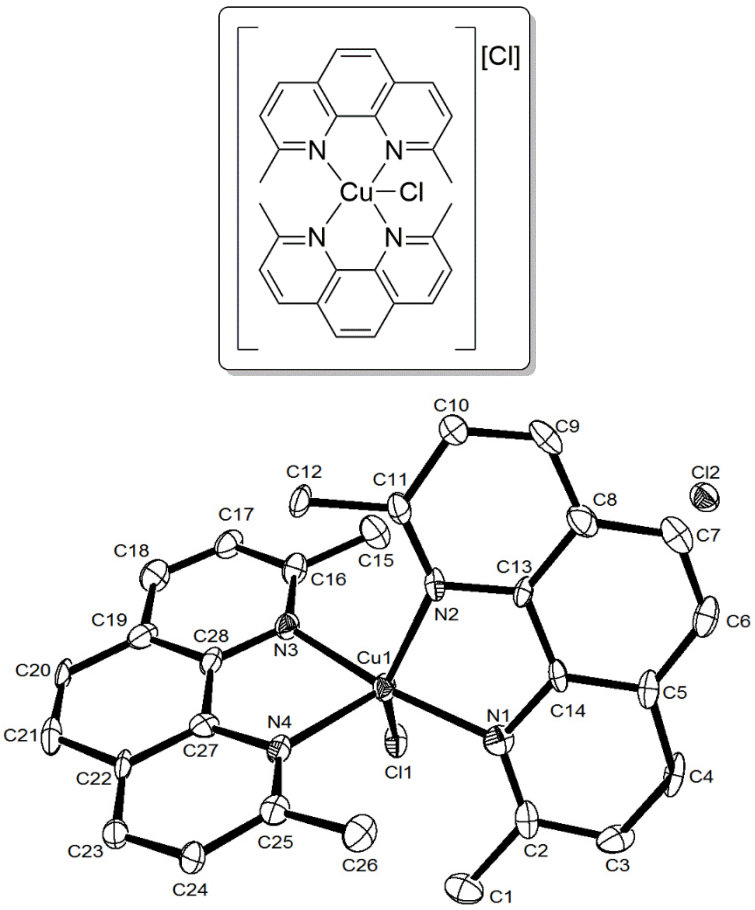

Figure 10-34: ORTEP plot of [Cu(DMP)$_2$(Cl)][Cl] at 50 % probability level for thermal ellipsoids. (Hydrogens are omitted.)

Table 10-34: Crystal data and structure refinement for $[Cu(DMP)_2(Cl)][Cl]$.

Identification code	s2897	
Empirical formula	C30 H32 Cl2 Cu N4 O2	
Formula weight	615.03	
Temperature	130(2) K	
Wavelength	0.71073 Å	
Crystal system	Monoclinic	
Space group	P 21/n	
Unit cell dimensions	a = 7.5624(13) Å	α= 90°.
	b = 23.930(4) Å	β= 93.135(3)°.
	c = 15.934(3) Å	γ = 90°.
Volume	2879.2(9) $Å^3$	
Z	4	
Density (calculated)	1.419 Mg/m^3	
Absorption coefficient	0.979 mm^{-1}	
F(000)	1276	
Crystal size	0.470 x 0.200 x 0.200 mm^3	
Theta range for data collection	1.537 to 27.876°.	
Index ranges	-9<=h<=9, -31<=k<=28, -20<=l<=20	
Reflections collected	26049	
Independent reflections	6825 [R(int) = 0.0826]	
Completeness to theta = 25.242°	100.0 %	
Absorption correction	Semi-empirical from equivalents	
Max. and min. transmission	1.0000 and 0.6737	
Refinement method	Full-matrix least-squares on F^2	
Data / restraints / parameters	6825 / 0 / 320	
Goodness-of-fit on F^2	1.085	
Final R indices [I>2sigma(I)]	R1 = 0.0977, wR2 = 0.2212	
R indices (all data)	R1 = 0.1303, wR2 = 0.2345	
Extinction coefficient	n/a	
Largest diff. peak and hole	0.904 and -1.793 $e.Å^{-3}$	

10.4.14 [Cu(2,9-dimethyl-1,10-phenanthroline)$_2$(Cl)][Cl] · 3 MeOH

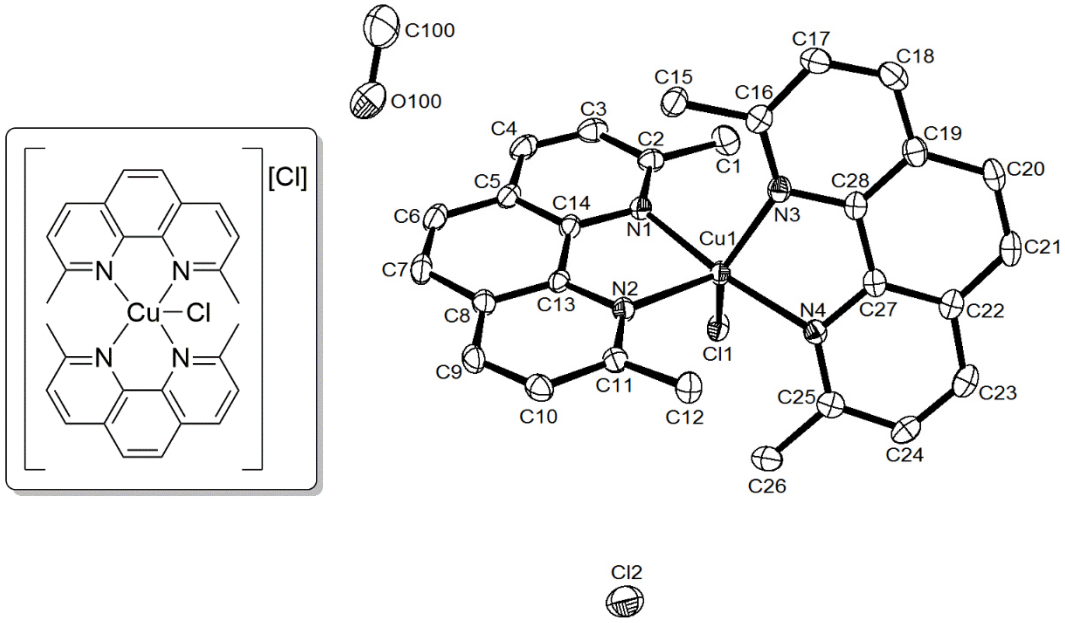

Figure 10-35: ORTEP plot of [Cu(2,9-dimethyl-1,10-phenanthroline)$_2$(Cl)][Cl] · 3 MeOH at 50 % probability level for thermal ellipsoids. (Hydrogens and 2 MeOH were omitted.)

Remarks:

Two of three methanol molecules were treated with Squeeze.

Table 10-35: Crystal data and structure refinement for [Cu(2,9-dimethyl-1,10-phenanthroline)$_2$(Cl)][Cl] · 3 MeOH.

Identification code	s2802s	
Empirical formula	C31 H36 Cl2 Cu N4 O3	
Formula weight	647.08	
Temperature	130(2) K	
Wavelength	0.71073 Å	
Crystal system	Monoclinic	
Space group	P 21/n	
Unit cell dimensions	a = 7.5948(9) Å	α= 90°.
	b = 23.990(3) Å	β= 94.360(2)°.
	c = 16.0656(18) Å	γ = 90°.
Volume	2918.7(6) Å^3	
Z	4	
Density (calculated)	1.473 Mg/m^3	
Absorption coefficient	0.972 mm^{-1}	
F(000)	1348	
Crystal size	0.470 x 0.360 x 0.200 mm^3	
Theta range for data collection	1.529 to 27.877°.	
Index ranges	-9<=h<=9, -31<=k<=28, -21<=l<=21	
Reflections collected	26926	
Independent reflections	6928 [R(int) = 0.0491]	
Completeness to theta = 25.242°	100.0 %	
Absorption correction	Semi-empirical from equivalents	
Max. and min. transmission	1.0000 and 0.7775	
Refinement method	Full-matrix least-squares on F^2	
Data / restraints / parameters	6928 / 0 / 343	
Goodness-of-fit on F^2	1.022	
Final R indices [I>2sigma(I)]	R1 = 0.0459, wR2 = 0.1040	
R indices (all data)	R1 = 0.0619, wR2 = 0.1106	
Extinction coefficient	n/a	
Largest diff. peak and hole	0.555 and -0.349 e.Å^{-3}	

10.4.15 [Cu$_2$-bis(μ-Cl)(2,9-dimethyl-1,10-phenanthroline)$_2$(Cl)$_2$]-A

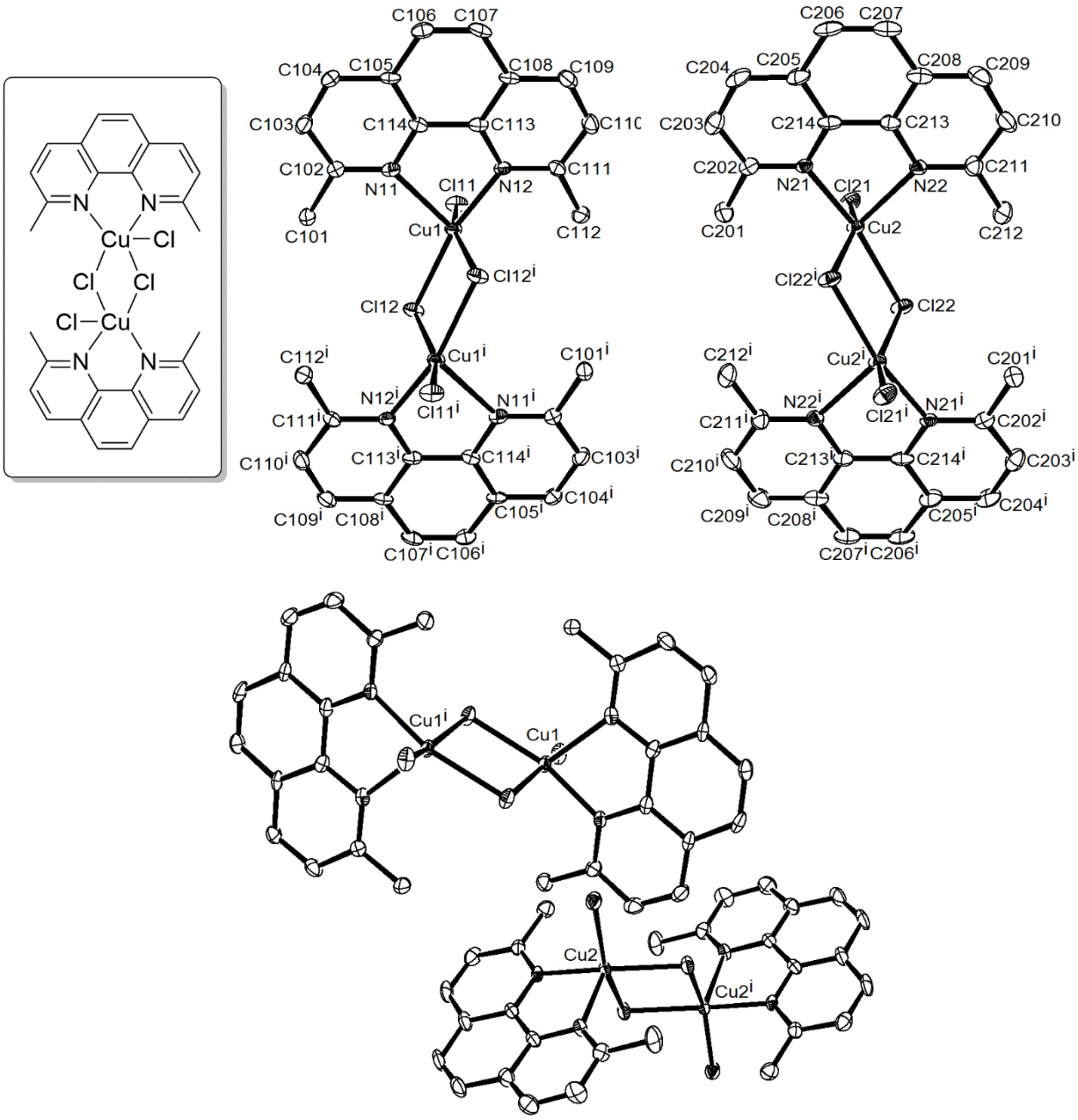

Figure 10-36: ORTEP plot of [Cu$_2$-bis(μ-Cl)(2,9-dimethyl-1,10-phenanthroline)$_2$(Cl)$_2$]-A at 50 % probability level for thermal ellipsoids. (Hydrogens were omitted.)

Table 10-36: Crystal data and structure refinement for [Cu_2-bis(μ-Cl)(2,9-dimethyl-1,10-phenanthroline)$_2$($Cl)_2$]-A.

Identification code	s2816	
Empirical formula	C28 H24 Cl4 Cu2 N4	
Formula weight	685.40	
Temperature	130(2) K	
Wavelength	0.71073 Å	
Crystal system	Triclinic	
Space group	P -1	
Unit cell dimensions	a = 9.440(2) Å	α= 103.844(5)°.
	b = 10.146(3) Å	β= 99.392(5)°.
	c = 15.715(4) Å	γ = 104.838(5)°.
Volume	1371.8(6) $Å^3$	
Z	2	
Density (calculated)	1.659 Mg/m^3	
Absorption coefficient	1.966 mm^{-1}	
F(000)	692	
Crystal size	0.410 x 0.200 x 0.030 mm^3	
Theta range for data collection	1.374 to 27.875°.	
Index ranges	-12<=h<=12, -13<=k<=13, -19<=l<=20	
Reflections collected	12871	
Independent reflections	6513 [R(int) = 0.0603]	
Completeness to theta = 25.242°	99.9 %	
Absorption correction	Semi-empirical from equivalents	
Max. and min. transmission	1.0000 and 0.5485	
Refinement method	Full-matrix least-squares on F^2	
Data / restraints / parameters	6513 / 0 / 347	
Goodness-of-fit on F^2	1.042	
Final R indices [I>2sigma(I)]	R1 = 0.0601, wR2 = 0.1085	
R indices (all data)	R1 = 0.1053, wR2 = 0.1266	
Extinction coefficient	n/a	
Largest diff. peak and hole	0.840 and -0.880 $e.Å^{-3}$	

10.4.16 [Cu_2-bis(μ-Cl)(2,9-dimethyl-1,10-phenanthroline)$_2$($Cl)_2$]-B

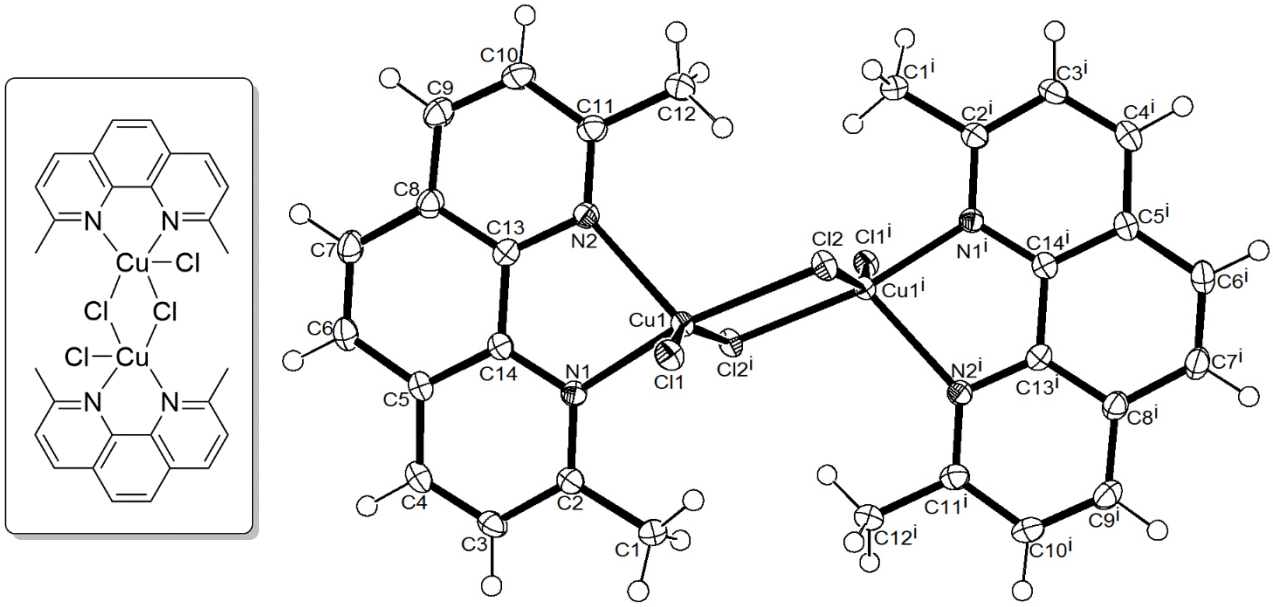

Figure 10-37: ORTEP plot of [Cu_2-bis(μ-Cl)(2,9-dimethyl-1,10-phenanthroline)$_2$($Cl)_2$]-B at 50 % probability level for thermal ellipsoids.

Table 10-37: Crystal data and structure refinement for [Cu_2-bis(μ-Cl)(2,9-dimethyl-1,10-phenanthroline)$_2$($Cl)_2$]-B.

Identification code	s2873	
Empirical formula	C28 H24 Cl4 Cu2 N4	
Formula weight	685.39	
Temperature	130(2) K	
Wavelength	0.71073 Å	
Crystal system	Triclinic	
Space group	P -1	
Unit cell dimensions	a = 7.2826(12) Å	α= 109.550(3)°.
	b = 9.3381(15) Å	β= 104.270(3)°.
	c = 10.9215(17) Å	γ = 93.580(3)°.
Volume	669.71(19) $Å^3$	
Z	1	
Density (calculated)	1.699 Mg/m^3	
Absorption coefficient	2.014 mm^{-1}	
F(000)	346	
Crystal size	0.400 x 0.190 x 0.170 mm^3	
Theta range for data collection	2.064 to 27.874°.	
Index ranges	-9<=h<=9, -12<=k<=12, -13<=l<=14	
Reflections collected	6406	
Independent reflections	3182 [R(int) = 0.0230]	
Completeness to theta = 25.242°	99.9 %	
Absorption correction	Semi-empirical from equivalents	
Max. and min. transmission	1.0000 and 0.6143	
Refinement method	Full-matrix least-squares on F^2	
Data / restraints / parameters	3182 / 0 / 175	
Goodness-of-fit on F^2	1.040	
Final R indices [I>2sigma(I)]	R1 = 0.0321, wR2 = 0.0757	
R indices (all data)	R1 = 0.0364, wR2 = 0.0793	
Extinction coefficient	n/a	
Largest diff. peak and hole	0.481 and -0.344 $e.Å^{-3}$	

10.4.17 [Cu(2,9-dimethyl-1,10-phenanthroline)$_2$(MeOH)][ClO$_4$]$_2$

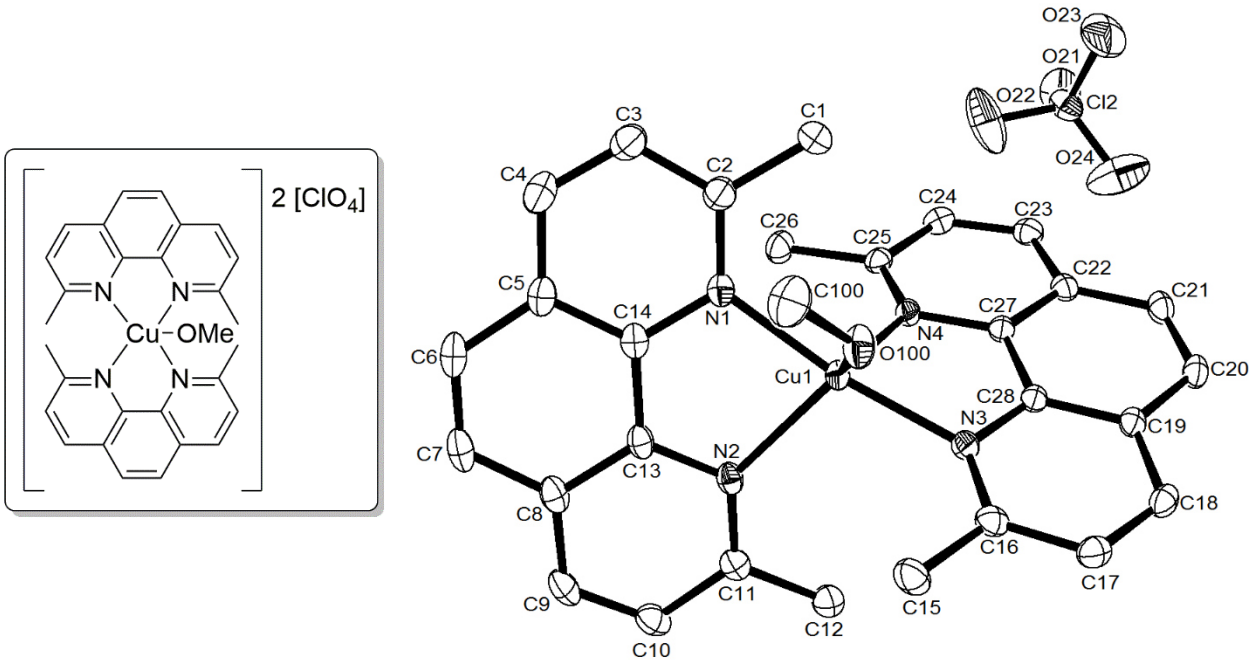

Figure 10-38: ORTEP plot of [Cu(2,9-dimethyl-1,10-phenanthroline)$_2$(MeOH)][ClO$_4$]$_2$ at 50 % probability level for thermal ellipsoids. (Hydrogens and one anion were omitted.)

Table 10-38: Crystal data and structure refinement for [Cu(2,9-dimethyl-1,10-phenanthroline)$_2$(MeOH)][ClO$_4$]$_2$.

Identification code	s2798	
Empirical formula	C29 H28 Cl2 Cu N4 O9	
Formula weight	710.99	
Temperature	130(2) K	
Wavelength	0.71073 Å	
Crystal system	Monoclinic	
Space group	P 21/c	
Unit cell dimensions	a = 13.8702(11) Å	α= 90°.
	b = 12.6903(10) Å	β= 100.752(2)°.
	c = 16.9768(13) Å	γ = 90°.
Volume	2935.7(4) Å^3	
Z	4	
Density (calculated)	1.609 Mg/m^3	
Absorption coefficient	0.989 mm^{-1}	
F(000)	1460	
Crystal size	0.470 x 0.440 x 0.360 mm^3	
Theta range for data collection	1.494 to 27.878°.	
Index ranges	-18<=h<=18, -15<=k<=16, -18<=l<=22	
Reflections collected	27372	
Independent reflections	6992 [R(int) = 0.0287]	
Completeness to theta = 25.242°	100.0 %	
Absorption correction	Semi-empirical from equivalents	
Max. and min. transmission	1.0000 and 0.8831	
Refinement method	Full-matrix least-squares on F^2	
Data / restraints / parameters	6992 / 1 / 415	
Goodness-of-fit on F^2	1.032	
Final R indices [I>2sigma(I)]	R1 = 0.0356, wR2 = 0.0906	
R indices (all data)	R1 = 0.0419, wR2 = 0.0949	
Extinction coefficient	n/a	
Largest diff. peak and hole	0.475 and -0.322 e.Å^{-3}	

10.4.18 [Cu(2,9-dimethyl-1,10-phenanthroline)$_2$(NO$_3$)][NO$_3$] · 6 H$_2$O

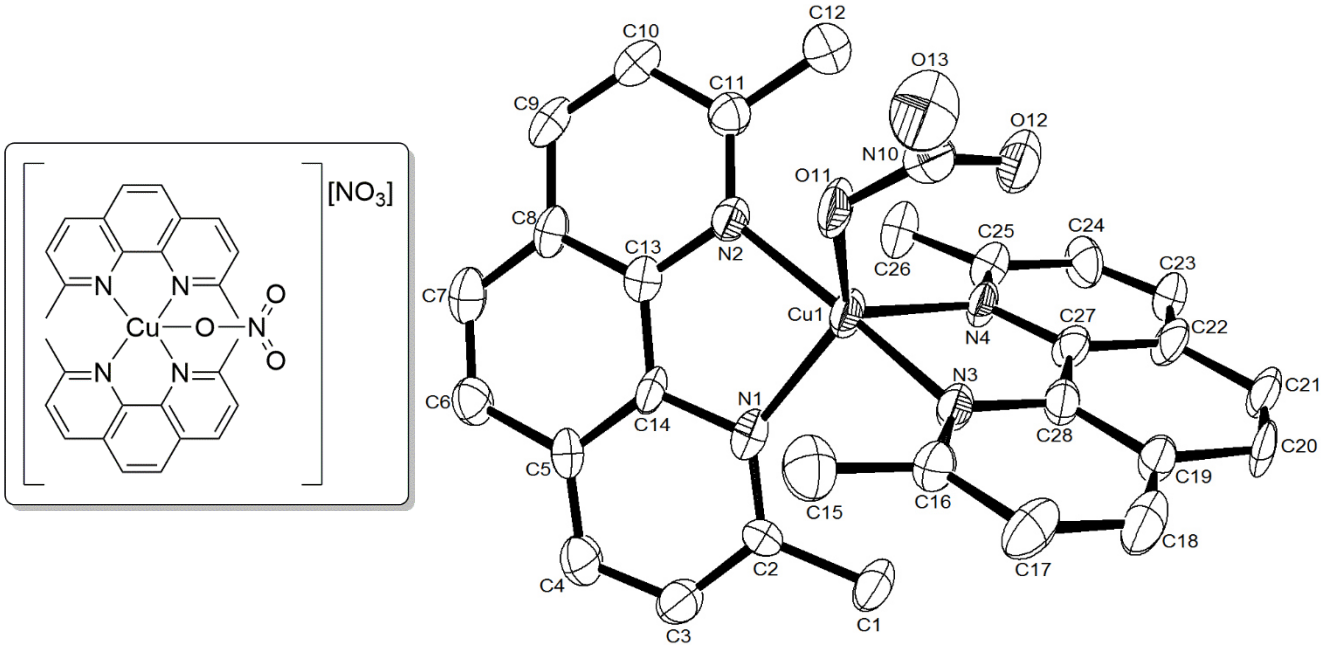

Figure 10-39: ORTEP plot of [Cu(2,9-dimethyl-1,10-phenanthroline)$_2$(NO$_3$)][NO$_3$] · 6 H$_2$O at 50 % probability level for thermal ellipsoids. (Hydrogens, six water molecules and one anion were omitted.)

Remarks:

Only seven of twelve hydrogen atoms of the water molecules could be determined. The crystallographic data is of poor quality.

Table 10-39: Crystal data and structure refinement for [Cu(2,9-dimethyl-1,10-phenanthroline)$_2$(NO$_3$)][NO$_3$] · 6 H$_2$O.

Identification code	s2830	
Empirical formula	C28 H36 Cu N6 O12	
Formula weight	712.17	
Temperature	130(2) K	
Wavelength	0.71073 Å	
Crystal system	Triclinic	
Space group	P -1	
Unit cell dimensions	a = 8.042(5) Å	α= 103.138(11)°.
	b = 14.243(8) Å	β= 93.093(12)°.
	c = 14.434(8) Å	γ = 93.567(10)°.
Volume	1603.0(16) Å^3	
Z	2	
Density (calculated)	1.475 Mg/m^3	
Absorption coefficient	0.753 mm^{-1}	
F(000)	742	
Crystal size	0.320 x 0.200 x 0.150 mm^3	
Theta range for data collection	1.472 to 27.876°.	
Index ranges	-10<=h<=10, -18<=k<=18, -18<=l<=16	
Reflections collected	14692	
Independent reflections	7598 [R(int) = 0.1786]	
Completeness to theta = 25.242°	99.9 %	
Absorption correction	Semi-empirical from equivalents	
Max. and min. transmission	1.0000 and 0.1352	
Refinement method	Full-matrix least-squares on F^2	
Data / restraints / parameters	7598 / 10 / 456	
Goodness-of-fit on F^2	0.918	
Final R indices [I>2sigma(I)]	R1 = 0.0916, wR2 = 0.1780	
R indices (all data)	R1 = 0.2364, wR2 = 0.2461	
Extinction coefficient	n/a	
Largest diff. peak and hole	0.753 and -1.020 e.Å^{-3}	

10.4.19 [Cu(1,10-phenanthroline-2,9diyl)dimethanol)$_2$][BF$_4$]$_2$

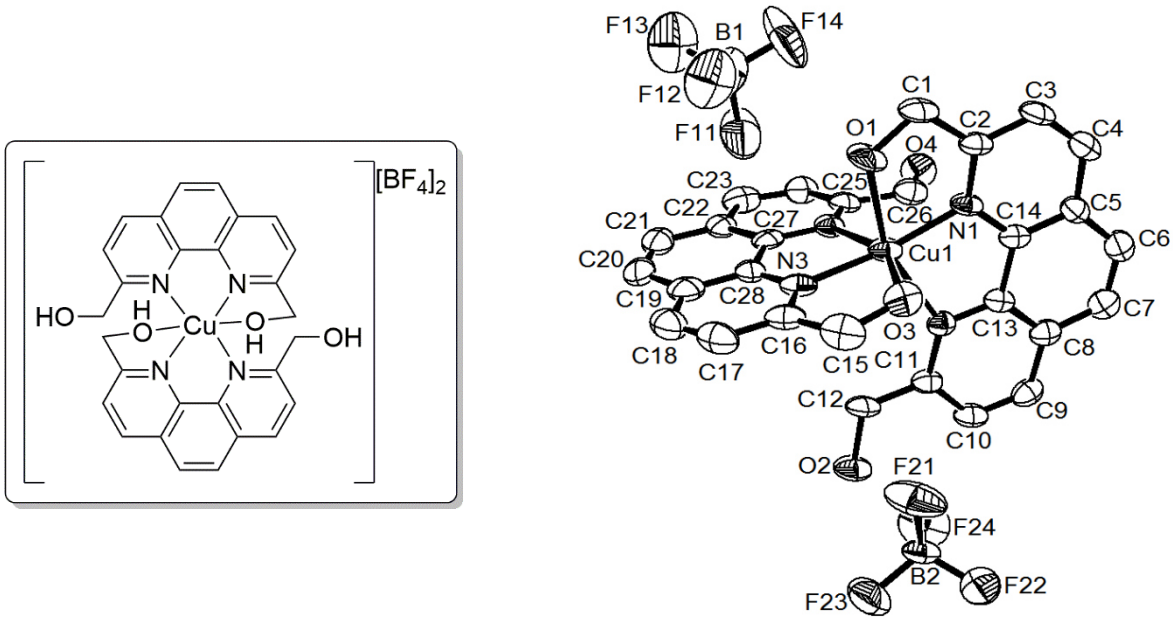

Figure 10-40: ORTEP plot of [Cu(1,10-phenanthroline-2,9diyl)dimethanol)$_2$][BF$_4$]$_2$ at 50 % probability level for thermal ellipsoids. (Hydrogens and one diethyl ether were omitted.)

Remarks:

Diethyl ether was treated with SQUEEZE. Two hydrogen atoms from the coordinating hydroxo functions could not be resolved. The crystallographic data is of poor quality.

Table 10-40: Crystal data and structure refinement for [Cu(1,10-phenanthroline-2,9diyl)dimethanol)$_2$][BF_4]$_2$.

Identification code	s2823	
Empirical formula	C32 H32 B2 Cu F8 N4 O5	
Formula weight	789.77	
Temperature	130(2) K	
Wavelength	0.71073 Å	
Crystal system	Triclinic	
Space group	P -1	
Unit cell dimensions	a = 12.031(6) Å	α= 103.335(9)°.
	b = 12.919(6) Å	β= 107.536(9)°.
	c = 13.266(6) Å	γ = 113.380(9)°.
Volume	1654.0(14) Å^3	
Z	2	
Density (calculated)	1.586 Mg/m^3	
Absorption coefficient	0.754 mm^{-1}	
F(000)	806	
Crystal size	0.480 x 0.220 x 0.210 mm^3	
Theta range for data collection	1.757 to 27.876°.	
Index ranges	-15<=h<=15, -16<=k<=16, -17<=l<=17	
Reflections collected	15199	
Independent reflections	7817 [R(int) = 0.0625]	
Completeness to theta = 25.242°	99.9 %	
Absorption correction	Semi-empirical from equivalents	
Max. and min. transmission	1.0000 and 0.2949	
Refinement method	Full-matrix least-squares on F^2	
Data / restraints / parameters	7817 / 0 / 426	
Goodness-of-fit on F^2	1.077	
Final R indices [I>2sigma(I)]	R1 = 0.0916, wR2 = 0.2010	
R indices (all data)	R1 = 0.1507, wR2 = 0.2238	
Extinction coefficient	n/a	
Largest diff. peak and hole	1.213 and -0.723 e.Å^{-3}	

10.4.20 [Cu(9-(carboxylic acid)-1,10-phenanthroline-2-dicarboxylato)$_2$] · 5 DMSO · MeOH

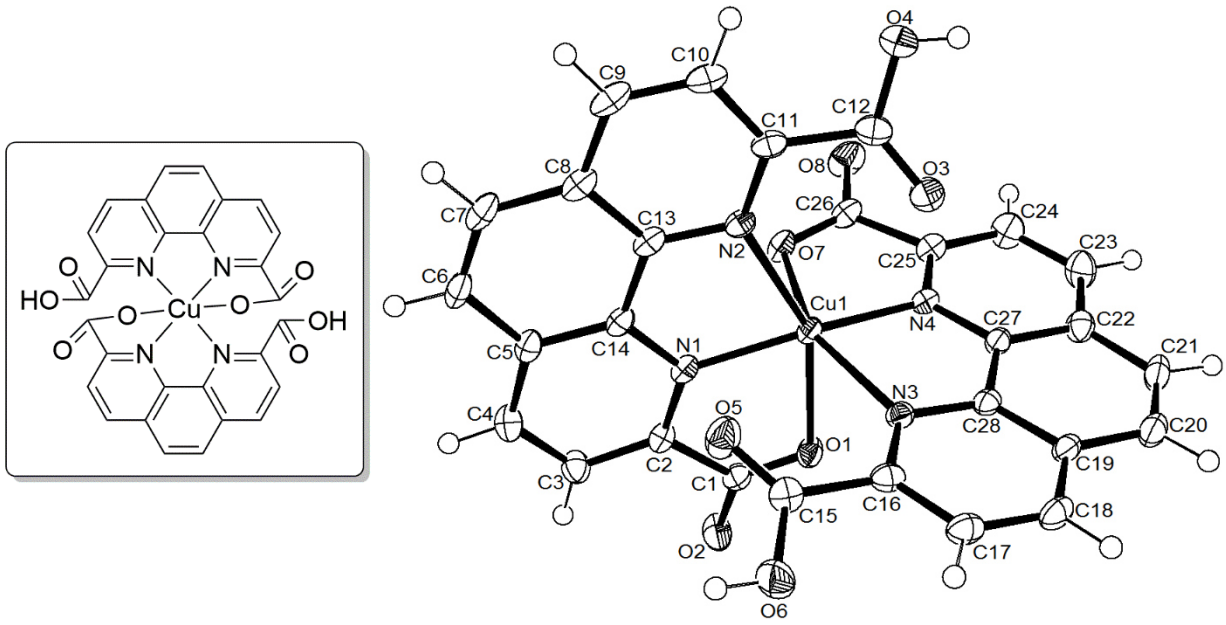

Figure 10-41: ORTEP plot of [Cu(9-(carboxylic acid)-1,10-phenanthroline-2-dicarboxylato)$_2$] · 5 DMSO · MeOH at 50 % probability level for thermal ellipsoids. (Five DMSO and one MeOH were omitted.)

Remarks:

One DMSO molecule is disordered over two position and the MeOH was treated with Squeeze.

Table 10-41: Crystal data and structure refinement for [Cu(9-(carboxylic acid)-1,10-phenanthroline-2-dicarboxylato)$_2$] · 5 DMSO · MeOH.

Identification code	s2821	
Empirical formula	C39 H48 Cu N4 O14 S5	
Formula weight	1020.65	
Temperature	130(2) K	
Wavelength	0.71073 Å	
Crystal system	Triclinic	
Space group	P -1	
Unit cell dimensions	a = 10.4170(13) Å	α= 72.872(2)°.
	b = 14.5399(18) Å	β= 79.105(3)°.
	c = 16.448(2) Å	γ = 72.434(3)°.
Volume	2256.1(5) Å^3	
Z	2	
Density (calculated)	1.502 Mg/m^3	
Absorption coefficient	0.785 mm^{-1}	
F(000)	1062	
Crystal size	0.490 x 0.370 x 0.190 mm^3	
Theta range for data collection	1.519 to 27.876°.	
Index ranges	-13<=h<=13, -18<=k<=19, -21<=l<=21	
Reflections collected	21448	
Independent reflections	10706 [R(int) = 0.0339]	
Completeness to theta = 25.242°	100.0 %	
Absorption correction	Semi-empirical from equivalents	
Max. and min. transmission	1.0000 and 0.6944	
Refinement method	Full-matrix least-squares on F^2	
Data / restraints / parameters	10706 / 0 / 587	
Goodness-of-fit on F^2	1.047	
Final R indices [I>2sigma(I)]	R1 = 0.0484, wR2 = 0.1170	
R indices (all data)	R1 = 0.0613, wR2 = 0.1254	
Extinction coefficient	n/a	
Largest diff. peak and hole	0.868 and -0.559 e.Å^{-3}	

10.4.21 [Cu(1,10-phenanthroline)$_2$(Cl)][Cl] · MeOH-A

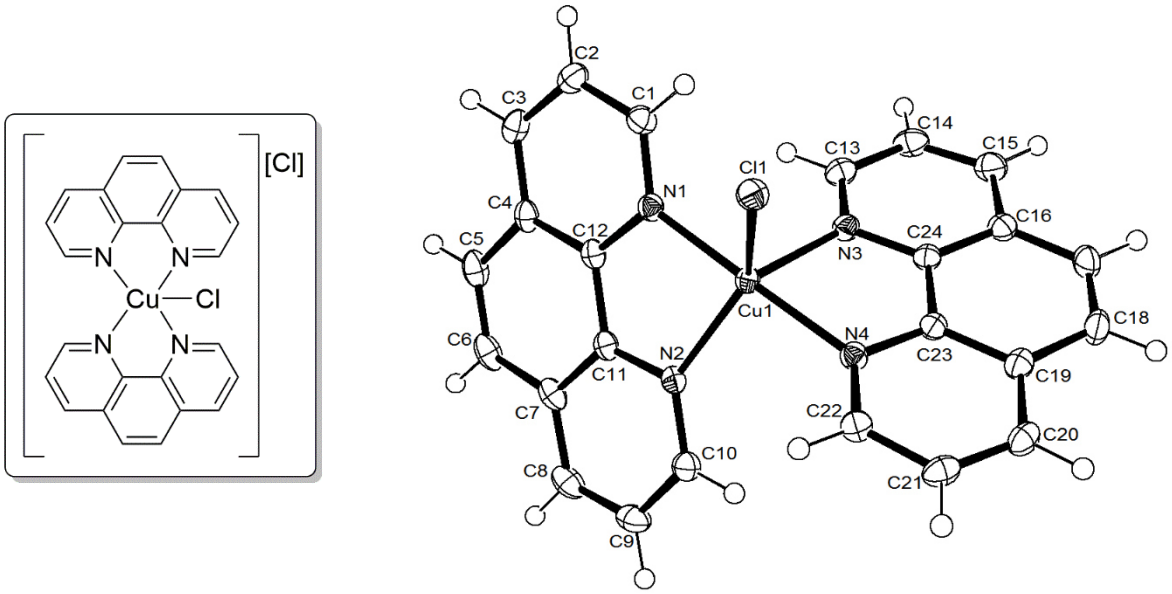

Figure 10-42: ORTEP plot of [Cu(1,10-phenanthroline)$_2$(Cl)][Cl] · MeOH-A at 50 % probability level for thermal ellipsoids. (One MeOH molecule and one chloride anion were omitted.)

Table 10-42: Crystal data and structure refinement for Cu(1,10-phenanthroline)2(Cl)][Cl] · MeOH-A.

Identification code	s2880	
Empirical formula	C25 H20 Cl2 Cu N4 O	
Formula weight	526.89	
Temperature	130(2) K	
Wavelength	0.71073 Å	
Crystal system	Monoclinic	
Space group	P 21/n	
Unit cell dimensions	a = 14.3319(17) Å	α= 90°.
	b = 10.6036(12) Å	β= 99.749(2)°.
	c = 14.7601(17) Å	γ = 90°.
Volume	2210.7(4) $Å^3$	
Z	4	
Density (calculated)	1.583 Mg/m^3	
Absorption coefficient	1.257 mm^{-1}	
F(000)	1076	
Crystal size	0.410 x 0.320 x 0.250 mm^3	
Theta range for data collection	1.832 to 27.877°.	
Index ranges	-18<=h<=18, -13<=k<=13, -19<=l<=19	
Reflections collected	20516	
Independent reflections	5269 [R(int) = 0.0366]	
Completeness to theta = 25.242°	100.0 %	
Absorption correction	Semi-empirical from equivalents	
Max. and min. transmission	1.0000 and 0.6170	
Refinement method	Full-matrix least-squares on F^2	
Data / restraints / parameters	5269 / 0 / 300	
Goodness-of-fit on F^2	1.072	
Final R indices [I>2sigma(I)]	R1 = 0.0351, wR2 = 0.0853	
R indices (all data)	R1 = 0.0450, wR2 = 0.0914	
Extinction coefficient	n/a	
Largest diff. peak and hole	0.694 and -0.307 $e.Å^{-3}$	

10.4.22 [Cu(1,10-phenanthroline)$_2$(Cl)][Cl] · MeOH-B

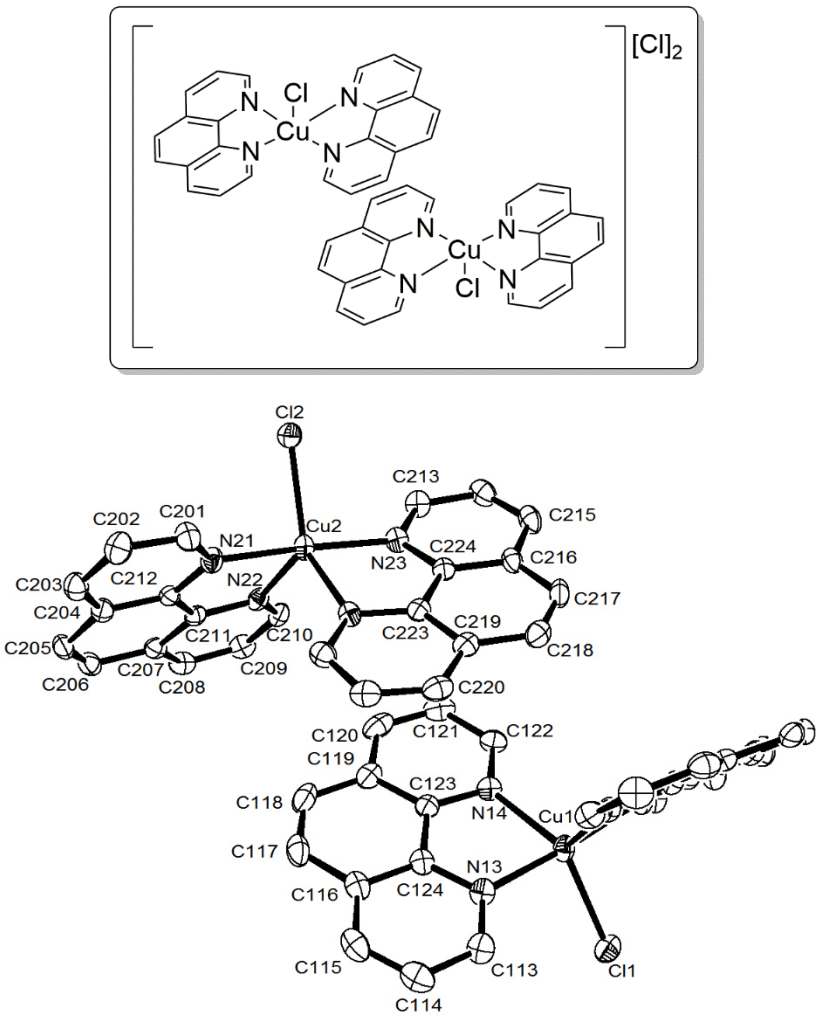

Figure 10-43: ORTEP plot of [Cu(1,10-phenanthroline)$_2$(Cl)][Cl] · MeOH-B at 50 % probability level for thermal ellipsoids. (Four MeOH molecule and two chloride anions were omitted.)

Table 10-43: Crystal data and structure refinement for [Cu(1,10-phenanthroline)$_2$(Cl)][Cl] · MeOH-B.

Identification code	s2881	
Empirical formula	C26 H24 Cl2 Cu N4 O2	
Formula weight	558.93	
Temperature	130(2) K	
Wavelength	0.71073 Å	
Crystal system	Orthorhombic	
Space group	P b c a	
Unit cell dimensions	a = 16.167(2) Å	α= 90°.
	b = 21.770(3) Å	β= 90°.
	c = 27.871(4) Å	γ = 90°.
Volume	9809(2) Å^3	
Z	16	
Density (calculated)	1.514 Mg/m^3	
Absorption coefficient	1.141 mm^{-1}	
F(000)	4592	
Crystal size	0.370 x 0.360 x 0.210 mm^3	
Theta range for data collection	1.731 to 27.878°.	
Index ranges	-21<=h<=21, -28<=k<=28, -36<=l<=36	
Reflections collected	90204	
Independent reflections	11703 [R(int) = 0.1305]	
Completeness to theta = 25.242°	100.0 %	
Absorption correction	Semi-empirical from equivalents	
Max. and min. transmission	1.0000 and 0.5140	
Refinement method	Full-matrix least-squares on F^2	
Data / restraints / parameters	11703 / 0 / 639	
Goodness-of-fit on F^2	1.033	
Final R indices [I>2sigma(I)]	R1 = 0.0552, wR2 = 0.1046	
R indices (all data)	R1 = 0.1073, wR2 = 0.1258	
Extinction coefficient	n/a	
Largest diff. peak and hole	0.726 and -0.421 e.Å^{-3}	

10.4.23 [Cu(1,10-phenanthroline)$_2$(Cl)][Cl] · 2 MeOH

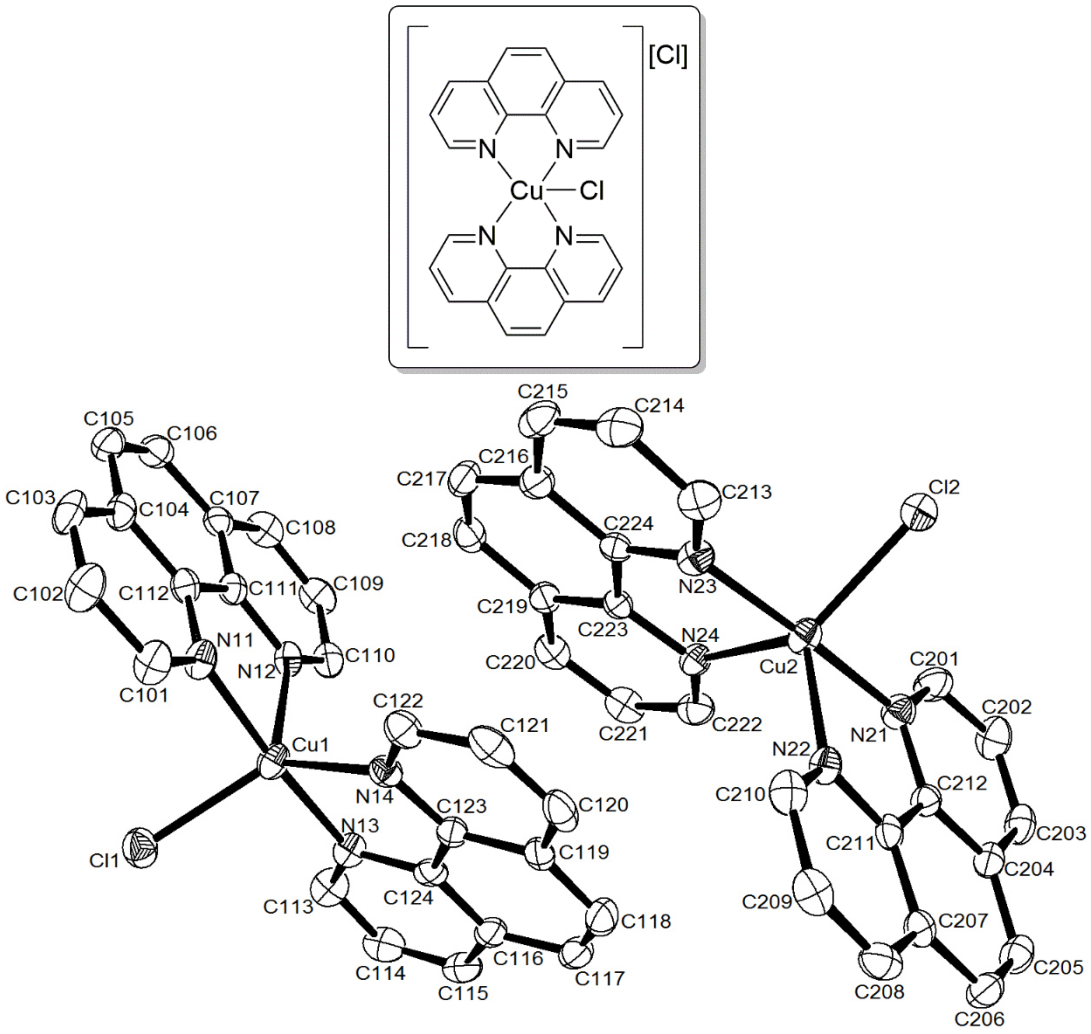

Figure 10-44: ORTEP plot of [Cu(1,10-phenanthroline)$_2$(Cl)][Cl] · 2 MeOH at 50 % probability level for thermal ellipsoids. (Hydrogens, two anions and four methanol molecules were omitted.)

Remarks:

Two crystallographic independent but chemical identical cations, anions and two methanol molecules were found in the asymmetric unit.

Table 10-44: Crystal data and structure refinement for [Cu(1,10-phenanthroline)$_2$(Cl)][Cl] · 2 MeOH.

Identification code	s2809	
Empirical formula	C26 H24 Cl2 Cu N4 O2	
Formula weight	558.93	
Temperature	130(2) K	
Wavelength	0.71073 Å	
Crystal system	Orthorhombic	
Space group	P b c a	
Unit cell dimensions	a = 16.1385(17) Å	α= 90°.
	b = 21.784(2) Å	β= 90°.
	c = 27.914(3) Å	γ = 90°.
Volume	9813.6(18) Å^3	
Z	16	
Density (calculated)	1.513 Mg/m^3	
Absorption coefficient	1.140 mm^{-1}	
F(000)	4592	
Crystal size	0.470 x 0.110 x 0.100 mm^3	
Theta range for data collection	1.732 to 27.877°.	
Index ranges	-21<=h<=21, -28<=k<=28, -32<=l<=36	
Reflections collected	90078	
Independent reflections	11710 [R(int) = 0.1535]	
Completeness to theta = 25.242°	100.0 %	
Absorption correction	Semi-empirical from equivalents	
Max. and min. transmission	1.0000 and 0.7037	
Refinement method	Full-matrix least-squares on F^2	
Data / restraints / parameters	11710 / 0 / 639	
Goodness-of-fit on F^2	0.906	
Final R indices [I>2sigma(I)]	R1 = 0.0517, wR2 = 0.0775	
R indices (all data)	R1 = 0.1237, wR2 = 0.0968	
Extinction coefficient	n/a	
Largest diff. peak and hole	0.697 and -0.445 e.Å^{-3}	

10.4.24 [Cu(1,10-phenanthroline)$_2$(Br)][Br] · 2 MeOH

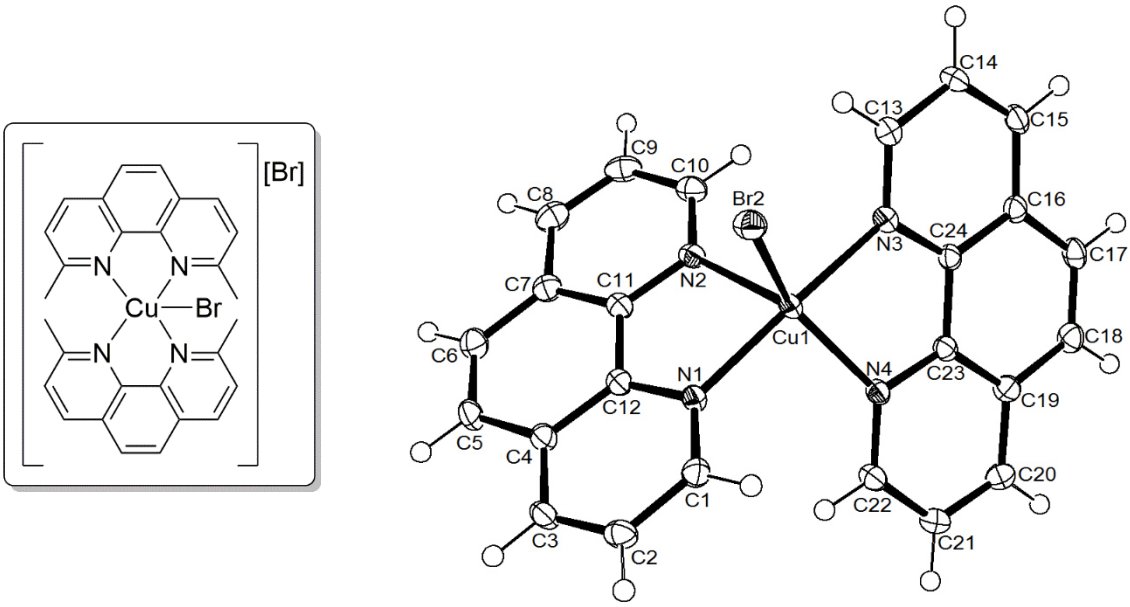

Figure 10-45: ORTEP plot of [Cu(1,10-phenanthroline)$_2$(Br)][Br] · 2 MeOH at 50 % probability level for thermal ellipsoids. (Two MeOH molecules were omitted.)

Table 10-45: Crystal data and structure refinement for [Cu(1,10-phenanthroline)$_2$(Br)][Br] · 2 MeOH.

Identification code	s2797	
Empirical formula	C26 H24 Br2 Cu N4 O2	
Formula weight	647.85	
Temperature	130(2) K	
Wavelength	0.71073 Å	
Crystal system	Triclinic	
Space group	P -1	
Unit cell dimensions	a = 8.2540(10) Å	α= 104.108(2)°.
	b = 10.9708(13) Å	β= 96.789(2)°.
	c = 15.3476(18) Å	γ = 110.766(2)°.
Volume	1227.8(3) Å^3	
Z	2	
Density (calculated)	1.752 Mg/m^3	
Absorption coefficient	4.176 mm^{-1}	
F(000)	646	
Crystal size	0.490 x 0.200 x 0.110 mm^3	
Theta range for data collection	1.404 to 27.876°.	
Index ranges	-10<=h<=10, -14<=k<=14, -20<=l<=18	
Reflections collected	11721	
Independent reflections	5841 [R(int) = 0.0236]	
Completeness to theta = 25.242°	100.0 %	
Absorption correction	Semi-empirical from equivalents	
Max. and min. transmission	1.0000 and 0.5281	
Refinement method	Full-matrix least-squares on F^2	
Data / restraints / parameters	5841 / 0 / 320	
Goodness-of-fit on F^2	1.032	
Final R indices [I>2sigma(I)]	R1 = 0.0308, wR2 = 0.0746	
R indices (all data)	R1 = 0.0386, wR2 = 0.0788	
Extinction coefficient	n/a	
Largest diff. peak and hole	0.784 and -0.372 e.Å^{-3}	

10.4.25 [Cu(1,10-phenanthroline)$_2$(NO$_3$)][NO$_3$] · MeOH

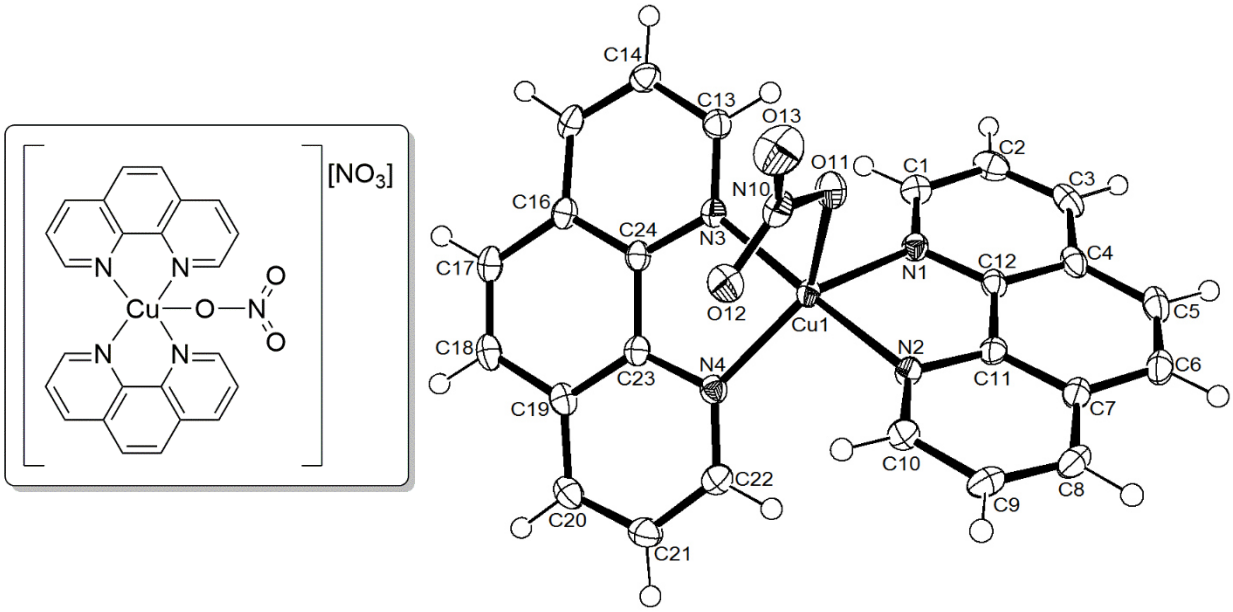

Figure 10-46: ORTEP plot of [Cu(1,10-phenanthroline)$_2$(NO$_3$)][NO$_3$] · MeOH at 50 % probability level for thermal ellipsoids. (One anion and one MeOH were omitted.)

Table 10-46: Crystal data and structure refinement for [Cu(1,10-phenanthroline)$_2$(NO$_3$)][NO$_3$] · MeOH.

Identification code	s2807	
Empirical formula	C25 H20 Cu N6 O7	
Formula weight	580.01	
Temperature	130(2) K	
Wavelength	0.71073 Å	
Crystal system	Triclinic	
Space group	P -1	
Unit cell dimensions	a = 7.4212(9) Å	α= 99.045(2)°.
	b = 10.9769(14) Å	β= 103.686(2)°.
	c = 15.4655(19) Å	γ = 102.520(2)°.
Volume	1165.7(3) Å^3	
Z	2	
Density (calculated)	1.652 Mg/m^3	
Absorption coefficient	0.999 mm^{-1}	
F(000)	594	
Crystal size	0.470 x 0.400 x 0.220 mm^3	
Theta range for data collection	1.948 to 27.875°.	
Index ranges	-9<=h<=9, -14<=k<=14, -20<=l<=19	
Reflections collected	11062	
Independent reflections	5537 [R(int) = 0.0213]	
Completeness to theta = 25.242°	99.9 %	
Absorption correction	Semi-empirical from equivalents	
Max. and min. transmission	1.0000 and 0.6880	
Refinement method	Full-matrix least-squares on F^2	
Data / restraints / parameters	5537 / 0 / 354	
Goodness-of-fit on F^2	1.055	
Final R indices [I>2sigma(I)]	R1 = 0.0365, wR2 = 0.0886	
R indices (all data)	R1 = 0.0424, wR2 = 0.0931	
Extinction coefficient	n/a	
Largest diff. peak and hole	0.479 and -0.336 e.Å^{-3}	

10.4.26 [Cu(1,10-phenanthroline)$_2$(CF$_3$SO$_3$)][CF$_3$SO$_3$]

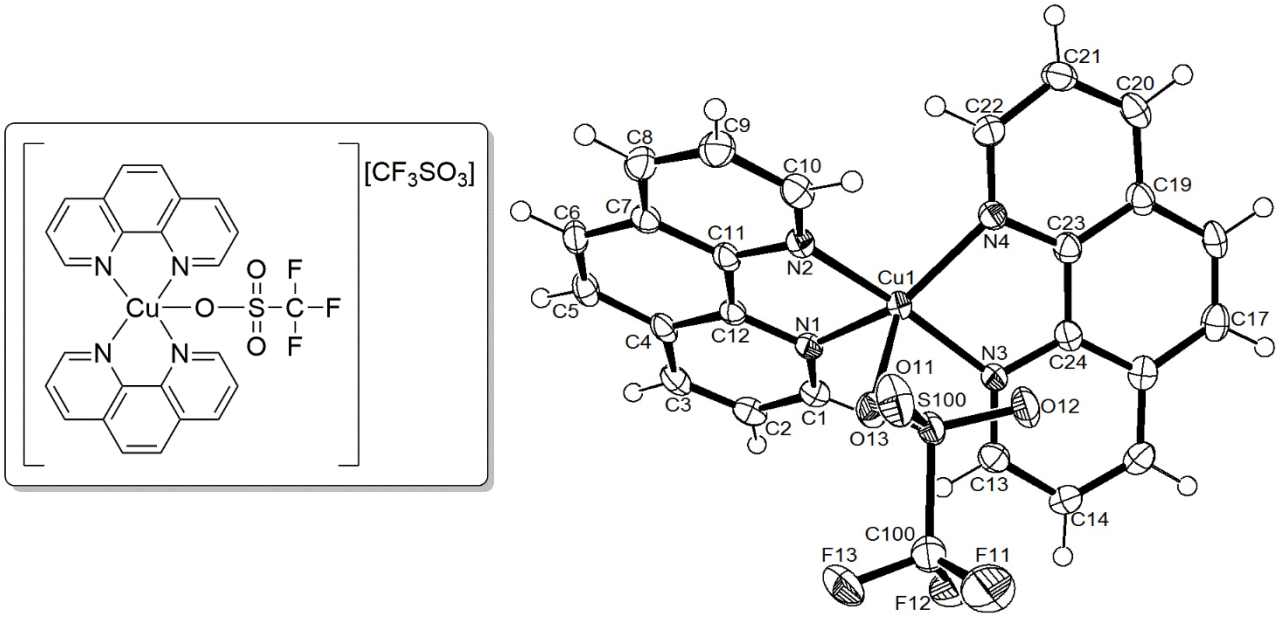

Figure 10-47: ORTEP plot of [Cu(1,10-phenanthroline)$_2$(CF$_3$SO$_3$)][CF$_3$SO$_3$] at 50 % probability level for thermal ellipsoids. (One anion was omitted.)

Table 10-47: Crystal data and structure refinement for [Cu(1,10-phenanthroline)$_2$(CF_3SO_3)][CF_3SO_3].

Identification code	s2822	
Empirical formula	C26 H16 Cu F6 N4 O6 S2	
Formula weight	722.09	
Temperature	130(2) K	
Wavelength	0.71073 Å	
Crystal system	Triclinic	
Space group	P -1	
Unit cell dimensions	a = 10.1410(19) Å	α= 68.376(4)°.
	b = 10.894(2) Å	β= 81.906(4)°.
	c = 13.386(2) Å	γ = 86.255(4)°.
Volume	1361.0(4) $Å^3$	
Z	2	
Density (calculated)	1.762 Mg/m^3	
Absorption coefficient	1.049 mm^{-1}	
F(000)	726	
Crystal size	0.370 x 0.220 x 0.200 mm^3	
Theta range for data collection	1.650 to 27.876°.	
Index ranges	-12<=h<=13, -14<=k<=14, -17<=l<=14	
Reflections collected	10928	
Independent reflections	5756 [R(int) = 0.0332]	
Completeness to theta = 25.242°	90.1 %	
Absorption correction	Semi-empirical from equivalents	
Max. and min. transmission	1.0000 and 0.5917	
Refinement method	Full-matrix least-squares on F^2	
Data / restraints / parameters	5756 / 0 / 406	
Goodness-of-fit on F^2	1.068	
Final R indices [I>2sigma(I)]	R1 = 0.0517, wR2 = 0.1012	
R indices (all data)	R1 = 0.0731, wR2 = 0.1313	
Extinction coefficient	n/a	
Largest diff. peak and hole	0.782 and -1.282 e.$Å^{-3}$	

10.4.27 [Cu$_2$-bis(μ-Cl)(1,10-phenanthroline)$_2$(Cl)$_2$]

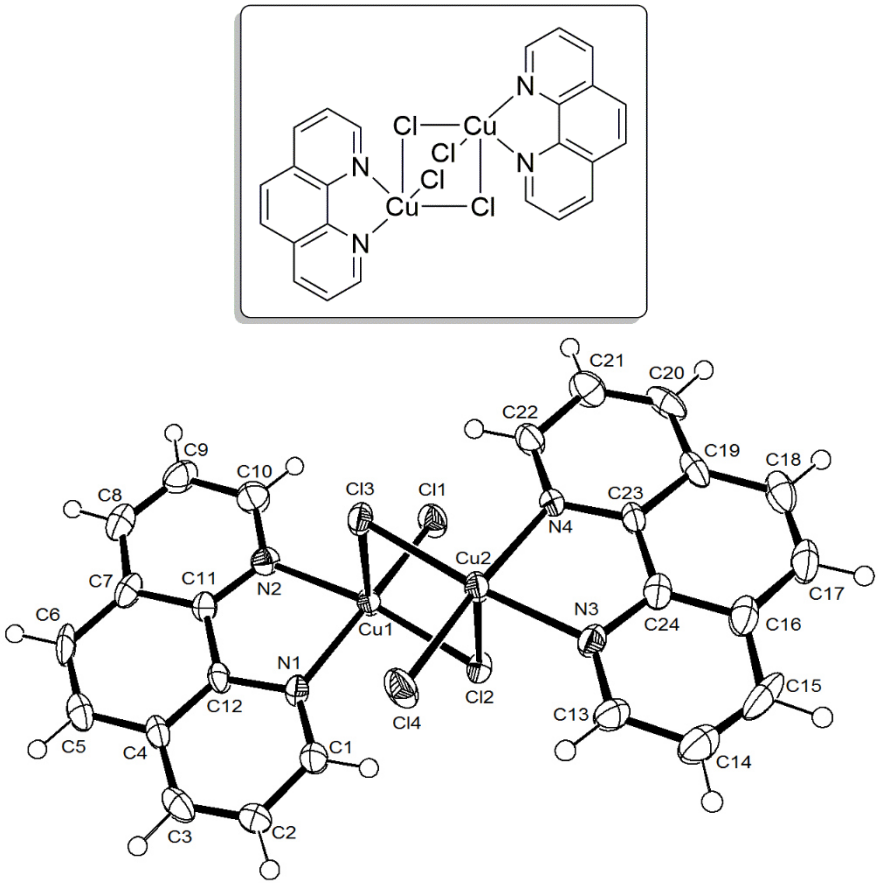

Figure 10-48: ORTEP plot of [Cu2-bis(μ-Cl)(1,10-phenanthroline)2(Cl)2] at 50 % probability level for thermal ellipsoids.

Table 10-48: Crystal data and structure refinement for [Cu_2-bis(μ-Cl)(1,10-phenanthroline)$_2$($Cl)_2$].

Identification code	s2896	
Empirical formula	C24 H16 Cl4 Cu2 N4	
Formula weight	629.29	
Temperature	130(2) K	
Wavelength	0.71073 Å	
Crystal system	Monoclinic	
Space group	C c	
Unit cell dimensions	a = 9.830(2) Å	α= 90°.
	b = 17.853(4) Å	β= 106.617(5)°.
	c = 13.291(3) Å	γ = 90°.
Volume	2235.0(9) $Å^3$	
Z	4	
Density (calculated)	1.870 Mg/m^3	
Absorption coefficient	2.405 mm^{-1}	
F(000)	1256	
Crystal size	0.210 x 0.200 x 0.180 mm^3	
Theta range for data collection	2.282 to 27.875°.	
Index ranges	-12<=h<=12, -23<=k<=23, -17<=l<=17	
Reflections collected	10520	
Independent reflections	4855 [R(int) = 0.0445]	
Completeness to theta = 25.242°	100.0 %	
Absorption correction	Semi-empirical from equivalents	
Max. and min. transmission	1.0000 and 0.7143	
Refinement method	Full-matrix least-squares on F^2	
Data / restraints / parameters	4855 / 2 / 308	
Goodness-of-fit on F^2	1.037	
Final R indices [I>2sigma(I)]	R1 = 0.0413, wR2 = 0.0753	
R indices (all data)	R1 = 0.0513, wR2 = 0.0810	
Absolute structure parameter	0.54(2)	
Extinction coefficient	n/a	
Largest diff. peak and hole	0.574 and -0.379 e.$Å^{-3}$	

10.4.28 [Cu_2-bis(μ-OH)(1,10-phenanthroline)$_2$($Cl)_2$]/[Cu_2-bis(μ-OH)(1,10-phenanthroline)$_2$($H_2O)_2$][$Cl]_2$ ratio 1:1 · 6 H_2O

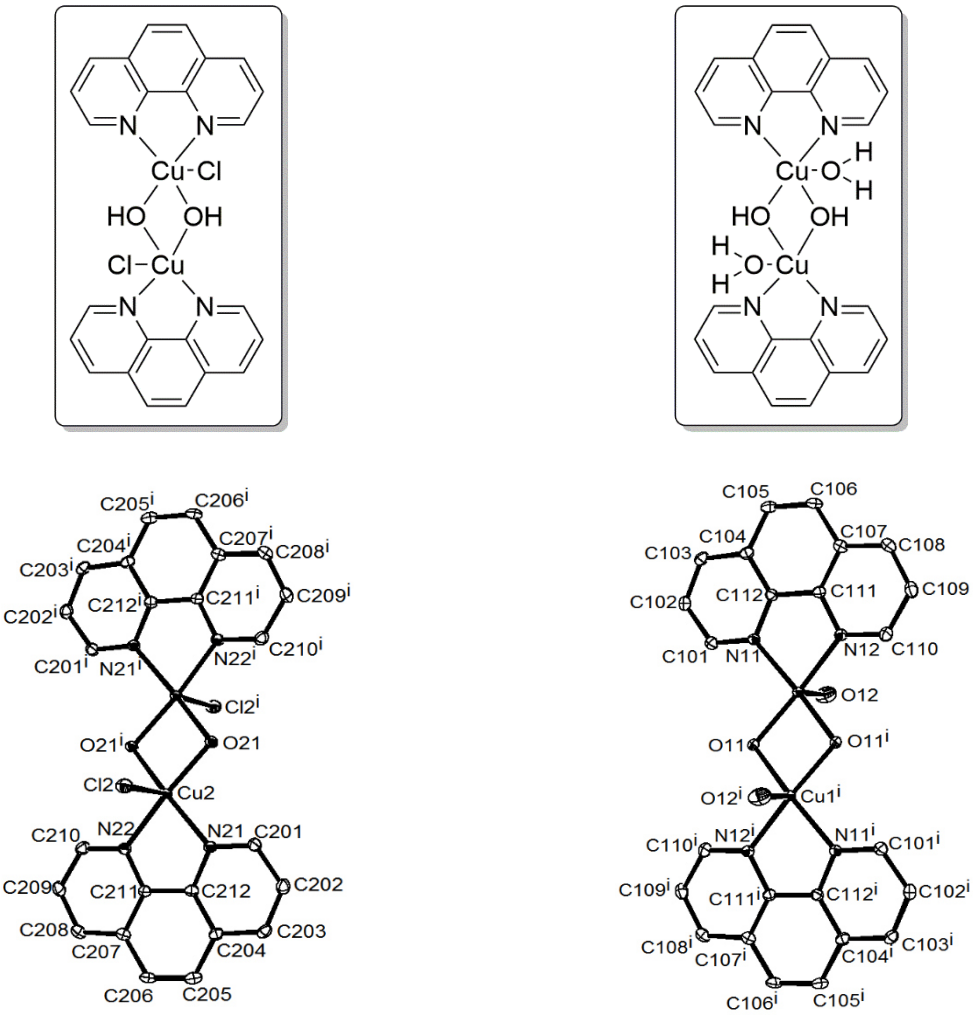

Figure 10-49: ORTEP plot of [Cu_2-bis(μ-OH)(1,10-phenanthroline)$_2$($Cl)_2$]/[Cu_2-bis(μ-OH)(1,10-phenanthroline)$_2$($H_2O)_2$][$Cl]_2$ ratio 1:1 · 6 H_2O at 50 % probability level for thermal ellipsoids. (Hydrogens, water and non-coordinating anions are omitted.)

Table 10-49: Crystal data and structure refinement for [Cu_2-bis(μ-OH)(1,10-phenanthroline)$_2$($Cl)_2$]/[Cu_2-bis(μ-OH)(1,10-phenanthroline)$_2$($H_2O)_2$][$Cl]_2$ ratio 1:1 · 6 H_2O.

Identification code	s2905	
Empirical formula	C48 H52 Cl4 Cu4 N8 O12	
Formula weight	1328.93	
Temperature	130(2) K	
Wavelength	0.71073 Å	
Crystal system	Triclinic	
Space group	P -1	
Unit cell dimensions	a = 8.7782(12) Å	α= 105.454(3)°.
	b = 9.3512(13) Å	β= 99.373(3)°.
	c = 16.427(2) Å	γ = 101.480(3)°.
Volume	1240.0(3) $Å^3$	
Z	1	
Density (calculated)	1.780 Mg/m^3	
Absorption coefficient	1.981 mm^{-1}	
F(000)	676	
Crystal size	0.370 x 0.310 x 0.280 mm^3	
Theta range for data collection	2.302 to 27.877°.	
Index ranges	-11<=h<=11, -11<=k<=12, -21<=l<=21	
Reflections collected	11722	
Independent reflections	5885 [R(int) = 0.0190]	
Completeness to theta = 25.242°	99.8 %	
Absorption correction	Semi-empirical from equivalents	
Max. and min. transmission	1.0000 and 0.8189	
Refinement method	Full-matrix least-squares on F^2	
Data / restraints / parameters	5885 / 11 / 377	
Goodness-of-fit on F^2	1.040	
Final R indices [I>2sigma(I)]	R1 = 0.0329, wR2 = 0.0869	
R indices (all data)	R1 = 0.0419, wR2 = 0.0925	
Extinction coefficient	n/a	
Largest diff. peak and hole	1.069 and -0.533 e.$Å^{-3}$	

10.4.29 $[Cu_2\text{-}(\mu\text{-}OH)(1,10\text{-phenanthroline})_4][BF4]_3$

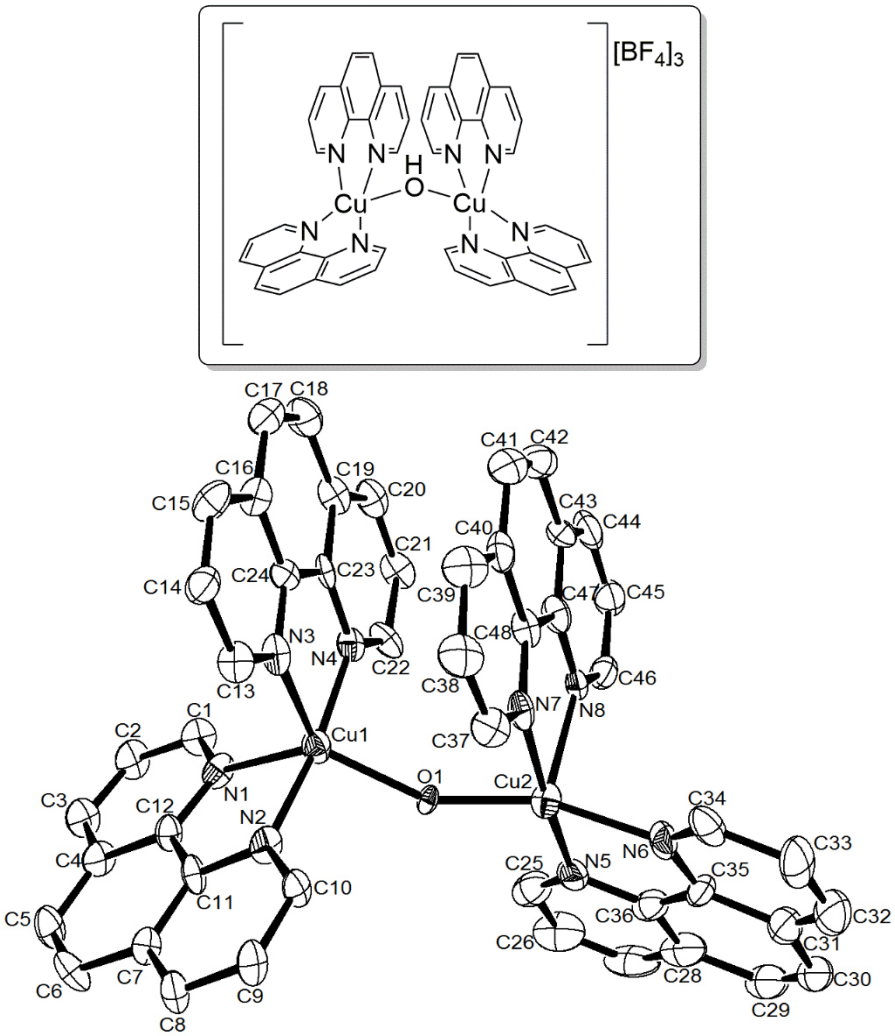

Figure 10-50: ORTEP plot of $[Cu_2\text{-}(\mu\text{-}OH)(1,10\text{-phenanthroline})_4][BF4]_3$ at 50 % probability level for thermal ellipsoids. (Hydrogens, three anions and one MeOH were omitted.)

Remarks:

The hydrogen atom of the bridging hydroxo group could not be resolved.

Table 10-50: Crystal data and structure refinement for $[Cu_2\text{-}(\mu\text{-}OH)(1,10\text{-phenanthroline})_4][BF4]_3$.

Identification code	s2818	
Empirical formula	C49 H37 B3 Cu2 F12 N8 O2	
Formula weight	1157.37	
Temperature	130(2) K	
Wavelength	0.71073 Å	
Crystal system	Monoclinic	
Space group	C c	
Unit cell dimensions	a = 19.574(5) Å	α= 90°.
	b = 15.620(4) Å	β= 96.758(6)°.
	c = 15.203(4) Å	γ = 90°.
Volume	4616(2) $Å^3$	
Z	4	
Density (calculated)	1.665 Mg/m^3	
Absorption coefficient	1.023 mm^{-1}	
F(000)	2336	
Crystal size	0.210 x 0.200 x 0.200 mm^3	
Theta range for data collection	1.672 to 27.878°.	
Index ranges	-25<=h<=23, -20<=k<=20, -19<=l<=19	
Reflections collected	21545	
Independent reflections	10110 [R(int) = 0.1068]	
Completeness to theta = 25.242°	100.0 %	
Absorption correction	Semi-empirical from equivalents	
Max. and min. transmission	1.0000 and 0.5281	
Refinement method	Full-matrix least-squares on F^2	
Data / restraints / parameters	10110 / 2 / 716	
Goodness-of-fit on F^2	1.030	
Final R indices [I>2sigma(I)]	R1 = 0.0785, wR2 = 0.1396	
R indices (all data)	R1 = 0.1334, wR2 = 0.1632	
Absolute structure parameter	0.30(3)	
Extinction coefficient	n/a	
Largest diff. peak and hole	0.520 and -0.725 $e.Å^{-3}$	

10.4.30 [Cu_2-bis(μ-OH)(1,10-phenanthroline)$_2$(H_2O)$_2$]/[Cu(1,10-phenanthroline)$_2$(CO_3)] 1:1 ratio · x H_2O

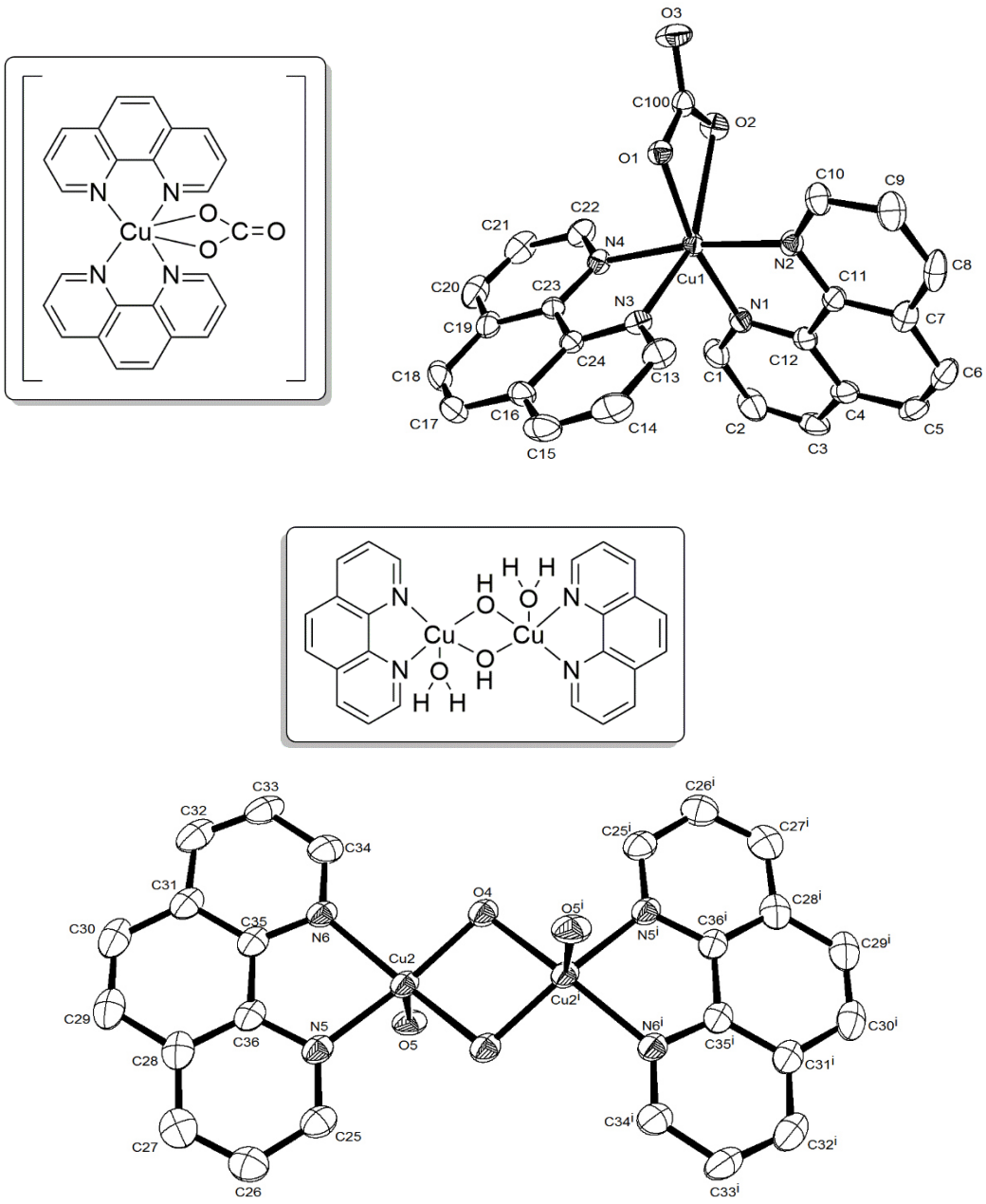

Figure 10-51: ORTEP plot of [Cu_2-bis(μ-OH)(Phen)$_2$(H_2O)$_2$] / [Cu(Phen)$_2$(CO_3)] 1:1 ratio · x H2O at 50 % probability level for thermal ellipsoids. (Hydrogens, anions and water were omitted.)

Remarks:

The headline represents the completed molecules from asymmetric unit. These atoms are indicated by an “i”. The exact number of solvent molecules could not be resolved. At least 22 molecules could be refined.

Table 10-51: Crystal data and structure refinement for [Cu_2-bis(μ-OH)(1,10-phenanthroline)$_2$(H_2O)$_2$] / [Cu(1,10-phenanthroline)$_2$(CO_3)] 1:1 ratio · x H2O.

Identification code	s2889s	
Empirical formula	C37 H49 Cu2 N6 O16	
Formula weight	960.90	
Temperature	130(2) K	
Wavelength	0.71073 Å	
Crystal system	Triclinic	
Space group	P -1	
Unit cell dimensions	a = 10.1221(10) Å	α= 74.900(2)°.
	b = 12.3025(12) Å	β= 80.711(2)°.
	c = 19.1117(18) Å	γ = 71.637(2)°.
Volume	2172.6(4) $Å^3$	
Z	2	
Density (calculated)	1.469 Mg/m^3	
Absorption coefficient	1.054 mm^{-1}	
F(000)	998	
Crystal size	0.470 x 0.250 x 0.200 mm^3	
Theta range for data collection	1.108 to 27.877°.	
Index ranges	-13<=h<=13, -16<=k<=15, -25<=l<=25	
Reflections collected	20775	
Independent reflections	10316 [R(int) = 0.0363]	
Completeness to theta = 25.242°	100.0 %	
Absorption correction	Semi-empirical from equivalents	
Max. and min. transmission	1.0000 and 0.6422	
Refinement method	Full-matrix least-squares on F^2	
Data / restraints / parameters	10316 / 35 / 647	
Goodness-of-fit on F^2	1.041	
Final R indices [I>2sigma(I)]	R1 = 0.0534, wR2 = 0.1253	
R indices (all data)	R1 = 0.0734, wR2 = 0.1369	
Extinction coefficient	n/a	
Largest diff. peak and hole	0.851 and -0.445 e.$Å^{-3}$	

10.4.31 [Cu(2,9-dimethyl-1,10-phenanthroline)$_2$(NO$_3$)][NO$_3$] · 6 H$_2$O

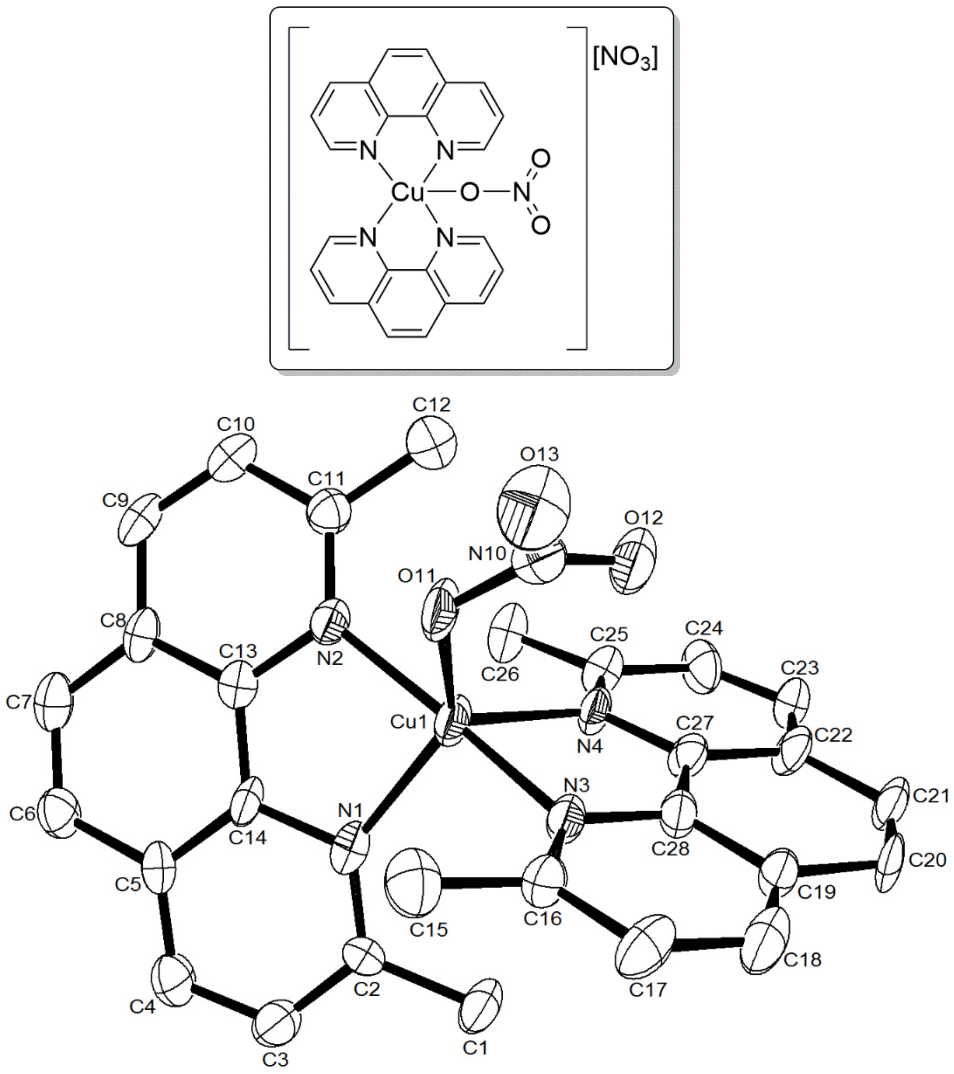

Figure 10-52: ORTEP plot of [Cu(2,9-dimethyl-1,10-phenanthroline)$_2$(NO$_3$)][NO$_3$] · 6 H$_2$O at 50 % probability level for thermal ellipsoids. (Hydrogens, six water molecules and one anion were omitted.)

Remarks:

Not every hydrogen atom of the incorporated water molecules could be determined.

Table 10-52: Crystal data and structure refinement for [Cu(2,9-dimethyl-1,10-phenanthroline)$_2$(NO$_3$)][NO$_3$] · 6 H$_2$O.

Identification code	s2830	
Empirical formula	C28 H36 Cu N6 O12	
Formula weight	712.17	
Temperature	130(2) K	
Wavelength	0.71073 Å	
Crystal system	Triclinic	
Space group	P -1	
Unit cell dimensions	a = 8.042(5) Å	α= 103.138(11)°.
	b = 14.243(8) Å	β= 93.093(12)°.
	c = 14.434(8) Å	γ = 93.567(10)°.
Volume	1603.0(16) Å^3	
Z	2	
Density (calculated)	1.475 Mg/m^3	
Absorption coefficient	0.753 mm^{-1}	
F(000)	742	
Crystal size	0.320 x 0.200 x 0.150 mm^3	
Theta range for data collection	1.472 to 27.876°.	
Index ranges	-10<=h<=10, -18<=k<=18, -18<=l<=16	
Reflections collected	14692	
Independent reflections	7598 [R(int) = 0.1786]	
Completeness to theta = 25.242°	99.9 %	
Absorption correction	Semi-empirical from equivalents	
Max. and min. transmission	1.0000 and 0.1352	
Refinement method	Full-matrix least-squares on F^2	
Data / restraints / parameters	7598 / 10 / 456	
Goodness-of-fit on F^2	0.918	
Final R indices [I>2sigma(I)]	R1 = 0.0916, wR2 = 0.1780	
R indices (all data)	R1 = 0.2364, wR2 = 0.2461	
Extinction coefficient	n/a	
Largest diff. peak and hole	0.753 and -1.020 e.Å^{-3}	

10.4.32 [Cu$_2$-bis(μ^2-hydroxo)-bis(DAPy-Ts)][BF$_4$]$_2$

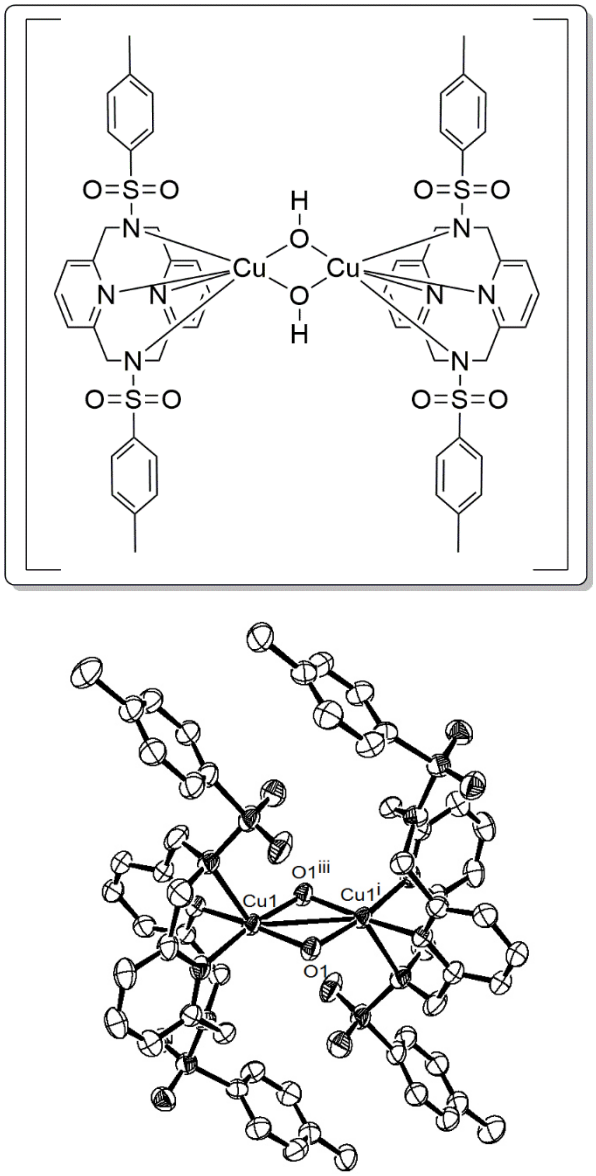

Figure 10-53: [Cu$_2$-bis(μ^2-hydroxo)-bis(DAPy-Ts)][BF$_4$]$_2$ at 50 % probability level for thermal ellipsoids. (Hydrogens and both tetrafluoroborate anions were omitted for clarity.).

Remarks:

The methyl hydrogens groups of the tosyl moieties are disordered over two locations.

Table 10-53: Crystal data and structure refinement for [Cu_2-bis(μ²-hydroxo)-bis(DAPy-Ts)][BF_4]$_2$.

Identification code	h2552	
Empirical formula	C58.50 H78 B2 Cl Cu2 F8 N8 O10.50 S4	
Formula weight	1525.68	
Temperature	130(2) K	
Wavelength	0.71073 Å	
Crystal system	Monoclinic	
Space group	C2/m	
Unit cell dimensions	a = 31.294(7) Å	α= 90°.
	b = 9.2648(18) Å	β= 98.296(7)°.
	c = 13.352(3) Å	γ = 90°.
Volume	3830.8(14) Å^3	
Z	2	
Density (calculated)	1.323 Mg/m^3	
Absorption coefficient	0.773 mm^{-1}	
F(000)	1580	
Crystal size	0.42 x 0.22 x 0.09 mm^3	
Theta range for data collection	1.32 to 27.88°.	
Index ranges	-40<=h<=41, -12<=k<=12, -17<=l<=17	
Reflections collected	18162	
Independent reflections	4854 [R(int) = 0.0304]	
Completeness to theta = 27.88°	99.9 %	
Absorption correction	Semi-empirical from equivalents	
Max. and min. transmission	0.9337 and 0.7372	
Refinement method	Full-matrix least-squares on F^2	
Data / restraints / parameters	4854 / 1 / 229	
Goodness-of-fit on F^2	1.068	
Final R indices [I>2sigma(I)]	R1 = 0.0436, wR2 = 0.1269	
R indices (all data)	R1 = 0.0502, wR2 = 0.1310	
Largest diff. peak and hole	0.737 and -0.296 e.Å^{-3}	

10.4.33 [Cu(DAPy-NH)Cl_2]

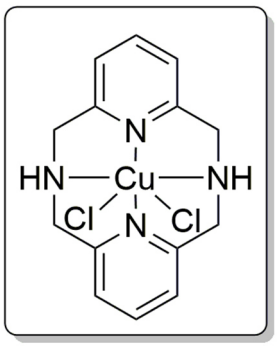

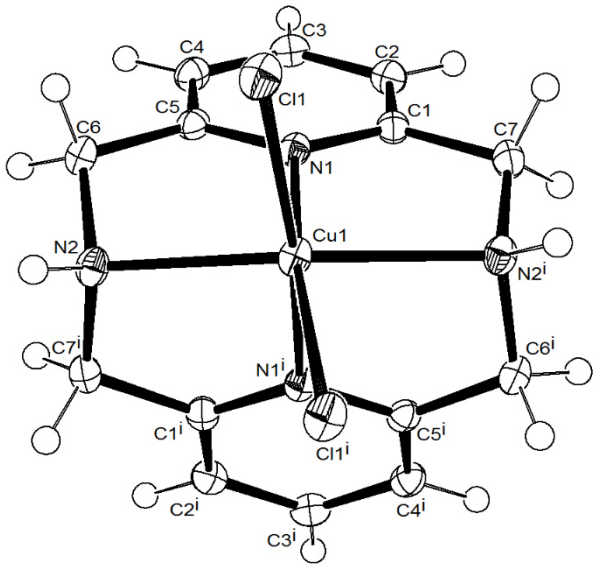

Figure 10-54: [Cu(DAPY-NH)Cl_2] at 50 % probability level for thermal ellipsoids. (One DCM molecule was omitted for clarity.)

Table 10-54: Crystal data and structure refinement for [Cu(DAPy-NH)Cl_2].

Identification code	h2580	
Empirical formula	C15 H18 Cl4 Cu N4	
Formula weight	459.67	
Temperature	130(2) K	
Wavelength	0.71073 Å	
Crystal system	Monoclinic	
Space group	C2/c	
Unit cell dimensions	a = 14.0668(14) Å	α= 90°.
	b = 14.6300(14) Å	β= 103.962(3)°.
	c = 8.8288(9) Å	γ = 90°.
Volume	1763.3(3) $Å^3$	
Z	4	
Density (calculated)	1.732 Mg/m^3	
Absorption coefficient	1.850 mm^{-1}	
F(000)	932	
Crystal size	0.48 x 0.20 x 0.19 mm^3	
Theta range for data collection	2.04 to 27.88°.	
Index ranges	-15<=h<=18, -19<=k<=19, -11<=l<=11	
Reflections collected	8101	
Independent reflections	2103 [R(int) = 0.0305]	
Completeness to theta = 27.88°	99.8 %	
Absorption correction	Semi-empirical from equivalents	
Max. and min. transmission	0.7201 and 0.4705	
Refinement method	Full-matrix least-squares on F^2	
Data / restraints / parameters	2103 / 0 / 110	
Goodness-of-fit on F^2	1.045	
Final R indices [I>2sigma(I)]	R1 = 0.0260, wR2 = 0.0666	
R indices (all data)	R1 = 0.0274, wR2 = 0.0675	
Largest diff. peak and hole	0.437 and -0.297 $e.Å^{-3}$	